

Constraining the Contribution of Isostasy and Dynamic Uplift at Venusian Volcanic Rises and Tessera Terrain: Implications for Rifting and Volcanism

Elyse Schinella



*Figure i. Venus's surface imaged using Magellan Synthetic Aperture Radar
(Credit: NASA/JPL)*

**A thesis submitted for the fulfillment of the degree:
Doctor of Philosophy
February, 2014**

**Department of Earth and Planetary Sciences,
Macquarie University, Sydney, Australia**



Contents

Abstract	9
Declaration and Certification	11
Preamble	12
Acknowledgments	14
Glossary of Scientific Terms and Units	16
1. Introduction	28
1.1 Rationale	28
1.2 Overview	29
1.3 Previous Studies	31
1.4 Study Areas	33
1.5 Aims	36
1.6 Thesis Structure	37
2. Global Planetary Background	40
2.1 Introduction	40
2.2 Geological Structures	43
2.2.1 Volcanic Rises	43
2.2.2 Volcanoes	43
2.2.3 Coronae	47
2.2.4 Crustal Plateaus and Tessera	50
2.2.5 Mountain Belts	51
2.2.6 Chamata (rifts)	53
2.2.7 Plains	53

2.2.8 Craters	58
2.3 The Venusian Interior	58
2.3.1 The Mantle	60
2.3.1.1 Mantle Composition	60
2.3.1.2 Thermal State and Convective Regime	63
2.3.1.3 Mantle Parameters	66
2.3.1.4 Mantle Plumes	70
2.3.1.5 Surface Manifestations of Mantle Plumes	71
2.3.2 The Thermal Lithosphere	74
2.3.2.1 Crustal Composition	74
2.3.2.2 Crustal Thickness	75
2.3.2.3 Lithospheric Rheology	77
2.3.2.4 Lithospheric Thickness	79
2.3.3 The Elastic Lithosphere	82
3. Methodology	86
3.1 Introduction	86
3.2 Geophysical Observables	87
3.3 Lithospheric Modelling Using LitMod3D	92
3.3.1 Introduction to LitMod3D	92
3.3.2 Thermal Field	93
3.3.3 Density and Pressure	95
3.3.4 Elevation	97
3.3.5 Regional Isostasy (Flexure)	98
3.3.6 Gravity and Geoid	98
3.3.7 Constraining the Lithospheric Structure Using GEO3Dmod	99

3.4 Dynamic Modelling Using CitcomS	100
3.4.1 Introduction and Fundamental Equations	100
3.4.2 Mesh Geometry	102
4. Constraining the Lithospheric Structure at Atla Regio, Venus:	
 Implications for Rifting and Melt Generation Rates	105
4.1 Introduction	106
4.2 Background	108
4.2.1 Thermal Lithosphere Thickness	108
4.2.2 Crustal Thickness	109
4.2.3 Elastic Lithospheric Thickness and Surface Heat Flow	110
4.3 Methodology	111
4.3.1 Introduction	111
4.3.2 Geophysical Observables	111
4.3.3 Lithospheric Modelling Using LitMod3D	114
4.3.4 Melt Generation Rates	121
4.3.5 Half-Space Cooling	126
4.3.6 Crustal Production Rates	127
4.4 Results	127
4.4.1 Constraining a Suitable Reference Column	127
4.4.2 Residuals	131
4.4.3 Profiles of Lithospheric Structure	131
4.4.4 Crustal and Lithospheric Thickness Maps	139
4.4.5 Thermal Structure of the Lithosphere	141
4.4.6 Compensation Mechanisms	141
4.5 Discussion	144

4.5.1 Constraining the Lithospheric Structure at Atla Regio	144
4.5.2 The Contribution of Flexure and Dynamic Uplift	147
4.5.3 Melt Generation Volumes and Rates	148
4.5.4 Half-Space Cooling Model	150
4.5.5 Crustal Production Rates	153
4.6 Conclusions	154
4.7 References	155
5. The Lithospheric Structure and Compensation of Beta Regio, Venus	166
5.1 Introduction	167
5.2 Background	170
5.2.1 Lithospheric Thickness	170
5.2.2 Crustal Thickness	171
5.2.3 Dynamic Compensation	172
5.2.4 Flexural Compensation	174
5.2.5 The East African Rift: A Terrestrial Analogy to Beta Regio	175
5.3 Methodology	176
5.3.1 Introduction	176
5.3.2 Geophysical Observables	176
5.3.3 Lithospheric Modelling	179
5.4 Results	185
5.4.1 Residuals	185
5.4.2 Lithospheric Profiles	188
5.4.3 Crustal and Lithospheric Thickness Maps	194
5.4.4 Flexural and Dynamic Compensation	196
5.5 Discussion	196

<i>Contents</i>	5
5.5.1 Lithospheric Structure	196
5.5.2 Compensation Mechanisms	201
5.5.3 Comparison with Atla Regio	203
5.6 Conclusions	205
5.7 References	206
 6. Lithospheric Structure and Compensation Mechanisms	
at Fortuna Tessera, Venus	215
6.1 Introduction	216
6.2 Background	219
6.2.1 Description	219
6.2.2 Crustal Thickness	223
6.2.3 Lithospheric Mantle Thickness	225
6.3 Methodology	226
6.3.1 Geophysical Observables	226
6.3.2 Lithospheric Modelling	229
6.4 Results	235
6.4.1 Residuals	235
6.4.2 Lithospheric Profiles	235
6.4.3 Crustal and Lithospheric Thickness Maps	239
6.4.4 Compensation Mechanisms	241
6.5 Discussion	243
6.5.1 Lithospheric Structure	243
6.5.2 Compensation Mechanisms	248
6.6 Conclusions	249
6.7 References	250

7. Constraining the Internal Dynamics of Venus and its Contribution to Topography at Atla and Beta Regio	258
7.1 Introduction	258
7.2 Background	261
7.2.1 Numerical Modelling	261
7.2.2 Localised Admittance and The Dynamic Contribution	264
7.3 Methodology	266
7.3.1 Introduction	266
7.3.2 Governing Equations	266
7.3.3 Physical Properties	268
7.3.4 Model Setup	270
7.3.5 Dynamic Topography and Geoid	271
7.3.6 Observed Topography and Geoid	273
7.3.7 Admittance and Correlation	274
7.4 Results	277
7.4.1 Rayleigh Number	277
7.4.2 Pre-exponential Factor	284
7.4.3 Internal Heating	284
7.4.4 Activation Energy	285
7.5 Discussion	291
7.5.1 CitcomS Modelling	291
7.5.2 Localised Admittance and Correlation	295
7.5.3 Implications of Partial Melting	303
7.6 Conclusions	307
7.7 References	308

8. Discussion	318
8.1 Lithospheric Modelling Discussion	318
8.1.1 Technique and Assumptions	318
8.1.2 Volcanism	320
8.1.3 Rifting	322
8.1.4 Elastic Lithospheric Thickness	324
8.1.5 Surface Heat Flow	325
8.2 Mantle Convection Modelling Discussion	328
8.2.1 Technique and Assumptions	328
8.2.2 Mantle Rheology	330
8.2.3 Mantle Convection	332
8.2.4 Lithosphere Thickness	332
8.3 Comparison between Lithospheric and Dynamic Modelling	333
8.3.1 Dynamic Compensation at Atla and Beta Regio	333
8.3.2 Pressure-Release Melting and Melt Generation Rates	335
8.4 Implications of Lithospheric and Dynamic Modelling	337
 9. Conclusions	 339
9.1 Introduction	339
9.2 Summary of Findings	340
9.2.1 Thermal Structure and Internal Dynamics	340
9.2.2 Compensation Mechanisms	341
9.3 Implications	343
9.4 Limitations	344
9.5 Future Work	345

10. References	347
-----------------------	------------

Appendix	383
-----------------	------------

A.1 CitcomS Input File	383
------------------------	-----

A.2 Processes Forming Volcanic Topography at Atla Regio, Venus	388
--	-----

A.3 Constraining Weathering Processes on Venus from Particle Size Distributions and Magellan Synthetic Aperture Radar (SAR)	412
--	-----

Abstract

Venus and Earth share a similar size, mass, density and volume, however surface conditions on each planet are very different. Venus has a surface temperature of $\sim 472^{\circ}\text{C}$, surface pressure over 90 bar, lacks surface water, and plate tectonics. These conditions make obtaining information about the interior difficult. Furthermore, a lack of integrated cross disciplinary studies of Venus's internal dynamics and topographic support mechanisms have resulted in highly unconstrained models of lithospheric structure.

This study aims to provide the first complete analysis of the processes compensating the observed topography at Atla Regio, Beta Regio, and Fortuna Tessera by modelling their lithospheric structure and internal dynamics. Atla and Beta Regio are rift-dominated volcanic rises and Fortuna Tessera is a crustal plateau. Atla Regio exhibits evidence for current or recent geological activity, whereas Beta Regio has the highest Geoid-to-Topography Ratio (GTRs), size, and volume of all the volcanic rises. In contrast, Fortuna Tessera comprises one of the oldest terrain units on Venus, but may provide long-wavelength support to the adjacent mountain belt, Maxwell Montes.

Both short and long wavelength processes can contribute to the support of the topography observed at each area. Airy isostasy and regional isostasy (flexure) provide short wavelength support, while thermal isostasy and dynamic uplift provide long wavelength support. By modelling the lithospheric structure below each area, we constrained the contribution of Airy isostasy, thermal isostasy, regional isostasy and dynamic uplift in shaping the topography observed within each area.

Lithospheric modelling found the thickest crust ($\sim 65\text{-}80$ km) is located at Fortuna Tessera, followed by the volcanoes ($\sim 30\text{-}75$ km) at Atla and Beta Regio. The crust below the central rift trough, Ganis Chasma, in Atla Regio is < 1 km in thickness. This compares to the crust below Devana Chasma in Beta Regio, which has a thickness of $\sim 15\text{-}25$ km. The thermal

lithosphere is thin below the rises (~50-100 km), but is thicker (~150-340 km) below Fortuna Tessera. The topography observed at each modelled area is primarily supported by a combination of Airy and thermal isostasy. Additional compensation mechanisms, however, are required within these areas such as regional isostasy and dynamic uplift. The dynamic support (at spherical harmonic degrees $< \sim 40$) required at each volcanic rise is further supported by a best-fit global convection model with an effective Rayleigh number of 2.5×10^7 , a non-dimensional internal heating of 40, a non-dimensional activation energy of 10, and a lower mantle three times more viscous than the upper mantle.

These findings have important implications for the current state of localised rifting and volcanism on Venus. At Atla Regio, the thin thermal lithosphere (~50-100 km), thin crust (< 1 km) along the central rift trough of Ganis Chasma, dynamic compensation (up to 1.5 km), and high surface heat flows ($\sim 26 \text{ mW m}^{-2}$) may facilitate ultra-slow rifting at a rate of $\sim 5\text{-}12 \text{ mm yr}^{-1}$ along Ganis Chasma. This rifting and the associated lithospheric thinning at Ganis Chasma, as well as the upwelling mantle plume below Atla Regio, results in pressure-release melting, which may be efficiently extracted to form the crust along this rift at a rate of $0.78 \text{ km}^3 \text{ yr}^{-1}$. In comparison, the thick crust (~15-25 km) below the central rift trough of Devana Chasma in Beta Regio suggests rifting may not be active. Furthermore, the localised dynamic compensation ($\sim 0.3 \text{ km}$) found for this area implies Beta Regio's high GTR, size, and swell volume are most likely caused from long wavelength thermal thinning of the lithosphere rather than a broad upwelling mantle plume presently located below the rise. This study demonstrates how rifting and tectonic deformation may exist on a planet without plate tectonics and has implications for studies of exoplanets and Earth's early evolution.

Declaration

This thesis is based on work carried out in the Department of Earth and Planetary Sciences at Macquarie University between February 2010 to February 2014. I hereby declare that all the models and interpretations are my own work, except for data and information published by others that has been appropriately acknowledged.

Certification

I certify that this thesis has not been submitted for a higher degree to any other institution. I further certify that this thesis is an original piece of research and any assistance in the preparation has also been appropriately acknowledged.

Elyse Schinella

February, 2014.

Preamble

This thesis is presented as a "Thesis by Publication", with Chapters 4 to 7 being papers, prepared for publication in peer-review journals. Each chapter follows a formatting and reference style similar to the *Journal of Geophysical Research*.

Attempts have been made to limit repetition between each chapter, however, Chapters 4 to 6 do represent self-contained, stand-alone papers that share similar methods and reference columns. Since the reference column is pivotal to the results presented for each area, the chosen reference column was explained in detail within each chapter.

I am the primary author on each chapter, and for Chapters 4 to 6, I was responsible for 95 % of the lithospheric modelling, in conjunction with a 5 % contribution for script development by J.C. Afonso and J. Fulla. I was also responsible for 95 % of the preparation of each manuscript and the images within, with a 5 % contribution fulfilled by co-authors. For Chapter 7, I was responsible for 90 % of the numerical modelling, with a 10 % contribution from S. Zhang and C. O'Neill for script development. I was also responsible for 95 % of the manuscript preparation and the images within, with a 5 % contribution fulfilled by C. O'Neill.

For all the chapters presented, figures and tables have been included within the text and labelled sequentially with respect to the chapter. For example, the figures in Chapter 1 are labelled as 1.1, 1.2, 1.3 etc. Figure and table numbers are in bold and the captions have a font size of 11 to differentiate these from the main text. Pagination begins after the title page and continues sequentially throughout the thesis.

The appendix also contains two peer-reviewed conference papers titled *Processes Forming Volcanic Topography at Atla Regio, Venus* and *Constraining Weathering Processes on Venus from Particle Size Distributions and Magellan Synthetic Aperture Radar (SAR)*. These were published in the proceedings of the 10th and 11th Australian Space Science Conference, respectively.

Acknowledgments

First and foremost I would like to thank my principal supervisor Craig O'Neill for the opportunity to study such an interesting and intellectually stimulating project. I am extremely grateful for the knowledge and skills I have learned throughout this project, as well as the constant support and guidance I received. I appreciate all the hard work and dedication taken by Craig to provide constructive feedback, revisions, and helpful suggestions for both thesis and scripts. I also appreciate all the time devoted to meetings and answering my endless questions.

Thank you to my co-supervisor Juan Carlos for all those long discussions on every aspect of LitMod3D and for being patient with my modifications, models, as well as the barrage of questions during every meeting. I also appreciate the time taken by Juan Carlos in providing constructive feedback and suggestions for this thesis.

I would also like to acknowledge Mark Lackie for his guidance and willingness to always answer questions through out my undergraduate years and for stopping by during my postgraduate studies for a chat.

I appreciate the time spent by the following people who answered questions and helped to get scripts working correctly:

- Javier Fulla, for the flexural calculation in LitMod3D, as well as the GUI.
- Siqi Zhang, for help with processing the dynamic topography obtained by CitcomS, and modifications to the sources, and tips on how to use Paraview.
- Thorsten Becker, for providing a the dynamic topography scaling relationship.
- Mark Wiczorek, for answering questions regarding SHTOOLS and providing the spherical harmonic model of Venus' topography.

I would like to acknowledge the Australian Postgraduate Award that I received to

undertake this research.

This thesis has solely utilised freely available software and data. Without this I would not have been able to access, modify, test, and develop my skills in programming. The data used in this study was obtained from the Planetary Data System Geosciences Node. The software used in this study includes:

- SHTOOLS
- Generic Mapping Tools
- Grace
- LitMod3D
- Tisc
- CitcomS
- Paraview

Thanks to all my colleges in the geophysics lab who provided support and encouragement including Cara, Rajat, Sam, Rusty, and Cameron, I wish you the best of luck in your future endeavors.

To my friends and especially my family Hildergard, Elizabeth, Rosina, Derek, Felicia, and Egon for providing emotional and financial support, encouragement, and for listening to me go on about Venus. I would like also like to make special mention of my parents - Sonya and Patrick- a daughter could not ask for more. You have always supported me in my pursuits, provided encouragement when I thought I could no longer go on, and never once doubted my abilities to excel. To my study "buddies" in feather and fur - Oreo, Buddy, Billy and Petey - thanks for your unconditional love, affection and companionship.

Glossary of Scientific Terms and Units*

A`a lava flow: a lava flow characterised by a rough and jagged surface.

Activation energy: the minimum amount of energy required to initiate a chemical reaction.

Activation volume: the difference between the volume of the reactants and the volume of the activated complex.

Adiabatic sub-lithospheric mantle: a layer of the mantle below the lithosphere dominated by adiabatic mantle convection.

Admittance: the variation of geoid and topography as a function of position and wavelength.

Airy isostasy: the state of equilibrium between the rigid lithosphere and a denser underlying layer.

Amoeboid: a smooth and featureless lowland area that has sharp "finger-like" boundaries.

Andesite: an extrusive igneous rock that has a composition between mafic and felsic.

Apparent Depth of Compensation (ADC): the depth where a lithospheric column reaches isostatic equilibrium.

Asthenosphere: a viscous, weak, and ductile layer of Earth's upper mantle.

Basalt: an extrusive iron-rich rock.

Bouguer correction: an equation that estimates the gravitational attraction associated with a mass of rock located between the measuring station and sea level.

Bouguer gravity: the anomaly found after removing the Bouguer correction from the free-air gravity.

Caldera: a cauldron-shaped depression formed after the collapse of a volcanic edifice.

Chasma (chasmata): a steep sided valley where the crust and lithosphere are undergoing extension. Also known as a rift.

Clapeyron curve: a line defining the transition between two-phases.

Clapeyron slope: the gradient of the Clapeyron curve.

Coherence: see correlation.

Compensation: the elevation of a geological landform is supported at depth by the lithospheric structure, upwarping and downwarping of the elastic lithosphere, and dynamic uplift from a mantle plume.

Complex ridged terrain: see tessera.

Convection: heat is transferred through the movement of fluids from hot regions to cold regions.

Episodic: characterised by periods of highly active convection and geological activity interspersed with periods of quiescence.

Sluggish-lid: characterised by disseminated deformation of a weak and viscous lid above a convective interior

Stagnant-lid: characterised by convection underneath a thick and motionless uppermost lid.

Core Mantle Boundary (CMB): the transition between the mantle and outer core.

Corona: an elevated ring-shaped structure.

Correlation: how well the geoid height anomaly shows similarities to elevation anomalies.

Crust: the outermost rigid layer of a planet.

Crustal plateau: an elevated region of flat terrain surrounded by steep sides.

Decompression melting: the melting caused from a decrease in pressure associated with lithospheric thinning or the impingement of a mantle plume on the base of the lithosphere.

Delamination: the process where the lithospheric mantle detaches from the crust and sinks into the interior.

Diabase: an intrusive igneous rock with with fine to medium sized grains.

Downwelling: the sinking of cold and dense material into the interior.

Dynamic uplift: a domal topographic high associated with the impingement of a mantle plume at the base of the lithosphere.

Eclogite: a rock formed from basalt under high temperatures and pressures.

Elastic lithosphere: a layer of the lithosphere that can endure elastic stresses over time.

Endothermic phase transition: an area where heat is absorbed as the lower density spinel transforms into denser perovskite. On Venus this transition may occur at a depth of 690 km.

Exothermic phase transition: heat is released as the lower density olivine transforms into the denser spinel. On Venus this transition may occur at a depth of 440 km.

Fast Fourier Transform (FFT): a mathematical equation that converts a time domain signal into a frequency domain signal or visa versa.

Fault: a fracture surface within the crust that results in displacement of the crustal blocks located on either side of the fault.

Fault zone: the near surface expression of a fault that can cover large areas (widths of > 1 km).

Felsic: an igneous rock with high concentrations ($\sim > 65\%$) of silicic minerals.

Finite-difference: a method where a model domain is first divided (discretised) into an equidimensional grid. At each grid point, the differential operator is estimated by substituting the derivatives in the finite-difference equation with differential quotients.

Finite-element: a method where a model domain is first divided (discretised) into a finite number of elements and solutions to differential equations, under the assumed boundary conditions, are estimated.

Flexure: the process where the elastic lithosphere bends due to loading. Downwarping of the elastic lithosphere occurs below the load, while upwarping occurs around the loading.

Fragmentation stage: the stage where reduced pressures allow the growth of bubbles (up to ~75 % of the total volume of magma) in ascending magma.

Free-air correction: a method that corrects for the change in gravitational attraction associated with increasing elevation.

Free-air gravity: the gravity anomaly after the gravity measurements have been corrected for elevation and latitude.

Gabbro: an intrusive igneous rock similar in composition to basalt.

Geoid: an equipotential surface that corresponds to average sea level.

Geoid to Topography Ratio (GTR): the change in geoid height with respect to the change in elevation as function of position.

Gravity (see Free-air gravity)

Half-space cooling model: a one-dimensional model of a semi-infinite half-space that experiences time-dependent heat conduction.

Highland: an extensive and elevated area on Venus's surface bounded by steep sides.

Hotspot: the surface manifestation of a mantle plume.

Igneous: a rock formed from the cooling of lava or magma on a planet's surface (extrusive) or within the crust (intrusive).

Internal heating: the heat from the interior of a planet caused from gravitational contraction during planetary accretion or the radioactive decay of elements.

Isostatic stagnant lid (ISL): the lithosphere is immobile and within isostatic equilibrium above a convective interior.

Lithosphere: the solid and rigid outer shell of a planet comprising the crust and lithospheric mantle.

Lithospheric mantle: the upper-most layer of the mantle or the lower-most layer of the thermal lithosphere below the crust.

Liquidus: the minimum temperature at which a material is entirely a liquid.

Mafic: a rock with high concentrations of magnesium and iron (44-55% silica content).

Magmatic underplating: the thickening of the lower crust as a result of ascending magma becoming trapped in the crust or at the moho.

Mantle diapir: a buoyant, low-density mantle upwelling possibly from a larger mantle plume that intrudes into the overlying rock. Mantle diapirs are usually narrower (< 300 km) than mantle plumes.

Mantle plume (or upwelling): an upwelling of hot material from the interior of a planet that contributes to volcanism.

Mean Planetary Radius (MPR): average distance from the centre of Venus to the surface.

Mechanical lithosphere: a part of the lithosphere that is strong enough to resist localised convection.

Melt generation rate: the rate of melt produced due to decompression within a plume or lithospheric thinning.

Metamorphic: the alteration of rock by high pressures and temperatures.

Metasomatism: the alteration of a rock's chemical composition by fluids.

Mid Ocean Ridge (MOR): a ridge-trough-ridge structure located on the ocean floor of the Earth where new oceanic crust is produced, causing the crust on either side to move apart.

E-MORB (Enriched Mid Ocean Ridge Basalts): rocks produced from melts that have been enriched in incompatible elements by the interaction of upwelling mantle associated with a hotspot.

N-MORB (normal mid-ocean ridge basaltic): produced by the partial melting of a depleted mantle.

Moho: the boundary between the crust and mantle.

Neutral buoyancy zone: a sub-surface area where the ascent of magma has stalled, resulting in a total density that is the same as the surrounding rock.

Newtonian rheology: stress and strain have a linear relationship, resulting in diffusion creep.

Node: the location where an unknown value is estimated.

Non-Newtonian rheology: stress and strain have a non-linear relationship that results in dislocation creep.

Nova: a starburst shaped feature comprising radial fractures, surrounded by lava flows extending outward from topographically high centres and small summit calderas

Nucleation stage: when an ascending volatile-rich magma reaches this stage, bubbles within the magma will form.

Overturn event (or resurfacing): occurs within an episodic convection regime whereby the lid becomes gravitationally unstable due to warmer internal temperatures causing widespread tectonism and volcanism.

Pahoehoe lava: a lava flow characterised by a smooth and ropey surface.

Partial melting: a process whereby only a fraction of the solid rock is melted.

Peridotite: an intrusive coarse grained rock comprising large quantities ($\sim > 65\%$) of mafic minerals.

Pervoskite: a mineral species comprising calcium titanium oxide.

Plains: broad, lowland areas that generally appear smooth (i.e. dark) in radar images.

Lobate: extensive areas (~ 300 km) that have an uneven surface texture and are usually associated with volcanoes.

Smooth: smooth area formed from the solidification of gently undulating lava flows.

Plate tectonics: the theory whereby the lithosphere is divided into multiple plates each moving over an asthenosphere. The boundaries between each interacting plate can be divergent, convergent or transform.

Pre-exponential factor: a number that signifies the collision frequency between reacting molecules and the orientation factor needed for the reaction.

Pyroclastic deposit: surface material formed as a result of the accumulation of rock from explosive eruptions.

Radiogenic elements: elements of uranium, thorium, and potassium produced as a result of radioactive decay.

Rayleigh number: a dimensionless number that characterises the onset of convection in a fluid layer.

Reference column: a reference lithospheric structure comprising a reference crustal and lithospheric mantle thickness.

Residual topography: topography remaining after the calculated topography from Airy and thermal isostasy is removed from the observed topography. The residual topography can be used to estimate the amount of topography that is supported by flexure and dynamic uplift.

Revolution: the amount of time it takes a planet to complete one orbit around a larger object (e.g. the Sun).

Ridge: an elongated, narrow elevated crest that extends for some distance.

Rift: see chasma.

Rotation: the amount of time a planet takes to complete one rotation around its central axis.

Runaway greenhouse effect: the theory where increased surface temperatures lead to greater quantities of atmospheric water vapour. This water vapour traps more heat and leads to higher surface temperatures. The cycle continues until all the liquid water on a planet's surface boils away.

Shield volcano: a broad volcano with low elevations and gently sloping sides.

Solidus: the temperature below which a material is entirely solid.

Spherical harmonics: functions that solve for the angular component of Laplace's equations in spherical coordinates.

Spinel: a mineral with octahedral crystals and a composition of aluminum and magnesium.

Subduction: a process where the boundary of one crustal plate is forced downwards under another.

Retrograde: proposed to occur around coronae. As the edge of the lithosphere sinks a trench is produced that moves backward over the surrounding lithosphere.

Surface heat flow: the rate of heat transmitted through a surface, per unit area.

Tessera (or complex ridged terrain): highly deformed areas of multiple intersecting ridges and troughs.

Thermal:

Isostasy: a process whereby changes in the thermal regime of the lithosphere produce elevation changes.

Lithosphere: comprises the crust and upper mantle where heat is transferred by conduction. Considered to be the depth to the 1300°C isotherm in this thesis.

Thinning: the process where the lithosphere is thinned at its base by convective heat transfer.

Triple-junction: the point on the surface of a planet where three rifts meet.

Trough: an elongated linear depression that has shallow elevations compared to a trench.

Upwelling: see mantle plume.

Volcanic degassing: occurs when volatiles contained within magma are subsequently released into the atmosphere.

Volcanic rise: a surface manifestation of an upwelling mantle plume.

Corona-dominated: a volcanic rise with extensive lava flows and no rifts.

Rift-dominated: volcanic rises that are dissected by a rift/s that extend beyond the rise.

Volcano-dominated: a volcanic rise comprising volcanic edifices and no rifts.

Wrinkle ridges: narrow, inclined ridges formed from compressional deformation.

Scientific Units*

Symbol	Description	Unit
A	plume channel thickness	m
a	radius of heated basal layer	m
B	Bouguer gravity	mGal
b	dynamic topography from the CMB [#]	m
BC	Bouguer correction	N kg ⁻¹
BC _{uncert}	Bouguer gravity uncertainty	mGal
B _{uncert}	Bouguer uncertainty	mGal
C	composition	
c	intercept value of the regression line	
c _p	heat capacity	J kg ⁻¹ K ⁻¹
D	dissipation number flexural rigidity	N m
d	depth particle size	m m
d _c	reference size relationship	m ⁻¹
E	absolute elevation Young's modulus activation energy	m Pa J mol ⁻¹
F	flexural parameter melt fraction	m
FA	free-air gravity	mGal
FA _{uncert}	free-air uncertainty	mGal
G	gravitational constant	N m ² kg ⁻²
g	gravitational acceleration	m s ⁻²
H	radiogenic heat production per unit volume	W m ⁻³
h _s	geoid anomaly at the surface	m
K	bulk modulus	Pa
k	thermal conductivity	W m ⁻¹ K ⁻¹
L	lithospheric thickness	m
L ₀	calibration constant	m
l	spherical harmonic degree	
M	melt volume	km ³
m	gradient of the line of	

	regression	
	spherical harmonic order	
P	pressure	Pa
Q	heat flow	W
R	universal gas constant	J mol ⁻¹ K ⁻¹
Ra	Rayleigh number	
RMSS	Root-Mean-Square slope	
R ₀	reference radius	m
r	radius	m
r _s	stagnation distance	m
s	dynamic topography from the surface	m
T	temperature	K
T _c	crustal thickness	m
T _e	elastic lithosphere thickness	m
Topo _{uncert}	topographic uncertainty	m
t	time	s
u	horizontal velocity	m s ⁻¹
V	activation volume	cm ⁻³ mol ⁻¹
W	cross-sectional area	m ²
w	width	m
x	distance	m
z	depth	m
Γ	phase function	
Φ	viscous dissipation	
α	coefficient of thermal expansion	K ⁻¹
β	compressibility	Pa ⁻¹
γ	slope of Clapeyron curve	Pa K ⁻¹
ΔT	temperature contrast surface to CMB [#]	K
δ_i	Kroneker delta tensor	
η	viscosity	Pa s
η_r	pre-exponential factor	
κ	thermal diffusivity	m ² s ⁻¹
λ	mass of a mantle plume	kg
ν	Poisson's ratio	
π	reduced pressure	Pa

ρ	density	kg m^{-3}
σ	reduced radial stress	Pa

* Referenced from *Basilevsky and McGill* [2007]; *Davies* [2000]; *Head et al.* [1992]; *Melosh* [2011]; *Reynolds* [1997]; *Schubert et al.* [2001]; and *Turcotte and Schubert* [2001].

1. Introduction

1.1 Rationale

Venus is enigmatic, it shares similar properties to Earth, but has unique surface conditions [Kaula and Phillips, 1981; Seeds, 2005; Solomon *et al.*, 1992]. The lack of multiple tectonic plates, long linear chains of volcanoes, and clear indicators of subduction suggest Venus lacks Earth-like plate tectonics. The scarcity and uniformity of impact craters indicate Venus's surface is young and it has experienced extensive tectonic and volcanic deformation [Anderson and Smrekar, 2006; Schaber *et al.*, 1992]. Global geological activity is not currently supported by Venus's mantle convection regime, however recent evidence shows localised areas may experience volcanism [Moresi and Solomatov, 1998; Solomatov and Moresi, 1996; Smrekar *et al.*, 2010; Turcotte, 1993].

The topographic shape of Venus's tectonic and volcanic landforms may be a combination of four short and long-wavelength processes including Airy isostasy, thermal isostasy, regional isostasy (flexure), and dynamic uplift that operate to compensate the structure of the lithosphere. For example, volcanic rises are considered to be surface expressions of mantle upwellings with some of the elevated topography (3-4 km) supported by dynamic uplift or long wavelength thermal thinning of the lithosphere [Kucinskas and Turcotte, 1994; Smrekar *et al.*, 1997]. This compares to crustal plateaus that lack dynamic uplift, but may be supported by crustal thickness variations (Airy isostasy) and regional isostasy.

The first aim of this study is to constrain the lithospheric structure and the contribution of Airy isostasy, thermal isostasy, regional isostasy, and dynamic uplift (obtained from the residual isostatic topography) in shaping the observed topography at two rift-dominated volcanic rises

Atla and Beta Regio and the crustal plateau, Fortuna Tessera. The second aim is to determine a plausible model of Venus's mantle convection and identify the contribution of dynamic uplift in supporting regional topography and geoid anomalies.

Previous studies, which have addressed each compensation mechanism as a single process, have resulted in highly variable estimates of the amount of dynamic support at Venusian rises as well as unconstrained average crustal and thermal lithospheric thickness estimates [e.g. *Grimm and Hess, 1997; James et al., 2013; Nimmo and McKenzie, 1996; Solomatov and Moresi, 1996; Stofan et al., 1995*]. The extensive, interconnected rift networks that dissect the large volcanic rises suggest deformation has been a complex process and variations in Venus's gravity and geoid imply a combination of both short and long wavelength contributions. It is unlikely compensation mechanisms on Venus act singularly rather, they occur together. By accounting for multiple components of topography, I present the first self-consistent study of the compensation mechanisms shaping the topography within selected regions on Venus. In turn, this study has important implications for current volcanism and rifting at selected areas on Venus.

1.2 Overview

Venus, the second planet from the Sun, is often considered Earth's twin since these planets share a similar size, mass, density, and volume [*Seeds, 2005*]. However, these two planets followed very different evolutionary paths. While Earth has life thriving under habitable conditions, surface water, average surface temperatures of $\sim 15^{\circ}\text{C}$ and ~ 1 bar surface pressures, conditions on Venus are extreme [*Lacis et al., 2010*]. A global runaway greenhouse effect has occurred on Venus as evidenced by its high surface temperatures (472°C), surface pressure (~ 90 bar), lack of surface water, and high abundance ratio of atmospheric deuterium

to hydrogen ($\sim 1.9 \times 10^{-2}$) [Grinspoon, 1993; Kulikov *et al.*, 2006; Lacis *et al.*, 2010; Rasool and Bergh, 1970; Seeds, 2005].

The high surface temperatures and pressures, in conjunction with a thick atmosphere, has made imaging and sampling the surface difficult, with missions requiring spectrometers and radar mapping capabilities. Multispectral mapping performed by Venera 13 in 1981-1982 and Vega 1 and 2 in 1984-1985 measured ferric compositions consistent with a basaltic crust at each landing site [Pieters *et al.* 1986]. The presence of basalt was then confirmed with in-situ analyses using Gamma-ray spectrometers and/or X-Ray fluorescence [Grimm and Hess, 1997]. These analyses, together with observations of shield volcanoes and expansive volcanic plains units, imply basaltic crust is abundant on Venus's surface [Wood, 1997]. The Magellan mission (1989-1994) was also successful in obtaining elevation and gravity data for most of the planet ($\sim 97\%$) and at much higher resolutions (120 to 300 m) than previous missions [Pettengill *et al.*, 1991]. Similar to Earth, Venus has a global network of rifts, volcanic rises, volcanoes, crustal plateaus, impact craters, calderas, and unique features, such as complex ridged terrain (tessera) and elevated ring-shaped structures (coronae) [Anderson and Smrekar, 2006].

The most recent mission, Venus Express (2005-2014), has focused on Venus's atmosphere and clouds and has measured the thermal emissivity of the surface. Thermal emissivity variations are indicative of different lava flow compositions, surface weathering, and in turn, surface age [Smrekar *et al.*, 2010]. The thermal emissivities obtained at Imdr, Themis, and Dione Regiones are indicative of young ages, $< 2.5 \times 10^5$ - 2.5×10^6 years [Smrekar *et al.*, 2010]. These ages are much younger than the Venus's surface age estimates of ~ 500 -750 Myr from impact crater studies [McKinnon *et al.*, 1997; Moresi and Solomatov, 1998; Schaber *et al.*, 1992].

Reasons for discrepancies in the surface ages estimated from the two different methods

include uncertainties associated with the crater production rate, mineralogy, and atmospheric composition [McKinnon *et al.*, 1997; Moresi and Solomatov, 1998; Schaber *et al.*, 1992; Smrekar *et al.*, 2010].

In spite of the many similarities in size, mass, density, and volume, Venus does not present evidence of Earth-like plate tectonics [Kaula and Phillips, 1981; Solomon *et al.*, 1992]. Plate tectonics may not occur on Venus due to the lack of surface water and the higher surface temperatures, which makes the crust more ductile than brittle [Bindschadler *et al.*, 1992; Phillips *et al.*, 1991; Zuber, 1987]. Also, the strong correlation of geoid and topography anomalies may imply Venus lacks an asthenosphere. Without an asthenosphere the mantle is strongly coupled to the crust and plate tectonics, as observed on Earth, is strongly inhibited [Phillips *et al.*, 1991].

Plate tectonics, and how easily a planet loses its internal heat, is a fundamental process contributing to its thermal, tectonic, and volcanic evolution, as well as the current topography, gravity, and geoid anomalies, observed on the surface [Reese *et al.*, 1998]. On Earth, subduction and rifting are important for interior heat loss, with some potential subduction sites being identified for Venus [Schubert and Sandwell, 1995] and possible current volcanic activity at localised rises [Bondarenko *et al.*, 2010; Smrekar *et al.*, 2010].

1.3 Previous Studies

The topographic shape of Venus's surface landforms are the result of short and long wavelength processes that act to compensate the observed topography at depth. Short-wavelength processes include Airy isostasy via crustal thickness variations or flexure. Long wavelength processes include thermal uplift, associated with the thinning of the lithosphere by

basal heating, or dynamic uplift, produced as a result of convective stresses within the mantle. Since both thermal uplift and dynamic uplift contribute to long-wavelength topography, discerning how much each mechanism contributes to surface topography is difficult.

In order to determine the contribution of each of these processes in supporting Venusian landforms we first need to discern the lithospheric structure, including crustal thickness, thermal and elastic lithosphere thickness and the dynamics of the mantle. In this study, the thermal lithosphere is considered to comprise the conductive region of the crust and upper mantle and the elastic lithosphere is the portion that can endure elastic stresses over time. Since Venus's surface conditions make seismic and borehole data acquisition unfeasible, the only reliable geophysical tools for studying the interior are geoid, gravity, and elevation data [James *et al.*, 2013]. However, these data sets are highly ambiguous, with different models producing different lithospheric structures and degrees of compensation [Orth and Solomatov, 2011; Pauer *et al.*, 2006; Schubert *et al.*, 1994; Smrekar and Phillips, 1991; Solomatov and Moresi, 1996; Turcotte, 1993]. This is compounded further by the tendency of previous authors to analyse the effect of a single process in shaping topography, rather than the multiple processes operating concurrently [e.g. Kucinskas and Turcotte, 1994; Moore and Schubert, 1995, 1997; Smrekar and Parmentier, 1996].

Average crustal thickness estimates range from 8-30 km and are strongly reliant on the density of the crust and the thermal gradient that was assumed [Grimm and Hess, 1997; Grimm and Solomon, 1988; James *et al.*, 2013; Konopliv and Sjogren, 1994; Simons *et al.*, 1994; Zuber, 1987]. The average range of lithospheric thickness estimates are also highly variable with some authors using Earth-like parameters to infer a thickness of 100 km, whereas others obtain thicker estimates (200-550 km) from stagnant-lid or episodic convection models [Orth and Solomatov, 2011; Pauer *et al.*, 2006; Schubert *et al.*, 1994; Smrekar and Phillips, 1991;

Solomatov and Moresi, 1996; Turcotte, 1993].

On Venus, the thickness of the elastic lithosphere is more constrained than crustal and thermal lithospheric thickness [*Barnett et al., 2000; Johnson and Sandwell, 1994; McKenzie and Nimmo, 1997*]. However, elastic lithospheric thickness indicates the flexural response at the time of loading, rather than the current lithospheric conditions. Craters, coronae, rifts, and volcanoes have been used in regional studies of flexure to yield elastic lithospheric thicknesses of ~25 km [*Barnett et al., 2002*] and ~6 to 34 km [*Johnson and Sandwell, 1994*], with a global average of ~30 km [*Barnett et al., 2000; Nimmo and McKenzie, 1998*].

Understanding the dynamic contribution stresses within the mantle can place on long wavelength topography and gravity is also highly unconstrained because very little is known about Venus's mantle, composition, and convective regime. Some studies have inferred a dry [*Grimm and Solomon, 1988; Kaula, 1995; Nimmo and McKenzie, 1998*] or wet Venusian mantle rheology [*Namiki and Solomon, 1998*]. Thermal buoyancy due to phase transitions and their influence on mantle convection have been the focus of a number of studies [*Benešová and Čížková, 2012; Huang et al., 2013; Schubert et al., 1997; Steinbach and Yuen, 1992; Weinstein, 1995, 1996*], with others inferring compositional buoyancy can also have a significant influence [*Dupeyrat and Sotin, 1995; Ogawa, 2000*]. A lack of consensus also exists with the type of convective regime with some suggesting sluggish-lid [*Ratcliff et al., 1997*], episodic [*Moresi and Solomatov, 1998; Turcotte, 1993*], or stagnant-lid convection [*Orth and Solomatov, 2011; Reese et al., 1998; Solomatov and Moresi, 1996*].

1.4 Study Areas: Atla and Beta Regio, and Fortuna Tessera

Atla and Beta Regio are rift-dominated volcanic rises, spanning distances of ~2000 km by

~2000 km and are located within Venus's equatorial and mid-latitudes, respectively (Figure 1.1) [Basilevsky and Head, 2007; Senske and Head, 1992]. These rises are sites of high geoid anomalies, large swell volumes, elevated volcanoes, and rifts that form triple junctions at the center of these areas [Basilevsky and Head, 2007; Senske and Head, 1992; Smrekar and Phillips, 1991; Stofan et al., 1995]. Impact craters at both rises exhibit tectonic and volcanic modification, the most notably being the presence of craters that dip outwards from the center of Atla Regio [Matias et al., 2004; Matias and Jurdy, 2005].

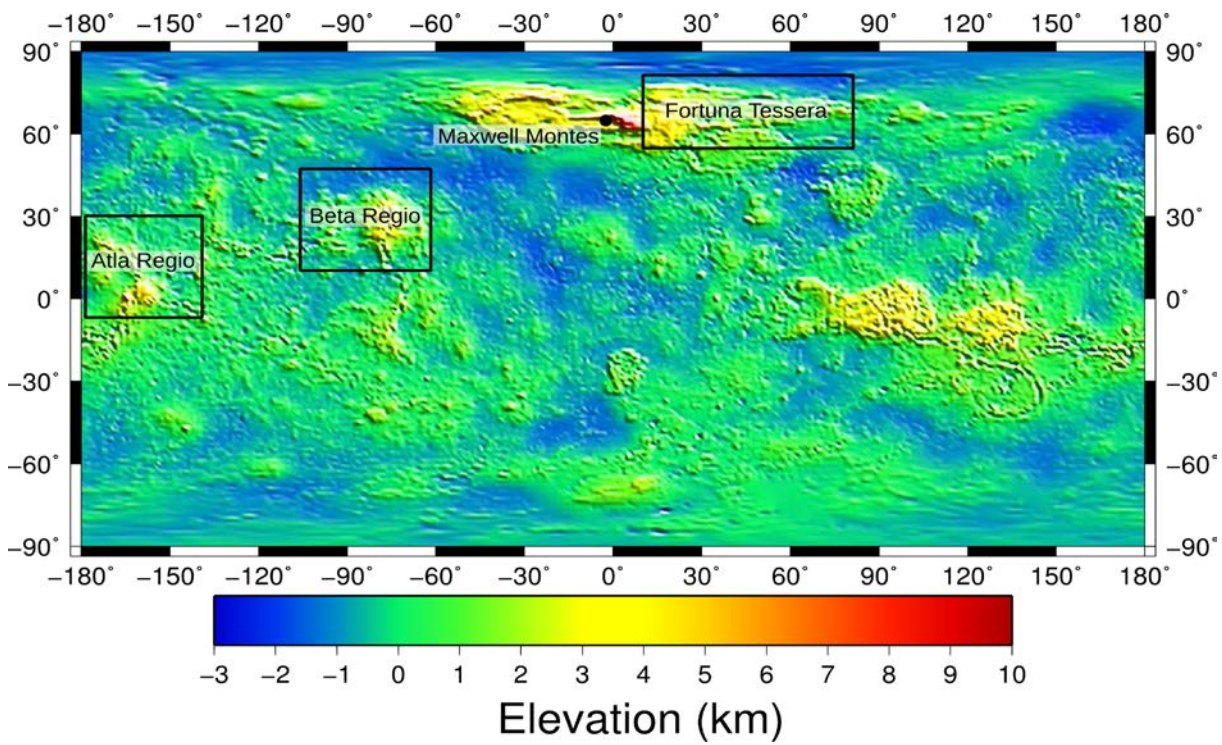


Figure 1.1. Map of Venus's global elevation showing the location of Atla and Beta Regio, within the equatorial and mid-latitudes, respectively. Fortuna Tessera is located near Venus's north pole, adjacent to Maxwell Montes (black circle), which has the highest elevation on Venus. This Mercator projected map has been referenced to Venus's Mean Planetary Radius (MPR), equal to 6051.848 km.

These rises require long-wavelength compensation mechanisms, since implausible crustal thicknesses (> 150 km) result if Airy isostasy operates only [Kucinskas and Turcotte, 1994]. In order to explain the elevated terrain of these areas, a number of authors have considered

thermal uplift with a thin (~88 km to 100 km) [Kucinskas and Turcotte, 1994; McGovern and Simons, 1995; Moore and Schubert, 1995, 1997; Phillips, 1994; Smrekar and Parmentier, 1996] or thick (300 km to 550 km) lithosphere [Orth and Solomatov, 2011; Solomatov and Moresi, 1996; Vezolainen *et al.*, 2004]. Most of these authors [Kucinskas and Turcotte, 1994; Moore and Schubert, 1995, 1997; Smrekar and Parmentier, 1996] used Apparent Depths of Compensation (ADCs) and Geoid-to-Topography Ratios (GTRs) to constrain their estimates, these methods may be unreliable, with melt generation rates being more useful in constraining the lithospheric thickness [Nimmo and McKenzie, 1998; Smrekar and Parmentier, 1996]. Observations of swell heights and numerical models of mantle upwellings, were also used to imply a minimum of ~1 km and up to ~5.7 km of the observed topography at these volcanic rises could be compensated dynamically [Kiefer and Hager, 1991; Stofan *et al.*, 1989; 1995; Vezolainen *et al.*, 2004]. Elastic lithospheric thicknesses at these volcanic rises were estimated from spectral admittance and the direct observation of topography and gravity, resulting in an average of 45 ± 3 km for Atla Regio [Phillips, 1994] and 10-20 km for Beta Regio [Simons *et al.*, 1997].

Fortuna Tessera is a crustal plateau, characterised by steep margins and complex ridged terrain [Bindschadler *et al.*, 1992]. Studies have inferred that the highly deformed nature of the tessera and relatively old age estimates could be associated with these areas having resisted the last global overturn event ~500 Myr ago or represent Venusian analogues to Earth's Archean cratons [Hansen, 2013; Romeo and Turcotte, 2008]. The nature of the terrain suggests compressional deformation where thick crust (20-60 km) compensates most of the complex topography [Vorder Bruegge and Head, 1989; Simons *et al.*, 1997; Zuber and Parmentier, 1990]. Elastic lithospheric thickness estimates are sparse for this area with one study inferring a 20 km thick elastic lithosphere [Simons *et al.*, 1997]. Constraining the thickness of the elastic lithosphere in Fortuna Tessera is important, since it can provide

information about Venus's past conditions, and possibly the stresses involved in this area's complex deformational history [*Foster and Nimmo*, 1996; *Johnson and Sandwell*, 1994]. No previous estimates of the thermal lithospheric thickness are available for Fortuna Tessera, but thermal thinning may be an important long-wavelength compensation mechanism, due to the close proximity of this area to Maxwell Montes.

1.5 Aims

The overall objective of this study is to provide the first complete investigation constraining the lithospheric structure and interior processes that support the topography observed at Atla Regio, Beta Regio, and Fortuna Tessera. The thesis is divided into two main parts, with the main goals identified below.

1. Lithospheric Modelling:

- a) To simultaneously constrain a suitable model of the 3D lithospheric structure below an area using elevation, geoid and Bouguer gravity observables.
- b) Utilise crustal, thermal lithospheric and elastic lithospheric thickness variations to discern the contribution of thermal, Airy and regional isostasy, and in part, dynamic uplift, in supporting the observed topography.

2. Mantle Convection Modelling:

- a) Use 3D spherical shell mantle convection simulations to identify the effects of varying Rayleigh number, pre-exponential factor, activation energy, and internal heating on Venus's internal dynamics, dynamic topography, and geoid.
- b) Use the best-fit model to understand the contribution of dynamic uplift to the elevation and geoid over regional upwellings and compare this to the amount required from the

lithospheric modelling.

- c) Perform localised admittance and correlation calculations on both the estimated, modelled, and observed geoid and elevation data to further constrain the contribution of long and short wavelength compensation mechanisms in supporting regional topography.

1.6 Thesis Structure

This thesis follows the formatting and reference style of the American Geophysical Union's *Journal of Geophysical Research*. The structure of this thesis follows guidelines set by Macquarie University for a Thesis by Publication. As a result, Chapters 4 to 7 are presented as stand-alone, self-contained papers, ready to be submitted for peer-review.

Chapter 2 provides a review of the previous studies related to the contents of this thesis, including examples and explanations of the tectonic, volcanic and tectono-volcanic terrains observed on the surface. It also outlines work relating to Venus's mantle and lithosphere including composition, thermal state, convective regime, crustal, thermal, and elastic lithospheric thicknesses.

Chapter 3 has three sub-sections. The first presents the elevation, geoid, and Bouguer gravity data sets that form the geophysical observables and help to constrain the lithospheric structure and internal dynamics of Venus's mantle. The second section outlines the lithospheric modelling software and the heat transfer, isostasy, pressure and density equations and the third section outlines the governing equations used in the global 3D spherical shell numerical models of Venus's internal dynamics.

Chapter 4 to 6 introduces the three study areas, Atla and Beta Regio, and Fortuna Tessera, respectively. The geological structures and geophysical anomalies of each region, their proposed lithospheric structure, and contribution of each mechanism in supporting the observed topography, are presented. Chapter 4, which considers Atla Regio, also provides estimates of melt generation rates and volumes from an upwelling mantle plume and possible spreading rates along its major rift.

Chapter 7 presents the global numerical models of Venus's interior and the influence of Rayleigh number, pre-exponential factor, internal heating, and activation energy on its convective regime, the dynamic topography, and geoid. The best-fit model is then used to determine if pressure-release melting can occur for different assumed mantle compositions. The dynamic topography and geoid obtained for the best-fit model is also used to determine the regional geoid and topography admittance and correlation. Comparisons are then made to estimated and observed values in order to constrain the contribution of long and short wavelength processes in shaping the topography within Atla and Beta Regio.

Chapter 8 combines the results from both the lithospheric modelling and mantle convection models to provide a self-consistent explanation of the mechanisms that contribute to producing the different landforms observed in each area. It also discusses these results, and their implications, in the context of previous work.

Chapter 9 summarizes the main conclusions from the previous chapters and outlines possible future studies.

Chapter 10 outlines all the references used in this study.

Appendix There are three sub-sections within the printed version of this thesis including two peer-reviewed conference papers and one input file used in the numerical modelling. The digital appendix also contains the output files for each lithospheric model.

2. Global Planetary Background

2.1 Introduction

Venus, the second planet from the Sun, shares a similar radius, mass, volume, and mean density as Earth (Table 2.1) [Seeds, 2005]. However, Venus's high surface temperatures ($\sim 472^{\circ}\text{C}$), surface pressure (~ 90 bar), and lack of surface water caused from a runaway greenhouse effect, are very different to conditions on Earth [Seeds, 2005]. Venus also rotates in a retrograde direction around its rotation axis compared to the other terrestrial planets that rotate in a prograde motion [Seeds, 2005]. The time it takes for Venus to complete one rotation around its axis is longer (243 Earth days) than the time (224.68 Earth days) it takes to complete one revolution around the Sun, making a Venusian day longer than its year. The slow rotation of Venus around its axis may have been caused from a large impact event in Venus's early history or from solar tidal forcing acting on the dense atmosphere [Seeds, 2005].

Numerous spacecraft have been sent to Venus [Moore, 2002]. Venus's dense atmosphere was a hindrance to the earlier missions; however, seven spacecraft carrying Gamma-Ray Spectrometers (GRS) and X-Ray Fluorescence instruments (XRF) were successful in obtaining surface samples [Grimm and Hess, 1997].

The first spacecraft to successfully sample Venus's surface rocks was Venera 8, north-west of Alpha Regio, in 1972 (Figure 2.1) [Moore, 2002]. This was followed by Venera 9 and 10, which landed, imaged, and sampled the surface close to Beta Regio in 1975 (Figure 2.1) [Moore, 2002]. In 1981, Venera 13 and 14 landed, photographing and sampling the surface in a plains region to the east of Phoebe Regio (Figure 2.1) [Moore, 2002]. In 1982, a plains

Table 2.1. Comparison of the properties of Venus and Earth*

Properties	Venus	Earth
Mass (10^{24} kg)	4.87	5.97
Radius (km)	6052	6371
Volume (10^{12} km³)	0.93	1.08
Density (kg m⁻³)	5243	5515
Gravity (m s⁻²)	8.87	9.81
Rotation Period (hours)	-5832.5	23.9
Orbital Period (days)	224.7	365.2
Surface Pressure (bars)	92	1.01
Surface Temperature (°C)	472	-50 to 50

* From *Seeds* [2005].

region close to Atla Regio and Aphrodite Terra, was imaged and sampled by Vega 1 and 2, respectively (Figure 2.1) [Moore, 2002].

The Magellan mission, however, only involved an orbiter that was used to map 97% of Venus's surface from 1990 to 1994 [Pettengill *et al.*, 1991]. Due to Venus's thick clouds, Magellan utilised high resolution (100 m) radar mapping capabilities, allowing the identification and imaging of numerous tectonic and volcanic landforms [Moore, 2002]. Data collected from the Magellan mission was also used to obtain maps of Venus's geoid, elevation, free-air gravity, and Bouguer gravity. Venus's surface features have elevations ranging from -3 km to 10 km, geoid anomalies ranging from -100 m to 150 m, free-air gravity anomalies ranging from -150 mGal to 550 mGal, and Bouguer gravity anomalies ranging from -1000 mGal to 400 mGal. The elevated (~3 km to 10 km) highlands, mountain regions, volcanoes, and volcanic rises correspond to areas of high geoid anomalies (~110 m to 180 m) and positive free air gravity anomalies (~75 mGal to 550 mGal). These elevated areas also

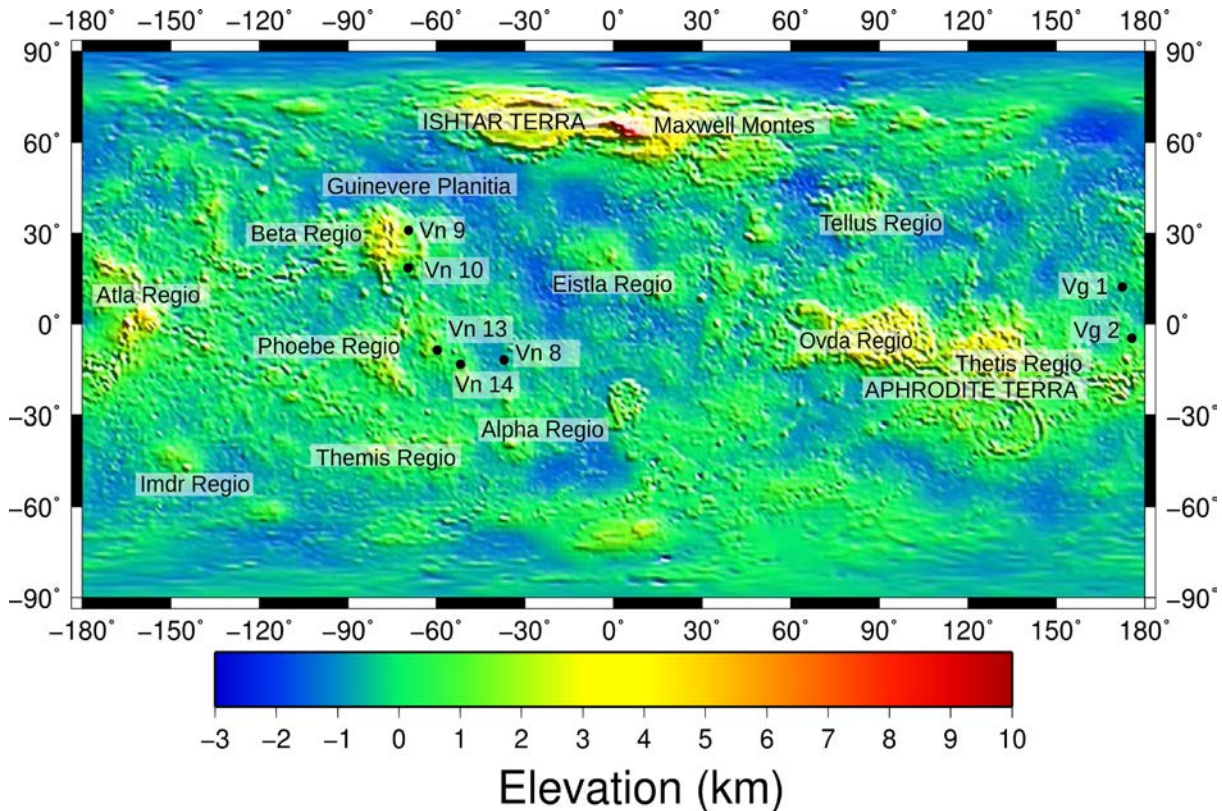


Figure 2.1. [Modified from *Grimm and Hess, 1997*]: Map showing the location of the Venera (Vn) landing sites, Vega (Vg) landing sites (black circles) and the main topographic features. This Mercator projected map of elevation, obtained from the Magellan mission to Venus, is referenced to Venus's Mean Planetary Radius (6051.848 km).

correspond to Bouguer gravity lows (-1000 mGal to -400 mGal) that imply these areas are compensated by low-density material at depth. The lowland (-3 to 2 km) plain regions correspond to areas of negative geoid anomalies (0 m to -100 m), negative free-air anomalies (0 mGal to -150 mGal), and positive Bouguer anomalies (0 mGal to 400 mGal).

In 2006, Venus Express arrived to study the atmospheric environment, with the Visible and Infrared Thermal Imaging Spectrometer providing information regarding surface emissivities at selected locations [Arnold *et al.*, 2008; Titov *et al.*, 2006].

2.2 Geological Structures

Venus's surface has a number of short and long wavelength tectonic, volcanic, and geologic structures including plains, volcanoes, volcanic rises, crustal plateaus, tessera, mountains, chasmata (rifts), craters, and coronae [Anderson and Smrekar, 2006; Moore, 2002]. The complexity of these landforms and their overlap (e.g. rifts and coronae on volcanic rises) indicate a plurality of geological processes have contributed to their formation. These landforms can be supported by a combination of Airy isostasy, thermal isostasy, regional isostasy (flexure), and dynamic uplift that operate within the short and long wavelengths. Short wavelength mechanisms operating to support these landforms are Airy isostasy, associated with crustal thickness variations and regional isostasy, associated with flexure of the elastic lithosphere. These landforms may be further compensated by long wavelength processes such as thermal isostasy associated with thinning of the thermal lithosphere and dynamic uplift produced from convective stresses within the mantle. Uncertainties in Venus's lithospheric structure, internal dynamics, and the parameters controlling mantle convection, in conjunction with each process being considered separately rather than concurrently, have resulted in highly unconstrained estimates of crustal thickness, lithospheric thickness, and the amount of dynamic support operating at these landforms [e.g. Grimm and Hess, 1997; James et al., 2013; Nimmo and McKenzie, 1996; Smrekar et al. 1997; Stofan et al., 1995; Solomatov and Moresi, 1996;].

2.2.1 Volcanic Rises

Volcanic rises have a broad, domical shape, and extend for large distances (1000-2500 km) [Anderson and Smrekar, 2006; McGill et al., 2010]. The ten rises on Venus's surface are Beta, Atla, Bell, Western Eistla, Eastern Eistla, Central Eistla, Laufey, Imdr, Themis, and Dione

Regiones [McGill *et al.*, 2010]. Three types of rises have been identified on Venus and include rift-dominated, volcano dominated, and coronae dominated [Smrekar *et al.*, 1997]. Rift-dominated volcanic rises, such as Atla and Beta Regio, are dissected by rifts, which form an interconnected global rift system (Figure 2.2) [Smrekar *et al.*, 1997]. These areas have the greatest swell heights (~ 2 km) of all the rises on Venus and also comprise elevated volcanoes, with one volcano (Maat Mons) reaching elevations up to to 8 km [Smrekar *et al.*, 1997].

If a rise has experienced limited extension, contains single or multiple large volcanoes (> 300 in diameter), and vast volcanic flows, it is considered volcano-dominated [Smrekar *et al.*, 1997]. Corona-dominated rises, such as Themis Regio, are characterised by extensive volcanism and coronae with diameters of 200 to 500 km [Smrekar *et al.*, 1997].

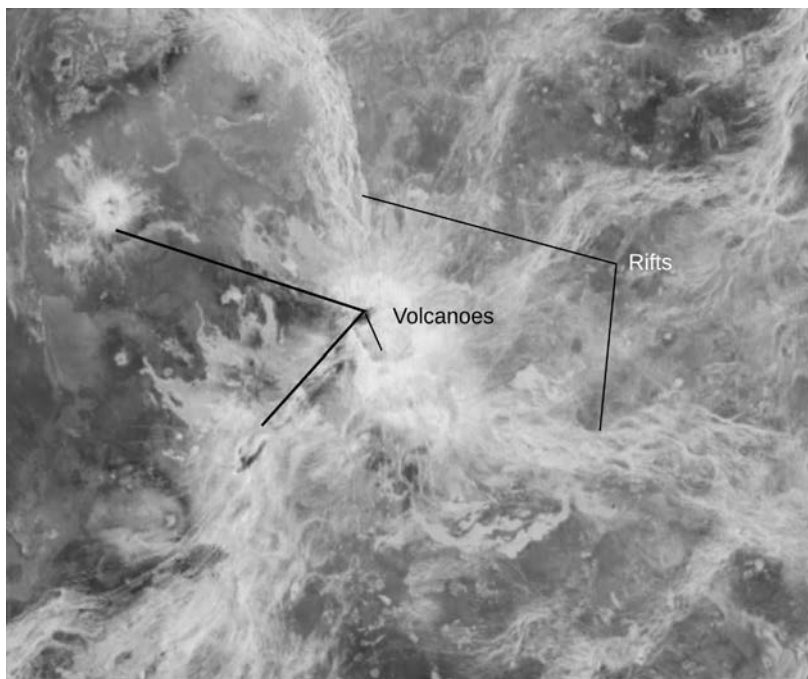


Figure 2.2. (Modified from USGS Map-A-Planet) Radar image of Atla Regio, a rift-dominated volcanic rise. This area is cut by large rifts and dotted with elevated volcanoes. Image width is ~ 2000 km. Radar bright regions represent rough surfaces, whereas radar dark areas represent smooth regions. Image centered at $195^\circ\text{E } 9^\circ\text{N}$.

2.2.2 Volcanoes

Large volcanoes, with their broad (100-600 km) diameters, radial lava flows, and high elevations (4-8 km), tend to occur within the volcanic rises of Atla, Beta, Phoebe, Themis, and Eistla Regio (Figure 2.3) [Head *et al.*, 1992; Ivanov and Head, 2011; Lopes *et al.*, 2010]. The preferential nature of large volcanoes to these regions could reflect a possible association with thermal uplift from the ascent of magma, or from elevation and atmospheric pressure relationships of neutral buoyancy zones [Head *et al.*, 1992; Steinberger *et al.*, 2010]. Neutral buoyancy zones are areas of halted magma ascent, whereby the magma accumulates resulting in higher volume volcanic eruptions [Ryan, 1994]. Some of these volcanoes, especially those on Imdr, Themis, and Dione Regiones, may be currently active [Bondarenko *et al.*, 2010; Smrekar *et al.*, 2010].

Surface processes and the physical properties of the interior can manipulate the style of volcanic activity and the morphology of the volcanoes observed. For example, the morphology of the large volcanoes observed on Venus's surface may be caused from the stresses associated with localised magma intrusion and flexural effects from localised edifice loading of the lithosphere [Galgana *et al.*, 2011; Head *et al.*, 1992; Ivanov and Head, 2013]. Even though Venus has a similar size and density to Earth, the high surface temperatures (730 K) and pressures (90 bar) could have important consequences for surface to near-surface volcanism [Head *et al.*, 1992]. The high surface temperatures on Venus should slow the radiative cooling of lava flows with the dense atmosphere acting to promote initial convective cooling. Initially, convective cooling dominates over radiative cooling, causing the volcanic flows to approach the solidus more rapidly than those on Earth [Head *et al.*, 1992]. As a result, lava flows on Venus are expected to extend one-fifth further and experience pahoehoe to `a`a transition faster than on Earth [Head *et al.*, 1992].

The high atmospheric pressures at the Mean Planetary Radius (MPR) would be effective in reducing explosive basaltic eruptions on Venus [Head *et al.*, 1992]. Ascending magmas containing volatiles, which remain soluble under certain pressures, transit through the nucleation and fragmentation stages before reaching the surface. At the nucleation stage the volatile rich magma produces bubbles if the atmospheric pressure is low compared to the nucleation pressure [Head *et al.*, 1992]. The fragmentation stage is associated with lower pressures that facilitate the growth of bubbles, which can now comprise up to ~75 % of the total volume of magma. As a result of the magma crossing the fragmentation stage, a more explosive eruption, similar to a Hawaiian fire-fountain, would occur. However, this type of eruption on Venus would be rare since the high pressure at Venus's MPR would exsolve less gas and an explosive basaltic eruption would not occur [Head and Wilson, 1992]. Therefore, lavas erupted onto the surface should retain a large proportion of exsolved volatiles [Cattermole, 1994].

On Earth ~0.1-0.4wt% H₂O is needed for explosive eruptions to occur, however, 1-3wt% H₂O would need to be exsolved at highland regions before explosive eruptions could occur on Venus [Head and Wilson, 1992]. Therefore, pyroclastic deposits are unlikely to occur on Venus's surface and even if these pyroclastic eruptions did occur, a pyroclastic cloud would be restricted to a size ~30% smaller than a plume on Earth, due to greater atmospheric resistance [Cattermole, 1994; Head and Wilson, 1992].

Atmospheric pressure also changes with altitude on Venus and can influence volatile exsolution, upper crustal densities, and neutral buoyancy zones [Head *et al.*, 1992]. If ascending magma has a volatile content similar to magma on Earth and is erupted below, or close to the MPR, then this magma could travel unimpeded to the surface [Head *et al.*, 1992]. However, 2 km above MPR, approximately half of the eruptions should be the result of the

direct ascent of magma, with the remaining eruptions arising from magma that has stalled below the surface in a neutral buoyancy zone [Head *et al.*, 1992]. This is important for volcanism on Venus, since lowland areas have experienced high quantities of lava outflow and highland areas have experienced small quantities of lava outflow from neutral buoyancy zones [Head *et al.*, 1992].

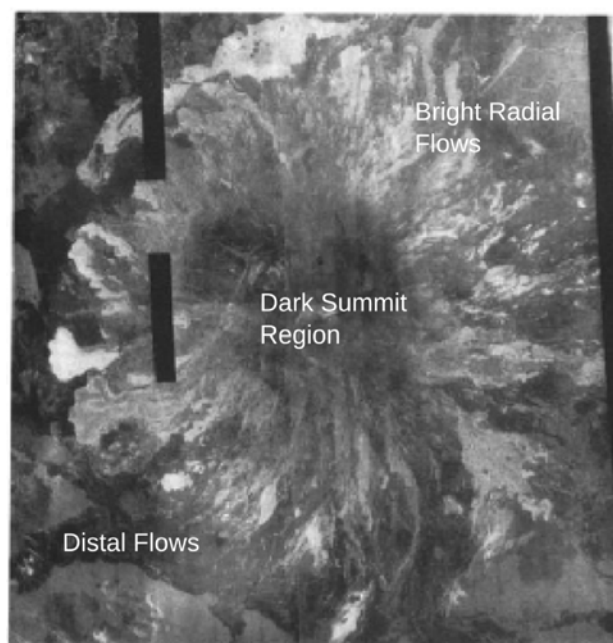


Figure 2.3. (Modified from Head *et al.*, 1992) Radar image showing a large volcano comprising of a central, dark summit, surrounded by radar bright, radial outflows. Radar dark (distal) flows occur toward the far extents of the volcano. Image width is 610 km and centered at -27°N 10°E . Key is similar to Figure 2.2.

2.2.3 Coronae

Similar to the large volcanoes, coronae mostly occur in the Atla-Beta region, Eistla Regio, and western Aphrodite Terra and may be associated with current mantle upwellings. However, they are absent in tessera terrain and sparse in lowland areas [Head *et al.*, 1992; Ivanov and Head, 2010]. Coronae are the most predominant volcano-tectonic feature on Venus's surface, comprising large concentric circular regions, ridges, and fractures that can reach diameters of

100 to 1000 km (Figure 2.4) [Head *et al.*, 1992; Krassilnikov *et al.*, 2012]. The two types of coronae observed on the surface are type 1, which comprise an annulus of concentric ridges and fractures and type 2, which have a partial annulus of ridges and fractures [Stofan *et al.*, 2001]. The interior of a corona can also have a number of volcanic or tectonic structures and the exterior can have a moat or trough (Figure 2.4) [Head *et al.*, 1992]. The occurrence of moats and an absence of lava flows make these features different to calderas [Head *et al.*, 1992]. Domes can also be associated with calderas possibly reflecting the evolution of magmas, since these magmas may have been more viscous [Head *et al.*, 1992].

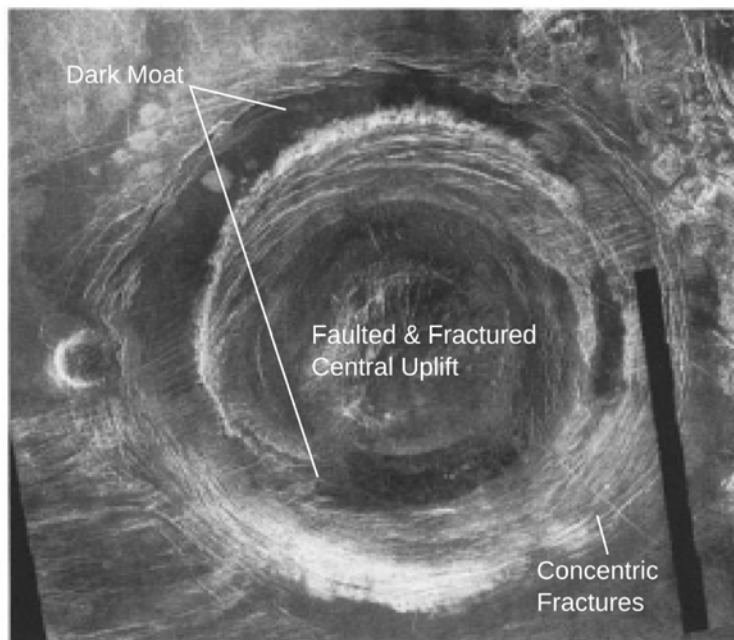


Figure 2.4. (Modified from Head *et al.*, 1992) Radar image showing a corona with a radar dark central uplift and moat, surrounded by radar bright concentric fractures. The width of the image is 372 km and the image is centered at -38°N 75°E in Aino Planitia. Key is similar to Figure 2.2.

Based on observations of coronae, Squyres *et al.* [1992] suggested that initial coronae development involved radial fracturing, in conjunction with domical uplift and volcanism, produced from mantle flow and radial stresses associated with a large rising diapir (Figure 2.5a) [Gerya, 2014; Hansen and Olive, 2009; McGill *et al.*, 2010].

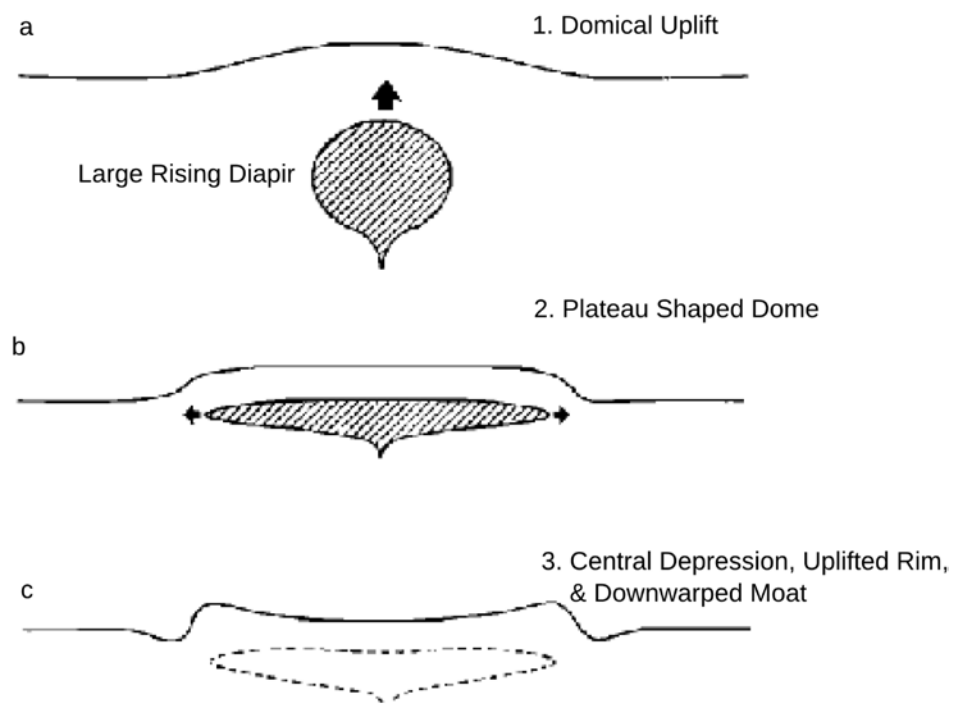


Figure 2.5. (Modified from *Squyres et al.*, 1992) Diagram showing the formation of a coronae. A) An ascending mantle plume produces mantle flow causing uplift that fractures the terrain and volcanism. B) The uplift becomes plateau-like as the plume flattens at the base of the lithosphere. C) As the plume cools, gravitational relaxation occurs, producing a moat, rim, central depression, and concentric fracturing.

During this stage of coronae formation, the uplifted dome appears similar to a nova [Krassilnikov and Head, 2002]. This diapir then flattens and encroaches onto the base of the lithosphere during a second stage of coronae formation, which results in gravitational relaxation of the uplift, producing a plateau shaped dome, rims, depressions, and moats (Figure 2.5b) [Squyres et al., 1992]. Crustal thickening most likely occurs at the boundaries of the plateau and crustal thinning at the centre of the plume [Squyres et al., 1992]. The thin diapir then cools, since it is located closer to the surface, allowing the lithosphere to experience gravitational relaxation and produce downwarped moat structures, an upwarped rim, and central depression (Figure 2.5c) [Squyres et al., 1992]. Concentric fractures located at the base and inward slopes of moat structures, as well as at the crest and outward slopes of the

rim, could have been produced during this stage by radial tensile stresses [Squyres *et al.*, 1992].

2.2.4 Crustal Plateaus and Tessera

Plateau-shaped, flat and topographically high (3-4 km), non-axisymmetric regions bounded by steep sides, commonly comprise complex ridged terrain or tessera on Venus [Bindschadler *et al.*, 1992]. Due to the presence of tessera terrain these areas appear rough with high radar backscatter [Bindschadler *et al.*, 1992; McGill *et al.*, 2010; Romeo and Turcotte, 2008]. Observations of topography, geology, and gravity have led Bindschadler *et al.* [1992] to propose that these areas were formed due to crustal thickening associated with mantle downwellings. Particularly, these authors note the lack of high Geoid-to-Topography Ratios (GTRs), absence of large Apparent Depths of Compensation (ADCs), presence of steep terrain, and lack of high gravity and topography anomalies as evidence for mostly compressional deformation [Bindschadler *et al.*, 1992].

Tesserae are wide (up to 1000s of km), sometimes equidimensional areas, which stand topographically higher than the surrounding plains and comprise multiple ridges and troughs, which gives this terrain its rough appearance in radar images (Figure 2.6) [Basilevsky and McGill, 2007]. These ridges and troughs can have spacings ranging from 5 km to 20 km and are crosscut at numerous angles from orthogonal to oblique (Figure 2.6) [Basilevsky, 1986; Basilevsky and Head, 2000]. Ridges of tessera terrain are usually located close to, and parallel to, the tessera margins [Solomon *et al.*, 1992]. Individual features comprising tessera terrain are usually consistent for ~100 km, but groups of features can maintain similar orientations

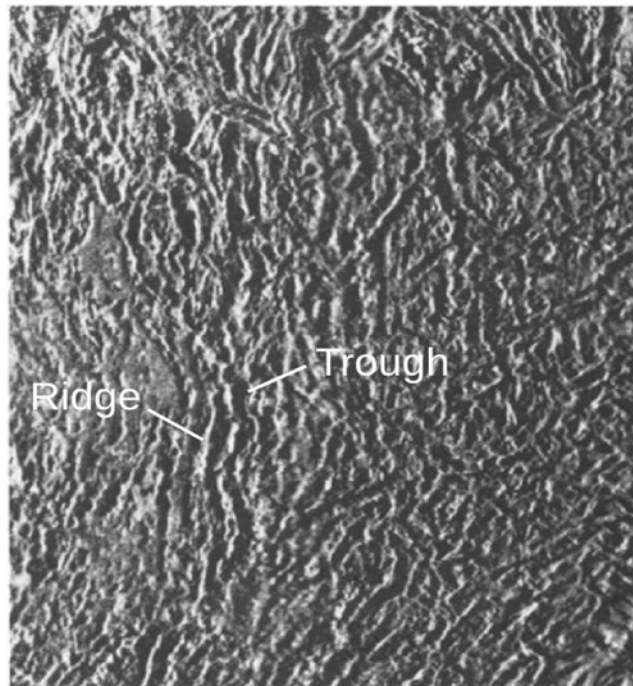


Figure 2.6. (Modified from *Bindschadler and Head*, 1992) Tessera are highly deformed areas comprising ridges and troughs. Image width is 500 km and centered at 67°N 16°E within Fortuna Tessera. Key is similar to Figure 2.2.

for ~1000 km [*Solomon et al.*, 1992].

2.2.5 Mountain Belts

Each topographically high mountain belt on Venus comprises groups of parallel ridges, which may imply they have a compressional origin (Figure 2.7) [*Basilevsky and McGill*, 2007].

Mountain belts usually merge with tessera terrain especially within Ishtar Terra [*Basilevsky and McGill*, 2007].

Mountain belt crests have very high radar reflectivity and appear bright in Magellan images that could be caused from either high altitude weathering of iron silicates or temperature controlled deposition of heavy metals and sulphides, sublimated from rocks at lower and

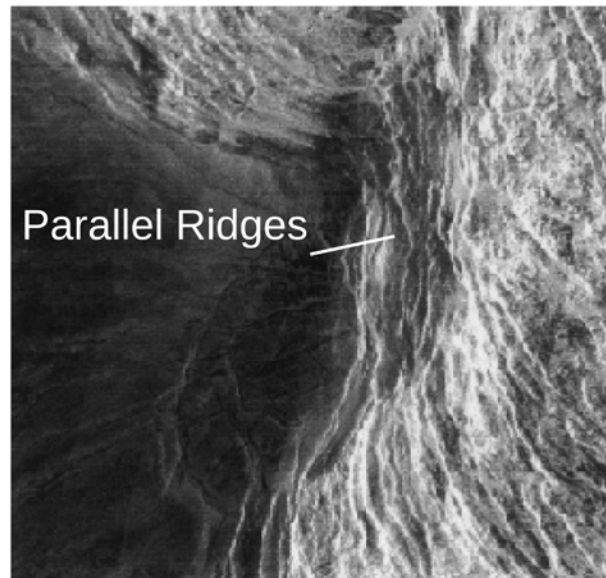


Figure 2.7. (Modified from *Basilevsky and Head, 2000*) Image showing the radar bright parallel ridges of the western margins of Maxwell Montes. Image width is ~ 150 km and centered at 358.5°E 64.5°N . Key is similar to Figure 2.2.

hotter elevations [*Basilevsky and McGill, 2007*].

Keep and Hansen [1994] proposed a "deformation-from-below" model for the formation of Maxwell Montes. This "deformation-from-below" model involved processes taking place within the crust and mantle, where the strong, upper crust was separated from the strong lower crust, by a weak zone. This weak zone could have operated as a decollement surface and/or a stress channel that would have permitted the upper crust to deform separately from the lower crust, propagating stresses from the lower crust/mantle to the upper crust [*Keep and Hansen, 1994*]. As a result, large stresses within the lower crust/mantle would have been able to cause deformation within the upper crust, forming Maxwell Montes [*Keep and Hansen, 1994*]. The lack of subsidence observed within this area could imply that the high elevation (up to 11 km) of Maxwell Montes is supported at depth by a thick crust [*Keep and Hansen, 1994; Phillips and Hansen, 1994*].

2.2.6 Chasmata or Rifts

Rift zone terrain, or chasmata, generally occur within, or close to, lowland regions [Basilevsky and Head, 2000; Solomon *et al.*, 1992]. These areas can extend for 100s to 1000s of km and be a few 100s of km in width [Basilevsky and Head, 2000]. Five main rifts, which form an interconnected global rift network, are observed on the surface and include Parga, Hecate, Dali, Devana, and Ganis Chasma (Figure 2.8) [McFadden *et al.*, 2006]. In conjunction with these large rifts, some shorter (100s of km) and narrower (~50 km to 80 km) rifts also occur on the surface [McFadden *et al.*, 2006]. Young rifts usually consist of topographic troughs, occurring a few kilometers below the surrounding non-rifted terrain, whereas the adjacent rims are topographically higher than the surrounding terrain [Basilevsky and Head, 2000]. Due to the low elevations of the central rift trough and the similarities between these features and terrestrial graben structures, these areas are most likely dominated by extension [Kryuchkov, 1990]. A number of rifts and coronae occur close to volcanic rises (Figure 2.8), which that may infer these features were produced due to mantle upwelling [McFadden *et al.*, 2006].

2.2.7 Plains

Plains are topographically low areas that have minor, but broad deformation [Phillips and Hansen, 1998]. Within Atla Regio lobate and smooth plains dominate and in Beta Regio, regional plains [Basilevsky and Head, 2000]. Regional plains comprise 50-60% of the surface of Venus and consist of smooth surfaces covered with flow-like structures, similar to solidified lava flows (Figure 2.9) [Basilevsky and McGill, 2007]. Regional plains can be dissected by narrow (~1-2km), slightly inclined, ridges 10s to 100s of kilometers in length, which are often called “wrinkle ridges” (Figure 2.9) [Basilevsky and McGill, 2007]. These

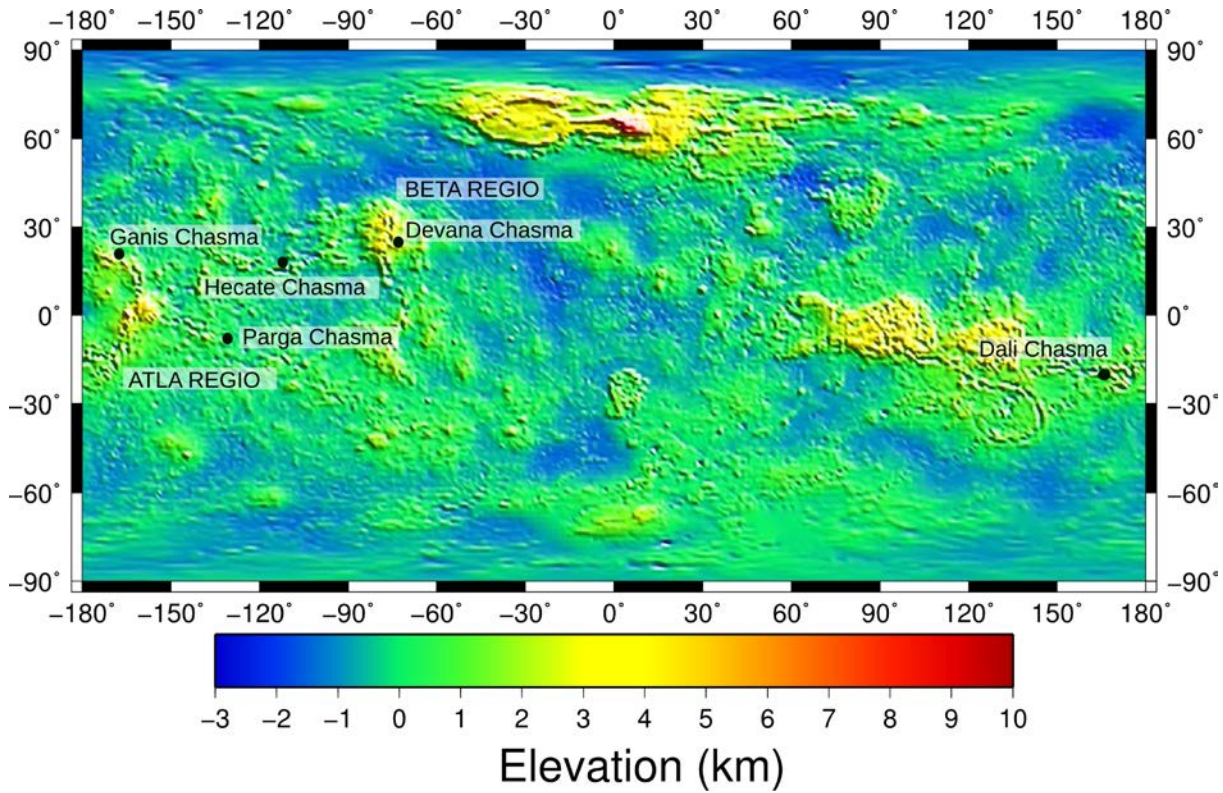


Figure 2.8. Elevation map showing the large rifts (black circles) on Venus, which reside close to the volcanic rises Atla and Beta Regio. This map is referenced to Venus's MPR, equal to 6051.848 km.

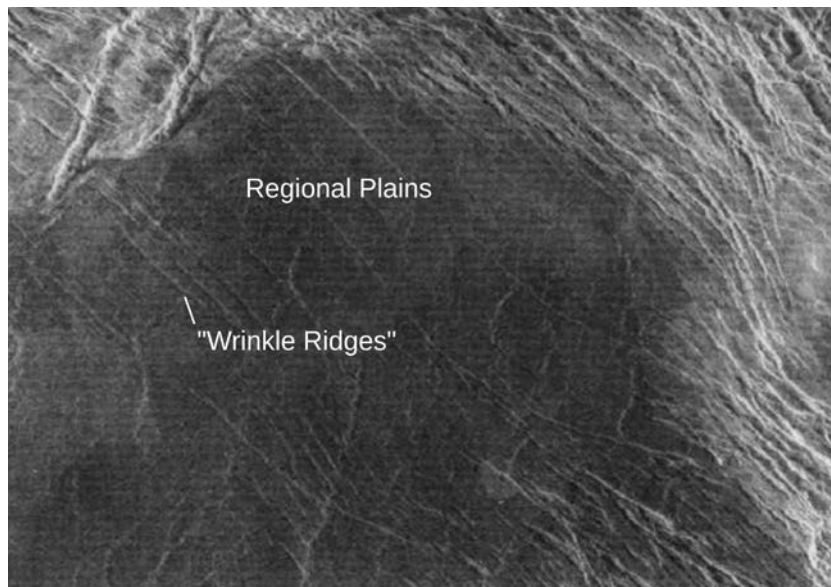


Figure 2.9. (Modified from *Basilevsky and Head, 2000*) Image showing the radar-dark regional plains dissected by the light grey "wrinkle ridges". Image width is ~150 km, centered at 348°E 38.2°S. Key is similar to Figure 2.2.

“wrinkle ridges” were produced by horizontal compression and the underlying plains were most likely formed by low viscosity lavas cascading down gentle inclines [Basilevsky and McGill, 2007]. Sinuous channels, ~2 km to 5 km in width and 100s of kilometers in length, are also observed within the plains [Basilevsky and McGill, 2007]. The origin of these channels is unknown, but their morphology indicates erosion by a substance such as lava [Basilevsky and McGill, 2007].

Lobate plains comprise ~10% of the surface of Venus, extend for large distances (up to 300 km), and tend to have an uneven texture shown by variable radar brightness (Figure 2.10) [Basilevsky and Head, 2007]. The close proximity of these flows to rift zones, large volcanoes, and coronae, in conjunction with their great length, suggest they may have formed from low viscosity basaltic lava [Basilevsky and Head, 2007]. The basaltic lava composition of these flows are consistent with the results obtained for a similar location from Venera 14 [Basilevsky and Head, 2002].

Smooth Plains comprise only a small percentage of the surface of Venus and are usually coupled with volcanic landforms, suggesting that they are fields of gently undulating lava flows [Basilevsky and Head, 2007]. Two types of smooth plains exist on Venus's surface, *amoeboids* and those associated with impact craters [Basilevsky and Head, 2000].

Amoeboid type smooth plains are defined by their "finger-like" sharp boundaries and are small featureless areas, although in some cases they contain slightly inclined shield volcanoes with summit craters (Figure 2.11) [Basilevsky and Head, 2000]. The boundaries of impact related smooth plains are not well defined as they are obscured by the fine ejecta associated with an impact (Figure 2.12) [Basilevsky and Head, 2000].

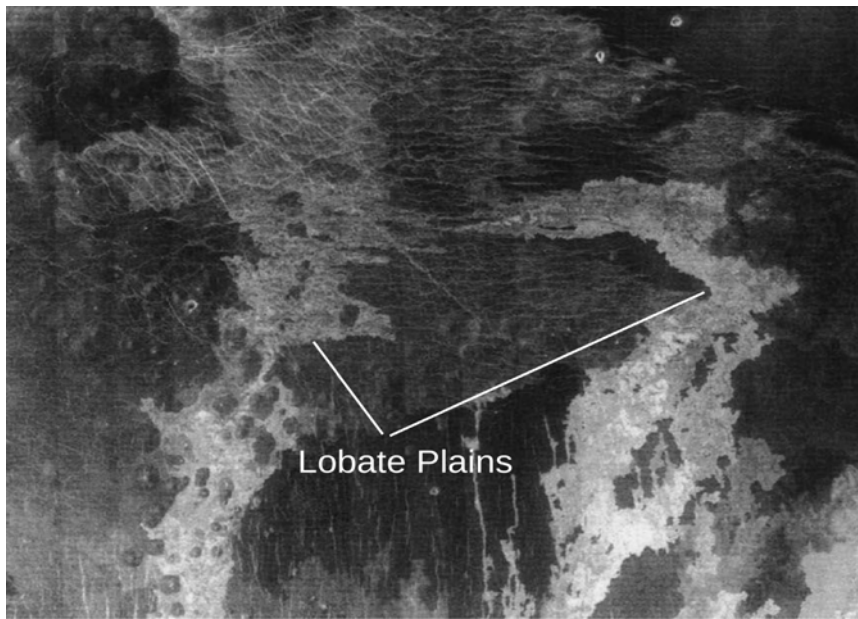


Figure 2.10. (Modified from *Basilevsky and Head, 2000*) Lobate plains, characterised by radar-bright flows dotted with radar-dark flows or "lobes". These lobate plains shown in this image radiate from the volcano Gula Mons, centered at 351.5°E 25.5°N and the area is ~220 km wide. Key is similar to Figure 2.2.

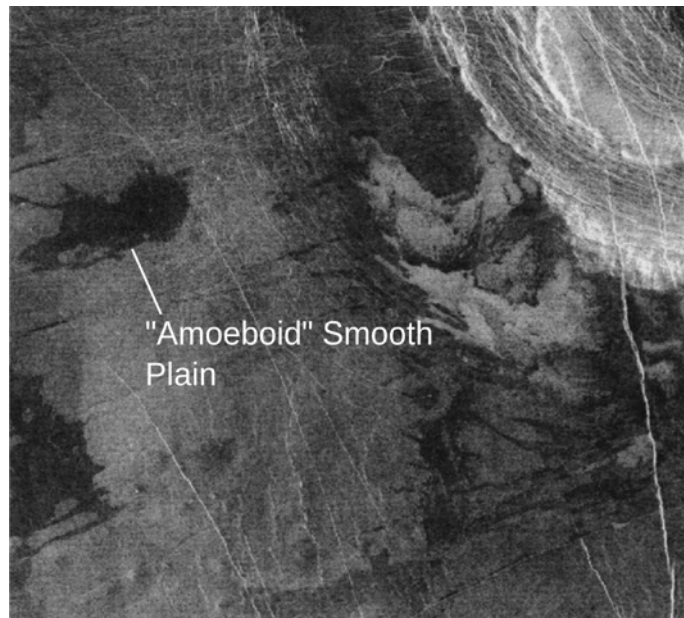


Figure 2.11. (Modified from *Basilevsky and Head, 2000*) Image showing the small, featureless, radar-dark *amoeboid* observed within a plains region centered at 85°E 27.7°S. Image width is ~130 km. Key is similar to Figure 2.2.

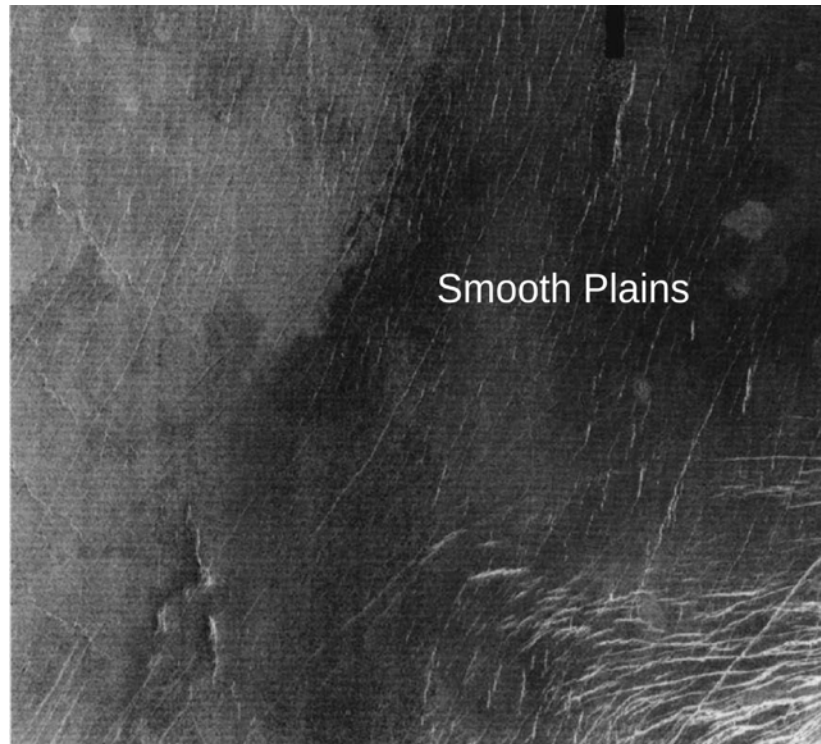


Figure 2.12. (Modified from *Basilevsky and Head, 2000*) The radar-dark smooth plains was most likely produced from the ejecta associated with the impact crater (located outside of the imaged area). Image width is ~220 km and is centered at 116.2°E 43.8°S. Key is similar to Figure 2.2.

Bindschadler et al. (1992) proposed that plains regions might be related to subsidence associated with young, asymmetric mantle downwellings, because the shape of these areas is generally circular, with bowl-shaped depressions when viewed in cross-section [*Bindschadler et al., 1992*]. The plains also correspond to negative gravity and geoid anomalies and lack associated hotspot structures such as coronae and volcanoes [*Bindschadler et al., 1992*]. Subsidence associated with downwellings would cause a negative gravity anomaly, since greater roots are required to compensate the subsidence. Subsidence on a sphere results in a decline in surface area resulting in compressional tectonism [*Bindschadler et al., 1992*]. However, compressional structures located over downwellings should be radial, which is not distinctly observed in these areas [*Bindschadler et al., 1992*].

2.2.8 Craters

Craters on the surface of Venus appear relatively pristine, with only ~281 and ~42 craters being disrupted by tectonic and volcanic deformation, respectively [Schaber *et al.*, 1992]. This suggests tectonic, volcanic, and weathering processes have not had a significant influence of the cratering record [Schaber *et al.*, 1992].

Similar to Mercury, Earth, Mars and the Moon, craters become more complex with increasing diameter [Herrick *et al.*, 1997]. Crater diameters of ~40 km usually mark the transition from a central peak crater to a ring crater [Schaber *et al.*, 1992]. Schaber *et al.* [1992] found that craters are uniformly distributed over Venus's surface and can occur as one of six types including multiple rings, double rings, central peaks, structure-less floors, irregular or multiple peaks. Multiple ringed, double ringed, central peaked, and peakless craters probably formed from the collision of high-velocity impactors with Venus's surface. This compares to irregular and multiple peaked craters that may have been produced from the concurrent collision of clustered fragments of a meteoroid [Schaber *et al.*, 1992].

2.3 The Venusian Interior

The radius, mass, density, and volume of Venus and Earth are comparable. This suggests that their interiors may be similar [Moore, 2002]. Venus should consist of a core, mantle and crust, similar to Earth (Figure 2.13) [Moore, 2002]. However, the current state of Venus's core is debatable and could be unsolidified, completely or partially solidified, or has yet to experience cooling and solidification [Solomatov and Zharkov, 1990]. The apparent lack of a magnetic field could be the result of Venus's slow rotation, lack of a liquid outer core or a metallic inner

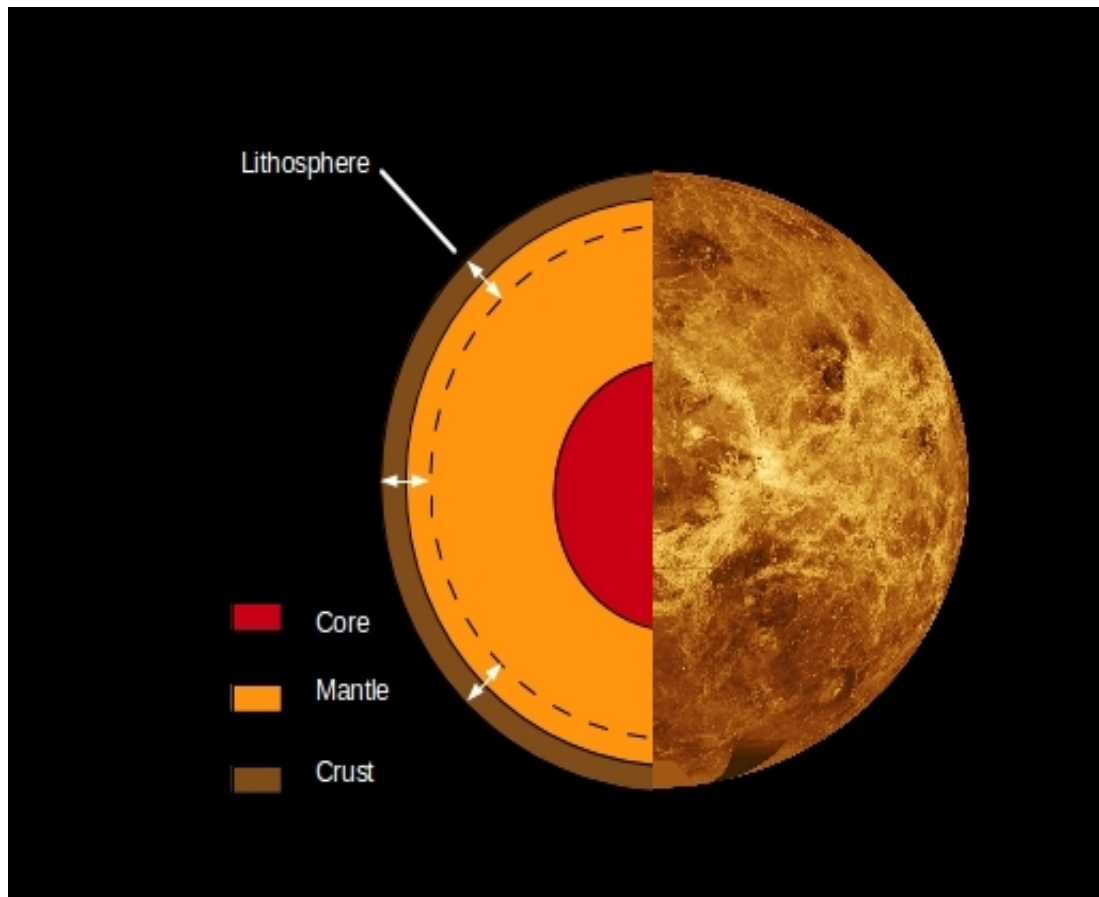


Figure 2.13. Image showing the interior structure of Venus, comprising a core, mantle, and crust. The lack of a magnetic field on Venus is suggestive of an absence of a liquid outer core or metallic inner core and the high correlation between geoid and topography anomalies implies Venus lacks an asthenosphere. The thermal lithosphere comprises the rigid outer portion of the crust and upper mantle, defined as the depth to the 1300°C isotherm.

core [Nimmo, 2002; Stevenson *et al.*, 1983].

The core extends for ~2940 km from the centre of Venus and is overlain by a dense mantle (Figure 2.13) [Moore, 2002]. The rock within the mantle moves via creep and convective motions act to transfer heat through the surface [Reese *et al.*, 1999; Schubert *et al.*, 1997]. The mantle is overlain by the crust, and from samples obtained by the Venera and Vega missions, is most likely basaltic in composition [Grimm and Hess, 1997]. The upper mantle and crust comprise the rigid portion of the lithosphere, where the thermal lithosphere is defined as the

depth to the 1300°C isotherm (Figure 2.13) [Fullea et al., 2009].

In comparison to Earth, Venus most likely lacks an asthenosphere between the crust and mantle. Without an asthenosphere or weak zone the mantle is strongly coupled to the crust, resulting in the high correlation of geoid and topography anomalies at the volcanic rises [Huang et al., 2013; Pauer et al., 2006; Phillips, 1990; Simons et al., 1997].

2.3.1 The Mantle

2.3.1.1 Mantle Composition

The mafic alkaline composition of the surface measured by Venera and Vega indicates Venus's mantle is anhydrous and carbonated compared to the usually uncarbonated and hydrated mantle composition of Earth [Huang et al., 2013; Kargel et al., 1993; Noack et al., 2012; Papuc and Davies, 2012; Smrekar and Sotin, 2012].

Despite these differences, the bulk composition and geochemistry of Venus's mantle is almost identical to Earth's suggesting nebular condensation, planetary accretion, and core formation were similar for both [Aitta, 2012; Elkins-Tanton et al., 2007; Kaula, 1995; Pham et al., 2011]. Furthermore, the planetary densities of Earth and Venus suggest they share similar core sizes and mantle compositions [Kargel et al., 1993].

Venusian surface compositions obtained from in situ analysis by the Verna and Vega landers resemble compositions of rocks obtained at Mid-Ocean Ridges (MOR) on Earth, implying Venus's iron oxide content in the mantle may be comparable [Grimm and Hess, 1997; Tackley, 2000; Shellnutt, 2013; Treiman, 2007]. Venera 14 and Vega 2 detected compositions similar to

normal mid-ocean ridge basaltic tholeiites (N-MORB) that are produced as a result of large degrees of partial melting of the mantle, which previously underwent melt extraction [Filliberto, 2014]. Venera 9 and 13, however, sampled compositions similar to Enriched MORB (E-MORB), which on Earth, are erupted on mid-ocean ridges that have been geochemically modified by neighboring hotspots [Filliberto, 2014; Nikolaeva and Ariskin, 1999].

Venera 10 and Vega 1 detected compositions of potassium, uranium, and thorium between both E and N MORB basalts [Kargel *et al.*, 1993]. The rocks sampled at these landing sites most likely formed from partial melting and fractionation from the mantle at high (> 1.8 GPa; Venera 13) pressure and low (< 0.2 GPa) pressure (Venera 14 and Vega 2) [Kiefer and Filiberto, 2009; Filiberto, 2009]. Rocks obtained at the Venera 13 landing site suggest Venus's mantle may not be totally devoid of water as rocks similar in composition require a hydrated mantle on Earth [Elkins-Tanton *et al.*, 2007; Filiberto, 2009; Namiki and Solomon, 1998]. The abundance of magnesia in the samples also indicated that fractional crystallization and crustal contamination was limited [Bonin, 2012; Hansen, 2007].

Venus, like Earth, is most likely differentiated based on the high potassium, uranium, and thorium abundances obtained by Venera 8 [Kargel *et al.*, 1993]. Venus's subchondritic ratios of potassium/thorium and potassium/uranium are also similar as Earth implying Venus did not undergo significantly higher volatile fractionation, even though Venus was closer to the Sun. This indicates Venus may have formed from intense "gravitational mixing" of planetesimals that existed within the inner Solar System before accretion [Tackley, 2000]. Venus may have also accreted less potassium compared to Earth as it condensed in a hotter part of the solar nebula [Kargel *et al.*, 1993].

Compositions measured by the Venera and Vega landers and radar imagery from Magellan imply most of Venus's surface is mafic in composition, suggesting these rocks were derived from partial melting of an ultramafic parent material, most likely the mantle [Shellnutt, 2013]. The degree of partial melting produced within a planet is determined by the elemental and mineral composition of the solid parent rock, the temperature, lithostatic pressure, and volatile concentrations [Nimmo and McKenzie, 1998]. For igneous rocks, the degree of partial melting also relies on the concentrations of potassium, uranium, and thorium [Nimmo and McKenzie, 1998]. Magma on Venus is most likely similar to that of Earth, being a partial melt of a peridotitic mantle comprising 80-231 ppm of potassium [Shellnutt, 2013].

One difference between the composition of Earth and Venus is the presence of water in the mantle [Grimm and Solomon, 1988; Kargel *et al.*, 1993; Kaula, 1995; Nimmo and McKenzie, 1998; Shellnutt, 2013]. The high surface temperatures and low partial pressure of water prevents it from being mixed into the interior causing a different petrologic and tectonic evolution on Venus, compared to Earth [Shellnutt, 2013].

Even though Venus's mantle may lack water, other volatiles could exist [Chassefière *et al.*, 2012]. For example, carbon dioxide abundances within Venus's mantle may be greater as the high surface temperatures and elevated carbon dioxide surface pressures permit in situ carbonate weathering of igneous rocks. The resulting carbon dioxide is incorporated into the crust and mantle causing a carbonated peridotitic Venusian mantle [Chassefière *et al.*, 2012; Kargel *et al.*, 1993]. These conditions are effective in producing alkaline mafic magmas compared to the hydrated peridotitic mantle of Earth, which results in siliceous magmas. The additional carbon dioxide within the interior of Venus depresses the peridotite liquidus and solidus of the mantle allowing small degrees of partial melting at low temperatures. Carbon dioxide can react with calcium and magnesium found in olivine and clinopyroxene effectively

moving the low-temperature liquidus to mafic or ultramafic compositions and, in turn, producing alkaline mafic melt [Kargel *et al.*, 1993].

2.3.1.2 Thermal State and Convective Regime

The concentrations of uranium, thorium, and potassium within Venus's mantle are assumed to be similar to those of Earth, with the heat produced from the decay of these radioactive elements fundamental for our understanding of the thermal state of the mantle [Aitta, 2012; Chassefière *et al.*, 2012; Elkins-Tanton *et al.*, 2007; Kargel *et al.*, 1993; Kaula, 1995; Pham *et al.*, 2011]. The style and rate of heat transfer have not been directly measured on Venus, however, using Earth scalings, Schubert *et al.* [1997] proposed the current heat loss from Venus is 2.91×10^{13} W and the average heat flow through the surface is 63 mWm^{-2} .

Heat loss through Venus's surface is an important mechanism, driving not only thermal convection within the mantle, but also tectonism and volcanism, while contributing to the current topography and gravity anomalies [Reese *et al.*, 1999; Schubert *et al.*, 1997]. Venus's lack of plate tectonics implies it is within a different convective regime than Earth [Huang *et al.*, 2013]. Convective regimes operating within Venus could include sluggish-lid, stagnant lid or episodic [Moresi and Solomatov, 1998; Orth and Solomatov, 2011; Reese *et al.*, 1999; Schubert *et al.*, 1997, Turcotte, 1993].

Sluggish-lid convection involves disseminated deformation of a weak, viscous lid, and this mobility may, depending on strain rates, permit significant horizontal advection, as per plate tectonics on Earth. In contrast, a stagnant-lid regime is characterised by conductive heat loss through an immobile lithosphere [Schubert *et al.* 1997]. Within the episodic convective regime, periods of stagnant-lid convection are intermingled with periods of tectonics and heat

loss [Moresi and Solmatov, 1998; Turcotte, 1993].

Due to the lack of evidence for large-scale volcanism and tectonism, Venus is most likely within the stagnant-lid regime and/or a quiescent period of the episodic regime [Reese *et al.*, 1998; Turcotte, 1993]. A stagnant-lid regime arises when a viscosity contrast of $> 10^4$ occurs between the surface and interior, making the lid rigid and stable enough to resist overturning (Figure 2.14) [Reese *et al.*, 1998; Solomatov, 1995]. Reese *et al.* [1999] found that viscosity at the base of the lithosphere contributed more to this convective regime than that of the underlying mantle. Compared to a mobile-lid regime, the convective mantle of a planet within a stagnant-lid regime must convect more rapidly in order to maintain an equal rate of heat transfer [Reese *et al.*, 1998; 1999]. These authors found a stagnant-lid regime, without large scale melting, results in conductive heat flows of 20 mWm^{-2} and are insufficient to cool the interior [Reese *et al.*, 1998].

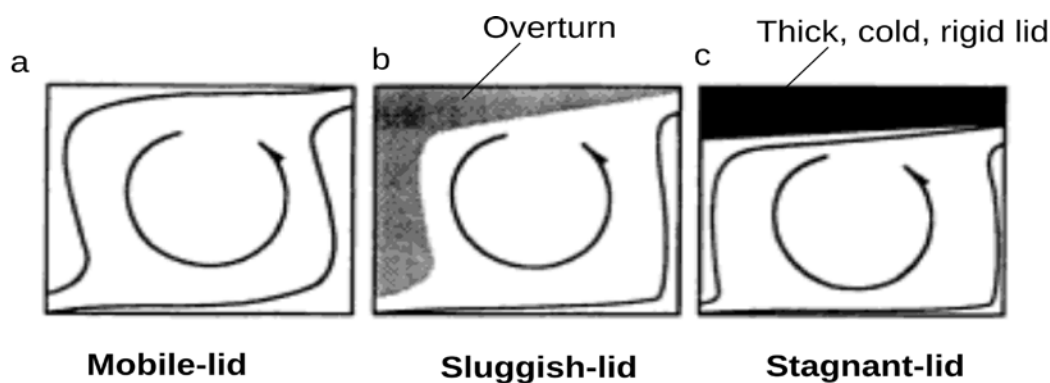


Figure 2.14. (Modified from Schubert *et al.*, 1997) The convective regime of Venus's mantle depends on the viscosity contrast between the mantle and lid. A) A small viscosity contrast results in mobile-lid convection, but increases to a sluggish-lid (B) as the viscosity contrast is increased. C) When the viscosity contrast is large enough a stagnant-lid regime is produced.

Venus's last global resurfacing may have been the result of an episodic convective regime, which is characterised by catastrophic lid overturns and volcanism interspersed with periods of quiescence [Orth and Solomatov, 2011; Pauer *et al.*, 2006; Schubert *et al.*, 1994; Smrekar

and Phillips, 1991; Solomatov and Moresi, 1996; Turcotte, 1993]. In an episodic convective regime the mantle is initially hotter and less viscous facilitating subduction of the lithosphere. This subduction is effective in lowering the temperature of the interior and slowing the vigour of convection, which causes the lithosphere to cool, thicken, and stabilise. As a result of the reduced heat loss, the interior heats up and the plume flux increases [Turcotte, 1993]. The thick lithosphere, which was already becoming unstable due to its negative buoyancy, is disturbed by this higher plume flux, starting a new period of activity [Turcotte, 1993].

Episodic overturns were found to occur within a stagnant-lid regime if the lithosphere is brittle and the yield stress was surpassed within the majority of the lid [Fowler and O'Brien, 1996; Solomatov and Moresi, 1996]. The friction coefficient may also play a role in episodic convection and is most likely higher on Venus compared to Earth due to a lack of volatiles, which makes it harder for the lithosphere to become mobile [Moresi and Solomatov, 1998].

Most authors [Orth and Solomatov, 2011; Pauer et al., 2006; Schubert et al., 1994; Smrekar and Phillips, 1991; Solomatov and Moresi, 1996; Turcotte, 1993] have suggested Venus is within either a stagnant-lid or episodic mode of convection, but Ratcliff et al. [1997] found a sluggish-lid regime produced convective structures similarly dispersed to geological structures observed on the surface. From 3D spherical shell convection models with temperature-dependent viscosity, these authors found lateral variations in viscosity altered the shape of the convective structures and vertical variations in viscosity impacted the lateral size of the convective structures. One unexpected result of this study was that the high viscosity variations (10^4) used for each model produced a sluggish-lid convective regime, rather than the expected stagnant-lid convective regime. This disparity was due to non-Newtonian viscosity or nonviscous lithospheric modification, which operated to decrease the total viscosity contrast between the lid and mantle and reduce the "effective" viscosity of the

lithosphere [Christensen, 1984; Ratcliff et al., 1997].

2.3.1.3 Mantle Parameters and Their Influence on the Evolution of Venus's Mantle

Steinbach and Yuen [1992] addressed the influence of phase transitions on the dynamics and evolution of Venus's mantle. Venus and Earth share similar properties and may have comparable exothermic (olivine to spinel) and endothermic (spinel to perovskite) phase transitions [Steinbach and Yuen, 1992]. However, these transition zones were suggested to occur at 490 km and 690 km, respectively, compared to those on Earth (410 km and 670 km), since Venus's elevated surface temperatures (730 K) and reduced pressure gradients (by ~10%) act to increase the depths and decrease the depth variations between the two zones [Steinbach and Yuen, 1992].

These phase boundaries were found to have important implications for evolutionary modelling of Venus's mantle since the exothermic boundary was associated with layered flow and episodic high heat flow [Steinbach and Yuen, 1992]. A large enough release of heat may have caused Venus's last catastrophic overturn resulting in a cooler interior, less vigorous, whole mantle convection, which may occur today [Steinbach and Yuen, 1992]. *Steinbach and Yuen* [1992] proposed the last catastrophic overturn event was a result of a change from layered to whole mantle convection, whereas *Weinstein* [1996] found that "avalanches" associated with the endothermic phase change, propagated by non-Newtonian rheology, may have caused Venus's last resurfacing.

However, this transition from layered to whole mantle convection is unable to explain the lack of recent large scale tectonic activity observed on Venus [Weinstein, 1996]. On Earth, plate tectonics is associated with a mobile-lid convective regime characterised by high Rayleigh

numbers ($> 10^6$) and a hydrated mantle [Schubert *et al.*, 2001]. Therefore, the lack of plate tectonics on Venus may be caused from an anhydrous mantle, a sluggish or stagnant-lid convective regime characterised by lower Rayleigh numbers ($< 10^6$) and a thick, rigid lithosphere that is unable to subduct [Schubert *et al.*, 2001].

The endothermic and exothermic phase changes and depths were also included in modelling completed by Huang *et al.* [2013]. However, these authors used global 3D spherical shell and constrained their results to global Venusian topography and geoid spectra. In addition to phase changes, the effects of varying the Rayleigh number, pre-exponential factor, and internal heating were also addressed [Huang *et al.*, 2013]. The best fit model to the observed topography and geoid spectra involved a Rayleigh number of 1.8×10^7 , a Clapeyron slope of $+3.5$ for the exothermic phase transition and -3.5 MPa K^{-1} for the endothermic phase transition, a non-dimensional pre-exponential factor of 1, and internal heating of 40 [Huang *et al.*, 2013]. The endothermic phase change promoted a reasonable number of long-wavelength mantle plumes [Huang *et al.*, 2013]. Similar to the previous authors, Huang *et al.* [2013] found the endothermic phase change had the greatest contribution to mantle convection, however they suggested that minor heat release was associated with this transition, which was not enough to promote catastrophic reworking of Venus's surface. One parameter that was not addressed by Huang *et al.* [2013] was activation energy. Activation energy has important implications for the temperature-dependent viscosity and style of creep within the mantle [Schubert *et al.*, 2001; Zhong *et al.*, 2008].

Benešová and Čížková [2012] also used 3D spherical models and depth-dependent viscosity to constrain the internal dynamics of Venus to observed topography and geoid spectra. These authors addressed the viscosity structure within the interior of Venus and the effects of internal heating and Rayleigh number on mantle dynamics. A model involving a 200 km thick thermal

lithosphere, upper mantle viscosity of 2×10^{21} Pa s and a steady increase in viscosity with depth, provided the closest fit to the observed topography and geoid spectra [Benešová and Čížková, 2012].

Schubert et al. [1997] used 3D spherical shell models with an exothermic and endothermic phase change at depths of 440 km and 740 km, respectively. However, these models did not assume stagnant-lid convection or strongly temperature dependent viscosity [*Schubert et al.*, 1997]. From their first model, which included phase changes, *Schubert et al.* [1997] found the mantle was composed of three regions: (1) downwelling planforms, where cold material accumulated at the endothermic transition (above 740 km); (2) upwellings and downwellings, between 740 km to 2000 km; and (3) extensive globules of cold material, dissected by narrow hot material, overlying the core-mantle-boundary (CMB) [*Schubert et al.*, 1997]. These authors then constrained their modelled topography and geoid to Venus's observed data and found that the most realistic boundary condition was between the free-slip and rigid cases [*Schubert et al.*, 1997]. In the second set of models, temperature-dependent viscosity was included with a rigid lid forming due to a significant viscosity contrast between the mantle and lithosphere [*Schubert et al.*, 1997]. At large viscosity contrasts of 10^4 - 10^5 a stagnant-lid formed and was dominated by small wavelength upwellings and downwellings [*Schubert et al.*, 1997]. Combining both phase changes and temperature-dependent viscosity, with a rigid-lid, lead to more layered mantle convection, decreasing the amount of heat transferred, compared to models involving constant viscosity and whole-mantle convection [*Schubert et al.*, 1997].

All of these previous models study thermal convection only and do not evaluate the effects of compositional buoyancy on mantle convection. *Dupeyrat and Sotin* [1995] model both thermal and compositional buoyancy associated with mantle differentiation and

heterogeneities, arising from a depleted mantle or the change of basalt into eclogite at depths greater than 50 km. In each of these cases a trade-off occurs between thermal and compositional buoyancy. In the first case the depleted mantle has a lower density occurring near the surface and mitigates downwellings. The depleted mantle that is transported to the base of the upper mantle will produce new upwellings and areas of partial melt due to chemical buoyancy [Dupeyrat and Sotin, 1995]. The decrease in mobility of the top layer and the trade-off between thermal and compositional buoyancy reduces heat flow through the surface and the transport of heat and mass within the interior [Dupeyrat and Sotin, 1995]. However, the converse is true when the transition of basalt into eclogite is included. In this case the dense eclogite permits downwellings and crustal overturn, while the compositional upwellings are reduced, resulting in greater heat and mass transfer, and low internal temperatures [Dupeyrat and Sotin, 1995]. It should be noted that these authors did not include temperature-dependent viscosity in their models, which would act to hinder the recycling of the lower crust [Armann and Tackley, 2012].

Temperature-dependent viscosity, in conjunction with compositional buoyancy and its effect on Venus's mantle convection, were addressed by Ogawa [2000]. In these models, the highly viscous lid participated in overturning and the reworked material accumulated at the base of the endothermic phase transition and altered the chemical layering in this zone [Ogawa, 2000]. As a result, "flushing events" occurred where large quantities of hot lower mantle was transported into the upper mantle, possibly causing resurfacing events and volcanic plains formation [Armann and Tackley, 2012; Ogawa, 2000].

Armann and Tackley [2012] addressed the thermochemical evolution of Venus using 2D stagnant-lid and episodic convection models. These models were constrained to Venus's observed topography, gravity, and surface history [Armann and Tackley, 2012]. An episodic

regime, instead of a stagnant-lid regime was the most consistent with observations, where resurfacing was initiated at regions of volcanically thickened crust before spreading globally [Armann and Tackley, 2012]. These models, unlike those of Turcotte [1993], result in a thin lithosphere and the maintenance of underlying mantle convection during periods of decreased activity. Within this regime, basalt was depleted within the upper mantle, causing the solidus to increase, which allowed the upkeep of a nearly constant heat flow through the surface and thinning of the lithosphere during quiescent periods [Armann and Tackley, 2012].

2.3.1.4 Mantle Plumes

Venus's lack of evidence for terrestrial plate tectonics could suggest that "intraplate" volcanism occurs, dominated by mantle plumes below a stagnant lid [Ernst and Desnoyers, 2004]. However, due to a possible stagnant-lid regime and higher viscosity mantle associated with the lack of volatiles, this "intraplate" volcanism may be different to what is observed on Earth [Ernst and Desnoyers, 2004]. In order to significantly transport enough heat through Venus's surface ~80 mantle plumes, each with a similar strength to the terrestrial Hawaiian plume ($3.6 \times 10^{11} \text{W}$) would be required [Schubert et al., 1997]. However, only nine or ten hotspots similar to the strength of the Hawaiian plume may be active at Venus's volcanic rises [Basilevsky and Head, 2007; Brian et al., 2004; Ivanov and Head, 2010; Smrekar et al., 2010; Smrekar and Sotin, 2012; Stofan et al., 1995; 2005]. Smaller plume conduits may also contribute to the support of Venus's 168 large (100 km - 1000 km diameter) volcanoes or 500 coronae [Ernst et al., 2007].

On Earth, mantle plumes should comprise a large head and narrow conduit tails, which require large viscosity variations ($>10^2$) within the hot thermal boundary layer to initiate upwelling (Figure 2.15) [Jellinek et al., 2002]. Jellinek et al. [1992] propose that these large viscosity

contrasts required for Earth's mantle plumes arises from cooling, associated with recycling of Earth's crust. Venus experiences minor cooling from a lack of plate tectonics, therefore the viscosity contrast at the hot boundary layer should be lower [Jellinek *et al.*, 2002]. Therefore, Venus's plumes should consist of large heads or "thermals" without narrow conduit tails (Figure 2.15) [Jellinek *et al.*, 2002]. The difference in structure of plumes on Venus could be important for the formation of corona and the lack of a magnetic field [Jellinek *et al.*, 2002].



Figure 2.15. (Modified from Jellinek *et al.*, 2002) Mantle plumes on Venus comprise a "thermal" and lack a narrow conduit, like those proposed for Earth.

Observations of coronae and surface age estimates can also reinforce the absence of Earth-like mantle plumes on Venus [Jellinek *et al.*, 2002]. Coronae usually have small diameters and since the surface of Venus is relatively young (~500 Myr), proposed coronae do not overlie plume tails, since they do not increase in size over time [Head *et al.*, 1992; Jellinek *et al.*, 2002; Nimmo and McKenzie, 1998].

2.3.1.5 Surface Manifestations of Mantle Plumes

Volcanic rises have been proposed by multiple authors to be the surface manifestation of an upwelling mantle plume based on expansive, domical shaped topography, large geoid anomalies (35 to 120 mGal), large ADCs, high GTRs, presence of extensive volcanism and

rifts [Bindschadler *et al.*, 1992; Pauer *et al.*, 2006; Phillips *et al.*, 1991; Smrekar and Phillips, 1999; Stein *et al.*, 2010; Steinberger *et al.*, 2010]. The shape of these rises, their diameters and the elevated topography, are consistent with the shape, diameter, and buoyancy of a plume head [Bindschadler *et al.*, 1992; Olson *et al.*, 1993].

Other large, isolated volcanoes, also have a similar morphology to the volcanoes associated with “thermals”, but lack rifts and geoid highs [Ernst and Desnoyers, 2004]. Mapping of graben fissures within this area (Guinevere Planitia-Beta Regio), found extensive (1000 km radius) radiating graben fissure networks, which could depict large dyke networks associated with the impingement of a “thermal” at the base of the lithosphere [Ernst and Buchan, 2003]. A lack of rifting and geoid highs could also represent older “thermals”, where topographic uplift and the associated thermal anomalies have declined [Ernst and Buchan, 2003].

From observations of topography, geoid, GTRs, and melt volumes at volcanic rises, the evolution of a mantle plume can be indirectly determined [Phillips *et al.*, 1991; Smrekar and Parmentier, 1996]. Particularly, the GTRs are important to determine how active a plume is, since this value will gradually decline over time [Phillips *et al.*, 1991; Smrekar and Parmentier, 1996].

A plume initially forms as a result of convective instability along the basal thermal boundary, and if hot material is transferred into the plume at a greater rate than the plume's ascent, a head will form [Phillips *et al.*, 1991; Smrekar and Parmentier, 1996]. Before the plume impinges onto the base of the lithosphere a high GTR occurs, with minimal topography and volcanism, due to extreme lithostatic pressures (Figure 2.16a) [Phillips *et al.*, 1991; Smrekar and Parmentier, 1996]. The plume head ascends to the base of the lithosphere, with the resulting stresses inducing rifting, pressure-release melting, widespread volcanism, and crustal

formation (Figure 2.16b) [Herrick and Phillips, 1992; Phillips, 1990; Phillips *et al.*, 1991; Smrekar and Parmentier, 1996]. When the plume head begins to level out, the drop in buoyancy pressure results in a decrease in dynamic uplift, gradual drop in GTR, and topographic subsidence (Figure 2.16c) [Phillips *et al.*, 1991; Smrekar and Parmentier, 1996]. The remaining topography not supported by dynamic uplift can be supported by crustal thickening or thermal lithospheric thinning [Morgan and Phillips, 1983; Phillips *et al.*, 1991].

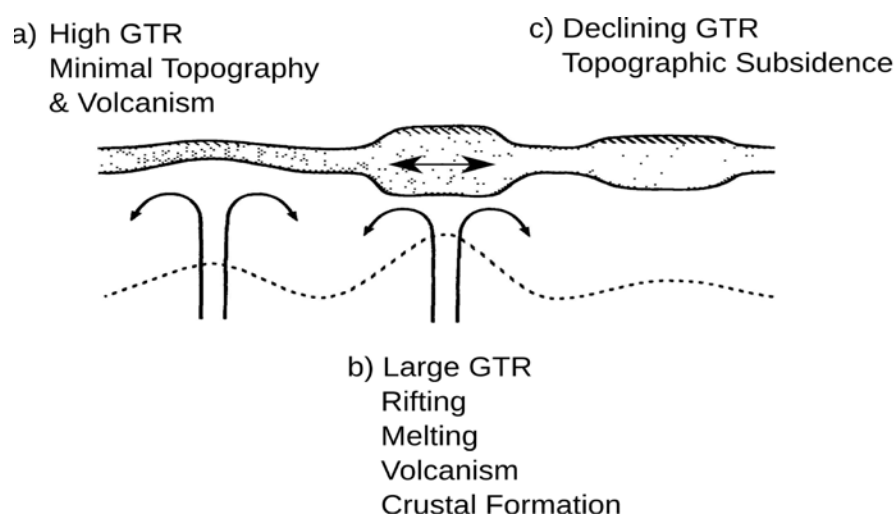


Figure 2.16. (Modified from Phillips *et al.*, 1991) The evolution of a mantle plume can be indirectly found from the features observed on the surface. A) The plume impinges onto the lithosphere and produces a high GTR, with limited topography and volcanism. B) The area undergoes dynamic uplift resulting in a high GTR, rifting, volcanism, and thick crust. C) As the plume dwindles, the GTR decreases and the topography subsides.

Recently, Venus Express used the Visible and Infrared Thermal Imaging Spectrometer (VIRTIS) to image three of these volcanic rises (Imdr, Themis, and Dione Regiones) [Smrekar *et al.*, 2010]. These rises correspond to high emissivity volcanic flows, suggesting these features are young, possibly volcanically active and sustained by mantle plumes [Smrekar *et al.*, 2010]. These authors proposed the large topographic rises on Venus were formed by primary plumes originating from the core-mantle boundary, with coronae being the result of

secondary plumes. When a large plume interacts with the upper-lower mantle boundary it can generate smaller plumes within the upper mantle, producing coronae [Stofan and Smrekar, 2005]. Venus most likely has 9 or 10 primary plumes, however 513 coronae were observed by Stofan and Smrekar [2005], with each being proposed as a possible secondary hotspot and plume.

2.3.2 The Thermal Lithosphere

2.3.2.1 Crustal Composition

Direct evidence for the composition of rocks on Venus's surface arose from the Vega and Venera landers [Grimm and Hess, 1997]. The uranium and potassium ratios occur within a similar range i.e. a factor of 3. These results suggest that metamorphic processes acting on Venus have not changed compositions of uranium, thorium, and potassium significantly via metasomatism; therefore potassium and uranium ratios could depict original bulk compositions [Grimm and Hess, 1997].

The composition of Venus's crust is likely to be basaltic (mafic composition), based on major oxide compositions and observations of the morphology of volcanoes [Grimm and Hess, 1997]. For example, shield volcanoes and their widespread flow deposits suggest low-viscosity, effusive eruption of lavas indicative of basalts [Head et al. 1992]. Uncertainty however, is inherent in this assumption due to; 1) large analytical errors; 2) the samples may represent soil produced via physical weathering and not pristine bedrock; 3) the samples could represent metamorphosed rocks that have had original minerals altered [Grimm and Hess, 1997].

2.3.2.2 Crustal Thickness

Based on Venus's relatively gentle hypsometry, *Grimm and Hess* [1997] suggested crustal thickness should not vary remarkably, except within the tessera areas. Other authors have also proposed thicker crust (35-60 km) is associated with tessera terrain [*Kucinskas and Turcotte*, 1994; *Nimmo and McKenzie*, 1998; *Simons et al.*, 1994; *Grimm*, 1994; *Zuber*, 1987], however, some suggest volcanic rises and plains regions will have a thinner crust, between 20-50 km and 10-40 km, respectively [*Konopliv and Sjogren*, 1994; *Grimm and Solomon*, 1988; *Nimmo and McKenzie*, 1998; *Phillips*, 1994; *Smrekar*, 1994].

Kucinskas and Turcotte [1994] proposed GTRs and compensation depths at each highland reflect different support mechanisms. Airy isostasy alone, via a crustal thickness of 50-60 km, was able to support the minor GTRs ($\sim 9 \text{ m km}^{-1}$ and $\sim 11 \text{ m km}^{-1}$) in Ovda and Thetis Regiones. Higher GTR areas, such as chasmata and the volcanic rises, produced an unlikely crustal thickness $> 160 \text{ km}$ [*Kucinskas and Turcotte*, 1994]. Using Airy isostasy alone, these authors proposed a combination of thermal thinning and crustal thickness variations support these areas [*Kucinskas and Turcotte*, 1994] .

Zuber and Parmentier [1990] also used Airy isostasy to determine the effects of crustal thickness variations on the isostatic elevation and short wavelengths ($\leq 30 \text{ km}$) of selected tessera terrain. From the first case of *Zuber and Parmentier* [1990], which involved a weak upper crust underlain by a strong upper mantle, the wavelengths between two adjacent features was reduced with higher elevations associated with a high thermal gradient (Table 2.2). However, broader distances were found to produce higher elevations due to a thicker crust (Table 2.2) [*Zuber and Parmentier*, 1990]. The second case assumed a strong upper crust was underlain by a weak upper mantle and showed a similar response as the previous case

[Zuber and Parmentier, 1990]. Increasing crustal thickness, however, had no effect on the wavelengths of features, but resulted in higher elevations (Table 2.2) [Zuber and Parmentier, 1990]. Zuber and Parmentier [1990] used this information to suggest that the different wavelengths of tessera observed within Fortuna Tessera was a result of variable crustal thickness directly relating to changes in elevation. However, they do note that this area may have been influenced by other processes such as thermal thinning and dynamic uplift.

Table 2.2* Influence of Thermal Gradient and Crustal Thickness

	Increasing Thermal Gradient	Increasing Crustal Thickness
Weak upper crust, strong upper mantle		
Isostatic Elevation	Increases	Increases
Wavelength	Decreases	Increases
Strong upper crust, weak upper mantle		
Isostatic Elevation	Increases	Increases
Wavelength	Decreases	Steady

*Modified from Zuber and Parmentier, [1990].

James *et al.* [2013] used a two-layered crustal thickness inversion and a reference crustal thickness of 15 km to propose Venus's average crustal thickness ranged between 8-25 km for a thermal gradient $< 15^{\circ}\text{C km}^{-1}$. Grimm and Solomon [1988] also proposed crustal thickness variations below craters may be representative of an average global crustal thickness since they share a similar elevation to the expansive plains regions. By constraining a viscous relaxation model to observed crater elevations, they used a 10 K km^{-1} thermal gradient and a weak lower crust to propose the crust was between 10-20 km thick [Grimm and Solomon, 1988]. This compares to Zuber [1987] who used the wavelengths of tectonic features to

determine an average crustal thickness ≤ 30 km, considering a thermal gradient ≤ 25 K km⁻¹, a weak lower crust and strong upper mantle.

Additionally, studies of Venus's global gravity spectral admittance suggest average crustal thickness should could range from 20-50 km, but is most likely around 30 km [Grimm and Hess, 1997]. However, this study infers the higher degree topography spherical harmonics are compensated by crustal processes only and not flexural or shallow mantle processes, possibly inflating these crustal thickness estimates [James *et al.*, 2013]. Each of these crustal thickness studies did not evaluate the effects of a dry rheology, and the associated large differential stress, on crustal thickness estimates [Mackwell *et al.*, 1998].

2.3.2.3 Lithospheric Rheology

Mackwell *et al.* [1998] simulated dry Venusian conditions to observe the high-temperature creep behaviour of diabase (a basaltic rock) to infer a model for the rheology of Venus's lithosphere, consistent with the dry basaltic compositions detected by the Venera and Vega landers. Dry diabase samples were taken from Columbia, South Carolina, Fredrick, and Maryland [Mackwell *et al.*, 1998]. The stress exponent n was determined for Columbia diabase ($n=4.8\pm0.6$) and Maryland diabase ($n=4.7\pm1.0$), accurate for dislocation-controlled creep [Mackwell *et al.*, 1998]. The mean activation energy Q for this creep was also determined for the Columbia diabase ($Q=488\pm35$ kJ mol⁻¹) and Maryland diabase ($Q=482\pm25$ kJ mol⁻¹) [Mackwell *et al.*, 1998].

Mackwell *et al.* [1998] simulated the past lithospheric structure of Venus via a model, which used a strain rate of $10\text{-}14$ s⁻¹, a crustal thickness of 7 km, a thermal gradient of 30 K km⁻¹ and a surface temperature of 470°C . A significant strength difference resulted across the crust-

mantle boundary, inferring significant decoupling [Mackwell *et al.*, 1998]. Therefore, formation of older, smaller tectonic features such as tessera can be supported by this model since a thin, strong upper crustal layer occurred above a weaker lower crust and strong upper mantle (Figure 2.17; SWS rheology or “jelly sandwich”) [Mackwell *et al.*, 1998].



Figure 2.17. (Modified from Burov and Watts, 2006) Cartoon showing a "Jelly Sandwich" rheology defined as a strong upper crust, underlain by a weak lower crust, and strong upper mantle. The weak lower crust acts to decouple the upper crust from the lithospheric mantle.

Mackwell *et al.* [1998] also simulated Venus's current lithospheric structure. In this model, a strain rate of $10\text{--}15\text{ s}^{-1}$, a crustal thickness of 15 km, a constant thermal gradient of 20 K km^{-1} and a surface temperature of 470°C was used. This resulted in a strong crust and a strong mechanical coupling between the crust and upper mantle, due to an absence of a significant strength variation across this boundary, inferring the absence of an underlying asthenosphere [Mackwell *et al.*, 1998]. A lower thermal gradient was also found to result in a strong lithosphere, where the upper mantle made a greater contribution to lithospheric strength [Mackwell *et al.*, 1998].

2.3.2.4 Lithospheric Thickness

Venus's lithospheric thickness is highly unconstrained with previous estimates varying from ~100 km at volcanic rises [Kucinskas and Turcotte, 1994; Moore and Schubert, 1997; Phillips, 1994], to global average estimates of ~100 km [Nimmo and McKenzie, 1996, 1998; Schubert *et al.*, 1994; Smrekar, 1994; Smrekar and Phillips, 1991], or up to 300-600 km, if an episodic or stagnant-lid convective regime is modelled [Orth and Solomatov, 2011; Solomatov and Moresi, 1996; Turcotte, 1993].

Schubert *et al.* [1997] suggested Venus's lithosphere is thin, based on calculations of the amount of heat transferred by conduction. Assuming a heat flux of 63 mW m^{-2} and a thermal conductivity of $3.3 \text{ W m}^{-1}\text{K}^{-1}$, the average thermal gradient and lithospheric thickness for Venus was found to be 19 K km^{-1} and 45 km, respectively [Schubert *et al.*, 1997]. Schubert *et al.* [1997] proposed this estimate may yield a larger lithospheric thickness if a higher number of radioactive elements are located in the lithosphere, or the thermal conductivity is greater for Venus.

The high GTRs of $\sim 25 \text{ m km}^{-1}$ and $\sim 32 \text{ m km}^{-1}$ for Atla and Beta Regio, lead Kucinskas and Turcotte [1994] to propose an initially 300 km thick thermal lithosphere was thinned to ~88 km and ~113 km at these rises, respectively. A further study in Ishtar Terra found that the GTR of $\sim 20 \text{ m km}^{-1}$ and $\sim 8 \text{ m km}^{-1}$ at Lakshmi Planum and Western Fortuna Tessera might be suggestive of the thermal thinning of a 300 to 400 km thick lithosphere to ~100 km [Kucinskas and Turcotte, 1994]. This thermal isostasy has less of a contribution moving eastwards, possibly inferring lithospheric delamination events were active towards the west. These authors noted that thermal isostasy within these areas may not arise from thinning, but from partial melting of a thick crust if a reasonable amount of radiogenic elements occur

within this layer [*Kucinskas and Turcotte, 1994*].

Moore and Schubert [1997] applied both a slow-thinning and two layer model to determine the lithospheric thickness below selected volcanic rises. By applying regression analysis to geoid and topography data sets, they inferred the resulting negative curvature was due to lithospheric thinning [*Moore and Schubert, 1997*]. The original lithospheric thickness of ~331 km for Atla Regio and ~396 km for Beta Regio were slowly thinned to minimum values of 88 km and 293 km, respectively in an attempt to fit the highest topography at these areas [*Moore and Schubert, 1997*].

The thermal lithospheric thickness below volcanic rises was also addressed by *Smrekar and Parmentier* [1996]. In this study, they used numerical modelling, in conjunction with temperature dependent viscosity and pressure release melting. They found a model with a thermal lithosphere of 100 km, underlain by 100-250 km thick depleted mantle layer, provided the most consistent results with GTRs, surface uplift, and melt volume estimates [*Smrekar and Parmentier, 1996*].

Based on ADCs and GTRs, *Smrekar and Phillips* [1991] and *Schubert et al.* [1994] studied selected Venusian highland areas, chasmata, and coronae to infer the ambient thermal lithospheric thickness on Venus is ~100 km thick. ADCs, however, may not be the most appropriate constraints on lithospheric thickness [*Nimmo and McKenzie, 1998*], with some authors showing that both depth-dependent and temperature-dependent viscosity can reduce the ADCs and can influence the resulting lithospheric thickness [*Moresi and Solomatov, 1998*; *Nimmo and McKenzie, 1998*; *Robinson et al., 1987*].

Nimmo and McKenzie [1996] suggested melt generation rates might be more useful to

constrain mechanical and thermal lithospheric thicknesses at volcanic rises. Using both a high (1336°C) and low (1163°C) potential temperature case they found that the thickness of the mechanical and thermal lithosphere should range between 20-150 km and $< \sim 170$ km, respectively, in order to match the possible melt generation rates.

Average lithospheric thicknesses may be much larger (200 to 400 km) if a numerical model involving temperature dependent viscosity and stagnant-lid convection are used [Solomatov and Moresi, 1996]. Within this model, the stagnant lithosphere experienced thermal thinning, however, a discrepancy existed with the rise experiencing a thicker thermal lithosphere (up to 550 km) than the average (200 to 400 km) [Solomatov and Moresi, 1996]. These results are inconsistent with previous authors [Kucinskis and Turcotte, 1994; Moore and Schubert, 1997; Phillips, 1994] who suggest that the volcanic rises are sites of mantle upwelling, which lead to thinner thermal lithosphere estimates compared to the global average.

Orth and Solomatov [2011] used an Isostatic Stagnant Lid (ISL) approach to evaluate the contribution of thermal thinning in producing the global topography and geoid of Venus. In the ISL approximation, topography and gravity can determine both the changes to the regional and mean lithospheric thickness, if the lid is within isostatic equilibrium. The amount of lithospheric thinning was varied between 5% to 75%, and in areas of high topography the amount of thermal thinning was limited to reasonable observations by the addition of a thick crustal layer [Orth and Solomatov, 2011]. The model that provided the best fit to Venus's topography and geoid had a very thick (560 km) lithosphere and involved lithospheric thinning of 50%, and a 50 km thick reference crust [Orth and Solomatov, 2011]. Both the amount of lithospheric thinning assumed and the global mean crustal thickness were found to have the greatest influence on the resulting mean lithospheric thickness [Orth and Solomatov, 2011].

Turcotte [1993] also suggested Venus's thermal lithosphere is ~300 km thick. This author used a simple half-space cooling model to infer the thickness of the lithosphere over time under an episodic convective regime [*Turcotte*, 1993]. This simplistic method relied on heating from below the lithosphere by an upwelling, delamination of the lithosphere, < 20% of radiogenic isotopes reside within the crust, and that the lithosphere is thinner than the mantle [*Turcotte*, 1993]. This background lithospheric thickness was used in a simple thermal isostasy equation relating the thickness of the thinned lithosphere to elevation, where an elevation of 3 km, similar to most of Venus's highlands, was found to be consistent with the thinning a thick (300 km) lithosphere [*Turcotte*, 1993].

2.3.3 The Elastic Lithosphere

Lithospheric flexure is inferred when a topographic low or moat is adjacent to a topographic high (Figure 2.18) [*Johnson and Sandwell*, 1994]. Whether flexural uplift or downwarping occurs depends on the type of terrain, with volcanic rises tending to produce flexural uplift near their margins, whereas chasmata and coronae are associated with downwarping of the lithosphere under loading [*Barnett et al.*, 2002].

Elastic lithospheric thickness estimates can be determined from either flexural modelling of topography observed on the surface or spectral gravity and topography [*Barnett et al.*, 2002; *Nimmo and McKenzie*, 1996]. Using these methods, elastic lithospheric thicknesses were found to be thin (8-40 km) below coronae [*Sandwell and Schubert*, 1992], shield volcanoes [*Kiefer and Potter*, 2000], rises [*Smrekar et al.*, 1997; *Smrekar and Stofan*, 1999] impact craters [*Brown and Grimm*, 1996a], large volcanoes [*McGovern and Solomon*, 1998], but may be thicker (~50 km) below concentric volcanic graben [*Rogers and Zuber*, 1998] and chasmata [*Brown and Grimm*, 1996b].

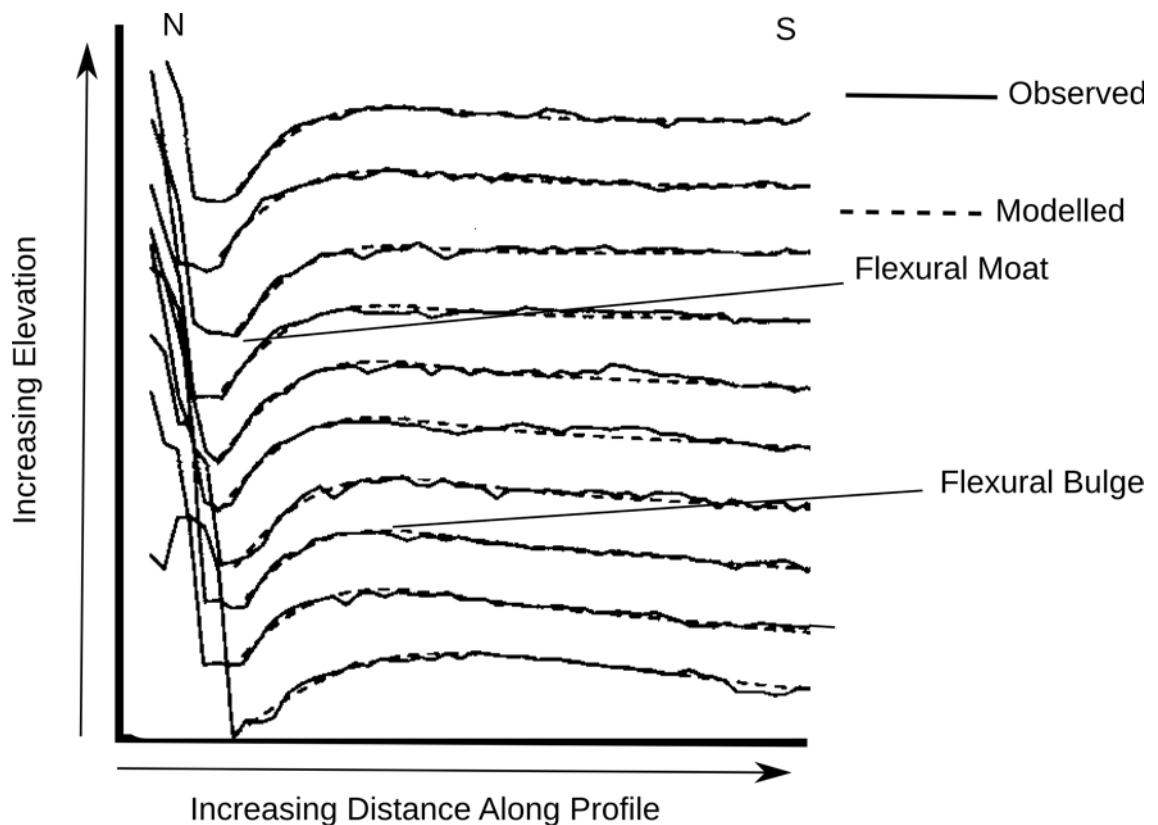


Figure 2.18. (Modified from *Johnson and Sandwell, 1994*) Observed altimetry profiles (solid line) overprinted with the Cartesian flexural responses from modelling (dashed line) at Nightingale corona.

For example, *Johnson and Sandwell [1994]* used topographic profiles and grids, in conjunction with 2D Cartesian and 2D axisymmetric thin elastic plate models, to produce estimates of the elastic thickness at seventeen areas. Loads were modelled as either linear (Cartesian), representing rifts or chasmata, or as rings (axisymmetric), representing coronae [*Johnson and Sandwell, 1994*]. The best-fit elastic lithospheric thickness for rifts ranged from ~12 km to ~34 km and ~6 km to ~22 km below the coronae [*Johnson and Sandwell, 1994*]. The smaller coronae features did not produce a flexural response, since the minor loads had trouble deforming a thick elastic plate [*Johnson and Sandwell, 1994*]. Instead, these features are most likely supported by other mechanisms, like thermal thinning or dynamic compensation [*Johnson and Sandwell, 1994*].

Long-wavelength topography generated by convective stresses were removed from the models through filtering of the gravity data set [Barnett *et al.*, 2002]. From these models, an elastic lithosphere thickness of ~25 km provided a reasonable fit below the selected rifts, coronae and moats surrounding volcanoes, but an average of 29 ± 6 km was more appropriate globally [Barnett *et al.*, 2002].

Barnett *et al.* [2000] also used spectral topography and gravity admittance to determine the elastic lithosphere thickness at selected regions on Venus. Flexure operates within the short wavelengths where the admittance becomes positive, arising from a density contrast between the load and the surrounding terrain [Barnett *et al.*, 2000]. By comparing theoretical curves to those from short wavelength admittances, an average elastic thickness of 21-23 km ($-2/+8$ km) was determined for Beta, Phoebe, Bell and Eistla regions [Barnett *et al.*, 2000]. These elastic thicknesses were heavily reliant on crustal density (2670 kg m^{-3}) and crustal thickness (16 km), where a similar elastic thickness can be represented by a thin, dense crust or a thick, light crust [Barnett *et al.*, 2000].

Global mapping using spectral admittances, similar to Barnett *et al.* [2002], in conjunction with top-loading (TL) and basal-loading (BL) models, were used by Anderson and Smrekar [2006] to determine variations in elastic thicknesses. Top-loading models involved a load that displaced the elastic lithosphere from above and a basal-loading model resulted in the elastic lithosphere being displaced from below [Anderson and Smrekar, 2006]. Observations of global admittance spectra were used to identify 35 areas of similar spectra and therefore, lithospheric structure [Anderson and Smrekar, 2006]. These 35 spectra were then correlated with the predicted admittance from top and basal-loading models to provide constraints on a range of possible estimates [Anderson and Smrekar, 2006]. By using bottom-loading, these authors found that the elastic lithosphere was thicker (up to ~100 km), particularly within the

plains regions [*Anderson and Smrekar, 2006*].

It should also be noted that all the elastic lithosphere thicknesses presented above do not reflect current conditions, but conditions when the feature was produced [*Johnson and Sandwell, 1994*].

3. Methodology

3.1 Introduction

This study presents the lithospheric structure and the mechanisms that support the topography below three areas: Atla Regio, Beta Regio, and Fortuna Tessera. Atla Regio was chosen as the first study area since it exhibits evidence for current or geologically recent activity and Beta Regio was chosen because it has the highest Geoid-to-Topography Ratio (GTR), swell volume, and diameter of all the Venusian rises [Basilevsky, 1993; Basilevsky and Head, 2002; Jurdy and Stoddard, 2007; Matias *et al.*, 2004; Matias and Jurdy, 2005; Smrekar and Phillips, 1991; Stofan *et al.*, 1995]. Fortuna Tessera was also chosen as tessera is unique to Venus, representing one of the oldest geological units on this planet [Basilevsky and Head, 2002]. The lithospheric structure and compensation mechanisms within Fortuna Tessera may also contribute to the formation of the neighbouring Maxwell Montes, the highest feature on Venus [Hansen *et al.*, 1998].

GEO3Dmod, which is discussed in Section 3.3, was useful in constraining the contribution of Airy, thermal, and regional isostasy (flexure) in supporting the observed topography within each study region and providing basic estimates of the amount of dynamic topography required. In this sense, dynamic topography represents the amount of residual topography, which was calculated by removing the total isostatic component (i.e. Airy isostasy, thermal isostasy, and regional isostasy) from the observed elevation. This value does not directly account for convective stresses within the mantle, however it does provide a useful benchmark for the CitcomS models of Venus's mantle convection as discussed in Section 3.4.

3.2 Geophysical Observables

The elevation data set used throughout this study was processed from the 719 degree and order spherical harmonic model, VenusTopo719, created by *Wieczorek* [2007]. This model is largely comprised of Magellan's Global Topography Data Record 3.2 (GTDR3.2), however Pioneer and Venera 15/16 altimetry were used to fill gaps in the data coverage (Figure 3.1) [Wieczorek, 2007]. The radial free-air gravity data set was obtained from Magellan's 180th degree and order spherical harmonic model SHGJ180u (Figure 3.2) [Konopliv *et al.*, 1999]. Both the topography and radial free-air gravity were referenced to 6051.848 km or Venus's Mean Planetary Radius (MPR) [Ford and Pettengill, 1992; Rappaport and Plaut, 1994].

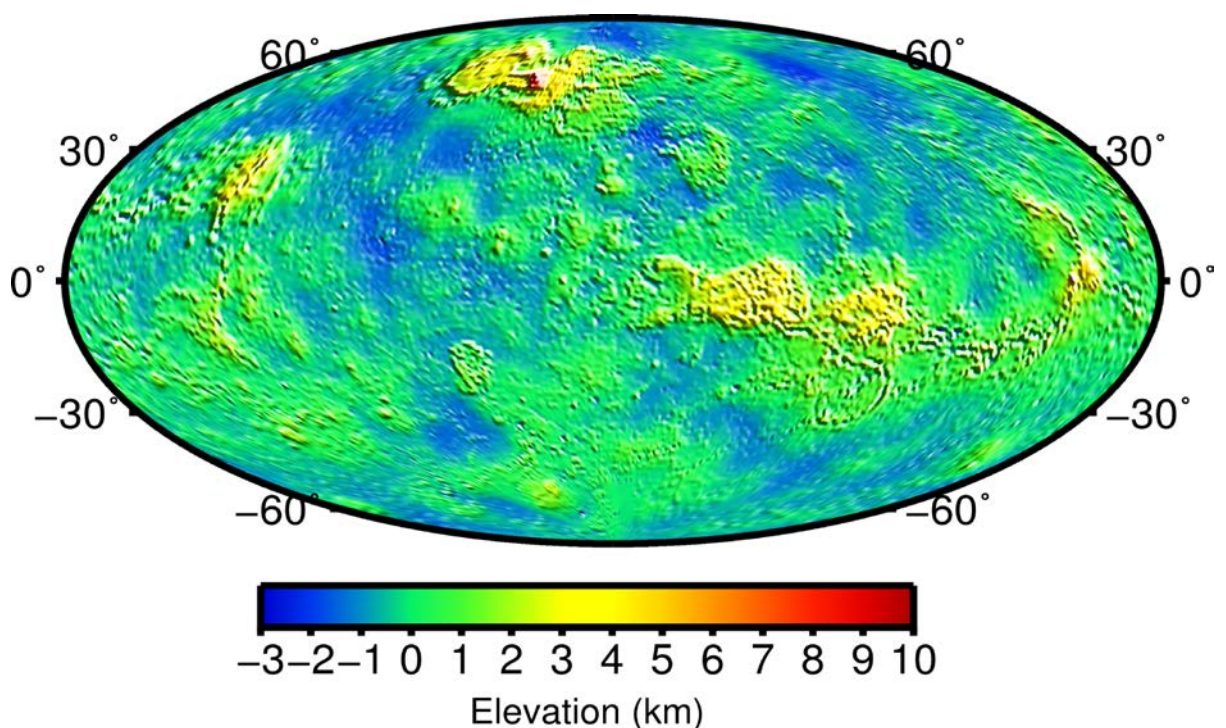


Figure 3.1. Venus's global elevation referenced to a Mean Planetary Radius (MPR) of 6051.848 km. Hammer projection centered at 60°E and overlain with a gradient image obtained from the elevation data set.

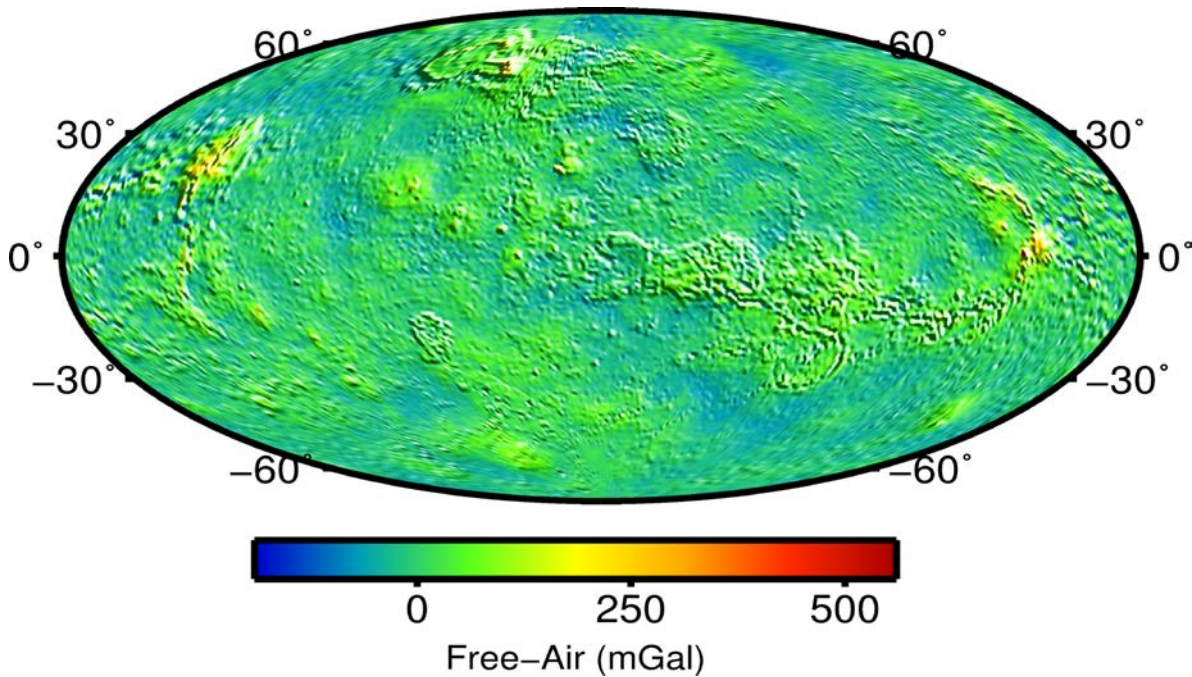


Figure 3.2. Venus's global free-air gravity evaluated at a radius of 6051.848 km. Hammer projection centered at 60°E and overlain with a gradient image obtained from the elevation data set.

The spherical harmonic software package SHTOOLS (<http://shtools.ipgp.fr/>) was used to convert the spherical harmonic models of topography (truncated beyond degree 719) and free-air gravity (truncated beyond degree 180) to a 2D grid format for visualisation purposes (Figure 3.1-3.2) [Wieczorek, 2007]. SHTOOLS relies on a number of FORTRAN 95 subroutines to complete transformations, reconstructions, rotations and spectral analysis of spherical harmonic coefficients [Wieczorek, 2007]. Elevation, free-air gravity, Bouguer gravity, and geoid height were then visualised using Generic Mapping Tools (GMT; <http://gmt.soest.hawaii.edu/>), as shown in Figures 3.1-3.5 [Wessel and Smith, 1991, 1998].

Both the free-air gravity and elevation data sets were used to calculate the Bouguer gravity (Figure 3.3). However, a Bouguer correction BC was applied first and accounts for the gravitational attraction of masses associated with an area's elevation (Equation 3.1). This correction assumes an infinite planar geometry and considers both the height of the

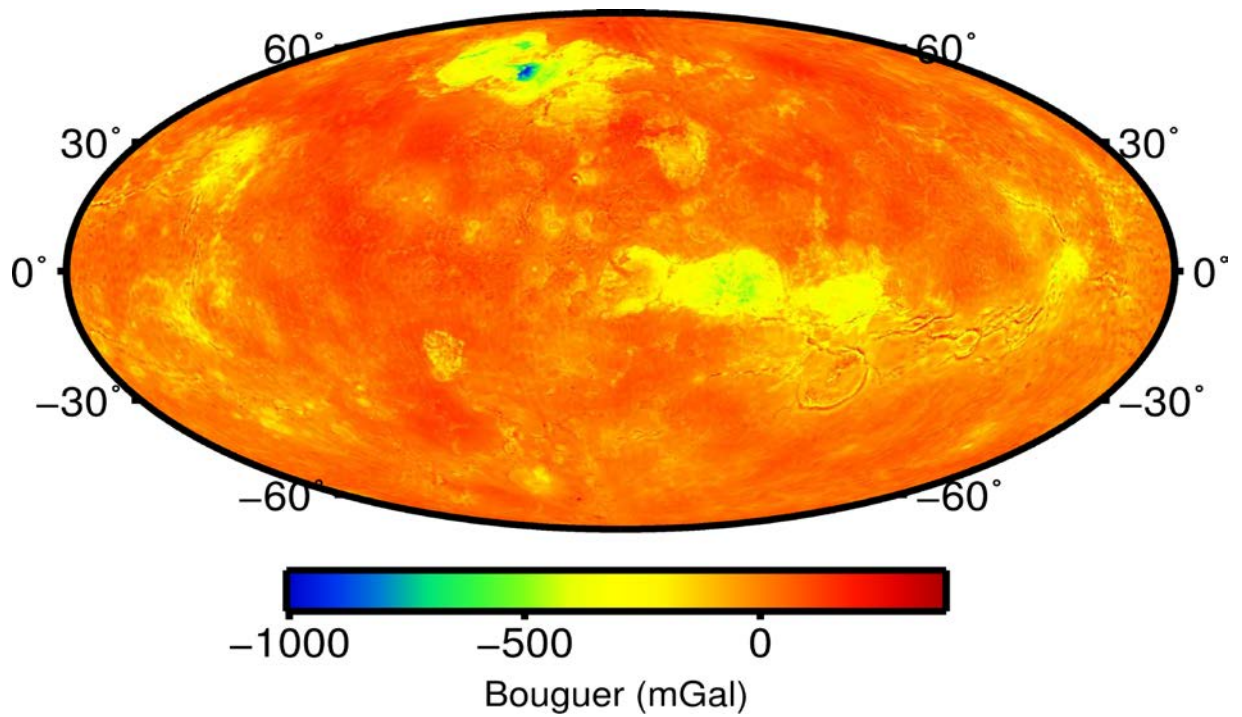


Figure 3.3. Venus's global Bouguer gravity. Hammer projection centered at 60°E and overlain with a gradient image obtained from the elevation data set.

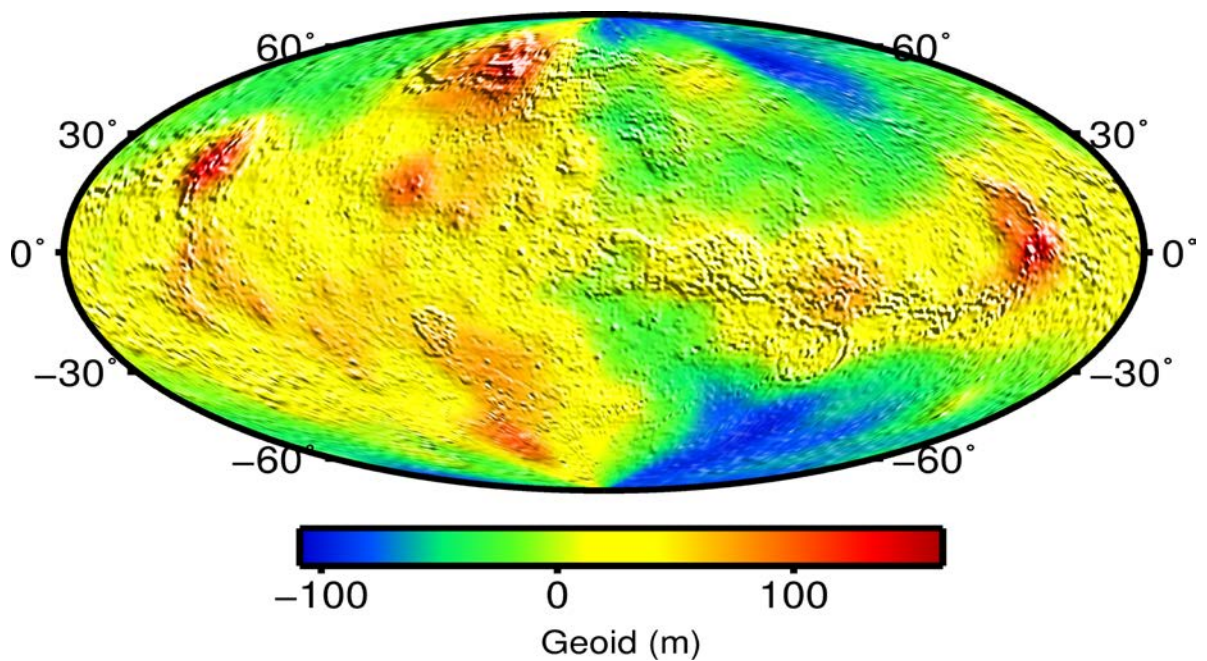


Figure 3.4. Venus's global geoid. Hammer projection centered at 60°E and overlain with a gradient image obtained from the elevation data set.

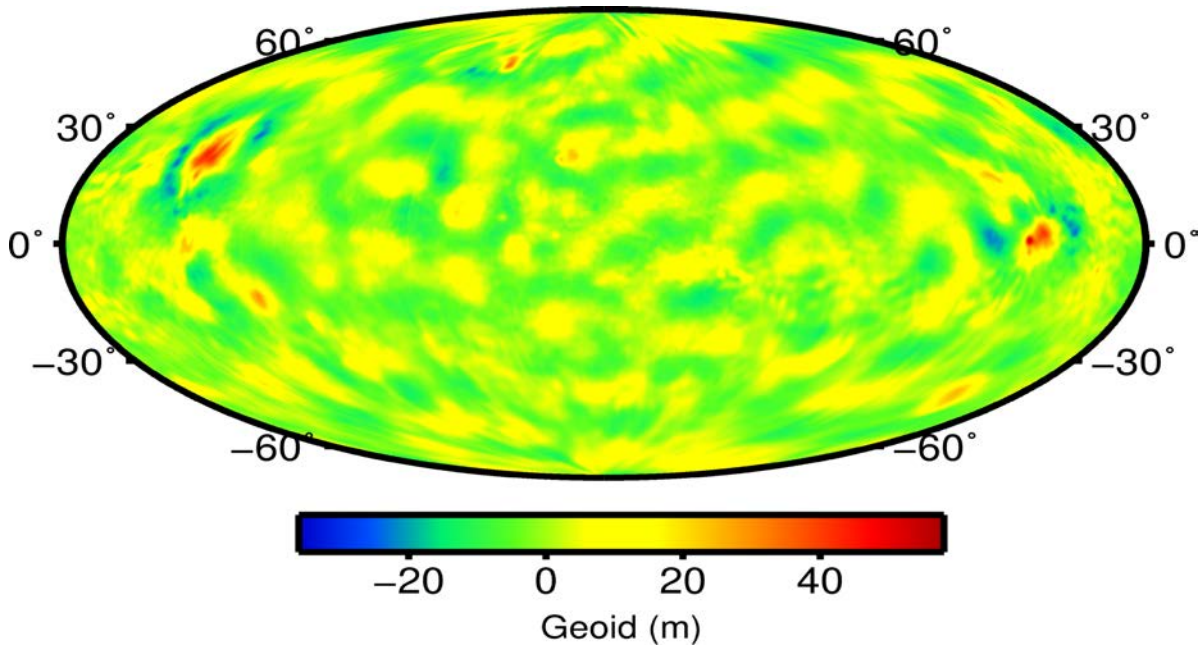


Figure 3.5. Venus's filtered geoid. A cosine-tapered high pass filter was applied to Venus's geoid to remove the contribution of deeper sources, greater than the total reference column thickness (440 km). Hammer projection centered at 60°E and overlain with a gradient image obtained from the elevation data set.

elevation h and density of the crust ρ_{crust} (2900 kg m^{-3}) [Turcotte and Schubert, 2001]:

$$BC = 2 \pi \rho_{crust} G h \quad (3.1)$$

where G is the universal gravitational constant $6.672 \times 10^{-11} \text{ N m}^2 \text{ kg}^{-2}$.

Finally, the Bouguer gravity B was obtained by removing the Bouguer correction BC from the free-air data set FA :

$$B = FA - BC \quad (3.2)$$

The free-air gravity was integrated through the 2D Fast Fourier Transform of Generic

Mapping Tools to obtain the geoid data set (Figure 3.4) similar to the method of *Sjogren*, [1997]; *Wessel and Smith* [1991, 1998]. In this transform, the space domain was converted into the frequency domain, where the free-air gravity was integrated by dividing the data by the radial wave number. The frequency domain was then transformed back into the space domain [Wessel and Smith, 1991, 1998].

The geoid data set contains anomalies from masses deeper than the total lithospheric depth (i.e. 440 km) assumed by GEO3Dmod and, as a result, was filtered using a cosine tapered high pass filter (Figure 3.5). This filter discarded all harmonic degrees < 9 , corresponding to wavelengths $> \sim 4225$ km and passed all harmonic degrees > 14 , corresponding to wavelengths $< \sim 2716$ km.

Each data set is associated with uncertainties. For the geoid data set this ranges from 0.1 to 2.3 m, with the maximum being used for the lithospheric modelling [Sjogren et al., 1997]. A maximum Root-Mean-Square (RMS) radial uncertainty of 400 m, associated with Magellan's GTDR3.2, is also assumed for the elevation data set. Even though the elevation data set is a composite from a number of different missions, Magellan mapped the majority ($\sim 97.4\%$) of the surface [Pettengill et al., 1991]. However, no estimates of the errors pertaining to the Bouguer gravity data are available for Venus. Both the topography and free-air gravity data sets were used to calculate Bouguer gravity with the uncertainty relating to the latter being calculated from the rules of error propagation [Bevington and Robinson, 1992; Taylor, 1982; Young, 1962]:

$$BC_{uncert} = Topo_{uncert} \times 2\pi \rho_{crust} G \quad (3.3)$$

where BC_{uncert} is the uncertainty associated with the Bouguer correction BC and $Topo_{uncert}$ is the

maximum topographic uncertainty of 400 m. Equation 3.3 resulted in a Bouguer correction uncertainty BC_{uncert} of 48.62 mGal.

The final uncertainty associated with the Bouguer gravity B_{uncert} was found by combining the uncertainty associated with the free-air gravity FA_{uncert} (12 mGal) and the uncertainty relating to the Bouguer correction BC_{uncert} :

$$B_{uncert} = \sqrt{[(FA_{uncert})^2 + (BC_{uncert})^2]} \quad (3.4)$$

Equation 3.4 resulted in a Bouguer uncertainty of 50.08 mGal.

3.3 Lithospheric Modelling Using GEO3Dmod

3.3.1 Introduction to GEO3Dmod

The geometry and temperature distribution of the thermal lithosphere below the three study locations were modelled using GEO3Dmod. GEO3Dmod is an interactive forward modelling software that uses a combination of FORTRAN subroutines and shell scripts to simultaneously solve heat transfer, isostasy, geoid, and Bouguer gravity equations to constrain the geometry and physical properties of the subsurface [Fullea *et al.*, 2009]. GEO3Dmod adopts a 3-dimensional approach that allows for greater detail, complexity and accuracy because geological structures are treated as finite bodies perpendicular from the modelled cross-sectional profile [Fullea, 2007]. Each body in GEO3Dmod is considered as a single layer with specific properties (e.g. temperature, density) set by the user, with the extents of each layer defined by an upper and lower surface (Figure 3.6) [Fullea *et al.*, 2009].

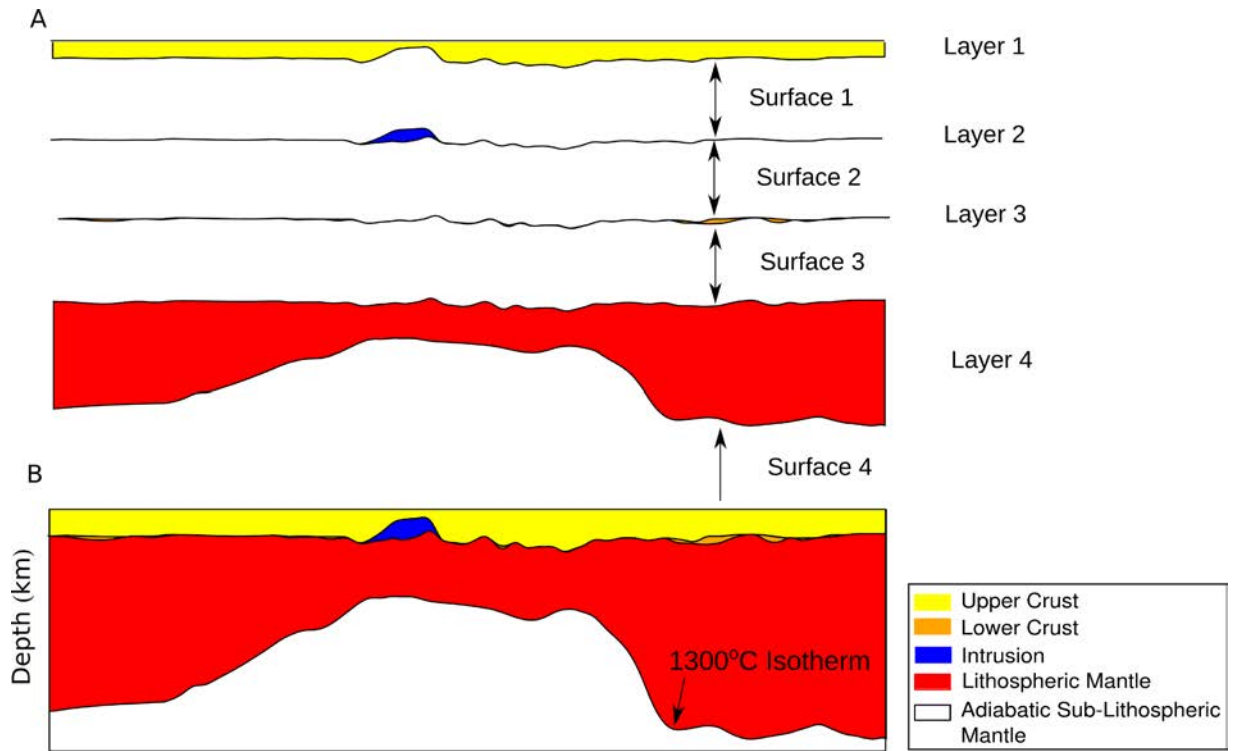


Figure 3.6. [Modified from *Fullea et al.*, 2009] (A) GEO3Dmod classifies each body as a separate layer with properties set by the user. Each layer is comprised of an upper and lower surface. (B) Each layer is subsequently joined to form the total cross-sectional lithospheric model.

GEO3Dmod is the simplified version of LitMod3D. GEO3Dmod uses simplified mantle properties and does not solve thermophysical or rheology equations [*Fullea et al.*, 2009]. Due to the high uncertainties surrounding the thermodynamics and rheology of Venus's interior this simplified approach is appropriate and useful in constraining the crustal and thermal lithospheric thickness.

3.3.2. Thermal Field

GEO3Dmod models the entire lithospheric structure to a depth of 440 km, which is the depth to the first phase transition on Venus [*Steinbach and Yuen*, 1992]. This model domain further comprises the conductive thermal lithosphere, comprising the crust and lithospheric mantle, down to the 1300°C isotherm (Figure 3.6) and the underlying sub-lithospheric mantle, which

is assigned a constant temperature in order to approximate an adiabatic, well-mixed, mantle (Figure 3.6). The finite-difference method is used by GEO3Dmod to solve the thermal field. The steady-state 3D thermal structure is represented by:

$$\nabla(k(\vec{x}) \nabla T(\vec{x})) = -H(\vec{x}) \quad (3.5)$$

where H is the radiogenic heat production per unit volume (W m^{-3}), k is the thermal conductivity ($\text{W m}^{-1} \text{K}^{-1}$), and T is the temperature. For this calculation, the lithosphere is depicted as a rectangular prism defined by a fixed temperature at the surface T_s and base T_a , with no heat flow perpendicular through the four vertical boundaries. The underlying adiabatic sub-lithospheric mantle has an invariable temperature T_a (Figure 3.7).

The finite-difference method the 3D model space is first discretised based on the number of N_x , N_y , N_z nodes in the x , y , and z domain, defined by the user. For each node and its nearest neighbour, T , k , and H of Equation 3.5 can be revised to:

$$\begin{aligned} & \frac{1}{(2\Delta x^2)} \left((k_{(i+1)jk} + k_{ijk}) T_{(i+1)jk} + (k_{ijk} + k_{(i-1)jk}) T_{(i-1)jk} - (k_{(i+1)jk} + 2k_{ijk} + k_{(i-1)jk}) T_{ijk} \right) \\ & + \left(\frac{1}{(2\Delta y^2)} \right) \left((k_{(ij+1)k} + k_{ijk}) T_{(ij+1)k} + (k_{ijk} + k_{(ij-1)k}) T_{(ij-1)k} - (k_{(ij+1)k} + 2k_{ijk} + k_{(ij-1)k}) T_{ijk} \right) \\ & + \left(\frac{1}{(2\Delta z^2)} \right) \left((k_{ijk+1} + k_{ijk}) T_{ijk+1} + (k_{ijk} + k_{(ijk-1)}) T_{(ijk-1)} - (k_{ijk+1} + 2k_{ijk} + k_{(ijk-1)}) T_{ijk} \right) = -H_{ijk} \end{aligned} \quad (3.6)$$

where i varies from 2 to N_{x-1} , j from 2 to N_{y-1} , and k from 2 to N_{z-1} .

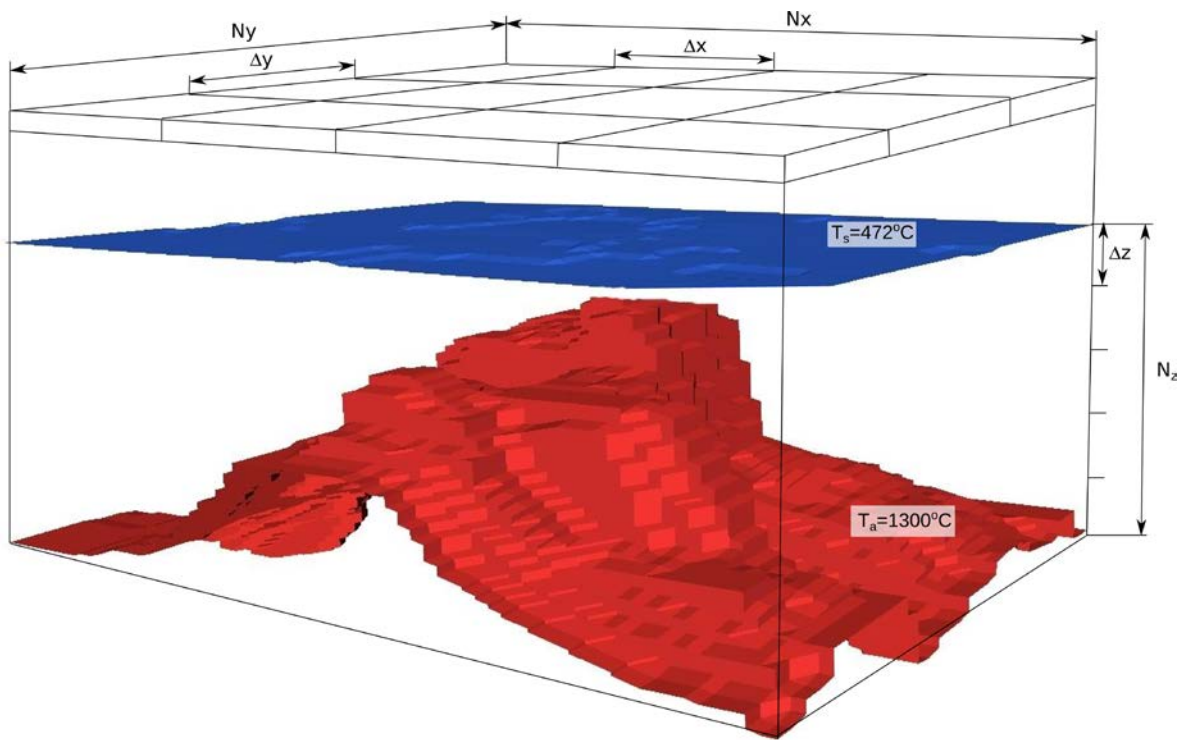


Figure 3.7. [Modified from *Fullea et al.*, 2009] The entire model domain is best depicted as a large block, composed of numerous sub-prisms centered at each node. The number of nodes in the x, y, and z direction are defined by the user. The number of nodes (N_x , N_y , N_z) are then used to discretise the numerical domain based on the Finite-Difference method. For calculation of the thermal field the upper boundary of the prism was set to Venus's surface temperature (472°C) and the basal boundary layer had a temperature of 1300°C.

3.3.3 Density and Pressure

GEO3Dmod calculates the pressure and density within a model after the thermal field is calculated [*Fullea et al.*, 2009]. The adiabatic sub-lithospheric mantle is assumed to have a constant density of 3200 kg m⁻³, but both the crust and lithospheric mantle densities are linearly temperature and pressure dependent. The crustal density ρ_c is calculated from:

$$\rho(T, P) = \rho_{oc} [1 - (T - T_o) \alpha_c + \beta_c (P - P_o)] \quad (3.7)$$

where ρ_{oc} is the crustal reference density at and the reference temperature T_o and pressure P_o , α_c and β_c are the thermal and pressure coefficients for the crustal layer, respectively.

When calculating the temperature-dependent density of the lithospheric mantle, the reference temperature and density are taken at the base of the thermal lithosphere. The density of the lithospheric mantle ρ_m is calculated from [Fullea, 2007]:

$$\begin{aligned}\rho_m &= \rho_o [1 - \alpha' T + \beta P] \\ \alpha' &= \frac{\alpha}{(1 + \alpha T_a)} \\ \rho_o &= \rho_a (1 + \alpha T_a)\end{aligned}\tag{3.8}$$

where ρ_o is the reference density at Temperature(T)=Pressure(P)=0, α' is the volumetric expansion coefficient for the lithospheric mantle, β is the pressure coefficient, α is the thermal expansion coefficient, and ρ_a is the density at the base of the thermal lithosphere.

Pressure and density are interdependent and connected via the pressure coefficient and lithostatic pressure $P(z)$:

$$P(z) = \int_0^z \rho(z') g dz' \tag{3.9}$$

where g is the gravitational acceleration on Venus (8.87 m s^{-2}).

As density changes with pressure, the increase in pressure from z_0 to z where $z > z_0$ can be calculated from:

$$\Delta P = g \rho(z_0)(z - z_0) \left(1 + \frac{(g \rho_0 \beta(z - z_0))}{2} \right) \quad (3.10)$$

3.3.4 Elevation

The calculation of absolute elevation E in GEO3Dmod depends on the concept of local isostasy and buoyancy of a rigid lithospheric column floating on a weaker underlying asthenosphere [Lachenbruch and Morgan, 1990; Turcotte and Schubert, 2001]. A lithospheric column's elevation is found from:

$$\begin{aligned} & \text{If } E < 0: \\ E &= \frac{\rho_a}{(\rho_a - \rho_{atmos})} \left(\frac{(\rho_a - \rho_l)}{\rho_a} L - L_0 \right) \\ & \text{If } E > 0: \\ E &= \frac{(\rho_a - \rho_l)}{\rho_a} L - L_0 \end{aligned} \quad (3.11)$$

where ρ_{atmos} is the density of the atmosphere (60 kg m^{-3}), ρ_a is the density of the adiabatic sub-lithosphere (3200 kg m^{-3}). The thermal lithospheric thickness L , the depth-averaged density of the lithosphere ρ_l and the calibration constant L_0 , depends on the chosen reference column [Fullea et al., 2009].

Absolute elevation calculations in GEO3Dmod do not consider dynamic contributions from thermal upwellings or downwellings within the adiabatic sub-lithospheric mantle. However, the geophysical observables (i.e. geoid) used to constrain the proposed lithospheric structure, can be filtered, as done in this study, to neglect these thermal perturbations [Fullea et al., 2009].

3.3.5 Regional Isostasy (Flexure)

Local isostasy is effective in compensating long wavelength topography, but shorter wavelengths may require elastic support [Fullea *et al.*, 2009]. GEO3Dmod incorporates the finite-difference code TISC (<https://sites.google.com/site/daniggcc/software/tisc>) [Garcia-Castellanos, 2002] to calculate regional isostasy, and assumes a 2D plate that has an effective elastic lithospheric thickness set by the user. The loads associated with the short-wavelength features correspond to deviations in pressure at the base of the model. These pressure variations are then used to calculate the vertical deflections of this elastic plate in response to loading [Fullea *et al.*, 2009].

3.3.6 Gravity and Geoid

Gravity and geoid calculations utilise the absolute density variations previously solved [Fullea *et al.*, 2009]. Each node within the discretised grid is centered within a rectangular prism, which has a linear depth-dependent density (Figure 3.8). The total gravity and geoid are then found by vertically grouping the gravity signature from each individual prism within each layer of the lithospheric column. Further details of the method can be found in Fullea *et al.* [2009].

However, the density variations at the boundaries of the model can have a significant influence on the modelled long-wavelength geoid. To account for these boundary effects, GEO3Dmod continues the lithospheric structure at the boundaries of a model to an additional distance of 10^6 km. For the geoid, however, small variations between the calculated and observed values can induce a regional long wavelength response in the calculated anomaly at the edge of a model. Therefore a best-fit plane is calculated from the observed geoid and

removed from

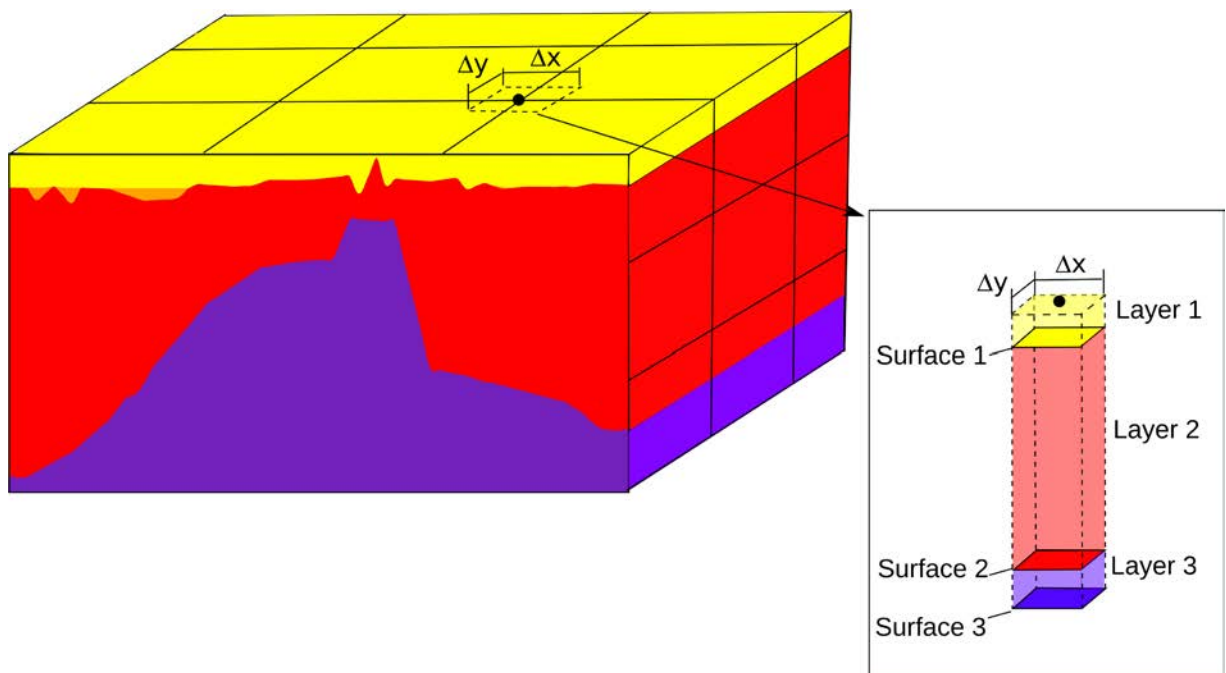


Figure 3.8. [Modified from *Fullea et al.*, 2009] The discretized grid is divided into nodes (black circle), each associated with a central vertical rectangular prism (inset; dashed prism), representing the lithospheric column. Each layer (inset) is sub-divided into a separate vertical prism (yellow, red, and purple prisms). The total gravity and geoid anomaly at each node was found by adding the potential field signature from each individual prism in the column.

the calculated geoid [*Fullea et al.*, 2009].

3.3.7 Constraining the Lithospheric Structure and Compensation Mechanisms Using GEO3Dmod

The structure of the lithosphere was constrained at each study area by comparing the calculated geoid, elevation, and Bouguer gravity responses from GEO3Dmod to the geophysical observables discussed in Section 3.2. The lithospheric structure was continually modified until the calculated responses fitted within error of the corresponding observed data sets.

The residual elevation $E_{residual}$ was used to assess the goodness-of-fit of a model and whether additional regional isostasy or dynamic uplift was required to support the topography within an area. $E_{residual}$ is estimated by subtracting the calculated response $E_{calculated}$ from the observed elevation $E_{observed}$:

$$E_{residual} = E_{observed} - E_{calculated} \quad (3.12)$$

where $E_{calculated}$ comprises the Airy and thermal isostatic responses for a proposed lithospheric structure.

The amount of dynamic uplift $E_{dynamic}$ at each area was estimated from:

$$E_{dynamic} = E_{observed} - E_{isostatic} \quad (3.13)$$

where $E_{isostatic}$ is the total isostatic elevation including Airy, thermal, and regional isostasy.

The dynamic uplift calculated from Equation 3.3 represents the amount of residual topography that can not be fitted isostatically by the lithospheric structure. This estimate does not directly account for convective stresses within the mantle, but provides a useful benchmark for the following models of Venus' mantle convection.

3.4 Dynamic Modelling Using CitcomS

3.4.1 Introduction and Fundamental Equations

CitcomS is a finite element method used to simulate thermal convection within a viscous,

compressible, and anelastic mantle, and for this study, it used a full 3D spherical shell geometry [Tan *et al.*, 2006; Zhong *et al.*, 2000]. Conservation of mass, energy and momentum determine the characteristics of mantle convection and are calculated from [Tan *et al.*, 2006; Zhong *et al.*, 2000]:

$$(\rho u_i)_{(i)} = 0 \quad (3.14)$$

$$-P_{(i)} + \left(\left(\eta (u_{(i,j)} - \frac{2}{3} u_{(k,k)} \delta_{(ij)}) \right)_{(i)} - \delta \rho g \delta_{(ir)} \right) = 0 \quad (3.15)$$

$$\rho c_p (T_{(t)} + u_i T_{(i)}) = \rho c_p \kappa T_{(ii)} - \rho \alpha g u_r T + \Phi + \rho (Q_{(L,t)} + u_i Q_{(L,i)}) + \rho H \quad (3.16)$$

where ρ , u , P , η , δ_{ij} , $\delta\rho$, g , T , c_p , κ , α , Φ , Q_L , H , is the density, velocity, dynamic pressure, viscosity, Kroneker delta tensor, density anomaly, gravitational acceleration, temperature, heat capacity, thermal diffusivity, thermal expansivity, viscous dissipation, latent heat arising from phase boundaries, and rate of heat production. In relation to the subscripts, i , j , and k are spatial indices, r is the radial direction, and t is time.

The density anomalies $\delta\rho$, considering phase boundaries, temperature and composition changes, are calculated from [Tan *et al.*, 2006; Zhong *et al.*, 2000]:

$$\delta\rho = -\alpha\rho(T - T_a) + \delta\rho_{ph}\Gamma + \delta\rho_{ch}C \quad (3.17)$$

where ρ and T_a are the radial lineaments of density and adiabatic temperature, $\delta\rho_{ph}$ is the density contrast crossing the phase boundary, $\delta\rho_{ch}$ density contrast due to composition, and C is the composition. Γ is the phase function, defined as [Tan *et al.*, 2006; Zhong *et al.*, 2000]:

$$\Gamma = \frac{1}{2} \left(1 + \tanh \left(\frac{\pi}{(\rho g w_{ph})} \right) \right) \quad (3.18)$$

$$\pi = \rho g (1 - r - d_{ph}) - \gamma_{ph} (T - T_{ph}) \quad (3.19)$$

where the reduced pressure, phase change depth, temperature, Clapeyron slope, and width are represented π , d_{ph} , T_{ph} , γ_{ph} , and w_{ph} , respectively.

Complex numerical modelling, particularly global simulations, require significant computational resources. In order to minimise the computational times required to run these simulations, the parameters used are scaled to non-dimensional values through Equations 3.20 to 3.34 [Tan et al., 2006; Zhong et al., 2000].

$$\begin{aligned} \rho &= \rho_0 \rho' & \alpha &= \alpha_0 \alpha' & g &= g_0 g' \\ \kappa &= \kappa_0 \kappa' & \eta &= \eta_0 \eta' & c_P &= c_{P0} c_P' \\ x_i &= R_0 x_i' & u_i &= (\kappa_0 / R_0) u_i' & T_0 &= \Delta T T_0' \\ T &= \Delta T (T' + T_0') & t &= R_0^2 / \kappa_0 t' & H &= \kappa_0 / R_0^2 c_{P0} \Delta T H' \\ P &= (\eta_0 \kappa_0 / R_0^2) P' & d_{ph} &= R_0 d_{ph}' & \gamma_{ph} &= ((\rho_0 g_0 R_0) / \Delta T) \gamma_{ph}' \end{aligned} \quad (3.20 \text{ to } 3.34)$$

where ρ_0 , α_0 , g_0 , κ_0 , η_0 , c_{P0} , R_0 are the reference density, thermal expansivity, gravitational acceleration, thermal diffusivity, viscosity, heat capacity, and radius, respectively. The primes represent the non-dimensional values. The surface temperature T_0 and temperature contrast between the surface and the Core Mantle Boundary (CMB) is ΔT .

3.4.2 Mesh Geometry

Global models involving a 3D spherical shell are divided into a mesh comprising 12 equidimensional caps as shown in Figure 3.9 [Tan et al., 2012]. The mesh, comprising the

caps (or elements), which are connected by nodes, is programmed to have properties which will characterise how the structure responds to loading conditions [Zienkiewicz *et al.*, 2005]. In map view (Figure 3.9), the caps are square in shape, with their edges positioned diagonally with respect to latitude and longitude. In a 3D global view the mesh and caps would appear similar to Figure 3.10.

Each cap within the mesh can be divided further by the number of x, y, and z computer processing domains (Figure 3.10). For the present study the total number of processors used were 96 (i.e. $12 \times 4 \times 2$) [Tan *et al.*, 2012].

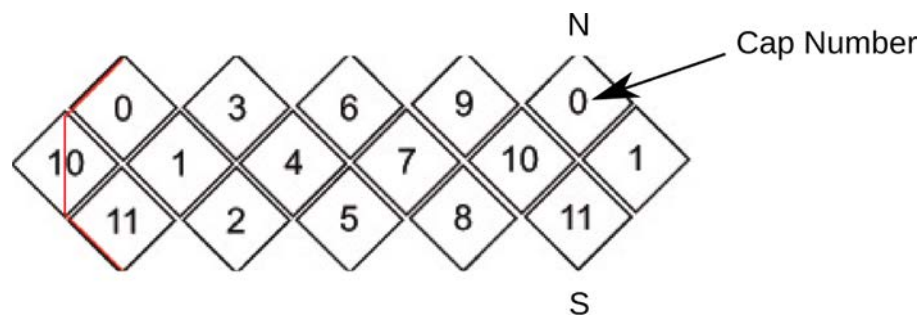


Figure 3.9. (Modified from Tan *et al.*, 2012) The global mesh used by CitcomS is divided into 12 equidimensional caps starting from 0 to 11. N and S are the north and south pole, respectively. The thin red line defines the 0 degree meridian.

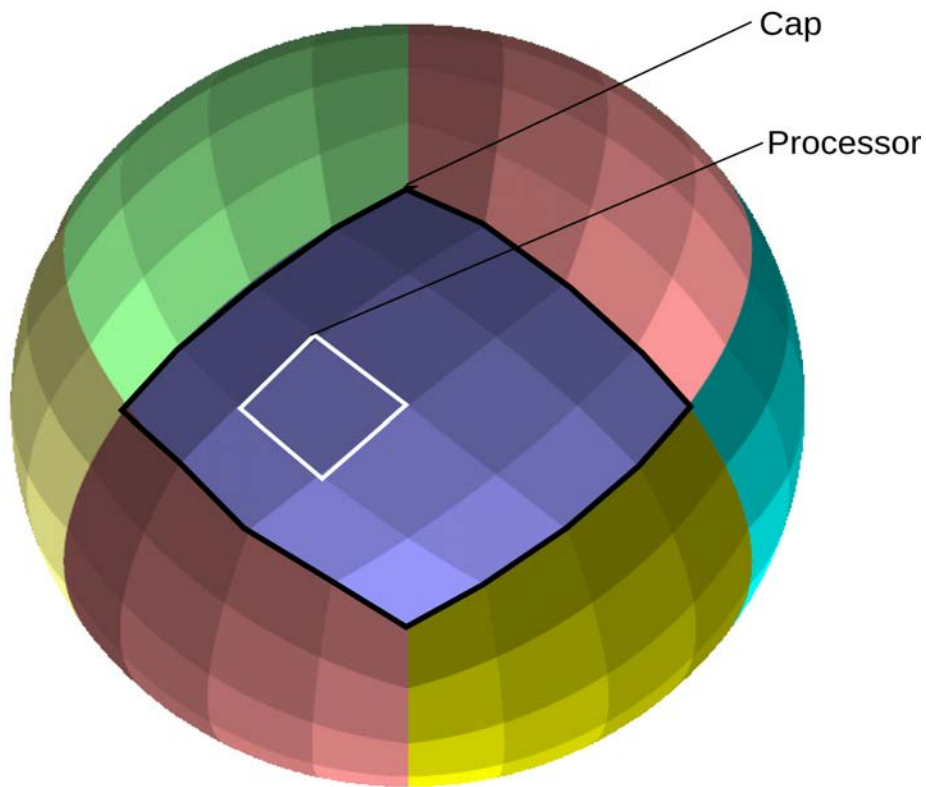


Figure 3.10. (Modified from *Tan et al.*, 2012) A 3D view of the mesh shown in Figure 3.9. The mesh is divided into 12 caps shown as distinct colours. The purple cap, defined by the solid black line, outlines the boundaries of one cap. Each cap can be sub-divided by the number of processors as shown by the varying colour intensities for each cap. For example, one processor is shown with its boundaries marked by the white solid square.

4. Constraining the Lithospheric Structure at Atla Regio, Venus: Implications for Rifting and Melt Generation Rates

Elyse Schinella, Juan Carlos Afonso, Craig O'Neill

Abstract. Atla Regio is a ~2000 km by ~2000 km equatorial volcanic rise, dissected by rifts, including the N-NW trending Ganis Chasma. Compared to other volcanic rises on Venus, Atla Regio exhibits evidence for possible recent and/or current geological activity. Lithospheric structure, especially thermal lithospheric thickness (or the depth to the 1300°C isotherm), is highly unconstrained on Venus, but is useful for delineating the mechanisms supporting the observed topography, calculating melt generation rates and spreading rates within a region. At Atla Regio, we use GEO3Dmod to (1) model the lithospheric structure, and (2) determine the contribution of Airy isostasy, thermal isostasy, regional isostasy (flexure) and dynamic uplift, in compensating the observed topography. We then combine our modelled crustal and lithospheric thickness estimates with analytical calculations and a half-space cooling model to estimate (3) melt generation rates from an upwelling mantle plume, (4) crustal production rates, and (5) rifting rates at Ganis Chasma. Using a reference crustal and thermal lithospheric thickness of 30 km and 300 km, respectively, we have found a thicker crust (30-60 km) and thermal lithosphere (~100-150 km) occurs below the volcanoes, while a thinner crust (<1 km) and lithosphere (50-60 km) occurs below Ganis Chasma. Most of the topography at Atla Regio is supported by Airy and thermal isostasy, followed by regional isostasy. Dynamic topography was considered to be the remaining topography after all isostatic compensation mechanisms were accounted for and ranged from ~0.5-1.5 km at the large volcanoes. For a dry mantle, a mantle temperature of 1300°C, a plume temperature of 1500°C, and a thermal

lithospheric thickness of 50 km, we found a melt volume of $2 \times 10^6 \text{ km}^3$ and a melt generation rate of $0.50 \text{ km}^3 \text{ yr}^{-1}$, below Ganis Chasma. Our findings also suggest Ganis Chasma is a site of current ultra-slow rifting ($\sim 5\text{-}12 \text{ mm yr}^{-1}$). The rate of crustal production ($0.78 \text{ km}^3 \text{ yr}^{-1}$) at Ganis Chasma implies rift-related volcanism and partial melt associated with an upwelling mantle plume may contribute to producing the new crust generated at this rift. This study has important implications since other young volcanic rises, like Beta Regio, may experience a similar lithospheric structure, compensation mechanisms, and current activity.

4.1 Introduction

Atla Regio consists of three large volcanic Mons: Maat Mons in the south-west, Ozza Mons in the south-east, and Sapas Mons in the north-west (Figure 4.1) [Senske and Head, 1992]. The area is also dissected by three large rift valley Chasmata: the southwest trending Dali Chasma, the northwesterly Ganis Chasma, and the eastward trending Parga Chasma, which form a triple junction rift at Ozza Mons (Figure 4.1) [Phillips, 1994; Senske and Head, 1992]. Based on observations of outwardly dipping and deformed craters, these features may still be geologically active, or have been active within the last 50 Myr [Basilevsky, 1993; Basilevsky and Head, 2002; Jurdy and Stoddard, 2007; Matias and Jurdy, 2005; Matias et al., 2004].

The extensional features, vast volcanic flows, broad swell morphology, high Geoid-to-Topography Ratios (GTRs), high elevation and geoid anomalies could also be attributed to long wavelength compensation from either thermal isostasy or dynamic uplift [Kiefer and Hager, 1991; Kucinskas and Turcotte, 1994; McGovern et al., 1995; Moore and Schubert, 1997; Phillips et al., 1991; Phillips, 1994; Senske and Head, 1992; Smrekar et al., 1997; Stofan et al., 1995]. Previous studies of the lithospheric structure at Atla Regio have also produced varied results, with some authors using elastic lithospheric thickness, thermal

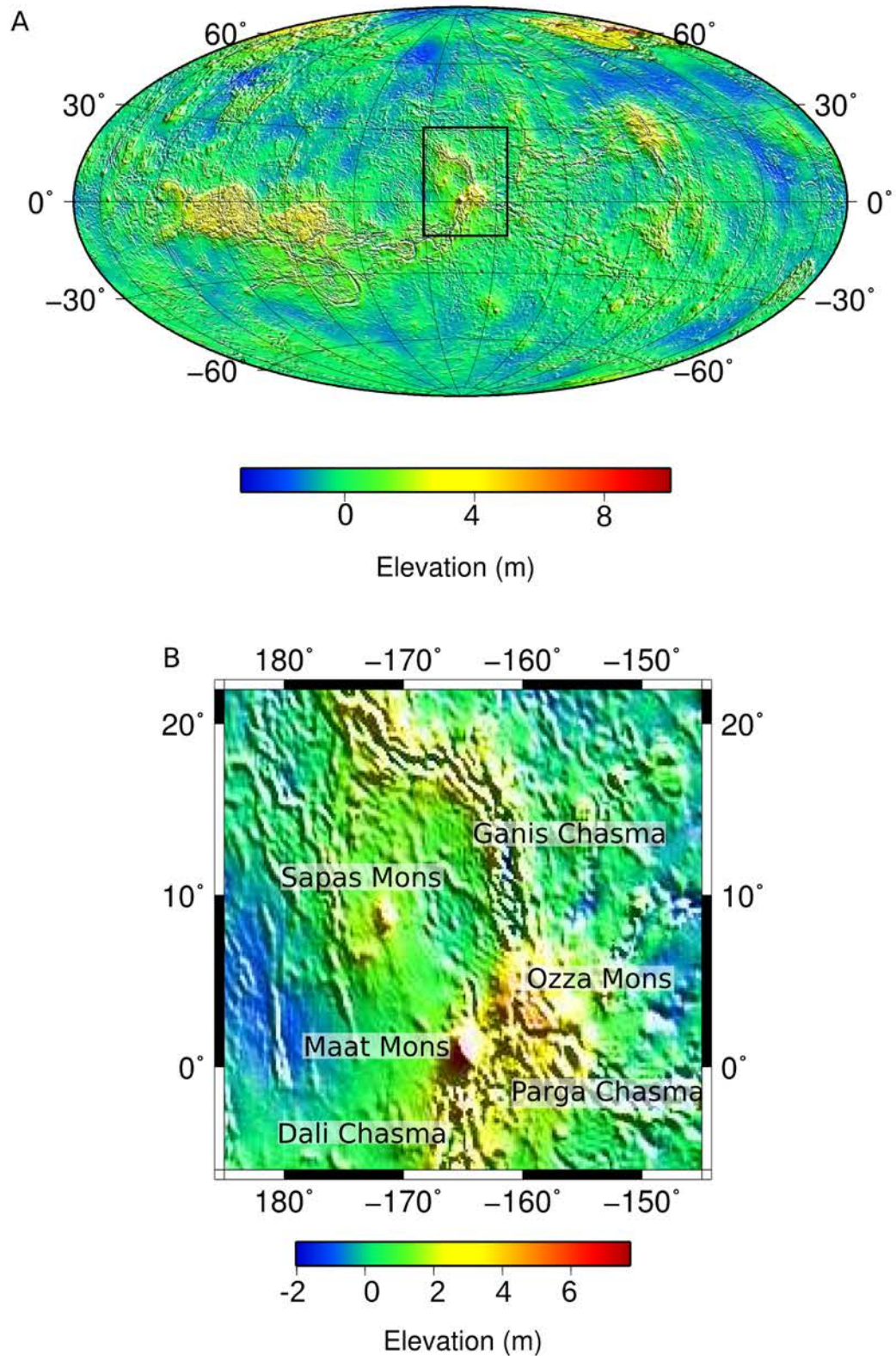


Figure 4.1. (A) Global elevation map, referenced to Venus's Mean Planetary Radius (MPR) of 6051.848 km. The black rectangle represents the location of Atla Regio, which comprises three elevated volcanic Mons and rift valley Chasmata (B). (B) shows the location of the features discussed in this study.

gradients, volcanic volumes, and observations of rifts and large volcanoes, to infer a thin (~100 km) thermal lithosphere with others using stagnant-lid convection models to imply a much thicker (300-400 km) thermal lithosphere [Kucinskas and Turcotte, 1994; Moore and Schubert, 1997; Orth and Solomatov, 2011; Phillips, 1994; Smrekar and Parmentier, 1996].

We aim to constrain the lithospheric structure and the mechanisms acting to support the observed topography at Atla Regio, using GEO3Dmod. GEO3Dmod is an interactive 3D forward modelling software, that simultaneously solves heat transfer, isostasy, geoid, and Bouguer gravity equations for a proposed lithospheric structure and outputs temperature, surface heat flow, gravity anomalies, absolute elevation, and geoid anomalies [Fullea *et al.*, 2009]. GEO3Dmod is the simplified version of LitMod3D as it uses simplified mantle properties and does not include thermophysical or rheological calculations. The high uncertainties associated with the thermodynamics and rheology of Venus's interior makes this simplified approach appropriate, which is especially useful in constraining the highly uncertain thickness of the lithosphere and crust. By constraining the thermal lithospheric structure, our study has important implications for melt generation rates, crustal production rates and the current state of rifting at Atla Regio.

4.2 Background

4.2.1 Thermal Lithospheric Thickness

A few studies have yielded estimates of the thermal lithospheric thickness at Atla Regio [Kucinskas and Turcotte, 1994; McGovern *et al.*, 1995; Moore and Schubert, 1997; Phillips, 1994; Smrekar and Parmentier, 1996]. Topography, geoid height, and GTRs, have been used to infer the thermal lithosphere has been thinned from ~300-350 km to ~88-100 km below

Atla Regio, with thermal isostasy contributing to the support of the observed topography [Kucinskas and Turcotte, 1994; Moore and Schubert, 1997; Phillips, 1994; Smrekar and Parmentier, 1996].

A more localised study of lithospheric thickness below Maat, Ozza, and Sapas Mons was completed by McGovern *et al.* [1995]. In this study, mechanical lithospheric thickness estimates were used to determine thermal gradients, and in turn, the thermal lithospheric thickness. These authors used a surface temperature of 500°C, a basal temperature of 1250°C, and a 3 W/mK thermal conductivity, similar to surface rocks. Using a mechanical lithospheric thickness of 50 km, surface heat flows of 15 ± 2 mW m⁻² were inferred for Maat and Ozza Mons and used to calculate a thermal lithosphere of 150 km. Sapas Mons, however, yielded a higher surface heat flow of 21 ± 2 mW m⁻², which resulted in a thermal lithospheric thickness of 107 km [McGovern *et al.*, 1995].

However, a thick thermal lithosphere (~300-400 km) may occur below Atla Regio if convection models and an Isostatic Stagnant Lid (ISL) approximation are used [Orth and Solomatov, 2011]. The ISL approximation involves a motionless lid, which is in isostatic equilibrium, and is located above a convecting mantle. In each of the ISL models, most of the topography was compensated from thermal thinning of the lithosphere, with the best-fit model requiring an average global crustal thicknesses of 50 km and 50% lithospheric thinning. This model resulted in an average lithospheric thicknesses of 560 km and 300-400 km below selected highlands and rises, with the plains regions having thicknesses ranging from 500-600 km.

4.2.2 Crustal thickness

Similar to the thermal lithospheric thickness, crustal thicknesses at selected sites on Venus are also uncertain [Nimmo and McKenzie, 1998]. If Airy isostasy applies, the crust below elevated areas (4-5 km high), should be 20-30 km thicker than the surrounding plains regions [Kiefer and Hager, 1991]. Other studies have suggested that volcanic rises on Venus have crustal thicknesses ranging between 20-50 km [Nimmo and McKenzie, 1998; Phillips, 1994; Smrekar, 1994] or 30 ± 13 km [Phillips, 1994]. Within the plains regions, crustal thicknesses may be 20-40 km thick [Grimm, 1994; Konopliv and Sjogren, 1994; Nimmo and McKenzie, 1998], with other studies suggesting a maximum of 25-30 km should occur within these areas [Banerdt and Golombek, 1988; Grimm and Solomon, 1988; Kiefer and Hager, 1991; Zuber and Parmentier, 1990].

Similar to some of Earth's hotspots, magmatic underplating may have occurred at Atla Regio, whereby melt from an upwelling mantle plume became impeded by the moho resulting in thickening of the lower crust [Smrekar *et al.*, 1997; White, 1993; Wolfe *et al.*, 1994]. Up to 25% of topography at Earth's hotspots can be isostatically compensated by residual melt associated with pressure-release melting [Morgan *et al.*, 1995; Smrekar *et al.*, 1997]. Venus and Earth share comparable volcanic and rise volumes, therefore this amount of compensation may be transferable to Venus [Smrekar *et al.*, 1997; Stofan *et al.*, 1995].

4.2.3 Elastic Lithospheric Thickness and Surface Heat Flow

Surface heat flow was estimated at Atla Regio from elastic lithospheric thicknesses and thermal gradients [Phillips, 1994]. Phillips [1994] assumed Atla Regio shares a similar thermal environment as the East African hot-spot and used an Earth-scaled heat flux of 74 mW m^{-2} as a guide to determine total heat flow within this area. A lower bound total heat flow of 80 mW m^{-2} and a temperature gradient of 20 K km^{-1} resulted in an elastic lithospheric

thickness of 20 km. This elastic lithospheric thickness estimate was significantly lower than the value found from spectral analysis (45 ± 3 km) leading *Phillips* [1994] to propose that Atla Regio should have a lower total heat flow (i.e. $< 80 \text{ mW m}^{-2}$) than what was ascertained from Earth scaling alone. *Smrekar* [1994] also used spectral admittance to calculate the elastic lithospheric thickness at Atla Regio, but combined this with top loading from volcanoes, to infer a value of 30 ± 5 km.

4.3 Methodology

4.3.1 Introduction

Lithospheric modelling below Atla Regio was conducted using the interactive 3D forward modelling tool, GEO3Dmod. GEO3Dmod models the lithospheric structure to the depth of the first phase transition [~ 440 km; *Steinbach and Yuen*, 1992] by simultaneously solving heat transfer, geopotential and isostasy equations. GEO3Dmod requires a suitable reference column, geophysical observables, and a lithospheric model that can comprise any number of crustal layers in conjunction with one lithospheric mantle layer. These layers are characterised by their density and thermal properties, which are defined by the user. The resulting output of GEO3Dmod includes 3D temperature and density distributions of the lithosphere and calculated responses of surface heat flow, elevation, geoid height, and Bouguer gravity. By simultaneously modelling these observables, rather than modelling them singularly, a highly constrained, self consistent lithospheric model is obtained [*Fullea et al.*, 2010].

4.3.2 Geophysical Observables

We used elevation, Bouguer gravity anomalies, and geoid height data sets to constrain our

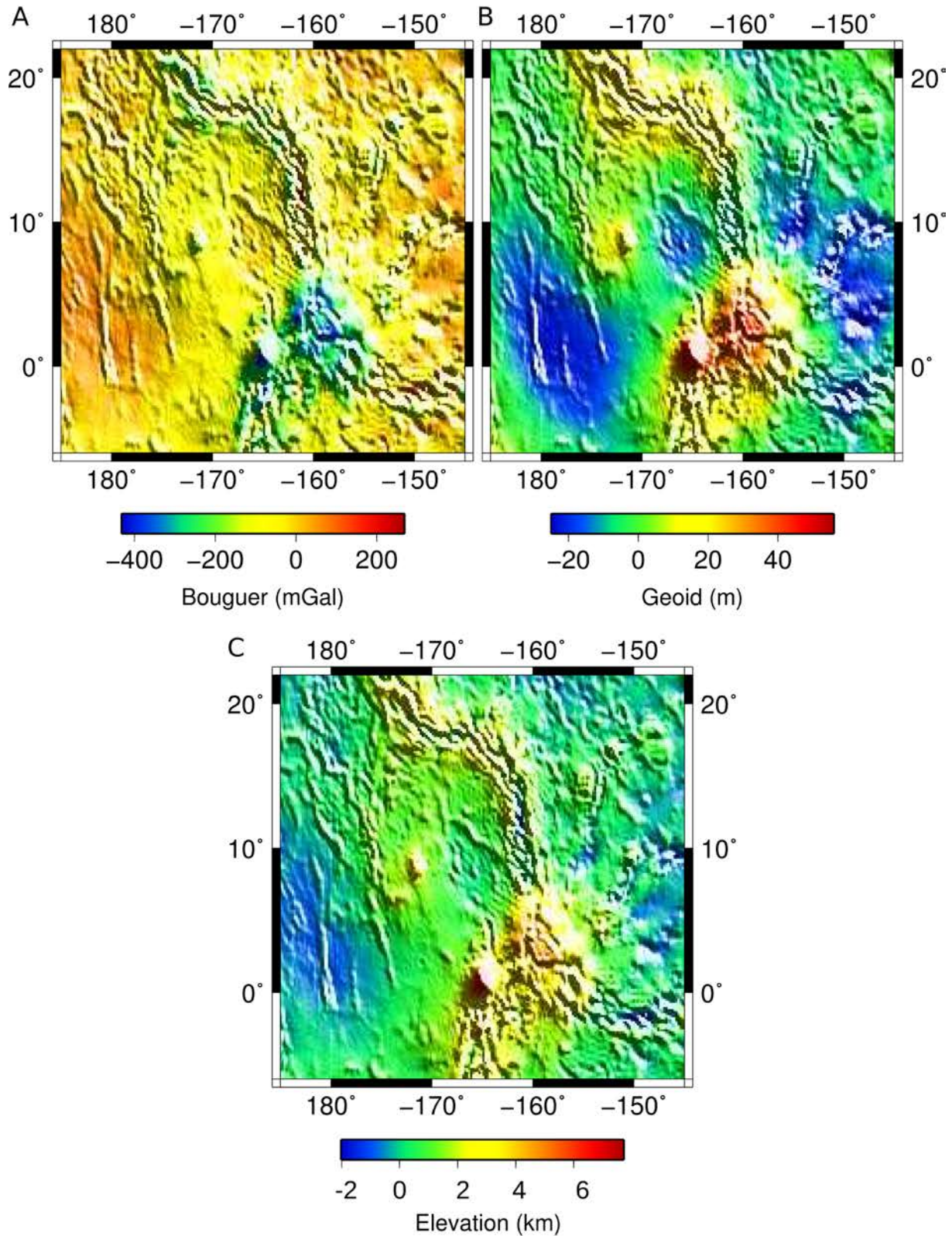


Figure 4.2. Maps of the geophysical observables at Atla Regio. (A) Bouguer gravity. (B) Geoid anomalies, filtered to represent a spherical harmonic degree and order $>\sim 14$. (C) Elevation referenced to Venus' Mean Planetary Radius (6051.848 km).

proposed lithospheric structure at Atla Regio (Figure 4.2). We obtained free-air gravity from the 180th degree and order spherical harmonic model SHGJ180u, which has a maximum uncertainty of 12 mGal [Konopliv *et al.*, 1999]. Bouguer gravity was obtained by subtracting a Bouguer correction from the free-air gravity, with the uncertainty (50 mGal) being calculated from the rules of error propagation (Figure 4.2A) [Bevington and Robinson, 1992; Taylor, 1982; Young, 1962]:

$$B = FA - BC \quad (4.1)$$

$$BC = 2 \pi \rho_{crust} G h \quad (4.2)$$

$$BC_{uncert} = Topo_{uncert} 2 \pi \rho_{crust} G \quad (4.3)$$

$$B_{uncert} = \sqrt{((FA_{uncert})^2 + (BC_{uncert})^2)} \quad (4.4)$$

where B , FA , BC , ρ_{crust} , G , h , B_{uncert} , FA_{uncert} and BC_{uncert} are the Bouguer anomaly, free-air gravity, Bouguer correction, density of the crust (2900 kg m⁻³), universal gravitational constant (6.672x10⁻¹¹ N m² kg⁻²), elevation and uncertainties relating to the Bouguer anomaly, free-air gravity and Bouguer correction, respectively.

The free-air gravity was also integrated through a 2D Fast Fourier Transform to obtain the geoid height (Figure 4.2B) similar to the method of Sjogren *et al.* [1997] and Wessel and Smith [1991, 1998]. This geoid data set has a maximum uncertainty of 2.3 m and contains anomalies from masses deeper than those assumed in our lithospheric modelling. Using a cosine tapered high pass filter all harmonic degrees < 9, corresponding to wavelengths > ~4225 km, were discarded and all harmonic degrees > 14, corresponding to wavelengths < ~2716 km, were passed.

The elevation data, obtained from *Wieczorek* [2007], is a 719 degree and order spherical harmonic model that includes Magellan's Global Topography Data Record 3.2 (GTDR3.2), Pioneer, and Venera 15/16 altimetry (Figure 4.2C). This elevation is also referenced to Venus's Mean Planetary Radius (MPR), equal to 6051.848 km [*Ford and Pettengill*, 1992]. Magellan mapped 97% of Venus's surface, therefore we assume a maximum Root-Mean-Square (RMS) radial uncertainty of 400 m in our modelling [*Rappaport et al.*, 1999].

4.3.3 Lithospheric Modelling Using GEO3Dmod

When using GEO3Dmod, a reference lithospheric structure must first be adopted before lithospheric modelling is initiated. The site of this column was located within the North Polar Plains, at 34.5°E 89°N, since this area has experienced less large scale deformation than the volcanic rises and highland regions (Figure 4.3). The North Polar Plains also correspond to elevations that are similar to Venus's MPR and vast lowland plains areas [*Solomon and Head*, 1990].

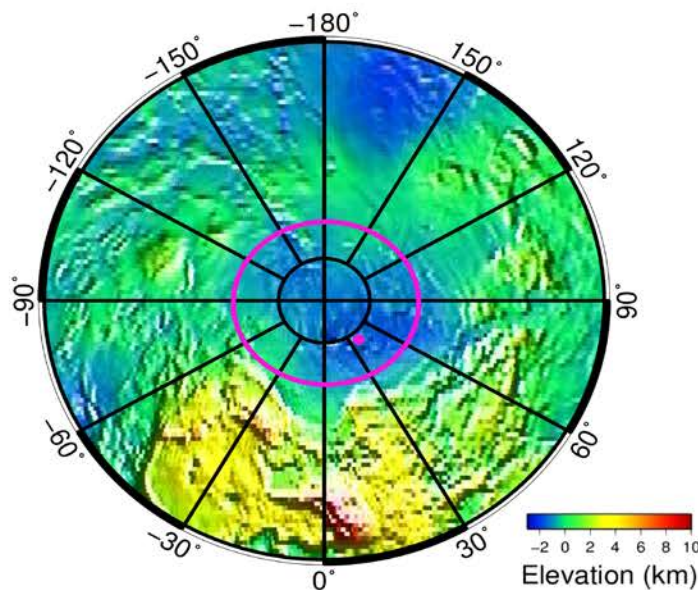


Figure 4.3. Location of the North Polar Plains, shown within the open, purple circle. The location of the reference column at 34.5°E 89°N is shown as the solid circle.

Due to the uncertainty associated with Venusian crustal and lithospheric thickness, three reference columns were adopted at the North Polar Plains and were used to derive a plausible lithospheric structure at Atla Regio (Table 4.1; Figure 4.4). Reference Column 1 has a thick crust (30 km) and a thermal lithospheric thickness of 300 km (Figure 4.4), consistent with previous global estimates [Grimm and Hess, 1997; Nimmo and McKenzie, 1998; Turcotte, 1993]. Reference Column 2 has a 300 km and 15 km thick lithosphere and crust, respectively, whereas Reference Column 3 has a thinner lithosphere (140 km), but a similar 15 km thick crust (Figure 4.4).

Table 4.1. Reference Column Parameters*

Reference Column	T_c (km)	L (km)	ρ_l (kg m ⁻³)	L_o (km)
1	30	300	3203	0.768
2	15	300	3227	-1.48
3	15	140	3206	0.786

* Where T_c , L , ρ_l , L_o are crustal thickness, lithospheric thickness, depth-averaged density of the lithosphere, and calibration constant, respectively.

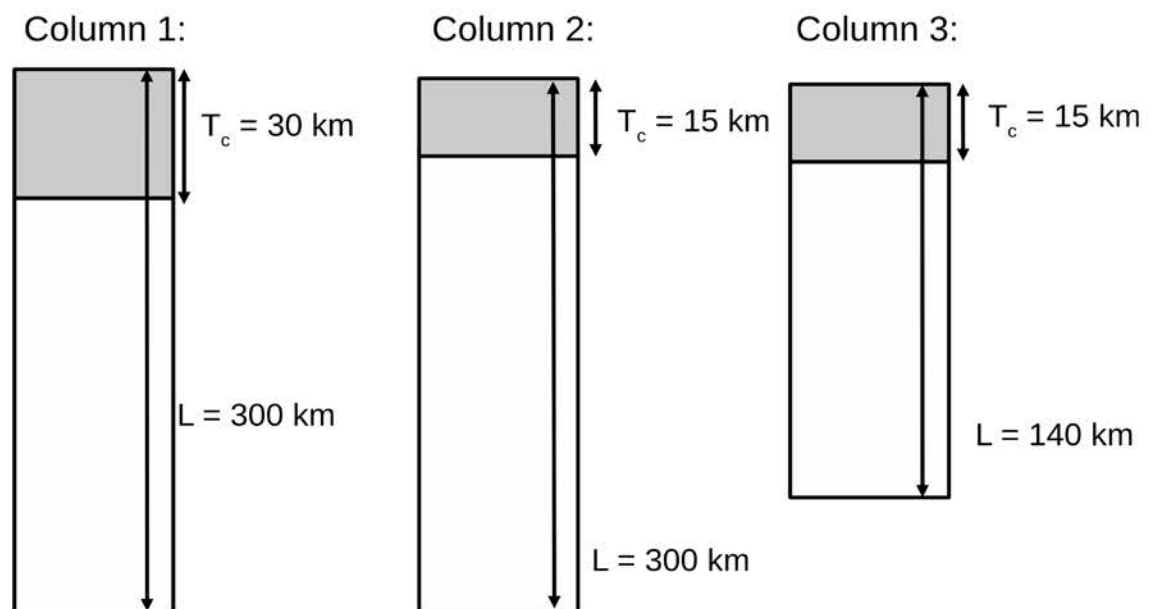


Figure 4.4. Schematic showing the three reference columns used in this study and their crustal and lithospheric thicknesses.

The choice of reference lithospheric structure can strongly influence the derived crustal and lithospheric thickness estimates within an area. In order to obtain the most suitable reference column, we performed a least squares analysis (also known as L2 normalisation) of each model obtained at Atla Regio for Reference Columns 1-3:

$$L2 = \sqrt{\sum \left(\frac{(\text{calculated} - \text{observable})}{\text{uncertainty}} \right)^2} \quad (4.5)$$

where *calculated* is the calculated model, *observable* is the geophysical observable, and *uncertainty* is the uncertainty of the geophysical observable at each x,y node (2240 total nodes) of the model.

For each reference column, we also evaluated the goodness of fit of the modelled responses to the observed responses by viewing profiles taken every 1°N throughout Atla Regio.

The absolute elevation E of any lithospheric column at Atla Regio required a calibration constant L_0 . This calibration constant was calculated from Equation 4.6 using the reference elevation, depth-averaged density of the lithosphere ρ_l , and lithospheric structure of each reference column (Figure 4.5) [Lachenbruch and Morgan, 1990]:

$$\begin{aligned} & \text{If } E \vee E_0 < 0: \\ E \vee E_0 &= \frac{\rho_a}{(\rho_a - \rho_{\text{atmos}})} \left(\frac{(\rho_a - \rho_l)}{\rho_a} L - L_0 \right) \\ & \text{If } E \vee E_0 > 0: \\ E \vee E_0 &= \frac{(\rho_a - \rho_l)}{\rho_a} L - L_0 \end{aligned} \quad (4.6)$$

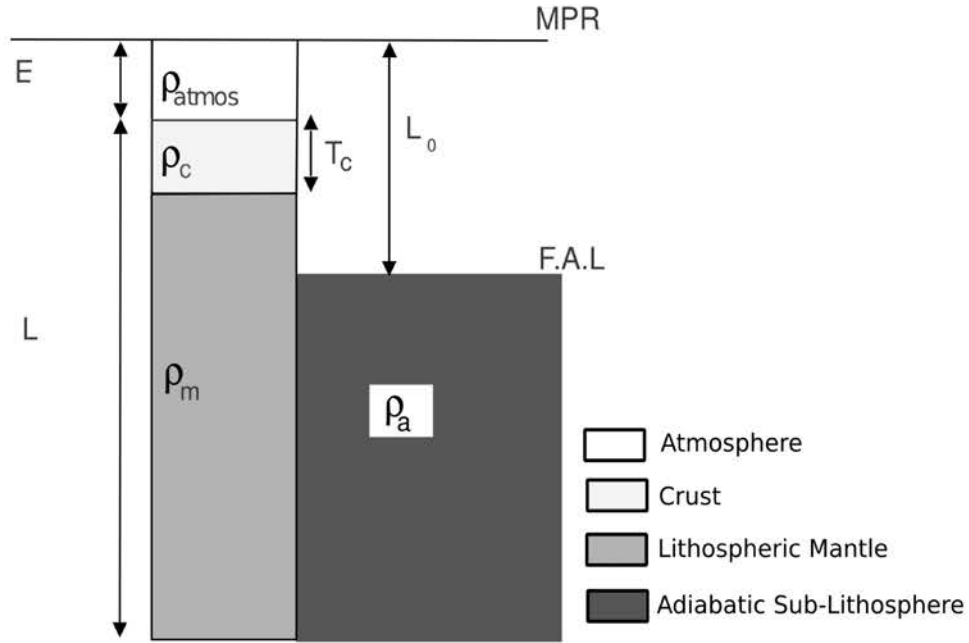


Figure 4.5. (Adapted from *Fullea et al. [2007]*) Notation for each lithospheric model at Atla Regio. E is the absolute elevation, T_c and L are the crustal and lithospheric thickness, respectively. The density of the atmosphere, crust, lithospheric mantle, and adiabatic sub-lithosphere are denoted by ρ_{atmos} , ρ_c , ρ_m and ρ_a . L_0 is the calibration constant, and represents the depth from the MPR to the Free-Asthenosphere Level (F.A.L.).

where ρ_{atmos} is the density of the atmosphere (60 kg m^{-3}), ρ_a is the density of the adiabatic sub-lithosphere (3200 kg m^{-3}), L is the thermal lithospheric thickness, L_0 is the calibration constant. The depth-averaged density of the lithosphere ρ_l is found by averaging the density output calculated by GEO3Dmod for the proposed lithospheric structure. Equation 4.6 was used when calculating the calibration constant L_0 for the reference elevation E_0 at the North Polar Plains (-1.069 km) and the absolute elevation E of any lithospheric column within the modelled area (Atla Regio).

The lithospheric model at Atla Regio has $70 \times 32 \times 204$ nodes and includes three layers, with properties shown in Table 4.2. Each layer has a different coefficient of thermal expansion and temperature-dependent density. The parameters shown in Table 4.2 are indicative of basalt,

diorite, gabbro, and peridotite. Basalt and gabbro are the most plausible compositions of the surface and sub-surface of Venus since both Venera and Vega landers sampled rocks with compositions similar to basalt [Grimm and Hess, 1997]. Also, volcanoes on Venus appear shield-like and have widespread flow deposits, which are indicative of effusive eruption of low-viscosity lavas, such as basalt [Head *et al.*, 1992]. For this study, we have assumed that Venus's crustal density is similar to Earth's crustal basaltic rocks ($\sim 2900 \text{ kg m}^{-3}$).

With greater depths, we expect that basalt will transition into gabbro, which has a density of $\sim 3000 \text{ kg m}^{-3}$ [Reynolds, 1997]. The low-density intrusion has a density (2500 kg m^{-3}) similar to diorite, which is more silicic in composition than basalt [Reynolds, 1997]. More silicic compositions have been proposed by some authors as being responsible for regions of high elevation on Venus whereas the intermediate compositions (diorite) are consistent with the geomorphological and geochemical data [Grimm and Hess, 1997; Jull and Arkani-Hamed, 1995; McKenzie *et al.*, 1992]. The fourth layer is the lithospheric mantle, which has a density similar to peridotite [Rogers, 2007].

Table 4.2. Layer parameters

Layer	Name	Density kg m^{-3}	Coefficient of thermal expansion ($\times 10^{-5}$) K^{-1}	Thermal conductivity W K^{-1}	Heat Production Rate ($\times 10^{-7}$) W m^{-3}	Pressure Coefficient ($\times 10^{-10}$)
1	Upper crust	2900	2.75	2.1	2.0	2.36
2	Intrusion	2500	1.60	3.0	2.0	2.44
3	Lower crust	3000	1.60	3.0	2.0	2.44
4	Lithospheric Mantle	3200	3.50	3.3	0.2	0

The thermal parameters of each layer shown in Table 4.2 were similar to those used by Afonso *et al.* [2005], Ranalli [1995], and Schubert *et al.* [2002]. Furthermore, the pressure coefficient

or compressibility β of each layer was derived from [Schubert *et al.*, 1997]:

$$K = \frac{E}{3(1-2\nu)} \quad (4.7)$$

$$\beta = \frac{1}{K}$$

where K is the bulk modulus, E is Young's modulus, and ν is Poisson's ratio.

Below the lithospheric mantle is the adiabatic sub-lithospheric mantle. This layer was not included in Table 4.1 since our model domain only extends through the conductive thermal lithosphere (i.e. the crust and lithospheric mantle or layers 1-4). The constant density of this layer (3200 kg m^{-3}), however, acts as a reference density for the density variations in the conductive thermal lithosphere.

GEO3Dmod also calculates the flexural response for a chosen elastic lithospheric thickness. Due to the uncertainty surrounding Atla Regio's elastic lithospheric thickness we ran each model with a constant value of 10 km, 30 km, and 50 km. One limitation of this study is that the flexural response was not iteratively solved. Instead, flexure was calculated from the residual topography, which was the difference between the calculated model response and the observables, after Airy and thermal isostasy were accounted for. From this residual topography we also derived an estimate for the amount of dynamic uplift by removing the isostatic and flexural contribution from the observed topography.

The modelled area at Atla Regio extends from 175°E to -145°E and -6°N to 22°N (Figure 4.6). We present three lithospheric profiles taken over Atla Regio and regional maps of crustal and lithospheric thickness. The location of each profile is shown in Figure 4.6.

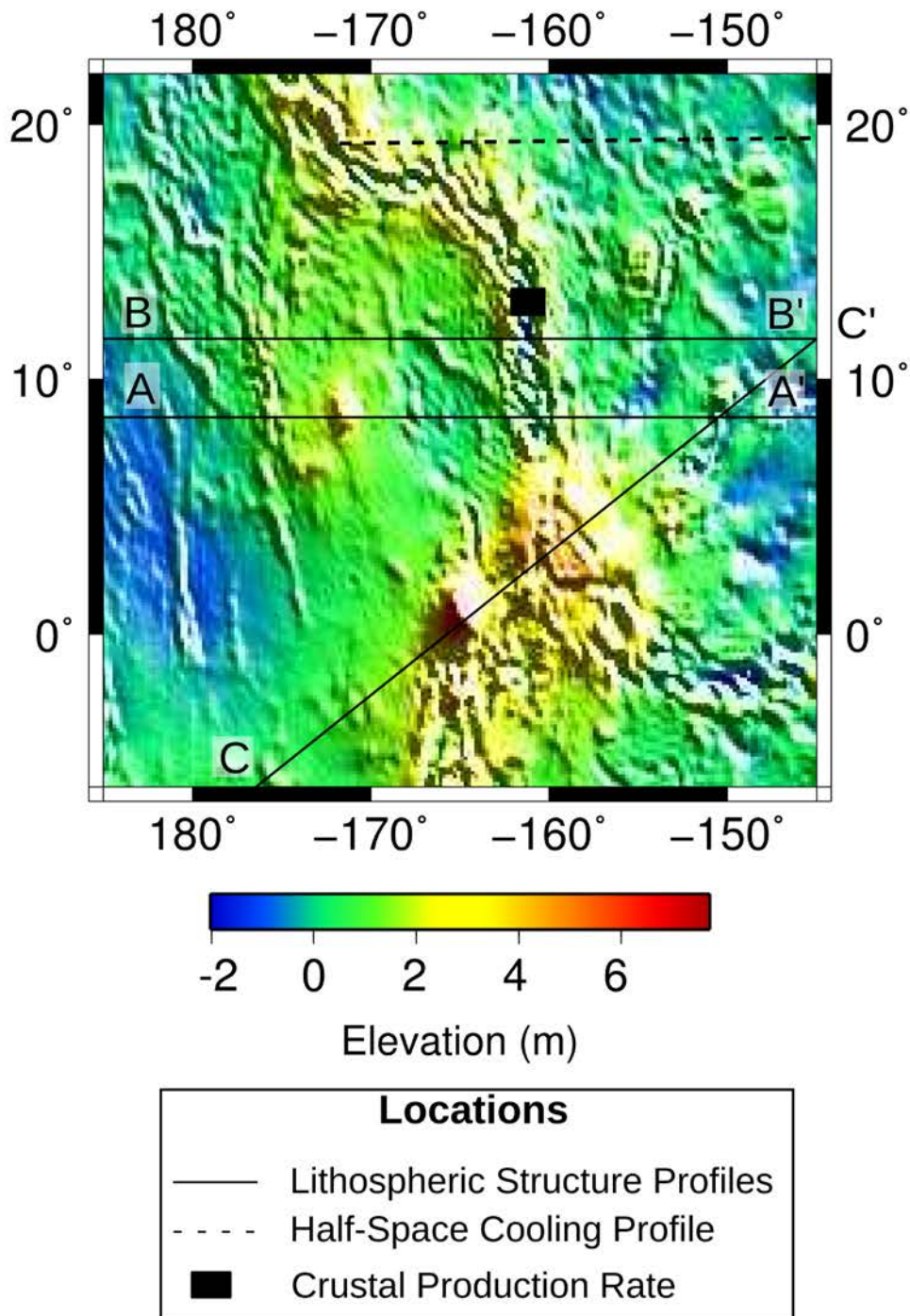


Figure 4.6. Elevation map showing the location of the lithospheric structure profiles (solid lines) discussed in Section 4.4.1 and the lithospheric thickness profiles used in the half-space cooling model (dashed). A portion of the profile A-A' (12°N) is also used in the half-space cooling model. The area used for the crustal production rate calculations is centered at the black, solid rectangle.

4.3.4 Melt Generation Rates

Our proposed lithospheric structure was constrained by comparing calculated melt generation rates, from a synthetic mantle plume, to previous estimates [Nimmo and McKenzie, 1998].

The amount of melt associated with an upwelling mantle plume is related to the temperature within the plume and the thickness of the lithosphere [Nimmo and McKenzie, 1998]. A thicker modelled thermal lithosphere will limit the amount of melt produced and extracted at the surface compared to a thinner modelled thermal lithospheric thickness. Mantle and plume temperature can also influence the amount of melt generated, therefore we chose to use two different mantle and plume temperatures, similar to Smrekar and Parmentier [1996].

To calculate melt generation rates, we assumed an axisymmetric plume structure within the lower mantle, similar to Olson *et al.* [1993] (Figure 4.7). The plume originates from a hot basal boundary layer, approximated by a disk with a radius of 1200 km. The upwelling mantle plume rises slowly upwards, comparable to vertically uniform Poiseuille flow [Olson *et al.*, 1993].

Plume temperature varies both vertically and radially [Schubert *et al.*, 2001]. Equations 4.8-4.11 address the variation of plume temperature and ascent velocity in the radial direction only. Figure 4.7 shows the parameters of the plume used in Equations 4.8-4.11. At each radial r increment (10 km), the temperature T_{plume} follows a Gaussian temperature distribution, best approximated by:

$$T_{plume} = T_{mantle} - T_{boundary} \exp\left(\frac{-r^2}{w_{plume}^2}\right) \quad (4.8)$$

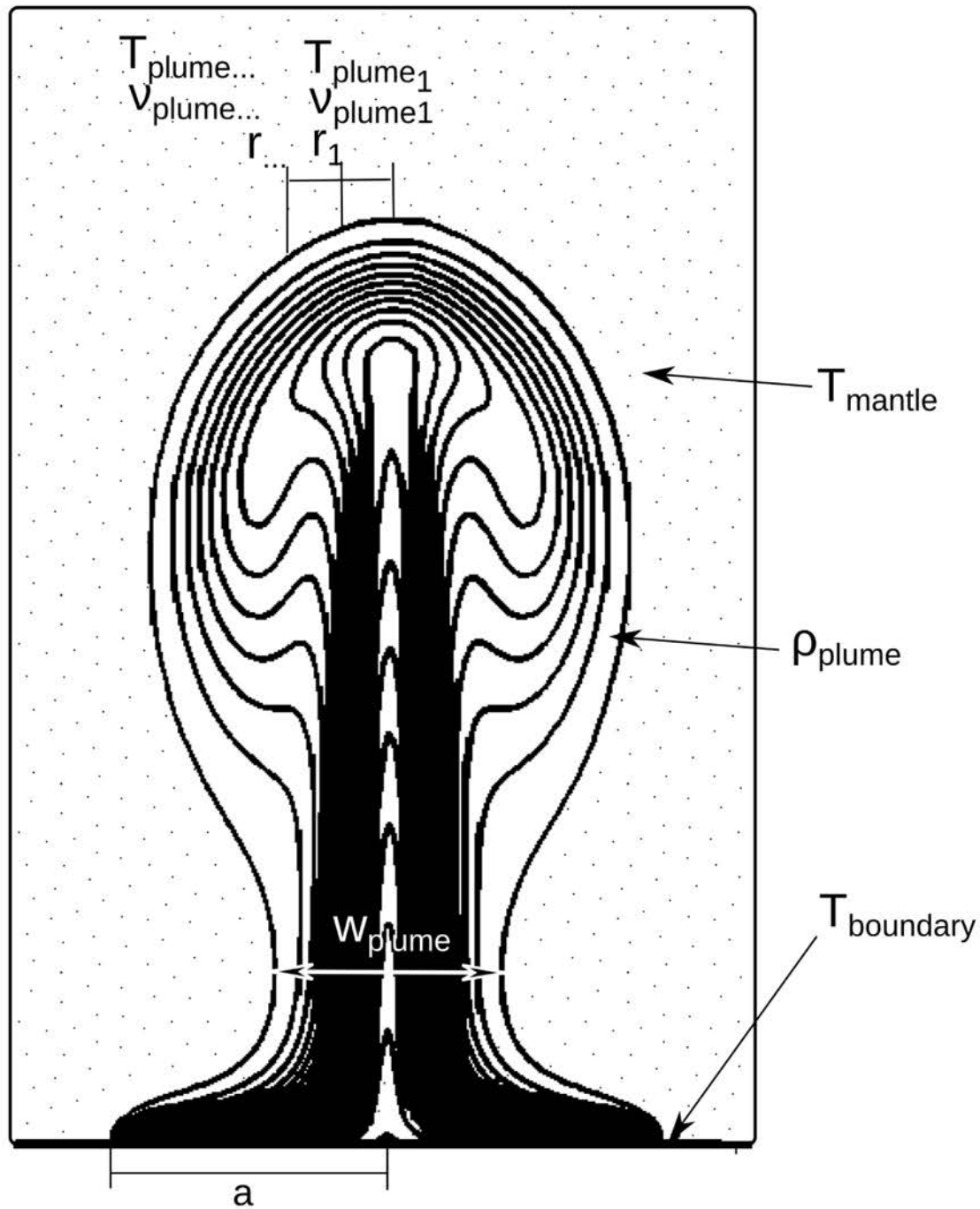


Figure 4.7. (Modified from *Olson et al.*, 1993) An axisymmetric mantle plume with the parameters used in Equations 4.8 to 4.11. T_{mantle} is the temperature of the mantle, T_{boundary} is the temperature at the basal boundary, w_{plume} is the thermal width of the plume, and a is the radius of the basal boundary. The ascent velocity of the plume v_{plume} and the temperature of the plume T_{plume} varies at each radial r increment.

where w_{plume} is the thermal width. For each of our cases, the plume's initial temperature T_{plume} is 1500°C and 1950°C, T_{mantle} is the temperature of the mantle (1300°C; 1700°C), and $T_{boundary}$ is the temperature of the basal boundary (2023.15 K).

The thermal width w_{plume} and structure of the plume depends on both the Rayleigh number Ra and radius of the heated basal boundary layer a [Olson *et al.*, 1993]:

$$w_{plume} = a \left(\frac{8}{3Ra} \right)^{(1/6)} \quad (4.9)$$

$$Ra = \frac{(\rho_{plume} \alpha g (T_{boundary} - T_{mantle}) a^3)}{(\kappa \eta)} \quad (4.10)$$

where ρ_{plume} is the density of the mantle plume (3250 kg m⁻³); α is the thermal expansivity (1×10⁻⁵ K⁻¹); g is the gravitational acceleration of Venus (8.87 m s⁻²), κ is the thermal diffusivity, a is the radius of the heated region at the base of the mantle plume (1200 km), and η is the viscosity at the background mantle temperature (1×10²² Pa s).

At each radial increment (10 km) the ascent velocity v_{plume} also varies, depending on the viscosity of the mantle that it is rising through, the thermal width w_{plumes} , and mass λ of the plume [Olson *et al.*, 1993]:

$$\lambda = \pi \rho_{plume} \alpha g (T_{boundary} - T_{mantle}) w_{plume} \quad (4.11)$$

$$v_{plume} = \frac{\lambda}{(4 \pi \eta)} \frac{(w_{plume}^2 - r^2)}{w_{plume}^2} \quad (4.12)$$

The temperature of the plume also varies with depth, thus we added a mantle adiabatic temperature gradient to each radial plume temperature. The adiabatic temperature gradient

$dT_{\text{mantle}}/dr_{\text{mantle}}$ of 0.36 K km^{-1} for Venus's upper mantle was found from [Fowler, 2004]:

$$\frac{dT_{\text{mantle}}}{dr_{\text{mantle}}} = \frac{(T \alpha g)}{c_p} \quad (4.13)$$

where T is set to 1700 K, c_p is the specific heat (1.25 J Kg C^{-1}), and α is the thermal expansivity ($3 \times 10^{-5} \text{ K}^{-1}$).

Before calculating the amount of melt produced, we first needed to calculate the temperature of the peridotite solidus T_s and liquidus T_l [McKenzie and Bickle, 1988]:

$$P = \frac{(T_s - 1100)}{136} + 4.968 \times 10^{-4} \exp[1.2 \times 10^{-2}(T_s - 1100)] \quad (4.14)$$

$$T_l = 1736.2 + 4.343P + \left[180 \tan^{-1} \left(\frac{P}{2.2169} \right) \right] \quad (4.15)$$

where P is in the units of GPa.

The pressure used in Equations 4.14 and 4.15 was then converted to depth assuming a geobaric gradient d^{-1} of 35 MPa km^{-1} for the mantle:

$$d = \frac{P}{(\Delta P \Delta d^{-1})} \quad (4.16)$$

By converting the pressure to depth, we could now calculate the melt fraction F for each depth increment (every 10 km) within the plume. We considered the depth of the plume at each radial increment to be limited by the thickness of the modelled thermal lithosphere (i.e. 50 km

and 100 km) and the depth where the temperature of the plume was less than the temperature of the solidus.

For each depth increment within the plume, the melt fraction was calculated, which is a function of the super-solidus temperature T_{ss} [McKenzie and Bickle, 1988]:

$$T_{ss} = \frac{(T_{plume} - T_s)}{(T_l - T_s)} \quad (4.17)$$

$$F = 2.0684T_{ss} - 4.0564T_{ss}^2 + 2.988T_{ss}^3 \quad (4.18)$$

So far Equations 4.8-4.18 assume only two dimensions, a radial and depth component. However, to estimate the melt volume, we considered the plume as a three dimensional cylinder, where the volume of melt is denoted by M :

$$M = \pi(r_2^2 - r_1^2) d F \quad (4.19)$$

where $r_2 - r_1$ is the radial distance between two points and d is the depth increment within the plume (every 10 km).

The ascent velocity for each radial annulus was then used in conjunction with the thickness of each depth slice (10 km) to determine the ascent time t :

$$t = \frac{d}{v_{plume}} \quad (4.20)$$

Using the melt volume M and time ascent time t for each radial annulus the melting rate R_p

was determined from:

$$R_p = \frac{M}{t} \quad (4.21)$$

A total melting rate and volume from the plume was then found by adding the melting rate and volume for each radial annulus, at each depth increment.

4.3.5 Half-Space Cooling

We use the modelled lithospheric thicknesses, in conjunction with a half-space cooling model, to determine the rate of rifting at Ganis Chasma. The lithospheric thickness profiles used to constrain the rifting rates were taken over two locations, 12°N and 19°N (Figure 4.6), where Ganis Chasma changes from trending northerly (at 12°N) to north-westerly (at 19°N). These profiles have an absolute temperature of 1300°C (1573 K) and represent the isotherm at the base of the lithosphere. We used Equation 4.22 to calculate how the lithospheric thickness y , varies with spreading rate u

$$\frac{(T - T_0)}{(T_1 - T_0)} = \text{erf} \left[\frac{y}{(2\sqrt{(kx/u)})} \right] \quad (4.22)$$

where $T - T_0$ is the temperature difference between the base of the lithosphere and the surface equal to 200 K, 400 K, 600 K, and 800 K, respectively [Turcotte and Schubert; 2001]. T_0 is the initial temperature below the plate (1573 K), T_1 is the surface temperature (693 K), x is the distance away from the center of the rift (0-2878 km), and κ is the thermal diffusivity ($1 \times 10^{-6} \text{ m}^2 \text{ s}^{-1}$). It should be noted that this technique only assumes vertical heat conduction, not

horizontal heat conduction [Turcotte and Schubert, 2001].

On Earth, the evolution of temperature in the boundary layer, represented by the half-space cooling model and Equation 4.22, assumes the existence of widespread plate tectonics. On Venus, if new crust is formed at a rift it should follow a similar cooling and thickening processes as crust formed at a rift on Earth. However, where subduction zones operate on Earth to destroy the crust, crustal destruction on Venus most likely occurs via retrograde localised subduction or compression and lithospheric delamination [Bilotti and Suppe, 1999; McGill, 1993; Schubert and Sandwell, 1995; Romeo and Turcotte, 2008; Turcotte, 1995]. Even though Venus lacks long linear volcanic chains, multiple tectonic plates, and clear evidence of crustal destruction, the process of conductive cooling of new crust is the same.

4.3.6 Crustal Production Rates

Crustal production rate R_c , calculated from the modelled crustal thicknesses and spreading rates, can be used to constrain the mechanisms that formed the crust at Ganis Chasma (Figure 4.6):

$$R_c = T_c u \quad (4.23)$$

where T_c is the crustal thickness obtained from lithospheric modelling and u is the half rate of spreading.

4.4 Results

4.4.1. Constraining a Suitable Reference Column

Our choice of reference column parameters can have a significant influence on our proposed lithospheric structure at Atla Regio. Reference Column 1 ($T_c=30$ km, $L=300$ km) produced the best-fit model, however, to test the influence of a thinner crust and the contribution of magmatic underplating in supporting topography we also used Reference Column 2 ($T_c=15$ km and $L=300$ km). We kept the crustal thickness the same (15 km) and chose to model a thinner (140 km) thermal lithosphere for Reference Column 3.

The least-squares analysis results indicate Reference Column 1 is the most suitable reference column at Atla Regio, compared to Reference Columns 2 and 3. From Table 4.3, Reference Column 1 has the least misfit between the observed and calculated geoid and elevation, with a slightly similar Bouguer gravity misfit as Reference Column 2. We were primarily concerned with fitting the geoid and elevation data sets, therefore the lithospheric structure of Reference Column 1 was chosen as being the most suitable for our modelling.

Table 4.3. Results from the least-squares analysis for each reference column

Model	Elevation (m)	Bouguer (mGal)	Geoid (m)
Ref. Column 1	1.61	16.21	203.78
Ref. Column 2	1.76	16.14	316.07
Ref. Column 3	1.78	17.33	247.68

Using Reference Columns 2 and 3 also produced lithospheric models that had a poor-fit between the modelled and observed elevations along the central rift trough of Ganis Chasma (Figure 4.8-4.9). Along this central rift trough, the crust required unrealistic thinning, above 0 km depth, in order to reduce the calculated topography to the observed topography (Figures 4.8-4.10). As a result of thinning the crust to these levels, the calculated geoid decreased and further lithospheric thinning was required. This thinning of the thermal lithosphere, however, had the effect of increasing the calculated elevation at the central rift trough. In order to

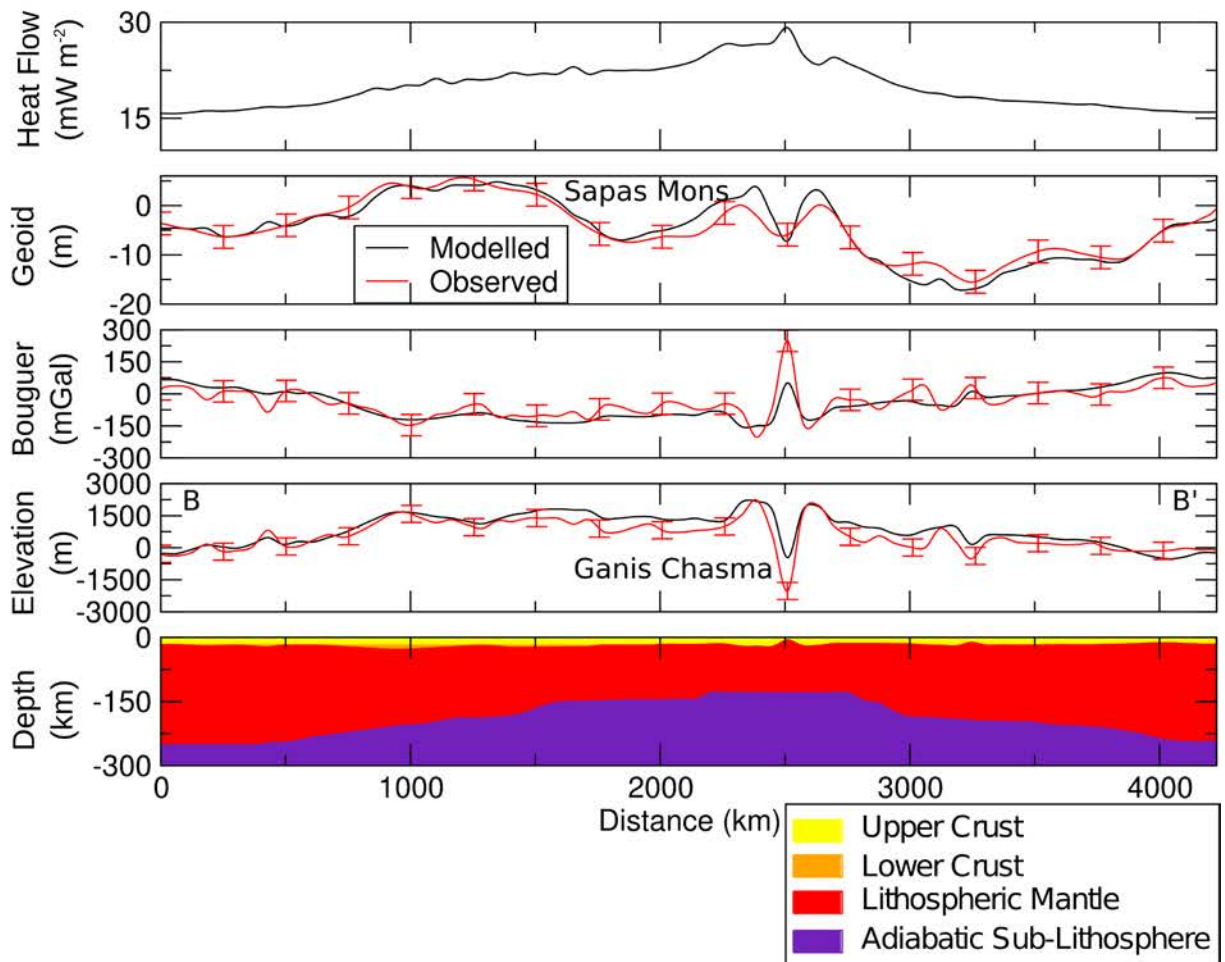


Figure 4.8. Lithospheric structure along Profile B-B', considering Reference Column 2 ($T_c=15$ km, $L=300$ km). The key is similar to Figure 4.9. The misfit between the forward modelled responses (black lines) and the observables (red lines) require implausible crustal (< 0 km) thinning. The upper crust, the lower crust, lithospheric mantle, and adiabatic sub-lithosphere are shown as the yellow, orange, red, and purple layers, respectively. No profiles of observed surface heat flow are available.

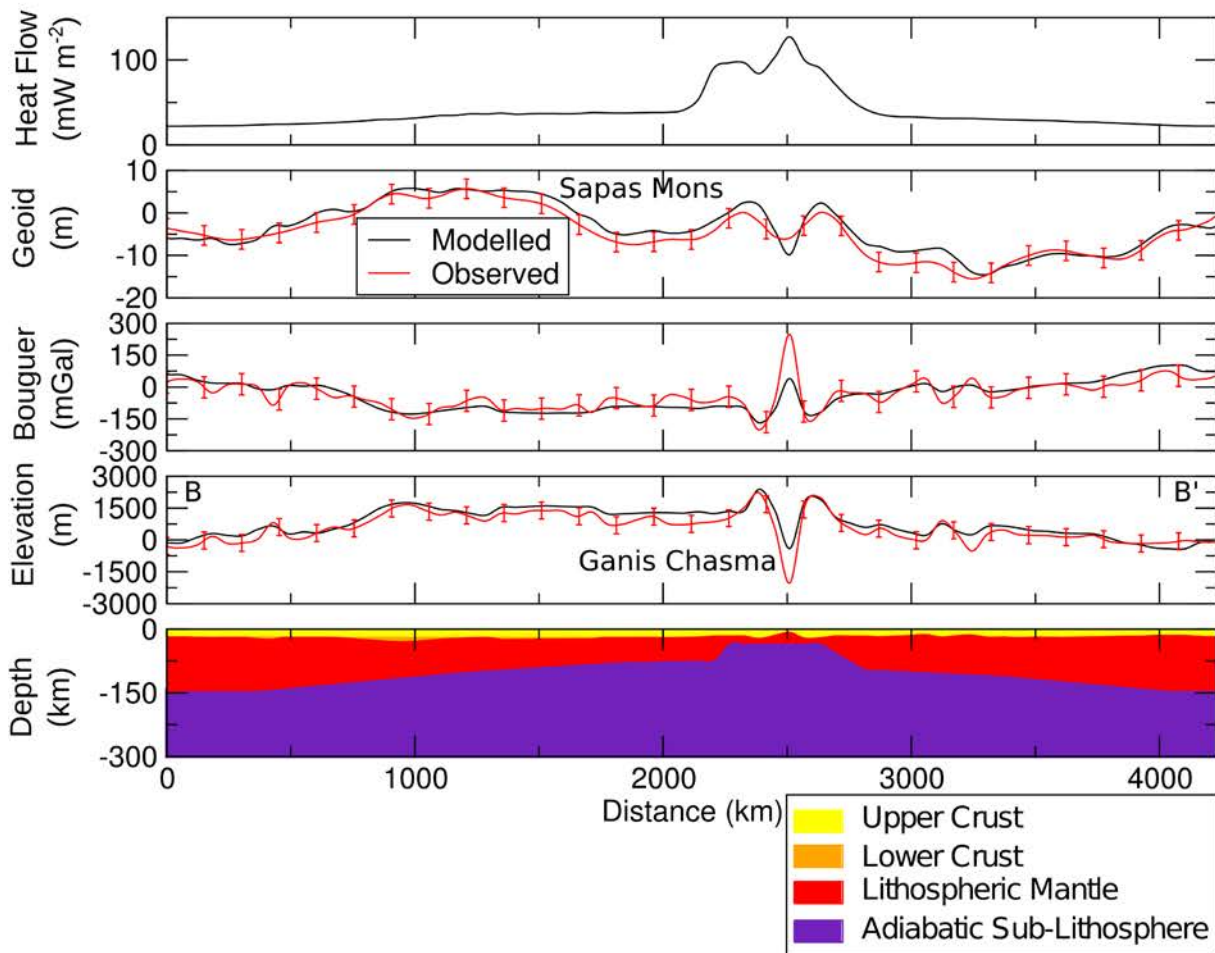


Figure 4.9. Reference Column 3 ($T_c=15$ km; $L=140$ km) results in very thin crustal and lithospheric thicknesses at Ganis Chasma. The misfit between the forward modelled responses (black lines) and the observables (red lines) require implausible crustal (< 0 km) and lithospheric thicknesses (< 25 km). Key is similar to Figure 4.8.

decrease the calculated elevation to the observed, further crust thinning (i.e. above 0 km) was required. An extremely thin modelled lithospheric thickness, such as that from Reference Column 3 (Figure 4.10), would also act as a minor impedance to upwelling melt, resulting in inconsistent melt generation rates [Nimmo and McKenzie, 1998]. Therefore, the poor-fit from the least-squares analysis and the model results suggest that Reference Columns 2 and 3 are not suitable reference lithospheric structures.

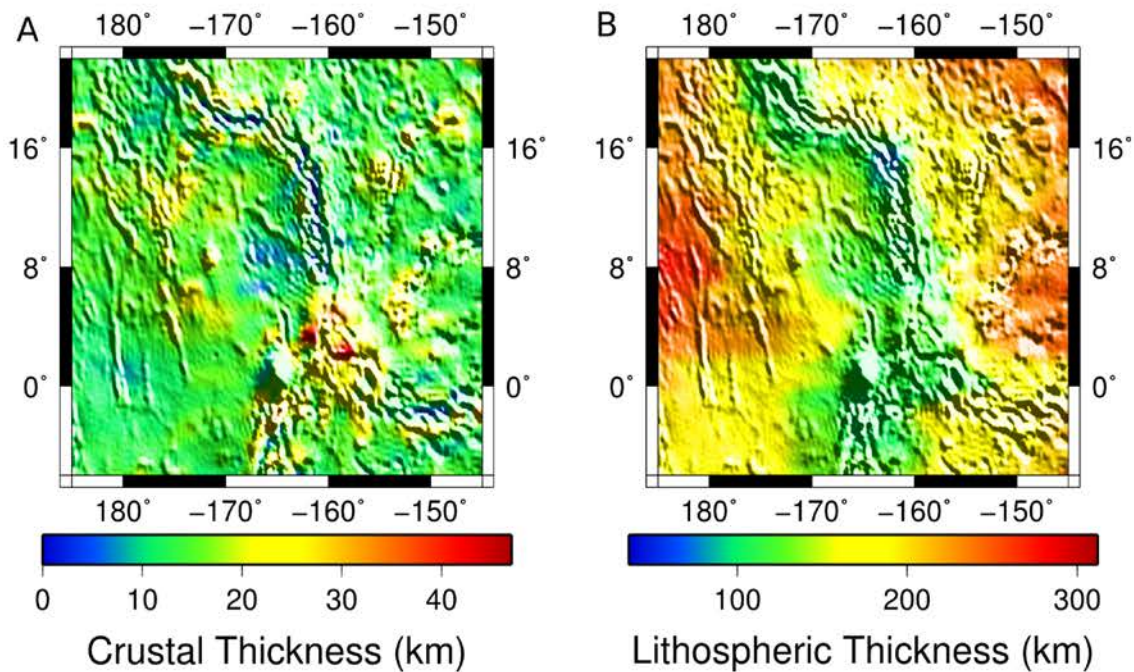
4.4.2 Residuals

Residuals for Reference Column 1 are shown in Figure 4.11. The residuals represent the model's misfit and can indicate either areas where additional compensation mechanisms are required or an unknown density structure that is not currently accounted for by the proposed lithospheric structure. Each residual histogram plot exhibits a Gaussian-like distribution with most of the residuals at 0% or within an error of 10% (Figure 4.12), implying most of the geophysical observables can be fitted by our lithospheric structure.

4.4.3 Profiles of Lithospheric Structure

Reference Column 1, which has a crustal and lithospheric thickness of 30 km and 300 km, respectively, provided the best-fit model to the geophysical observables. Considering this model, profile A-A' runs from 175°E to -145°W at 8°N and includes Sapas Mons and Ganis Chasma (Figure 4.13). Multiple rift troughs are evident and have crustal thicknesses ranging between ~0.4-20 km (Figure 4.13). In order to fit the elevated rift shoulders of Ganis Chasma, a thick crust (24-42 km) is required at a distance of ~2400 km and ~2700 km. The thermal

Reference Column 2



Reference Column 3

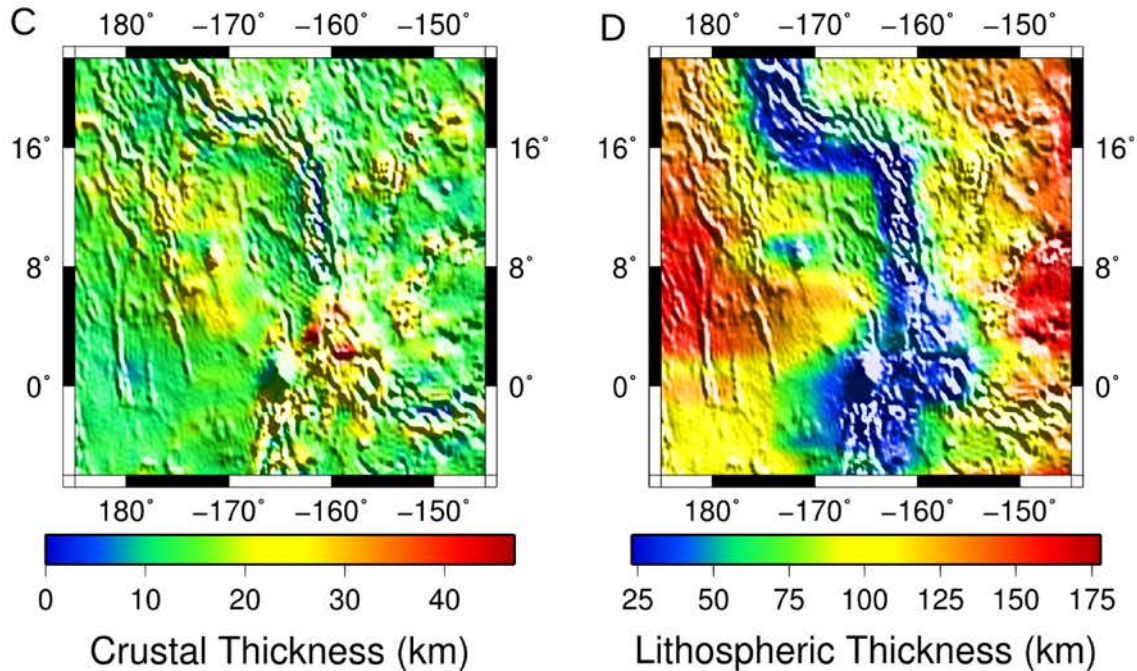


Figure 4.10. Crustal and thermal lithospheric thickness at Atla Regio using Reference Column 2 (A-B) and Reference Column 3 (C-D). Both reference columns result in unrealistic crustal thicknesses (0 km) below the central rift trough of Ganis Chasma and Reference Column 3 results in an unrealistic lithospheric thickness (< 25 km) below Ganis Chasma.

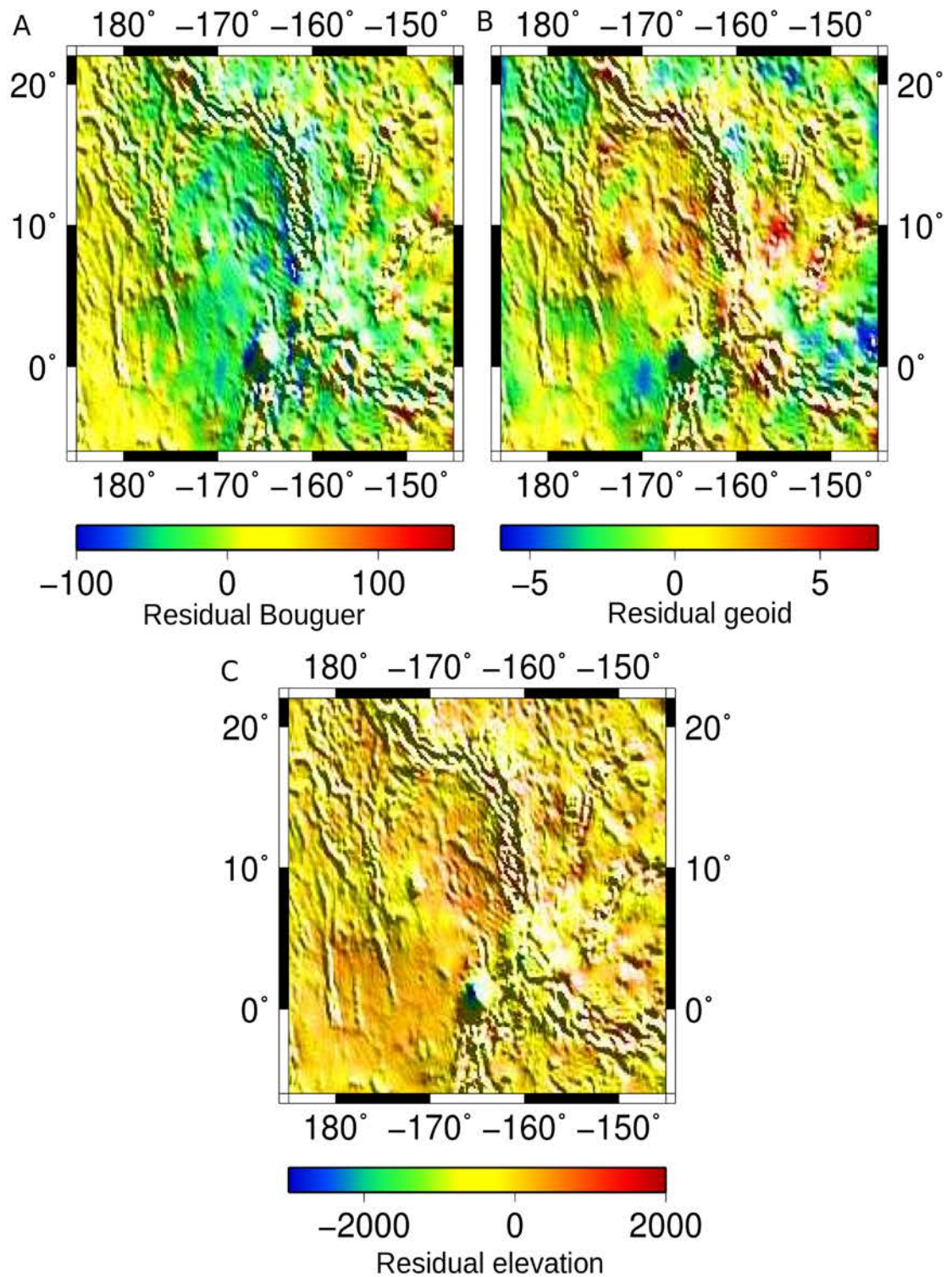


Figure 4.11. Residual Bouguer gravity (A), residual geoid (B), and residual elevation (C) maps are useful in delineating where additional compensation mechanisms are required. The negative geoid anomalies and elevation at Maat and Ozza Mons suggest additional mechanisms are required to support this area.

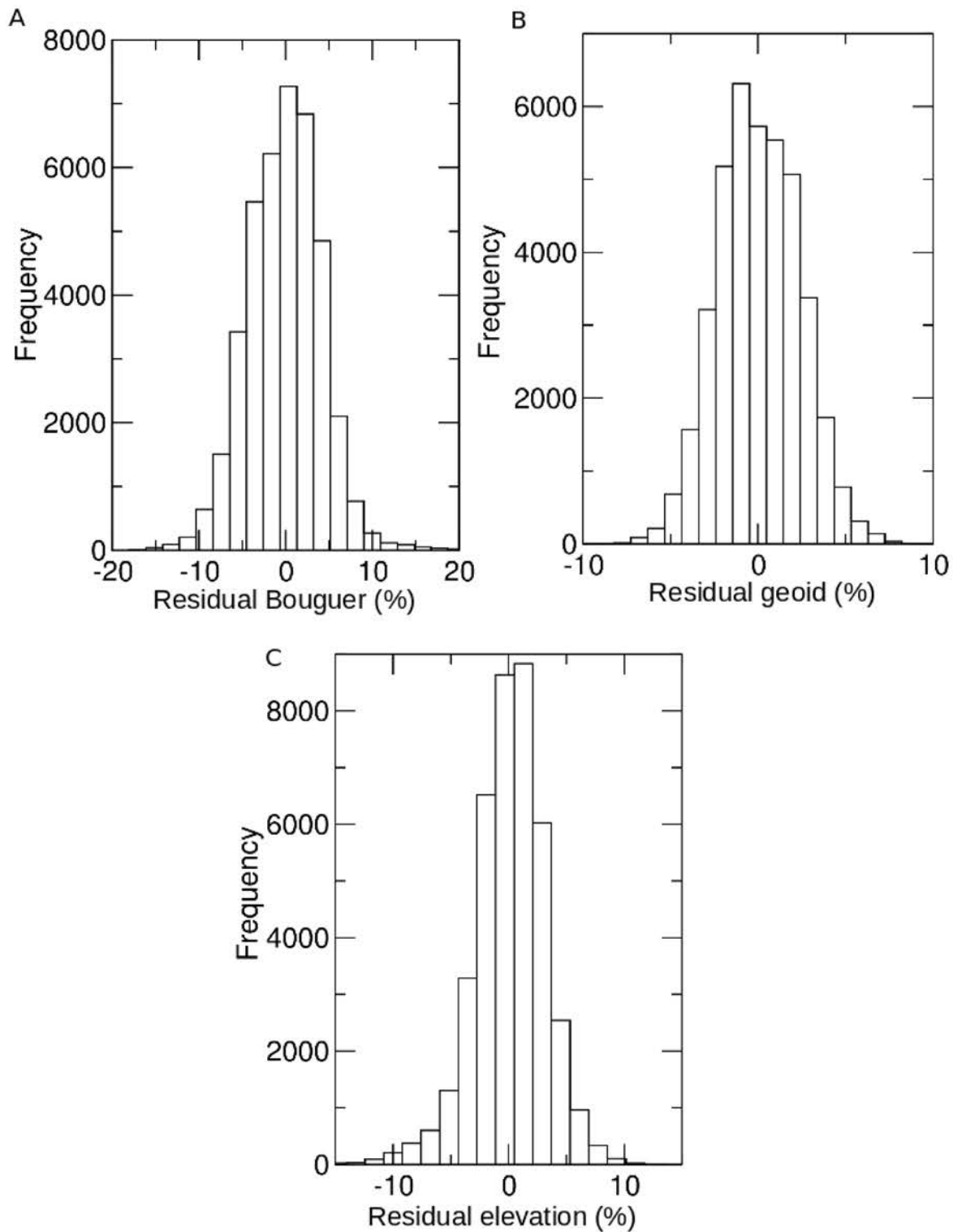


Figure 4.12. Histogram plots of (A) residual Bouguer gravity, (B) residual geoid, and (C) residual elevation. Residuals are shown as a percentage of the total magnitude range for each observable. Each histogram plot exhibits a Gaussian-like distribution, with the majority of the residuals being within 10% error.

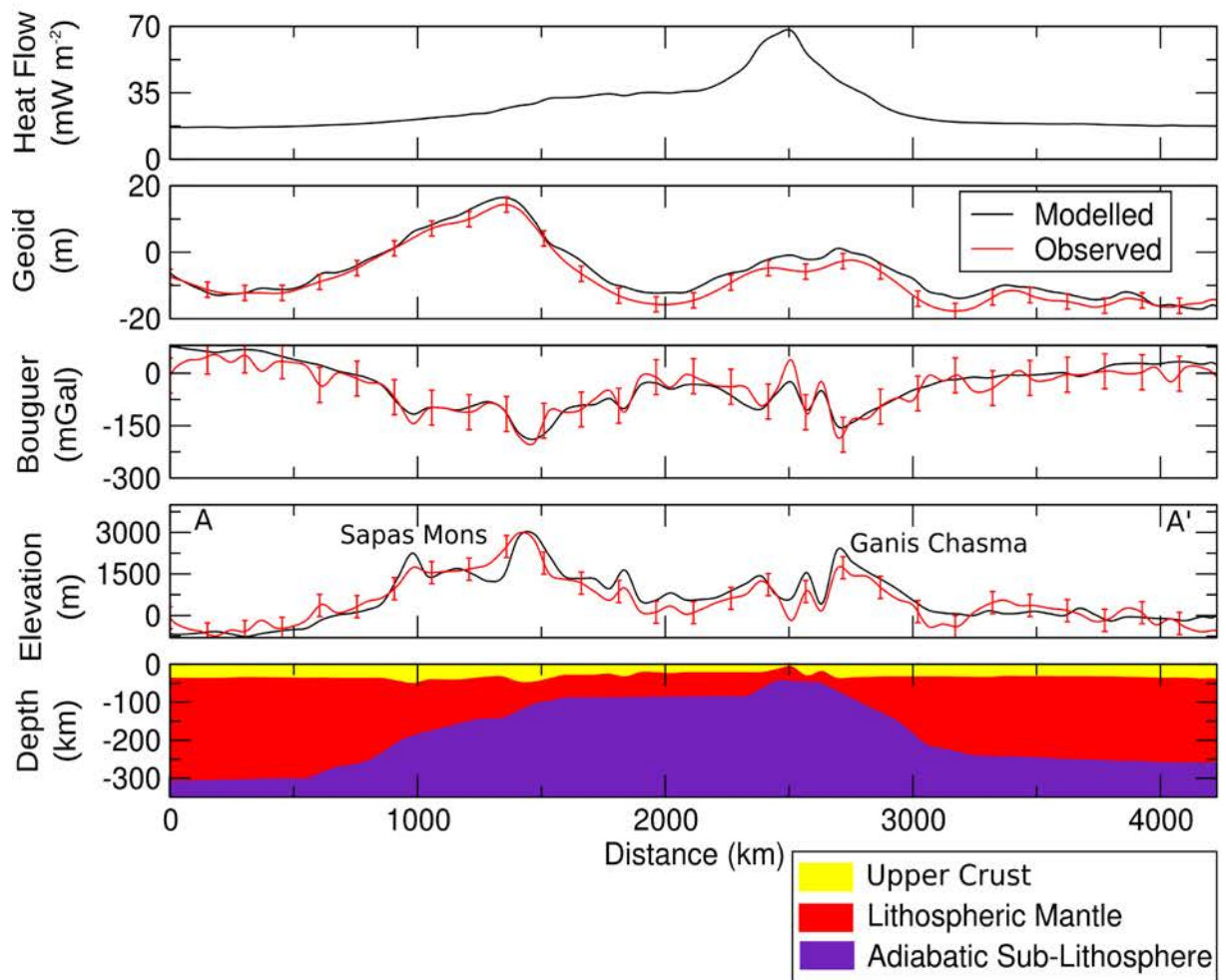


Figure 4.13. Modelled lithospheric structure along Sapas Mons and Ganis Chasma from 175°E to -145°W at 8°N. The proposed lithospheric structure was modified until the forward modelled responses (black lines) were within error of each observable (red lines). The upper crust, lithospheric mantle, and adiabatic sub-lithosphere are shown as the yellow, red, and purple layers, respectively. No profiles of observed surface heat flow are available.

lithosphere below Ganis Chasma is thin, approximately 50 km, but this thickens to ~100 km below Sapas Mons and 250-305 km in the surrounding plains regions (Figure 4.13). Surface heat flow is greatest (68 mW m^{-2}) at Ganis Chasma, followed by Sapas Mons ($\sim 27 \text{ mW m}^{-2}$) with the plains surrounding the volcanic rise having the lowest values ($16\text{-}19 \text{ mW m}^{-2}$; Figure 4.13).

Profile B-B' extends over one of the deepest parts of Ganis Chasma from 175°E to -145°W at 12°N (Figure 4.14). Even though Sapas Mons is not apparent in the topography, it is in the geoid, which is slightly higher towards the west of this profile (Figure 4.14). The crust below the central trough at Ganis Chasma is thin ($\sim 2.4 \text{ km}$) at a distance of $\sim 2520 \text{ km}$, but thickens towards the rift shoulders at a distance of $\sim 2400 \text{ km}$ and $\sim 2600 \text{ km}$ ($\sim 30\text{-}36 \text{ km}$; Figure 4.14). Crustal thicknesses within the surrounding plains regions range from $20\text{-}30 \text{ km}$, but thicken ($\sim 40\text{-}45 \text{ km}$) below the western sinuous ridges, between 0 and 500 km . The thicker crust below the sinuous ridges is attributed to thick, localised roots of lower crust, which are required below this area to support the slightly higher elevations location here, compared to the surrounding plains regions. Below Ganis Chasma the lithosphere is thin ($\sim 55 \text{ km}$), but thickens towards the west ($\sim 100 \text{ km}$) and within the plains ($\sim 195\text{-}290 \text{ km}$). Ganis Chasma also exhibits the highest heat flow ($38\text{-}55 \text{ mW m}^{-2}$) compared to the surrounding volcanic rise and plains regions ($17\text{-}21 \text{ mW m}^{-2}$; Figure 4.14).

Profile C-C' dissects Maat and Ozza Mons from 180°E -8°N to -145°E 12°N (Figure 4.15). The proposed lithospheric structure is able to fit the geoid and Bouguer gravity, but is unable to compensate all of the topography at Maat and Ozza Mons (Figure 4.15). Along this profile, the crust and lithosphere are thicker below Ozza Mons (up to 52 km and 112 km , respectively) compared to Maat Mons (up to 39 km and 100 km , respectively) due to the low density intrusion in the lower crust (Figure 4.15).

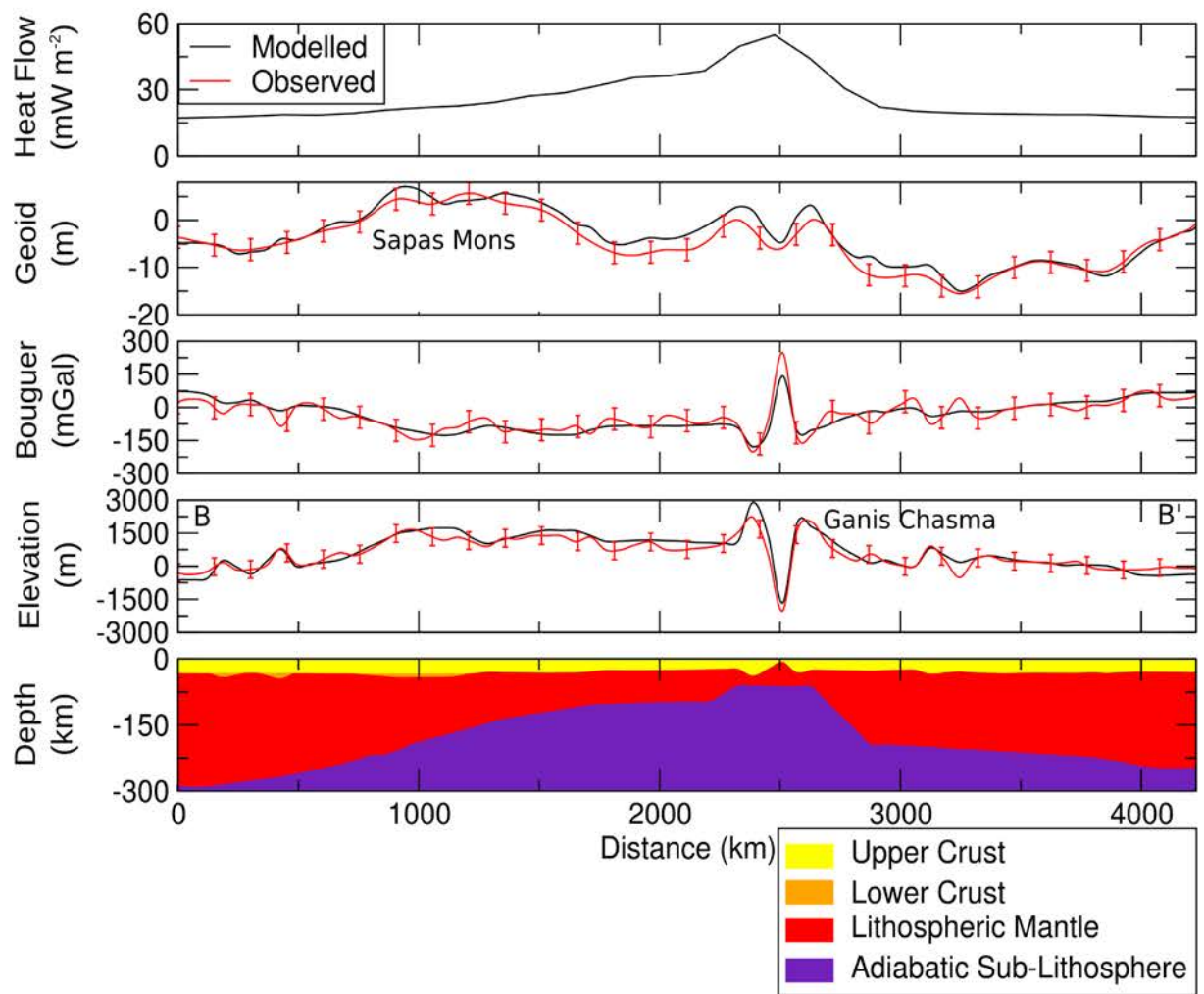


Figure 4.14. Modelled lithospheric structure along Ganis Chasma and Sapas Mons from 175°E to -145°W at 12°N. Key is similar to Figure 4.13, however a gabbroic lower crust (orange) is required below Sapas Mons.

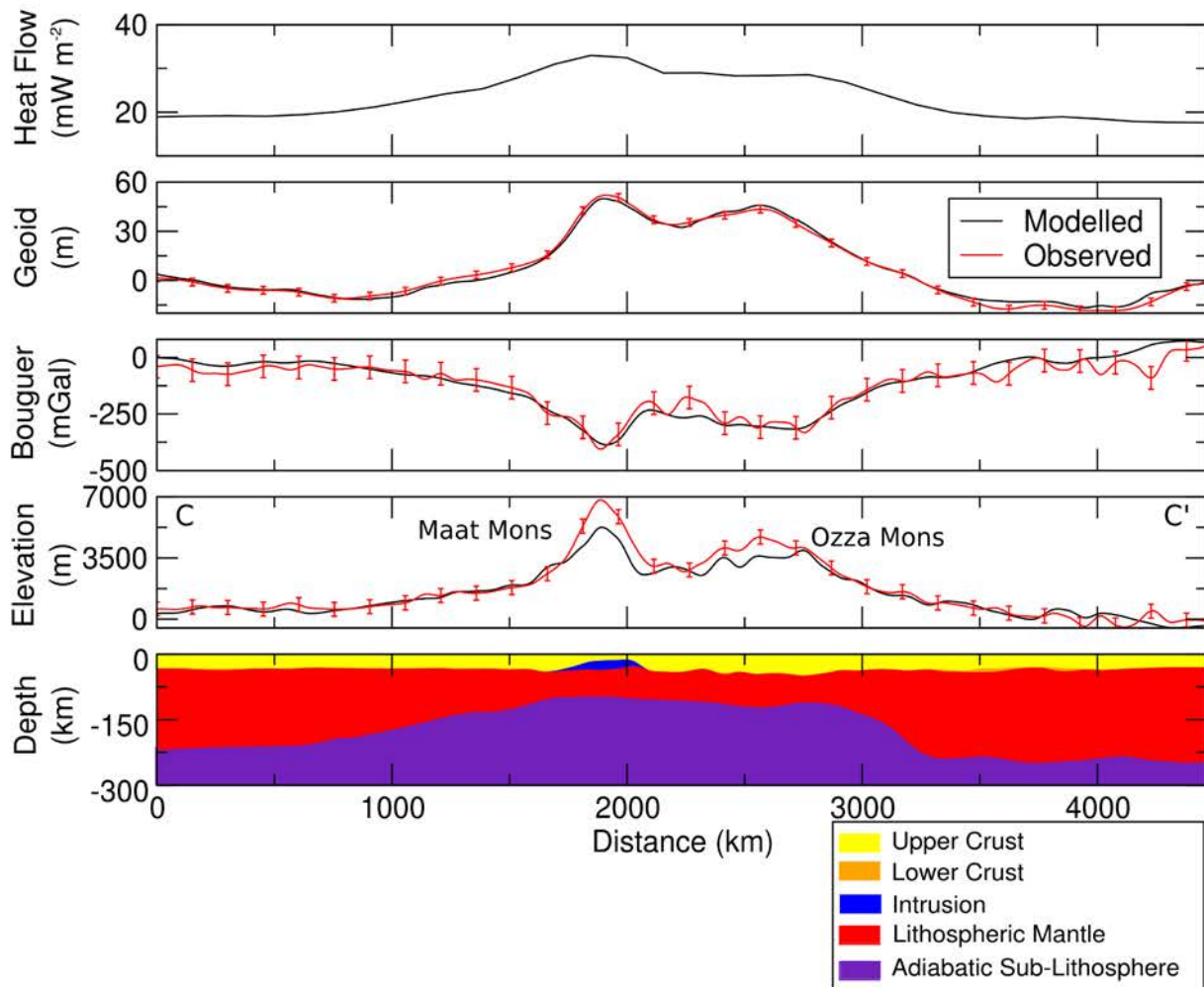


Figure 4.15. The modelled lithospheric structure below Maat and Ozza Mons between 180°E -8°N to -145°E 12°N. The key is similar to Figure 4.13. Localised gabbroic crust (orange) is required below the volcanic constructs (distances between ~3500-4000 km), with a dioritic intrusion (blue) also being required below Maat Mons.

This low density intrusion is assumed to represent a low density magma chamber or partial melting associated with Maat Mons. This low density intrusion reduces the overall density below Maat Mons, with the model requiring a thinner crust and lithosphere, compared to Ozza Mons (Figure 4.15). The thinner modelled crust and lithosphere below Maat Mons results in a higher calculated elevation and a better fit between the calculated and observed elevations at Maat Mons. We attempted to add more intrusion to the crust, however the fit to the geoid and the Bouguer gravity became degraded and the lithospheric structure became unrealistic (i.e. no mantle lithosphere). As a result, we focused on fitting the observed geoid rather than the elevation since the geoid dataset was filtered to represent anomalies from masses that had similar depths as our lithospheric model. This compares to the elevation dataset, which was not filtered and could include topographic contributions from mantle plumes occurring at greater depths than those assumed in our lithospheric models.

Figure 4.15 shows plains regions to the west have slightly thinner crustal and lithospheric thicknesses (32-38 km and 210-220 km, respectively) compared to the eastern plains (~36-45 km and 235-250 km, respectively). The thicker crustal estimates within the eastern plains regions are associated with localised areas of lower crust that were required to obtain a better fit to the geoid and topography observables. These plains regions correspond to low surface heat flows (17-19 mW m⁻²) compared to Maat (32 mW m⁻²) and Ozza Mons (28 mW m⁻²).

4.4.4 Crustal and Lithospheric Thickness Maps

The elevated topography at Atla Regio corresponds to high geoid and low Bouguer anomalies (Figure 4.2). The volcanoes within Atla Regio also tend to correspond to a negative Bouguer response, since the excess mass of the volcano is isostatically compensated by a 'root' of low density crustal material, low-density partial melting, or a magma chamber (Figure 4.2). Also

the geoid high of this area correlates to high topography, which could imply Venus lacks an asthenosphere (Figure 4.2) [Phillips *et al.*, 1991].

Crustal roots, 30-60 km thick, occur below Ozza, Maat, and Sapas Mons (Figure 4.16A). Localised patches of crustal thickening (~40-45 km) also occur at the volcanic constructs to the north-east, along the north-west trending arms of Ganis Chasma, and the sinuous ridges to the north-west (Figure 4.16A).

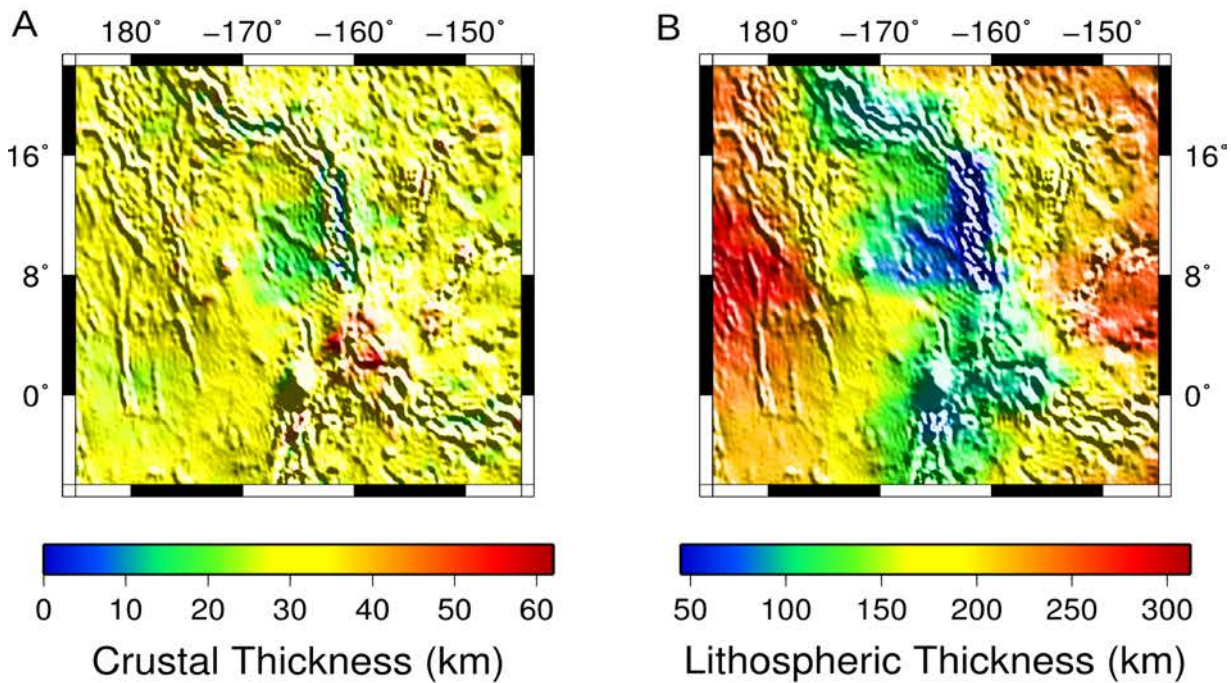


Figure 4.16. Modelled crustal and lithospheric thicknesses using Reference Column 1 ($T_c = 30$; $L = 300$ km). (A) The large volcanoes have thick crustal roots and the central trough of Ganis Chasma has a thin crust. (B) A thin lithosphere occurs below the central volcanic rise, but increases towards the distal plains regions.

The thinnest crust $\sim < 1$ to 1 km occurs along the deepest trough sections of Ganis Chasma, particularly between 8°N-15°N, surrounded by a crust ~ 15 -25 km thick (Figure 4.16A). The deepest trough sections of Ganis Chasma are associated with the thinnest (~ 50 -60 km)

lithosphere (Figure 4.16B), followed by slightly thicker lithosphere (~95-140 km) below the volcanoes. Moving outwards from the central volcanic rise to the surrounding plains regions, the thermal lithosphere gradually thickens until it reaches depths of 225-310 km (Figure 4.16B).

4.4.5 Thermal Structure of the Lithosphere

A 3D model of the temperature distribution for the proposed lithospheric structure is shown in Figures 4.17 and 4.18. In Figure 4.17, the plains regions to the south-west were removed in order to view the temperature distribution beneath Maat, Ozza, and Sapas Mons. From Figure 4.17, the base of the thermal lithosphere, represented by the 1300°C isotherm, is fairly shallow below Maat and Sapas Mons (~100 km), but thickens below Ozza Mons (~110 km) and the surrounding plains regions (~200-350 km).

Figure 4.18 shows the variation of thermal lithospheric thickness with the changing orientation of Ganis Chasma. Ganis Chasma has a thin thermal lithosphere towards the south of the area (~50 km), which gradually thickens (~150 km) towards the north, where the rift begins to change orientation from N-S to N-NW.

4.4.6 Compensation Mechanisms

Most of the observed topography at Atla Regio is primarily supported by Airy and thermal isostasy (Figure 4.19). Ozza, Maat, and Sapas Mons, however, appear to require additional compensation mechanisms, such as dynamic uplift or flexure (Figure 4.19C).

Using our proposed model for Reference Column 1, we tested if flexure could compensate

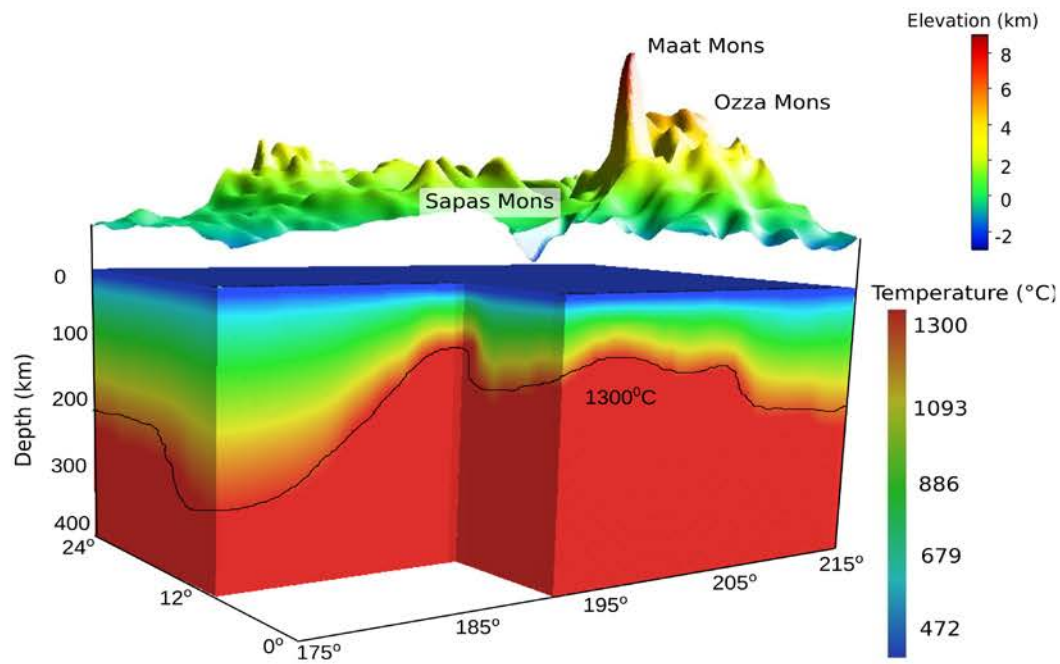


Figure 4.17. A 3D model of the temperature distribution below Maat, Ozza, and Sapas Mons. The south-western plains regions were removed for clarity.

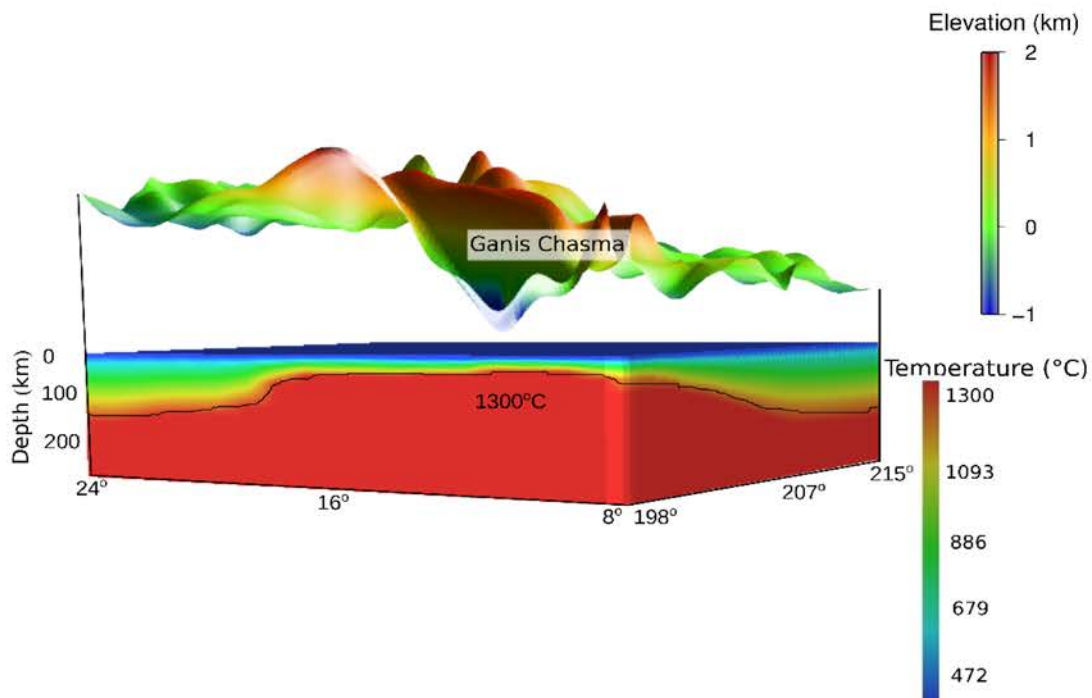


Figure 4.18. A 3D model of the temperature distribution along Ganis Chasma. The area to the south, comprising Ozza and Maat Mons, as well as the area to the west of Ganis Chasma, were removed for clarity.

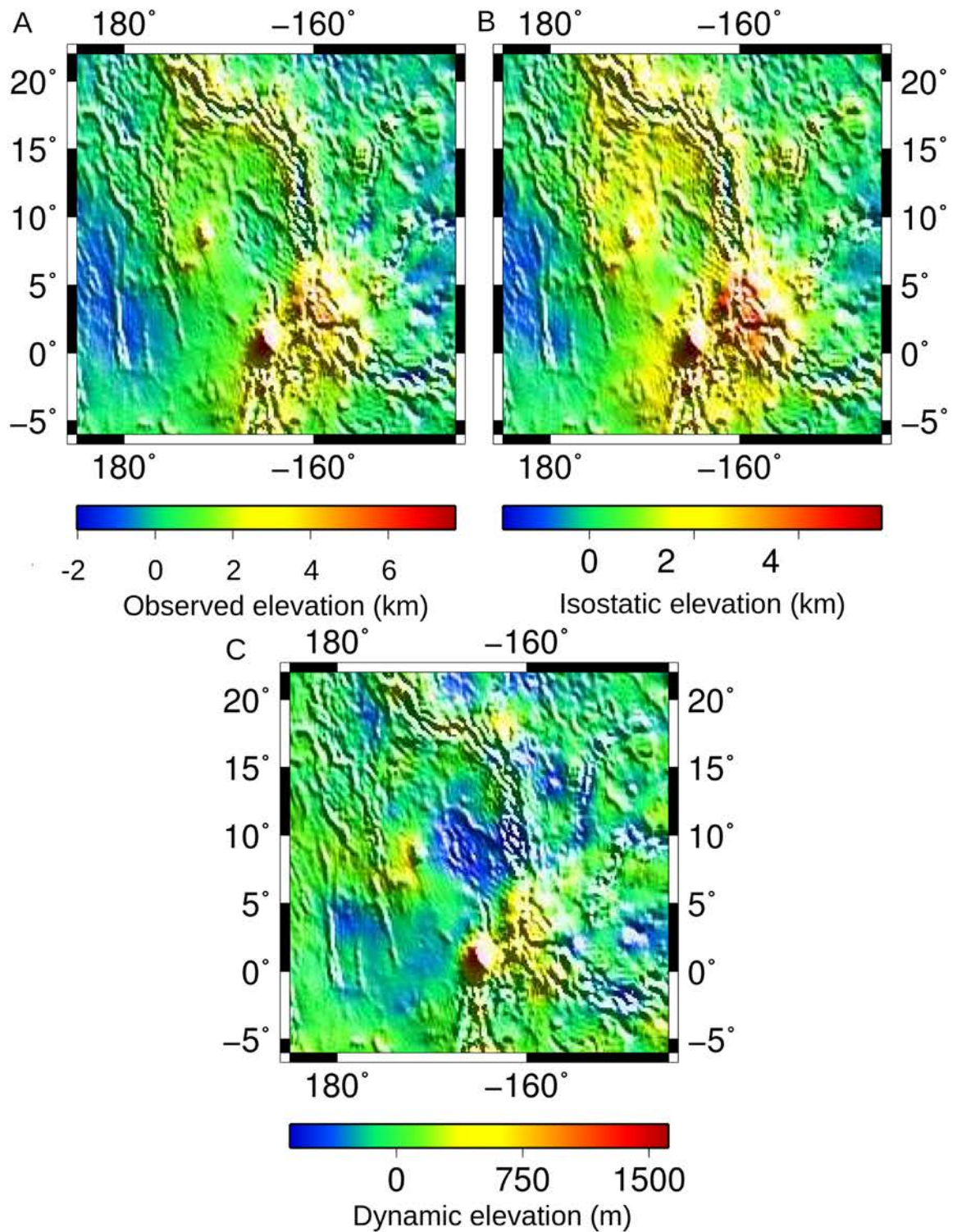


Figure 4.19. The contribution of each mechanism to supporting Atla Regio's observed elevation (A). (B) Airy and thermal isostasy compensates most of the topography within this region. (C) Dynamic uplift (assuming an elastic lithosphere thickness of 50 km) also contributes to the support of the observed elevation at Maat, Ozza, and Sapas Mons. The dynamic elevation was found by subtracting the isostatic and flexural elevation from the observed elevation.

some or all of the remaining topography at Maat and Ozza Mons (Figure 4.20). Flexure at Maat Mons can compensate additional topography, up to 1.5 km, 1.1 km, and 1.0 km if an elastic lithospheric thickness of 50 km, 30 km, and 10 km, is used respectively (Figure 4.20). However, at Ozza and Sapas Mons flexure is able to compensate slightly less topography, up to ~0.5 km, ~0.3 km, and ~0.25 km, for an elastic lithosphere thickness of 50 km, 30 km, and 10 km, respectively (Figure 4.20). A 50 km thick elastic lithosphere produces the most reasonable additional compensation at Maat Mons, as required by the residuals. However, flexure does not compensate all of this remaining topography, with dynamic uplift also being required. Significantly greater dynamic compensation (up to ~1.5 km) occurs at Maat Mons with Ozza and Sapas Mons having slightly less (up to ~0.7 km; Figure 4.19).

4.5 Discussion

4.5.1 Constraining the Lithospheric Structure at Atla Regio

Using Reference Column 1 ($T_c=30\text{km}$; $L=300\text{km}$), we obtained thermal lithospheric thicknesses ranging from ~50-60 km below Ganis Chasma, ~100-150 km below the volcanoes, and ~225-300 km below the surrounding plains regions. Previous studies have suggested the topography of Ganis Chasma is similar to the ultra-slow Gakkel Ridge [Stoddard and Jurdy, 2011], and from our study these two areas may exhibit similar crustal and thermal lithospheric thicknesses. The modelled thermal lithospheric thickness of ~50-60 km below Ganis Chasma, is similar to the possible ~40-50 km thicknesses at the Gakkel Ridge, obtained from models of long-period surface waves [Pasyanos, 2010]. Coakley and Cochran [1998], assuming a crustal density of 2900 kg m^{-3} , obtained thin ($< 4 \text{ km}$) crust below the Gakkel Ridge, similar to what we obtain for Ganis Chasma for the same crustal density.

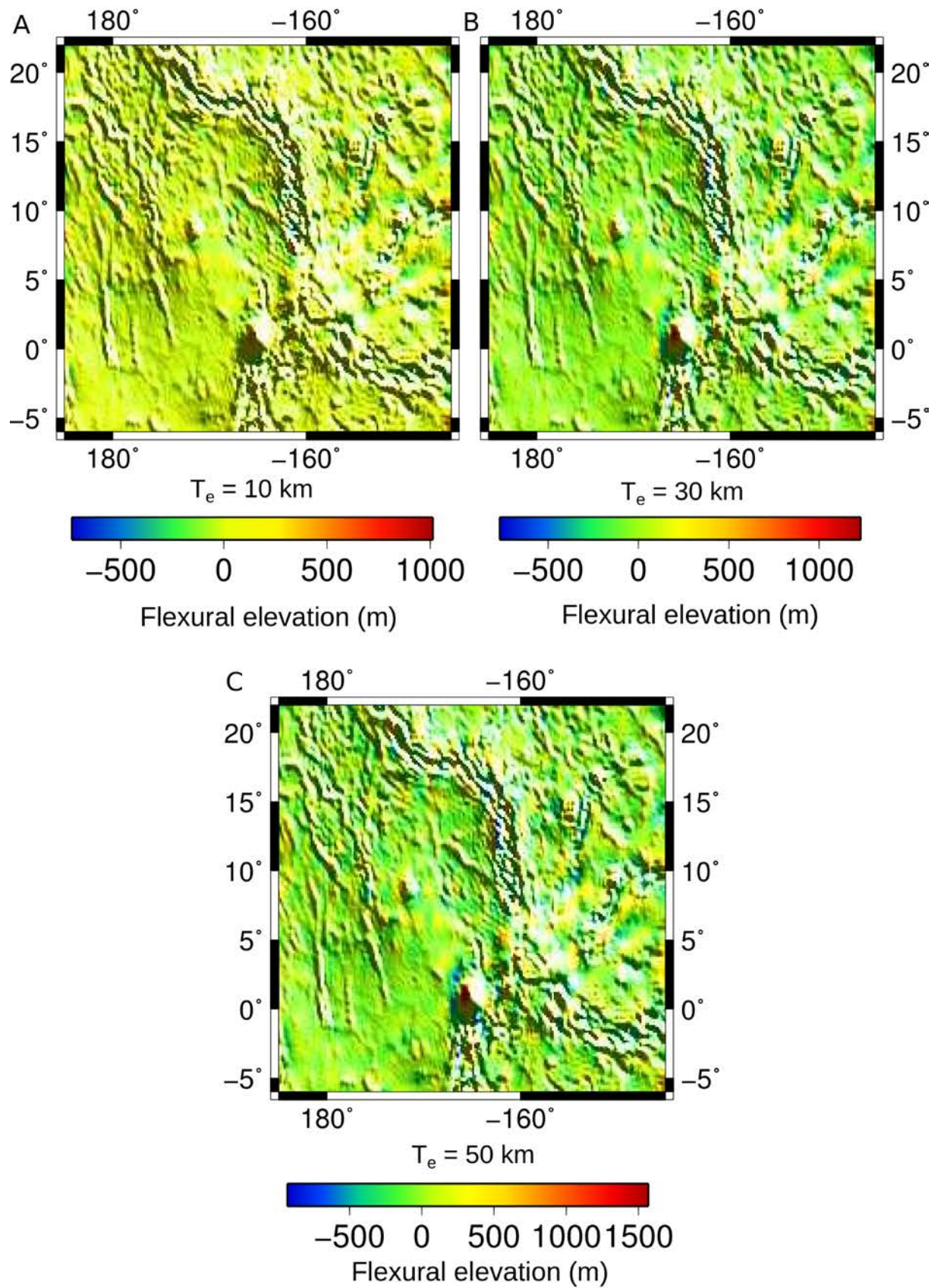


Figure 4.20. The amount of residual topography compensated by flexure assuming a constant elastic lithosphere thickness of (A) 10 km, (B) 30 km, and (C) 50 km.

Atla Regio also shows similarities to the Yellowstone hotspot [Stoddard and Jurdy, 2011]. From Ps and Sp receiver functions, the Yellowstone hotspot could have lithospheric and crustal thicknesses of ~120-140 km and 50 km, respectively [Miller and Levander, 2010]. However, the lithosphere could be as thin as 80-90 km and the crust could be ~30 km thick if S-wave receiver functions are used [Kumar *et al.*, 2012]. From our models, both the crust and thermal lithosphere at Atla Regio share similar thicknesses to those at Yellowstone.

The volcanic rise, except for Ganis Chasma between 8°N to 15°N, has a similar thermal lithospheric thickness (~100 km thick) to the range (88-100 km) provided by previous studies [Kucinskas and Turcotte, 1994; Moore and Schubert, 1997; Phillips, 1994; Smrekar and Parmentier, 1996]. Previous authors [Kucinskas and Turcotte, 1994; Phillips, 1994] have also suggested that the thermal lithosphere within the plains regions should have a thickness of ~300 km. Our modelled plains thermal lithospheric thicknesses are close (~250 km) in most of the area, with a small portion thickening to 300 km in the west centered at 10°N. One reason for our slightly lower plains thermal lithospheric thicknesses could be that our modelled area did not extend into “true” lowland plains regions, with the plains to the east and west still being influenced by the volcanic rise and rifts. This can also be observed in the elevation map of the modelled area (Figure 4.1). Most of the modelled “plains” regions have elevations of 0-2 km, when true lowland plains regions could be considered as having elevations of -2 to 0 km [Garvin *et al.*, 1985].

The thermal lithospheric thickness below Atla Regio may be much thicker if an Isostatic Stagnant-Lid approximation is used [Orth and Solomatov, 2011]. Based on a crustal thickness of 50 km and a maximum lithospheric thinning of 50%, the thermal lithosphere below Atla Regio may range between 300-500 km, much thicker than that obtained by our modelling [Orth and Solomatov, 2011]. Compared to our models, these authors did not assume a

reference lithospheric thickness, instead their results were strongly influenced by the amount of thinning they assumed in their model [Orth and Solomatov 2011]. They also chose to model longer wavelength geoid and topography (1901-19013 km) compared to our models (< ~2716 km).

The modelled thermal lithospheric thicknesses show a reasonable correlation to those previously suggested, however the crustal thicknesses vary. Phillips [1997] used a crustal thickness of 38 ± 9 km at Atla Regio. Plains crustal thicknesses tend (~29-35 km) to lie within this proposed range, however the crust is thicker at the volcanoes and thinner Ganis Chasma. The most significant factor contributing to differences between the modelled crustal thicknesses and that of previous authors is the reference crustal and lithospheric thickness.

Another factor that could influence our proposed lithospheric structure is our choice of layer parameters. Samples from the Venera and Vega mission and the morphology of Venus's volcanoes suggest the surface is predominately basaltic, however, some areas may have silicic to intermediate compositions [Grimm and Hess, 1997; Jull and Arkani-Hamed, 1995; McKenzie *et al.*, 1992]. If different densities or thermal parameters were used, then one would expect a different lithospheric structure and, in turn, different quantities of isostatic and dynamic compensation.

4.5.2 The Contribution of Flexure and Dynamic Uplift

Considering our proposed lithospheric structure, isostatic compensation is the most dominant mechanism of support at Atla Regio. However, the residuals and models reinforce that Airy and thermal isostasy alone is unable to compensate all the topography at Maat and Ozza Mons and that dynamic and/or flexural compensation is most likely required. Dynamic

compensation at Atla Regio is inferred from observations of heavy extensional and volcanic activity, rise morphology, localised geoid and topography highs [*Senske and Head, 1992; Smrekar et al., 1997; Smrekar and Phillips, 1991*]. The amount of dynamic compensation from our models was similar (2.5 km) to that proposed by *Stofan et al. [1995]*. Mantle plumes usually contribute to long-wavelength topographic compensation, however, our models require dynamic compensation, in localised areas such as Maat, Ozza, and to a lesser extent, Sapas Mons. These results may suggest these areas are supported by localised mantle upwellings, similar to those responsible for the formation of coronae and other Venusian shield volcanoes [*Herrick et al., 2005; Smrekar et al., 1997; Stofan et al., 1997*]. Our models may also underestimate the amount of dynamic compensation occurring at Atla Regio since the main function of GEO3Dmod is to determine the amount of isostatic compensation occurring within an area.

A 50 km thick elastic lithosphere provided the most consistent flexural support, as required from the residual topography, and is close to the maximum estimates (48 km) from previous authors [*Phillips, 1994; Phillips et al., 1991; Smrekar, 1994*]. However, one should also consider these flexural results as an oversimplification of the actual flexure at Atla Regio. In our modelling we have assumed a uniform elastic lithosphere thickness everywhere, but the actual elastic lithosphere thickness would vary between the central volcanic rise and the surrounding plains.

4.5.3 Melt Generation Volumes and Rates

The amount of melt associated with an upwelling mantle plume is related to the temperature within the plume and the thickness of the lithosphere [*Nimmo and McKenzie, 1998*]. The thin lithosphere below Ganis Chasma acts as a minor impedance producing greater melt volumes,

and in turn results in higher melt generation rates than a thick thermal lithosphere (Table 4.4). Previous melt generation rate estimates for Atla Regio are lacking. However, an average melt generation rate for Venus's volcanic rises of $\sim 0.4 \text{ km}^3 \text{ yr}^{-1}$ was estimated by dividing global melting rates by the number of hypothesized plumes [Nimmo and McKenzie, 1998].

Table 4.4. Melt Generation Volumes and Rates

Case	Mantle Temperature (°C)	Plume Temperature (°C)	Lithospheric Thickness 50 km		Lithospheric Thickness 100 km	
			Melt Volume ($\times 10^6 \text{ km}^3$)	Melt Generation Rate ($\text{km}^3 \text{ yr}^{-1}$)	Melt Volume ($\times 10^6 \text{ km}^3$)	Melt Generation Rate ($\text{km}^3 \text{ yr}^{-1}$)
1	1300	1500	0.20	0.50	0	0
2	1500	1700	0.89	2.7	0.35	1.1

Case 1 results in no melt being generated for a 100 km thick lithosphere (Table 4.4), however melt is generated for a thinner (50 km) lithosphere. For Case 2, both lithospheric thicknesses result in partial melting (Table 4.4), with a 50 km thick lithosphere generating a higher melt volume ($8.9 \times 10^5 \text{ km}^3$) and rate ($2.7 \text{ km}^3 \text{ yr}^{-1}$) compared to a 100 km thick lithosphere ($3.5 \times 10^5 \text{ km}^3$ and $1.11 \text{ km}^3 \text{ yr}^{-1}$, respectively). Considering previous melt generation volumes (10^4 - 10^6 km^3) and rates ($0.4 \text{ km}^3 \text{ yr}^{-1}$) [Smrekar and Parmentier, 1996; Nimmo and McKenzie, 1998], a thinner (50 km) lithosphere, with a mantle temperature of 1300°C and plume temperature of 1500°C , provides the most consistent estimates. This case can be used to infer partial melting may occur below Ganis Chasma, where the lithosphere is thinner, with an absence of melt at the volcanoes.

A number of factors can influence these estimates, however, including the methods used by previous authors to determine melt generation rates and our assumed mantle rheology.

Comparing our melt generation rates to those obtained from global estimates may be unreliable since each Venusian rise exhibits different characteristics and evolutions. Atla Regio has the greatest volume of volcanics of all the Venusian rises and evidence for possible geological activity, which could contribute to greater than average melt generation rates [Matias and Jurdy, 2005; Stoddard and Jurdy, 2011; Stofan, 1995].

The fraction of melt, and in turn, the melt volume and rate, also depends on whether a wet or dry mantle solidus is assumed, with very little evidence existing for either on Venus [Smrekar and Sotin, 2012]. High surface temperatures, slow relaxation of impact craters, and evidence for extensive volcanism that would have acted to devolatilize the crust and upper mantle, imply a dry mantle composition [Grimm and Solomon, 1988; Kaula, 1990; Mackwell et al. 1998; Reese et. al., 1991]. Our melt generation volumes and rates have assumed a dry peridotite solidus [McKenzie and Bickle, 1988; Watson and McKenzie, 1991]. If a wet peridotite mantle solidus was used instead, the melt volumes and rates would increase, since water reduces the temperatures required for melting, with melting occurring over a broader range of temperatures [Inoue, 1994].

Also the melt generation rate calculations do not consider current, ultra-slow spreading where conduction dissipates heat, reducing the amount of melt generated [Bown and White, 1994]. If this was included it may have reduced the volumes and rates found in Case 2 to more consistent values.

4.5.4 Half-Space Cooling Model

Our modelled lithospheric thickness can also be used to constrain spreading rates at Ganis Chasma, since this area may experience geological activity [Basilevsky, 1993; Basilevsky and

Head, 2002; Jurdy and Stoddard, 2007; Matias and Jurdy, 2005; Matias et al., 2004].

Previous authors propose Ganis Chasma should be within a similar ultra-slow regime as the Gakkel Ridge, which spreads at a full rate of approximately 6-13 mm yr⁻¹ [*Stoddard and Jurdy, 2011; Coakley and Cochran, 1998*].

Figure 4.21 shows the results from the half-space cooling model. The 200 K, 400 K, 600 K, and 800 K isotherms represent the temperature difference between the base of the lithosphere and the surface. These isotherms are overprinted with the basal thermal lithospheric isotherm taken at 12°N and 19°N (Figure 4.14 & 4.15). This isotherm has an absolute temperature of 1573.15 K or (1300°C). Our modelled absolute basal lithospheric isotherm shows a poor correlation with half-rates of spreading between 10-13 mm yr⁻¹, but show a closer correlation with slower rates between 2.5-6 mm yr⁻¹, especially with greater distance away from the center of the rift (Figure 4.21). Moving outwards from the rift, the depth of each isotherm increases due to cooling of the lithosphere. No significant differences in spreading rate is apparent for a thin (50 km) or (100 km) thick thermal lithosphere below Ganis Chasma, with both of these supporting full spreading rates between 5-12 mm yr⁻¹. These are consistent with the ultra-slow regime, but the spreading rates at Ganis Chasma are slower than those proposed for the Gakkel Ridge.

If Ganis Chasma is currently rifting locally then some form of crustal compression or subduction must also operate to conserve Venus's total surface area [*Bilotti and Suppe, 1999; McGill, 1993; Schubert and Sandwell, 1995; Turcotte, 1995*]. Crustal compression, indicated by the presence of wrinkle ridges, may occur within the plains regions surrounding a volcanic rise. Wrinkle ridges comprise anticlines and thrust faults that can accommodate regional shortening of up to 5% [*Bilotti and Suppe, 1999*]. These wrinkle ridges are commonly found in the lowland plains regions, below a geoid of height of 20 m, and appear to circumscribe an

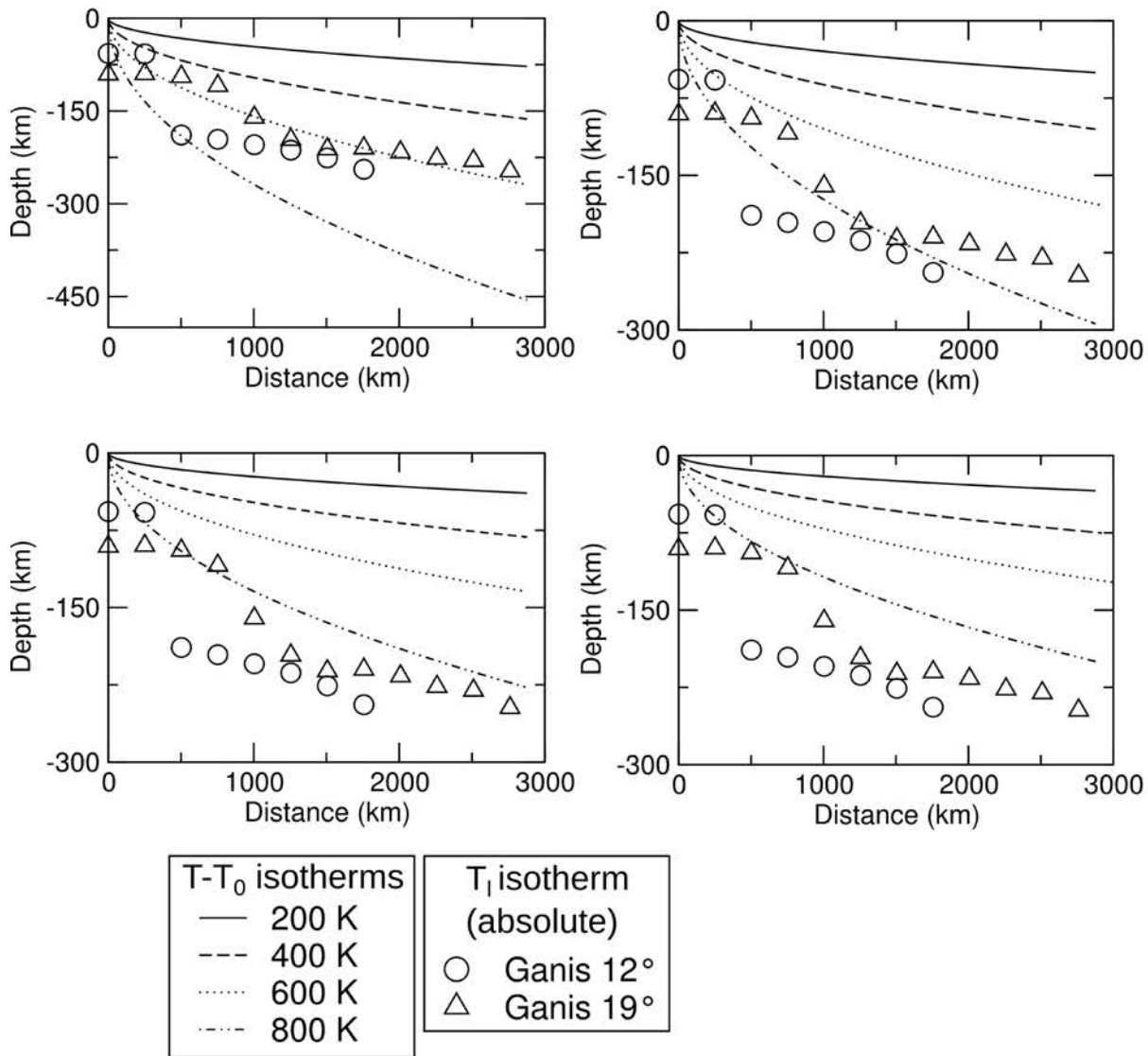


Figure 4.21. Lithospheric thickness obtained from the half-space cooling model assuming a spreading half-rate of: (A) 2.5 mm yr⁻¹; (B) 6 mm yr⁻¹; (C) 10 mm yr⁻¹; and (D) 13 mm yr⁻¹. The thermal lithospheric isotherm taken at 12°N and 19°N, which represent an absolute temperature of 1573.15 K or (1300°C) are used to constrain these spreading rates. The 200 K, 400 K, 600 K, and 800 K isotherm represent the temperature difference between the surface and base of the lithosphere.

associated volcanic rise [Bilotti and Suppe, 1999; Sandwell et al., 1997]. Atla Regio, however, lacks these concentric structures, possibly suggesting this rise formed after these features were emplaced [Bilotti and Suppe, 1999].

Another mechanism that may occur within the plains regions surrounding Atla Regio is localised retrograde subduction. *Schubert and Sandwell* [1995] proposed that a rift could change to a subduction zone as it propagates from a volcanic rise into the plains regions where the lithosphere is cold, thick, and gravitationally unstable. Localised rifting and subduction may operate concurrently on Venus, however our lithospheric model at Atla Regio did not extend into the distant lowland regions.

Even though the mechanisms of crustal destruction are highly uncertain on Venus, the slow-spreading rates found at Ganis Chasma imply that the mechanism acting to accommodate the additional crust produced at this rift most likely occurs within the plains located outside of the modelled region.

4.5.5 Crustal Production Rates

Crustal thicknesses obtained from the proposed lithospheric structure are also useful when calculating the rates of crustal production along Ganis Chasma between 8°N to 15°N. By comparing the crustal production rates to the melt generation rates found in Section 4.5.3 we can constrain the mechanisms that have contributed to crustal production in Atla Regio.

Higher full spreading rates (12 mm yr⁻¹) correspond to greater crustal production rates (2.75 km³ yr⁻¹) than slower rates (5 mm yr⁻¹) of spreading (0.78 km³ yr⁻¹). The lower rate of crustal production (0.78 km³ yr⁻¹) associated with a slower (5 mm yr⁻¹) spreading ridge is consistent with the melt generation rate (0.50 km³ yr⁻¹) found for this area, which may imply all the partial melt is extracted efficiently, cooling and solidifying to form the crust. However, this melt can not form all of the crust produced at Ganis Chasma, with localised rifting most likely operating concurrently to produce pressure-release melting and possible rift-related volcanism.

4.6 Conclusions

A reference column with a 30 km thick crust and 300 km thick thermal lithosphere provides the most plausible lithospheric structure below Atla Regio. Crustal thicknesses below Atla Regio range from being thin (< 1 km) at the central rift trough of Ganis Chasma, to 30-60 km at the volcanoes and ~ 30 km within the surrounding plains. The thermal lithosphere also shows a similar relationship with a shallow lithosphere occurring below the volcanic rise (~ 50 -150 km) compared to the plains (~ 225 -300 km). The best-fit lithospheric structure found in this study implies Airy and thermal isostasy compensates most (~ 1.5 to 5 km) of the observed topography at Atla Regio, with an additional ~ 0.3 to 1.5 km of flexural support and ~ 0.5 to 1.5 km of dynamic compensation, being required at the volcanoes.

Both the modelled lithospheric structure and the chosen reference column were also constrained further by melt generation rate and volume calculations. Assuming a dry solidus, a mantle temperature of 1300°C and a plume temperature of 1500°C , the thin (50 km) thermal lithosphere below Ganis Chasma results in a melt generation rate ($0.5 \text{ km}^3 \text{ yr}^{-1}$) and volume ($2.5 \times 10^5 \text{ km}^3$) that is consistent with previous estimates [Nimmo and McKenzie, 1998; Smrekar and Parmentier, 1996].

Even though Venus is considered to be within a stagnant-lid convective regime [Orth and Solomatov, 2011; Solomatov and Moresi, 1996] does not mean that the surface is entirely stationary, with some areas, such as Ganis Chasma, possibly experiencing localised spreading on the order of $\sim 5 \text{ mm yr}^{-1}$, but may reach rates of up to $\sim 12 \text{ mm yr}^{-1}$. This rate of rifting is within an ultra-slow regime, but is slower than similar locations on Earth. At Ganis Chasma, the partial melt associated with an upwelling mantle plume below Atla Regio and rift-related volcanism, may form the new crust at a rate of $0.78 \text{ km}^3 \text{ yr}^{-1}$. The findings presented in this

study have important implications for the lithospheric structure, compensation mechanisms and current state of localised rifting at other Venusian rises that share similar geological features and geophysical anomalies to Atla Regio.

4.7 References

- Afonso, J. C., G. Ranalli, and M. Fernández (2005), Thermal expansivity and elastic properties of the lithospheric mantle: results from mineral physics of composites, *Physics of the Earth and Planetary Interiors*, 149, 279-306, doi: 10.1016/j.pepi.2004.10.003.
- Banerdt, W. B., and M. P. Golombek (1988), Deformational Models of Rifting and Folding on Venus, *Journal of Geophysical Research*, 93(B5), 4759-4772, doi:198810.1029/JB093iB05p04759.
- Basilevsky, A. T. (1993), Age of rifting and associated volcanism in Atla Regio Venus, *Geophysical Research Letters*, 20(10), 883-886.
- Basilevsky, A. T., and J. W. Head (2002), Venus: Timing and rates of geologic activity, *Geology*, 30(11), 1015 -1018, doi:10.1130/0091-7613(2002)030<1015:VTAROG>2.0.CO;2.
- Bevington, P. R., and D. K. Robinson (1992), *Data reduction and error analysis for the physical sciences*, McGraw-Hill Inc, New York.
- Bilotti, F., and J. Suppe (1999), The Global Distribution of Wrinkle Ridges on Venus, *Icarus*, 139(1), 137–157, doi:10.1006/icar.1999.6092.
- Bown, J. W., and R. S. White (1994), Variation with spreading rate of oceanic crustal

thickness and geochemistry, *Earth and Planetary Science Letters*, 121(3–4), 435–449, doi:10.1016/0012-821X(94)90082-5.

Coakley, B. J., and J. R. Cochran (1998), Gravity Evidence of Very Thin Crust at the Gakkel Ridge (Arctic Ocean), *Earth and Planetary Science Letters*, 162(1–4), 81–95, doi:10.1016/S0012-821X(98)00158-7.

Davies, G.F. (2000), *Dynamic Earth: Plates, Plumes and Mantle Convection*, 472 pp., Cambridge University Press, Cambridge, New York.

Ford, P.G. and G.H. Pettengill (1992), Venus topography and kilometer-scale slopes, *Journal of Geophysical Research*, 97(E8), 13103-13114.

Fowler, C. M. R. (2004), *The Solid Earth: An Introduction to Global Geophysics*, 2nd ed., Cambridge University Press, United Kingdom.

Fullea, J., J. C. Afonso, J. A. D. Connolly, M. Fernàndez, D. García-Castellanos, and H. Zeyen (2009), LitMod3D: An Interactive 3-D Software to Model the Thermal, Compositional, Density, Seismological, and Rheological Structure of the Lithosphere and Sublithospheric Upper Mantle, *Geochemistry Geophysics Geosystems.*, 10, Q08019 , 21 pp., doi:2009 10.1029/2009GC002391.

Fullea, J., M. Fernàndez, J. C. Afonso, J. Vergés, and H. Zeyen (2010), The structure and evolution of the lithosphere-asthenosphere boundary beneath the Atlantic-Mediterranean Transition Region, *Lithos*, 120, 74-95. doi: 10.1016/j.lithos.2010.03.003 .

Fullea, J., M. Fernàndez, H. Zeyen, and J. Vergés (2007), A rapid method to map the crustal and lithospheric thickness using elevation, geoid anomaly and thermal analysis. Application to the Gibraltar Arc System, Atlas Mountains and adjacent zones,

Tectonophysics, 430(1-4), 97–117, doi:10.1016/j.tecto.2006.11.003.

Garvin, J. B., J. W. Head, G. H. Pettengill, and S. H. Zisk (1985), Venus Global Radar Reflectivity and Correlations With Elevation, *Journal of Geophysical Research*, 90(B8), 6859-6871, doi:198510.1029/JB090iB08p06859.

Grimm, R.E. (1994), The Deep Structure of Venusian Plateau Highlands, *Icarus*, 112(1), 89-103, doi:10.1006/icar.1994.1171.

Grimm, R. E., and P. C. Hess (1997), The crust of Venus, in *Venus II: Geology, Geophysics, Atmosphere and Solar Wind Environment*, 1205–1244, The University of Arizona Press, Arizona.

Grimm, R. E., and S. C. Solomon (1988), Viscous Relaxation of Impact Crater Relief on Venus: Constraints on Crustal Thickness and Thermal Gradient, *Journal of Geophysical Research*, 93(B10), 11911-11929, doi:10.1029/JB093iB10p11911.

Head, J. W., L. S. Crumpler, J. C. Aubele, J. E. Guest, and R. S. Saunders (1992), Venus volcanism: classification of volcanic features and structures, associations, and global distribution from Magellan data, *Journal of Geophysical Research*, 97(E8), 13,153-13,197, doi:10.1029/92JE01273.

Herrick, R. R., J. Dufek, and P. J. McGovern (2005), Evolution of large shield volcanoes on Venus, *Journal of Geophysical Research*, 110, E01002, doi:10.1029/2004JE002283.

Inoue, T. (1994), Effect of water on melting phase relations and melt composition in the system $\text{Mg}_2\text{SiO}_4\text{-MgSiO}_3\text{-H}_2\text{O}$ up to 15 GPa, *Physics of the Earth and Planetary Interiors*, 85(3–4), 237–263, doi:10.1016/0031-9201(94)90116-3.

Jull, M. G., and J. Arkani-Hamed (1995), The implications of basalt in the formation and

- evolution of mountains on Venus, *Physics of the Earth and Planetary Interiors*, 89(3–4), 163–175, doi:10.1016/0031-9201(95)03015-O.
- Jurdy, D. M., and P. R. Stoddard (2007), The coronae of Venus: Impact, plume, or other origin?, *Geological Society of America Special Papers*, 430, 859–878, doi:10.1130/2007.2430(40).
- Kaula, W. M. (1990), Venus: A Contrast in Evolution to Earth, *Science*, 247(4947), 1191–1196, doi:10.1126/science.247.4947.1191.
- Kiefer, W. S., and B. H. Hager (1991), A Mantle Plume Model for the Equatorial Highlands of Venus, *Journal of Geophysical Research*, 96(E4), 20,947–20,966, doi:10.1029/91JE02221.
- Konopliv, A., and W. L. Sjogren (1994), Venus Spherical Harmonic Gravity Model to Degree and Order 60, *Icarus*, 112(1), 42–54, doi:10.1006/icar.1994.1169.
- Kucinskas, A. B., and D. L. Turcotte (1994), Isostatic Compensation of Equatorial Highlands on Venus, *Icarus*, 112(1), 104–116, doi:10.1006/icar.1994.1172.
- Kumar, P., X. Yuan, R. Kind, and J. Mechie (2012), The Lithosphere-Asthenosphere Boundary Observed with USArray Receiver Functions, *Solid Earth*, 3(1), 149–159, doi:10.5194/se-3-149-2012.
- Lachenbruch, A. H., and P. Morgan (1990), Continental extension, magmatism and elevation; formal relations and rules of thumb, *Tectonophysics*, 174, 39–62.
- Mackwell, S. J., M. E. Zimmerman, and D. L. Kohlstedt (1998), High-temperature deformation of dry diabase with application to tectonics on Venus, *Journal of Geophysical Research: Solid Earth*, 103(B1), 975–984, doi:10.1029/97JB02671.

- Matias, A., and D.M. Jurdy (2005), Impact craters as indicators of tectonic and volcanic activity in the Beta-Atla-Themis region, Venus, *Geological Society of America Special Papers*, 388, 825 -839, doi:10.1130/0-8137-2388-4.825.
- Matias, A., Jurdy, D.M, and Stoddard, P.R (2004), Stereo imaging of impact craters in the Beta-Atla-Themis (BAT) region, Venus., *35th Lunar and Planetary Science Conference*, 2.
- McGill, G. E. (1993), Wrinkle ridges, stress domains, and kinematics of Venusian plains, *Geophysical Research Letters*, 20(21), 2407–2410, doi:10.1029/93GL02635.
- McGovern, P., Simons, M, and S. Solomon (1995), Estimates of elastic lithosphere thickness and heat flux beneath large volcanoes on Venus, *26th Lunar and Planetary Science Conference*, 941-942.
- McKenzie, D. (1994), The Relationship between Topography and Gravity on Earth and Venus, *Icarus*, 112(1), 55-88, doi:10.1006/icar.1994.1170.
- McKenzie, D., and M. J. Bickle (1988), The Volume and Composition of Melt Generated by Extension of the Lithosphere, *Journal of Petrology*, 29(3), 625–679.
- McKenzie, D., P. G. Ford, C. Johnson, B. Parsons, D. Sandwell, S. Saunders, and S. C. Solomon (1992), Features on Venus generated by plate boundary processes, *Journal of Geophysical Research: Planets*, 97(E8), 13533–13544, doi:10.1029/92JE01350.
- Miler, M. S., and Levander (2010), Lithospheric Structure Beneath the Western US using USArray Data, *IRIS Core Proposal*, 3, II–148.
- Moore, W. B., and G. Schubert (1995.), Lithospheric thickness and mantle/lithosphere density contrast beneath Beta Regio, Venus, *Geophysical Research Letters*, 22(4), 429-432,

doi:199510.1029/94GL02055.

Moore, W. B., and G. Schubert (1997), Venusian Crustal and Lithospheric Properties from Nonlinear Regressions of Highland Geoid and Topography, *Icarus*, 128(2), 415-428, doi:10.1006/icar.1997.5750.

Moresi, L., and B. Parsons (1995), Interpreting gravity, geoid, and topography for convection with temperature dependent viscosity: Application to surface features on Venus, *Journal of Geophysical Research*, 100(E10), 21,155-21,171, doi:199510.1029/95JE01622.

Morgan, J. P., W. J. Morgan, and E. Price (1995), Hotspot melting generates both hotspot volcanism and a hotspot swell?, *Journal of Geophysical Research*, 100(B5), 8045-8062, doi:199510.1029/94JB02889.

Nimmo, F., and D. McKenzie (1998), Volcanism and tectonics on Venus, *Annual Reviews of Earth and Planetary Science*, 26(1), 23-51, doi:10.1146/annurev.earth.26.1.23.

Olson, P., G. Schubert, and C. Anderson (1993), Structure of Axisymmetric Mantle Plumes, *Journal of Geophysical Research: Solid Earth*, 98(B4), 6829–6844, doi:10.1029/92JB01013.

Orth, C. P., and V. S. Solomatov (2011), The isostatic stagnant lid approximation and global variations in the Venusian lithospheric thickness, *Geochemistry Geophysics Geosystems*, 12(7), 1525-2027.

Pasyanos, M. E. (2010), Lithospheric thickness modeled from long-period surface wave dispersion, *Tectonophysics*, 481(1–4), 38–50, doi:10.1016/j.tecto.2009.02.023.

Phillips, R. (1994), Estimating Lithospheric Properties at Atla Regio, Venus, *Icarus*, 112(1),

147-170, doi:10.1006/icar.1994.1175.

Phillips, R. J., R. E. Grimm, and M. C. Malin (1991), Hot-Spot Evolution and the Global Tectonics of Venus, *Science*, 252(5006), 651 -658, doi:10.1126/science.252.5006.651.

Ranalli, G. (1995) *Rheology of the Earth*, Chapman and Hall, London.

Rappaport, N. J., A. S. Konopliv, A. B. Kucinskias, and P. G. Ford (1999), An Improved 360 Degree and Order Model of Venus Topography, *Icarus*, 139(1), 19–31, doi:10.1006/icar.1999.6081.

Reese, C. C., V. S. Solomatov, and L.-N. Moresi (1999), Non-Newtonian Stagnant Lid Convection and Magmatic Resurfacing on Venus, *Icarus*, 139(1), 67–80, doi:10.1006/icar.1999.6088.

Reynolds, J. M. (1997), An introduction to applied and environmental geophysics, John Wiley and Sons, West Sussex, England.

Rogers, N. (2008), *An introduction to our dynamic planet*, Cambridge University Press, United Kingdom.

Romeo, I., and D. L. Turcotte (2008), Pulsating continents on Venus: An explanation for crustal plateaus and tessera terrains, *Earth and Planetary Science Letters*, 276(1–2), 85–97, doi:10.1016/j.epsl.2008.09.009.

Sandwell, D. T., C. L. Johnson, F. Bilotti, and J. Suppe (1997), Driving Forces for Limited Tectonics on Venus, *Icarus*, 129(1), 232–244, doi:10.1006/icar.1997.5721.

Schubert, G., and D. T. Sandwell (1995), A Global Survey of Possible Subduction Sites on Venus, *Icarus*, 117(1), 173–196, doi:10.1006/icar.1995.1150.

- Schubert, G., V. S. Solomatov, P. J. Tackley, and D. L. Turcotte (1997), *Mantle convection and the thermal evolution of Venus*, 1245-1288, The University of Arizona Press, Arizona.
- Schubert, G., D. L. Turcotte, and P. Olson (2001), *Mantle convection in the earth and planets*, 912 pp., Cambridge University Press, Cambridge, New York.
- Schubert, G., and D. L. Turcotte (2002), *Geodynamics*, 456 pp., Cambridge University Press, New York.
- Senske, D. A., and J. W. Head (1992), Atla Regio, Venus: Geology and origin of a major equatorial volcanic rise, *LPI Contributions*, 789, 107-109.
- Sjogren, W. L., W. B. Banerdt, P. W. Chodas, A. S. Konopliv, G. Balmino, J. P. Barriot, J. Arkani-Hamed, T. R. Colvin, and M. E. Davies (1997), The Venus gravity field and other geodetic parameters, in *Venus II: Geology, Geophysics, Atmosphere and Solar Wind Environment*, 1125–1161, The University of Arizona Press, Arizona.
- Smrekar, S. E. (1994), Evidence for Active Hotspots on Venus from Analysis of Magellan Gravity Data, *Icarus*, 112(1), 2-26, doi:10.1006/icar.1994.1166.
- Smrekar, S. E., W. S. Kiefer, and E. R. Stofan (1997), Large Volcanic Rises on Venus, in *Venus II: Geology, Geophysics, Atmosphere and Solar Wind Environment*, 845-878, The University of Arizona Press, Arizona.
- Smrekar, S. E., and E. M. Parmentier (1996), The interaction of mantle plumes with surface thermal and chemical boundary layers: Applications to hotspots on Venus, *Journal of Geophysical Research*, 101(B3), 5397-5410, doi:199610.1029/95JB02877.
- Smrekar, S. E., and R. J. Phillips (1991), Venusian highlands: geoid to topography ratios and their implications, *Earth and Planetary Science Letters*, 107(3-4), 582-597.

- Smrekar, S. E., and C. Sotin (2012), Constraints on mantle plumes on Venus: Implications for volatile history, *Icarus*, 217(2), 510–523, doi:10.1016/j.icarus.2011.09.011.
- Solomatov, V. S., and L.-N. Moresi (1996), Stagnant lid convection on Venus, *Journal of Geophysical Research*, 101(E2), 4737–4753, doi:199610.1029/95JE03361.
- Solomon, S. C., and J. W. Head (1990), Lithospheric flexure beneath the Freyja Montes Foredeep, Venus: Constraints on lithospheric thermal gradient and heat flow, *Geophysical Research Letters*, 17(9), 1393–1396, doi:199010.1029/GL017i009p01393.
- Steinbach, V., and D. A. Yuen (1992), The effects of multiple phase transitions on Venusian mantle convection, *Geophysical Research Letters*, 19(22), 2243–2246, doi:10.1029/92GL02319.
- Stoddard, P. R., and D. M. Jurdy (2011), Topographic comparisons of uplift features on Venus and Earth: implications for Venus tectonics, *Icarus*, 524–533, doi:10.1016/j.icarus.2011.09.003.
- Stofan, E. R., V. E. Hamilton, D. M. Janes, and S. E. Smrekar (1997), Coronae on Venus: morphology and origin, in *Venus II: Geology, Geophysics, Atmosphere and Solar Wind Environment*, 931–965, The University of Arizona Press, Arizona.
- Stofan, E. R., S. E. Smrekar, D. L. Bindshadler, and D. A. Senske (1995), Large topographic rises on Venus: Implications for mantle upwelling, *Journal of Geophysical Research*, 100(E11), 23317–23327, doi:10.1029/95JE01834.
- Ranalli, G. (1995) *Rheology of the Earth*, Chapman and Hall, London.
- Reynolds, J. M. (1997), *An introduction to applied and environmental geophysics*, John Wiley

and Sons, West Sussex, England.

Rogers, N. (2008), *An introduction to our dynamic planet*, Cambridge University Press, United Kingdom.

Taylor, J. R. (1982), *An introduction to error analysis*, University Science Books, Mill Valley, California.

Turcotte, D. L. (1993), An Episodic Hypothesis for Venusian Tectonics, *Journal of Geophysical Research*, 98(E9), 17,061–17,068, doi:199310.1029/93JE01775.

Turcotte, D. L. (1995), How does Venus lose heat?, *Journal of Geophysical Research: Planets*, 100(E8), 16931–16940, doi:10.1029/95JE01621.

Turcotte, D. L., and Schubert (2001), *Geodynamics*, 2nd ed., Cambridge University Press, New York.

Watson, S., and D. a. N. McKenzie (1991), Melt Generation by Plumes: A Study of Hawaiian Volcanism, *Journal of Petrology*, 32(3), 501–537, doi:10.1093/petrology/32.3.501.

Wessel, P., and W. H. F. Smith (1991), Free Software Helps Map and Display Data, *EOS Transactions, American Geophysical Union*.

Wessel, P., and W. H. F. Smith (1998), New, improved version of Generic Mapping Tools released, *EOS Transactions, American Geophysical Union*, 79(49), 579.

Wieczorek, M. A. (2007), Gravity and Topography of the Terrestrial Planets, *Treatise on Geophysics*, 165–206.

White, R. S. (1993), Melt Production Rates in Mantle Plumes, *Philosophical Transactions of the Royal Society of London. Series A: Physical and Engineering Sciences*, 342(1663),

137 -153, doi:10.1098/rsta.1993.0010.

Wolfe, C. J., M. K. McNutt, and R. S. Detrick (1994), The Marquesas archipelagic apron: Seismic stratigraphy and implications for volcano growth, mass wasting, and crustal underplating, *Journal of Geophysical Research*, 99(B7), 13,591-13,608, doi:199410.1029/94JB00686.

Young, H. D. (1962), *Statistical treatment of data*, McGraw-Hill Inc, New York.

Zuber, M. T., and E. M. Parmentier (1990), On the relationship between isostatic elevation and the wavelengths of tectonic surface features on Venus, *Icarus*, 85(2), 290-308, doi:10.1016/0019-1035(90)90118-S.

5. The Lithospheric Structure and Compensation Mechanisms at Beta Regio, Venus

Elyse Schinella, Juan Carlos Afonso, and Craig O'Neill

Abstract. Beta Regio is a ~2500 km by ~2000 km rift-dominated volcanic rise located within Venus's mid-latitudes. Beta Regio shares similar tectonic and volcanic land forms to other volcanic rises, however, its large swell volume and high Geoid-to-Topography Ratios (GTRs) are uncharacteristic of Venusian volcanic rises and could be produced by a range of mechanisms, including crustal thickening, dynamic uplift, volcanism, and thermal thinning of the lithosphere. In order to constrain the contribution of each of these mechanisms in shaping Beta Regio's topography we first need to determine the lithospheric structure below this rise. However, previous estimates of Beta Regio's lithospheric structure are highly unconstrained, especially the thermal lithospheric thickness, with estimates ranging from being thin (~100-200 km) to thick (~300-550 km). At Beta Regio we aim to constrain the (1) lithospheric structure, (2) compensation mechanisms acting to support the topography, and (3) cause of the large swell volumes and GTRs. We use the interactive forward modelling software, GEO3Dmod, to model the lithospheric structure below Beta Regio using a reference crustal and lithospheric thickness of 30 km and 300 km, respectively. Our proposed lithospheric structure comprises thick (~30-75 km) crustal roots below the volcanoes and widespread tessera terrain (~30-75 km). A thinner crust (~15-25 km) occurs below the central rift trough, which are flanked by a thicker crust (~25-40 km) at the rift shoulders. The thermal lithosphere gradually thickens moving outwards from the central volcanic rise (~60-100 km) into the surrounding plains regions (~375 km). Beta Regio's topography is primarily supported by Airy isostasy and thermal isostasy, with some regional isostasy (flexure) and localised dynamic

uplift ($\sim < 0.3$ km). In this study, dynamic topography is considered to be the topography remaining after the isostatic topography was removed from the observed topography. An absence of broad scale dynamic compensation required by our model implies Beta Regio's high swell volume and GTR is due to a thick crust associated with the observed tessera terrain and long wavelength thermal thinning of the lithosphere. This minor dynamic compensation, in conjunction with a thick (~ 15 km) crust below the central rift trough of Ganis Chasma, may imply this area is not undergoing current localised rifting and volcanism.

5.1 Introduction

Beta Regio extends from -105°E to -55°E and 14°N to 42°N (Figure 5.1). The rise itself has elevations of ~ 2 to 3 km above Venus's Mean Planetary Radius (MPR), increasing up to 4 km at the two large shield volcanoes, Theia and Rhea Mons (Figure 5.1) [Basilevsky and Head, 2007]. The earliest geological unit emplaced at Beta Regio was a northern region of tessera terrain and was closely followed by the formation of Rhea Mons. Both of these units were later being dissected by the north-south striking Devana Chasma [Basilevsky and Head, 2007]. Devana Chasma is part of an interconnected global rift system [Basilevsky and Head, 2007], forming a triple junction at Theia Mons and extending below 1 km of Venus's MPR [Ernst et al., 2003; Stofan et al., 1989]. Theia Mons overlies the western portion of this rift to the south, and has also been dissected by later rifting [Basilevsky and Head, 2007].

Beta Regio is the main focus of this study, however we have also chosen to include Asteria Regio (Figure 5.1). Asteria Regio is located between -100°E to -90°E and 20°N to 38°N in the modelled area and appears similar to a plateau, reaching elevations up to 1 - 2 km, much lower than Beta Regio (Figure 5.1) [Smrekar and Phillips, 1991]. A region with slightly higher

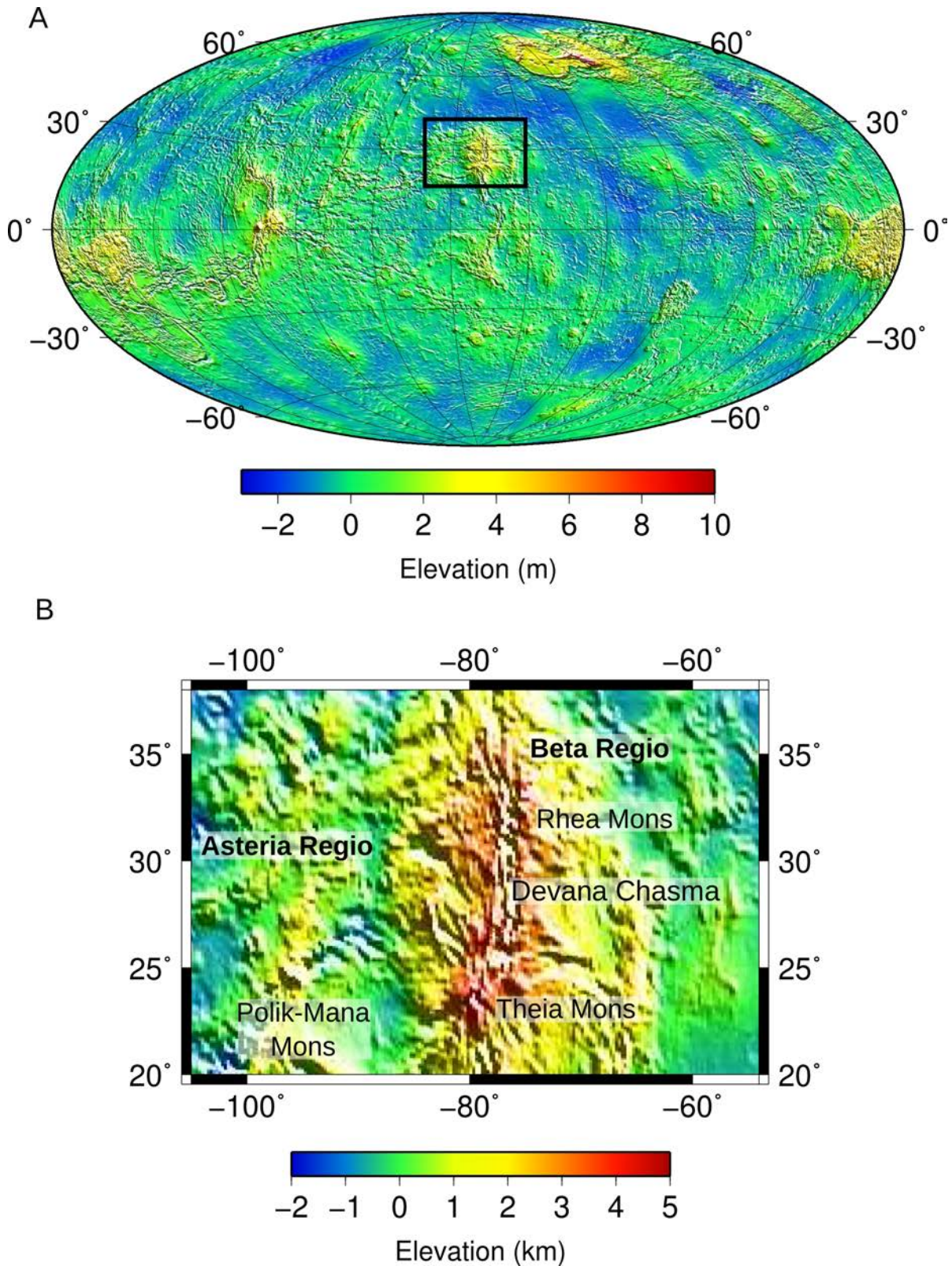


Figure 5.1. (A) Beta Regio is located within Venus's mid-latitudes. (B) Elevation map, referenced to a Mean Planetary Radius (MPR) of 6051.848 km, overlain with the location of the major features discussed in this study.

elevation (~ 4 km) occurs towards the south, corresponding to the volcano Polik-Mana Mons (Figure 5.1). Asteria lacks the broad domical shape that is characteristic of other volcanic rises considered to experience mantle upwelling, which could suggest this area requires either no, or very minor, dynamic compensation [Smrekar *et al.*, 1997].

Compared to other Venusian volcanic rises, Beta Regio has the largest swell volume, diameter, and GTR [Smrekar and Phillips, 1991; Stofan *et al.*, 1995]. However, the processes contributing to these differences and the observed topography, are not clearly defined with some authors favouring dynamic uplift [Kiefer and Hager, 1991; Smrekar and Phillips, 1991; Smrekar *et al.*, 1997; Vezolainen *et al.*, 2004] or significant thermal thinning [Kucinskas and Turcotte, 1994; Moore and Schubert, 1995]. In addition, the lithospheric structure, which can help to determine the contribution of each process in shaping Beta Regio's topography, is also very unconstrained. Lithospheric thickness is particularly ambiguous, with estimates of 100-550 km fitting the observed elevations and GTRs equally well [Kiefer and Hager, 1991; Kucinskas and Turcotte, 1994; McKenzie, 1994; Moore and Schubert, 1997; Moresi and Parsons, 1995; Orth and Solomatov., 2011; Smrekar *et al.*, 1997; Smrekar and Phillips, 1991; Solomatov and Moresi, 1996].

This study aims to constrain the crustal and lithospheric thickness variations, the extent of Airy isostasy, thermal isostasy, dynamic uplift, and flexure (regional isostasy) in shaping the topography observed at Beta Regio. We use GEO3Dmod, the simplified version of LitMod3D, to calculate solutions to isostasy, geopotential, and heat transfer equations for a plausible lithospheric structure [Fullea *et al.*, 2009]. Compared to LitMod3D, GEO3Dmod does not consider the thermodynamics or rheology of the interior. Considering these parameters are highly unknown on Venus, the simplified approach of GEO3Dmod was chosen to constrain the highly uncertain thermal lithospheric structure (or depth to the 1300°C isotherm) below

Beta Regio. By constraining the lithospheric structure, we were able to infer the cause of Beta Regio's uncharacteristically high GTRs, size, and swell volume. It also allows us to compare with other Venusian rises to determine if Beta Regio is a site of localised rifting and volcanism.

5.2 Background

5.2.1 Lithospheric Thickness

A thin (100-200 km) thermal lithosphere below Beta Regio can explain observations of recent volcanism, extension, dynamic support, melt generation rates, and large Apparent Depths of Compensation (ADCs; 244 to 296 km) [Leftwich *et al.*, 1999; Smrekar *et al.*, 1997; Smrekar and Phillips, 1991; Stofan *et al.*, 1995]. A number of authors have inferred Beta Regio's large GTRs ($\sim 31 \text{ m km}^{-1}$) represent thermal thinning of the lithosphere associated with an upwelling mantle plume [Kucinkas and Turcotte, 1994; Moore and Schubert, 1995; Senske *et al.*, 1991].

Kucinkas and Turcotte [1994] used geoid and topography data from Magellan, in conjunction with isostatic models, to estimate Beta Regio's lithosphere has thinned from around 369 km to ~ 113 km. They also proposed that this lithospheric thinning was responsible for compensating most of the topography observed in this area.

Moore and Schubert [1995] also used isostatic models, a maximum elevation of 3.3 km, a mantle-lithosphere density contrast of 2.5-3% and a mantle temperature of 800-1000 K, to determine that the lithosphere was thinned from ~ 135 -162 km to present values of ~ 108 -135 km. However, the high mantle temperature variations used in their model would produce extensive melt and widespread volcanic terrain, which is not currently observed at Beta Regio

[Moore and Schubert, 1995].

Numerical models of stagnant-lid convection are consistent with a thick (300-550 km) thermal lithosphere [Leftwich *et al.*, 1999; Orth and Solomatov, 2011; Smrekar, 1994; Solomatov and Moresi, 1996; Vezolainen *et al.*, 2004]. Vezolainen *et al.* [2004] used a maximum elevation of 4 km and a GTR of 30 m km^{-1} in their numerical models to determine a 400 km thick thermal lithosphere occurs below Beta Regio. In order to explain the much thinner lithospheric thickness estimates obtained from melt generation rates, Vezolainen *et al.* [2004] proposed the lithosphere may have been as thin as 100-200 km during formation. A thinner lithosphere during formation is also inferred from tightly spaced (5 km) faults at Rhea Mons [Stofan *et al.*, 1989]. One discrepancy with their results is the thickening of the thermal lithosphere with time. They confirm Beta Regio does not exhibit subsidence and is currently being uplifted, but do not address how the lithosphere has cooled and thickened over time, without the topography subsiding.

5.2.2 Crustal Thickness

Beta Regio's crustal structure has also been studied using different techniques [Leftwich *et al.*, 1999; McKenzie, 1994; Simons *et al.*, 1997]. From admittance studies of gravity and topography and numerical modelling, McKenzie [1994] proposed a thin crust at the center of Devana Chasma is flanked by a thicker crust at the rift shoulders. These crustal variations can form when an upwelling mantle plume impinges onto the base of the lithosphere, whereby the additional heat decreases the viscosity in the lower crust, enabling it to migrate and pool outwards from the plume's center [McKenzie, 1994]. The force of this migrating lower crustal material could produce rifting in the upper crust at the center of the plume and thrusting at the rift flanks [McKenzie, 1994].

Leftwich et al. [1999] used free-air gravity and topography with Airy-Heiskanen isostasy models to also determine a thin (3 km) crust was prevalent at the central trough of Devana Chasma, with the adjacent rift shoulders and remaining areas having a thicker crust (up to 38 km). The thicker crust below the rift shoulders is most likely caused from volcanism and intrusion of magma into the lower crust [*Leftwich et al.*, 1999].

In Beta Regio, areas over the volcanic rise, located away from Devana Chasma, exhibit crustal thicknesses ranging from 20-30 km [*Leftwich et al.*, 1999]. A similar range (20-40 km) of crustal thicknesses over the Beta Regio rise were also found from geoid and topography spectral admittance studies by *Simons et al.* [1997].

Kucinskas and Turcotte [1994] used an Airy Isostasy model where Beta Regio's topography was supported by crustal roots of low or constant density, in a higher density mantle. This model resulted in implausible crustal thicknesses of 244 km at Beta Regio, implying this observed topography may be predominately supported by thermal isostasy [*Kucinskas and Turcotte*, 1994].

5.2.3 Dynamic Compensation

A mantle plume or mantle diapir may provide dynamic compensation at Beta Regio, as evidenced from the presence of volcanoes, rifts, an elevated domal morphology, and high geoid anomalies [*Basilevsky and Head*, 2007; *Kiefer and Hager*, 1991; *Vezolainen et al.*, 2004]. In a model proposed by *Senske et al.* [1991] a mantle plume encompassing both Beta and Asteria Regio caused dynamic uplift and the associated volcanic edifice formation and rifting of the extensive and preexisting tessera terrain. However, these authors note that this model is unable to account for the tessera terrain that formed prior to Beta Regio [*Senske et*

al., 1991].

Spectral admittance studies have found isostatic compensation alone can-not support all of the topography at Venus's large volcanic rises [Smrekar, 1994]. Compensation depths would be extremely large if Airy isostasy is the only compensation mechanism acting at Beta Regio [Kiefer and Hager, 1991; Kucinskas and Turcotte, 1994]. Also the elevated topography and geoid at Beta Regio requires a thick crust (up to 60 km) if an Airy isostatic model is assumed, whereas a rifting model has a limited compensation contribution (20-30 %) [Kiefer and Hager, 1991; Smrekar and Phillips, 1991]. Kiefer and Hager [1991] proposed dynamic uplift explains Beta Regio's high geoid and topography, with the associated stresses being high enough to initiate rifting. This may be further supported by the common north-south orientation of both Devana Chasma and Beta Regio [Basilevsky and Head, 2007; Senske and Head, 1992].

Rathbun *et al.* [1999] further addressed the relationship between a mantle plume and rifting at Beta Regio. In this study they calculated the amount of extension at each rift and found up to 27 km of extension along the northern arm of Devana Chasma (between Theia and Rhea Mons) [Rathbun *et al.*, 1999]. Hoop, or circumferential, strain is a function of both vertical and radial displacement and was used to estimate the amount of dynamic uplift within Beta Regio [Rathbun *et al.*, 1999]. Moving outwards from Theia Mons, localised, low strain anomalies occur, suggesting volcanic infilling [Rathbun *et al.*, 1999]. However, adjacent to Theia Mons, on the Beta Regio rise, the hoop strain and dynamic uplift reached up to 2.5% and ~3 km, before decreasing to ~0.1% and ~800 m, respectively within the plains. Without considering the influence of Theia Mons, the higher hoop strain over the volcanic rise compared to the plains regions could suggest current mantle plume activity [Rathbun *et al.*, 1999].

Vezolainen et al. [2004] also proposed dynamic uplift may be currently operating within Beta Regio from numerical models, the preservation of craters, and a lack of observational evidence for subsidence. Their results suggest Beta Regio has experienced dynamic uplift over ~ 800 Myr, initiated prior to ~ 375 Ma, continuing to the present day.

Previous estimates for the amount of dynamic compensation at Beta Regio has ranged from 0.2 km to 5.7 km [*Kiefer and Hager*, 1991; *Stofan et al.*, 1995; *Vezolainen et al.* 2004]. The higher dynamic uplift estimates were obtained from numerical modelling and varied depending on the Rayleigh number and viscosity structure used. This compares to the minimum value that was estimated from the flow direction of a lava channel, which appears to have formed due to volcanism before dynamic uplift influenced this area [*Smrekar et al.*, 1997; *Stofan et al.*, 1995].

5.2.4 Flexural Compensation

Elastic lithospheric thicknesses obtained from flexural studies using residual topography and Cartesian models were carried out over the western and eastern flanks of Davana Chasma at $281^{\circ}\text{E } 17^{\circ}\text{N}$ and $284^{\circ}\text{E } 17^{\circ}\text{N}$, respectively [*Barnett et al.*, 2002]. Rift flanks can experience maximum flexural uplift, when the adjacent lithosphere experiences loading due to the emplacement of the rift [*Kiefer and Swafford*, 2006]. The western profile has a much thinner elastic lithospheric thickness of ~ 36 km compared to the eastern flank (~ 67 km) [*Barnett et al.*, 2002]. Flexural studies completed by *Senske* [1993] across Devana Chasma showed the greatest correlation to the observed topography when a 20-40 km thick elastic lithosphere was used. However, a much thinner range of elastic lithospheric thicknesses, between 10-20 km, at Beta Regio were found from spectral admittance studies [*Simons et al.*, 1997].

5.2.5 The East-African Rift: A Terrestrial Analogy to Beta Regio

The evolution and orientation of rift associated fault systems at Beta Regio are analogous to that of the East African Rift (EAR), suggesting Devana Chasma closely resembles a continental rift [Foster and Nimmo, 1996; Stofan *et al.*, 1989]. Both of these rifts appear to have undergone minimal extension ($3\text{-}5\text{ mm yr}^{-1}$), with the EAR experiencing a maximum of 10 km in some places and up to 20 ± 10 km at Devana Chasma [Foster and Nimmo, 1996; Senske *et al.*, 1991].

Devana Chasma and the EAR share similar characteristics [Foster and Nimmo, 1996; Nimmo and McKenzie, 1996], thus their crustal and thermal lithospheric thickness estimates may also be comparable. Long period surface wave dispersion can be used to estimate lithospheric thickness [Pasyanos, 2010]. The eastern branch of the EAR, which includes the Ethiopian rift, was found to have a thin thermal lithosphere (40-100 km) compared to the thicker thermal lithosphere (100-140 km) along the western branch [Pasyanos, 2010]. A thin thermal lithosphere along the EAR is further supported by bore hole heat flow measurements [Artemieva, 2006; Pasyanos, 2010]. These thermal models produced similar lithospheric thicknesses, with the eastern branch of the EAR exhibiting a thinner lithosphere (60-100 km), compared to the western branch (100-120 km) [Artemieva, 2006; Pasyanos, 2010].

Similar to Devana Chasma, the EAR also exhibits crustal thickness variations between the central trough and shoulders. Along the eastern branch of the EAR, a thinner crust is located below the graben (30 km) compared to a thicker, flanking crust (35-40 km) [Achauer *et al.*, 1992; Chorowicz, 2005]. However, a thinner crust, between 15-30 km, occurs along the western branch of the EAR, near Lake Malawi [Chorowicz, 2005; Morley, 1989].

5.3 Methodology

5.3.1. Introduction

To model the thermal lithospheric structure below Beta Regio we used the interactive 3D forward modelling software, GEO3Dmod [Fullea *et al.*, 2010]. Input data required for modelling includes geophysical observables, a suitable reference column structure, and a thermal lithospheric model, which is determined by the user. The entire model domain extends to the depth of the first phase transition [~ 440 km; Steinbach and Yuen, 1992] and can comprise any number of crustal layers and one lithospheric mantle layer. The user is also required to define the density and thermal properties of each layer. GEO3Dmod then simultaneously solves heat transfer, geopotential, and isostasy equations before outputting 3D temperature and density distributions as well as calculated responses of Bouguer gravity, geoid height, surface heat flow, and elevation. By modelling these observables simultaneously we obtained a highly constrained, self-consistent lithospheric model rather than a highly unconstrained model that is commonly obtained from modelling each observable singularly [Fullea *et al.*, 2010].

5.3.2 Geophysical Observables

We used topography and gravity data obtained from the Magellan, Pioneer, and Venera missions to Venus to determine a plausible lithospheric structure at Beta Regio. Venus's elevation data set is the 719 degree and order spherical harmonic model of Wieczorek [2007], consisting of Magellan's Global Topography Data Record 3.2 (GTDR3.2), Pioneer, and Venera 15/16 altimetry (Figure 5.2). This resulting elevation was referenced to Venus's Mean Planetary Radius (MPR), equal to 6051.848 km.

This topography, in conjunction with the 180th degree and order spherical harmonic model of Venus's radial gravity [Konopliv *et al.*, 1999], was used to determine the Bouguer gravity B (Figure 5.2):

$$B = FA - BC \quad (5.1)$$

$$BC = 2 \pi \rho_{crust} G h \quad (5.2)$$

where FA , BC , ρ_{crust} , G , and h is the free-air gravity, Bouguer correction, crustal density (2900 kg m⁻³), universal gravitational constant (6.672x10⁻¹¹ N m² kg⁻²), and elevation, respectively.

A 2D Fast Fourier Transform was also applied to the free-air gravity to determine the geoid data set (Figure 5.2) using a similar method as Sjogren *et al.* [1997], Wessel and Smith [1991; 1998]. We filtered the geoid using a cosine-tapered high pass filter in order to remove anomalies from depths greater than our lithospheric model (< ~400 km). This filter discarded all degrees < ~14 (wavelengths < ~2716 km), effectively removing the the long-wavelength (dynamic) contribution of deep mantle anomalies to the geoid [Jiménez-Munt *et al.*, 2010].

Each of these data sets were associated with uncertainties. Most (97%) of the elevation data set was obtained from Magellan's Global Topography Data Record 3.2, therefore we assumed a maximum Root-Mean-Square error of 400 m for this data set in our modelling [Rappaport *et al.*, 1999].

The geoid was calculated to have a maximum uncertainty of 2.3 m by Sjogren *et al.* [1997] and this value was also used when modelling. The Bouguer gravity was calculated from a Bouguer correction involving both the topography and free-air gravity data sets and the

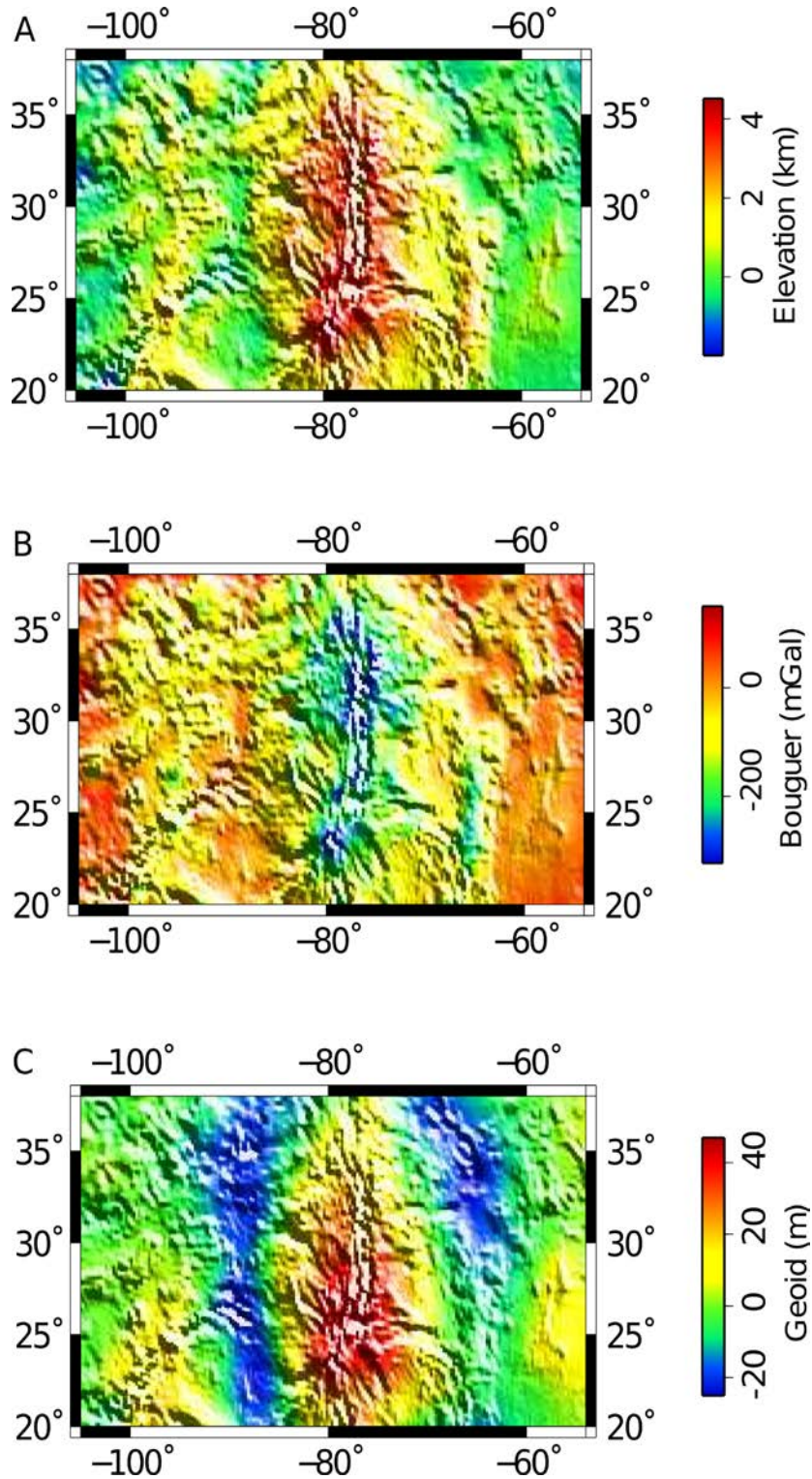


Figure 5.2. Maps of geophysical observables used in our lithospheric modelling at Beta Regio. (A) Elevation referenced to a Mean Planetary Radius (MPR) of 6051.848 km. (B) Bouguer gravity. (C) Geoid anomalies corresponding to a spherical harmonic degree and order $> \sim 14$ and wavelengths $< \sim 2716$ km.

uncertainty pertaining to this data was calculated from the rules of error propagation

[Bevington and Robinson, 1992; Taylor, 1982; Young, 1962]:

$$BC_{uncert} = Topo_{uncert} 2 \pi \rho_{crust} G$$

$$B_{uncert} = \sqrt{((FA_{uncert})^2 + (BC_{uncert})^2)}$$
(5.3-5.4)

where BC_{uncert} is the uncertainty relating to the Bouguer correction, $Topo_{uncert}$ is the maximum topographic uncertainty (400 m), FA_{uncert} is the maximum uncertainty of the free-air gravity equal to 12 mGal [Konopliv *et al.*, 1999]. Substituting each of these values into Equations 5.3 and 5.4 resulted in a Bouguer uncertainty of 50 mGal.

5.3.3 Lithospheric Modelling

GEO3Dmod was used to model crustal and lithospheric thickness variations below Beta Regio in order to determine the extent of isostatic and dynamic compensation in supporting the observed elevations within this region. GEO3Dmod requires a reference column with a suitable lithospheric structure located within an area that has undergone minimal tectonic and volcanic modification [Fullea *et al.*, 2010]. For Venus, this reference column was located within the North Polar Plains at 34.5°E 89°N, and was assumed to have a 30 km thick crust (T_c) and 300 km thick thermal lithosphere (L), consistent with previous global estimates (Figure 5.3) [Grimm and Hess, 1997; Nimmo and McKenzie, 1998; Turcotte, 1993].

Previous lithospheric modelling at Atla Regio has also addressed the effects of using thinner reference values of 15 km for the crust and 140 km for the thermal lithosphere (Refer to Chapter 4 for additional details). By performing a least-squares analysis for each reference

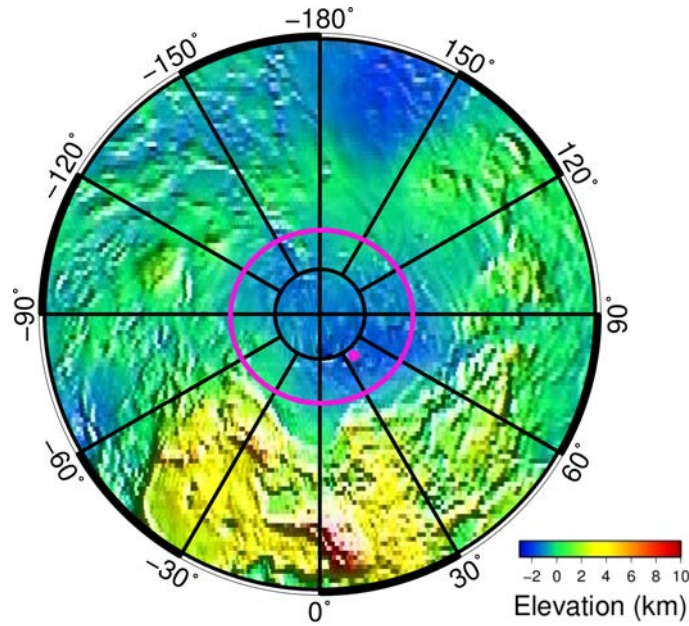


Figure 5.3. The location of the North Polar Plains and our reference column shown as the large purple and small circle, respectively. The average elevation (-1.069 km) of the North Polar Plains also corresponds to the elevation at our reference column located at 34.5°E 89°N.

column, we found that reference columns using a thinner crust and thermal lithosphere resulted in a greater misfit between the calculated and observed geoid and elevation at Atla Regio (Table 5.1). A reference column using a thick crust (30 km) and lithosphere (300 km) resulted in a slightly higher Bouguer misfit than one with a thinner crust (15 km). We were primarily concerned with fitting the geoid and elevation data sets, thus the reference column with a 30 km thick crust and 300 km thick lithosphere was considered the most appropriate lithospheric structure at the North Polar Plains.

Table 5.1. Results from the least-squares analysis for each reference column

Model	Elevation (m)	Bouguer (mGal)	Geoid (m)
$T_c=30$ km; $L=300$ km	1.61	16.21	203.78
$T_c=15$ km; $L=300$ km	1.76	16.14	316.07
$T_c=15$ km; $L=140$ km	1.78	17.33	247.68

The other reference columns also produced calculated responses of geoid, Bouguer gravity, and elevation that showed a weak correlation to the observables and implausible crustal thinning below Atla Regio's central rift ($\sim < 0$ km).

Our chosen reference column was constrained further from melt generation rates calculated at Ganis Chasma in Atla Regio [Nimmo and McKenzie, 1998]. For example, a reference column with $T_c = 30$ km and $L = 300$ km resulted in a modelled lithospheric structure below Ganis Chasma that yielded a melt generation rate of $0.5 \text{ km}^3 \text{ yr}^{-1}$ and a melt volume of $0.20 \times 10^6 \text{ km}^3$, consistent with previous estimates [Nimmo and McKenzie, 1998; Smrekar and Paramentier, 1996].

The elevation (-1.069 km) at the location of this reference column ($34.5^\circ\text{E } 89^\circ\text{N}$) corresponds to the average elevation of the North Polar Plains between $-180^\circ\text{E } 85^\circ\text{N}$ and $180^\circ\text{E } 90^\circ\text{N}$, implying this reference lithospheric structure may be suitable not only for the North Polar Plains, but also the expansive lowland plains regions that occur at similar elevations (Figure 5.3) [Solomon and Head, 1990].

The absolute elevation E of a lithospheric column at Beta Regio is dependent on its depth-averaged density of the lithosphere ρ_l and a calibration constant L_0 . Therefore, the calibration constant can be calculated for a reference lithospheric structure if the reference elevation E_0 is known. For our reference column, the depth-averaged density of the lithosphere (3203 kg m^{-3}) was found by averaging the total densities of the lithospheric column to a depth of 300 km. This value, in conjunction with reference elevation E_0 of -1.069 km, was used with Equation 5.5 to find a calibration constant L_0 , equal to 0.768 km (Figure 5.4) [Lachenbruch and Morgan, 1990]. Therefore, Equation 5.5 can be used to either calculate the elevation E of a lithospheric column at Beta Regio or can be used with a reference elevation E_0 to calculate the

calibration constant:

$$\begin{aligned}
 & \text{If } E \vee E_0 < 0: \\
 E \vee E_0 &= \frac{\rho_a}{(\rho_a - \rho_{atmos})} \left(\frac{(\rho_a - \rho_l)}{\rho_a} L - L_0 \right) \\
 & \text{If } E \vee E_0 > 0: \\
 E \vee E_0 &= \frac{(\rho_a - \rho_l)}{\rho_a} L - L_0
 \end{aligned} \tag{5.5}$$

where L is the lithospheric thickness (300 km), ρ_{atmos} and ρ_a are the densities of the overlying atmosphere (60 kg m^{-3}) and adiabatic sub-lithosphere (3200 kg m^{-3}), respectively.

The lithospheric model at Beta Regio has a resolution of 70x28x600 nodes and includes three layers, with properties shown in Table 5.2. The first, second, and third layers corresponded to the basaltic upper crust, gabbroic lower crust, and peridotitic lithospheric mantle, respectively (Table 5.2).

Most of Venus's surface and sub-surface is mafic in composition as indicated by the composition of samples obtained during the Venera and Vega missions and the morphology of volcanoes [Grimm and Hess, 1997; Head et al., 1992]. Considering these observations, Venus's crust most likely has a similar density to Earth's crustal basaltic rocks ($\sim 2900 \text{ kg m}^{-3}$), with this basalt ultimately transitioning into denser gabbro and peridotite at greater depths [Reynolds, 1997; Rogers, 2007].

Each of the layers presented in Table 5.2 have variable coefficients of thermal expansion and temperature-dependent densities, with layers one and two also having pressure-dependent densities (Table 5.2).

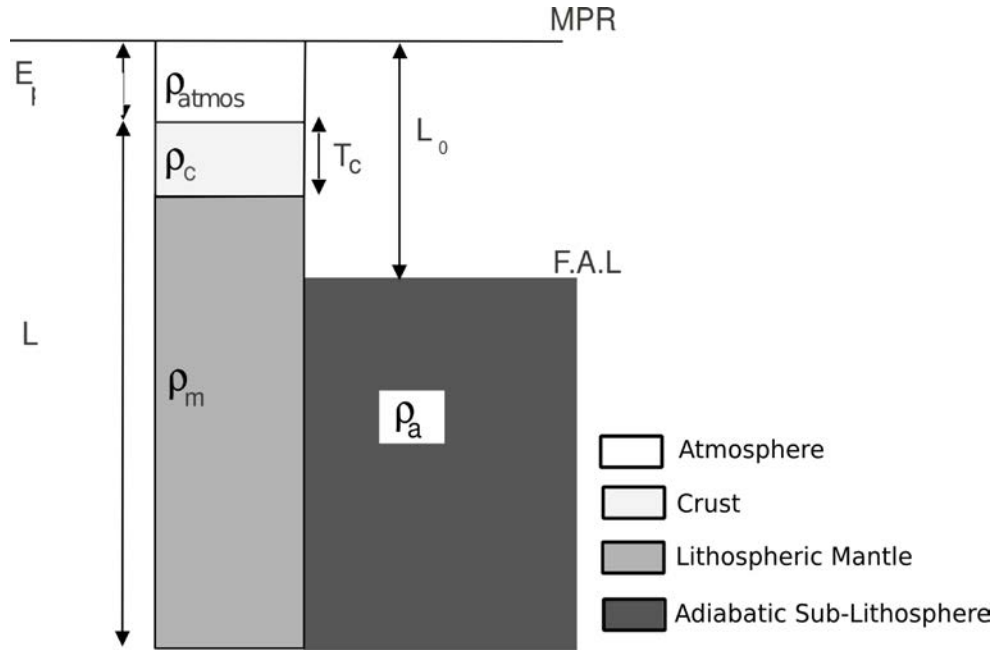


Figure 5.4. (Adapted from *Fullea et al.*, 2007) Notation for each lithospheric model at Beta Regio. E is the absolute elevation, T_c and L are the crustal and lithospheric thickness, respectively. The density of the atmosphere, crust, lithospheric mantle, and adiabatic sub-lithosphere are denoted by ρ_{atmos} , ρ_c , ρ_m and ρ_a . L_0 is the calibration constant, and represented the depth from the MPR to the Free-Asthenosphere Level (F.A.L.).

Table 5.2. Layer parameters

Layer	Name	Density (kg m^{-3})	Coefficient of thermal expansion ($\times 10^{-5}$) K^{-1}	Thermal conductivity W K^{-1}	Heat Production Rate ($\times 10^{-7}$) W m^{-3}	Pressure Coefficient ($\times 10^{-10}$)
1	Upper crust	2900	2.75	2.1	2.0	2.36
2	Lower crust	3000	1.60	3.0	2.0	2.44
3	Lithospheric Mantle	3200	3.50	3.3	0.2	0

The coefficient of thermal expansion and heat production rate for each layer in Table 5.2 are similar to those used by *Afonso et al.* [2005]; *Ranalli* [1995]; and *Schubert et al.* [2002]. The the compressibility β of each layer was calculated by taking the inverse of the bulk modulus K of basalt, gabbro, and peridotite [Table 5.2; *Schubert et al.*, 1997]:

$$K = \frac{E}{3(1-2\nu)} \quad (5.6)$$

$$\beta = \frac{1}{K}$$

where E is Young's modulus and ν is Poisson's ratio.

Properties of the adiabatic sub-lithospheric mantle, which underlies the thermal lithosphere were not included in Table 5.2, since this layer is outside of our model domain. However, the constant density (3200 kg m^{-3}) of this layer acts as a reference for the density variations in the thermal lithosphere.

Residuals, found by subtracting the calculated response associated with a chosen lithospheric structure from the observed response, were useful in determining whether additional compensation mechanisms, such as flexure and dynamic uplift, are required to support the observed topography. Additionally, histogram plots of these residuals as a percentage of the total magnitude range for each observable are also useful in determining the "goodness-of-fit" of the chosen lithospheric model.

GEO3Dmod calculates the flexural response for a given elastic lithospheric thickness [Fullea *et al.*, 2009]. Due to the uncertainty surrounding the elastic lithospheric thickness at Beta Regio, we chose to model a range of values including 10 km, 30 km, and 50 km. This flexural response was calculated from the residual topography that remained after the effects of Airy and thermal isostasy were removed from the observed topography. Therefore, the flexural response was not iteratively solved. The amount of dynamic compensation was also found from the residual topography by removing the isostatic and flexural contribution from the observed topography.

The modelled area at Beta Regio extended from -55°E to -105°E and 20°N to 38°N (Figure

5.5). We present both regional maps of crustal and lithospheric thickness, as well as three lithospheric profiles taken over Theia Mons, Rhea Mons, and Asteria Regio, as shown in Figure 5.5.

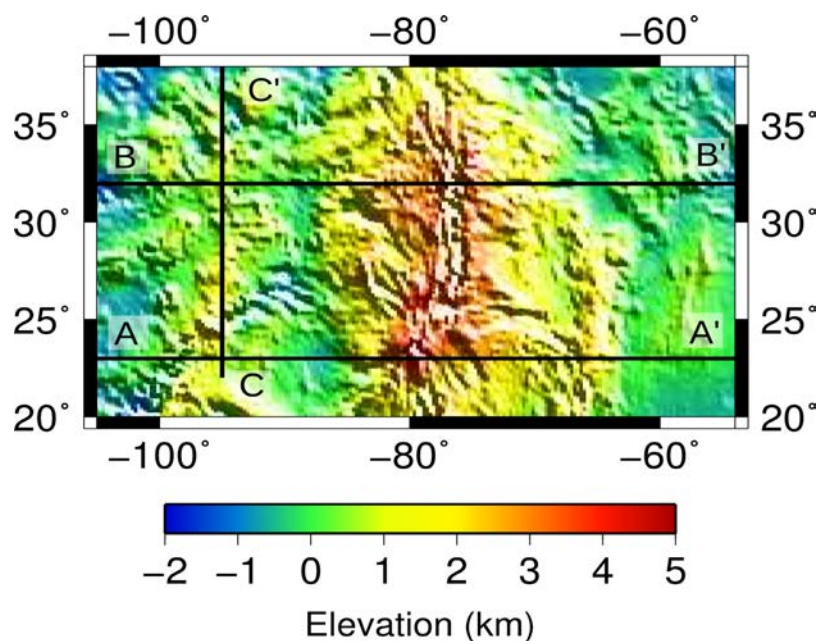


Figure 5.5. Elevation map of Beta Regio showing the location of the three profiles discussed in this study. A-A' , B-B' , and C-C' extend over Theia Mons, Rhea Mons, and Asteria Regio, respectively.

5.4 Results

5.4.1 Residuals

Residuals represent a model's misfit and are useful in locating areas where additional compensation is required (Figure 5.6). This misfit may also represent a density structure that is not accounted for by the current lithospheric structure. From Figure 5.7 each histogram plot exhibits a Gaussian-like distribution implying the proposed lithospheric structure and in turn, Airy and thermal isostasy, can compensate most of the observed topography. From Figure 5.6C the elevation residuals are low in the region along Devana Chasma, between 25°N to 29°N, suggesting another compensation mechanism may be required for topographic support.

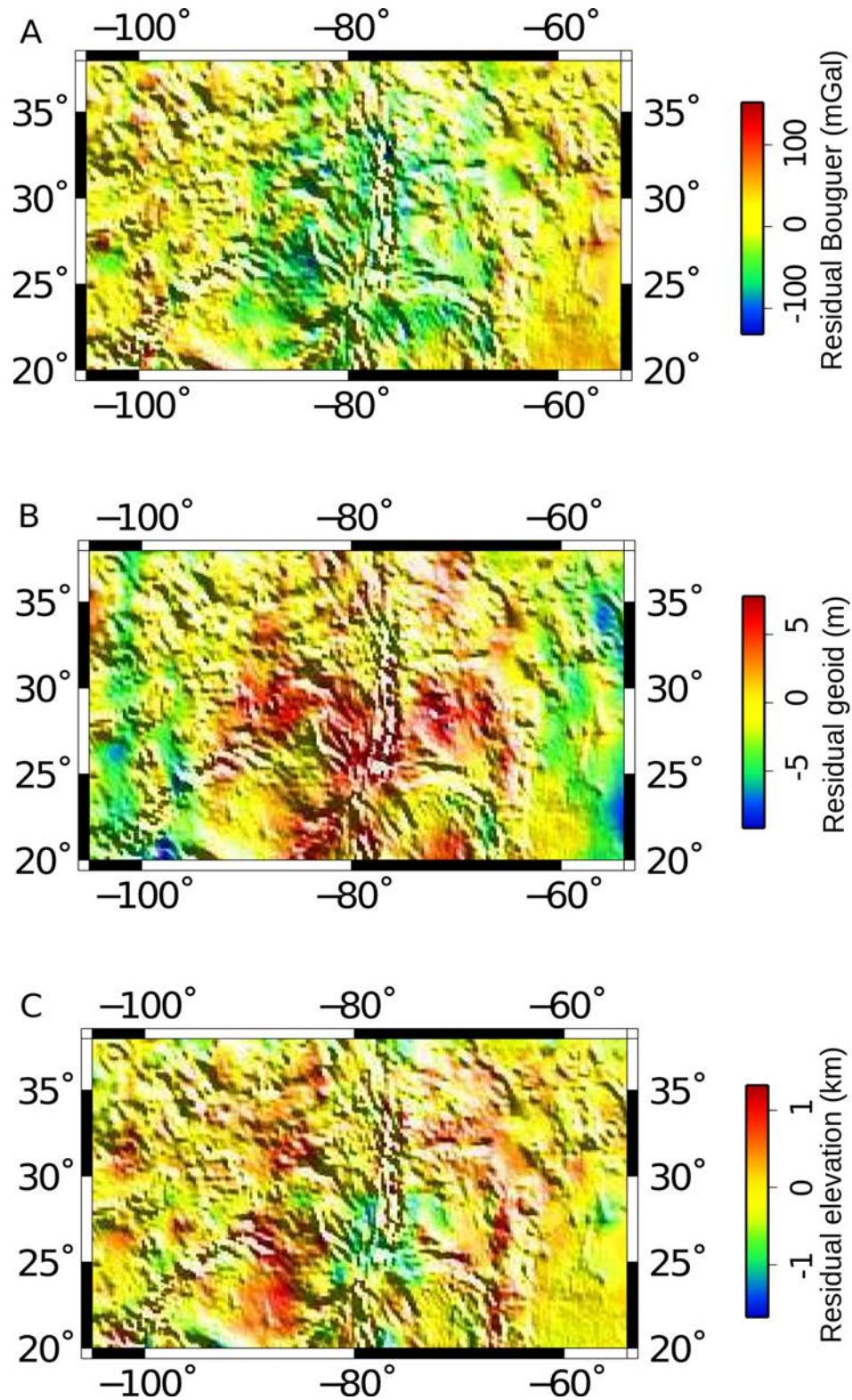


Figure 5.6. Maps of residual Bouguer gravity (A), residual geoid (B), and residual elevation (C).

Residuals were found by subtracting the calculated model from the observables.

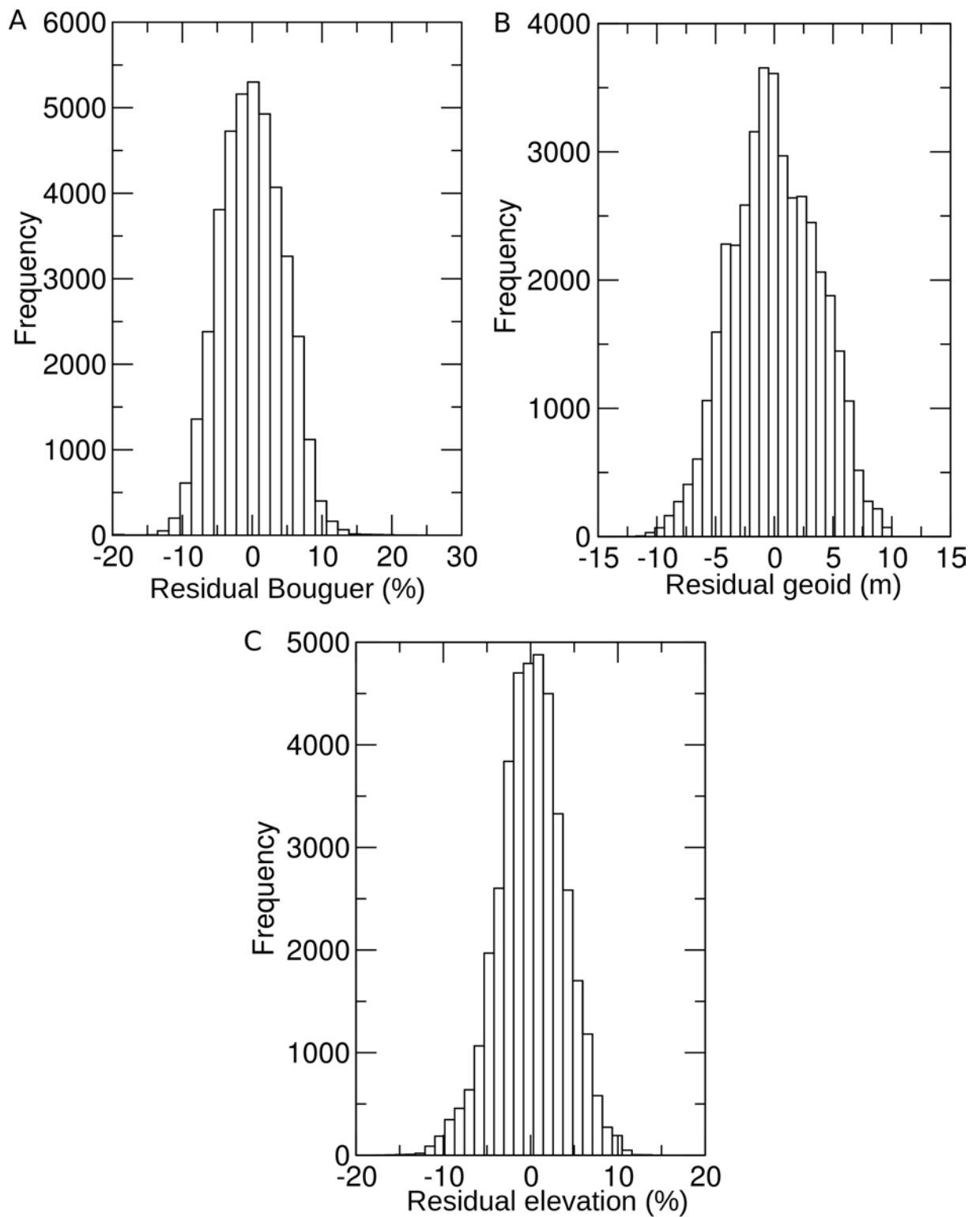


Figure 5.7. Histogram plots of (A) residual Bouguer gravity, (B) residual geoid, and (C) residual elevation residuals. Residuals are shown as a percentage of the total magnitude range for each observable. Each histogram plot exhibits a Gaussian-like distribution, with the majority of the residuals being within 10% error.

5.4.2 Lithospheric Profiles

Figure 5.8 shows an easterly profile over Theia Mons along 23°N. The crust is the thickest (65-73 km) at Theia Mons with less occurring at Asteria Regio (48 km) and the plains (~36 km). From both the lithospheric structure (Figure 5.8) and thermal structure (Figure 5.9) the lithosphere is thin (100 km) below Beta Regio, but thickens at Asteria Regio (~230) and the plains regions (292-352 km). The thin lithosphere below Beta Regio corresponds to higher surface heat flows (29-30 mW m⁻²) compared to the thicker plains regions (15-19 mW m⁻²) and Asteria Regio (16-18 mW m⁻²).

Another easterly profile was also taken over the summit of Rhea Mons at 32°N (Figure 5.10). Rhea Mons and the surrounding tessera experience similar crustal thicknesses ranging from 50-56 km, however Asteria Regio has a crustal thickness comparable to the previous profile (40-48 km). Rhea Mons shares a similar lithospheric thickness (100 km) and thermal structure to Theia Mons (Figure 5.10 and 5.11). The lithosphere at the tessera terrain is relatively thin (138 km), compared to Asteria Regio (272 km), and the surrounding plains regions (280-320 km). Surface heat flow is highest at Rhea Mons (30-35 mW m⁻²) compared to the tessera (29 mW m⁻²), Asteria Regio (16-17 mW m⁻²), and the plains (15-18 mW m⁻²).

A northerly profile, taken over Asteria Regio at -95°E from 22°N to 38°N, is shown in Figure 5.12. Most of Asteria Regio has thick (60-76 km) crustal roots. The profile crosses a tessera unit towards the north, centered at ~1350 km, which has crustal thicknesses ranging from 40-60 km. From Figures 5.12 and 5.13 the lithosphere gradually thickens (260 to 264 km) from Asteria Regio to the northern tessera and plains regions (394 km). Compared to Theia and Rhea Mons, the surface heat flows below this rise are lower (17-19 mW m⁻²) with values similar to the plains regions. Between 1200 to 1500 km the modelled responses are slightly

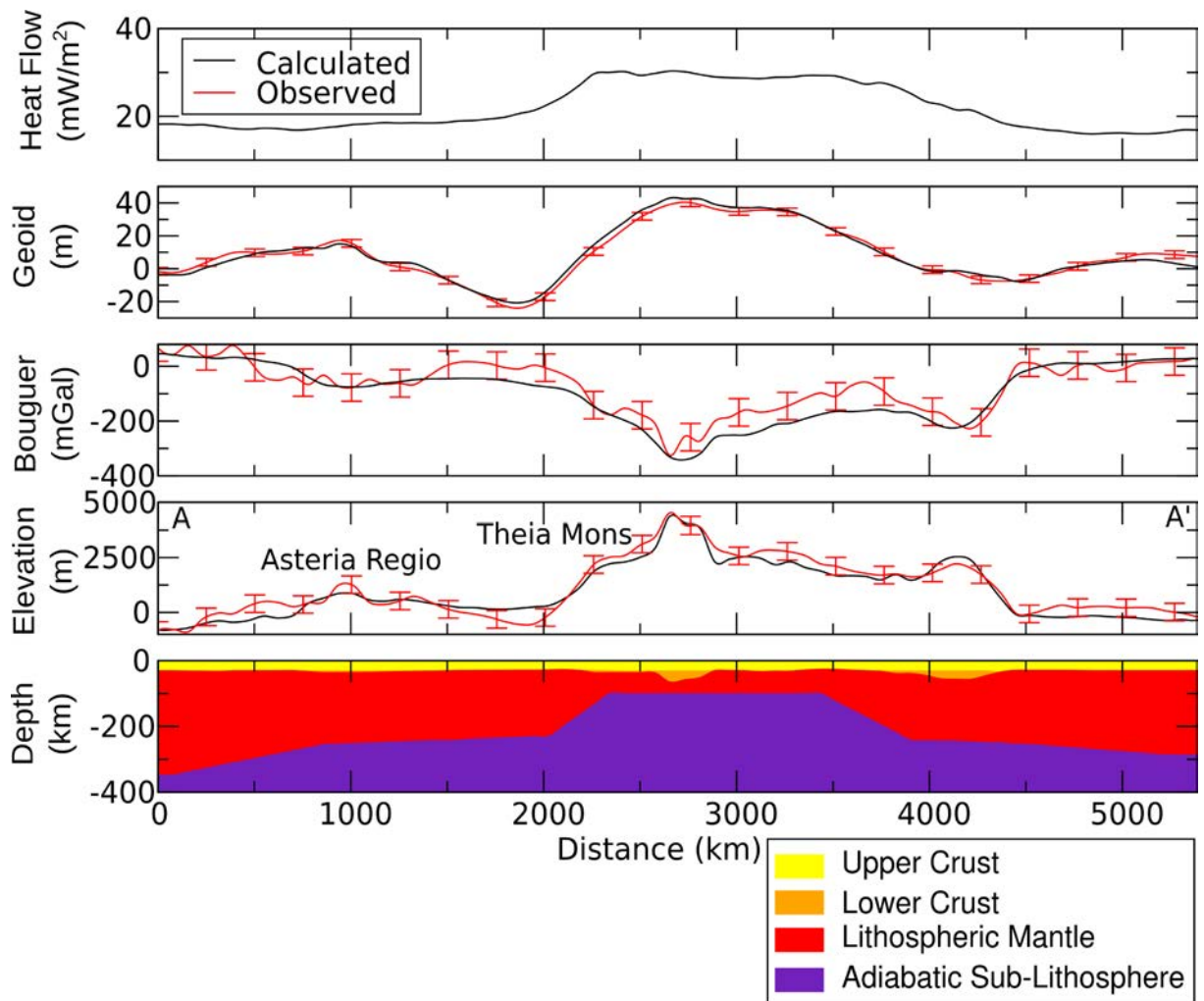


Figure 5.8. Easterly profile taken along 23°N over Asteria Regio, and Theia Mons (located on the Beta Regio rise). The calculated model responses, based on the proposed lithospheric structure, are shown by the black lines. The red error bars represent the uncertainty associated with each respective geophysical observable (red lines). The upper crust, lower crust, lithospheric mantle, and adiabatic sub-lithosphere are shown as the yellow, orange, red, and purple layers, respectively. No observed surface heat flow is available.

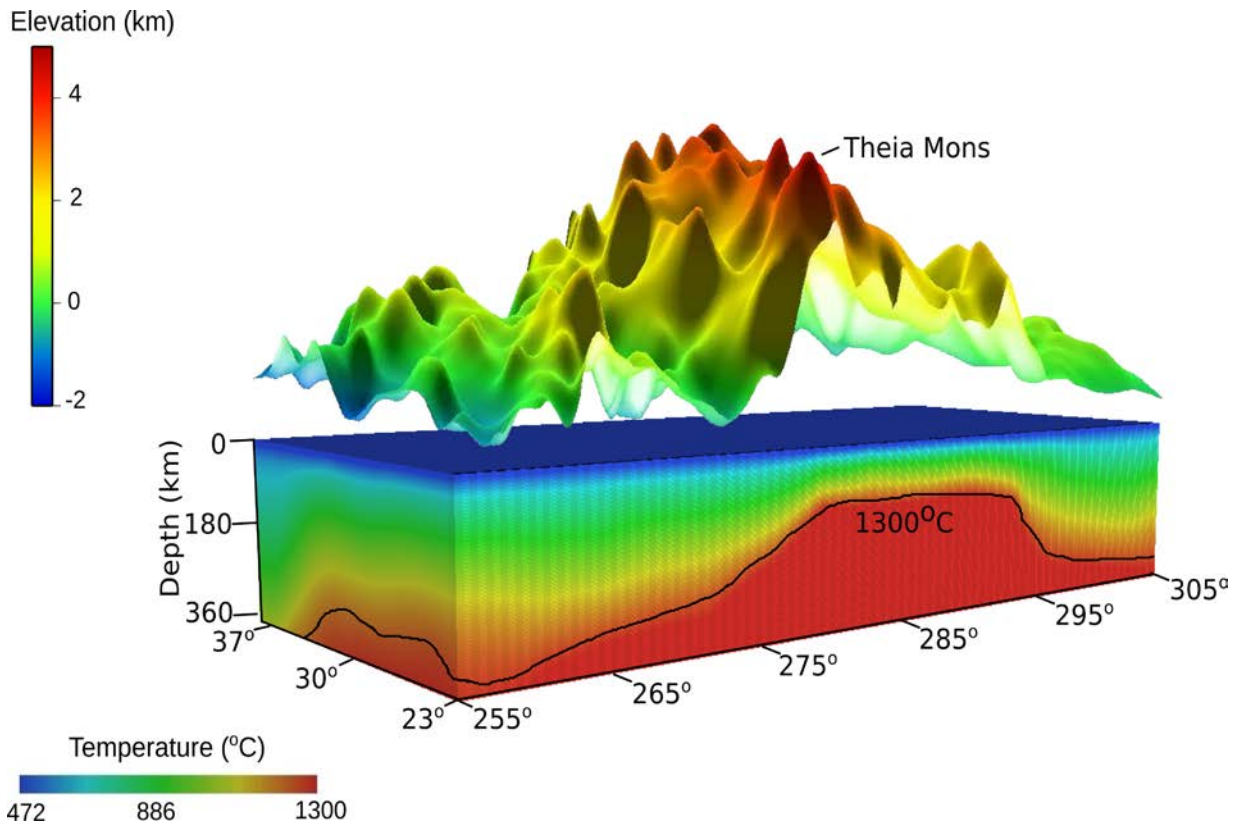


Figure 5.9. The thermal structure below Theia Mons along 23°N. The thermal structure and topography between 20°N to 22°N was removed for clarity.

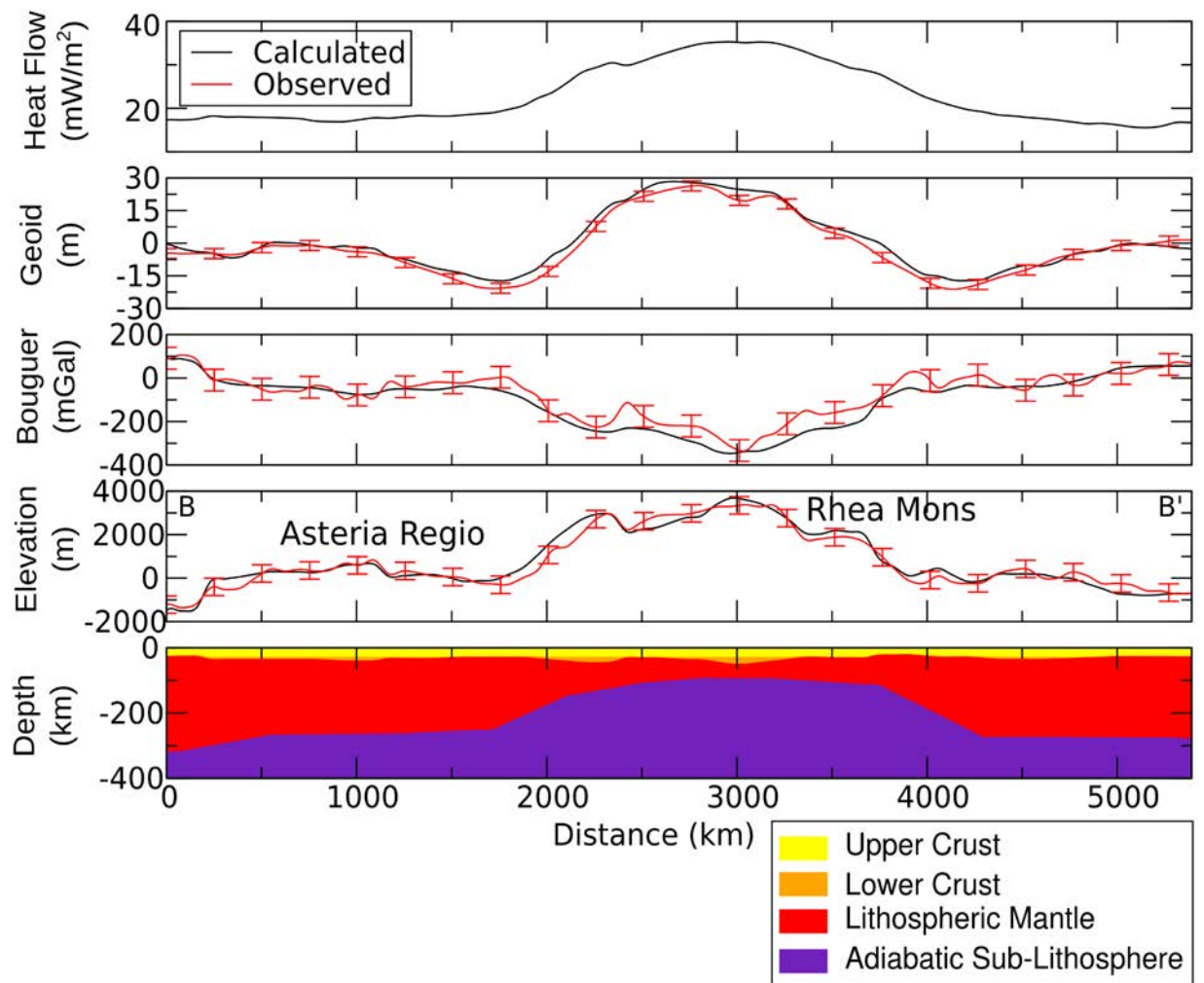


Figure 5.10. Easterly profile taken over 32° N showing the lithospheric structure at Asteria Regio and Rhea Mons. Key is similar to Figure 5.8.

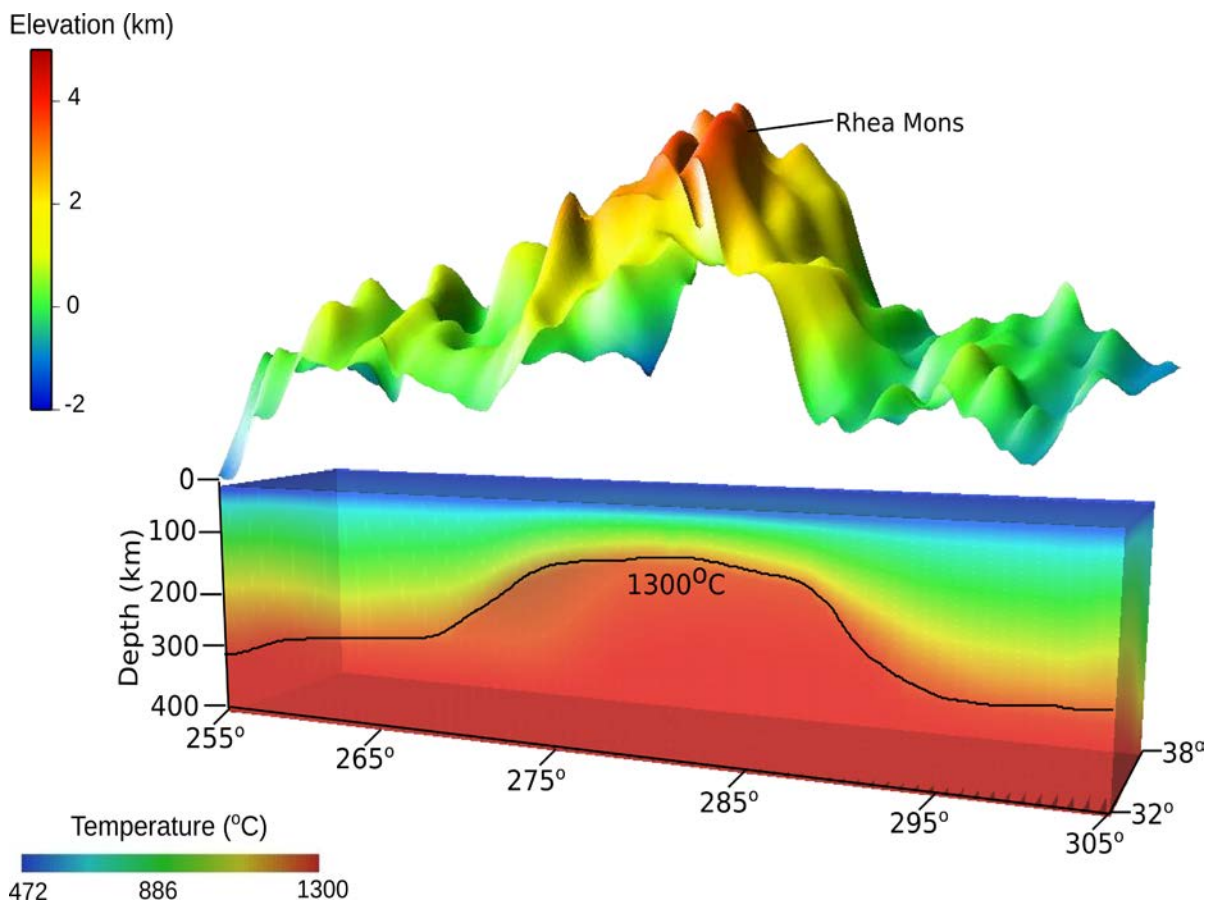


Figure 5.11. Thermal structure below Rhea Mons along 32°N. The thermal structure and topography between 20°N to 31°N was removed for clarity.

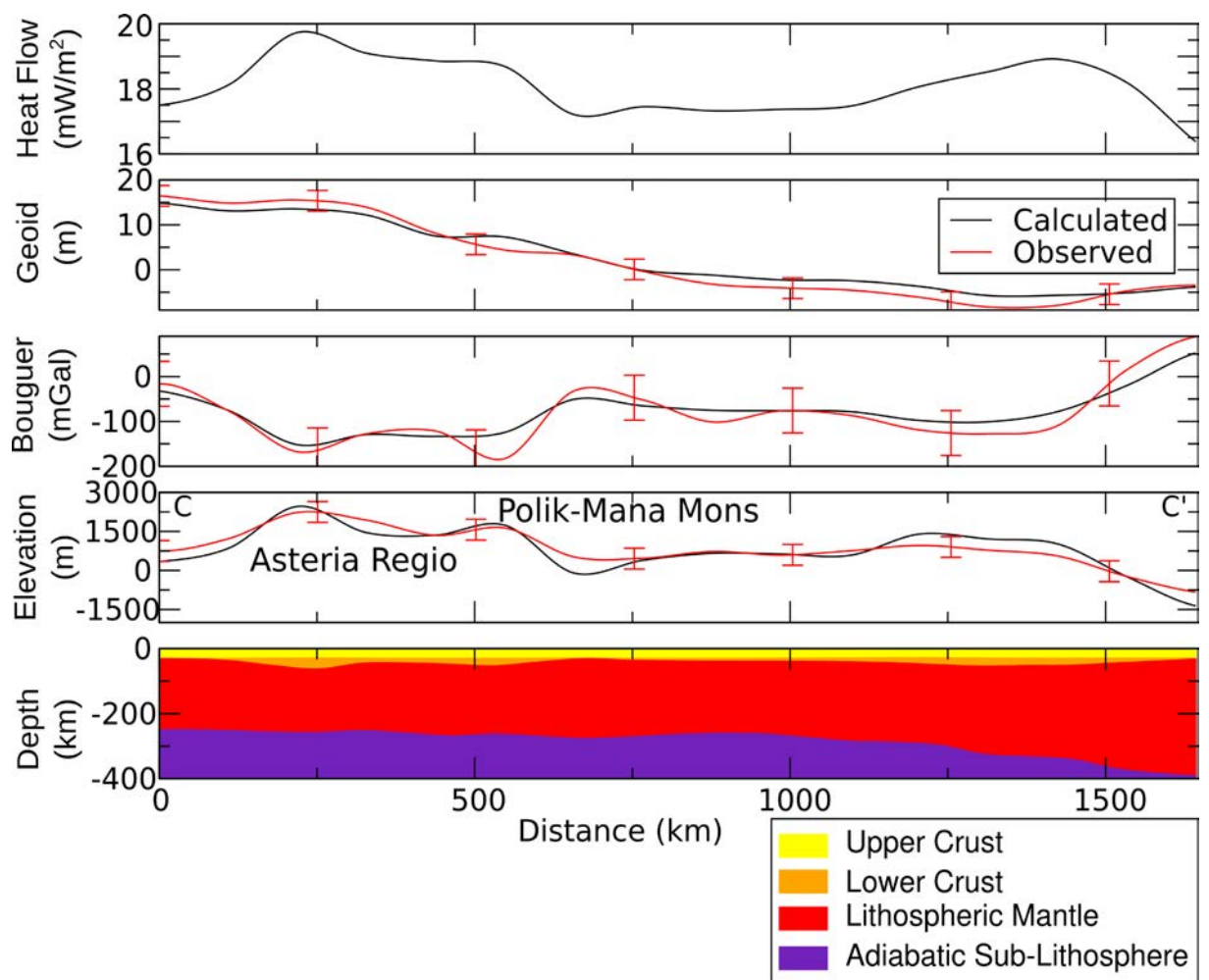


Figure 5.12. Lithospheric structure over Asteria Regio and Polik-Mana Mons. This profile is located at -95°E and extends from 22°N to 38°N . Key is similar to Figure 5.6.

slightly higher than the observed elevation, Bouguer gravity, and geoid height. However, most the calculated responses are within error, and should have no significant influence on the dynamic topography and flexural estimates covered in Sections 5.4.4.

5.4.3 Crustal and Lithospheric Thickness Maps

Beta Regio exhibits thick crustal roots below the summits of Theia and Rhea Mons (40-70 km; Figure 5.14A). Asteria Regio has crustal thicknesses of ~30-45 km, thickening to 65 km at the summit of Polik-Mana Mons. The central trough of Devana Chasma corresponds to a thin crust (~15-25 km) surrounded by a thicker (25-50 km) crust at the rift shoulders. The tessera terrain towards the north, surrounding Rhea Mons, also has a thick crust (up to ~75 km), however where the volcanic rise transitions into the surrounding plains regions, the crust is thinner (25-40 km).

Beta Regio has thinner lithospheric thicknesses than the surrounding plains regions and Asteria Regio (Figure 5.14B). A thin (~60-100 km) lithosphere occurs below Devana Chasma, Theia, and Rhea Mons. However, towards the northern extents of Rhea Mons, a gradual thickening of the lithosphere to 150 km occurs as the rise diffuses into the northern plains region. Asteria Regio, exhibits a thick lithosphere (~200-300 km), with Polik-Mana Mons requiring the thickest thermal lithosphere (280-290 km) of all the volcanoes in the studied region. Moving outwards from the volcanic rises the thermal lithosphere gradually thickens towards the plains regions (~300-400 km).

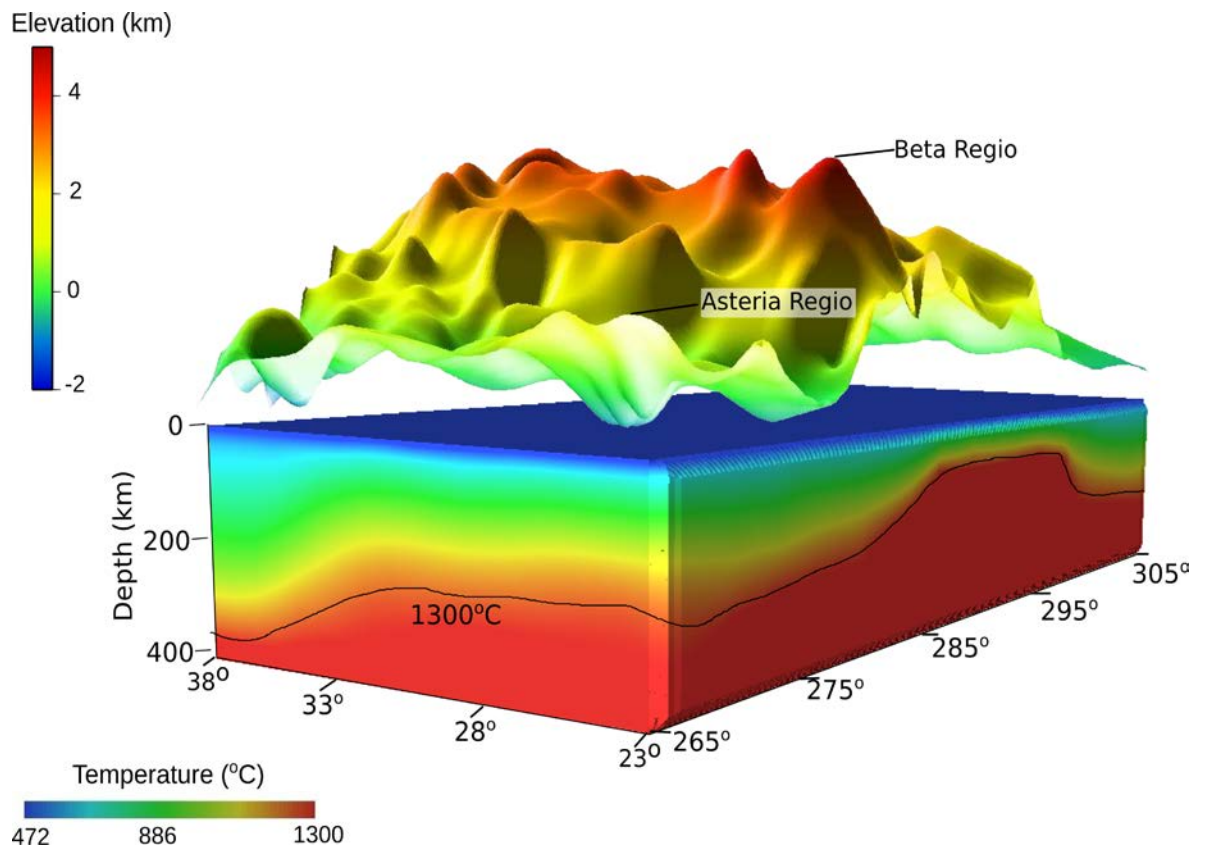


Figure 5.13. The thermal structure below Asteria Regio along -95°E . The thermal structure and topography between -105°E to -96°E was removed for clarity.

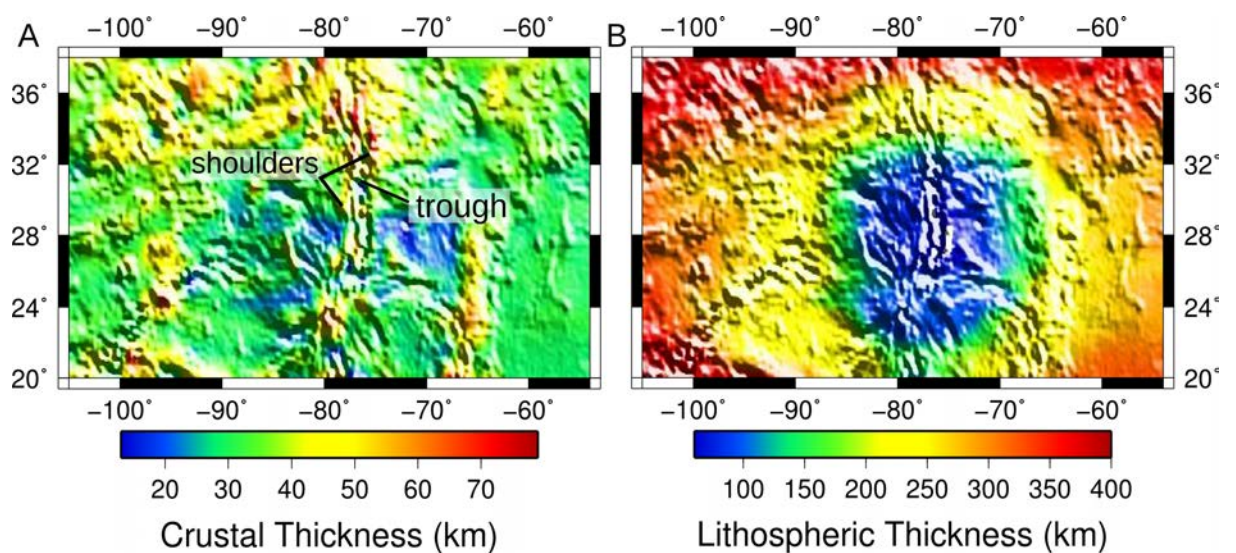


Figure 5.14. Modelled crustal (A) and lithospheric thicknesses (B) at Beta Regio. The location of the central trough and adjacent rift shoulders are shown on (A).

5.4.4 Flexural and Dynamic Compensation

Most of the topography at Beta Regio and Asteria Regio is compensated by local isostasy only (Figure 5.15B). Assuming flexure operates as the only additional compensation mechanism at Beta Regio, each elastic lithospheric thickness could contribute to different amounts of flexural support (Figure 5.16). A 50 km thick elastic lithosphere provides flexural support that shows a closer correlation to the residual elevation (Figure 5.16C). For a 50 km thick elastic lithosphere the largest amount (~ 2 km) of flexural support occurs to the north of Theia Mons, along the elevated and rifted rise, between 25°N and 29°N (Figure 5.16C). Flexural support is ~ 0.5 km at Theia Mons and < 0.5 km at Rhea Mons.

The amount of dynamic compensation at Beta Regio was determined by subtracting the local and regional isostatic compensation, based on a 50 km thick elastic lithosphere, from the observed elevation. Minor ($< \sim 0.3$ km) dynamic uplift is required at localised volcanic constructs and centered at $\sim 32^{\circ}\text{N}$ along Rhea Mons (Figure 5.15C). This contrasts to Theia Mons, Devana Chasma between 25°N to 29°N , and Polik-Mana Mons that require no additional dynamic support (Figure 5.15C).

5.5 Discussion

5.5.1 Lithospheric Structure

Our modelling indicates that most of Beta Regio exhibits crustal thicknesses similar to those (20-40 km) found from previous studies [James *et al.*, 2013; Leftwich *et al.*, 1999; Simons *et al.*, 1997].

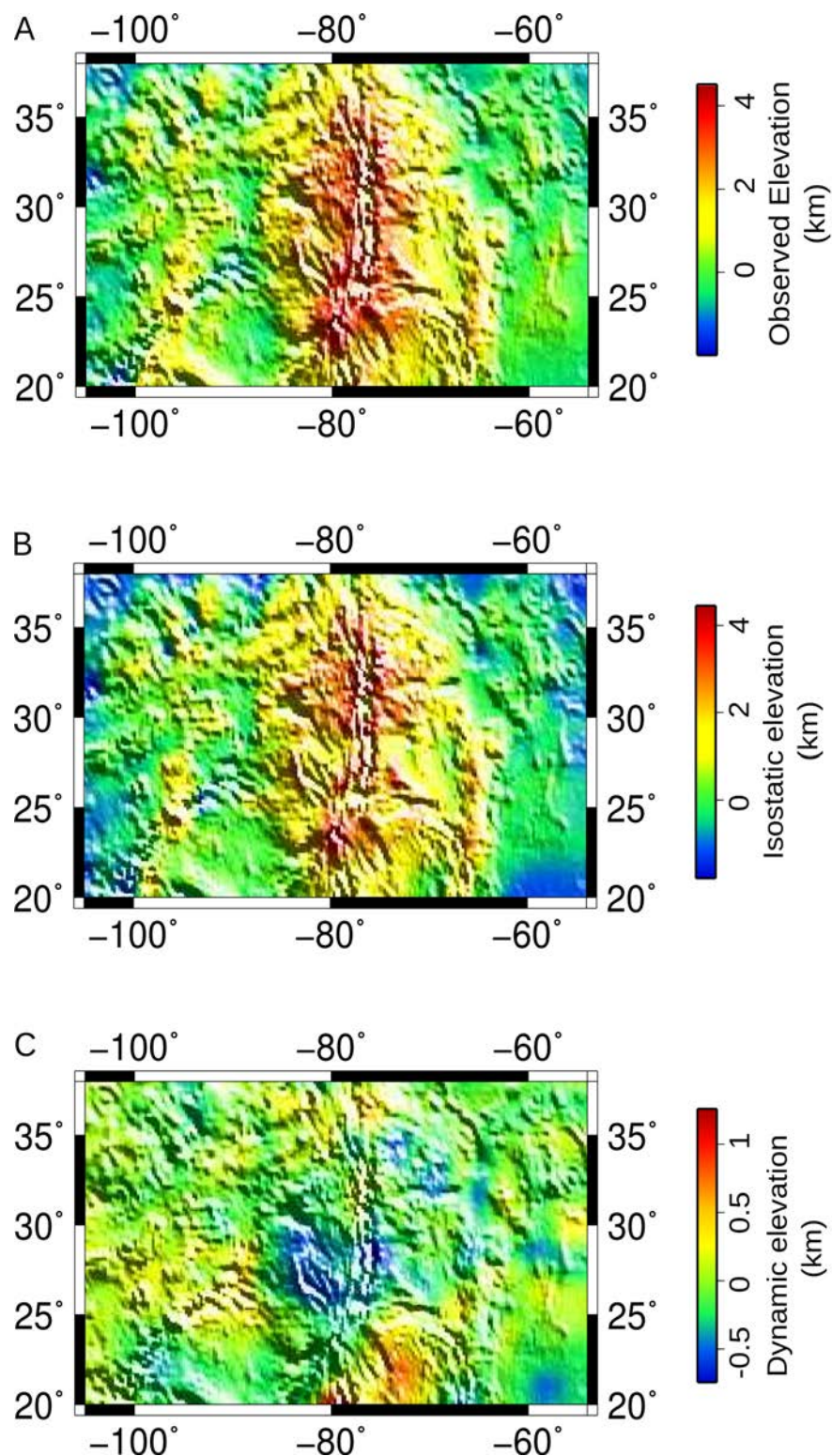


Figure 5.15. (A) The observed elevation at Beta Regio. (B) The amount of topography compensated by Airy and thermal isostasy found from our proposed lithospheric structure. (C) The amount of dynamic compensation at Beta Regio was found by subtracting the isostatic and flexural component (assuming an elastic lithosphere of 50 km) from the observed elevation.

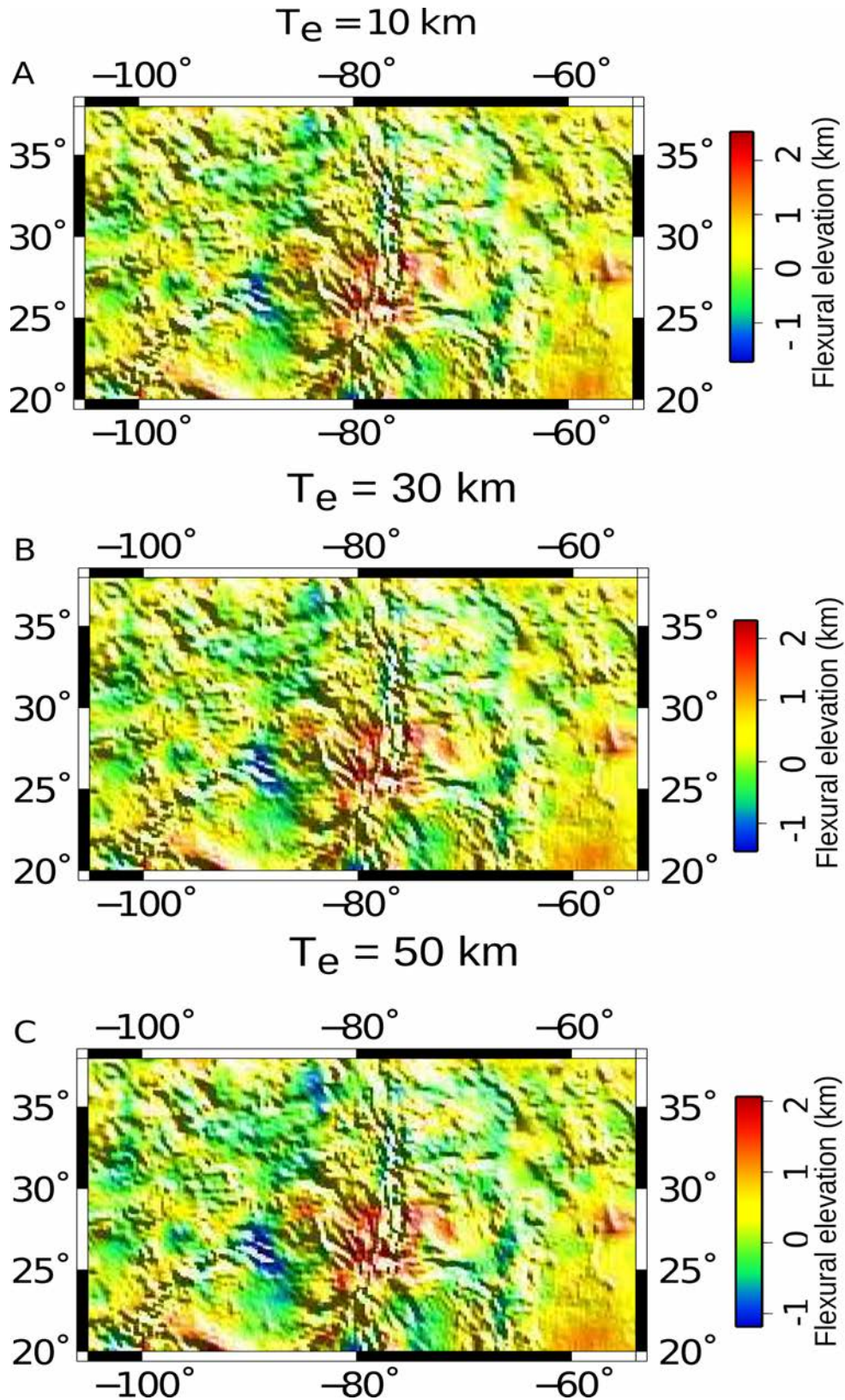


Figure 5.16. The amount of residual topography compensated by flexure at Beta Regio for an elastic lithosphere thickness of 10 km (A), 30 km (B), and 50 km (C).

A thicker (40-75 km) crust is associated with the tessera unit surrounding Rhea Mons and the volcanoes, respectively. This thicker crust is consistent with very early compressional deformation for the tessera, as well as localised volcanism at Theia and Rhea Mons, which occurred much later [Basilevsky and Head, 2007; Leftwich *et al.*, 1999].

Similar to McKenzie [1994], we obtain thin crustal values below the central trough of Devana Chasma, surrounded by a thicker crust below the adjacent rift shoulders. However, we found that the crust below the central trough of Devana Chasma was thicker (15-25 km) than that proposed by McKenzie [1994], whereas the rift shoulders have similar crustal thicknesses, between 30-40 km.

Crustal thicknesses along the EAR may be comparable to those at Devana Chasma, since these rifts share common characteristics [Foster and Nimmo, 1996; Nimmo and McKenzie, 1996; Stofan *et al.*, 1989]. From our lithospheric modelling, the crust below Devana Chasma's central trough and rift shoulders are consistent with those found by Achauer *et al.* [1992], Chorowicz [2005], and Morley [1989], along the western and eastern rift of the EAR, respectively.

The elevated rift shoulders surrounding Devana Chasma are not associated with volcanic edifice formation, since the highest uplifts occur away from the volcanoes, between 25°N to 29°N (Figure 5.1). Instead these elevated rift shoulders could suggest thermal uplift that may contribute to the compensation of the central rift trough [Chorowicz, 2005; Zuber and Parmentier, 1989].

Our results show Devana Chasma is a site of localised crustal thinning, but broader lithospheric thinning. Under these conditions, elevated rift shoulders may occur if horizontal

temperature variations produce localised, small-scale convection [Zuber and Parmentier, 1989]. The thin crustal thicknesses associated with Devana Chasma become harder to see when it crosses Theia Mons, since the central trough becomes shallower and the width decreases, which may be attributed to volcanic infilling [Stofan *et al.*, 1995].

The plains regions on the flanks of the volcanic rise experience crustal thicknesses of ~20-30 km and are consistent with previous global estimates of 20-30 km [Grimm and Hess, 1997; Nimmo and McKenzie, 1998; Solomon and Head, 1990].

The GTRs of Beta Regio may also suggest the underlying lithosphere has been thermally thinned [Kucinskas and Turcotte, 1994; Moore and Schubert, 1995]. Our results also show thermal thinning of the lithosphere to ~65-80 km along the elevated and rifted terrain from 24°N to 29°N and to ~100-150 km below Theia and Rhea Mons. The region of terrain between 24°N to 29°N, which experiences a thin thermal lithosphere, corresponds to the location of Beta Regio's geoid high (Figure 5.1) and recent stages of rifting [Stofan *et al.*, 1989]. The 100 km thick thermal lithosphere below Theia and Rhea Mons are similar to those from previous authors, however, the modelled lithospheric thicknesses along Devana Chasma are thinner [Kucinskas and Turcotte, 1994; Moore and Schubert, 1995].

Devana Chasma may also experience a similar lithospheric thickness to the EAR [Foster and Nimmo, 1996; Nimmo and McKenzie, 1996; Stofan *et al.*, 1989]. Considering previous estimates of the lithospheric thickness at the EAR from long period surface wave dispersion [Pasyanos, 2010] and bore hole heat flow measurements [Artemieva, 2006], the modelled lithospheric thickness at Devana Chasma (~60-100 km) shows a closer correlation with the eastern branch of the EAR (40-100 km).

Isostatic stagnant-lid models have provided much thicker (300-550 km) lithospheric thickness estimates, with our model corresponding to these values only within the plains regions surrounding Beta Regio [Orth and Solomatov, 2011]. If we were to test these lithospheric thicknesses below Beta Regio we would first need to use a thicker reference lithosphere (eg. 400 km) below the North Polar Plains. At Beta Regio, thickening the lithosphere to 300 km below the volcanic rise, would require us to reduce the lithospheric thickness within the surrounding plains regions to values $> \sim 500$ km. As a result of thickening the lithosphere, crustal thicknesses would have to increase in order to maintain isostatic equilibrium. These new values would be inconsistent with previous studies, especially a 500 km thick thermal lithosphere, which exceeds the depth of the exothermic phase transition proposed for Venus [Steinbach and Yuen, 1992].

The crustal and lithospheric thickness estimates that we have obtained from our modelling may not reflect the current lithospheric structure at Beta Regio if the surface and sub-surface compositions are not basaltic, gabbroic, or peridotitic. Even though surface samples and the morphology of volcanoes imply a predominately basaltic surface, some areas may have silicic to intermediate compositions [Grimm and Hess, 1997; Head *et al.*, 1992; Jull and Arkani-Hamed, 1995; McKenzie *et al.*, 1992]. The use of more silicic to intermediate surface and subsurface compositions could result in a different lithospheric structure and different quantities of isostatic and dynamic compensation.

5.5.2 Compensation Mechanisms

From our lithospheric modelling, most of the topography at Beta Regio was isostatically compensated, via crustal and lithospheric thickness variations. However, previous authors have suggested a minimum of 0.2 km and up to 5.7 km of dynamic uplift could occur at this

rise [Kiefer and Hager, 1991; Smrekar *et al.*, 1997; Stofan *et al.*, 1995; Vezolainen *et al.*, 2004]. At Beta Regio, these minimum estimates of the amount of dynamic compensation are similar to those (0 to < 0.3 km) found by our study. Our study also results in localised dynamic uplift even though mantle plumes contribute to the support of long-wavelength topography. From our study, both the magnitude and wavelength of the dynamic compensation may be greater if the amount of isostatic or flexural compensation was over estimated.

It should also be noted that the flexural response for a 50 km thick elastic lithosphere appears to generate a "pseudo" dynamic uplift at a localised region of Devana Chasma centered at $-80^{\circ}\text{E } 20^{\circ}\text{N}$. This "pseudo" dynamic uplift is not a real dynamic response, instead it is a result of the low flexural response (~ 1 km) that acts to reduce the calculated isostatic component. When this total isostatic (Airy, thermal, and flexural) component is removed from the observed response, it results in a dynamic response that is greater than what was required from the residual elevation. The converse is also true for an overestimation of the flexural response. A negative dynamic uplift occurs towards the west of Devana Chasma and is most likely the result of an overestimation (~ 2 km) of the flexural response that, in turn, results in a higher total isostatic component than the observed elevation. When this overestimated total isostatic component is removed from the observed elevation it leads to a negative dynamic component.

Our results imply some dynamic uplift is required within localised regions of Beta Regio and no dynamic compensation or a mantle upwelling occurs below Asteria Regio. This is consistent with the observed plateau morphology, low elevation, geoid lows, and absence of widespread extension [Smrekar *et al.*, 1997].

Out of the three modelled thicknesses, a 50 km thick elastic lithosphere provided flexural support, consistent with the residual topography. However, this elastic lithosphere is slightly

thicker than the upper limit of previous estimates (~ 40 km) [Senske, 1993; Simons *et al.*, 1997]. These differences could arise from the constant elastic lithosphere used by GEO3Dmod when performing the flexural calculations, since the real thickness would vary between the volcanic rise and plains regions.

5.5.3 Comparison with Atla Regio

Atla and Beta Regio are both rift-dominated volcanic rises on Venus, sharing similar tectonic and volcanic features. The large rifts—Devana Chasma in Beta Regio and Ganis Chasma in Atla Regio—contain similar sized fractures, graben, and rift troughs [Michaels *et al.*, 1992; Senske *et al.*, 1992]. Each of these rises have expansive domal topography, large apparent depths of compensation, high geoid, and topography anomalies [Senske and Head, 1992; Smrekar *et al.*, 1997]. However, one difference between these rises is the large swell volumes and GTRs of Beta Regio, compared to Atla Regio [Stofan *et al.*, 1995]. GTRs are related to the depth and compensation mechanism at long wavelengths, with higher GTRs suggesting deeper compensation mechanisms such as thermal and dynamic uplift, volcanism, and a thick crust [Sandwell and Renkin, 1988; Stofan *et al.*, 1995]. The higher swell volume and presence of tessera terrain at Beta Regio [Stofan *et al.*, 1995] is consistent with our thicker modelled crust (~ 70 km) within this area.

Both Atla and Beta Regio require localised areas (diameters ranging from 250-500 km) of dynamic uplift (For more details, refer to Chapter 4). However, the magnitude of this dynamic uplift varies significantly with Beta Regio requiring $< \sim 0.3$ km and Atla Regio $< \sim 1.5$ km. Both models also infer that most of the observed topography is supported by a combination of lithospheric thinning (thermal isostasy) and crustal thickness variations (Airy isostasy). Each area exhibits a thin thermal lithosphere below the main rift and volcanoes (50-100 km),

compared to the surrounding plains regions (250-375 km). Beta Regio does not require significant and broad scale dynamic uplift from our lithospheric modelling and, as a result, the higher GTR at this rise is most likely associated with thermal thinning.

Flexure (regional isostasy) has a greater contribution than dynamic uplift in supporting the residual topography at these volcanic rises and is useful in constraining the elastic lithospheric thickness. Flexural support is greater at the rift shoulders in Beta Regio and at Maat Mons in Atla Regio, with a 50 km thick elastic lithosphere providing support consistent with the residual topography.

Some authors have proposed Beta Regio is currently experiencing upwelling [Vezolainen *et al.*, 2004]. However, others have used the degree of modification and dip direction of craters at both volcanic rises to infer current and/or more recent geological activity has occurred at Atla compared to Beta Regio [Basilevsky and Head, 2002; Matias and Jurdy, 2005]. These crater observations are consistent with our modelling results where Atla Regio requires greater topographic support from dynamic uplift, compared to Beta Regio, further implying mantle upwelling and the associated partial melting has been more recent at Atla Regio than Beta Regio.

From topographic cross-correlation methods, Devana Chasma and Ganis Chasma show similarities to Earth's ultra-slow spreading Gakkel Ridge [Stoddard and Jurdy, 2011]. However, considering the lithospheric models between each area and the minor dynamic uplift required at Beta Regio, it is unlikely that Devana Chasma is currently rifting within localised areas or undergoing rift-related volcanism. This is consistent with the slightly thicker modelled thermal lithosphere (~60 km) and much thicker crust (~15 km) below the central rift trough of Devana Chasma, compared to Ganis Chasma and the Gakkel Ridge (~40-50 km and

< 4 km, respectively) [Coakley and Cochran, 1998].

5.6 Conclusions

The topographic variations at Beta Regio are a combination of crustal thickness variations (Airy isostasy) and lithospheric thinning (thermal isostasy), with flexure and very minor dynamic uplift (< ~0.3 km). We have modelled the lithospheric structure and found that an integrated solution of Bouguer gravity, geoid height, and elevation, can be obtained for models with thick crustal roots (~30-75 km) and a thin thermal lithosphere (~60-100 km) below the rise. Devana Chasma and the terrestrial EAR show geological similarities, with modelled crustal and lithospheric thicknesses showing a closer correlation to the eastern branch of the EAR. Asteria Regio has a thick thermal lithosphere and requires no dynamic support, consistent with the observed morphology, low elevation, and low geoid anomalies observed at this rise.

Even though Beta Regio shares similar tectonic and volcanic characteristics to Atla Regio, the large swell volume and GTRs are uncharacteristic of Venusian rises. Large, broad scale dynamic uplift was not required by our model, which may imply Beta Regio's high swell volumes are most likely the result of the thick crust below the tessera terrain. A lack of dynamic compensation also implies the higher GTRs at Beta Regio are caused from long-wavelength thermal thinning of the lithosphere. A lack of dynamic compensation and the thick crust at the central rift trough of Devana Chasma, in conjunction with an absence of modified and dipping craters [Basilevsky and Head, 2002; Matias and Jurdy, 2005], may imply rifting and volcanism is currently absent at Beta Regio.

5.7 References

- Achauer, U., P. K. H. Maguire, J. Mechie, W. V. Green, and KRISP working group (1992), Some remarks on the structure and geodynamics of the Kenya Rift, *Tectonophysics*, 213, 257–268, doi:10.1016/0040-1951(92)90262-5.
- Afonso, J. C., G. Ranalli, and M. Fernández (2005), Thermal expansivity and elastic properties of the lithospheric mantle: results from mineral physics of composites, *Physics of the Earth and Planetary Interiors*, 149, 279–306, doi:10.1016/j.pepi.2004.10.003.
- Artemieva, I. M. (2006), Global $1^\circ \times 1^\circ$ thermal model TC1 for the continental lithosphere: Implications for lithosphere secular evolution, *Tectonophysics*, 416(1–4), 245–277, doi:10.1016/j.tecto.2005.11.022.
- Barnett, D. N., F. Nimmo, and D. McKenzie (2002), Flexure of Venusian lithosphere measured from residual topography and gravity, *Journal of Geophysical Research*, 107, 21, doi:200210.1029/2000JE001398.
- Basilevsky, A. T., and J. W. Head (2002), Venus: Analysis of the degree of impact crater deposit degradation and assessment of its use for dating geological units and features, *Journal of Geophysical Research*, 107, 38, doi:200210.1029/2001JE001584.
- Basilevsky, A. T., and J. W. Head (2007), Beta Regio, Venus: Evidence for uplift, rifting, and volcanism due to a mantle plume, *Icarus*, 192(1), 167–186, doi:10.1016/j.icarus.2007.07.007.
- Bevington, P. R., and D. K. Robinson (1992), *Data reduction and error analysis for the physical sciences*, McGraw-Hill Inc, New York.

- Coakley, B. J., and J. R. Cochran (1998), Gravity Evidence of Very Thin Crust at the Gakkel Ridge (Arctic Ocean), *Earth and Planetary Science Letters*, 162(1–4), 81–95, doi:10.1016/S0012-821X(98)00158-7.
- Chorowicz, J. (2005), The East African rift system, *Journal of African Earth Sciences*, 43(1–3), 379–410, doi:10.1016/j.jafrearsci.2005.07.019.
- Ernst, R., D. Desnoyers, J. Head, and E. Grosfils (2003), Graben–fissure systems in Guinevere Planitia and Beta Regio (264°–312°E, 24°–60°N), Venus, and implications for regional stratigraphy and mantle plumes, *Icarus*, 164(2), 282–316, doi:10.1016/S0019-1035(03)00126-X.
- Foster, A., and F. Nimmo (1996), Comparisons between the rift systems of East Africa, Earth and Beta Regio, Venus, *Earth and Planetary Science Letters*, 143(1-4), 183–195, doi:10.1016/0012-821X(96)00146-X.
- Fullea, J., M. Fernàndez, J. C. Afonso, J. Vergés, and H. Zeyen (2010), The structure and evolution of the lithosphere-asthenosphere boundary beneath the Atlantic-Mediterranean Transition Region, *Lithos*, 120, 74-95. doi: 10.1016/j.lithos.2010.03.003.
- Fullea, J., M. Fernàndez, H. Zeyen, and J. Vergés (2007), A rapid method to map the crustal and lithospheric thickness using elevation, geoid anomaly and thermal analysis. Application to the Gibraltar Arc System, Atlas Mountains and adjacent zones, *Tectonophysics*, 430(1-4), 97–117, doi:10.1016/j.tecto.2006.11.003.
- Grimm, R. E., and P. C. Hess (1997), The crust of Venus, in *Venus II: Geology, Geophysics, Atmosphere and Solar Wind Environment*, 1205–1244, The University of Arizona Press, Arizona.

- Head, J. W., L. S. Crumpler, J. C. Aubele, J. E. Guest, and R. S. Saunders (1992), Venus volcanism: classification of volcanic features and structures, associations, and global distribution from Magellan data, *Journal of Geophysical Research*, 97(E8), 13,153–13,197, doi:10.1029/92JE01273.
- James, P. B., M. T. Zuber, and R. J. Phillips (2013), Crustal thickness and support of topography on Venus, *Journal of Geophysical Research Planets*, 17, doi:10.1029/2012JE004237.
- Jiménez-Munt, I., M. Fernàndez, J. Vergés, J. C. Afonso, D. Garcia-Castellanos, and J. Fulla (2010), Lithospheric structure of the Gorringer Bank: Insights into its origin and tectonic evolution, *Tectonics*, 29, 16 pp., doi:10.1029/2009TC002458.
- Jull, M. G., and J. Arkani-Hamed (1995), The implications of basalt in the formation and evolution of mountains on Venus, *Physics of the Earth and Planetary Interiors*, 89(3–4), 163–175, doi:10.1016/0031-9201(95)03015-O.
- Kiefer, W. S., and B. H. Hager (1991), A Mantle Plume Model for the Equatorial Highlands of Venus, *Journal of Geophysical Research*, 96(E4), 20,947–20,966, doi:10.1029/91JE02221.
- Kiefer, W. S., and L. C. Swafford (2006), Topographic analysis of Devana Chasma, Venus: implications for rift system segmentation and propagation, *Journal of Structural Geology*, 28(12), 2144–2155, doi:10.1016/j.jsg.2005.12.002.
- Konopliv, A. S., W. B. Banerdt, and W. L. Sjogren (1999), Venus Gravity: 180th Degree and Order Model, *Icarus*, 139(1), 3–18, doi:10.1006/icar.1999.6086.
- Kucinskas, A. B., and D. L. Turcotte (1994), Isostatic Compensation of Equatorial Highlands on Venus, *Icarus*, 112(1), 104–116, doi:10.1006/icar.1994.1172.

- Leftwich, T. E., R. R. B. von Frese, H. R. Kim, H. C. Noltimier, L. V. Potts, D. R. Roman, and L. Tan (1999), Crustal analysis of Venus from Magellan satellite observations at Atalanta Planitia, Beta Regio, and Thetis Regio, *Journal of Geophysical Research*, 104(E4), 8441–8462.
- Matias, A., and D. M. Jurdy (2005), Impact craters as Indicators of Tectonic and Volcanic Activity in the Beta-Atla-Themis Region, Venus, *Geological Society of America Special Papers*, 388, 825–839, doi:10.1130/0-8137-2388-4.825.
- McKenzie, D. (1994), The Relationship between Topography and Gravity on Earth and Venus, *Icarus*, 112(1), 55–88, doi:10.1006/icar.1994.1170.
- McKenzie, D., P. G. Ford, C. Johnson, B. Parsons, D. Sandwell, S. Saunders, and S. C. Solomon (1992), Features on Venus generated by plate boundary processes, *Journal of Geophysical Research: Planets*, 97(E8), 13533–13544, doi:10.1029/92JE01350.
- Michaels, G. A., R. S. Saunders, and E. R. Stofan (1992), Morphology of Regional Fracture Systems on Venus, *Abstracts of the Lunar and Planetary Science Conference*, 23, 903–904.
- Moore, W. B., and G. Schubert (1995), Lithospheric thickness and mantle/lithosphere density contrast beneath Beta Regio, Venus, *Geophysical Research Letters*, 22(4), 429–432, doi:10.1029/94GL02055.
- Moore, W. B., and G. Schubert (1997), Venusian Crustal and Lithospheric Properties from Nonlinear Regressions of Highland Geoid and Topography, *Icarus*, 128(2), 415–428, doi:10.1006/icar.1997.5750.
- Moresi, L., and B. Parsons (1995), Interpreting gravity, geoid, and topography for convection with temperature dependent viscosity: Application to surface features on Venus,

Journal of Geophysical Research, 100(E10), 21,155–21,171,
doi:199510.1029/95JE01622.

Morley, C. K. (1989), Extension, detachments, and sedimentation in continental rifts (with particular reference to East Africa), *Tectonics*, 8(6), 1175–1192,
doi:10.1029/TC008i006p01175.

Nimmo, F., and D. McKenzie (1996), Modelling plume-related uplift, gravity and melting on Venus, *Earth and Planetary Science Letters*, 145(1-4), 109–123, doi:10.1016/S0012-821X(96)00200-2.

Nimmo, F., and D. McKenzie (1998), Volcanism and Tectonics on Venus, *Annual Review of Earth and Planetary Science*, 26(1), 23–51, doi:10.1146/annurev.earth.26.1.23.

Orth, C. P., and V. S. Solomatov (2011), The isostatic stagnant lid approximation and global variations in the Venusian lithospheric thickness, *Geochemistry Geophysics Geosystems*, 12(7), 1525–2027.

Pasyanos, M. E. (2010), Lithospheric thickness modeled from long-period surface wave dispersion, *Tectonophysics*, 481(1–4), 38–50, doi:10.1016/j.tecto.2009.02.023.

Ranalli, G. (1995) *Rheology of the Earth*, Chapman and Hall, London.

Rappaport, N. J., A. S. Konopliv, A. B. Kucinskas, and P. G. Ford (1999), An Improved 360 Degree and Order Model of Venus Topography, *Icarus*, 139(1), 19–31,
doi:10.1006/icar.1999.6081.

Rathbun, J. A., D. M. Janes, and S. W. Squyres (1999), Formation of Beta Regio, Venus: Results from measuring strain, *Journal of Geophysical Research*, 104(E1), 1917–1927, doi:199910.1029/1998JE900026.

- Reynolds, J. M. (1997), *An introduction to applied and environmental geophysics*, John Wiley and Sons, West Sussex, England.
- Rogers, N. (2008), *An introduction to our dynamic planet*, Cambridge University Press, United Kingdom.
- Sandwell, D. T., and M. L. Renkin (1988), Compensation of swells and plateaus in the north Pacific: No direct evidence for mantle convection, *Journal of Geophysical Research: Solid Earth*, 93(B4), 2775–2783, doi:10.1029/JB093iB04p02775.
- Schubert, G., V. S. Solomatov, P. J. Tackley, and D. L. Turcotte (1997), *Mantle convection and the thermal evolution of Venus*, 1245-1288, The University of Arizona Press, Arizona.
- Schubert, G., and D. L. Turcotte (2002), *Geodynamics*, 456 pp., Cambridge University Press, New York.
- Senske, D. A. (1993), Rifting at Devana Chasma, Venus: Structure and estimation of the effective thickness of the elastic lithosphere, *In Lunar and Planetary Inst., Twenty-Fourth Lunar and Planetary Science Conference. Part 3: N-Z*, 1277-1278.
- Senske, D. A., and J. W. Head (1992), Atla Regio, Venus: Geology and Origin of a Major Equatorial Volcanic Rise, *Papers presented to the International Colloquium Venus*, 107–109.
- Senske, D. A., J. W. Head, E. R. Stofan, and D. B. Campbell (1991), Geology and structure of Beta Regio, Venus: Results from Arecibo Radar Imaging, *Geophysical Research Letters*, 18(6), 1159–1162.
- Senske, D. A., G. G. Schaber, and E. R. Stofan (1992), Regional Topographic Rises on Venus: Geology of Western Eistla Regio and Comparison to Beta Regio and Atla Regio, *Journal of Geophysical Research*, 97(E8), 13395-13420.

- Simons, M., S. C. Solomon, and B. H. Hager (1997), Localization of gravity and topography: constraints on the tectonics and mantle dynamics of Venus, *Geophysical Journal International*, 131(1), 24–44, doi:10.1111/j.1365-246X.1997.tb00593.x.
- Sjogren, W. L., W. B. Banerdt, P. W. Chodas, A. S. Konopliv, G. Balmino, J. P. Barriot, J. Arkani-Hamed, T. R. Colvin, and M. E. Davies (1997), The Venus gravity field and other geodetic parameters, in *Venus II: Geology, Geophysics, Atmosphere and Solar Wind Environment*, 1125–1161, The University of Arizona Press, Arizona.
- Smrekar, S. E. (1994), Evidence for Active Hotspots on Venus from Analysis of Magellan Gravity Data, *Icarus*, 112(1), 2–26, doi:10.1006/icar.1994.1166.
- Smrekar, S. E., W. S. Kiefer, and E. R. Stofan (1997), Large Volcanic Rises on Venus, in *Venus II: Geology, Geophysics, Atmosphere and Solar Wind Environment*, 845–878, The University of Arizona Press, Arizona.
- Smrekar, S. E., and E. M. Parmentier (1996), The Interaction of Mantle Plumes with Surface Thermal and Chemical Boundary Layers: Applications to Hotspots on Venus, *Journal of Geophysical Research*, 101(B3), 5397–5410, doi:10.1029/95JB02877.
- Smrekar, S. E., and R. J. Phillips (1991), Venusian Highlands: Geoid to Topography Ratios and their Implications, *Earth and Planetary Science Letters*, 107(3-4), 582–597, doi:10.1016/0012-821X(91)90103-O.
- Solomatov, V. S., and L.-N. Moresi (1996), Stagnant Lid Convection on Venus, *Journal of Geophysical Research*, 101(E2), 4737–4753, doi:199610.1029/95JE03361.
- Solomon, S. C., and J. W. Head (1990), Lithospheric Flexure Beneath the Freyja Montes Foredeep, Venus: Constraints on Lithospheric Thermal Gradient and Heat Flow, *Geophysical Research Letters*, 17(9), 1393–1396,

doi:199010.1029/GL017i009p01393.

Steinbach, V., and D. A. Yuen (1992), The effects of multiple phase transitions on Venusian mantle convection, *Geophysical Research Letters*, 19(22), 2243-2246.

Stoddard, P. R., and D. M. Jurdy (2011), Topographic comparisons of uplift features on Venus and Earth: implications for Venus tectonics, *Icarus*, 524-533,

doi:10.1016/j.icarus.2011.09.003.

Stofan, E. R., J. W. Head, D. B. Campbell, S. H. Zisk, A. F. Bogomolov, O. N. Rzhiga, A. T. Basilevsky, and N. Armand (1989), Geology of a rift zone on Venus: Beta Regio and Devana Chasma, *Geological Society of America Bulletin*, 101(1), 143 –156, doi:10.1130/0016-7606(1989)101<0143:GOARZO>2.3.CO;2.

Stofan, E. R., S. E. Smrekar, D. L. Bindschadler, and D. A. Senske (1995), Large Topographic Rises on Venus: Implications for Mantle Upwelling, *Journal of Geophysical Research*, 100(E11), 23317–23327, doi:10.1029/95JE01834.

Taylor, J. R. (1982), *An introduction to error analysis*, University Science Books, Mill Valley, California.

Turcotte, D. L. (1993), An Episodic Hypothesis for Venusian Tectonics, *Journal of Geophysical Research*, 98(E9), 17,061–17,068, doi:199310.1029/93JE01775.

Turcotte, D. L., and Schubert (2001), *Geodynamics*, 2nd ed., Cambridge University Press, New York.

Vezolainen, A. V., V. S. Solomatov, A. T. Basilevsky, and J. W. Head (2004), Uplift of Beta Regio: Three-dimensional models, *Journal of Geophysical Research*, 109(E08007), doi:200410.1029/2004JE002259.

- Wessel, P., and W. H. F. Smith (1991), Free Software Helps Map and Display Data, *EOS Transactions, American Geophysical Union*.
- Wessel, P., and W. H. F. Smith (1998), New, improved version of Generic Mapping Tools released, *EOS Transactions, American Geophysical Union*, 79(49), 579.
- Wieczorek, M. A. (2007), Gravity and Topography of the Terrestrial Planets, *Treatise on Geophysics*, 165–206.
- Young, H. D. (1962), *Statistical treatment of data*, 96 pp., McGraw-Hill Inc, New York.
- Zuber, M. T., and E. M. Parmentier (1989), Lithospheric necking: a dynamic model for rift morphology, *Earth and Planetary Science Letters*, 373–383, doi:10.1016/0012-821X(86)90147-0.

6. Lithospheric Structure and Compensation Mechanisms at Fortuna Tessera, Venus

Elyse Schinella, Juan Carlos Afonso, Craig O'Neill

Abstract. Tessera terrain is characterised by a complex network of ridges and troughs, commonly associated with crustal plateaus, which reside at higher elevations than the surrounding terrain. One example is Fortuna Tessera that forms the eastern portion of the extensive (~5600 km) highland region Ishtar Terra. Fortuna Tessera is divided into two areas; Eastern Fortuna Tessera and Western Fortuna Tessera, with each exhibiting different types of tessera terrain. Previous thermal lithospheric thickness (or the depth to the 1300°C isotherm) estimates are lacking within this area. Thermal lithospheric thickness estimates are particularly important, since long-wavelength thermal thinning may contribute to the support of Maxwell Montes, a 11 km high Mountain belt that lies adjacent to Western Fortuna Tessera. We aim to constrain the lithospheric structure, particularly the lithospheric thickness, and compensation mechanisms acting to support the observed topography. We use the interactive forward modelling software, GEO3Dmod, to model the lithospheric structure below Fortuna Tessera using a reference crustal and lithospheric thickness of 30 km and 300 km, respectively. Our model shows a decrease in crustal thickness and an increase in thermal lithospheric thickness moving from Western to Eastern Fortuna Tessera. Western Fortuna Tessera corresponds to crustal and lithospheric thicknesses of ~80 km and ~150 km and Eastern Fortuna Tessera has thicknesses of ~65 km and ~340 km, respectively. Most of the topography within Fortuna Tessera is supported by Airy isostasy, with some thermal and regional isostasy required at Western Fortuna Tessera and the chasmata, respectively. The thick crust (~80 km) that are underlain by a comparatively thin thermal lithosphere (~150 km)

at Western Fortuna Tessera may imply long-wavelength support of Maxwell Montes.

6.1 Introduction

Tessera terrain are elevated areas, appearing bright in radar images, due to their rugged appearance and complex intersecting ridges and troughs [Basilevsky, 1986; Vorder Bruegge and Head, 1989; Gilmore *et al.*, 1997; Hansen *et al.*, 1999]. Tessera are the oldest terrain on Venus and may have survived the last global over-turning event [Basilevsky and Head, 2002; Hansen, 2013; Romeo and Turcotte, 2008]. Highland regions are commonly sites of extensive tessera terrain, such as Ishtar Terra, a northern latitude highland region that is bounded by Fortuna Tessera between $\sim 15^{\circ}\text{E}$ to 82°E and 65°N to 70°N (Figure 6.1) [Hansen and Phillips, 1995]. The close proximity of both of these regions implies compensation mechanisms and deformational processes operating within Fortuna Tessera must be applicable to those operating within Ishtar Terra [Keep and Hansen, 1994].

Fortuna Tessera is divided by an elongated depression into Eastern Fortuna Tessera ($\sim 10^{\circ}\text{E}$ to $\sim 30^{\circ}\text{E}$) and Western Fortuna Tessera ($\sim 30^{\circ}\text{E}$ to $< 60^{\circ}\text{E}$; Figure 6.1) [Hansen, 2013; Kucinskas *et al.*, 1996; Riley *et al.*, 1995]. Towards the distal margins of Western Fortuna Tessera lies the 11 km high mountain belt, Maxwell Montes [Vorder Bruegge and Head, 1989; Ivanov and Head, 2009]. Structures within Western Fortuna Tessera closely resemble features in Maxwell Montes, such as parallel ridges and troughs, rather than features from Eastern Fortuna Tessera [Vorder Bruegge and Head, 1989; Keep and Hansen, 1994; Pritchard *et al.*, 1997]. The variations in the types of tessera terrain observed between Western and Eastern Fortuna Tessera may suggest these two terrains have experienced a different evolution [Ivanov and Head, 2009].

The small Apparent Depths of Compensation (ADCs), small Geoid-to-Topography Ratios

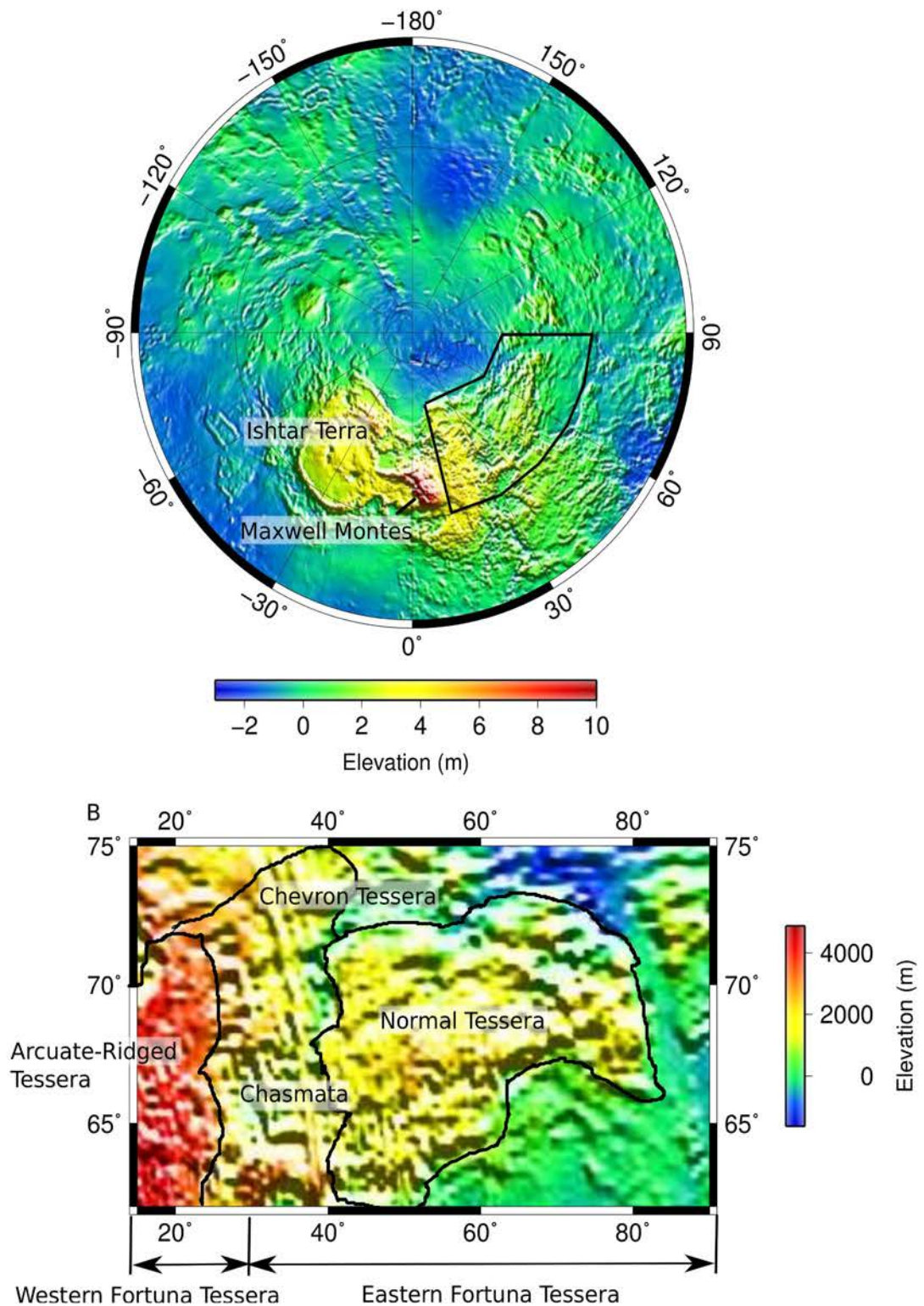


Figure 6.1. (A) Location map of Fortuna Tessera. Fortuna Tessera resides to the east of Maxwell Montes and comprises Eastern Ishtar Terra. (B) Map of our modelled area showing the major features discussed in this study. We have addressed the same terrains (encompassed by the thick black lines), and apply the same nomenclature, as *Vorder Bruegge and Head* [1989, 1990].

(GTRs), gravity lows, and absence of domal morphologies suggest Fortuna Tessera does not require dynamic compensation [Bindschadler *et al.*, 1992; Grimm, 1994; Hansen *et al.*, 1999; Simons *et al.*, 1997; Smrekar and Phillips, 1991]. This has led some authors to propose the topography within Fortuna Tessera is compensated predominately by Airy isostasy, with some also inferring flexural support from a 20 km thick elastic lithosphere and thermal thinning of an initially thick (~300 to ~400 km) lithosphere [Vorder Bruegge and Head, 1989; Kucinskas *et al.*, 1996; Simons *et al.*, 1997]. Estimates of crustal thickness variations are available for Fortuna Tessera, with the area exhibiting a westwards increase in elevation and deformational intensity, corresponding to increasing crustal thicknesses from values of ~35 to 40 km in the east to ~60 km in the west [Vorder Bruegge and Head, 1989; Ivanov, 1988; Zuber and Parmentier, 1990]. A previous study found thermal isostasy contributes to the topography at Western Fortuna Tessera, however estimates of the amount of thermal thinning that has occurred was not provided [Kucinskas *et al.*, 1996]. In addition, if we are to assume lithospheric thickness does not vary within Western Fortuna Tessera, then unreasonably thick crust (<150 km) would occur below this region.

This study aims to provide estimates of the lithospheric thickness below Fortuna Tessera, in conjunction with crustal thickness, to constrain the compensation mechanisms operating within this area. To do this we use GEO3Dmod, a simplified version of LitMod3D, which solves heat transfer, isostasy, geoid, and Bouguer gravity equations, and provides temperature, surface heat flow, gravity anomalies, absolute elevation, and geoid anomalies for a proposed lithospheric structure [Fullea *et al.*, 2009]. GEO3Dmod differs from LitMod3D in that it does not solve for the thermodynamics or rheology of the interior. These two mechanisms are highly unknown on Venus, thus the simplified approach of GEO3Dmod was more appropriate and beneficial in constraining the unknown thermal lithospheric structure below Fortuna Tessera. An understanding of the thermal structure and compensation mechanisms operating

within Fortuna Tessera has important implications for studies addressing the long-wavelength compensation of Maxwell Montes and can provide insight into the evolution of the much larger Ishtar Terra province.

6.2 Background

6.2.1 Description

Fortuna Tessera exhibits different types of tessera terrain—Sub-Parallel Ridged, Arcuate-Ridged, Chevron, Normal, and Ribbons—that formed from either compression or extension [Bindschadler and Head, 1991; Vorder Bruegge and Head, 1989; Hansen and Willis, 1998; Pritchard *et al.*, 1997]. Bindschadler and Head [1991] found the portion of Fortuna Tessera closest to Maxwell Montes was dominated by Sub-Parallel Ridged terrain. Sub-Parallel Ridged terrain comprises north-east to south-west orientated sub-parallel ridges and troughs, with some dissected by $\sim 60^\circ$ NE and $\sim 60^\circ$ NW lineations. Spacing between adjacent ridges range from 10-15 km and can extend over distances of 50-150 km. The elongated, symmetric, and cyclic nature of the ridges and the similarities to structures observed in Maxwell Montes, lead Bindschadler and Head [1991] to propose this terrain had a compressional origin. Strike-slip or shear deformation may have operated concurrently or after, producing the lineations and dissecting the pre-existing ridges [Bindschadler and Head, 1991].

Vorder Bruegge and Head [1989] also studied tessera terrain surrounding Maxwell Montes (Figure 6.1). Arcuate-Ridged Tessera resides on a wide plateau at an elevation of ~ 5 km (Figure 6.2) [Vorder Bruegge and Head, 1989]. Moving eastwards this terrain transitions into Chevron Tessera, which has elevations between 3-4 km and appears “buckled” from significant alteration by cross-cutting ridges [Vorder Bruegge and Head, 1989]. Scarps within

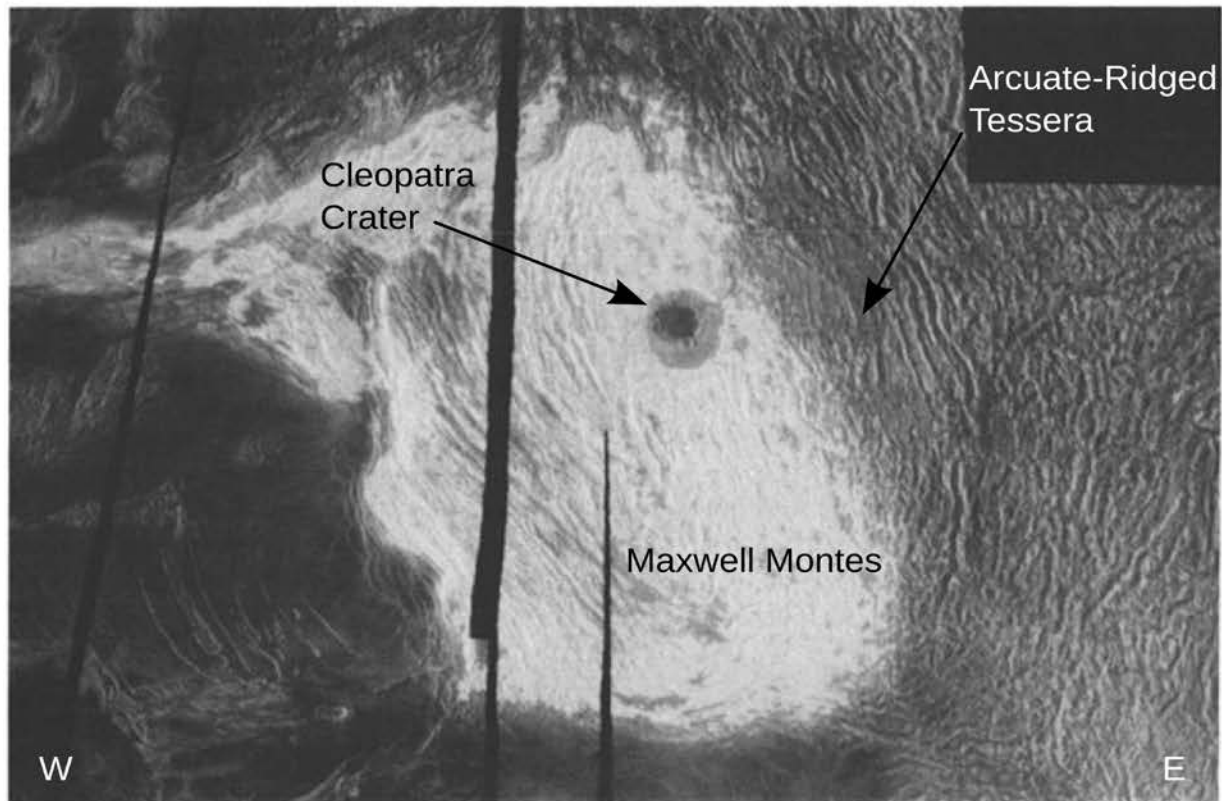


Figure 6.2. (Modified from *Keep and Hansen* [1994]) Radar image of Maxwell Montes and the adjacent Arcuate-Ridged Tessera, characterised by parallel ridges and troughs that merge into the eastern most extents of Maxwell Montes. The image is centered at $\sim 5^{\circ}\text{E } 65.6^{\circ}\text{N}$. Black N-S trending regions are missing data. Radar dark regions represent smooth surfaces and radar bright regions represent rough surfaces.

this tessera occur singularly or paired, with the former producing deep troughs [*Vorder Bruegge and Head*, 1989]. A north-south trough, containing smooth plains material, bounds the eastern extents of the Chevron Tessera, whereby the transition into this trough is marked by high scarps [*Vorder Bruegge and Head*, 1989]. Chevron Tessera is dotted with localised (50-200 km), topographically low areas of smooth plains material, that appear younger than the surrounding tessera [*Bindschadler and Head*, 1991]. Eastern Fortuna Tessera is located next to this trough, with elevations of 1-4 km [*Vorder Bruegge and Head*, 1989; *Ivanov and Head*, 2009]. This area is characterised by Normal Tessera, which comprise long-wavelength, normal-angular cross-cutting ridges and troughs, with spacings of 5-25 km.

A north-west to south-west trending ridge belt borders the Arcuate-Ridged and Chevron Tessera, consisting of parallel ridges with short 5-15 km spacings [Bruegge and Head, 1989]. The Arcuate-Ridged and Chevron Tessera may have originated as Normal Tessera that later experienced east-west convergence and significant compressional deformation [Vorder Bruegge and Head, 1989]. Vorder Bruegge and Head [1989] propose Maxwell Montes was initially located further east and was transported over ~1000 km, along two east-west and northeast/southwest shear zones, to its current location. This hypothesis can explain the increasing elevations, thicker crust, and increasing terrain complexity from Eastern to Western Fortuna Tessera.

Vorder Bruegge and Head [1989] proposed Chevron Tessera formed solely by compressional deformation, although other authors [Gilmore *et al.*, 1997; Hansen and Willis, 1998; Kiefer and Hager, 1991; Pritchard *et al.*, 1997] suggested this terrain may have experienced extensional and compressive forces. Chasmata located within the Chevron Tessera (Figure 6.1) exhibit parallel radar-bright and radar-dark lineament pairs characteristic of extensional grabens [Kiefer and Hager, 1991]. Compressional features may have been formed by up slope flow, however extensional graben may have been formed by down slope flow caused from increased crustal basal heat flow associated with lithospheric delamination [Kiefer and Hager, 1991; Sukhanov, 1986].

Western and South-Western Fortuna Tessera also consists of Ribbon-Tessera Terrain characterised by parallel, alternating, tightly spaced, radar-bright and radar dark ridges and scarps, separated by radar-dark elongated, thin, flat, and shallow troughs (Figure 6.3) [Ghent and Tibuleac, 2002; Hansen *et al.*, 1999; Hansen and Willis, 1998; Pritchard *et al.*, 1997]. Tensile-Fracture Ribbons are restricted to South-Western Fortuna Tessera and may have formed by the extension of a brittle layer, ~0.3-2 km thick, overlying a ductile lower layer

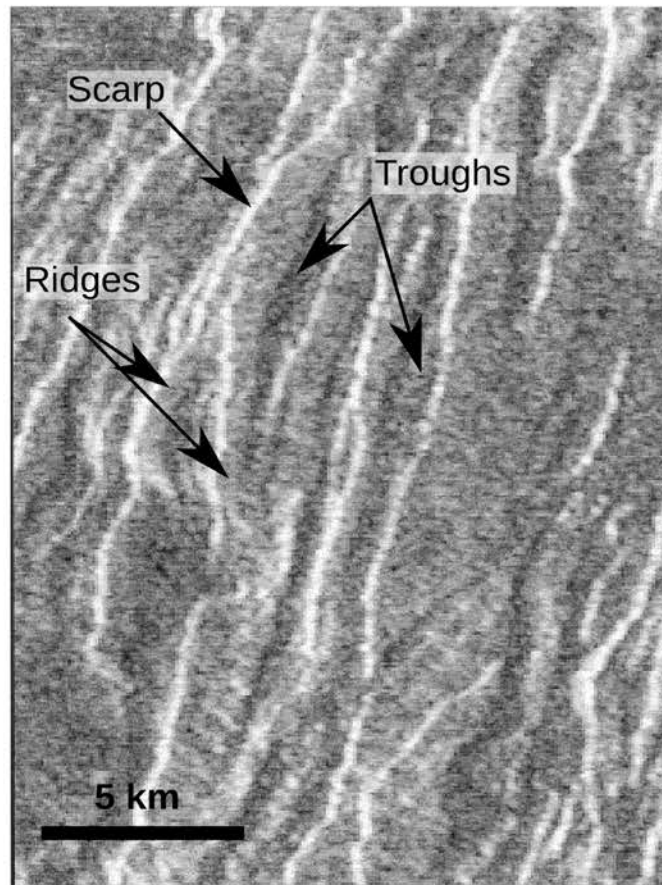


Figure 6.3. (Modified from *Hansen and Willis, 1998*) Ribbon terrain located within southwestern Fortuna Tessera is characterised by radar-dark troughs adjacent to radar-bright or radar-dark lineaments. Scarps facing the radar appear bright. This image is centered at 12°E 58°N. Radar dark regions represent smooth surfaces and radar bright regions represent rough surfaces.

[*Ghent and Tibuleac, 2002; Hansen and Willis, 1998*]. *Pritchard et al. [1997]* also identified a number of other structures within Western Fortuna Tessera (between 10°E to 20°E), including folds, graben, and warps. Folds may have formed during the movement of Maxwell Montes to its present location and are similar to the Arcuate-Ridged Tessera identified by *Vorder Bruegge and Head [1989]*. The combination of these structures —ribbons, folds, warps, and grabens—imply Western Fortuna Tessera has undergone early surface extension, followed by compression, and late extension [*Pritchard et al., 1997*].

Western Fortuna Tessera forms the eastern most portion of Ishtar Terra, an expansive (~5600

km) highland region located in Venus's high latitudes (Figure 6.1) [Kucinskas *et al.*, 1996]. Ishtar Terra's dimensions and high elevations (3-10 km) imply long-wavelength support, which may contribute to the topography observed within Fortuna Tessera. Two models can account for the formation of Ishtar Terra and include both upwelling or downwelling mantle flow [Kaula *et al.*, 1997]. Mantle upwelling below Ishtar Terra is effective in providing support for the long-wavelength potential field and topography data, but is unable to account for the compressional deformation that may have formed the mountain belt Maxwell Montes [Basilevsky, 1986; Kaula *et al.*, 1997; Grimm and Phillips, 1990,1991; Phillips *et al.*, 1991; Pronin, 1986]. A downwelling model or a model involving horizontal normal forces at Ishtar's boundaries is consistent with the compressional structures observed and the thick crust that most likely supports the high elevations of this terrain [Bindschadler *et al.*, 1990; Bindschadler and Parmentier, 1990; Kaula *et al.*, 1997; Kiefer and Hager, 1991; Lenardic *et al.*, 1991; Roberts and Head, 1990]. A thickened residuum layer, associated with a downwelling, could also support Ishtar Terra [Hansen and Phillips, 1995]. The shorter wavelength structures, such as Maxwell Montes, could be supported by crustal thickness variations and imbricated lower crustal material compounded below the mountain due to ponding of a residuum layer (Figure 6.4) [Hansen and Phillips, 1995]. The high elevations of Maxwell Montes, if supported by Airy isostasy variations only, would require a basaltic crust thicker than 60 km. However, the gabbro-garnet granulite eclogite phase transition would reduce the buoyancy associated with this crust if the surface has an age greater than 50 Ma, implying the composition of these areas may be silicic [Jull and Arkani-Hamed, 1995; Kucinskas *et al.*, 1996; Namiki and Solomon, 1993; Vorder Bruegge and Head, 1991].

6.2.2 Crustal Thickness

Ivanov [1988] and Zuber and Parmentier [1990] proposed the spacing of tectonic features in

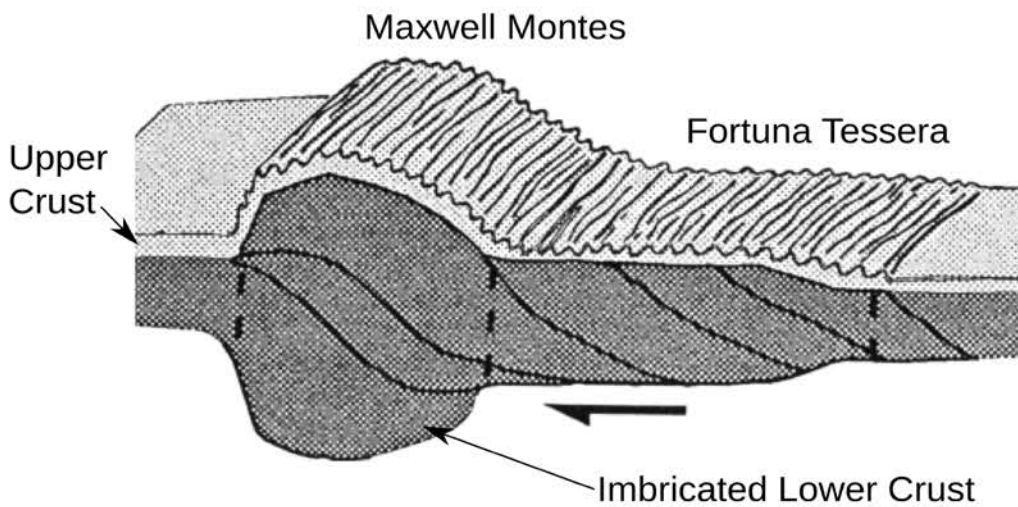


Figure 6.4. (Modified from *Keep and Hansen, 1994*) The high elevations of Maxwell Montes is supported by imbricated and thickened lower crust. The upper crust deforms, due to westward compression, to produce the observed tessera terrain in Fortuna Tessera.

Fortuna Tessera were directly related to crustal thickness and elevation. *Ivanov [1988]* found the high average band spacings (11.5 km) and elevations (4 km) could be supported by thick (30-45 km) basaltic crustal roots. However, a more detailed study addressing the variation of band spacing with elevation for each tessera terrain could constrain the crustal thickness variations further [*Zuber and Parmentier, 1990*]. An estimate of the regional crustal and elastic lithospheric thickness at Fortuna Tessera was also made by *Simons et al. [1997]*. These authors used Venus's topography, gravity, and spectral admittance to estimate a 20 km thick crust and elastic lithosphere [*Simons et al., 1997*].

The variations of crustal thickness with elevation for each of the tessera terrains were addressed in more detail by *Vorder Bruegge and Head [1989]*. By using an Airy isostatic model with a reference crustal thickness of 15 km these authors found the crust gradually thicken moving westwards over Fortuna Tessera. The Normal and Chevron Tessera, had thicknesses of ~35 km and ~40 km, respectively, increasing to ~60 km within the Arcuate-Ridged Tessera [*Vorder Bruegge and Head, 1989*].

An Airy isostatic model, in conjunction with GTRs, was also used by *Kucinskas et al.* [1996] to determine the dominant compensation mechanisms operating within Fortuna Tessera. Western Fortuna Tessera has a GTR of $\sim 8 \text{ m km}^{-1}$ suggesting this area is supported equally by Airy isostasy and thermal isostasy associated with lithospheric delamination [*Kucinskas et al.*, 1996]. However, the thermal uplift within Western Fortuna Tessera could also be produced by partial melting of thick crust if the quantities of surface radiogenic isotopes were similar to those at depth [*Kucinskas et al.*, 1996]. The lower GTR ($\sim 4 \text{ m km}^{-1}$) within Eastern Fortuna Tessera implies topography is supported by Airy isostasy only [*Kucinskas et al.*, 1996]. The absence of thermal isostasy in Eastern Fortuna Tessera may imply delamination has not occurred recently, allowing the thermal lithosphere to cool and thicken, and the topography to relax [*Kiefer and Hager*, 1991; *Kucinskas et al.*, 1996].

6.2.3 Lithospheric Mantle Thickness

Romeo and Turcotte [2008] found that the dominant deformation mechanism operating within a tessera region is directly related to the ratio between the crustal and lithospheric mantle thickness. To determine these ratios, analytical models were used to simulate the force balance on a crustal plateau. The ratio between the thickness of the crust and lithospheric mantle determined the equilibrium force balance [*Romeo and Turcotte*, 2008]. From this model, compressional deformation was found to dominate if the crust is less than 2/5 of the lithospheric mantle thickness, with the terrain collapsing if the crustal thickness is greater than 2/5 of lithospheric mantle thickness [*Romeo and Turcotte*, 2008]. The tessera and its inliers could have originated from two phases of deformation if delamination of the lithospheric mantle from the crust has occurred. No delamination results in compression and elevated plateau morphology supported by a thick crust, whereas delamination produces extension, grabens, and intratessera volcanism [*Romeo and Turcotte*, 2008]. These tessera terrains may

have resisted global overturn with the present elevations being directly related to the variations in lithospheric mantle thickness following this event. Considering the equilibrium force balance model, the lithospheric mantle thickness associated with a plateau's elevation varies with respect to the assumed crustal density [Romeo and Turcotte, 2008]. For a crustal density of 2750 kg m^{-3} , a thin mantle lithosphere (40 km) could support small elevations (2 km), whereas a thicker mantle lithosphere (90 km) could support higher elevations (4 km) [Romeo and Turcotte, 2008].

6.3 Methodology

6.3.1 Introduction

The interactive 3D forward modelling software, GEO3Dmod was used to model the thermal lithospheric structure below Fortuna Tessera [Fullea *et al.*, 2010]. The user is required to choose an appropriate reference column structure and thermal lithospheric model. The lithospheric model, which extends to the depth of the first phase transition [$\sim 440 \text{ km}$; Steinbach and Yuen, 1992], can comprise numerous crustal layers and one lithospheric mantle layer, defined by densities and thermal properties set by the user. Heat transfer, geopotential, and isostasy equations are then solved simultaneously. The output from these equations include 3D temperature and density distributions as well as calculated responses of Bouguer gravity, geoid, surface heat flow, and elevation. The simultaneous modelling of each observable results in a highly constrained, self-consistent final lithospheric model [Fullea *et al.*, 2010].

6.3.2 Geophysical Observables

Elevation, Bouguer gravity, and geoid height constitute the geophysical observables for our lithospheric modelling at Fortuna Tessera (Figure 6.5). The 719 degree and order spherical harmonic model by *Wieczorek* [2007] formed the elevation data set (Figure 6.5) and consisted of the Global Topography Data Record 3.2 (GTDR3.2), obtained from the Magellan mission to Venus. However, Pioneer and Venera 15/16 altimetry were also used within the modelled area (Figure 6.5), between 31°N to 55°N, to cover a gap within the GTDR3.2 [*Riley et al.*, 1995; *Wieczorek*, 2007]. A Root-Mean-Square (RMS) radial uncertainty of 400 m was adopted as the uncertainty pertaining to the elevation, which was referenced to 6051.848 km or Venus's Mean Planetary Radius (MPR) [*Rappaport et al.*, 1999; *Wieczorek*, 2007].

The free-air gravity was obtained from the 180th degree and order spherical harmonic model SHGJ180u and assumes a maximum uncertainty of 12 mGal [*Konopliv et al.*, 1999]. A Bouguer Correction BC was then subtracted from the free-air gravity to obtain the Bouguer gravity B (Figure 6.5):

$$BC = 2 \pi \rho_{crust} G h \quad (6.1)$$

$$B = FA - BC \quad (6.2)$$

where ρ_{crust} is the density of the crust (2900 kg m⁻³); G is the universal gravitational constant 6.672×10^{-11} N m² kg⁻², h is the elevation, and FA is the free-air gravity.

Using the rules of error propagation [*Bevington and Robinson*; 1992; *Taylor*, 1982; *Young*, 1962], this data set has a maximum uncertainty (B_{uncert}) of 50 mGal from:

$$BC_{uncert} = Topo_{uncert} 2 \pi \rho_{crust} G \quad (6.3)$$

$$B_{uncert} = \sqrt{((FA_{uncert})^2 + (BC_{uncert})^2)} \quad (6.4)$$

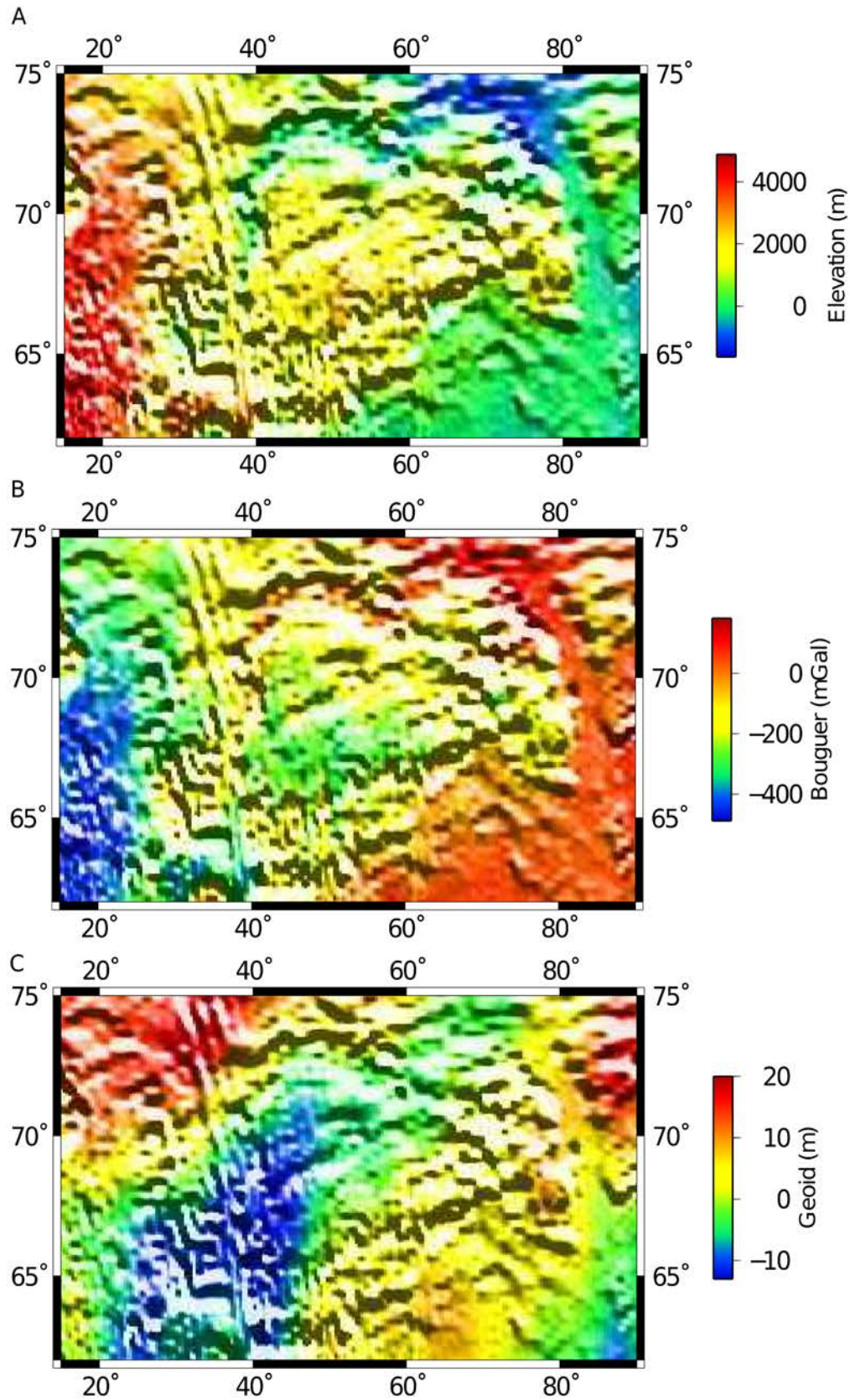


Figure 6.5. Geophysical observables of (A) elevation, referenced to a Mean Planetary Radius (MPR) of 6051.848 km. (B) Bouguer gravity, and (C) filtered geoid. The geoid represented spherical harmonic degrees $>\sim 14$ or wavelengths $<\sim 2716$ km.

where BC_{uncert} is the uncertainty associated with the Bouguer correction BC , $Topo_{\text{uncert}}$ is the maximum topographic uncertainty of 400 m, FA_{uncert} is the maximum uncertainty (12 mGal) for the free-air gravity data set.

A 2D Fast Fourier Transform was used to integrate the free-air gravity field to derive the geoid data set (Figure 6.5) and is similar to the method performed by *Sjogren et al.* [1997], *Wessel and Smith* [1991; 1998]. The lithospheric model extends to relatively shallow depths ($< \sim 400$ km) and, as a result, the geoid data set was filtered using a cosine-tapered high pass filter to remove the contribution of deep mantle anomalies [*Jiménez-Munt et al.*, 2010]. As a result, the filtered geoid data set corresponds to all degrees $> \sim 14$ (wavelengths $< \sim 2716$ km). This data set has an uncertainty of 2.3 m.

6.3.3 Lithospheric Modelling

Before modelling Fortuna Tessera we first had to assume a suitable reference column (Figure 6.6). The location of this reference column was taken at $34.5^\circ\text{E } 89^\circ\text{N}$, within the North Polar Plains, since it is absent of large scale tectonism, volcanism, and weathering (Figure 6.7). This region has a similar elevation to Venus's Mean Planetary Radius (MPR) and lowland plains, acting as a possible analogue for $\sim 65\%$ of Venus's surface [*Solomon and Head*, 1990]. The structure of this reference column comprises a 300 km thick lithosphere and 30 km thick crust, similar to global estimates [*Grimm and Hess*, 1997; *Nimmo and McKenzie*, 1998; *Turcotte*, 1993]. A thinner reference crust (15 km) and lithosphere (140 km thick) were also trialled in previous lithospheric modelling at Atla Regio (see Chapter 4 for additional details).

From a least-squares analysis of each reference column, we found that reference columns using a thinner crust and thermal lithosphere resulted in a greater misfit between the

calculated and observed geoid and elevation at Atla Regio (Table 6.1). We were primarily concerned with fitting the elevation and geoid data, rather than the Bouguer gravity, therefore a reference column with a crustal thickness of 30 km and lithospheric thickness of 300 km was chosen as the most appropriate lithospheric structure.

Table 6.1. Results from the least-squares analysis for each reference column

Model	Elevation (m)	Bouguer (mGal)	Geoid (m)
$T_c=30$ km; $L=300$ km	1.61	16.21	203.78
$T_c=15$ km; $L=300$ km	1.76	16.14	316.07
$T_c=15$ km; $L=140$ km	1.78	17.33	247.68

The thinner reference columns also produced unrealistic crustal thicknesses ($\sim < 0$ km) below Ganis Chasma and generated calculated geoid, Bouguer gravity and elevation responses that showed a poor correlation to the observed data.

Melt generation volumes and rates, calculated at Atla Regio, were also used to indirectly constrain the lithospheric structure occurring below the North Polar Plains. Reference column 1 produced a modelled lithospheric structure below Ganis Chasma that yielded a rate ($0.5 \text{ km}^3 \text{ yr}^{-1}$) and volume ($0.20 \times 10^6 \text{ km}^3$) of melt similar to previous estimates ($0.4 \text{ km}^3 \text{ yr}^{-1}$ and 10^4 - 10^6 km^3 , respectively) [Nimmo and McKenzie, 1998; Smrekar and Parmentier, 1996]. Therefore, lithospheric modelling, melt generation rate and volume calculations, and previous global estimates, imply the reference lithospheric structure below the North Polar Plains may be a 30 km thick crust underlain by a 300 km thick thermal lithosphere [Grimm and Hess, 1997; Nimmo and McKenzie, 1998; Turcotte, 1993].

An average elevation of the North Polar plains was calculated between -180°E 85°N and 180°E 90°N , which also corresponds to an elevation of -1.069 km at 34.5°E 89°N (Figure 6.7). Using the reference lithospheric structure, and density output from GEO3Dmod, a depth

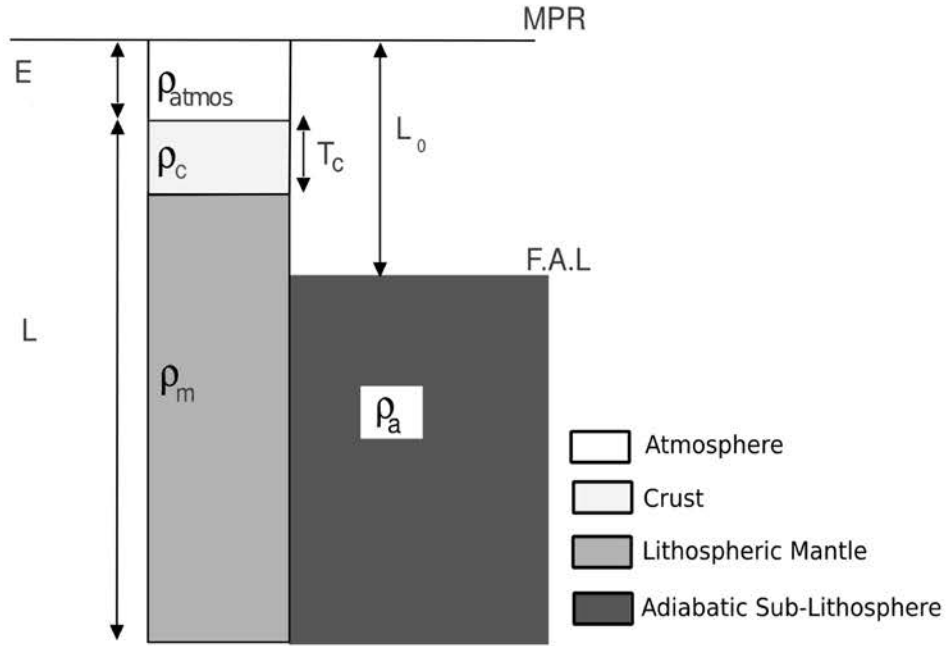


Figure 6.6. (Adapted from [Fullea *et al.*, 2007]) Notation for each lithospheric model at Fortuna Tessera. E is the absolute elevation, T_c and L are the crustal and lithospheric thickness, respectively. The density of the atmosphere, crust, lithospheric mantle, and adiabatic sub-lithosphere are denoted by ρ_{atmos} , ρ_c , ρ_m and ρ_a . L_0 is the calibration constant, and represents the depth from the MPR to the Free-Asthenospheric Level (F.A.L.).

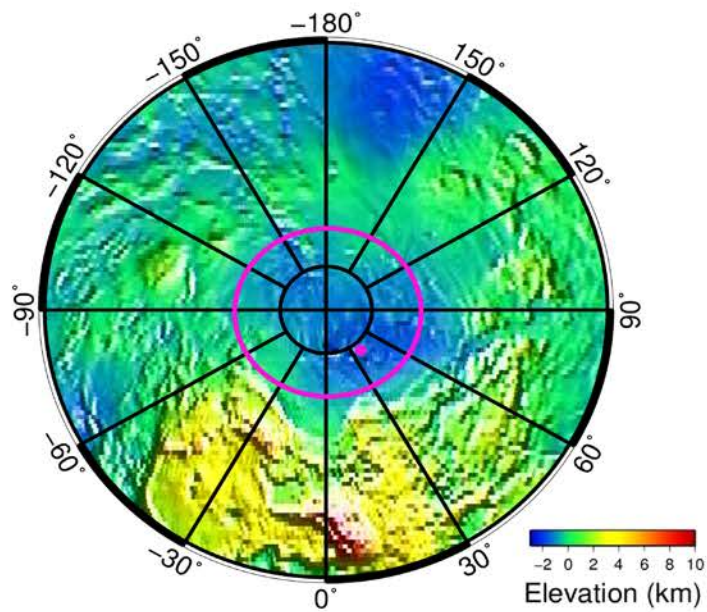


Figure 6.7. The location of the North Polar Plains. An average elevation (-1.069 km) was found for the area encompassed within the large purple circle. This average elevation also corresponds to the elevation at 34.5°E 89°N (small purple circle), which was the location of our reference column.

averaged lithospheric density of 3203 kg m^{-3} was calculated at this point. Using both the reference elevation E_0 (-1.069 km) and depth-averaged density of the lithosphere ρ_l , the calibration constant L_0 (0.768 km) was determined from Equation 6.5 [Lachenbruch and Morgan, 1900]. Once the calibration constant was calculated, Equation 6.5 was then used to calculate the absolute elevation E of any lithospheric column at Fortuna Tessera.

$$\begin{aligned}
 &\text{If } E \vee E_0 < 0: \\
 E \vee E_0 &= \frac{\rho_a}{(\rho_a - \rho_{atmos})} \left(\frac{(\rho_a - \rho_l)}{\rho_a} L - L_0 \right) \\
 &\text{If } E \vee E_0 > 0: \\
 E \vee E_0 &= \frac{(\rho_a - \rho_l)}{\rho_a} L - L_0
 \end{aligned} \tag{6.5}$$

where ρ_{atmos} is the density of the atmosphere (60 kg m^{-3}), ρ_a is the density of the adiabatic sub-lithosphere (3200 kg m^{-3}), L is the thermal lithospheric thickness (300 km), ρ_l is the depth-averaged density of the lithosphere (3203 kg m^{-3}), L_0 is a calibration constant that corresponded to the depth to the free asthenosphere, F.A.L, which does not experience any loading.

The lithospheric model at Fortuna Tessera has $90 \times 30 \times 300$ nodes and includes two layers, with properties shown in Table 6.2. The first layer comprises the crust and represents basalt and layer two is the lithospheric mantle that has values similar to peridotite (Table 6.2). We have assumed that these layers have densities and thermal parameters as similar rocks located on Earth, with this assumption being supported by the composition of samples obtained during the Venera and Vega missions and the morphology of Venus's volcanoes [Grimm and Hess, 1997; Head et al., 1992].

Layer one and two has a variable coefficient of thermal expansion and temperature-dependent density, with layer one also having a pressure-dependent density (Table 6.2). The thermal parameters and densities of each layer were obtained from *Afonso et al.* [2005], *Ranalli* [1995], *Reynolds* [1997], *Rogers* [2007], and *Schubert et al.* [2002], whereas the compressibility β was calculated from *Schubert et al.* [1997]:

$$K = \frac{E}{(3(1-2\nu))} \quad (6.6)$$

$$\beta = \frac{1}{K}$$

where K is the bulk modulus, E is Young's modulus, and ν is Poisson's ratio of each composition.

The properties of the adiabatic sub-lithospheric mantle were not included in Table 6.2 since this layer underlies the thermal lithosphere and lies outside of our model domain. This constant density (3200 kg m^{-3}) of this layer, however, acts as a reference for the density variations in the overlying conductive thermal lithosphere.

Table 6.2. Layer parameters

Layer	Name	Density (kg m^{-3})	Coefficient of thermal expansion ($\times 10^{-5}$) K^{-1}	Thermal conductivity W K^{-1}	Heat Production Rate ($\times 10^{-7}$) W m^{-3}	Pressure coefficient ($\times 10^{-10}$)
1	Crust	2900	2.75	2.1	2.0	2.36
2	Lithospheric Mantle	3200	3.50	3.3	0.2	0

Regional isostasy or flexure was also calculated by GEO3Dmod for an assumed elastic lithospheric thickness. For our modelled we assumed an elastic lithospheric thickness of 10 km, 30 km, and 50 km. In this study, flexure was not iteratively solved, instead it was

calculated from the residual topography remaining after Airy and thermal isostasy were removed from the observed elevation. This residual topography was also useful in estimating the amount of dynamic compensation required to support the observed topography and was found by removing the calculated isostatic and flexural contribution from the observed topography.

Our modelled area at Fortuna Tessera extends from 62°N to 75°N and 15°E to 90°E (Figure 6.8). We present both regional maps of crustal and lithospheric thickness, as well as two lithospheric profiles taken over the various tessera terrain within Fortuna Tessera. We chose to adopt the same tessera terrain nomenclature of *Vorder Bruegge and Head* [1989, 1990] when presenting these results. The location of the profiles taken over our modelled area are shown in Figure 6.8.

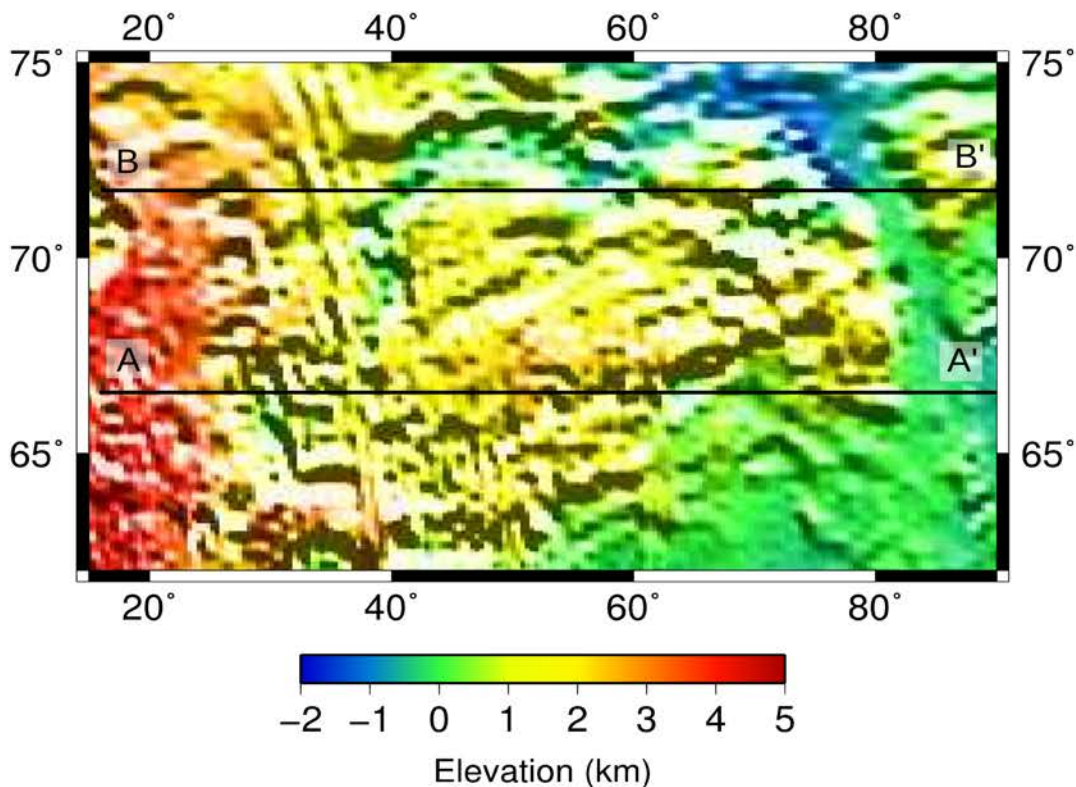


Figure 6.8. Elevation map of Fortuna Tessera showing the location of the two profiles (A-A' and B-B').

6.4 Results

6.4.1 Residuals

Residuals, found by subtracting the calculated model from the observables, represent the model's misfit or an unknown density structure and are useful in locating areas where additional compensation is required (Figure 6.9). From Figure 6.10 each histogram plot exhibits a Gaussian-like distribution with most of the residuals at 0% or within an error of ~10%.

6.4.2 Lithospheric Profiles

Figures 6.11 and 6.12 show the lithospheric structure along 67°N. An area of poor-fit occurs between 1500-2000 km, however, this is a short-wavelength (i.e. ~500 km) feature does not influence our modelled results and compensation mechanisms that support the long wavelength tessera surrounding this area. From Figure 6.11, the crust tends to thin further along the profile, with the thickest crust (~70 km) corresponding to the Arcuate-Ridged Tessera (0-500 km), followed by the Chevron Tessera (~60-70 km; 500-1350 km) and the Normal Tessera (~60-50 km; 1350-7800 km). The Chevron Tessera and Normal Tessera are separated by a rift (at ~1600 km) and its associated thin crust (~25 km).

The thermal lithosphere thickens from the Arcuate-Ridged and Chevron Tessera (255-275 km) to the Normal Tessera and plains regions (~335 km; Figure 6.11 and 6.12). A thinner thermal lithosphere below the Arcuate-Ridged Tessera results in higher surface heat flow (~22 mW m⁻²) compared to the other tessera units (18-19 mW m⁻²; Figure 6.11).

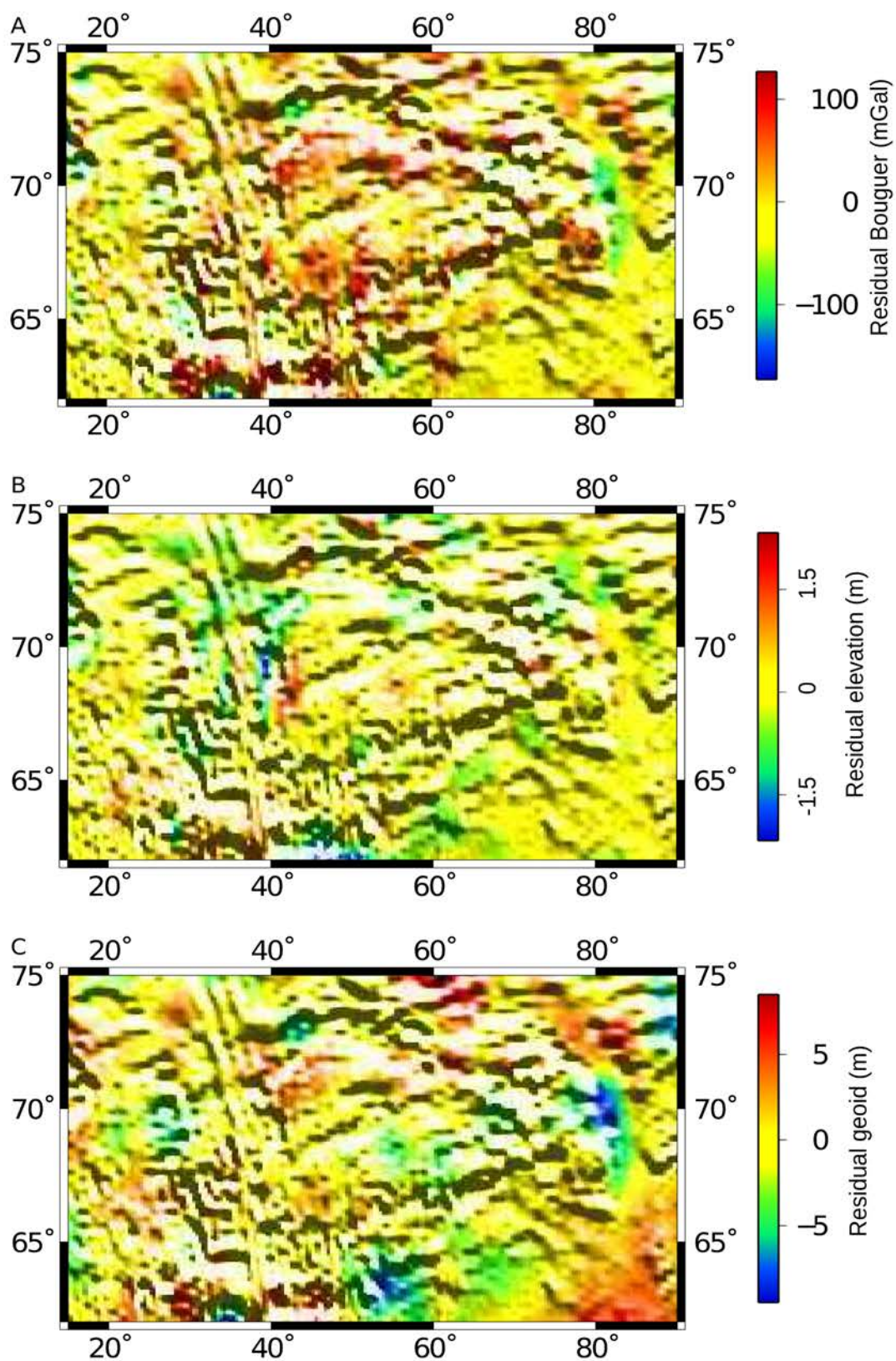


Figure 6.9. Maps of residual Bouguer gravity (A), residual elevation (B), and residual geoid (C). The residuals were found by subtracting the calculated model from the observables.

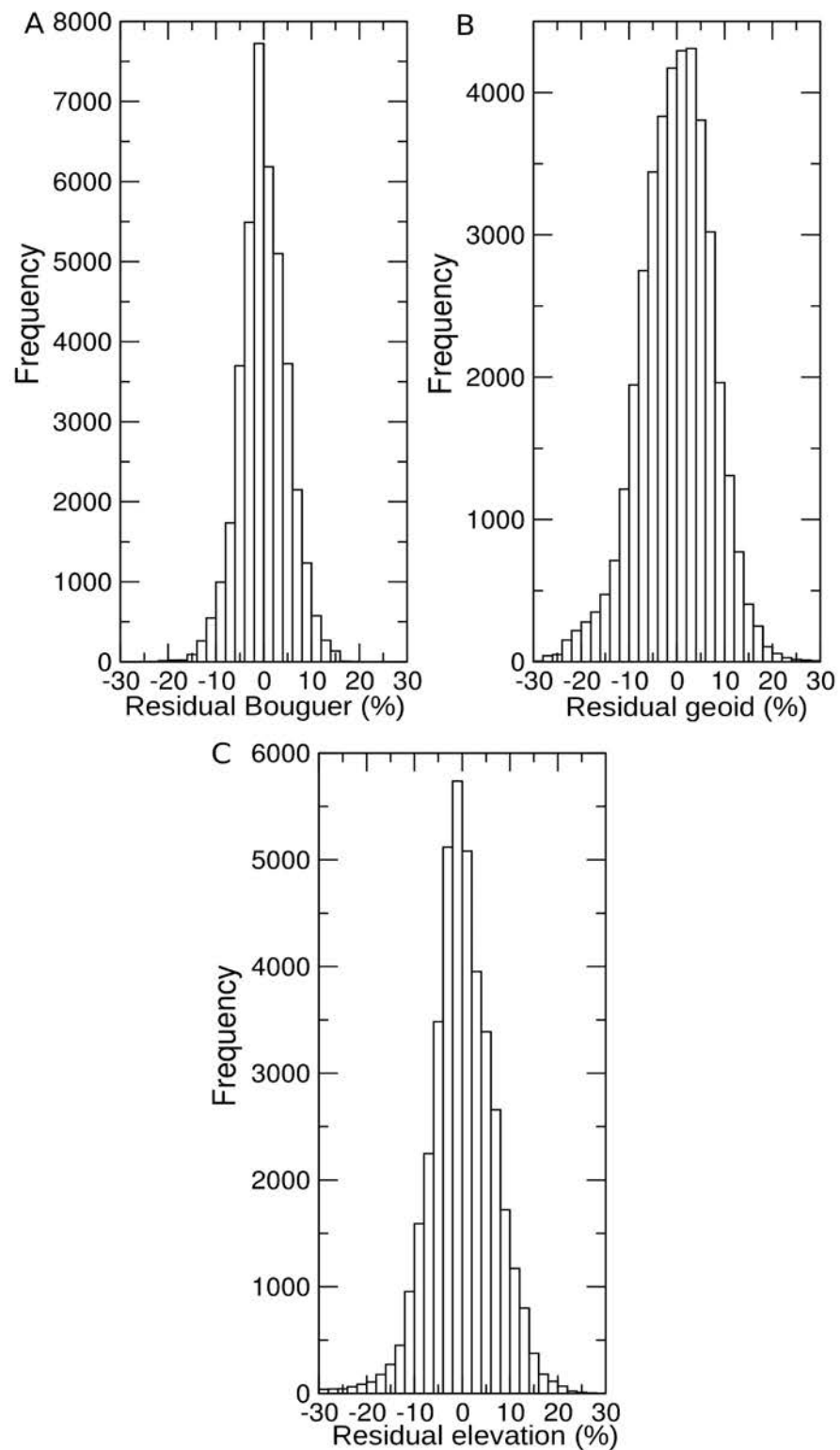


Figure 6.10. Histogram plots of (A) residual Bouguer gravity, (B) residual geoid, and (C) residual elevation, shown in Figure 6.9. Residuals are shown as a percentage of the total magnitude range for each observable.

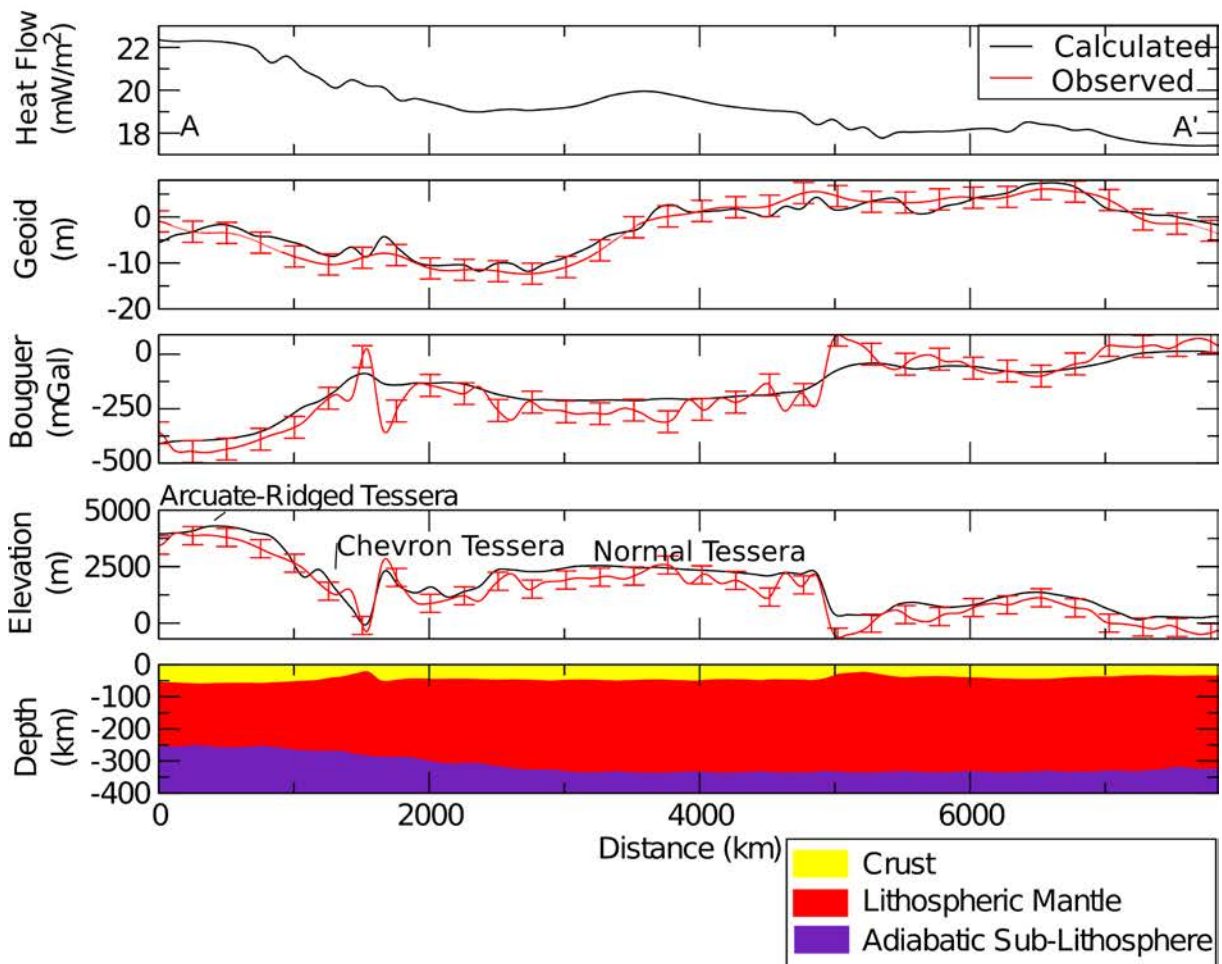


Figure 6.11. Lithospheric structure over the three main tessera terrains addressed in this study. This profile was taken along 67°N, extending from 16°E to 90°E (A-A' in Figure 6.8). The calculated responses, based on the proposed lithospheric structure are shown by the black lines. The red error bars represent the uncertainty associated with each respective geophysical observable (red line). The crust, lithospheric mantle, and adiabatic sub-lithosphere are shown as the yellow, red, and purple layers, respectively. No observed surface heat flow is available.

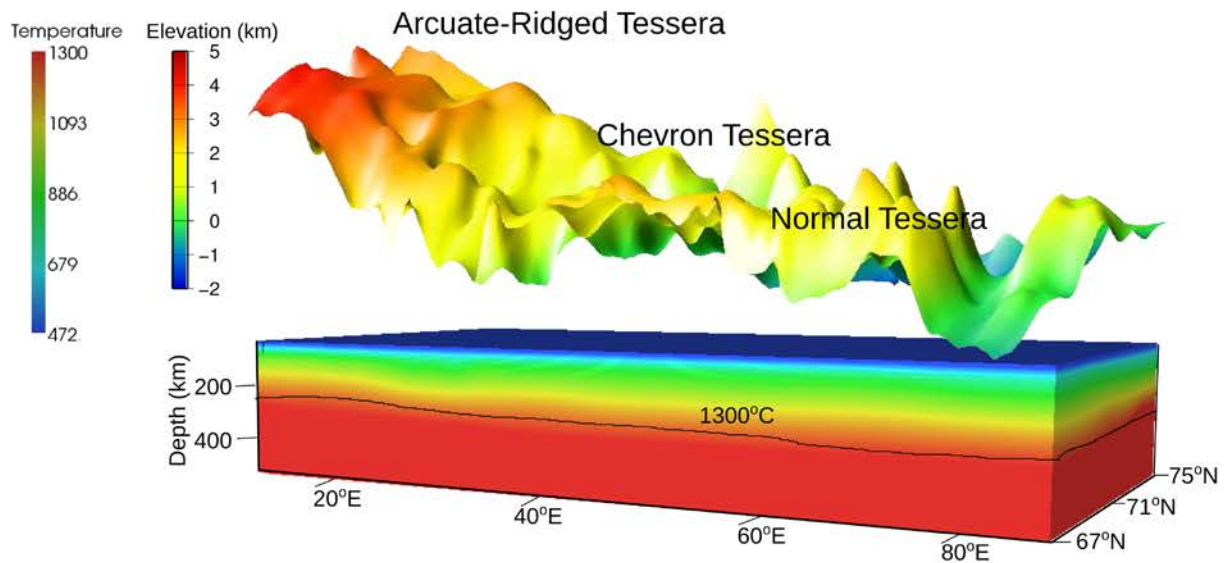


Figure 6.12. The thermal structure from 16°E to 90°E and 67°N to 75°N. The thermal structure and topography between 62°N to 66°N was removed for clarity.

At 72°N, only the Chevron and Normal Tessera remain (Figure 6.13). The Normal Tessera has a thick crust (52-63 km) and is interspersed with plains units and their associated thinner crust (35-50 km). Chevron Tessera corresponds to a thick crust (52-70 km) especially between distances of 250-1000 km. Chevron tessera (~310-350 km) also correspond to slightly thinner thermal lithospheric thicknesses compared to the Normal Tessera and plains regions (~350 km) (Figures 6.13 and 6.14). Higher ($\sim 21.5 \text{ mW m}^{-2}$) surface heat flows occur in the Chevron and Normal Tessera within Western Fortuna Tessera compared to the Normal Tessera in the east ($16\text{-}17.5 \text{ mW m}^{-2}$).

6.4.3 Crustal and Lithospheric Thickness Maps

Regional maps of crustal thickness variations also show an overall thinning of the crust when moving towards the east (Figure 6.15A). The Arcuate-Ridged Tessera corresponds to a thick (50-80 km) crust, whereas a thinner crust occurs within the Normal Tessera (50-65 km) and

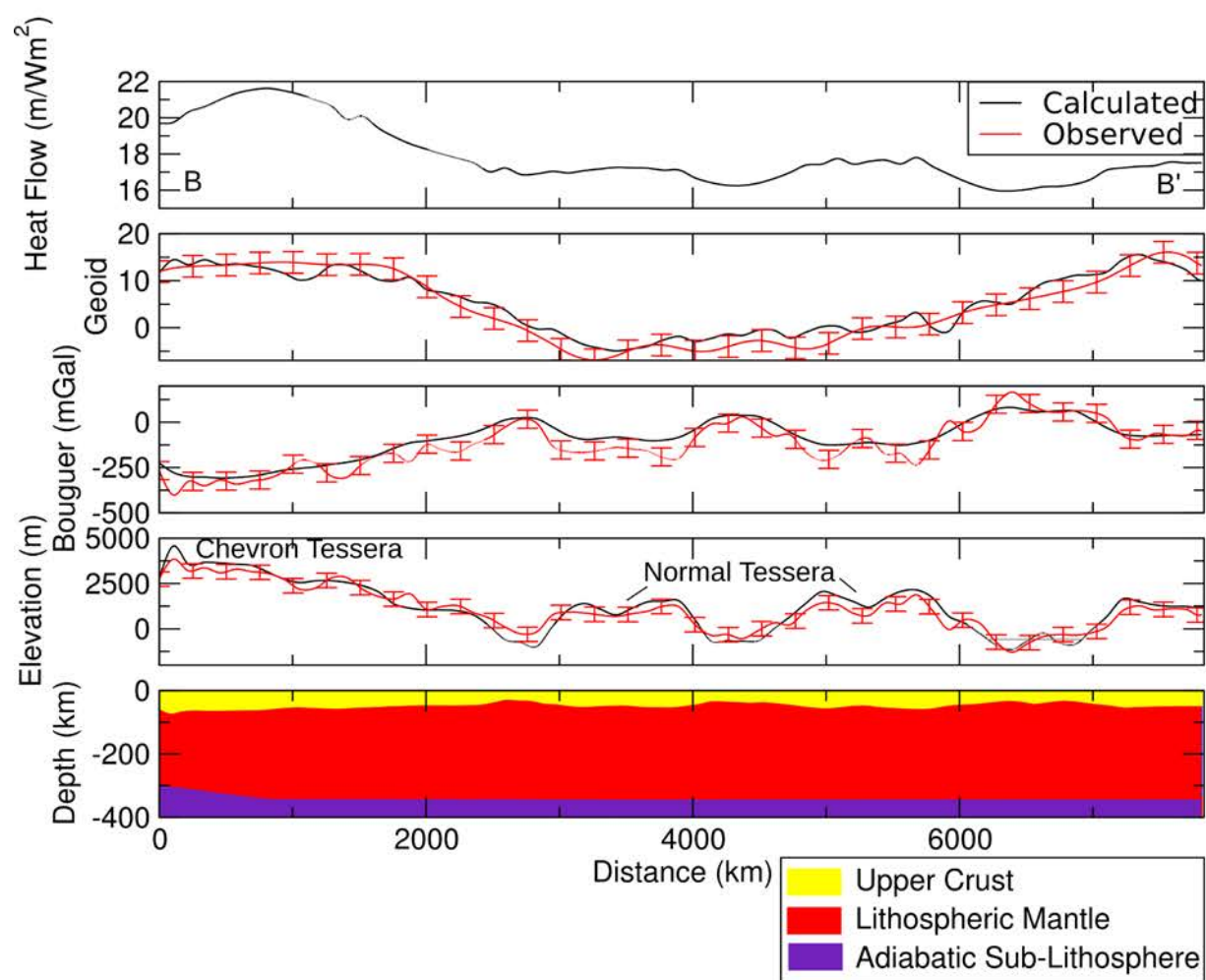


Figure 6.13. The lithospheric structure along 72°N, extending from 16°E to 90°E (B-B' in Figure 6.8).

Key is similar to Figure 6.11.

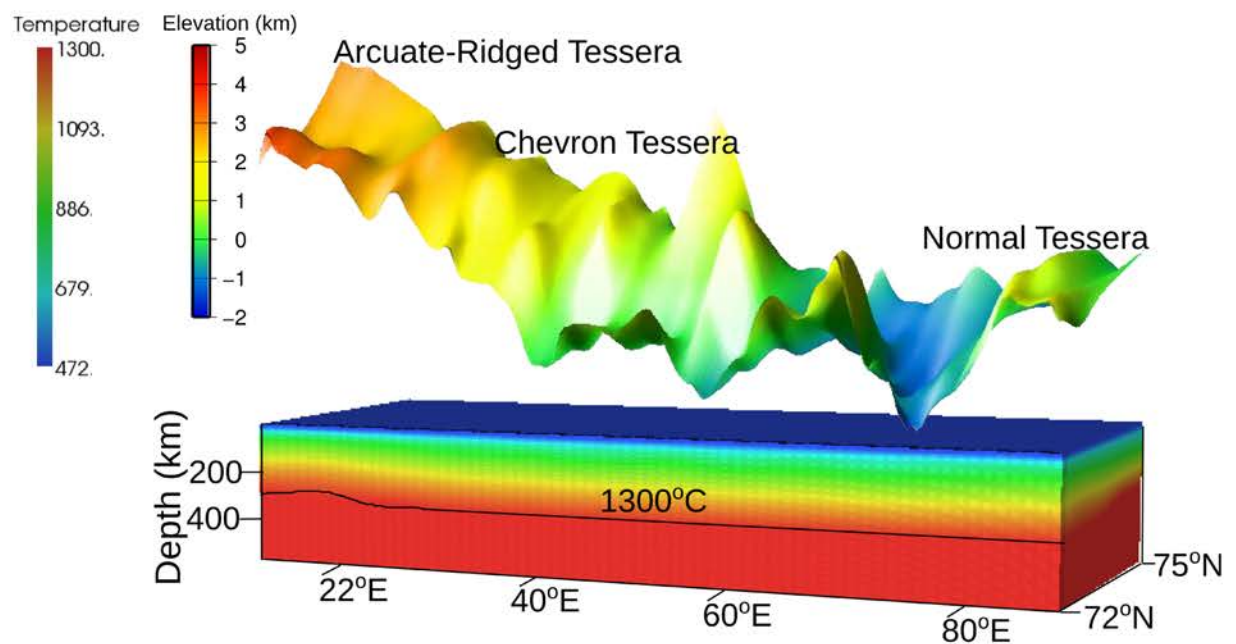


Figure 6.14. The thermal structure from 16°E to 90°E and 72°N to 75°N. The thermal structure and topography between 62°N to 71°N was removed for clarity.

the plains regions (35-45 km). The Chevron and Normal Tessera has been dissected by chasmata, corresponding to a thin (25-30 km) crust below the central trough, flanked by a thicker crust at the adjacent rift shoulders (35-45 km). The Chevron Tessera surrounding these rifts have localised areas of thick crust (50-75 km). The lithosphere is thin near the Arcuate-Ridged Tessera especially to the south-west, towards the summit of Maxwell Montes (Figure 6.15B). As the area surrounding Maxwell Montes diffuses northwards, the thermal lithosphere below the Arcuate-Ridged Tessera thickens to 275-300 km. The Chevron Tessera, Normal Tessera, and the distal eastern plains units require minor lithospheric thickness variations with values ranging from 330-340 km thick (Figure 6.15B).

6.4.4 Compensation Mechanisms

Most of the observed elevations at Fortuna Tessera is supported by a combination of Airy and

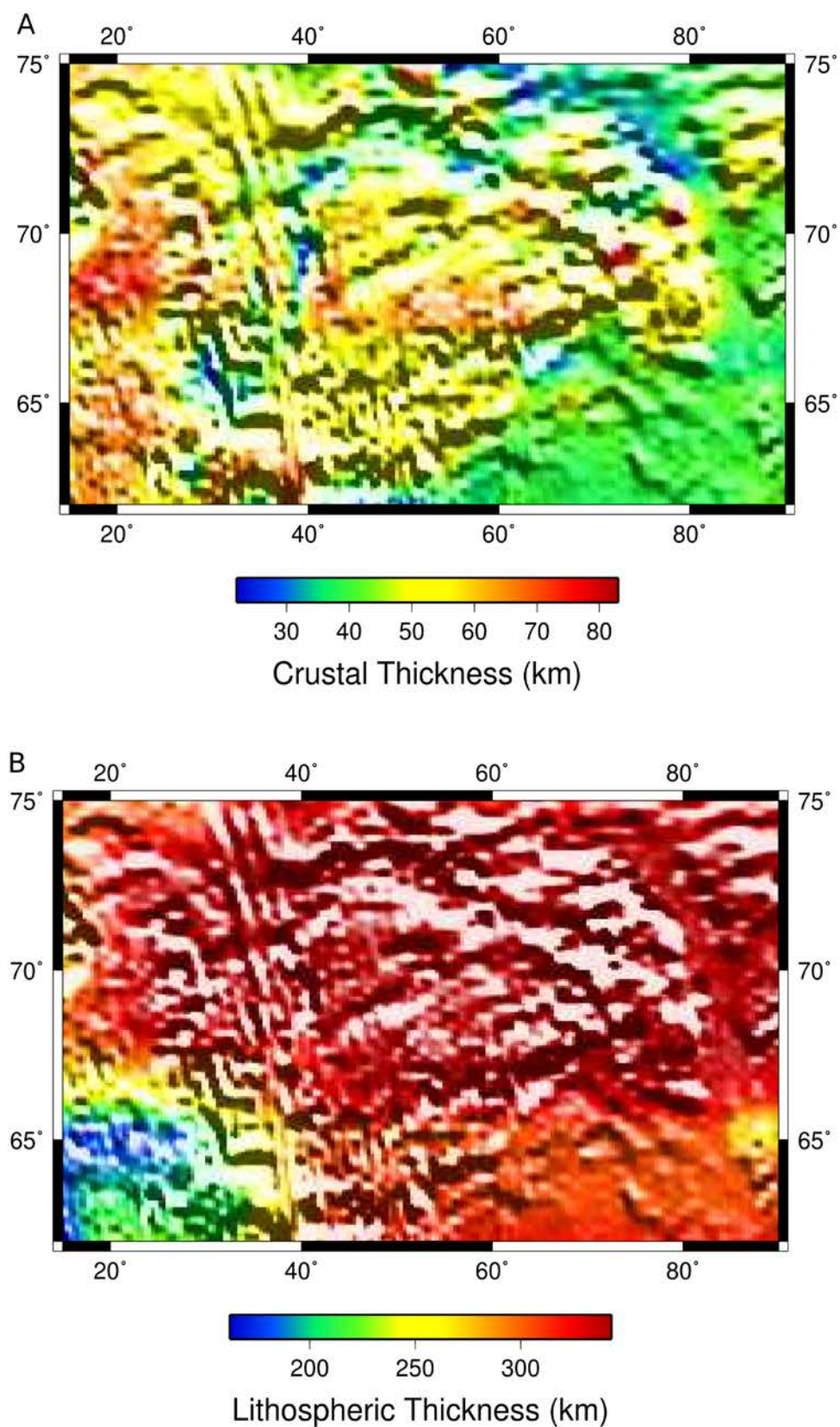


Figure 6.15. The results of our proposed lithospheric structure, comprising crustal (A) and lithospheric (B) thickness variations, at Fortuna Tessera.

thermal isostasy (Figure 6.16A-B). However, some additional support (~ 0.7 km) is required along the chasmata (Figure 6.17).

The amount of flexural support obtained at Fortuna Tessera appears similar even though the assumed elastic lithosphere thickness varied from 10 km, 30 km, and 50 km (Figure 6.17). However, it should be noted that the quantity of flexural support for each of these elastic lithospheric thicknesses are also over estimated when compared to the amount of additional compensation required from the residuals (Figure 6.9).

The dynamic compensation was estimated by removing both the isostatic and flexural support from the observed topography. Considering a thin elastic lithosphere thickness of 10 km, dynamic uplift may provide minor (0-500 m) compensation to the tessera terrain, particularly the Arcuate-Ridged and Normal Tessera (Figure 6.17C). A mantle plume is generally considered to influence the long-wavelength topography of an area, however our study has found dynamic uplift contributes to localised compensation only. These localised dynamic uplift estimates (of 0-500 m) are most likely associated with the uncertainty of the observed elevation data set (± 400 m) rather than an underlying mantle plume.

6.5 Discussion

6.5.1 Lithospheric Structure

We found the different tessera terrains have a thicker crust, with less variation between the Arcuate-Ridged and Chevron Tessera, compared to previous authors [Vorder Bruegge and Head, 1989]. The Arcuate-Ridged, Chevron, and Normal Tessera had thicknesses ranging from 50-80 km, 25-70 km, 25-65 km, respectively, however Vorder Bruegge and Head [1989]

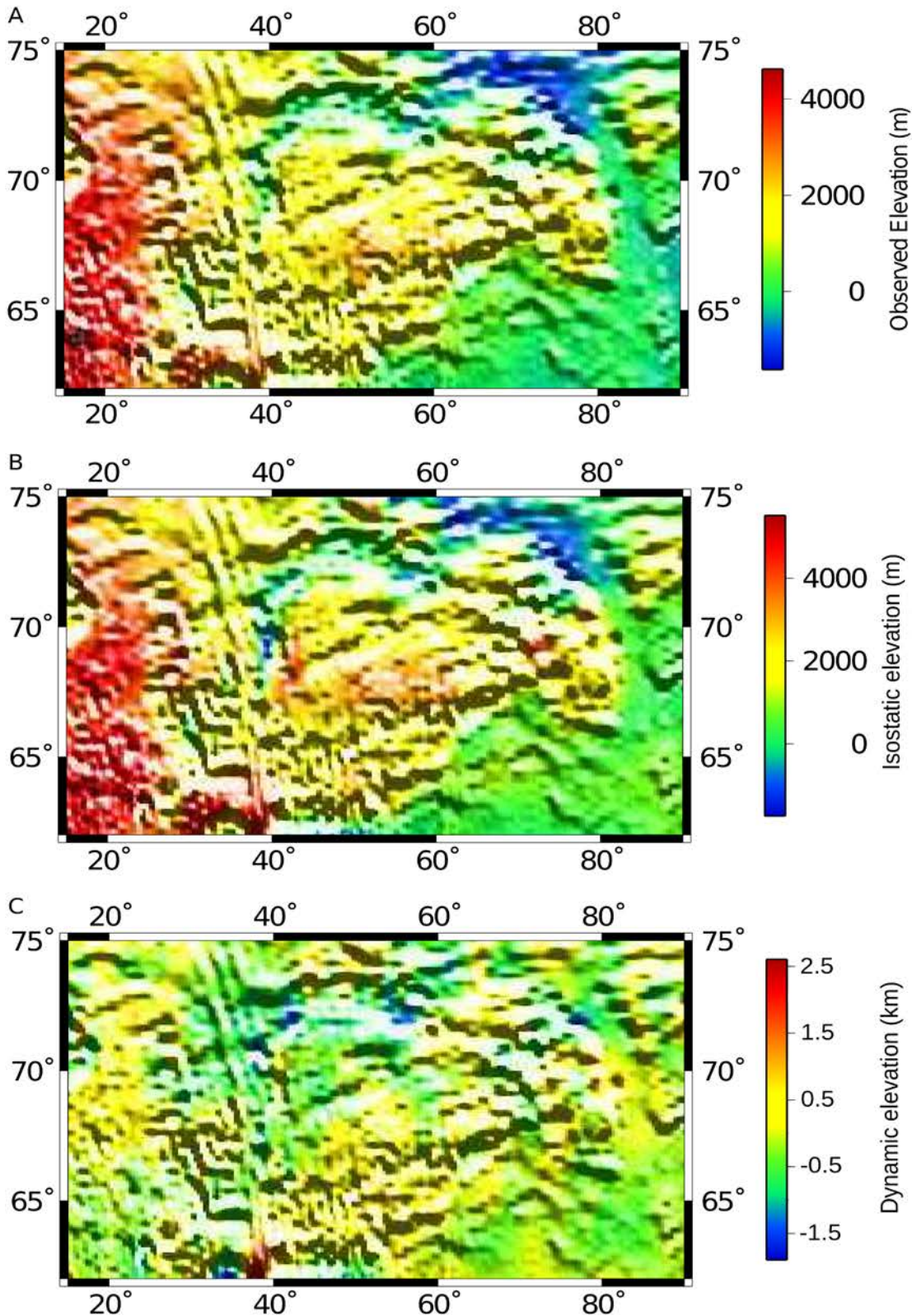


Figure 6.16. (A) The observed elevation at Fortuna Tessera. (B) The amount of topography compensated by Airy and thermal isostasy found from our proposed lithospheric structure. (C) The amount of dynamic elevation found by subtracting the isostatic and flexural component (based on an elastic lithosphere thickness of 10 km) from the observed elevation.

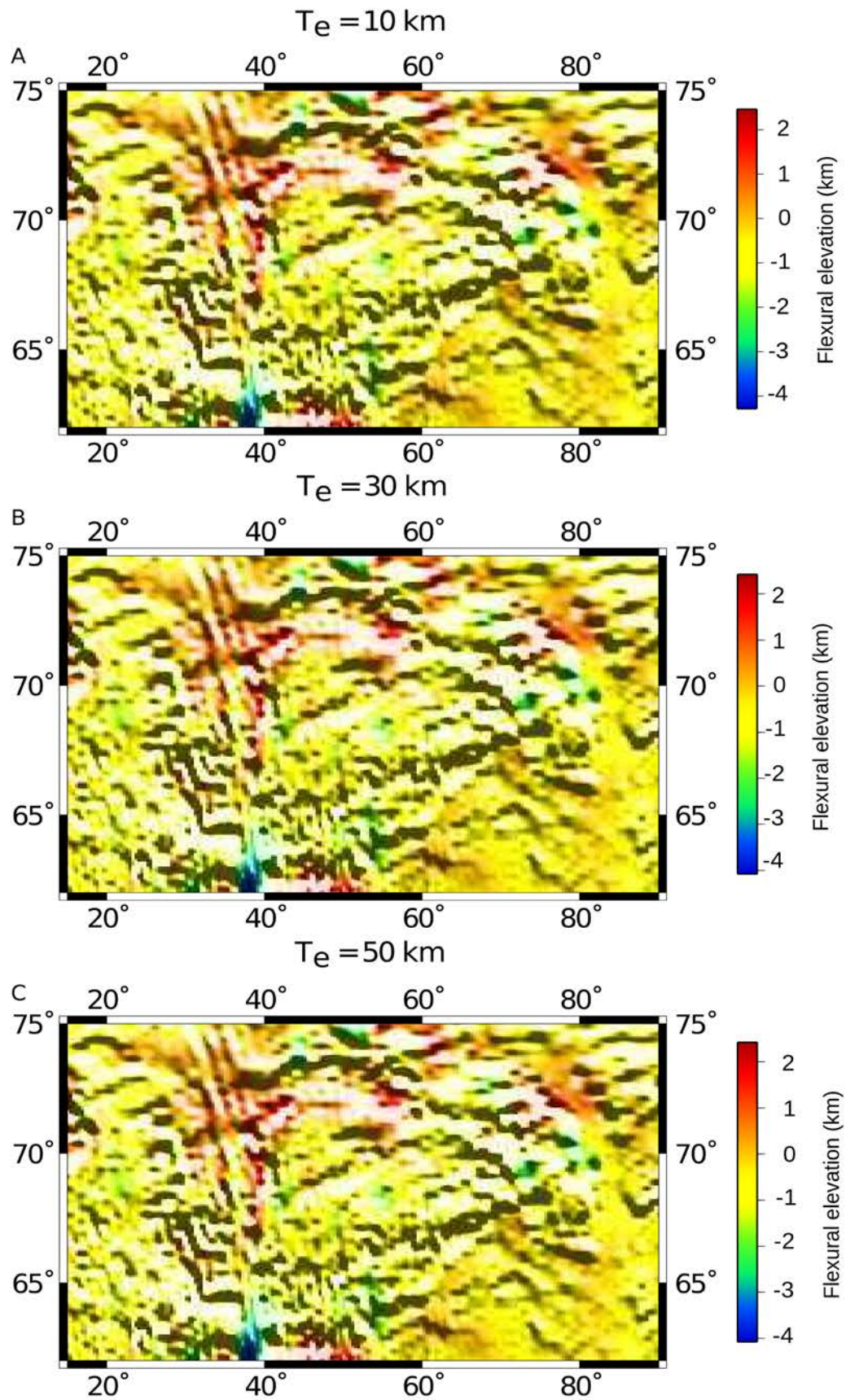


Figure 6.17. The amount of residual topography compensated by flexure at Fortuna Tessera for an elastic lithosphere thickness of 10 km (A), 30 km (B), and 50 km (C).

found crustal thicknesses of 50-70 km, 25-62 km, and 17-50 km for the same terrains. The main factor causing differences in crustal thickness between the studies is the assumed reference crustal thickness. *Vorder Bruegge and Head* [1989] used a 15 km thick reference crust, whereas our model used 30 km, and resulted in thick crust below the tessera terrain.

Romeo and Turcotte [2008] proposed compression dominated tessera formation if the crustal thickness was less than 2/5 of the lithospheric mantle thickness after a subduction event. The tessera terrain towards the east and north-west of Fortuna Tessera follow this relationship [Figure 6.18], confirming previous interpretations of a compressional origin for this region [Vorder Bruegge and Head, 1989]. *Romeo and Turcotte* [2008] also suggested the plateau elevations of tessera terrain, which potentially survived global, episodic over-turning, were proportional to the thickness of the lithospheric mantle that remained after delamination. These authors used force balance equations to determine the relationship between plateau elevation and mantle lithospheric thickness for different crustal densities [Romeo and Turcotte, 2008]. By adopting a continental crustal density (2750 kg m^{-3}) and a 7 km thick initial crust, very thin (40 km) initial mantle lithospheric thicknesses were proposed to support low elevations (2 km) compared to a thicker initial mantle lithosphere (90 km) that supported higher elevations (4 km) [Romeo and Turcotte, 2008]. However, if a basaltic composition and crustal density (2900 kg m^{-3}) were used, a much thicker ($\sim 110 \text{ km}$) initial lithospheric mantle could support a plateau elevation of 4 km [Romeo and Turcotte, 2008].

The increase in crustal thickening and lithospheric thinning from Eastern to Western Fortuna Tessera required in our model is consistent with the results obtained by *Kucinskas et al.* [1996]. These authors proposed the decline in GTRs from Western to Eastern Fortuna Tessera correspond to a decline in the thermal effects that accompany delamination, and increasing

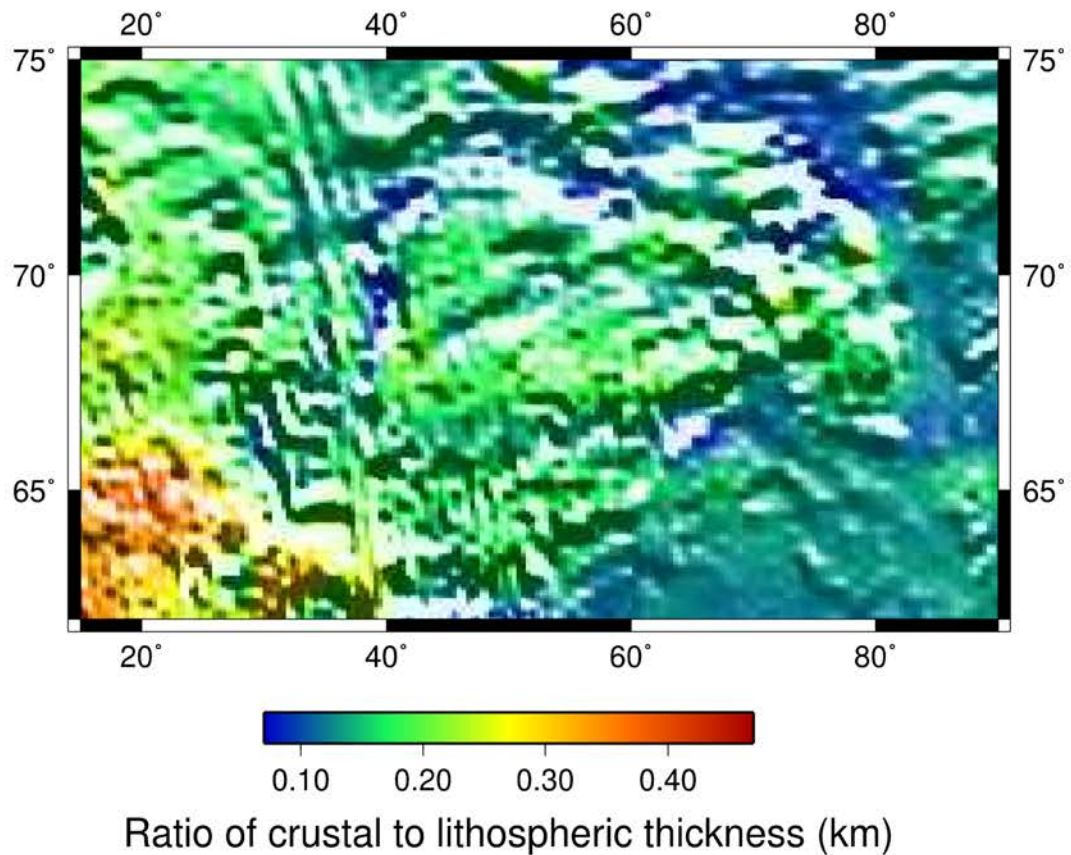


Figure 6.18. Map of the ratio of crustal to thermal lithospheric thickness. The tessera terrain located towards the east and north-west of Fortuna Tessera have a ratio $< 2/5$ (or 0.4) implying compressional deformation contributed to the formation of this terrain.

topographic relaxation [Kucinskas *et al.*, 1996].

In our lithospheric modelling, we have assumed that the surface and sub-surface is predominately mafic in composition. However, if the composition of the crust and lithospheric mantle at Fortuna Tessera is intermediate or basic in composition, as suggested to occur in some areas, then our model may not represent a realistic lithospheric structure [Grimm and Hess, 1997; Head *et al.*, 1992; Jull and Arkani-Hamed, 1995; McKenzie *et al.*, 1992].

6.5.2 Compensation Mechanisms

Our models show most of the topography at Fortuna Tessera is supported by Airy isostasy from crustal thickness variations, consistent with previous studies [*Bindshadler et al.*, 1992; *Vorder Bruegge and Head*, 1989; *Grimm*, 1994; *Hansen et al.*, 1999; *Ivanov*, 1988; *Simons et al.*, 1997; *Smrekar and Phillips*, 1991; *Zuber and Parmentier*, 1990]. However, significant (~150 km) amounts of thermal thinning is required within Western Fortuna Tessera near Maxwell Montes, but is not required in Eastern Fortuna Tessera. This decline in thermal thinning is consistent with the drop in GTRs from Western to Eastern Fortuna Tessera [*Kucinskis et al.*, 1996].

Most of the topography at Fortuna Tessera is supported by Airy and thermal isostasy, however our model requires minor (~0.7 km) flexural support from a thin (10 km) elastic lithosphere at the chasmata. A 10 km thick elastic lithosphere is favoured as it provides a flexural elevation estimate that is consistent with the residual topography. This elastic lithospheric thickness is also consistent with an upper limit of 10 km found from folding models and band spacing estimates [*Solomon and Head*, 1984]. However, GEO3Dmod also assumes that the elastic lithospheric thickness is constant through out the area. This may not be appropriate for Fortuna Tessera due to its close proximity to Maxwell Montes, with the high elevations (11 km) of this mountain range acting as a significant load.

Most of the topography at Fortuna Tessera is associated with minor (~< 500 m) dynamic uplift that could actually represent the uncertainty associated with the observed elevation data set. A few localised areas of dynamic uplift (~1 to 2.5 km) also occurs, with one such area being centered at 38°E 62°N. However, the magnitude of this dynamic uplift is greater (2.5 km; Figure 6.16C) than what is required from the residual elevation (0.8 km; Figure 6.14B). This

response is most likely caused from the over estimation of flexural loading associated with assuming a constant elastic lithospheric thickness throughout Fortuna Tessera (~4 km; Figure 6.17A). Fortuna Tessera's low GTRs, low ADCs, low geoid anomalies, anti-correlation of geoid and topography anomalies, lack of large-scale extension, and plateau morphology also implies dynamic compensation is not required to support the observed topography [Bindschadler *et al.*, 1992; Vorder Bruegge and Head, 1989; Grimm, 1994; Hansen *et al.*, 1999; Ivanov, 1988; Simons *et al.*, 1997; Smrekar and Phillips, 1991; Zuber and Parmentier, 1990].

6.6 Conclusions

This study presents the first estimates of thermal lithospheric thickness below Fortuna Tessera. Even though crustal thickness increases from ~50-55 km to ~55-70 km with higher elevations moving from east to west, our model shows thermal lithospheric thickness will decrease from ~340 km to 150 km, respectively. The three different tessera terrains in Fortuna Tessera and their associated elevation differences are primarily supported by Airy isostasy, with some thermal isostasy being required in the tessera closest to Maxwell Montes. Our proposed lithospheric structure fits the observed elevations within the tessera units very well and no additional compensation mechanisms are required within these areas, however the chasmata do require localised flexural support (~0.7 km).

The thinner thermal lithosphere in Western Fortuna Tessera occurs close to the summit of Maxwell Montes, which may imply this area requires long-wavelength compensation from thermal isostasy. Thermal compensation within this area also has important implications for delamination models proposed for Ishtar Terra, implying further that delamination may be currently occurring within Western Fortuna Tessera [Kucinskas *et al.*, 1996].

6.7 References

- Afonso, J. C., G. Ranalli, and M. Fernández (2005), Thermal expansivity and elastic properties of the lithospheric mantle: results from mineral physics of composites, *Physics of the Earth and Planetary Interiors*, 149, 279-306, doi:10.1016/j.pepi.2004.10.003.
- Basilevsky, A.T. (1986), Structure of central and eastern areas of Ishtar Terra and some problems of Venusian tectonics, *Geotektonika*, 20, 282-288.
- Basilevsky, A. T., and J. W. Head (2002), Venus: Timing and rates of geologic activity, *Geology*, 30(11), 1015 –1018, doi:10.1130/0091-7613(2002)030<1015:VTAROG>2.0.CO;2.
- Bevington, P. R., and D. K. Robinson (1992), *Data reduction and error analysis for the physical sciences*, New York, McGraw-Hill Inc.
- Bindschadler, D. L., and J. W. Head (1991), Tessera Terrain, Venus: Characterization and Models for Origin and Evolution, *Journal of Geophysical Research*, 96(B4), 5889–5907, doi:10.1029/90JB02742.
- Bindschadler, D. L., and E. M. Parmentier (1990), Mantle flow tectonics: The influence of a ductile lower crust and implications for the formation of topographic uplands on Venus, *Journal of Geophysical Research: Solid Earth*, 95(B13), 21329–21344, doi:10.1029/JB095iB13p21329.
- Bindschadler, D. L., G. Schubert, and W. M. Kaula (1990), Mantle flow tectonics and the origin of Ishtar Terra, Venus, *Geophysical Research Letters*, 17(9), 1345–1348, doi:10.1029/GL017i009p01345.

- Bindschadler, D. L., G. Schubert, and W. M. Kaula (1992), Coldspots and hotspots: Global tectonics and mantle dynamics of Venus, *Journal of Geophysical Research: Planets*, 97(E8), 13495–13532, doi:10.1029/92JE01165.
- Fullea, J., J. C. Afonso, J. A. D. Connolly, M. Fernàndez, D. García-Castellanos, and H. Zeyen (2009), LitMod3D: An Interactive 3-D Software to Model the Thermal, Compositional, Density, Seismological, and Rheological Structure of the Lithosphere and Sublithospheric Upper Mantle, *Geochemistry, Geophysics, Geosystems*, 10, 21 pp., doi:2009 10.1029/2009GC002391.
- Fullea, J., M. Fernàndez, J. C. Afonso, J. Vergés, and H. Zeyen (2010), The structure and evolution of the lithosphere-asthenosphere boundary beneath the Atlantic-Mediterranean Transition Region, *Lithos*, 120, 74-95. doi: 10.1016/j.lithos.2010.03.003 .
- Fullea, J., M. Fernàndez, H. Zeyen, and J. Vergés (2007), A rapid method to map the crustal and lithospheric thickness using elevation, geoid anomaly and thermal analysis. Application to the Gibraltar Arc System, Atlas Mountains and adjacent zones, *Tectonophysics*, 430(1-4), 97–117, doi:10.1016/j.tecto.2006.11.003.
- Ghent, R. R., and I. M. Tibuleac (2002), Ribbon spacing in Venusian tessera: Implications for layer thickness and thermal state, *Geophysical Research Letters*, 29, 4 pp., doi:200210.1029/2002GL015994.
- Gilmore, M. S., M. A. Ivanov, J. W. Head, and A. T. Basilevsky (1997), Duration of tessera deformation on Venus, *Journal of Geophysical Research: Planets*, 102(E6), 13357–13368, doi:10.1029/97JE00965.
- Grimm, R. E. (1994), Recent deformation rates on Venus, *Journal of Geophysical Research: Planets*, 99(E11), 23163–23171, doi:10.1029/94JE02196.

- Grimm, R. E., and P. C. Hess (1997), The crust of Venus, in *Venus II: Geology, Geophysics, Atmosphere and Solar Wind Environment*, 1205–1244, The University of Arizona Press, Arizona.
- Grimm, R. E., and R. J. Phillips (1990), Tectonics of Lakshmi Planum, Venus: Tests for Magellan, *Geophysical Research Letters*, 17(9), 1349–1352, doi:10.1029/GL017i009p01349.
- Grimm, R. E., and R. J. Phillips (1991), Gravity anomalies, compensation mechanisms, and geodynamics of western Ishtar Terra, Venus, *Journal of Geophysical Research*, 96, 8305–8324, doi:10.1029/91JB00055.
- Hansen, V. L. (2013), Venus crustal plateaus and an analog for Archean cratons and SCLM, *Mineralogical Magazine*, 77(5), 1255.
- Hansen, V. L., B. K. Banks, and R. R. Ghent (1999), Tessera terrain and crustal plateaus, Venus, *Geology*, 27(12), 1071–1074, doi:10.1130/0091-7613(1999)027<1071:TTACPV>2.3.CO;2.
- Hansen, V. L., and R. J. Phillips (1995), Formation of Ishtar Terra, Venus: Surface and gravity constraints, *Geology*, 23(4), 292–296, doi:10.1130/0091-7613(1995)023<0292:FOITVS>2.3.CO;2.
- Hansen, V. L., and J. J. Willis (1998), Ribbon Terrain Formation, Southwestern Fortuna Tessera, Venus: Implications for Lithosphere Evolution, *Icarus*, 132(2), 321–343, doi:10.1006/icar.1998.5897.
- Head, J. W., L. S. Crumpler, J. C. Aubele, J. E. Guest, and R. S. Saunders (1992), Venus volcanism: classification of volcanic features and structures, associations, and global distribution from Magellan data, *Journal of Geophysical Research*, 97(E8), 13,153–

13,197, doi:10.1029/92JE01273.

Ivanov, M. A. (1988), The results of morphometric study of the tessera terrain of Venus from Venera 15/16 data, *Abstracts of the Lunar and Planetary Science Conference*, 19, 537–538.

Ivanov, M. A., and J. W. Head (2009), Geological mapping of the Fortuna Tessera quadrangle (V-2), Venus: Preliminary results, *40th Lunar and Planetary Science Conference*.

Jiménez-Munt, I., M. Fernández, J. Vergés, J. C. Afonso, D. Garcia-Castellanos, and J. Fulla (2010), Lithospheric structure of the Gorringer Bank: Insights into its origin and tectonic evolution, *Tectonics*, 29, 16 pp., doi:10.1029/2009TC002458.

Jull, M. G., and J. Arkani-Hamed (1995), The implications of basalt in the formation and evolution of mountains on Venus, *Physics of the Earth and Planetary Interiors*, 89(3–4), 163–175, doi:10.1016/0031-9201(95)03015-O.

Kaula, W.M., Lenardic, A., Bindshadler, D.L., and J. Arkani-Hamed (1997), Ishtar Terra, in *Venus II: Geology, Geophysics, Atmosphere and Solar Wind Environment*, 879-900, The University of Arizona Press, Arizona.

Keep, M., and V. L. Hansen (1994), Structural history of Maxwell Montes, Venus: Implications for Venusian mountain belt formation, *Journal of Geophysical Research: Planets*, 99(E12), 26015–26028, doi:10.1029/94JE02636.

Kiefer, W. S., and B. H. Hager (1991), Mantle Downwelling and Crustal Convergence: A Model for Ishtar Terra, Venus, *Journal of Geophysical Research*, 96(E4), 20,967–20,980, doi:10.1029/91JE02219.

Konopliv, A. S., W. B. Banerdt, and W. L. Sjogren (1999), Venus Gravity: 180th Degree and Order Model, *Icarus*, 139(1), 3–18, doi:10.1006/icar.1999.6086.

- Kucinskas, A. B., D. L. Turcotte, and J. Arkani-Hamed (1996), Isostatic compensation of Ishtar Terra, Venus, *Journal of Geophysical Research*, 101(E2), 4725–4736, doi:10.1029/95JE02979.
- Lenardic, A., W. M. Kaula, and D. L. Bindshadler (1991), The tectonic evolution of Western Ishtar Terra, Venus, *Geophysical Research Letters*, 18(12), 2209–2212, doi:10.1029/91GL02734.
- Lachenbruch, A. H., and P. Morgan (1990), Continental extension, magmatism and elevation; formal relations and rules of thumb, *Tectonophysics*, 174, 39–62.
- Namiki, N., and S. C. Solomon (1994), Impact crater densities on volcanoes and coronae on venus: implications for volcanic resurfacing, *Science*, 265(5174), 929–933, doi:10.1126/science.265.5174.929.
- Nimmo, F., and D. McKenzie (1998), Volcanism and Tectonics on Venus, *Annual Review of Earth and Planetary Sciences*, 26(1), 23–51, doi:10.1146/annurev.earth.26.1.23.
- Phillips, R. J., R. E. Grimm, and M. C. Malin (1991), Hot-Spot Evolution and the Global Tectonics of Venus, *Science*, 252(5006), 651 –658, doi:10.1126/science.252.5006.651.
- Pritchard, M. E., V. L. Hansen, and J. J. Willis (1997), Structural evolution of western Fortuna Tessera, Venus, *Geophysical Research Letters*, 24(18), 2339–2342.
- Pronin, A.A. (1986) The structure of Lakshmi Plateau, an indication of asthenosphere horizontal flows on Venus, *Geotectonika*, 20, 271-280.
- Ranalli, G. (1995) *Rheology of the Earth*, Chapman and Hall, London.
- Rappaport, N. J., A. S. Konopliv, A. B. Kucinskas, and P. G. Ford (1999), An Improved 360 Degree and Order Model of Venus Topography, *Icarus*, 139(1), 19–31,

doi:10.1006/icar.1999.6081.

Reynolds, J. M. (1997), *An introduction to applied and environmental geophysics*, John Wiley and Sons, West Sussex, England.

Riley, K. M., R. C. Anderson, and B. J. Peer (1995), Lineament analysis of Fortuna Tessera, Venus: Results from an ongoing study, *Abstracts of the Lunar and Planetary Science Conference*, 26.

Roberts, K. M., and J. W. Head (1990), Western Ishtar Terra and Lakshmi Planum, Venus: Models of formation and evolution, *Geophysical Research Letters*, 17(9), 1341–1344.

Rogers, N. (2008), *An introduction to our dynamic planet*, Cambridge University Press, United Kingdom.

Romeo, I., and D. L. Turcotte (2008), Pulsating continents on Venus: An explanation for crustal plateaus and tessera terrains, *Earth and Planetary Science Letters*, 276(1–2), 85–97, doi:10.1016/j.epsl.2008.09.009.

Schubert, G., V. S. Solomatov, P. J. Tackley, and D. L. Turcotte (1997), *Mantle convection and the thermal evolution of Venus*, 1245–1288, The University of Arizona Press, Arizona.

Schubert, G., and D. L. Turcotte (2002), *Geodynamics*, 456 pp., Cambridge University Press, New York.

Simons, M., S. C. Solomon, and B. H. Hager (1997), Localization of gravity and topography: constraints on the tectonics and mantle dynamics of Venus, *Geophysical Journal International*, 131(1), 24–44, doi:10.1111/j.1365-246X.1997.tb00593.x.

Sjogren, W. L., W. B. Banerdt, P. W. Chodas, A. S. Konopliv, G. Balmino, J. P. Barriot, J. Arkani-Hamed, T. R. Colvin, and M. E. Davies (1997), The Venus gravity field and

other geodetic parameters, in *Venus II: Geology, Geophysics, Atmosphere and Solar Wind Environment*, 1125–1161, The University of Arizona Press, Arizona.

Smrekar, S. E., and R. J. Phillips (1991), Venusian Highlands: Geoid to Topography Ratios and their Implications, *Earth and Planetary Science Letters*, 107(3-4), 582–597, doi:10.1016/0012-821X(91)90103-O.

Solomon, S. C., and J. W. Head (1984), Venus banded terrain: tectonic models for band formation and their relationship to lithospheric structure, *Journal of Geophysical Research*, 89, 6885–6897.

Solomon, S. C., and J. W. Head (1990), Lithospheric Flexure Beneath the Freyja Montes Foredeep, Venus: Constraints on Lithospheric Thermal Gradient and Heat Flow, *Geophysical Research Letters*, 17(9), 1393–1396, doi:199010.1029/GL017i009p01393.

Steinbach, V., and D. A. Yuen (1992), The effects of multiple phase transitions on Venusian mantle convection, *Geophysical Research Letters*, 19(22), 2243–2246, doi:10.1029/92GL02319.

Sukhanov, A. L. (1986), Parquet: Regions of areal plastic dislocations, *Geotectonics*, 20, 294–305.

Taylor, J. R. (1982), *An introduction to error analysis*, Mill Valley, California, University Science Books.

Turcotte, D. L. (1993), An Episodic Hypothesis for Venusian Tectonics, *Journal of Geophysical Research*, 98(E9), 17,061–17,068, doi:199310.1029/93JE01775.

Vorder Bruegge, R. W. V., and J. W. Head (1989), Fortuna Tessera, Venus: Evidence of horizontal convergence and crustal thickening, *Geophysical Research Letters*, 16(7),

699–702, doi:10.1029/GL016i007p00699.

Vorder Bruegge, R. W. V., and J. W. Head (1990), Tectonic Evolution of Eastern Ishtar Terra, Venus, *Earth Moon Planets*, 50-51(1), 251–304, doi:10.1007/BF00142396.

Wieczorek, M. A. (2007), Gravity and Topography of the Terrestrial Planets, *Treatise on Geophysics*, 165–206.

Young, H. D. (1962), *Statistical treatment of data*, New York, McGraw-Hill Inc.

Zuber, M. T., and E. M. Parmentier (1990), On the relationship between isostatic elevation and the wavelengths of tectonic surface features on Venus, *Icarus*, 85(2), 290–308, doi:10.1016/0019-1035(90)90118-S.

7. Constraining the Internal Dynamics of Venus and its Contribution to Topography at Atla and Beta Regio

Elyse Schinella and Craig O'Neill

Abstract. Venus and Earth share many similar characteristics such as size, mass, volume, and density, however the factors controlling Venus's internal dynamics, and the contribution these have in shaping the observed surface topography at the volcanic rises Atla and Beta Regio, are highly unconstrained. We use 3D spherical shell numerical simulations with temperature- and pressure-dependent viscosity to estimate the contribution of varying the Rayleigh number, internal heating, pre-exponential factor, and activation energy to Venus's internal dynamics. The best-fit model to Venus's observed geoid and topography uses an effective Rayleigh number of 2.5×10^7 , internal heating of 40, activation energy of 10, and a lower mantle 3 times more viscous than the upper mantle. To constrain the amount of dynamic uplift occurring at Atla and Beta Regio, localised admittance and correlation calculations were also performed for two upwelling plumes and compared to estimated and observed values. Long wavelength dynamic support is required at both rises and can contribute ~ 1.5 km and ~ 0.5 km to the observed topography and 120 m and 110 m to the observed geoid at Atla and Beta Regio, respectively. Our findings imply ~ 60 locations, such as volcanoes and coronae, may be supported by localised upwellings. These upwelling mantle plumes may facilitate partial melting, up to $\sim 21\%$, and possible volcanism, if the mantle is hydrated.

7.1 Introduction

Stresses associated with either stagnant-lid or episodic mantle convection may currently

contribute to localised volcanism and the support of volcanic rises and coronae.

Approximately 9 large Venusian volcanic rises have been attributed to topographic compensation associated with primary upwelling mantle plumes, while ~513 coronae may be representative of secondary plumes [Smrekar and Sotin, 2012; Stofan *et al.*, 1995; Stofan and Smrekar, 2005]. Two such large volcanic rises are Atla and Beta Regio located along Venus's equator and within the mid-latitudes, respectively (Figure 7.1) [Basilevsky and Head, 2007; Senske and Head, 1992]. These rises most likely have a mantle plume origin based on their high elevations (3-4 km), high geoid anomalies (~120-150 m), domal morphologies, presence of volcanoes, large dissecting rifts, high Geoid-to-Topography Ratios (GTRs) and peaks in the geoid and topography admittance at low spherical harmonic degrees [Basilevsky and Head, 2007; Kiefer and Hager, 1991; Moresi and Parsons, 1995; Senske and Head, 1992; Simons *et al.*, 1994, 1997; Smrekar and Phillips, 1991; Vezolainen *et al.*, 2004]. Since both thermal thinning of the lithosphere and dynamic uplift can contribute to the long-wavelength support of these rises, dynamic uplift estimates are highly unconstrained, ranging from a minimum of 200 m to 5.7 km [Kiefer and Hager, 1991; Stofan *et al.*, 1989, 1995; Vezolainen *et al.*, 2004]. This ambiguity regarding the amount of dynamic topography is further compounded by the difficulty in constraining suitable mantle parameters. Three-dimensional spherical shell mantle convection simulations have been applied to Venus [Huang *et al.*, 2013; Smrekar and Sotin, 2012], but have primarily focused on the influence of varying Rayleigh number, the pre-exponential factor, mantle viscosity, Core-Mantle Boundary (CMB) temperature, Clapeyron slope magnitude, and internal heating.

These previous models either do not include phase transitions and pressure-dependent viscosity or do not address the effect of varying activation energy, which can significantly influence the temperature-dependency of viscosity, wavelengths of convective structures, lid thickness, and the resulting dynamic topography and geoid [Christensen, 1984; Zhong *et al.*,

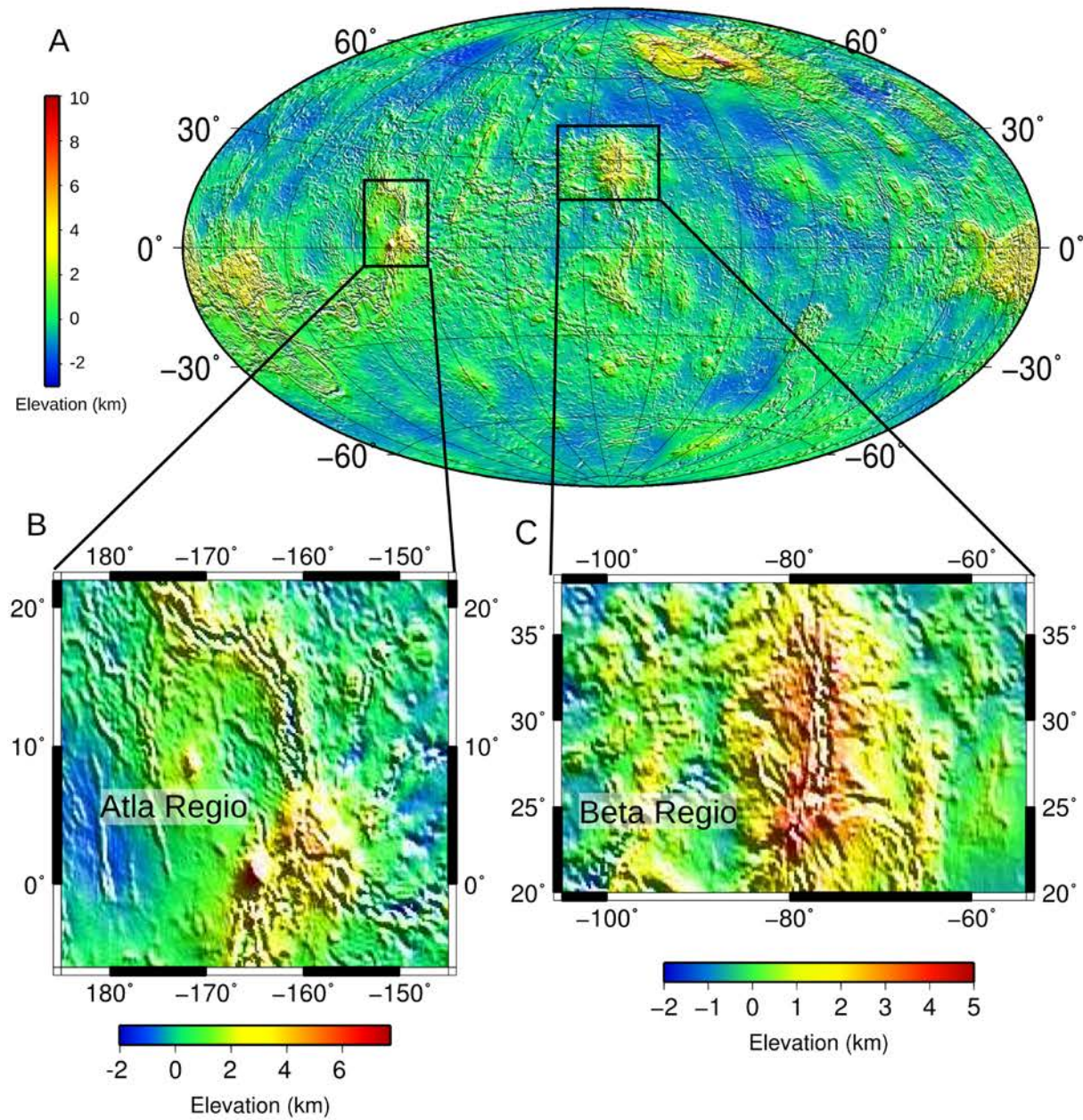


Figure 7.1. (A) Global elevation map showing Atla Regio located along Venus's equator and Beta Regio within the mid-latitudes. (B-C) Regional elevation maps of Atla and Beta Regio.

2000].

Unlike other studies that have used 2D geometries or regional models to constrain Venus's mantle dynamics and its contribution to the observed geoid and topography at Atla and Beta Regio, our study combines 3D global spherical shell convection models with localised

admittance and correlation calculations [Benešová and Čížková, 2012; Kiefer and Hager, 1991; McKenzie, 1994; Pauer *et al.*, 2006; Solomatov and Moresi, 1996; Vezolainen *et al.*, 2004]. CitcomS, a finite-element numerical software, was used to model 3D mantle convection, in conjunction with SHTOOLS, a spherical harmonic software package, which was used to calculate the localised geoid and topography admittance and correlation [Simons *et al.*, 1997; Tan *et al.*, 2006; Wieczorek and Simons, 2005, 2007; Zhong *et al.*, 2000]. This study has important implications for our understanding of Venus's internal dynamics, possible current volcanic activity and the contribution of long-wavelength compensation mechanisms in supporting the observed topography at Atla and Beta Regio.

7.2 Background

7.2.1 Numerical Modelling

Huang *et al.* [2013] recently constrained a model of Venus's mantle convective structure to global geoid and topography spectra. Assuming both temperature and pressure-dependent viscosity, the best fit model, which also reproduced the number (~ 8) of hypothesized mantle plumes on Venus, involved a Rayleigh number of 1.8×10^7 , a non-dimensional internal heating ratio of 40, uniform viscosity, pre-exponential factor of 1, Clapeyron slope magnitudes of ± 3.5 MPa K⁻¹, and an activation energy of 150 kJ mol⁻¹, corresponding to a Newtonian rheology. However, higher activation energies (430-540 kJ mol⁻¹), representing a non-Newtonian rheology, may be more appropriate for Venus if the mantle is dry [Grimm and Solomon, 1988; Kaula, 1995; Nimmo and McKenzie, 1998; Solomatov and Moresi, 1996].

The influence of both a low (154 kJ mol⁻¹) and high (485 kJ mol⁻¹) activation energies on Venus's internal dynamics was modelled by Smrekar and Sotin [2012]. Lower activation

energies (240-300 kJ mol⁻¹) result in thin conductive lids (180 km), lower mantle temperatures (1681 K), and more buoyant upwellings, than higher values [Smrekar and Sotin, 2012; Solomatonov and Moresi, 1996]. This study was effective in constraining the contribution of activation energy to Venus's internal dynamics, however it did not address the contribution that these values have on the wavelength of convective structures or the observed geoid and topography.

Whether pressure-dependent viscosity, and in turn phase change transitions, should be included in numerical models of Venus's interior is also debatable [Huang *et al.*, 2013; Smrekar and Sotin, 2012]. Including these phase transitions in models of Venus's mantle convection could have a significant influence on the dynamics of the interior, promoting layered rather than whole mantle convection, and facilitating higher internal heating ratios as the interior transfers less heat [Reese *et al.*, 1998; Steinbach and Yuen, 1992].

The depths to these phase changes are also different to those proposed for Earth [Steinbach and Yuen, 1992]. Venus's diminished pressure gradients (by ~10%) act to increase the depths of the phase changes to 490 km and 690 km and the 730 K surface temperature steepens the upper mantle "geotherms", reducing the depth between the two transitions [Steinbach and Yuen, 1992]. In contrast, Smrekar and Sotin [2012] chose not to include pressure-dependent viscosity, including the effects of phase transitions, because of the high uncertainties surrounding Venus's activation volume, adiabatic and isoviscous temperature gradients.

The viscosity configuration of Venus's interior mantle is also highly unconstrained and has been the focus of a number of studies [Benešová and Čížková, 2012; Pauer *et al.*, 2006; Ratcliff *et al.*, 1997; Schubert *et al.*, 1997]. Ratcliff *et al.* [1997] addressed the effects of increasing the viscosity contrast between the lid and upper mantle on convection. With higher

viscosity contrasts (10^4 to 10^5) and a Rayleigh number of 10^5 , convection occurs within a stagnant-lid regime where mantle flow becomes localised, characterised by narrower upwellings within linear downwellings [Ratcliff *et al.*, 1997; Schubert *et al.*, 1997]. Higher viscosity contrasts between the lid and upper mantle enhances a rigid lithosphere producing intense convection with slight variations in temperature, where heat is transported quickly, but at reduced amounts [Schubert *et al.*, 1997].

Stagnant-lid convection and the resulting highly viscous lid is also facilitated when temperature-dependent viscosity is included in simulations [Schubert *et al.*, 1997]. However, the convective regime can become more sluggish if temperature-dependent viscosity is combined with phase change transitions. Schubert *et al.* [1997] used a constant Rayleigh number of 10^6 and a Clapeyron slope of 2 MPa K^{-1} and -4 MPa K^{-1} at a depth of 440 km and 740 km, respectively. Within the sluggish-lid convective regime, significant layering was promoted by laterally extensive, symmetrical downwellings. The significant stresses within the upper boundary layer, where these downwellings propagated from, reduced their negative buoyancy making them unable to infiltrate the positive buoyancy of the phase change transition, increasing the tendency for layered mantle convection and a reduction of heat loss through the surface.

Previous studies that have varied the activation energy have not included phase changes, whereas those that have included phase changes have assumed a constant activation energy [Huang *et al.*, 2013; Schubert *et al.*, 1997; Smrekar and Sotin, 2012]. This study, however, considers a broad range of activation energies, includes temperature- and pressure-dependent viscosity and the endothermic and exothermic phase transitions, within a realistic 3D spherical shell geometry.

7.2.2 Localised Admittance and The Dynamic Contribution

Mantle dynamics within a planet can be indirectly constrained to a planet's observed geoid and topography. Geoid and topography are related by an admittance function, which is the covariation of geoid height and elevation, where the magnitude and sign of the admittance, depends on both wavelength and position [Simons *et al.*, 1997]. A number of authors have used GTRs to constrain the compensation mechanisms occurring at Atla and Beta Regio. In its most basic sense, GTR is similar to admittance, and related to the change in geoid height divided by topography, varying only as a function of position. Admittance can provide a greater constraint since it also includes wavelength and does not require us to assume the topography is compensated at a particular depth [Simons *et al.*, 1997].

Simons *et al.* [1997] used spatio-spectral localisation of geoid and topography data to calculate the spectral admittance and delineate whether surface features are compensated due to dynamic forces within the mantle or isostatic mechanisms. Considering the global admittance of geoid and topography, the volcanic rises have a higher admittance than the crustal plateaus and tessera. For degree 8 the admittance at Atla Regio ranges from ~ 32 to 36 m km^{-1} , followed by Beta Regio (~ 28 to 32 m km^{-1}), while at degree 16 the admittance decreases to $\sim 20 \text{ m km}^{-1}$ and 24 m km^{-1} , respectively [Simons *et al.*, 1997]. These values are in agreement with those of an earlier study that resulted in admittance values of $20\text{-}25 \text{ m km}^{-1}$ for Atla Regio and 30 m km^{-1} for Beta Regio at degrees $10\text{-}20$ [Simons *et al.*, 1994]. The admittance at Atla and Beta Regio imply these areas are dynamically compensated from mantle upwellings with some contribution from a thick crust associated with the observed volcanism and the associated intrusion of magma [Simons *et al.*, 1994].

The admittance or the geoid and topography observed at Atla and Beta Regio was reproduced

by convection models [Benešová and Čížková, 2012], non-linear axisymmetric convective models [McKenzie, 1994], cylindrical axisymmetric numerical models [Kiefer and Hager, 1991], and geodynamic inversions [Pauer *et al.*, 2006]. Results from each of these methods could fit the data equally well even though they used different Rayleigh numbers, viscosity structures and values of lithospheric thickness.

A Rayleigh number of $\sim 10^6$ was found to produce a gravity and topography admittance of 50 mGal km⁻¹ at Atla and Beta Regio [McKenzie, 1994]. A similar Rayleigh number of 10^6 , in conjunction with an isoviscous model, or a Rayleigh number of 10^7 and a viscosity contrast of 10 between the lid and upper mantle, were also found to match the observed geoid and topography within these areas [Kiefer and Hager, 1991].

The properties of the lithosphere could also influence the observed geoid and topography with Pauer *et al.* [2006] proposing the a thick lithosphere and constant viscosity, or a highly viscous lithosphere with a gradual increase in viscosity, could fit the observables equally well. Benešová and Čížková [2012] were able to constrain these parameters further with a model involving a 200 km thick lithosphere, a 2×10^{21} Pa s upper mantle viscosity, a Rayleigh number of 2.8×10^6 and a slight increase of viscosity with depth [Benešová and Čížková, 2012].

These previous studies have either not used a 3D spherical shell geometry of Venus's mantle convection or they have assumed that the high observed admittance, at low spherical harmonic degrees within Atla and Beta Regio, is only attributed to convective stresses within the mantle. This study, however, used global convection models to produce a dynamically self-consistent convective structure and assumes that the long wavelength compensation at these rises is not solely related to dynamic uplift.

7.3 Methodology

7.3.1 Introduction

We used CitcomS and varied the Rayleigh number, pre-exponential factor, internal heating, and activation energy in order to understand how these parameters can influence Venus's internal dynamics [Tan *et al.*, 2006; Zhong *et al.*, 2000]. Each model included temperature- and pressure-dependent viscosity with each simulation having free-slip boundary conditions at the surface and basal boundary. Lithospheric thickness evolves during the simulation and is dependent on the chosen thermal parameters. The lithospheric thickness we calculated for each model was found by taking an average depth for each cap between the non-dimensional temperature range of 0.48 to 0.52.

To model these complex global mantle convection simulations within reasonable computational time frame, each dimensional parameter was scaled to non-dimensional values, as outlined in sections (7.3.2 to 7.3.4). All non-dimensional values are shown as primes ('). To constrain the most plausible mantle parameters for Venus, geoid and topography data obtained from each model run was compared to observed geoid and topography. Equations relating to how geoid and topography are calculated in CitcomS are outlined in section 7.3.5.

7.3.2 Governing equations

The mantle convection modelled by CitcomS depends on the following equations relating to the conservation of mass, energy and momentum [Tan *et al.*, 2006; Zhong *et al.*, 2000]:

$$(\rho u_i)_{(,i)} = 0 \quad (7.1)$$

$$-P_{(,i)} + \left(\left(\eta(u_{(i,j)} - \frac{2}{3} u_{(k,k)} \delta_{(ij)}) \right)_{(,i)} - \delta \rho g \delta_{(ir)} \right) = 0 \quad (7.2)$$

$$\rho c_P (T_{(,t)} + u_i T_{(,i)}) = \rho c_P \kappa T_{(,ii)} - \rho \alpha g u_r T + \Phi + \rho (Q_{(L,t)} + u_i Q_{(L,i)}) + \rho H \quad (7.3)$$

where ρ is the density, u is the velocity, P is the dynamic pressure, η is the viscosity, δ_{ij} Kroneker delta tensor, $\delta\rho$ is the density anomaly, g is the gravitational acceleration, T is the temperature, c_P is the heat capacity, κ is the thermal diffusivity, α is the thermal expansivity, Φ is the viscous dissipation, Q_L is the latent heat from the phase boundaries, and H is the heat production rate. In relation to the subscripts, i, j , and k are spatial indices, r is the radial direction, and t is time.

The density anomalies $\delta\rho$ depend on the temperature, composition, and phase changes within the mantle and are calculated from [Tan et al., 2006; Zhong et al., 2000]:

$$\delta\rho = -\alpha\rho(T - T_a) + \delta\rho_{ph}\Gamma + \delta\rho_{ch}C \quad (7.4)$$

where ρ , T_a , $\delta\rho_{ph}$, $\delta\rho_{ch}$, and C are the radial lineaments of density, adiabatic temperature, density contrast crossing the phase boundary, density contrast due to composition, and the composition. The phase function, Γ is defined as [Tan et al., 2006; Zhong et al., 2000]:

$$\Gamma = \frac{1}{2} \left(1 + \tanh \frac{\pi}{(\rho g w_{ph})} \right) \quad (7.5)$$

$$\pi = \rho g (1 - r - d_{ph}) - \gamma_{ph} (T - T_{ph})$$

where π , d_{ph} , T_{ph} , γ_{ph} , and w_{ph} are the reduced pressure, initial phase change depth, phase change temperature, the Clapeyron slope of the phase change, and phase change width, respectively.

7.3.3 Physical Properties

Rayleigh number controls the vigour of convection of a fluid that experiences basal heating and cooling from above. Mantle thickness is usually used to calculate Rayleigh number, however, CitcomS scales this parameter using planetary radius [Tan *et al.*, 2006; Zhong *et al.*, 2008]:

$$Ra = \frac{(\rho_0 g_0 \alpha_0 \Delta T R_0^3)}{(\eta_0 \kappa_0)} \quad (7.6)$$

where ρ_0 , g_0 , α_0 , ΔT , R_0 , κ_0 , and η_0 are the reference density, gravitational acceleration, thermal expansivity, temperature change between the Core-Mantle-Boundary (CMB) and the surface, radius of Venus, viscosity, and thermal diffusivity, respectively. The values for each of these parameters are shown in Table 7.1.

Table 7.1. Dimensional Mantle Convection Parameters

Parameter*	Symbol	Value
Density	ρ_0	3300 kg m ⁻³
Gravitational acceleration	g_0	8.87 m s ⁻²
Thermal expansivity	α_0	2x10 ⁻⁵ K
Temperature contrast	ΔT	2500 K
Radius	R_0	6050 km
Viscosity	η_0	2x10 ²¹ Pa s
Thermal diffusivity	κ_0	8.1x10 ⁻⁷ m ² s ⁻¹
Inner radius	r_c	3330 km
Surface temperature	T_s	730 K
Activation energy	E^*	1.5x10 ⁶ J mol ⁻¹ to 4.2x10 ⁶ J mol ⁻¹
Activation volume	V^*	1.5 cm ⁻³ mol ⁻¹
Dissipation number	D	0.89
Gas constant	R	8.3 J mol ⁻¹ K ⁻¹

*Reference values, taken from Huang *et al.* [2013].

The mantle viscosity η' depends on both temperature and pressure, with variations in the pre-exponential factor η_r' and its influence on the viscosity contrast between the upper and lower mantle being a focus of this study. The non-dimensional viscosity calculated from Equation 7.7 is both temperature and pressure dependent [Tan *et al.*, 2006; Zhong *et al.*, 2008]. The pressure dependency of viscosity is represented in Equation 7.7 through the non-dimensional radial position r' and core radius r_{core}' since pressure increases with greater depths through the mantle:

$$\eta' = \eta_r' \exp \left[\frac{(E' + V'(1 - r'))}{(T' + T_s')} - \frac{(E' + V'(1 - r_{core}'))}{(1 + T_s)} \right] \quad (7.7)$$

$$E' = \frac{(E^*)}{(R \Delta T)} \quad (7.8)$$

$$V' = \frac{(\rho_0 g_0 D V^*)}{(R \Delta T)} \quad (7.9)$$

where E' and V' are the non-dimensional values of activation energy E^* and volume V^* , R is the gas constant, and D is the dissipation number (Table 7.1). The parameters r_{core}' , T' and T_s' are the non-dimensional core radius, temperature, and surface temperature, respectively.

The endothermic and exothermic boundaries can have a significant influence on upwelling and downwelling mantle plumes. These phase transitions can cause changes to the properties and dynamics of upwelling mantle plumes [Bossman and Keken, 2013] and, in turn, the lithospheric thickness, melting, and volcanism [Schubert and Goldman, 2012]. During a model simulation, the depths of the phase changes vary in response to upwelling and downwellings. For example, an upwelling mantle plume interacting with the endothermic phase change can result in the upward shift of the transition and release of latent heat, causing the plume to become more buoyant [Schubert *et al.*, 2001]. These phase changes can cause

density, viscosity, composition, temperature, and latent heat changes within an upwelling or downwelling.

Huang et al. [2013] found an exothermic Clapeyron slope of +3.5 Pa K⁻¹ and an endothermic Clapeyron slope of -3.5 Pa K⁻¹ reproduced the most realistic number of mantle plumes on Venus, the observed geoid height, and observed topography.

This value was non-dimensionalised using [*Tan et al.*, 2006; *Zhong et al.*, 2008]:

$$\gamma_{ph}' = \frac{(\gamma_{ph} \Delta T)}{(\rho_0 g_0 R_0)} \quad (7.10)$$

The magnitude of the phase change remained the same for both transitions, however, the sign changed to +3.5 Pa K⁻¹ for the exothermic phase change (olivine to spinel) and -3.5 Pa K⁻¹ for the endothermic phase change (spinel to perovskite).

The depths of these phase changes d_{ph} are fixed and occur at depths of 490 km and 690 km [*Huang et al.*, 2013; *Steinbach and Yuen*, 1992]. The non-dimensional d_{ph}' values of these depths were found from [*Tan et al.*, 2006; *Zhong et al.*, 2008]:

$$d_{ph}' = \frac{d_{ph}}{R_0} \quad (7.11)$$

7.3.4 Model Setup

Each of the governing equations presented in Section 7.3.2 are performed in a 3D spherical shell domain. This spherical shell is divided into 12 equidimensional caps where

each of these caps are further subdivided into 96 elements.

Each model used four layers representing the depth to the base of the lithosphere, the depth to the 440 km phase change, the depth to the 690 km phase change, and the depth to the CMB, respectively. For each model, we altered the activation energy E' , Rayleigh number Ra' , and internal heating H' . The pre-exponential factor η_r' for layers 2 and 3 was also changed (Table 7.2).

Table 7.2. Modelled Input Parameters*

Case	$Ra'\dagger$	H'	$\eta_r'^{**}$	E'
1	2×10^8	40	1	7.20
2	2×10^7	40	1	7.20
3	2×10^6	40	1	7.20
4	2×10^8	40	1	7.20
5	2×10^8	40	30	7.20
6	2×10^7	40	0.1	7.20
7	2×10^7	20	1	7.20
8	2×10^7	40	3	20.7
9	7×10^7	20	3	20.7
10	7×10^7	30	3	22
11	9×10^7	30	3	20
12	2×10^8	30	3	20
13	2×10^8	40	3	16
14	2×10^8	40	3	10

* Parameters are Rayleigh number Ra' , internal heating H' , pre-exponential factor η_r' , activation energy E' .

† Rayleigh number as considered by CitcomS i.e. scaled to Venus's radius.

** Pre-exponential factor for layer 3 (depth to the 690 km phase transition), except for Case 6 that has a value 0.1 for layer 2 (depth to the 490 km phase transition).

7.3.5 Dynamic Topography and Geoid

CitcomS calculates the dynamic topography, under free-slip boundary conditions, by assuming that the vertical (normal) stresses occurring on the surface of the upper boundary are due to

surface deformities [Tan *et al.*, 2012]. For the surface and CMB, the dimensionless dynamic topography (s' , b') and gravitational potential (φ_s' , φ_b') for each spherical harmonic degree l were found from [Zhong *et al.*, 2008]:

$$s' = \sigma_{rrs}' + q_s \varphi_s' \quad (7.12)$$

$$b' = \sigma_{rrb}' + q_b \varphi_b' \quad (7.13)$$

$$\varphi_s' = \frac{1}{(2l+1)} \left[\left(r_b' \frac{(r_b')}{(r_t')} \right)^{(l+1)} b + r_t' s' - r_o' \left(\frac{(r_o')}{(r_t')} \right)^{(l+1)} \right] \quad (7.14)$$

$$\varphi_b' = \frac{1}{(2l+1)} \left[r_b' + r_t' \left(\frac{(r_b')}{(r_t')} \right)^l s' - r_o' \left(\frac{(r_b')}{(r_o')} \right)^l \right] \quad (7.15)$$

where σ_{rrs}' and σ_{rrb}' are the reduced radial stress at the surface and CMB, respectively. The dimensionless delta function buoyancy is r_o' and the radial location of the surface is $r_t' = 1$ and CMB is $r_b' = 0.55$. The parameters q_s and q_b are found from Zhong *et al.* [2008]:

$$q_s = \frac{(4\pi G R_0 \Delta \rho_t)}{g_0} \quad (7.16)$$

$$q_b = \frac{(4\pi G R_0 \Delta \rho_b)}{g_0} \quad (7.17)$$

where the density contrast across the surface $\Delta \rho_t$ and CMB $\Delta \rho_b$ are 3300 kg m^{-3} and 5400 kg m^{-3} , respectively. The dimensional radius R_0 is 6050 km, the gravitational acceleration g_0 is 8.87 m s^{-2} , and the universal gravitational constant G is $6.67 \times 10^{-11} \text{ m}^3 \text{ kg}^{-1} \text{ s}^{-2}$.

The surface potential φ_s' can then be used with Equation 7.18 to determine the dimensionless geoid anomalies h_s' at the surface [Zhong *et al.*, 2008]:

$$h_s' = \frac{(\varphi_s')}{g_0} \quad (7.18)$$

Both the non-dimensional dynamic topography s' and geoid h_s' at the surface can be scaled to dimensional values using [Moresi and Parsons, 1995]:

$$s = s' \frac{(\eta_0 \kappa_0)}{(R_0^2 \rho_0 g_0)} \quad (7.19)$$

$$h_s = h_s' \frac{(2 \pi G \eta_0 \kappa_0)}{(g_0^2 R_0)} \quad (7.20)$$

where η_0 , κ_0 , ρ_0 , σ_0 is the reference viscosity, thermal diffusivity, density, and surface density, respectively.

7.3.6 Observed Topography and Geoid

In order to constrain Venus's internal mantle dynamics and the parameters controlling convection we compared the modelled geoid and topography output from CitcomS to observed data sets of topography and geoid (Figure 7.2). The topography data set is the 719 degree and order spherical harmonic model from *Wieczorek* [2007] and was referenced to a Mean Planetary Radius of 6051.848 km. Most of the topography in this data set originated from Magellan's Global Topography Data Record 3.2 (GTDR 3.2) with gaps in data coverage filled by Pioneer and Venera 15/16 altimetry [Wieczorek, 2007]. A 2D Fast Fourier Transform was used to integrate the 180th degree and order spherical harmonic model (SHGJ180u) of Venus's free-air gravity to obtain the geoid data set [Sjogren *et al.*, 1997; Wessel and Smith, 1991, 1998].

From Figure 7.2 areas of high topography are associated with highlands, mountain belts, and volcanic rises such as Ishtar Terra, Maxwell Montes, Atla and Beta Regio. These areas of high topography are strongly correlated to high geoid anomalies. This positive correlation between geoid and topography on Venus, unlike that observed on Earth, has lead some authors to propose Venus lacks an asthenosphere [Bindschadler *et al.*, 1992; Höink *et al.*, 2012; Kaula *et al.*, 1994; Phillips *et al.*, 1991; Richards *et al.*, 2001].

7.3.7 Admittance and Correlation

Localised spectral admittance and correlation was calculated using SHTOOLS for both the observed topography and geoid, as well as the estimated and modelled dynamic topography at each location [Wieczorek and Simons, 2005]. Before the admittance and correlation functions were solved, we first had to define one spatial and spectral axisymmetric localisation window, which were defined by an angular radius α [Wieczorek and Simons, 2005]. The parameters used for each of these windows, at each area, are shown in Table 7.3 and were calculated from:

$$\alpha = 2 \arctan \frac{r}{2D} \quad (7.21)$$

where D is the radius of Venus, equal to 6051 km and r is the angular radius for each area.

Multiple orthogonal tapers have been used in this study since they have been found to provide uniform energy distribution over the concentration area, representing the feature better than that of a single taper [Wieczorek and Simons, 2005]. For each taper used, the window was moved to the position defined by the center coordinates within the spherical harmonic geometry and then expanded to the space domain. The geoid and topography data were then

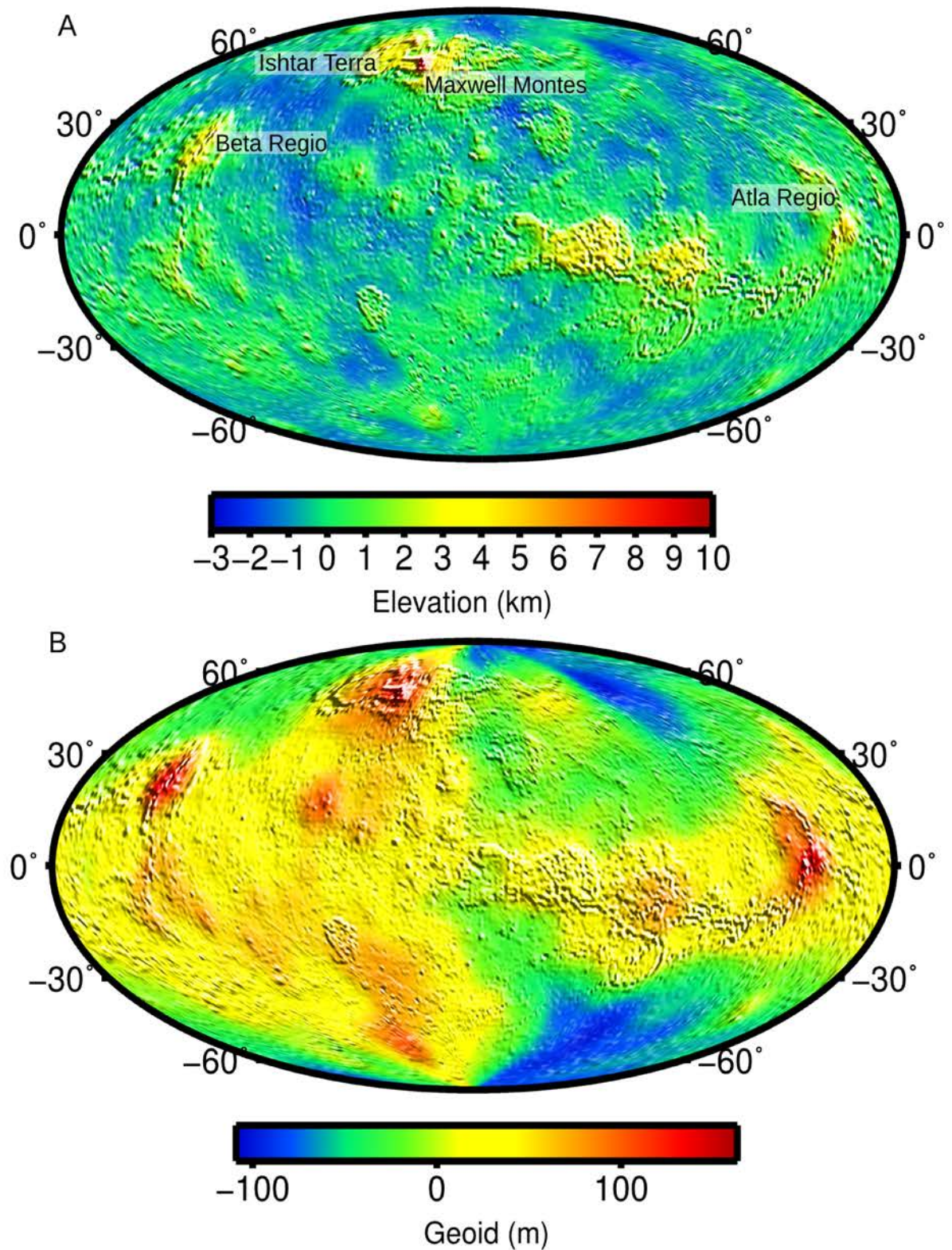


Figure 7.2. (A) Global map of Venus's elevation and (B) Geoid. Areas of high elevation and high geoid anomalies correspond to highlands, mountain belts, and volcanic rises. The elevation map is referenced to a Mean Planetary Radius of 6051.848 km.

Table 7.3. Localisation Window Parameters

Area	Angular Radius (°)	Radius of Area (km)	Center Longitude (°E)	Center Latitude (°N)
Atla Regio [*]	14	1500	195	8
Beta Regio [*]	12	1250	280	29
Plume 1 [†]	14	1500	152	-15
Plume 2 [†]	12	1250	35	-30

^{*} Using Venus's total observed topography and geoid.

[†] Using the dynamic topography and geoid from Case 14.

multiplied by this window, with the result being expanded in spherical harmonics using a Fourier transformation [Wieczorek and Simons, 2005].

The cross-power spectra $S_{\Phi\Gamma}(l)$ was then found from Equations 7.22 and 7.23 for each taper, with the multitaper estimate being found by taking an average:

$$S_{(\Phi\Gamma)}(l) = \sum_{m=-l}^l \Phi_{lm} \Gamma_{lm} \quad (7.22)$$

$$\begin{aligned} \Phi_{lm} \Gamma_{lm} = & \frac{1}{(4\pi)} \int_{\Omega} [h(\theta)f(\Omega)] Y_{lm}(\Omega) d\Omega \\ & \cdot \frac{1}{(4\pi)} \int_{\Omega} [h(\theta)g(\Omega)] Y_{lm}(\Omega) d\Omega \end{aligned} \quad (7.23)$$

where l is the degree, m is the order, with Φ_{lm} and Γ_{lm} being the spherical harmonic coefficients of the two windowed fields. The function $h(\theta)$ is the axisymmetric window, $f(\Omega)$ and $g(\Omega)$ are two arbitrary functions defined on the sphere Ω .

In the simplest case, admittance can be defined as the change in geoid height with elevation, with the correlation being how well the geoid anomalies match the elevation anomalies [Simons *et al.*, 1994]. The multitaper admittance $Z_{(\Phi\Gamma)}$ and correlation $\gamma_{(\Phi\Gamma)}$ estimate of $f(\Omega)$ and $g(\Omega)$ for degree l was found from:

$$Z_{(\phi\Gamma)}(l) = \frac{(S_{(\phi\Gamma)}(l))}{(S_{(\phi\phi)}(l))} \quad (7.24)$$

$$\gamma_{(\phi\Gamma)}(l) = \frac{(S_{(\phi\Gamma)}(l))}{\sqrt{(S_{(\phi\phi)}(l))S_{(\Gamma\Gamma)}(l)}} \quad (7.25)$$

7.4 Results

Each model case shown in Table 7.4 was run until convection was steady-state and within the stagnant-lid regime characterised by a thick immobile lid. The effects of varying Rayleigh number, pre-exponential factor, internal heating, and activation energy are discussed in Sections 7.4.1 to 7.4.4.

7.4.1 Rayleigh Number

Cases 1-3 have variable Rayleigh numbers and fixed pre-exponential factors of 1 and internal heating values of 40 (Table 7.4). Case 1 has a high Rayleigh number (2×10^8), dynamic topography of up to ~ 4 km and geoid highs of 300 m over numerous, narrow, localised upwellings (Figures 7.3-7.5A). In the temperature and velocity slices shown, the hotter upwelling plumes have lower vertical velocities than the colder downwellings (Figures 7.6-7.7A). The vigorous convection associated with the higher Rayleigh number is also efficient at transferring heat from the interior and thinning the lithosphere (~ 204 km).

Cases 2 and 3 have lower Rayleigh numbers, 2×10^7 and 2×10^6 , respectively (Table 7.4). Less vigorous convection produces lower elevations and higher geoid anomalies over sites of mantle upwelling (Figures 7.3-7.4B-C). The morphology of these plumes also change with decreasing Rayleigh number, with the plume head becoming more elongated (Figure 7.5B-C).

Table 7.4. Modelled Input Parameters and Output*

Case	$Ra'\dagger$	H'	η_r^{**}	E'	T_l (km)	Dynamic Topography (km)	Geoid (m)
1	2×10^8	40	1	7.20	204	-1.9 to 4.2	-286 to 327
2	2×10^7	40	1	7.20	270	-0.19 to 0.25	-320 to 325
3	2×10^6	40	1	7.20	313	-0.30 to 0.30	-480 to 470
4	2×10^8	40	1	7.20	197	-2.2 to 2.6	-265 to 309
5	2×10^8	40	30	7.20	198	-3.8 to 3.0	-713 to 682
6	2×10^7	40	0.1	7.20	230	-0.21 to 0.50	-680 to 959
7	2×10^7	20	1	7.20	389	-0.47 to 0.70	-1106 to 1376
8	2×10^7	40	3	20.7	340	-0.40 to 0.30	-120 to 110
9	7×10^7	20	3	20.7	489	-0.86 to 0.64	-1100 to 900
10	7×10^7	30	3	22	384	-0.24 to 0.13	-150 to 123
11	9×10^7	30	3	20	383	-0.23 to 0.17	-153 to 139
12	2×10^8	30	3	20	383	-0.60 to 0.59	-303 to 245
13	2×10^8	40	3	16	267	-5.1 to 2.2	-858 to 632
14	2×10^8	40	3	10	223	-1.9 to 2.1	-256 to 261

* Input parameters are Rayleigh number Ra' , internal heating H' , pre-exponential factor η_r , activation energy E' , lithospheric thickness T_l .

† Rayleigh number as considered by CitcomS i.e. scaled to Venus's radius.

** Pre-exponential factor for layer 3 (depth to the 690 km phase transition), except for Case 6 that has a value 0.1 for layer 2 (depth to the 490 km phase transition).

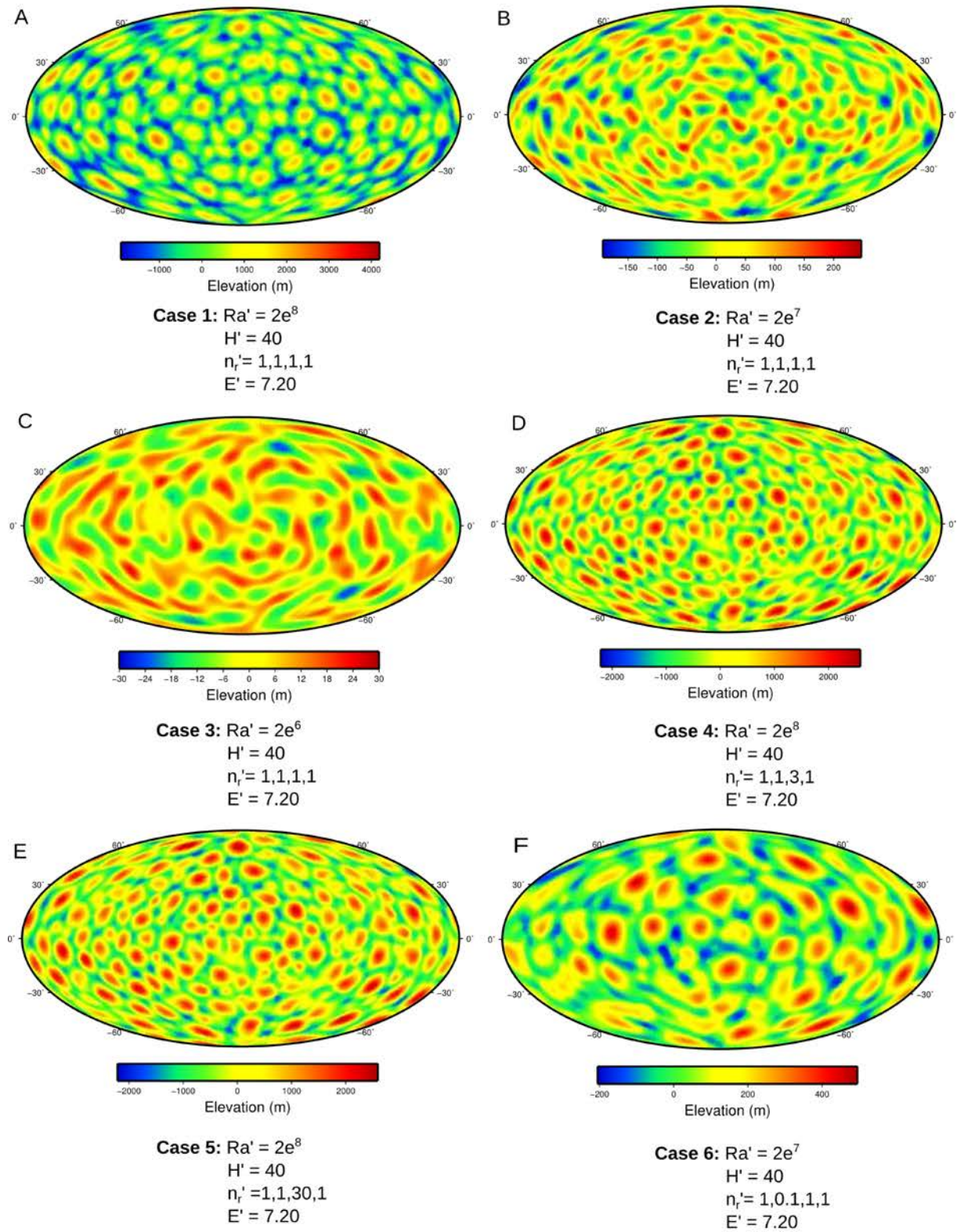


Figure 7.3. Maps of dynamic topography for Cases 1-6 (A-F). The non-dimensional values of Rayleigh number Ra' , internal heating H' , activation energy E' , and pre-exponential factor η_r' for the lid, depth to the first and second phase change and the CMB, are also shown for each case.

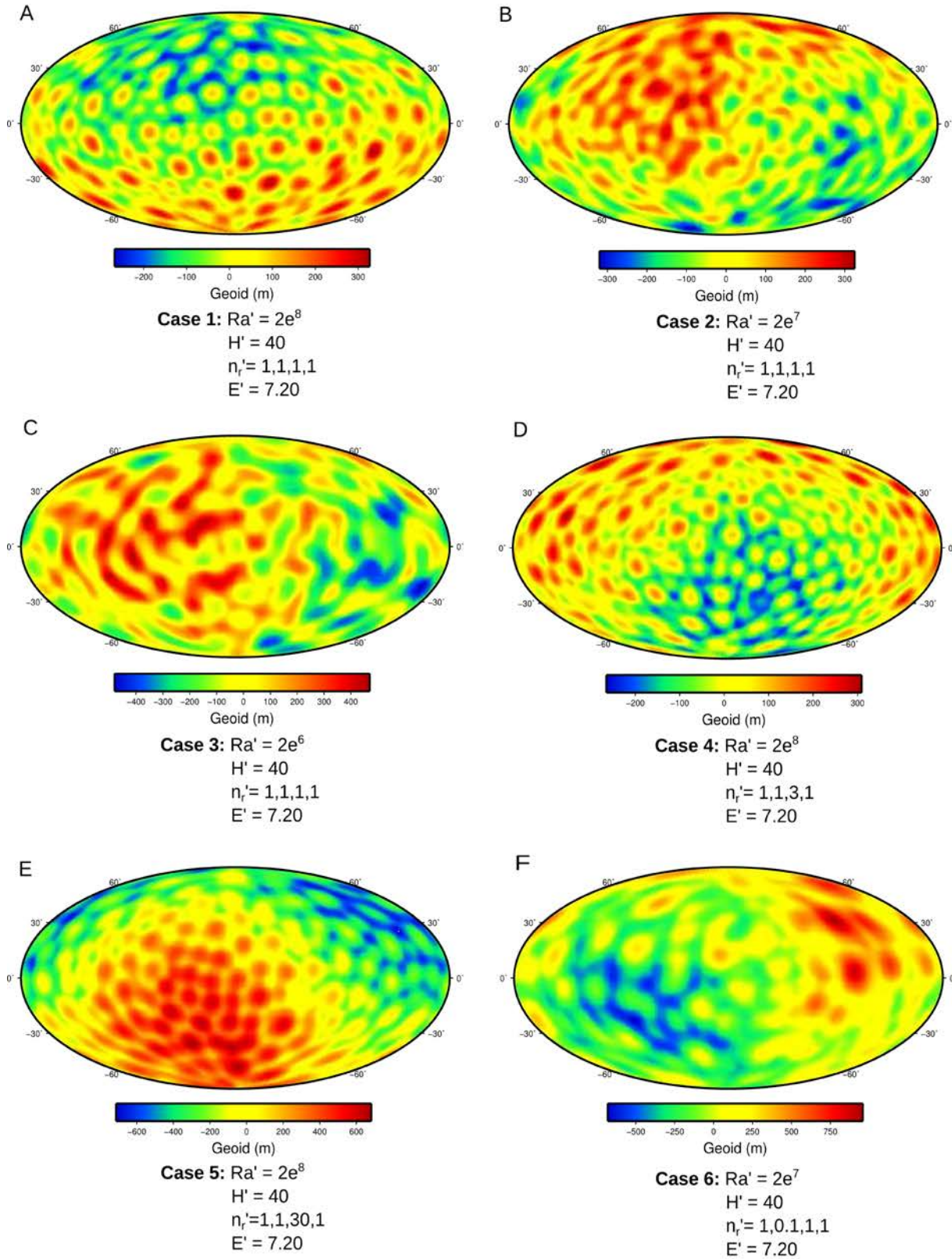


Figure 7.4. Modelled geoid for Cases 1-6.

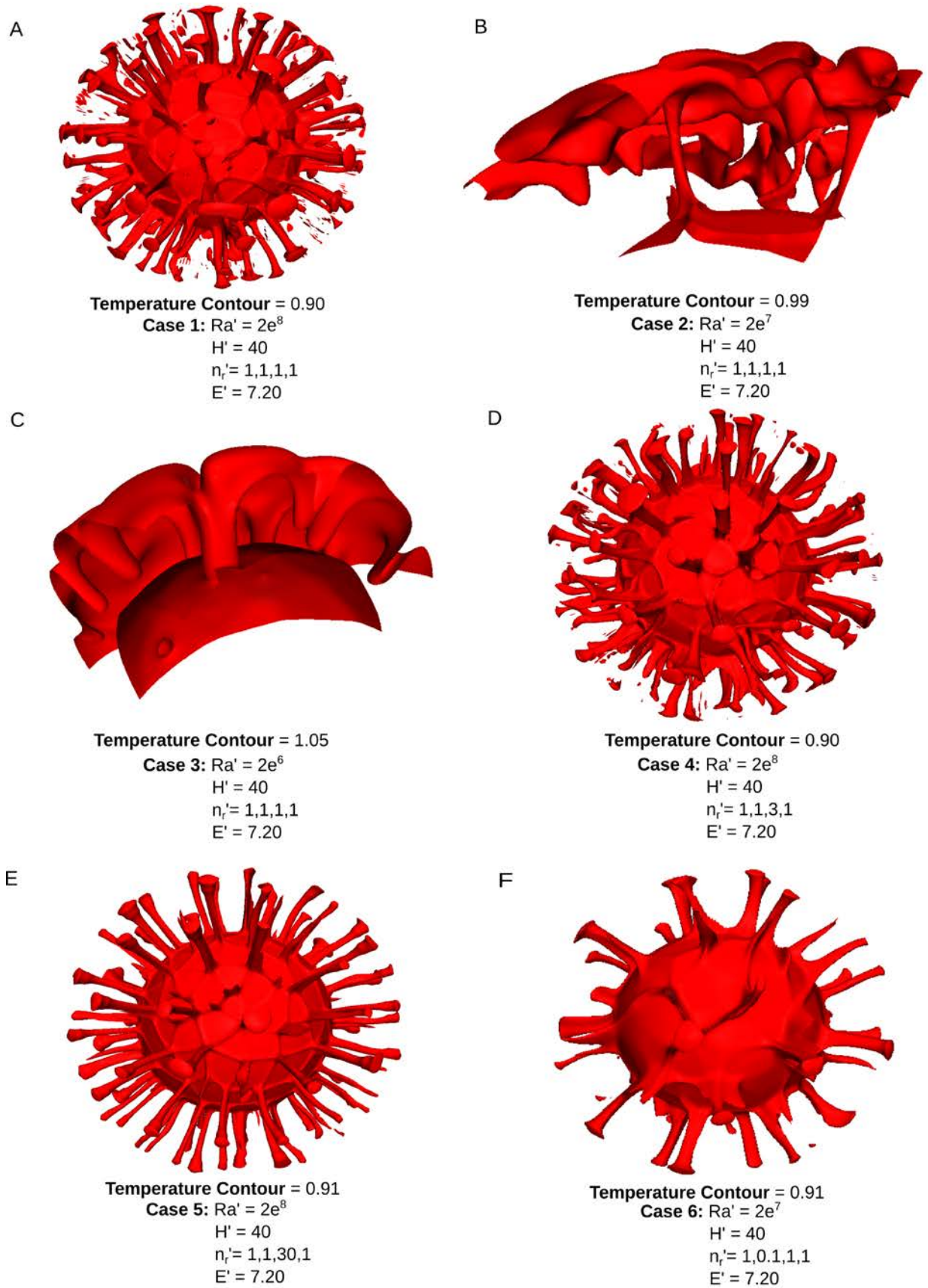


Figure 7.5. Contour plots for Cases 1-6.

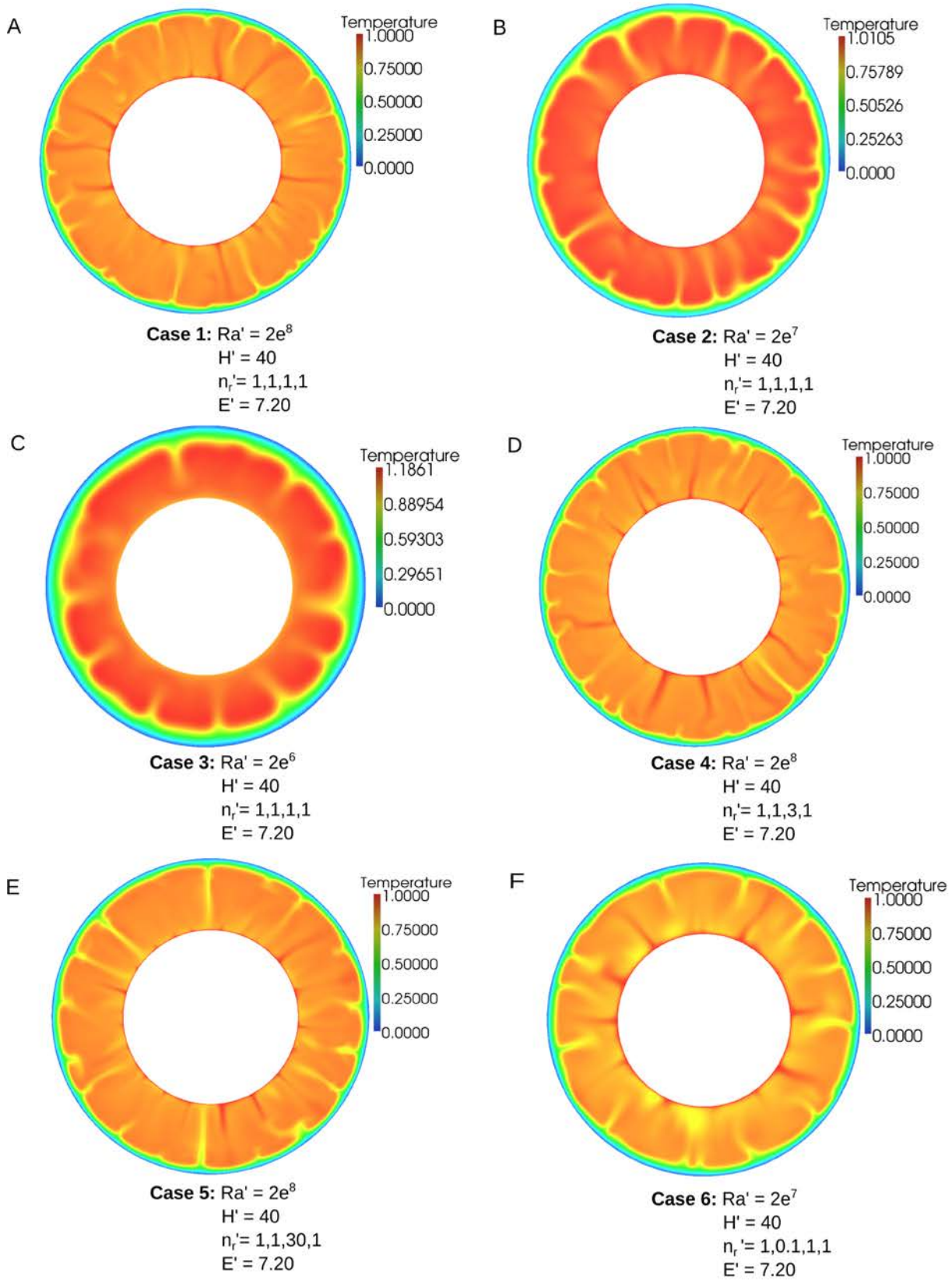


Figure 7.6. Temperature slices for Cases 1-6.

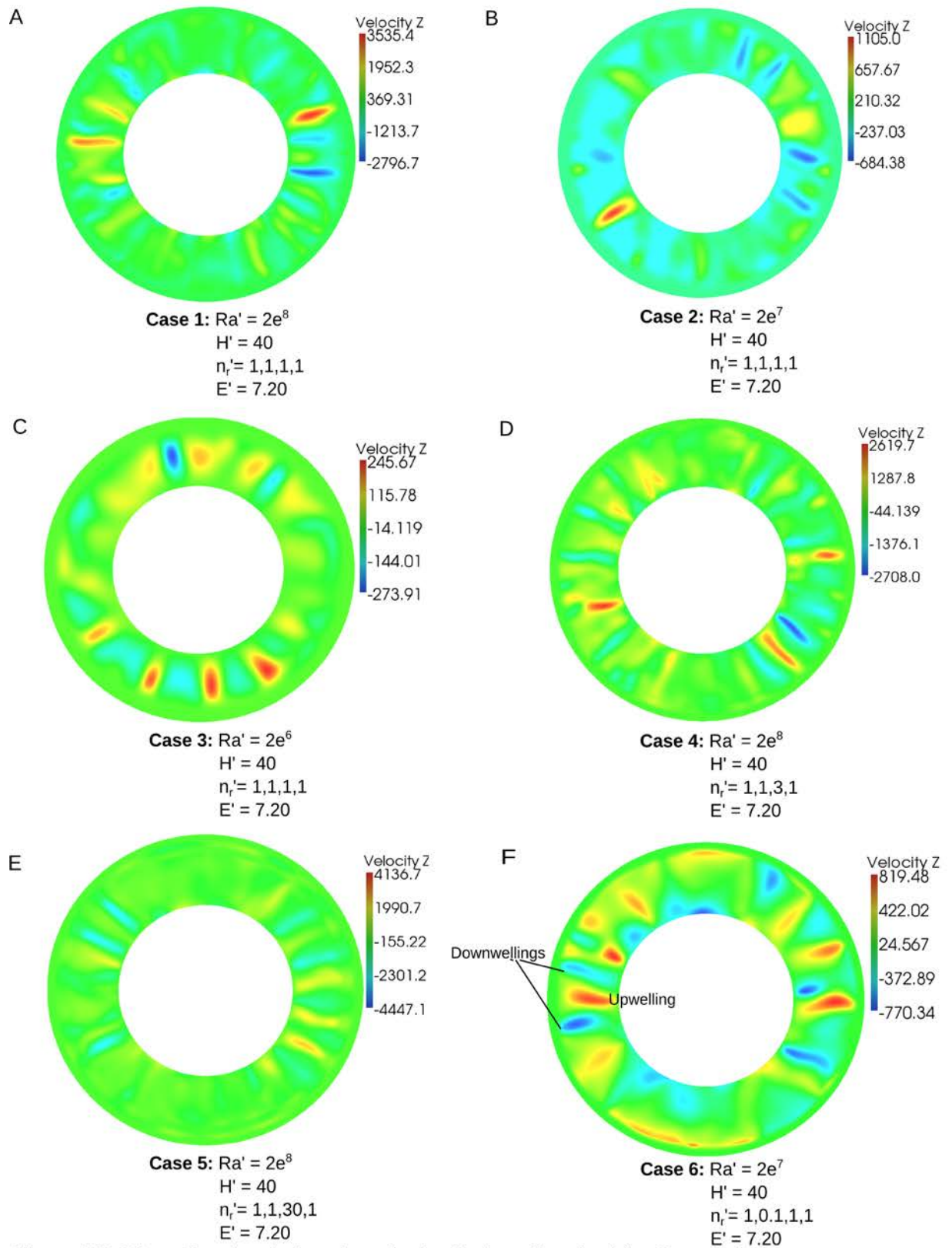


Figure 7.7. Slices showing the interior velocity (in the z direction) for Cases 1-6.

Since convection becomes less effective at transferring heat to the surface with a lower Rayleigh number, less thermal thinning occurs for Case 3 (313 km) compared to Case 2 (270 km). Case 2 is associated with hot, slow upwellings, but these are absent in Case 3, where cold, fast moving downwellings dominate (Figures 7.6-7.7B-C).

7.4.2 Pre-exponential Factor

The pressure-dependency of viscosity was modelled by changing the pre-exponential factor of either the lower mantle (Cases 4 and 5) or upper mantle (Case 6). We have modelled this viscosity increase due to pressure by making the lower mantle a factor of 3 and 30 times more viscous than the upper mantle (Case 4 and 5).

Increasing the viscosity within the lower mantle results in more elongated, but lower magnitude, elevation anomalies (~ 2.5 km for Case 4 and ~ 2.8 km for Case 5; Figure 7.3D-E). The geoid height for these upwellings do not vary significantly between Case 1 and Case 4, but do vary considerably for Case 5 (Figure 7.4D-E). Case 4 and 5 have numerous upwellings, the velocity of which is lower for the former case (Figures 7.5-7.7D-E).

An asthenosphere was also modelled in Case 6 by reducing the pre-exponential factor of the upper mantle by a factor of 10. In contrast to Case 2, an asthenosphere produces similar lithospheric thickness estimates, but higher dynamic topography and geoid anomalies (Figure 7.3-7.4F). This case also shows an interesting feature where a slow moving downwelling is associated with a high velocity upwelling plume (Figures 7.6-7.7F).

7.4.3 Internal Heating

Internal heating is from the decay of radioactive isotopes within the mantle. Case 7 has a lower non-dimensional internal heating (20) compared to previous cases, with a Rayleigh number of 2×10^7 . This case results in low elevations (~ 700 m), with extremely high geoid anomalies (~ 1300 m; Figures 7.8- 7.9G). A lower internal heating also results in fewer upwelling mantle plumes, with the ones that do occur having wider diameters (Figure 7.10G). Compared to Case 2, which has a similar Rayleigh number, activation energy, and pre-exponential factor, Case 7 has slightly cooler, but more pronounced upwellings, with the lithosphere being significantly thicker (by 119 km; Figure 7.11G).

7.4.4 Activation Energy

For Cases 8-12 the pre-exponential factor was set to 3 for the lower mantle. A factor of 3 increase was chosen for the lower mantle compared to a factor of 30, or a uniform mantle viscosity, since it provided the most reasonable geoid and topography for Cases 1, 4 and 5 (Table 7.4).

Higher activation energies in Cases 8-12 have the effect of decreasing the geoid and elevation, when the internal heating remains at 30 or 40. One effect of a high internal heating (30-40) and high activation energy is that the elevation is strongly reduced, with increased thickening of the lid (> 300 km; Figure 7.8H,J,K,L). In order to increase the elevation, the internal heating was reduced (Case 9), but this strongly influences the magnitude of the geoid in comparison to the geoid obtained from Cases 8, 10 and 11 (Table 7.4; Figure 7.9H,I,J,K). However, one consequence of an activation energy above ~ 10 and internal heating of 30 or 40 is the reduction and/or absence of upwellings due to a lower temperature contrast between the plume and surrounding mantle (Figures 7.10-7.12H,J,K,L). Instead high-velocity downwellings (Figure 7.12H,J,K,L) and drips occur off the base of a thick (~ 380 km), cold

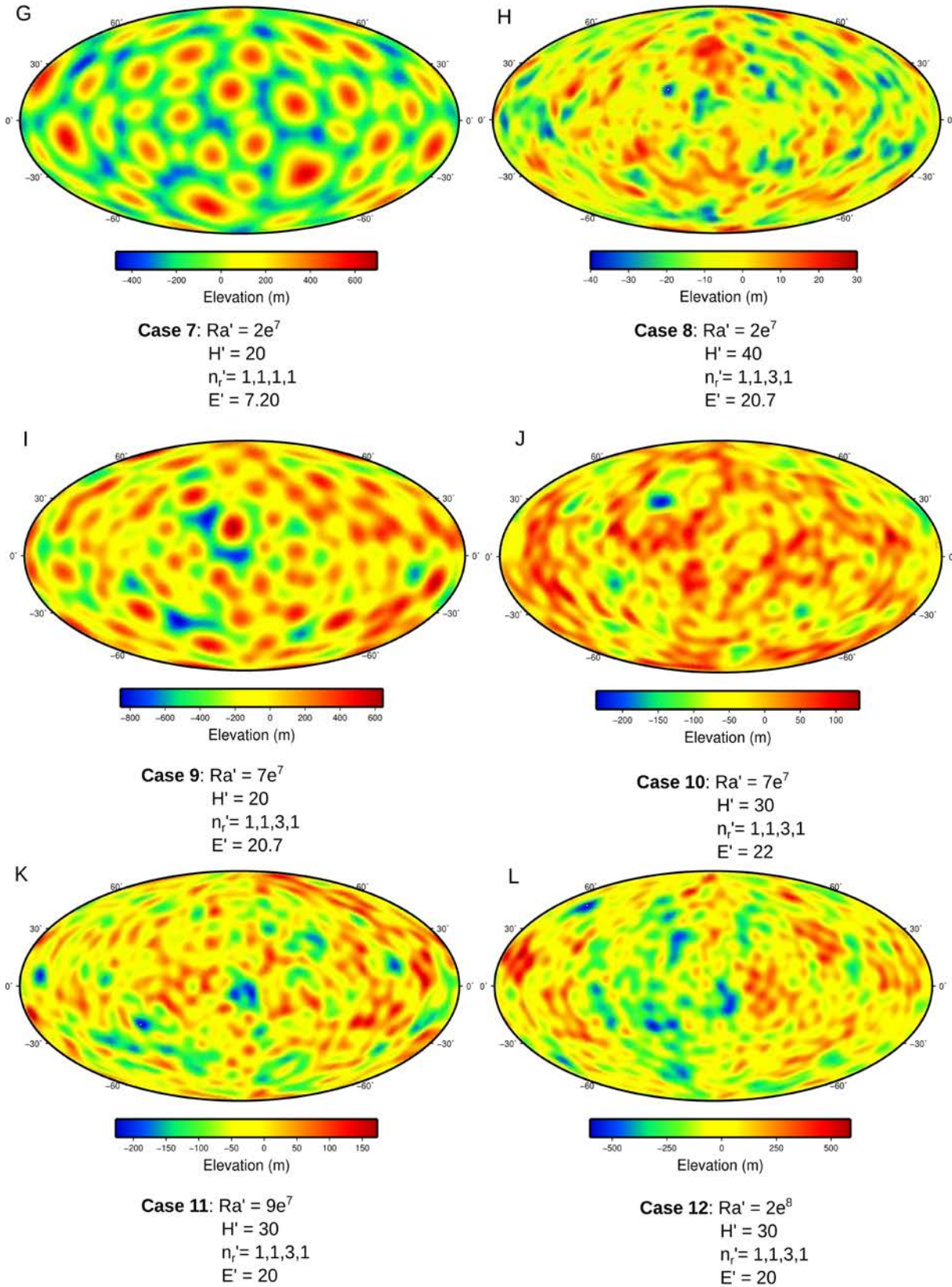


Figure 7.8. Dynamic topography maps associated with Cases 8-12.

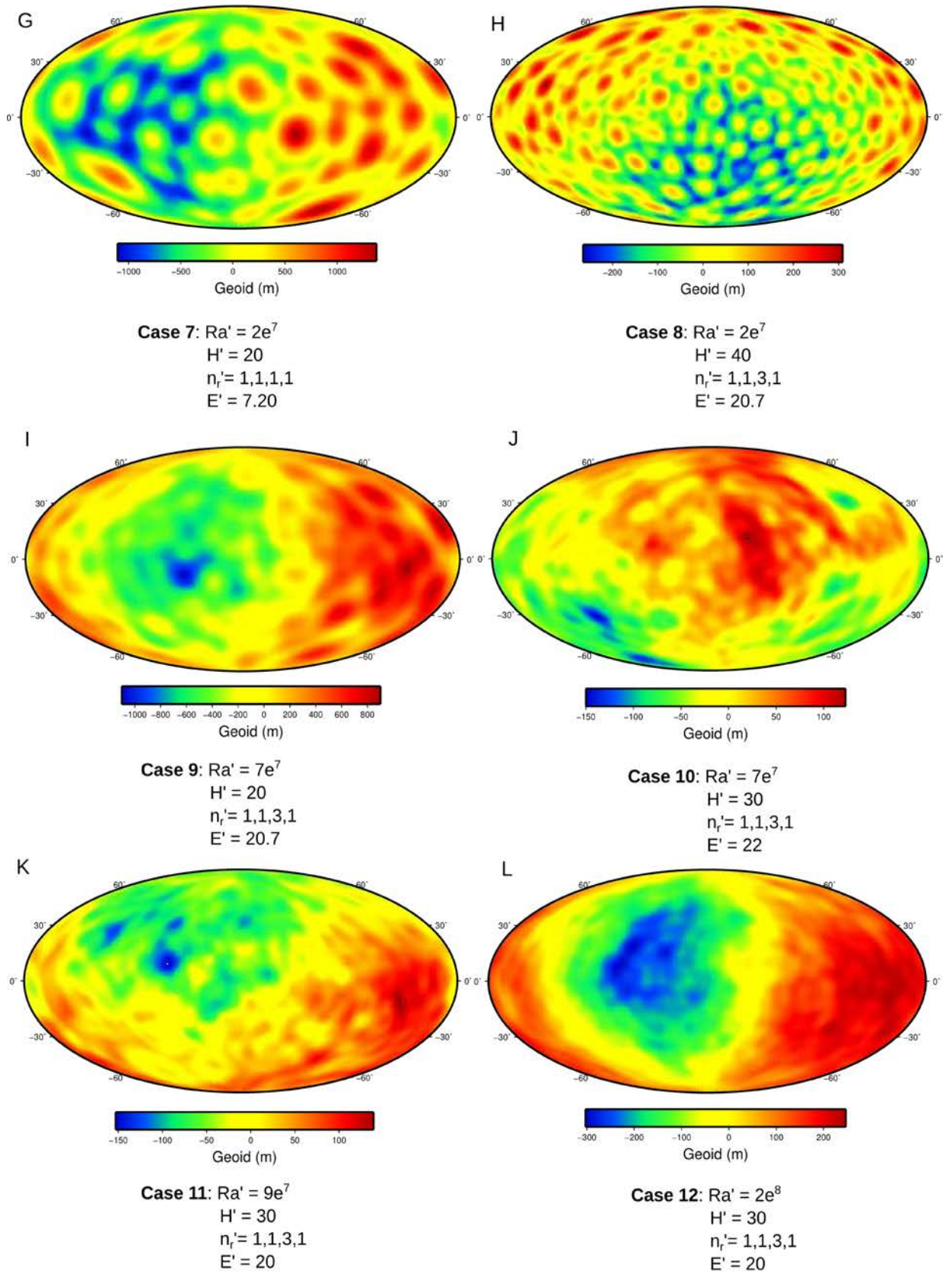


Figure 7.9. Modelled geoid for Cases 7-12.

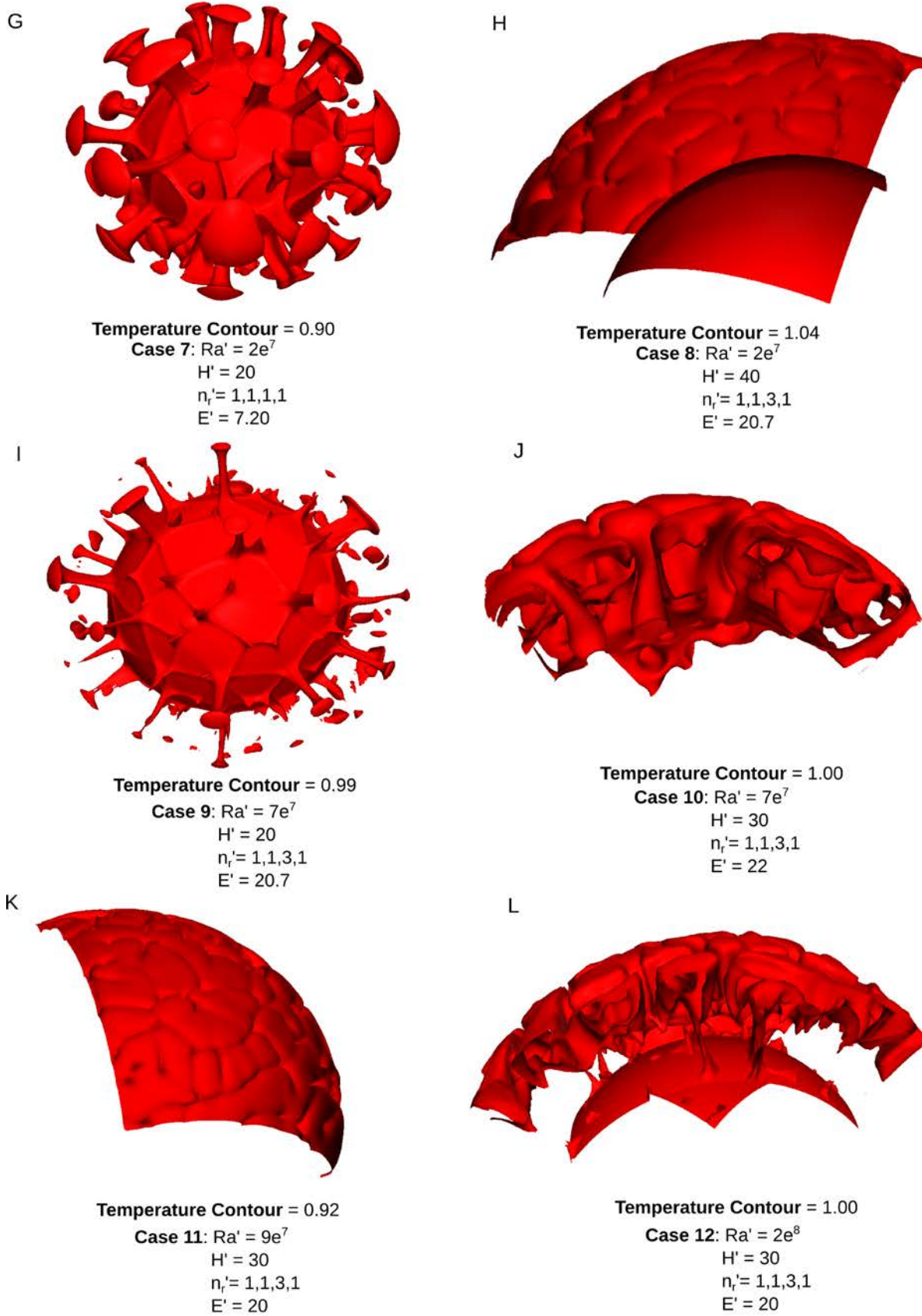


Figure 7.10. Contour plots for Cases 7-12.

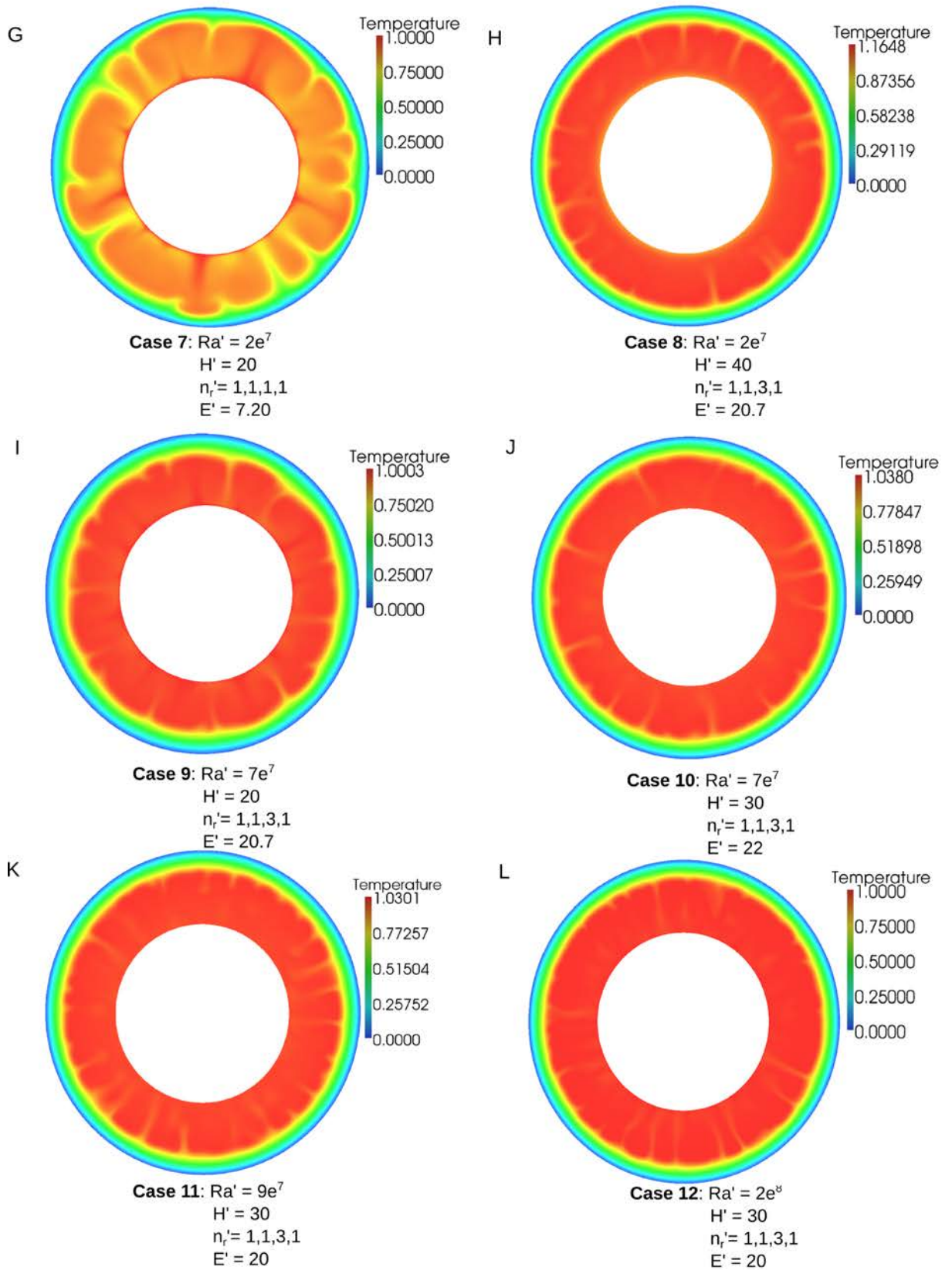


Figure 7.11. Temperature slices for Cases 7-12.

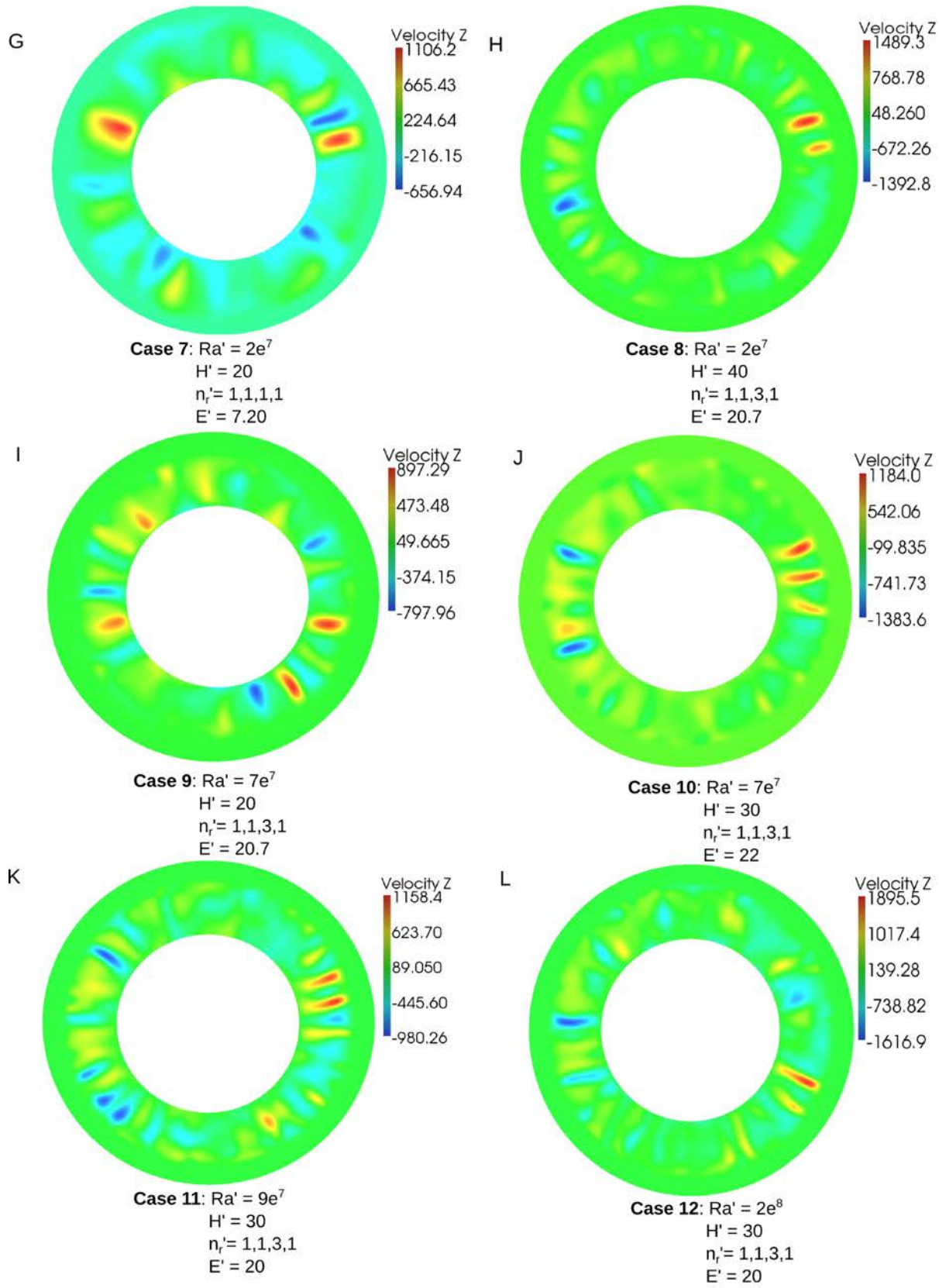


Figure 7.12. Slices showing the interior velocity (in the z direction) for Cases 7-12.

stagnant-lid (Figure 7.11H,J,K,L).

Previous cases have shown vigorous convection results in both upwellings and higher topography. Case 12 uses an internal heating of 30 and a Rayleigh number of 2×10^8 , which produces a few long-wavelength upwellings with modest elevations (Figures 7.8I and 7.10I). Combining an internal heating of 40, Rayleigh number of 2×10^8 , and activation energies of 16 and 10 for Cases 13 and 14, respectively, provides a model with reasonable elevation, with Case 14 also providing plausible geoid anomalies (Figures 7.13-7.14M-N). More hot, slowly rising plumes are obtained for Case 14 compared to Case 13, due to the lower activation energy (Figures 7.15-7.17M-N).

7.5 Discussion

7.5.1 CitcomS Modelling

Case 14 ($Ra=2 \times 10^8$, $H=40$, $E=10$) provides the most reasonable geoid and topography anomalies of all the models studied. The effective Rayleigh number for this case is 2.5×10^7 similar to the value proposed for Earth ($\sim 6 \times 10^7$) [Fowler, 2004]. This lower effective Rayleigh number is consistent with Venus's dry mantle composition, which could result in a higher effective viscosity [Arkani-Hamed *et al.*, 1993; Kaula, 1990; Steinbach and Yuen, 1992].

Both the high Rayleigh number and internal heating in Case 14 leads to ~ 60 mantle upwellings that have the effect of thinning the lid to an average value of ~ 223 km. The number of plumes found in this case are much higher than the ~ 9 -12 plumes proposed for Venus [McKenzie, 1994; Smrekar and Sotin, 2012; Stofan *et al.*, 1995]. These larger plumes

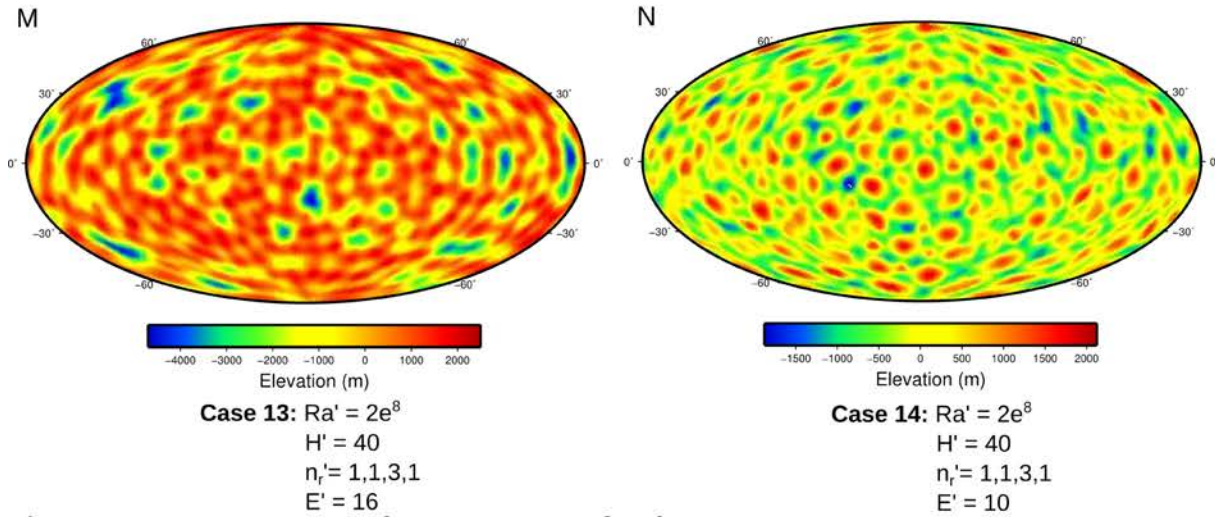


Figure 7.13. Dynamic topography maps associated with Cases 13-14.

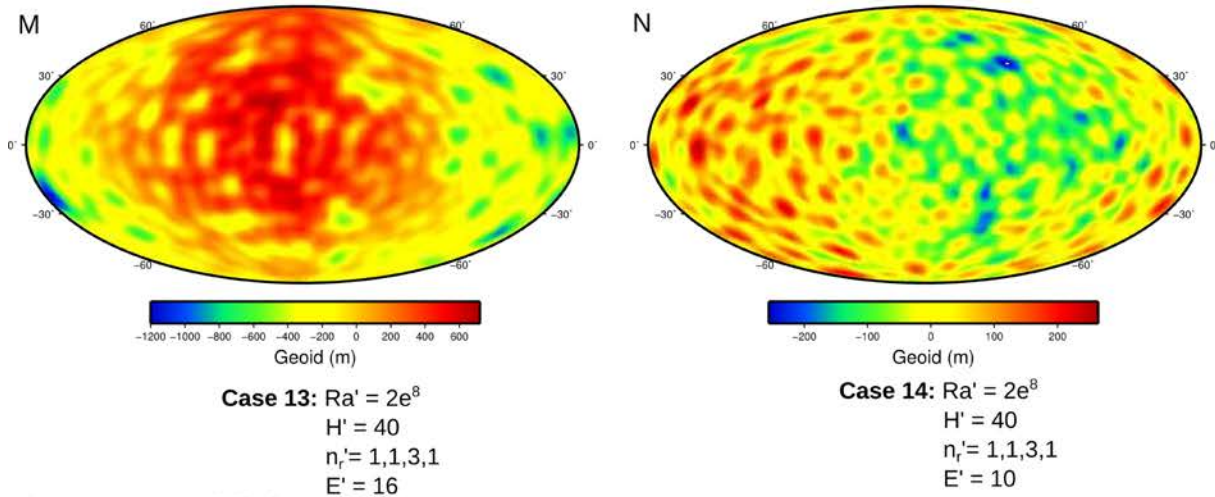


Figure 7.14. Modelled geoid for Cases 13-14.

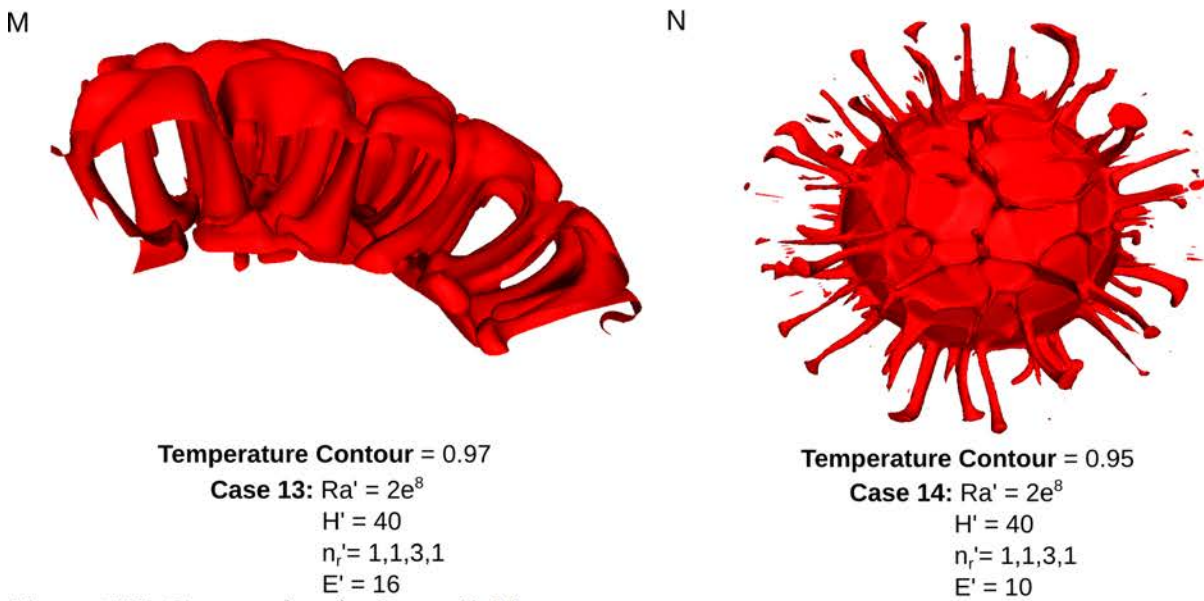


Figure 7.15. Contour plots for Cases 13-14.

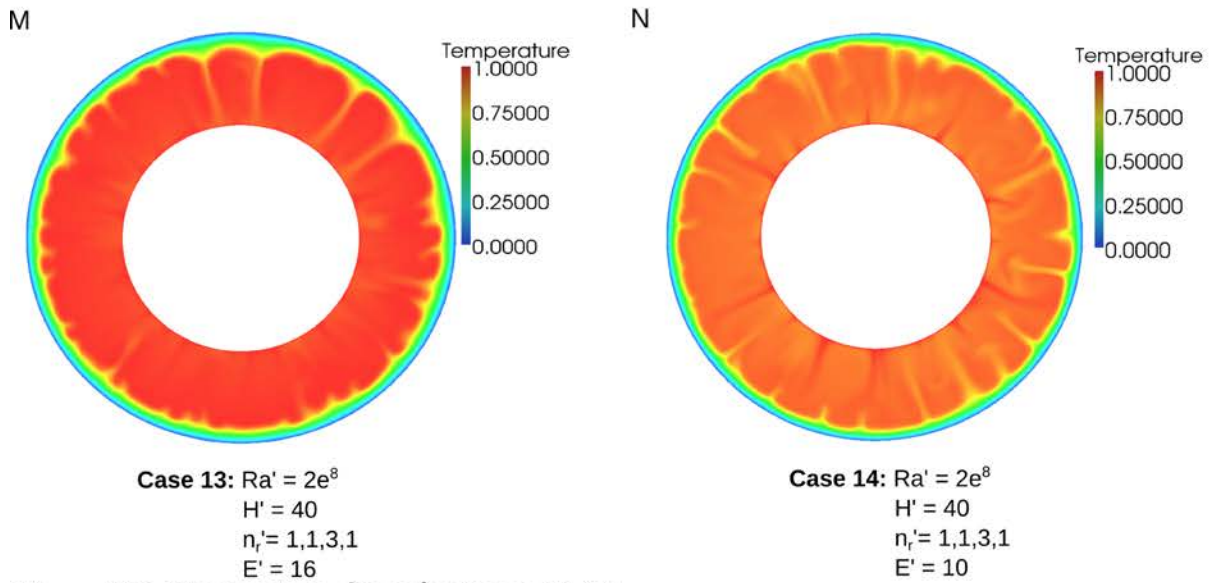


Figure 7.16. Temperature slices for Cases 13-14.

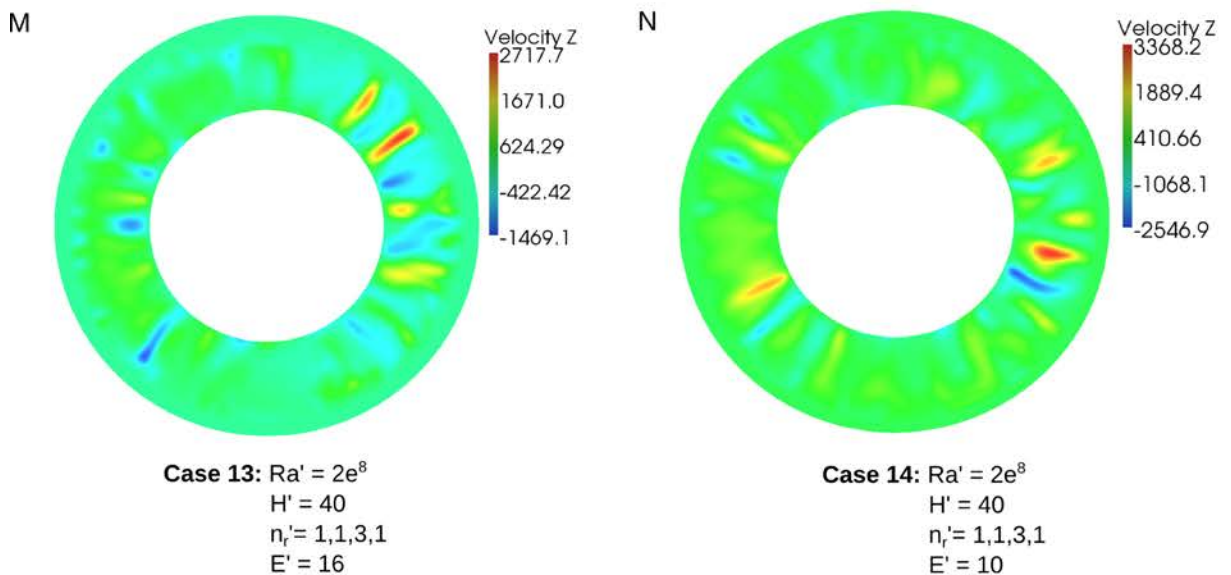


Figure 7.17. Slices showing the interior velocity (in the z direction) for Cases 13-14.

tend to correspond to the volcanic rises, however, the 513 coranae observed on the surface may also be sites of localised mantle upwelling [Musser and Squyres, 1997; Solomon and Head, 1991; Squyres et al., 1993; Stofan and Smrekar, 2005]. Some have proposed the small diameter of these features could imply shallow secondary upwellings [Stofan and Smrekar, 2005], rather than deep seated plumes. However, our study would favour that these represent narrow upwellings similar to those expected with a more vigorously convecting mantle and one that includes a realistic temperature-dependent viscosity [Schubert et al., 1990]. Differences in the number of plumes found also depends on the assumed core radius, a

highly unconstrained parameter on Venus, with variations of up to ~700 km [Konopliv and Yoder, 1996; Smrekar and Sotin, 2012]. Our models use a core radius of 3330 km, whereas a lower value would reduce the number of plumes due to a smaller surface area of the core and a thicker mantle [Smrekar and Sotin, 2012].

Uncertainty exists surrounding the activation energy on Venus. For example, high activation energies should result from the lack of surface water and lower activation energies should result from the higher surface temperatures [Bindschadler *et al.*, 1990]. Higher and lower activation energies are also associated with a dry or wet mantle dominated by diffusion and dislocation creep, respectively. Even though uncertainty regarding the water content of Venus's mantle exists, some authors favour a dry rheology based on observations of extensive lava flows and large volcanoes, which imply an early period of volcanism and devolatilisation of the sub-surface in conjunction with the observed gradual relaxation of impact features [Grimm and Solomon, 1988; Kaula, 1990; Mackwell *et al.*, 1998; Reese *et al.*, 1999].

Compared to other studies that have used a limited range of activation energies [Smrekar and Sotin, 2012], this study shows that varying the activation energy, and indirectly the temperature-dependence of viscosity, can make a significant impact on the convection within the interior, the dynamic topography and geoid. However, one consequence of using activation energies higher than ~9 is that the models become chaotic and time-dependent rather than steady-state [van den Berg *et al.*, 1993; Christensen, 1984]. We also found that higher activation energies promote temperature-dependent viscosity, fewer upwellings and thick rigid lids, which contribute to variations in the modelled geoid and topography. Previous authors have also noted that low activation energies should promote long wavelength convection features compared to higher values [Zhong *et al.*, 2000], however we found that Rayleigh number also makes a significant contribution.

Higher activation energies tend to represent a more realistic non-Newtonian rheology, dominated by dislocation creep. However, Case 14 that uses a non-dimensional activation energy of 10 (208 kJ mol^{-1}) approximates a Newtonian rheology, dominated by diffusion creep. This value is within the range ($150\text{--}360 \text{ kJ mol}^{-1}$) used by previous authors for a similar rheology [Huang *et al.*, 2013; van Hunen *et al.*, 2005]. The style of creep could also vary from diffusion to dislocation if the grain size of the mantle material changes as a function of stress associated with recrystallisation and dislocation of the original grains into subgrains [Christensen, 1984; Weertman, 1970].

The dynamic topography of $\sim 2 \text{ km}$ for Case 14 is lower than the $\sim 3\text{--}4 \text{ km}$ total observed elevation at the volcanic rises. This implies that these areas are compensated by a combination of long-wavelength dynamic uplift associated with convective stresses within the mantle in conjunction with short wavelength mechanisms, such as Airy isostasy and flexure, which have not been included in this modelling. Most of the plumes associated with Case 14 also correspond to geoid anomalies $\leq 180 \text{ m}$, similar to the observed, however five localised areas have anomalies higher than 200 m .

7.5.2 Localised Admittance and Correlation

Figure 7.18 shows the localised admittance and correlation for Atla and Beta Regio for degrees greater than 5. All the following admittance and correlation profiles are truncated at degrees < 5 , corresponding to very long wavelength ($\sim 1512 \text{ km}$) structures at approximately mid-mantle depths. High admittance and correlation values at lower spherical harmonic degrees imply long-wavelength dynamic support from deep mantle structures such as mantle plumes. This compares to high admittance and correlation values at higher spherical harmonic degrees that imply support from short-wavelength processes such as Airy isostasy

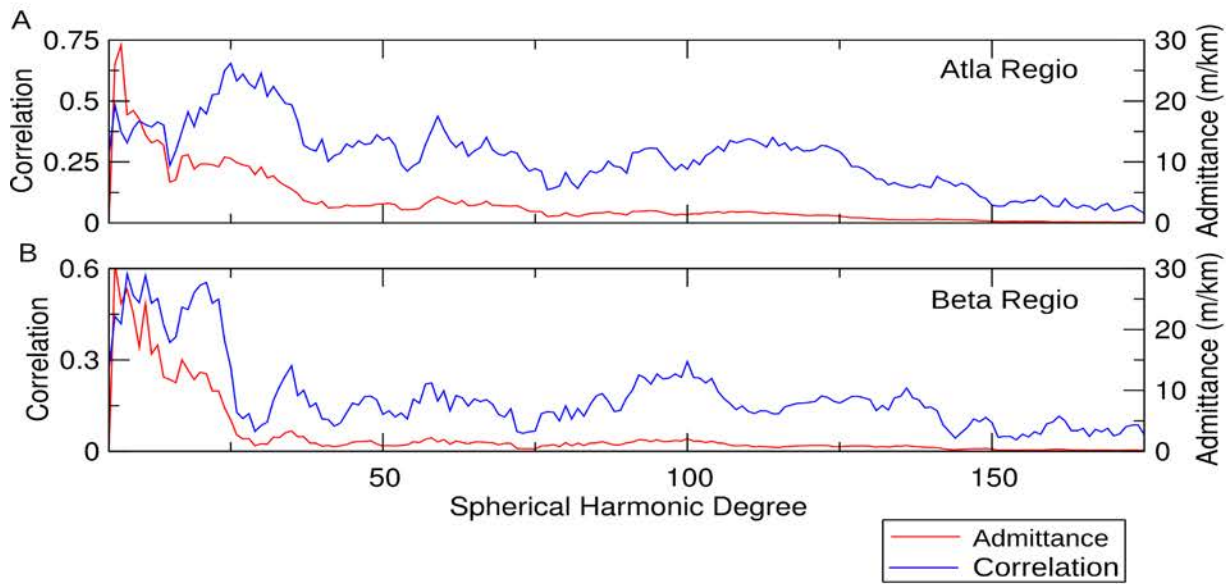


Figure 7.18. Observed geoid and topography admittance and correlation at Atla Regio (A) and Beta Regio (B), using windowing parameters shown in Table 7.3. Both the admittance and correlation were truncated at degrees < 5 . The observed topography used in the localised admittance and correlation calculations included contributions from both short wavelength isostatic and flexural effects and long wavelength dynamic effects.

and flexure. For our study, we are particularly interested in high admittance and correlation values at low spherical harmonic degrees since these indicate long wavelength dynamic support from a mantle plume/s.

Both Atla and Beta Regio exhibit higher observed admittance and correlation values at lower spherical harmonic degrees corresponding to longer wavelength dynamic effects. The two volcanic rises have an admittance of $\sim 30 \text{ m km}^{-1}$ at degree ~ 7 , with Atla Regio showing a more gradual decline of admittance to $\sim 3 \text{ m km}^{-1}$ at degree ~ 38 , compared to Beta Regio ($\sim 2 \text{ m km}^{-1}$ at degree ~ 27 ; Figure 7.18).

In regards to the correlation, Atla Regio has the highest (0.4-0.6) between degrees 5 and 30, with the peak at degree 24 (Figure 7.18A). For Beta Regio, the correlation shows a similar

trend as the admittance at degrees less than ~ 27 where the correlation is ~ 0.55 (Figure 7.18B). At both volcanic rises, the topography and geoid of shorter wavelength features, characterised by higher degrees, are positively correlated with values ranging between 0.1 to 0.4.

Localised admittance and correlation was also completed using the dynamic topography and geoid data generated for Case 14 with similar window dimensions as shown in Table 7.3 (Figures 7.19-7.20). Two plumes centered at $150^\circ\text{E } -15^\circ\text{N}$ and $-30^\circ\text{E } 33^\circ\text{N}$, respectively were chosen since these areas have similar geoid highs as those observed at Atla and Beta Regio (Figure 7.21). Figure 7.19 and 7.20 show the modelled long wavelength dynamic topography and geoid admittance and correlation for Plume 1 and Plume 2, respectively (Blue solid and dashed lines; Figures 7.10-7.20). The observed admittance and correlation for Atla and Beta Regio, shown in Figure 7.18, is also included on these figures, however the topography and geoid used includes contributions from both short wavelength isostatic and flexural effects and long wavelength dynamic effects.

These short wavelength isostatic effects were addressed in previous 3D lithospheric modelling at Atla and Beta Regio that simultaneously constrained the lithospheric structure below each rise to geophysical observables including elevation, Bouguer gravity, and geoid height (Refer to Chapters 4 and 5 for further details). By constraining the lithospheric structure we were able to discern the contribution of Airy, thermal and regional isostasy in shaping the observed topography at each rise. However, not all of the observed topography could be compensated by these mechanisms. This remaining topography, which is the difference between the observed and that associated with isostasy, was inferred to represent a simple estimate of the amount of dynamic compensation an area requires (Figure 7.22). This estimated dynamic topography and the corresponding geoid data (representing wavelengths $< \sim 2716$ km) were then used to calculate the estimated admittance and correlation profiles (red solid and red

dashed lines) shown in Figures 7.19-7.20.

At degrees $< \sim 30$ the modelled and estimated dynamic topography and geoid generally correspond to higher admittance estimates ($26\text{-}80 \text{ m km}^{-1}$) than those obtained when considering the total observed topography at Atla Regio ($18\text{-}25 \text{ m km}^{-1}$; Figure 7.19). The admittance highs at degrees < 10 are also much broader when using the observed and modelled dynamic topography, while narrower admittance peaks occur when using the estimated dynamic topography (Figure 7.19). At degrees $> \sim 30$ the admittance for each data set decreases implying the contribution from dynamic effects decrease with shorter wavelengths at Atla Regio.

At Atla Regio, the correlation using the modelled dynamic topography and geoid ranges from 0.1 to 0.6 at degrees < 30 , whereas using the total observed topography and geoid results in correlations of 0.2 to 0.6 at degrees < 40 (Figure 7.19B). However, very low 0 to 0.2 correlation occurs when comparing the estimated dynamic topography and observed geoid. These low correlation values, and the narrow peaks in the associated admittance spectra, are the result of localised dynamic uplift at Atla Regio (Figure 7.19 & 7.22A). For example, areas that have a high geoid, but don't need dynamic topography will result in a low correlation value, while the localised areas of high dynamic topography will create peaks in the resulting admittance rather than a broad response (Figure 7.19 & 7.22A).

The observed admittance ranges from $6\text{-}30 \text{ m km}^{-1}$ for degrees $< \sim 25$ at Beta Regio (Figure 7.20A). However, a higher admittance is obtained when considering the estimated or modelled dynamic topography, reaching values up to 62 m km^{-1} and 47 m km^{-1} , respectively. For degrees < 26 , the observed geoid and total topography show correlations ranging from 0.36 to 0.57, the estimated admittance has values ranging from 0 to 0.24 and the modelled admittance

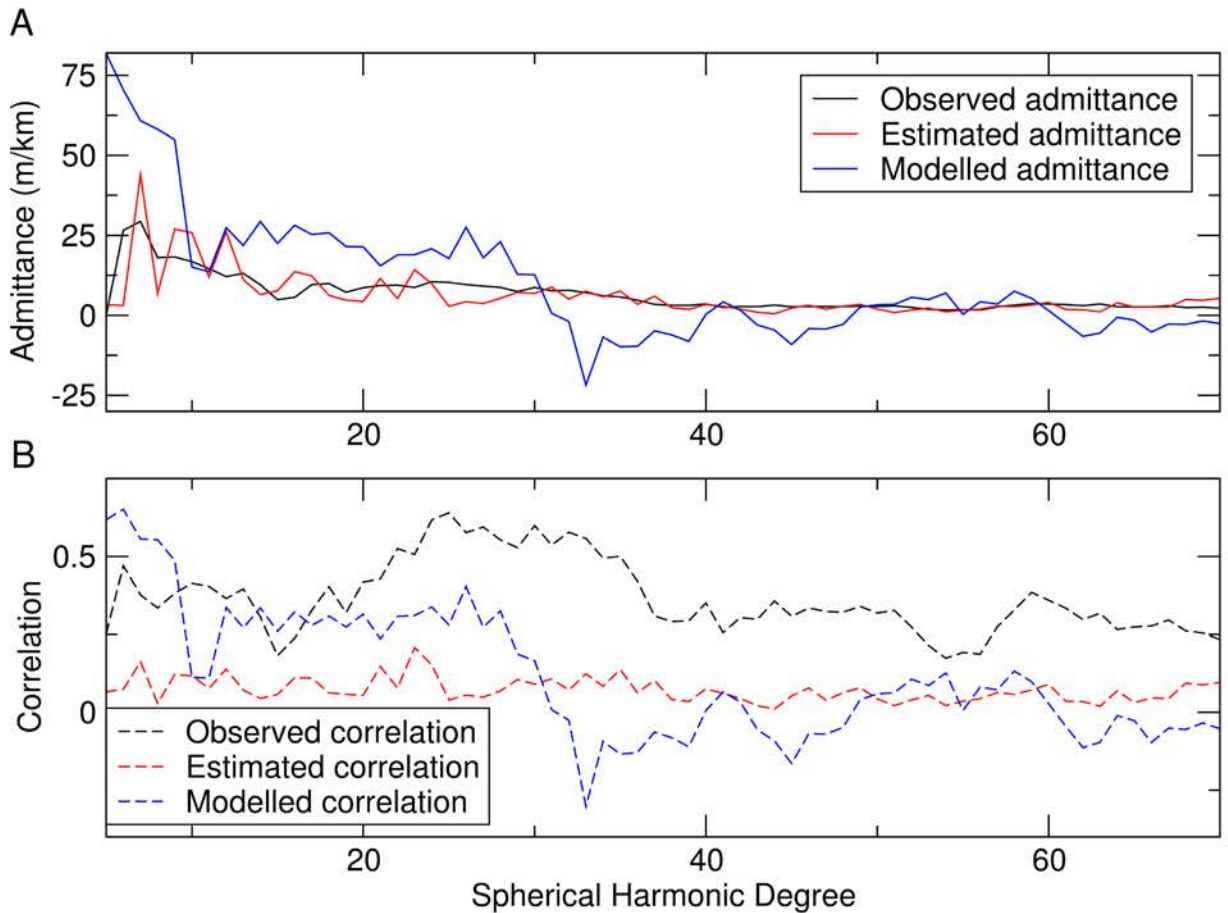


Figure 7.19. (A-B) The geoid and topography admittance and correlation for Atla Regio and Plume 1.

(A) The solid black line represents the geoid and topography admittance using the total observed topography and geoid containing both short wavelength isostatic effects and long wavelength dynamic effects. The red solid line represents the estimated admittance using the dynamic topography found from Chapter 4. This long-wavelength dynamic topography was found by removing the short wavelength topography associated with Airy, thermal and regional isostasy from the observed total topography. The geoid data used in the estimated admittance calculations was the same as that used in Chapter 4 and represented all wavelengths $< \sim 2716$ km. The solid blue line represents the admittance using the modelled long wavelength dynamic topography and geoid from Case 14 for Plume 1. (B) The observed correlation (black dashed line), estimated correlation (red dashed), and modelled correlation (dashed blue line) using the same respective data sets as the admittance. Similar windowing parameters were also used in order to maintain consistency with the observed admittance and correlation as shown in Figure 7.18.

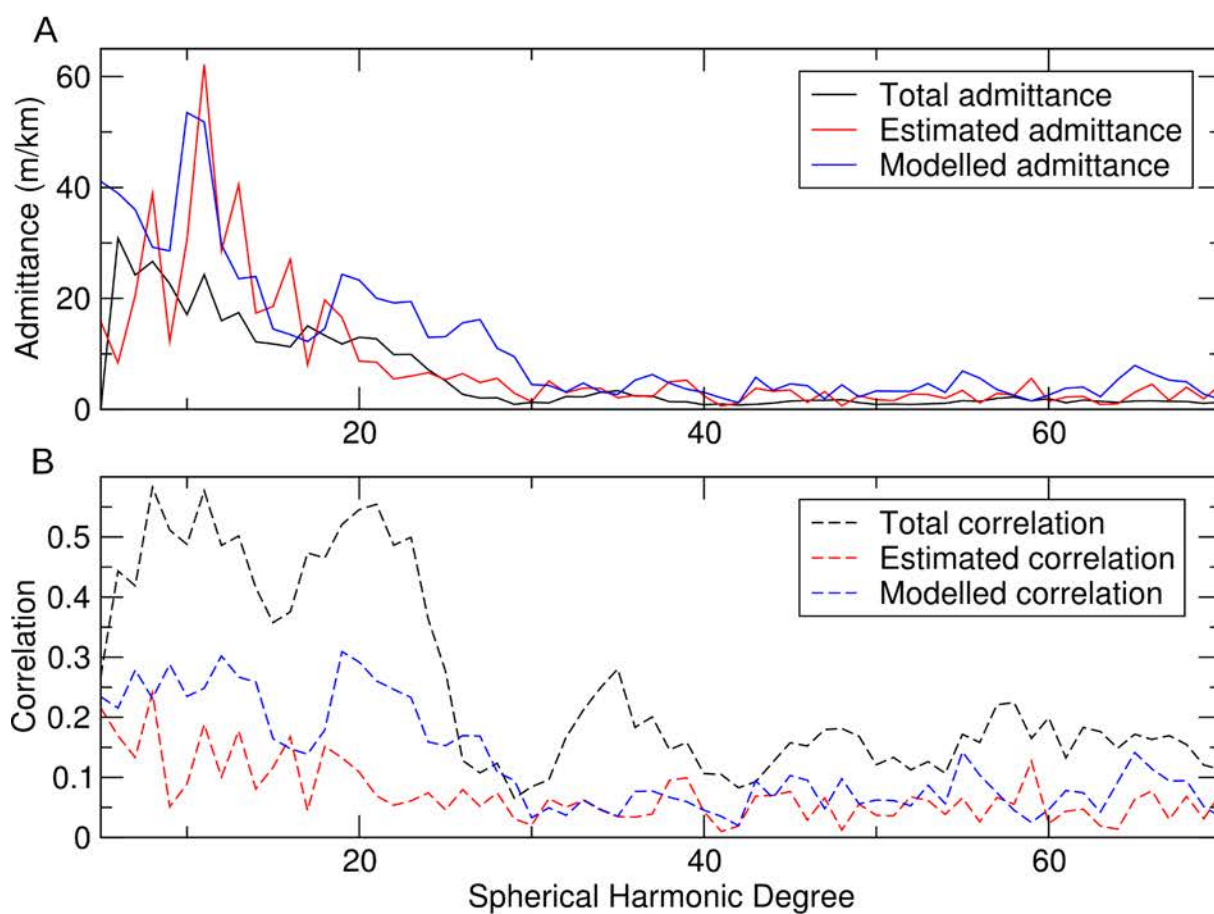


Figure 7.20. The geoid and topography admittance (A) and correlation (B) for Beta Regio and Plume 2. Key as per Figure 7.19, but for Beta Regio.

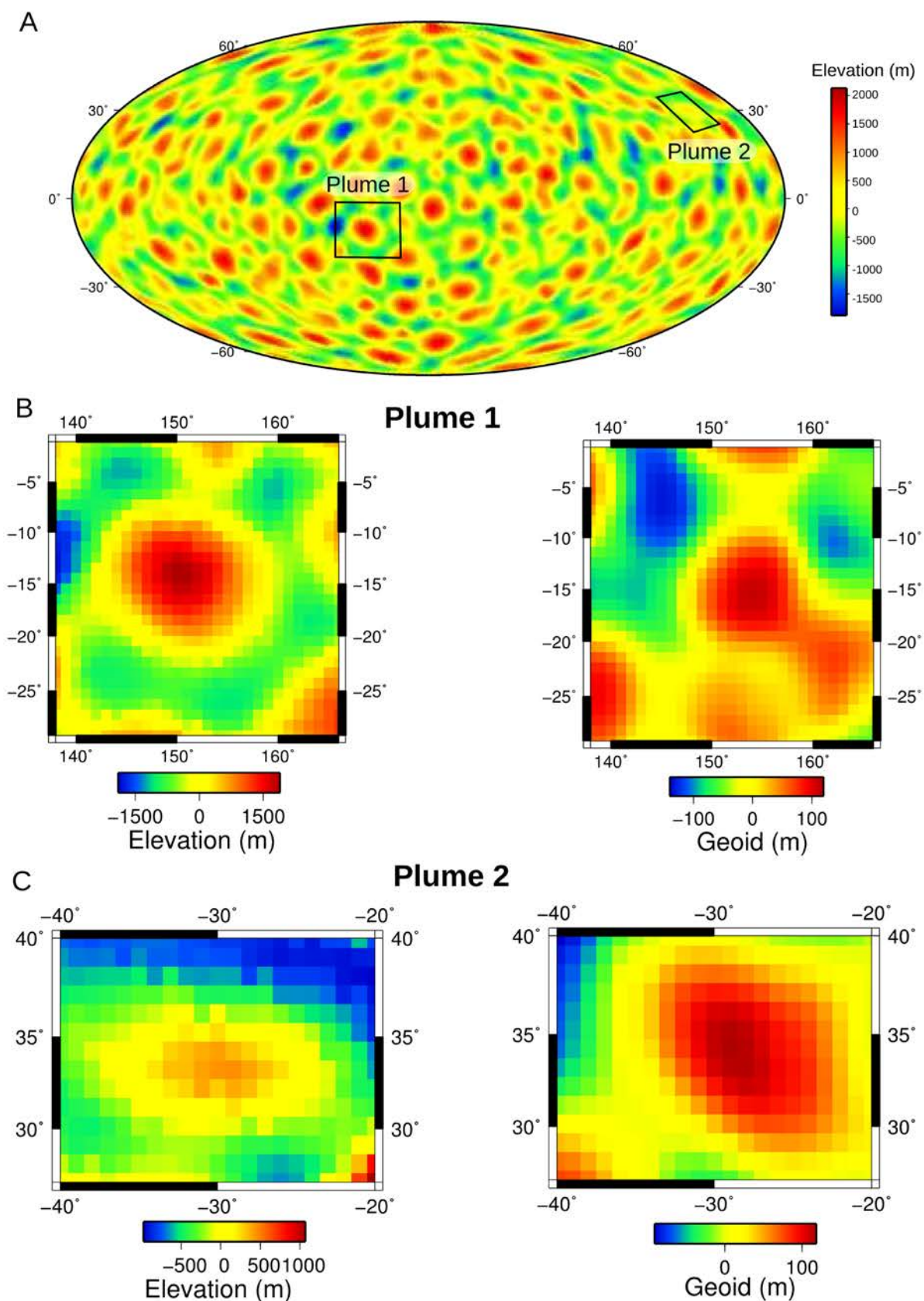


Figure 7.21. (A) Global map of the modelled dynamic topography obtained from Case 14, with the location of Plume 1 and 2 shown as the black rectangles. (B-C) The local dynamic topography and geoid obtained from Case 14 for Plume 1 (B) and Plume 2 (C). North is to the top of the page.

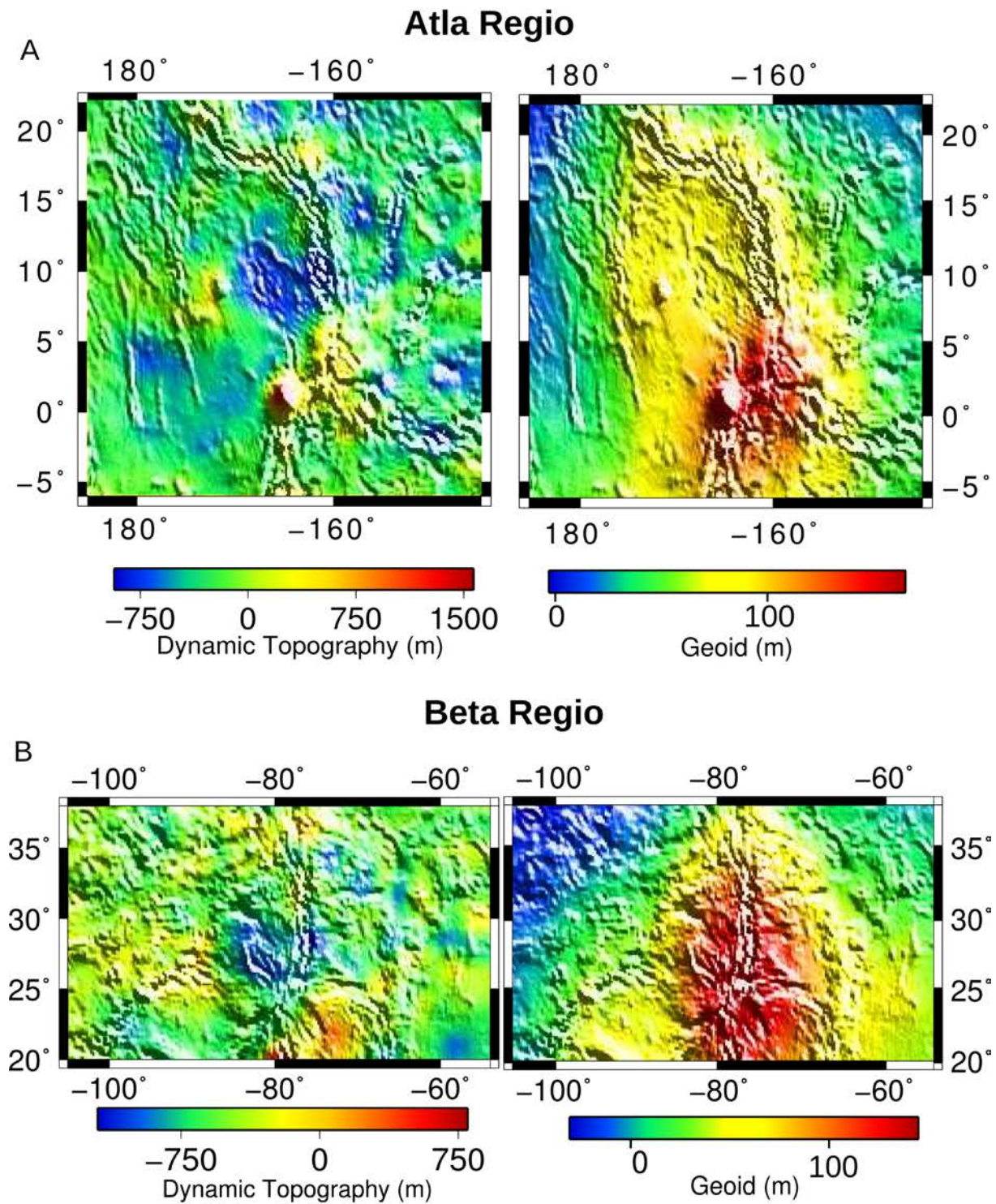


Figure 7.22. The amount of dynamic topography found by removing the isostatic contribution from the total observed topography at Atla Regio (A) and Beta Regio (B). The dynamic topography is localised compared to the broad geoid highs that occur at each rise and results in low correlation as seen in Figures 7.19 and 7.20.

has values between 0.15 to 0.36 (Figure 7.20A). Similar to Atla Regio, the estimated correlation is lower because the dynamic topography is restricted locally, compared to the expansive geoid high (Figure 7.22B). The modelled correlation is also lower than the observed because the modelled geoid anomaly, corresponding to Plume 2, is more elongate in the NW-SW direction than the modelled dynamic topography (Figure 7.21).

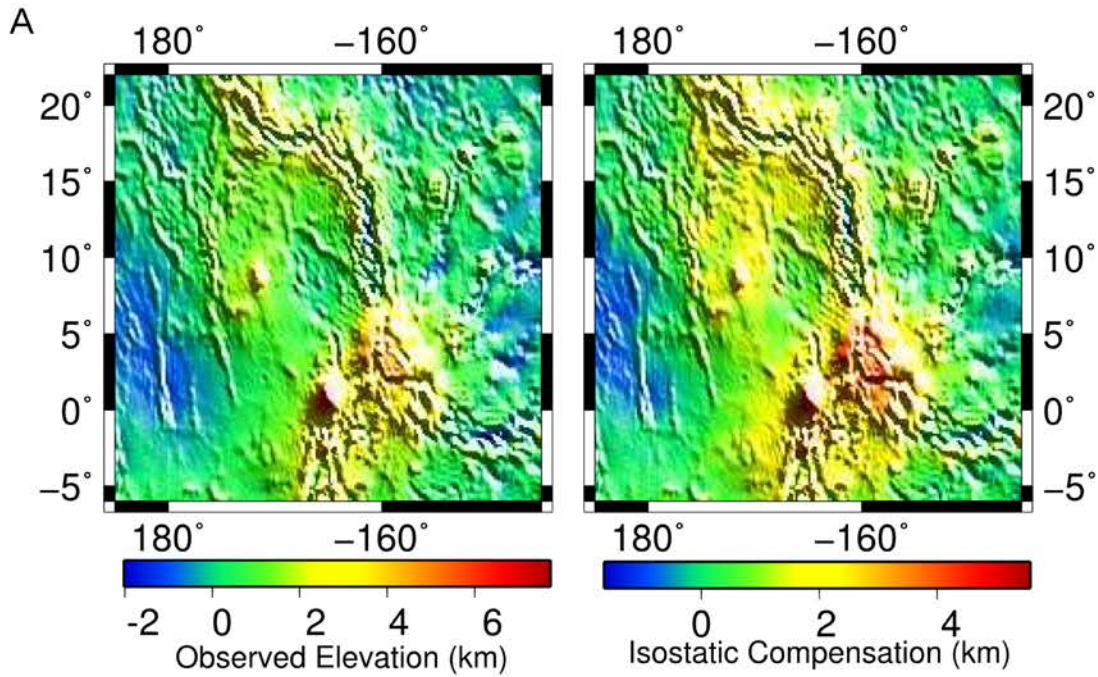
The high admittance and low correlations at degrees $< \sim 35$ -40 obtained for Atla and Beta Regio, using the modelled and estimated dynamic topography, imply additional long wavelength isostatic compensation is required. This is consistent with previous results obtained from lithospheric modelling, where thermal isostasy was found to contribute significantly to the long-wavelength topography and geoid anomalies observed at these rises (Refer to Chapter 4 and 5 for more details; Figure 7.23).

7.5.3 Implications for Partial Melting

The thermal structure of the interior found from Case 14 can be useful in determining if pressure release melting is plausible under the assumed conditions, especially since recent studies infer geologically recent or current surface volcanism [Smrekar *et al.*, 2010]. To determine if pressure release melting could occur, a suitable solidus needs to be adopted. This is particularly difficult for Venus due to the uncertainties surrounding the rheology of the mantle and the composition of peridotite, which can influence the location of the solidus [Hirschmann, 2000].

Figure 7.26 shows the horizontally averaged temperature with respect to depth for Case 14, scaled using a surface temperature of 730 K, a temperature contrast of 1000 K, and an adiabatic temperature gradient of 0.36 K km^{-1} [Fowler, 2004]. Three solidi are also shown

Atla Regio



Beta Regio

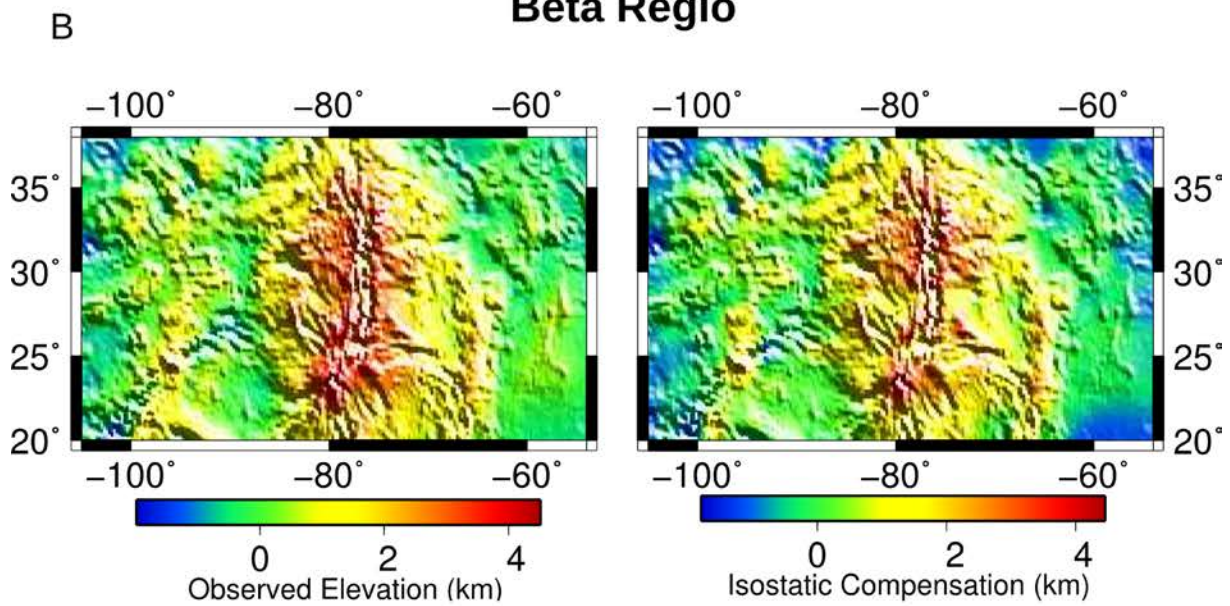


Figure 7.23. The observed elevation and isostatic compensation for long-wavelength thermal thinning. The isostatic compensation maps also include short-wavelength compensation from crustal thickness variations.

including a wet solidus [Gerya *et al.*, 2006], a dry peridotite solidus [Basaltic Volcanism Study Project, 1981], a dry KLB-1 peridotite solidus up to a pressure of 22.5 GPa [Hertzberg *et al.*, 2000], and one liquidus of garnet peridotite [McKenzie and Bickle, 1988]. These three solidi were calculated from Equations 7.26-7.28 with the liquidus from Equation 7.29 [Basaltic Volcanism Study Project, 1981; Gerya *et al.*, 2006; Hertzberg *et al.*, 2000; McKenzie and Bickle, 1988]. The equations for the solidi are:

$$T(K) = 1350 + 0.0001P(GPa) \text{ for dry peridotite} \quad (7.26)$$

$$T(K) = \left(\frac{405.15}{GPa}\right)P + 1375.15; P < 22.5 GPa \text{ for dry KLB-1 peridotite} \quad (7.27)$$

$$T(K) = 1240 + \frac{49.8}{(P(GPa) + 0.323)}; P < 2.4 GPa \quad \text{for wet peridotite} \quad (7.28)$$

$$T(K) = 1266 - 11.8P(GPa) + 3.5P^2; P > 2.4 GPa$$

and the liquidus:

$$T(^{\circ}C) = 1736.2 + 4.343P + 180 \arctan\left(\frac{P}{2.2169}\right) \text{ for garnet peridotite} \quad (7.29)$$

It should be noted that this liquidus crosses the wet solidus at a depth of ~560 km (Figure 7.26) and comparing the two below these depths becomes problematic and unreliable. From Figure 7.26, the horizontally averaged temperature profile for Case 14 touches, but does not cross, the wet solidus. The temperature profile taken at the center of Plume 1, however, does cross the same solidus, initiating partial melting at a depth of ~200 km and generating a maximum melt fraction of 0.21 or 21 % (See Figure 7.26 for description). Even though the garnet peridotite liquidus is not directly comparable to the peridotite solidi, in the absence of other information, it does provide a simple estimate of the percentage of partial melt possibly associated with an upwelling mantle plume.

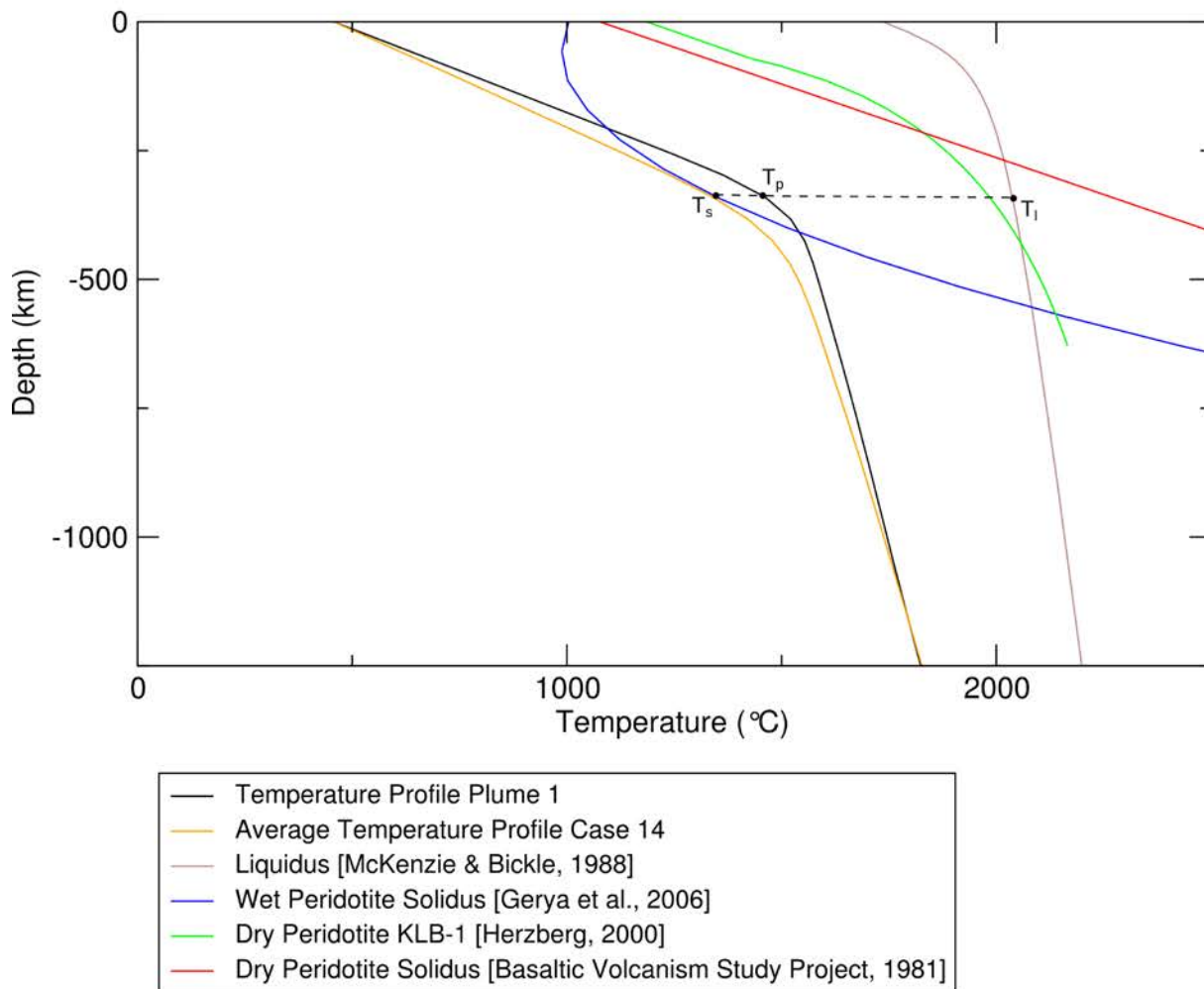


Figure 7.24. Wet melting occurs for the temperature profile taken at Plume 1 (150°E and -15°N) with no wet melting occurring for the horizontally averaged temperature profile from Case 14 or the dry peridotite solidi. The fraction of melt generated was calculated from *McKenzie and Bickle* [1988], using the supersolidus temperature found from $(T_p - T_s)/(T_l - T_s)$, as shown on the diagram.

Both the average temperature profile and the temperature profile from the plume do not cross the dry solidus (Figure 7.24). Within our models the lid is immobile, and does not fault, however, if localised motion of the lid was accounted for, then dry melting may be possible. For example, if rifting occurs above an upwelling mantle plume the lithosphere could be quite thin, resulting in a steeper "geotherm", which may be able to cross the dry solidi and produce dry melting.

Venus's solidus and liquidus are also highly unconstrained since its exact composition is not known [Smrekar and Sotin, 2012]. However, our results imply a hydrated mantle is more conducive to melting in areas of thermal thinning associated with an upwelling mantle plume. Venus's mantle may be hydrated if the high surface pressures act to reduce volatile degassing and cause magma to become impeded within the crust and mantle [Elkins-Tanton *et al.*, 2007; Head and Wilson, 1992.; Papale, 1997]. Furthermore, localised areas of Venus's mantle, which have undergone melting, may have volatile concentrations of 1-2% [Aubaud *et al.*, 2004; Koga *et al.*, 2003; Namiki and Solomon, 1998].

7.6 Conclusions

This study has constrained the parameters contributing to Venus's internal dynamics, topography and geoid both globally and locally. Our best-fit model involves an effective Rayleigh number of 2.5×10^7 , internal heating of 40, a pre-exponential factor of 3 for the lower mantle and an activation energy of 10. Unlike previous 3D spherical shell models, we used a range of activation energies and discovered this parameter significantly influences the resulting geoid, topography, and lid thickness, while making the models more time-dependent.

Atla and Beta Regio both exhibit high observed geoid and topography admittance and

correlation values at low spherical harmonic degrees, implying long wavelength compensation. Since thermal thinning and dynamic uplift both contribute to long wavelength support, discerning the contribution of each mechanism can be difficult. From our best-fit model, up to ~1.5 km and ~0.5 km of the observed topography and 110 m and 120 m of the observed geoid at Atla and Beta Regio, respectively is supported by convective stresses within the mantle, with the remaining long wavelength topography being supported by thermal thinning of the lithosphere.

The number (~60) of upwellings generated from this model is higher than the number of volcanic rises observed on the surface (~9-12) [McKenzie, 1994; Stofan *et al.*, 1995], with these remaining upwellings possibly corresponding to the numerous coronae, volcanoes, and rifts observed on the surface. Our best-fit model also has important implications for volcanism associated with an upwelling mantle plume, if Venus's mantle is hydrated.

7.7 References

- Aubaud, C., E. H. Hauri, and M. M. Hirschmann (2004), Hydrogen partition coefficients between nominally anhydrous minerals and basaltic melts, *Geophysical Research Letters*, 31(20), L20611, doi:10.1029/2004GL021341.
- Arkani-Hamed, J., G. G. Schaber, and R. G. Strom (1993), Constraints on the thermal evolution of Venus inferred from Magellan data, *Journal of Geophysical Research: Planets*, 98(E3), 5309–5315, doi:10.1029/93JE00052.
- Basaltic Volcanism Study Project (1981) *Basaltic Volcanism on the Terrestrial Planets*, Pergamon Press, Oxford.
- Basilevsky, A. T., and J. W. Head (2007), Beta Regio, Venus: Evidence for uplift, rifting, and

- volcanism due to a mantle plume, *Icarus*, 192(1), 167–186,
doi:10.1016/j.icarus.2007.07.007.
- Benešová, N., and H. Čížková (2012), Geoid and topography of Venus in various thermal convection models, *Studia Geophysica Geodaetica*, 56(2), 621–639,
doi:10.1007/s11200-011-0251-7.
- van den Berg, A. P., P. E. van Keken, and D. A. Yuen (1993), The effects of a composite non-Newtonian and Newtonian rheology on mantle convection, *Geophysical Journal International*, 115(1), 62–78, doi:10.1111/j.1365-246X.1993.tb05588.x.
- Bindschadler, D. L., G. Schubert, and W. M. Kaula (1990), Mantle flow tectonics and the origin of Ishtar Terra, Venus, *Geophysical Research Letters*, 17(9), 1345–1348,
doi:10.1029/GL017i009p01345.
- Bindschadler, D. L., G. Schubert, and W. M. Kaula (1992), Coldspots and hotspots: Global tectonics and mantle dynamics of Venus, *Journal of Geophysical Research: Planets*, 97(E8), 13495–13532, doi:10.1029/92JE01165.
- Bossman, A.B., and P.E. Keken (2013), Dynamics of plumes in a compressible mantle with phase changes: implications for phase boundary topography, *Physics of the Earth and Planetary Interiors*, 224, p 21-31.
- Christensen, U. (1984), Convection with pressure- and temperature-dependent non-Newtonian rheology, *Geophysical Journal of the Royal Astronomical Society*, 77(2), 343–384,
doi:10.1111/j.1365-246X.1984.tb01939.x.
- Elkins-Tanton, L. T., S. E. Smrekar, P. C. Hess, and E. M. Parmentier (2007), Volcanism and volatile recycling on a one-plate planet: Applications to Venus, *Journal of Geophysical Research: Planets*, 112, E04S06, doi:10.1029/2006JE002793.

- Fowler, C. M. R. (2004), *The Solid Earth: An Introduction to Global Geophysics*, 2nd ed., Cambridge University Press, United Kingdom.
- Gerya, T. V., J. A. D. Connolly, D. A. Yuen, W. Gorczyk, and A. M. Capel (2006), Seismic implications of mantle wedge plumes, *Physics of the Earth and Planetary Interiors*, 156(1–2), 59–74, doi:10.1016/j.pepi.2006.02.005.
- Grimm, R. E., and S. C. Solomon (1988), Viscous Relaxation of Impact Crater Relief on Venus: Constraints on Crustal Thickness and Thermal Gradient, *Journal of Geophysical Research*, 93(B10), 11911–11929, doi:10.1029/JB093iB10p11911.
- Head, J. W. and L. Wilson (1992), Magma reservoirs and neutral buoyancy zones on Venus: implications for the formation and evolution of volcanic landforms, *Journal of Geophysical Research*, 97(E3), 3877–3903, doi:10.1029/92JE00053.
- Herzberg, C., P. Raterron, and J. Zhang (2000), New experimental observations on the anhydrous solidus for peridotite KLB-1, *Geochemistry, Geophysics, Geosystems*, 1(11), 1051, doi:10.1029/2000GC000089.
- Hirschmann, M. M. (2000), Mantle solidus: Experimental constraints and the effects of peridotite composition, *Geochemistry, Geophysics, Geosystems*, 1(10), 2000GC000089, doi:10.1029/2000GC000070.
- Höink, T., A. Lenardic, and M. Richards (2012), Depth-dependent viscosity and mantle stress amplification: implications for the role of the asthenosphere in maintaining plate tectonics, *Geophysical Journal International*, 191(1), 30–41, doi:10.1111/j.1365-246X.2012.05621.x.
- Huang, J., A. Yang, and S. Zhong (2013), Constraints of the topography, gravity and volcanism on Venusian mantle dynamics and generation of plate tectonics, *Earth and*

Planetary Science Letters, 362, 207–214, doi:10.1016/j.epsl.2012.11.051.

van Hunen, J., S. Zhong, N. M. Shapiro, and M. H. Ritzwoller (2005), New evidence for dislocation creep from 3-D geodynamic modeling of the Pacific upper mantle structure, *Earth and Planetary Science Letters*, 238(1–2), 146–155, doi:10.1016/j.epsl.2005.07.006.

Kaula, W. M. (1990), Venus: A Contrast in Evolution to Earth, *Science*, 247(4947), 1191–1196, doi:10.1126/science.247.4947.1191.

Kaula, W. M. (1995), Venus reconsidered, *Science*, 270(5241), 1460–1464.

Kaula, W. M., T. Owen, S. K. Runcorn, and D. C. Tozer (1994), The Tectonics of Venus [and Discussion], *Philosophical Transactions of the Royal Society London*, 349(1690), 345–355, doi:10.1098/rsta.1994.0137.

Kiefer, W. S., and B. H. Hager (1991), Mantle Downwelling and Crustal Convergence: A Model for Ishtar Terra, Venus, *Journal of Geophysical Research*, 96(E4), 20,967–20,980, doi:10.1029/91JE02219.

Koga, K., E. Hauri, M. Hirschmann, and D. Bell (2003), Hydrogen concentration analyses using SIMS and FTIR: Comparison and calibration for nominally anhydrous minerals, *Geochemistry, Geophysics, Geosystems*, 4(2), 1019, doi:10.1029/2002GC000378.

Konopliv, A. S., and C. F. Yoder (1996), Venusian k2 tidal Love number from Magellan and PVO tracking data, *Geophysical Research Letters*, 23(14), 1857–1860, doi:10.1029/96GL01589.

Mackwell, S. J., M. E. Zimmerman, and D. L. Kohlstedt (1998), High-temperature deformation of dry diabase with application to tectonics on Venus, *Journal of Geophysical Research: Solid Earth*, 103(B1), 975–984, doi:10.1029/97JB02671.

- McKenzie, D. (1994), The Relationship between Topography and Gravity on Earth and Venus, *Icarus*, 112(1), 55–88, doi:10.1006/icar.1994.1170.
- McKenzie, D., and M. J. Bickle (1988), The Volume and Composition of Melt Generated by Extension of the Lithosphere, *Journal of Petrology*, 29(3), 625–679.
- Moresi, L., and B. Parsons (1995), Interpreting Gravity, Geoid, and Topography for Convection with Temperature Dependent Viscosity: Application to Surface Features on Venus, *Journal of Geophysical Research*, 100(E10), 21,155–21,171, doi:199510.1029/95JE01622.
- Musser, G. S., and S. W. Squyres (1997), A coupled thermal-mechanical model for corona formation on Venus, *Journal of Geophysical Research: Planets*, 102(E3), 6581–6595, doi:10.1029/96JE03044.
- Namiki, N., and S. C. Solomon (1998), Volcanic degassing of argon and helium and the history of crustal production on Venus, *Journal of Geophysical Research: Planets*, 103(E2), 3655–3677, doi:10.1029/97JE03032.
- Nimmo, F., and D. McKenzie (1998), Volcanism and Tectonics on Venus, *Annual Review of Earth and Planetary Sciences*, 26(1), 23–51, doi:10.1146/annurev.earth.26.1.23.
- Papale, P. (1997), Modeling of the solubility of a one-component H₂O or CO₂ fluid in silicate liquids, *Contributions to Mineralogy and Petrology*, 126(3), 237–251, doi:10.1007/s004100050247.
- Pauer, M., K. Fleming, and O. Čadež (2006), Modeling the dynamic component of the geoid and topography of Venus, *Journal of Geophysical Research*, 111(E11), doi:10.1029/2005JE002511.
- Phillips, R. J., R. E. Grimm, and M. C. Malin (1991), Hot-Spot Evolution and the Global

- Tectonics of Venus, *Science*, 252(5006), 651–658, doi:10.1126/science.252.5006.651.
- Ratcliff, J. T., P. J. Tackley, G. Schubert, and A. Zebib (1997), Transitions in thermal convection with strongly variable viscosity, *Physics of the Earth and Planetary Interiors*, 102(3–4), 201–212, doi:10.1016/S0031-9201(97)00013-7.
- Reese, C. C., V. S. Solomatov, and L.-N. Moresi (1998), Heat transport efficiency for stagnant lid convection with dislocation viscosity: Application to Mars and Venus, *Journal of Geophysical Research: Planets*, 103(E6), 13643–13657, doi:10.1029/98JE01047.
- Reese, C. C., V. S. Solomatov, and L.-N. Moresi (1999), Non-Newtonian Stagnant Lid Convection and Magmatic Resurfacing on Venus, *Icarus*, 139(1), 67–80, doi:10.1006/icar.1999.6088.
- Richards, M. A., W.-S. Yang, J. R. Baumgardner, and H.-P. Bunge (2001), Role of a low-viscosity zone in stabilizing plate tectonics: Implications for comparative terrestrial planetology, *Geochemistry, Geophysics, Geosystems*, 2(8), 1026, doi:10.1029/2000GC000115.
- Schubert, G., D. Bercovici, and G. A. Glatzmaier (1990), Mantle Dynamics in Mars and Venus: Influence of an Immobile Lithosphere on Three-Dimensional Mantle Convection, *Journal of Geophysical Research*, 95(B9), 14,105–14,129, doi:10.1029/JB095iB09p14105.
- Schubert, G., and C.A.P. Goldman (2012), Mantle plume interaction with an endothermic phase change, *Journal of Geophysical Research*, 100, B5, 8245–8256.
- Schubert, G., V. S. Solomatov, P. J. Tackley, and D. L. Turcotte (1997), *Mantle convection and the thermal evolution of Venus*, 1245–1287, The University of Arizona Press, Tucson.
- Schubert, G., D. L. Turcotte, and P. Olson (2001), *Mantle convection in the earth and planets*,

Cambridge University Press, New York.

Senske, D. A., and J. W. Head (1992), Atla Regio, Venus: Geology and Origin of a Major Equatorial Volcanic Rise, *Papers presented to the International Colloquium Venus*, pp. 107–109.

Simons, M., B. H. Hager, and S. C. Solomon (1994), Global Variations in the Geoid/Topography Admittance of Venus, *Science*, 264(5160), 798–803, doi:10.1126/science.264.5160.798.

Simons, M., S. C. Solomon, and B. H. Hager (1997), Localization of gravity and topography: constraints on the tectonics and mantle dynamics of Venus, *Geophysical Journal International*, 131(1), 24–44, doi:10.1111/j.1365-246X.1997.tb00593.x.

Sjogren, W. L., W. B. Banerdt, P. W. Chodas, A. S. Konopliv, G. Balmino, J. P. Barriot, J. Arkani-Hamed, T. R. Colvin, and M. E. Davies (1997), The Venus gravity field and other geodetic parameters, in *Venus II: Geology, Geophysics, Atmosphere and Solar Wind Environment*, 1125–1161, The University of Arizona Press, Arizona.

Smrekar, S. E., and R. J. Phillips (1991), Venusian Highlands: Geoid to Topography Ratios and their Implications, *Earth and Planetary Science Letters*, 107(3-4), 582–597, doi:10.1016/0012-821X(91)90103-O.

Smrekar, S. E., and C. Sotin (2012), Constraints on mantle plumes on Venus: Implications for volatile history, *Icarus*, 217(2), 510–523, doi:10.1016/j.icarus.2011.09.011.

Smrekar, S. E., E. R. Stofan, N. Mueller, A. Treiman, L. Elkins-Tanton, J. Helbert, G. Piccioni, and P. Drossart (2010), Recent Hotspot Volcanism on Venus from VIRTIS Emissivity Data, *Science*, 328(5978), 605–608, doi:10.1126/science.1186785.

Solomatov, V. S., and L.-N. Moresi (1996), Stagnant Lid Convection on Venus, *Journal of*

Geophysical Research, 101(E2), 4737–4753, doi:199610.1029/95JE03361.

Solomon, S. C., and J. W. Head (1991), Fundamental issues in the geology and geophysics of venus, *Science*, 252(5003), 252–260, doi:10.1126/science.252.5003.252.

Squyres, S. W., D. M. Janes, G. Schubert, D. L. Bindschadler, J. E. Moersch, D. L. Turcotte, and E. R. Stofan (1993), The spatial distribution of coronae and related features on Venus, *Geophysical Research Letters*, 20(24), 2965–2968, doi:10.1029/93GL00866.

Steinbach, V., and D. A. Yuen (1992), The effects of multiple phase transitions on Venusian mantle convection, *Geophysical Research Letters*, 19(22), 2243–2246, doi:10.1029/92GL02319.

Stofan, E. R., J. W. Head, D. B. Campbell, S. H. Zisk, A. F. Bogomolov, O. N. Rzhiga, A. T. Basilevsky, and N. Armand (1989), Geology of a rift zone on Venus: Beta Regio and Devana Chasma, *Geological Society of America Bulletin*, 101(1), 143–156, doi:10.1130/0016-7606(1989)101<0143:GOARZO>2.3.CO;2.

Stofan, E. R., and S. E. Smrekar (2005), Large topographic rises, coronae, large flow fields, and large volcanoes on Venus: Evidence for mantle plumes?, *Geological Society of America Special Papers*, 388, 841–861, doi:10.1130/0-8137-2388-4.841.

Stofan, E. R., S. E. Smrekar, D. L. Bindschadler, and D. A. Senske (1995), Large Topographic Rises on Venus: Implications for Mantle Upwelling, *Journal of Geophysical Research*, 100(E11), 23317–23327, doi:10.1029/95JE01834.

Tan, E., E. Choi, P. Thoutireddy, M. Gurnis, and M. Aivazis (2006), GeoFramework: Coupling multiple models of mantle convection within a computational framework, *Geochemistry, Geophysics, Geosystems*, 7(6), Q06001, doi:10.1029/2005GC001155.

Tan, E., M. Gurnis, L. Armendariz, L. Strand, and S. Kientz (2012), *CitcomS User Manual*

Version 3.2.0, Computational Infrastructure for Geodynamics (CIG).

Vezolainen, A. V., V. S. Solomatov, A. T. Basilevsky, and J. W. Head (2004), Uplift of Beta Regio: Three-dimensional models, *Journal of Geophysical Research*, 109, E08007, doi:200410.1029/2004JE002259.

Weertman, J. (1970), The creep strength of the Earth's mantle, *Reviews of Geophysics*, 8(1), 145–168, doi:10.1029/RG008i001p00145.

Wessel, P., and W. H. F. Smith (1991), Free Software Helps Map and Display Data, *EOS Transactions, American Geophysical Union*.

Wessel, P., and W. H. F. Smith (1998), New, improved version of Generic Mapping Tools released, *EOS Transactions, American Geophysical Union*, 79(49), 579.

Wieczorek, M. A. (2007), Gravity and Topography of the Terrestrial Planets, *Treatise on Geophysics*, 165–206.

Wieczorek, M. A., and F. J. Simons (2005), Localized spectral analysis on the sphere, *Geophysical Journal International*, 162, 655–675.

Wieczorek, M. A., and F. J. Simons (2007), Minimum-Variance Multitaper Spectral Estimation on the Sphere, *Journal of Fourier Analysis and Applications*, 13(6), 665–692, doi:10.1007/s00041-006-6904-1.

Zhong, S., A. McNamara, E. Tan, L. Moresi, and M. Gurnis (2008), A benchmark study on mantle convection in a 3-D spherical shell using CitcomS, *Geochemistry, Geophysics, Geosystems*, 9(10), Q10017, doi:10.1029/2008GC002048.

Zhong, S., M. T. Zuber, L. Moresi, and M. Gurnis (2000), Role of temperature-dependent viscosity and surface plates in spherical shell models of mantle convection, *Journal of*

Geophysical Research: Solid Earth, 105(B5), 11063–11082,

doi:10.1029/2000JB900003.

8. Discussion

8.1 Lithospheric Modelling Discussion

8.1.1 Technique and Assumptions

Studies addressing the processes supporting Venus's topography have tended to focus solely on the role of either regional isostasy, dynamic uplift and mantle convection, or Airy and thermal isostasy [Anderson and Smrekar, 2006; Barnett *et al.*, 2000; Grimm and Hess, 1997; James *et al.*, 2013; Johnson and Sandwell, 1994; Kiefer and Hager, 1991; Kucinskas *et al.*, 1996; Kucinskas and Turcotte, 1994; Moore and Schubert, 1995, 1997; Orth and Solomatov, 2011; Schubert *et al.*, 1994; Solomatov and Moresi, 1996; Stofan *et al.*, 1995]. Instead of analysing each of these processes separately, a more complete approach is required, since the complexity of Venus's surface implies multiple compensation mechanisms are operating concurrently. This is the first integrated, cross-disciplinary study addressing the contribution of long and short wavelength processes in compensating the observed topography at Atla and Beta Regio as well as Fortuna Tessera.

Lithospheric modelling used a 3D, rather than a 2D approach, which allowed for more realistic and complex lithospheric structures. For example, models using 3 dimensions assume a body extends to a finite distance along strike of the current cross-section, whereas a 2D approach considers the same body to be infinite.

Before modelling an area, which has undergone tectonic and volcanic modification, a suitable reference column had to be defined first. GEO3Dmod requires this column to be taken at a geographical coordinate, such as 34.5°E 89°N, within the North Polar Plains [Fullea *et al.*,

2009]. Plains regions exhibit minimal deformation, compared to other regions, with their emplacement and majority of deformation ceasing ~ 700 Myr ago [Phillips, 1998]. The North Polar Plains are particularly interesting as they share an elevation that is close to Venus's Mean Planetary Radius (MPR) [Solomon and Head, 1990]. Therefore, this reference lithospheric structure could represent a large proportion of the surface since 65% of plains regions reside within 0.5 km of Venus's MPR [Pettengill et al., 1980; Solomon and Head, 1990].

On Venus average lithospheric thickness estimates range from being thin (~ 100 km) to thick (~ 300 - 600 km) [Nimmo and McKenzie, 1996,1998; Orth and Solomatov, 2011; Schubert et al., 1994; Smrekar, 1994; Smrekar and Phillips, 1991; Solomatov and Moresi, 1996; Turcotte, 1993]. Most authors also propose Venus's crust, on average, is between 15 km and 30 km thick [Grimm and Hess, 1997; James et al., 2013; Zuber, 1987]. Due to these inconsistencies surrounding both the average crustal and lithospheric thickness of Venus, three reference lithospheric structures were assumed in the study at Atla Regio. The first reference column used a 30 km thick crust and 300 km thick thermal lithosphere. The second reference column used a similar lithospheric thickness (300 km), but adopted a 15 km thick crust. The third reference column, however, used a much thinner lithospheric thickness (140 km) with a crustal thickness of 15 km. Using a thinner (140 km) reference lithospheric thickness shifted the modelled lithospheric thickness to a shallower depths, with almost a direct relationship occurring between thinning the reference lithospheric thickness and the modelled lithosphere. For example, using Reference Column 3 resulted in the lithosphere below the modelled plains to be ~ 150 km thinner, compared to those found for Reference Column 1. Considering this relationship, if the reference lithosphere was 400 km thick, a maximum modelled lithospheric thickness of ~ 500 km and ~ 445 km would result below the plains regions at Beta Regio and Fortuna Tessera, respectively. Therefore, an extremely thick (> 400 km) reference lithosphere was not adopted since the base of the resulting modelled thermal lithosphere, particularly

within the plains regions, would occur below the first phase transition (~440-490 km)

[Schubert *et al.*, 1997; Steinbach and Yuen, 1992].

A thick reference thermal lithosphere was also not favoured after considering previous numerical modelling results [Solomatov and Moresi, 1996]. These models imply Venus has a maximum average lithospheric thickness of 200-400 km, with the same model yielding lithospheric thicknesses of 400-550 km below Beta Regio [Solomatov and Moresi, 1996]. However, Beta Regio is a volcanic rise, with strong evidence (e.g. rifts, expansive volcanic flows, high topography and geoid anomalies) indicating it should experience thermal thinning, resulting in a thinner than average lithospheric thickness (i.e. < 200 km) [Kucinskas and Turcotte, 1994; Moore and Schubert, 1997].

From Chapter 4, it was found that a thinner lithospheric thickness (140 km) or crust (15 km) would also produce implausible ($\sim < 1$ km) crustal and lithospheric thinning below Ganis Chasma in Atla Regio. All of these results imply a thick reference crust (30 km) and thermal lithosphere (300 km) is the most feasible lithospheric structure at the North Polar Plains. The melt generation volumes and rates obtained for the proposed lithospheric structure at Atla Regio, which were similar to those obtained from previous studies, also indirectly constrain these chosen reference column parameters. By constraining a suitable reference column at the North Polar Plains, this study was able to indirectly estimate the lithospheric structure below the vast plains regions, and in turn, approximately ~65 % of Venus's surface.

8.1.2 Volcanism

Deviations in the crustal structure below the volcanoes addressed within Atla and Beta Regio may indicate differences in magma composition and eruptive style. Sapas and Ozza Mons in

Atla Regio, and Theia and Rhea Mons in Beta Regio, were underlain by a thick upper crustal layer and lower crust of basalt and gabbro, respectively. This structure, however, was unable to fit the highest volcano on Venus, Maat Mons, and required a low density dioritic intrusion in a basaltic upper crust. Geochemical measurements at the Venera and Vega landing sites imply a primarily basaltic composition, further evidenced by volcanoes that exhibit shield-like morphologies, profuse and extensive lava flows [Grimm and Hess, 1997; Head *et al.*, 1992]. Due to the limited number of samples taken, a basaltic composition may not be representative of the entire crust, with no samples taken near Maat Mons [Grimm and Hess, 1997]. Some authors have proposed more silicic compositions are required to explain the elevated terrain of Ishtar Terra and steep-sided domes [Grimm and Hess, 1997; Jull and Arkani-Hamed, 1995; McKenzie *et al.*, 1992]. A crust that has a mafic to intermediate silica content, such as diorite, is plausible considering both geochemical and geomorphological constraints [Grimm and Hess, 1997].

A felsic magma composition, with high silica and volatile content, can result in more explosive eruptions on Earth [Self, 2006]. Pioneer detected an increase in SO₂ within Venus's upper atmosphere during its orbit, which some authors inferred was due to recent volcanic activity [Glaze, 1999; Glaze *et al.*, 2011; Robinson *et al.*, 1995]. In order for a volcano to erupt this SO₂ high into Venus's atmosphere, an explosive volcanic event was required within the recent geological history [Robinson *et al.*, 1995]. Robinson *et al.* [1995] used the lack of craters on the volcanic flanks of Maat Mons, and stratigraphically young lava flows, to imply this volcano was recently active.

The intrusion of more silica- and volatile-rich magma, as evidenced by the dioritic intrusion, could have resulted in an explosive eruption, facilitated by the low atmospheric pressure (~55 bars) and volatile exsolution (~2 wt% H₂O) that occurs at Maat Mons's elevation [Head and

Wilson, 1992; Robinson *et al.*, 1995]. However, the extensive lava flows and gentle slopes of this volcano suggests a more basaltic composition of extruded lavas [Robinson *et al.*, 1995]. To overcome these contradictions, Robinson *et al.* [1995] proposed highly volatile basaltic magmas (~5 wt% H₂O) produced an explosive Plinian eruption at Maat Mons, contributing to the spike in SO₂ detected within Venus's upper atmosphere by Pioneer. It is expected that pyroclastic deposits would have resulted from this explosive eruption, however none have been observed [Robinson *et al.*, 1995].

8.1.3 Rifting

Thinning of the thermal lithosphere can facilitate rifting on the terrestrial planets [Spohn and Schubert, 1983]. Atla and Beta Regio are both sites of extensive (~200 km) thermal thinning and exhibit evidence of geologically recent and current activity [Basilevsky, 1993; Basilevsky and Head, 2002; Jurdy and Stoddard, 2007; Matias *et al.*, 2004; Matias and Jurdy, 2005].

Considering the lithospheric models, the crustal and thermal lithosphere are thinner (< 4 km and ~50 km, respectively) at Ganis Chasma in Atla Regio compared to Devana Chasma in Beta Regio (~15 km and ~60 km, respectively). Also, studies completed at both rises have found craters dip outwards from the central rise at Atla Regio whereas the craters in Beta Regio exhibit random dip orientations. However, the low number (3) of impact craters observed in Beta Regio suggest these might not be a representative sample [Matias *et al.*, 2004; Matias and Jurdy, 2005]. The lithospheric modelling results found at Beta Regio are consistent with geologically recent activity, however, rifting may occur at rates between 5-12 mm yr⁻¹ in localised regions along Ganis Chasma.

If Ganis Chasma is rifting, creating new crust in the process, then some form of crustal

destruction must also be occurring in order to maintain Venus's total surface area. Two processes have been proposed to destroy the lithosphere on Venus including retrograde localised subduction and delamination [Schubert and Sandwell, 1995; Turcotte, 1995]. Schubert and Sandwell [1995] proposed Venusian coronae and chasmata share similar topographic and flexural morphologies to subduction zones on Earth. These authors also suggest that both rifting and subduction operate closely together, with rifting acting to initially fracture the lithosphere, allowing subduction to occur. The subduction of the lithosphere would occur along the rift's side when it moves outwards to areas of cooler, thicker lithosphere, changing from a rift at the volcanic rise, to a subduction zone within the plains [Schubert and Sandwell, 1995]. Localised rifting may operate within Atla Regio, but no evidence of localised subduction was observed within the lithospheric model as it did not extend into the vast lowland areas surrounding this volcanic rise.

New crust produced at a zone of rifting may also be destroyed by delamination after crustal compression at crustal plateaus and tessera inliers [Romeo and Turcotte, 2008; Turcotte, 1995]. The crust and lithospheric mantle thickens and uncouples due to compression, with the gravitationally unstable lithospheric mantle participating in subduction [Arkani-Hamed, 1993; Buck, 1992; Romeo and Turcotte, 2008; Turcotte, 1995]. However, this process may be limited on Venus, since decoupling of the crust and lithospheric mantle would be hindered if the lower crust is dry [Mackwell *et al.*, 1998].

Due to the proposed slow-spreading rates associated with Ganis Chasma, the surrounding plains regions, rather than distal crustal plateaus and tessera terrain, most likely accommodate this additional crust. Plains regions on Venus exhibit wrinkle ridges, which are anticlines and thrust faults, and are responsible for regional shortening by 2-5% [Bilotti and Suppe, 1999; McGill, 1993]. Bilotti and Suppe [1999] proposed that some upwellings below volcanic rises

were associated with compressional wrinkle ridges within the plains regions, with these features also showing parallel orientations to the rise's topography and geoid contours. A similar trend was also observed by *Sandwell et al.* [1997] who calculated Venus's global strain field and compared this to geological observations. These authors found that extensional structures correlated with high geoid and topography and compressional structures were associated with low geoid and topography anomalies. These compressional structures include wrinkle-ridges, which occur below a geoid height of 20 m and below Venus's MPR. However, Atla Regio showed a high correlation to strain and a lack of concentric wrinkle-ridges implying a thin, young thermal lithosphere, and recent activity [*Bilotti and Suppe*, 1999; *Sandwell et al.*, 1997], further reinforcing the results found in Chapter 4.

8.1.4 Elastic Lithospheric Thickness

Observations of Venus's high topography and geoid anomalies and unrelaxed craters imply a thick, strong elastic lithosphere capable of compensating topography over the last ~500 Myr of Venus's geological history [*Grimm and Solomon*, 1988; *Phillips et al.*, 1997; *Schubert et al.*, 1994]. Observations of an area's geological features and history are useful when interpreting elastic lithospheric thickness estimates. For example, a thin elastic lithosphere could imply an area is predominantly supported by isostatic compensation or that the area has been recently active [*Anderson and Smrekar*, 2006; *Nimmo and McKenzie*, 1998]. This relationship is similar to that observed between the modelled terrains, where the older tessera terrain of Fortuna Tessera is dominated by isostatic compensation and a thin (10 km) elastic lithosphere. A thicker (50 km) elastic lithosphere was found to be more appropriate at the volcanic rises of Atla and Beta Regio. Within these areas the volcanoes, Maat and Oza Mons in Atla Regio and Theia Mons in Beta Regio, and can not be supported solely by isostasy, but require additional compensation from flexure. However, localised rifting at Ganis Chasma in

Atla Regio implies this area should have a locally variable elastic lithosphere. This variation between modelled and real values are caused from the assumption of a uniform elastic lithospheric thickness in flexural calculations completed by GEO3Dmod. On Venus, the elastic lithosphere at these volcanic rises would vary between both the rifts and volcanoes, as well as the entire volcanic rise and the surrounding plains regions. These variations confirm geological activity on Venus may not have ceased at ~700 Ma, since a uniform elastic lithosphere would be expected after ~100 Myr [Anderson and Smrekar, 2006; McKinnon *et al.*, 1997].

8.1.5 Surface Heat Flow

Lithospheric structure and surface heat flow are directly related to Venus's thermal history, global heat loss, volcanism, and tectonism [Reese *et al.*, 1999; Solomon and Head, 1982; Turcotte, 1993]. Heat transfer through the lithosphere on terrestrial planets can occur within three "tectonic" regimes including plate recycling, stagnant-lid lithospheric conduction, and advection of heat during volcanism [Solomon and Head, 1982]. Assuming Hawaiian-type hotspot volcanism, ~80 to 10^4 active hotspots are required to efficiently extract the total heat flow from Venus, implying most of Venus's surface would need to be covered by hotspots [Schubert *et al.*, 1997; Solomon and Head, 1982]. Plate recycling is responsible for most (65%) of the heat lost from the interior of Earth, however, evidence of a similar process is unclear on Venus [Nimmo and McKenzie, 1998; Solomon and Head, 1982]. Considering Venus lacks evidence for plate tectonics, including multiple tectonic plates and linear volcanic chains, the mechanisms that transport heat through the surface are important [Turcotte, 1995]. Venus and Earth share a similar mass and surface area, and possibly, heat loss per mass [Brown and Grimm, 1999; Solomon and Head, 1982; Turcotte, 1995]. No surface heat flow measurements have been made for Venus with estimates provided by scaling Earth based

values [Brown and Grimm, 1999; Solomon and Head, 1982; Turcotte, 1995]. From Earth scaling, the average global heat loss and surface heat flow were found to range from 2.91 to 3.4×10^{13} W and 63 to 78 mW m⁻², respectively. In contrast, convection models resulted in a wider range of estimates, between 15 to 80 mW m⁻² [Arkani-Hamed and Toksöz, 1984; Brown and Grimm, 1999; Phillips, 1998; Solomatov and Moresi, 1996; Solomon and Head, 1982; Turcotte, 1995]. Scaling Venusian heat flow to Earth can involve errors since the quantity of radiogenic elements may be different and the mantle masses of each planet may not scale with the global mass ratio [Brown and Grimm, 1999].

On Earth, high surface heat flows correspond to volcanic areas, with areas exhibiting tectonism having lower values [Turcotte and Schubert, 2001]. Estimates of Venus's global average surface heat flow are available, however, regional estimates are lacking [Brown and Grimm, 1999; Solomon and Head, 1982; Turcotte, 1995]. We also assume the crust comprises similar concentrations of uranium, thorium, and potassium as Earth, since both planets should have formed close together within the protoplanetary disk and Venera and Vega measurements reflect alkali basalts and tholeiites [Basilevsky *et al.*, 1992; Elkins-Tanton *et al.*, 2007; Grimm and Hess, 1997; Kaula *et al.*, 1994; Nimmo and McKenzie, 1996, 1998; Solomon and Head, 1982; Wood *et al.*, 1981].

From lithospheric modelling, higher surface heat flows were associated with the volcanic rises compared to Fortuna Tessera (Table 8.1). By taking an average of the surface heat flow and area at each location, the conductive heat loss and the percentage that this contributes to the global heat loss, can be estimated (Table 8.1).

Both volcanic rises constitute 2.73% of Venus's global surface area and contribute 0.96% to Venus's global heat loss, while Fortuna Tessera represents 1.68 % and 0.41% of total surface

area and global heat loss, respectively (Table 8.1). The highest average surface heat flow occurred at Beta Regio (26.5 mW m⁻²), closely followed by Atla Regio (25.6 mW m⁻²), with Fortuna Tessera sharing a similar value to the plains regions (~17.5 mW m⁻²; Table 8.1). Therefore, these volcanic rises have surface heat flows that are ~43-60 % greater than that at the plains and tessera regions, caused by the thinner modelled thermal lithosphere and greater conductive heat transfer within these areas.

Table 8.1. Average surface heat flow, heat loss and percentage heat loss at each modelled area

Region	Beta Regio		Atla Regio		Fortuna Tessera
	Rise	Plains	Rise	Plains	Tessera
Location (easting)	270°E-290°E	300°E-306°E	185°E-210°E	175°E-180°E	40°E-90°E
Location (northing)	20°N-38°N	20°N-38°N	6°S-22°N	6°S-22°N	62°N-75°N
Average Surface Heat Flow (mW m⁻²)*	26.5	16.6	25.6	17.9	18.0
Surface Area (x10⁶ km²)	4.27	1.28	8.30	1.66	7.71
Percentage Surface Area (%)[‡]	0.93	0.28	1.8	0.36	1.68
Heat Loss[†] (x10¹¹ W)	1.13	0.212	2.12	0.297	1.39
Percentage Heat Loss (%)[#]	0.33	0.063	0.63	0.087	0.41

*The average surface heat flow calculated for the proposed lithospheric structure at each area.

†Found by multiplying the surface area by the mean surface heat flow [Turcotte and Schubert, 2001].

‡Found by dividing the surface area of each feature by Venus's total surface area equal to 4.6x10⁸ km².

#The conductive heat loss for each area expressed as a percentage of the global total heat loss of Venus.

These surface heat flows and their contribution to Venus's total global heat loss are significantly lower than previous estimates since the conductive component is considered only, without contributions from mantle convection and advection from magma ascent.

Advection of heat may actually dominate over conduction if these areas are active, similar to locations on Earth [Jaupart, 2007]. Changes in surface emissivity can imply surface temperature changes associated with volcanism [Mueller *et al.*, 2008]. Higher (by 5%) than average atmospheric flux correlates to higher surface thermal emissivities at volcanic rises (Themis, Indr and Phoebe Regio), coronae and volcanoes within Lade Terra, which may indicate extrusive volcanism [Mueller *et al.*, 2008]. However, these anomalies are relatively stable over time with very small (20 K) variations in temperature implying the heat associated with these higher emissivity areas may not be associated with present volcanism [Smrekar *et al.*, 2010].

It should be noted that the higher heat flows found at Atla and Beta Regio, compared to Fortuna Tessera, are contradictory to the proposed elastic lithospheric thicknesses for each area. The proposed elastic lithospheric thickness at Atla Regio and Beta Regio (50 km), as well as and Fortuna Tessera (10 km), were chosen based on how consistent the resulting flexural topography was to the residual topography. However, two assumptions can influence our proposed elastic lithospheric thickness for each area. The first is the assumption that the elastic lithospheric is constant throughout the modelled area and the second is the assumption that the topography compensated by Airy and thermal isostasy has not been overestimated or underestimated. If the Airy and thermal isostasy has been overestimated or underestimated then the resulting required flexural contribution could correlate to a thinner elastic lithosphere at areas of high surface heat flow (i.e. Atla and Beta Regio) or a thicker elastic lithosphere at areas with low surface heat flow (i.e. Fortuna Tessera).

8.2 Mantle Convection Modelling Discussion

8.2.1 Technique and Assumptions

Numerical modelling presented in Chapter 7 used a 3D spherical shell geometry since it produces a realistic convective structure, and when mantle viscosity and phase changes are incorporated, reproduces the number of plumes more accurately than regional models [Huang *et al.*, 2013]. Each numerical simulation also assumed viscosity varied with temperature, depth, and pressure. Even though temperature and depth dependent viscosity have been included in previous models [e.g. Huang *et al.*, 2013; Ogawa, 2000; Schubert *et al.*, 1997; Smrekar and Sotin, 2012; Solomatov and Moresi, 1996] some uncertainty surrounds the effect of pressure on viscosity [Smrekar and Sotin, 2012].

In this study, phase transitions and the pre-exponential factor have contributed to a variation of viscosity with depth and pressure. Although the depth of the endothermic and exothermic phase transitions can vary by 50 km between authors, it is assumed that Venus's high surface temperature (730 K) and lower pressure gradient (~10% less) makes these transitions occur deeper and closer together than those on Earth [Huang *et al.*, 2013; Schubert *et al.*, 1997; Steinbach and Yuen, 1992].

Another uncertainty is the degree to which pressure will cancel or exceed the effect of temperature on viscosity [Smrekar and Sotin, 2012]. If this does occur, the lower mantle would have a higher viscosity relative to the upper mantle, which can be simulated by numerical models through variations in the pre-exponential factor [Schubert *et al.*, 2001]. Most models shown in Chapter 7 have an increase in viscosity between the upper and lower mantle by a factor of 3 and 30. A value of 3 produces consistent modelled elevation and geoid anomalies compared to a higher value (30). This implies viscosity increases gradually with depth, similar to previous findings [Benešová and Čížková, 2012; Pauer *et al.*, 2006].

One disadvantage of using a spherical geometry is that the number of plumes generated by a

model are strongly influenced by the radius of the core assumed [Smrekar and Sotin, 2012]. This value is highly unconstrained for Venus, varying by a minimum of 700 km [Konopliv and Yoder, 1996]. This study has assumed a value of 3330 km, similar to Huang *et al.* [2013], however Smrekar and Sotin [2012] assumed a lower value of 3120 km. The smaller surface area associated with a smaller core and a thicker mantle will reduce the number of upwellings. Internal heating, which was set to a non-dimensional value of 40 for the best-fit model presented in Chapter 7, can also influence the number of plumes. A high value results in a hotter mantle and a smaller temperature contrast across the basal boundary layer, fostering plume formation [Smrekar and Sotin, 2012].

Thermal and chemical buoyancy drives mantle convection and can contribute to mantle plume formation. Previous authors studying chemical buoyancy found that partial melt, magmatism and the change of basalt into eclogite beyond 50 km depth, can influence mantle convection [Armann and Tackley, 2012]. Chemical buoyancy was included in the numerical models (Chapter 7), however partial melting, magmatism and the basalt to eclogite phase change were not directly modelled. However, it is expected that magmatism, and the associated depleted mantle, would decrease the number of downwellings, but enhance upwellings at the base of the upper mantle due to chemical buoyancy [Dupeyrat and Sotin, 1995]. This process would result in a reduction of surface heat flow and lower internal heat and mass transfer [Dupeyrat and Sotin, 1995]. However, the converse is true if the basalt to eclogite transition is included whereby upwellings become limited and downwellings are promoted due to the denser eclogite, making the transport of heat and mass easy [Dupeyrat and Sotin, 1995].

8.2.2 Mantle Rheology

No direct evidence inferring Venus's mantle is hydrated or dehydrated has been found. A low

or high activation energy can act as an indicator of a wet or dry mantle, respectively, with the best-fit model found in Chapter 7 having a low activation energy (208 kJ mol^{-1}) and possibly resulting in wet melting at an upwelling mantle plume.

Most of Venus's mantle has most likely degassed in the past, producing the thick atmosphere, a small amount (1-2 %) of the remaining volatiles may still occur within the interior in areas that have suffered melting [Aubaud *et al.*, 2004; Koga *et al.*, 2003; Namiki and Solomon, 1998]. On Earth, downwelling of the volatile rich lithosphere at subduction zones aids in replenishing volatiles in the mantle, however this processes is debatable for Venus, with lithospheric delamination being favoured instead [Hamilton and Stofan, 1996; McKenzie *et al.*, 1992; Romeo and Turcotte, 2008; Schubert and Sandwell, 1995; Smrekar *et al.*, 2007]. As the lithosphere sinks after delamination it can experience heating from the upper mantle, releasing volatiles into the mantle [Smrekar *et al.*, 2007]. Compared to Earth, Venus's high surface pressures can limit the amount of volatile degassing from lavas more effectively and stall the ascent of magma in the crust and upper mantle [Elkins-Tanton *et al.*, 2007; Head and Wilson, 1992.; Papale, 1997].

Venus's mantle could also be dry, as evidenced by the lack of asthenosphere, lack of viscous relaxation of impact craters, and stagnant-lid convective regime [Grimm and Solomon, 1988; Smrekar *et al.*, 2007]. The dehydration of Venus's interior could have produced its stronger lithosphere and facilitated the transition from mobile-lid convection to a stagnant-lid regime [Moresi and Solomatov, 1998; Smrekar *et al.*, 2007]. This transition can be enhanced further by a reduction of hydrated minerals and pore fluid in fault zones, which effectively increase the yield strength of the lithosphere and limit modification by convective stresses [Moresi and Solomatov, 1998].

8.2.3 Mantle Convection

All models presented in Chapter 7 exhibit stagnant-lid convection, characterised by an immobile, cold, and thick conductive lid. A similar regime was also adopted by *Huang et al.* [2013], *Orth and Solomatov* [2011]; *Reese et al.* [1999] and *Solomatov and Moresi* [1996], based on the lack of observed geologically recent global volcanism and tectonics. However, a stagnant-lid regime has difficulty accounting for the observed tectonic and volcanic features. In order to account for these observations and the approximately uniform surface age of Venus, *Turcotte* [1993] inferred a stagnant-lid convection regime could be disrupted by periods of plate tectonics.

The present study is concerned with constraining the current conditions and not Venus's evolution, therefore a stagnant-lid regime was modelled instead of an episodic regime. However, the high internal heating (non-dimensional value of 40) associated with the best-fit model may imply the interior is heating up before the next global overturn. This episodic convective regime could also be modelled directly by varying the yield stress of the lithosphere [*Moresi and Solomatov*, 1998].

8.2.4 Lithospheric Thickness

The best-fit numerical model presented in Chapter 7 yielded an average global lithospheric thickness of ~223 km. This value was thinner (by ~77 km) than the assumed reference lithospheric thickness (300 km) at the North Polar Plains for the lithospheric modelling. The thinner average lithospheric thickness obtained from the numerical model is most likely the result of the high number of upwellings (~60) that were found to occur for the best-fit model, which act to thin the conductive lid and force a thinner average. The best-fit numerical model

also exhibits a few localised areas that share a similar elevation to that of the North Polar Plains (~ 1.6 km) and correspond to downwellings, where it is expected that the thermal lithosphere within these areas would approach values closer to 300 km.

8.3. Comparison between Lithospheric and Dynamic Modelling

8.3.1. Dynamic Compensation at Atla and Beta Regio

As shown in Chapter 7, localised geoid and topography admittance and correlation results for Atla and Beta Regio imply these areas require dynamic compensation. This is consistent with the domal morphology, high elevations, high geoid anomalies, presence of rifts and volcanoes, in conjunction with the lithospheric modelling results presented in Chapters 4-5 [*Basilevsky and Head, 2007; Senske and Head, 1992; Smrekar and Phillips, 1991; Stofan et al., 1995*]. For example, lithospheric modelling at Beta Regio required a maximum dynamic uplift of ~ 0.5 km, whereas Atla Regio required 0.5 km at Ozza and Sapas Mons and up to 1.5 km at Maat Mons.

Fortuna Tessera, however, has a low admittance and correlation (Figure 8.1) and can be supported by a combination of Airy and thermal isostasy, as shown in Chapter 6. The lack of dynamic uplift that was required within this area agrees with observations including low apparent depths of compensation, geoid lows, and a lack of domal morphology [*Bindschadler et al., 1992; Vorder Bruegge and Head, 1989; Grimm, 1994; Hansen et al., 1999; Ivanov, 1988; Simons et al., 1997; Smrekar and Phillips, 1991; Zuber and Parmentier, 1990*].

Numerical modelling was used in order to constrain the required range of dynamic uplift needed from lithospheric modelling at Atla and Beta Regio. Based on the best-fit model

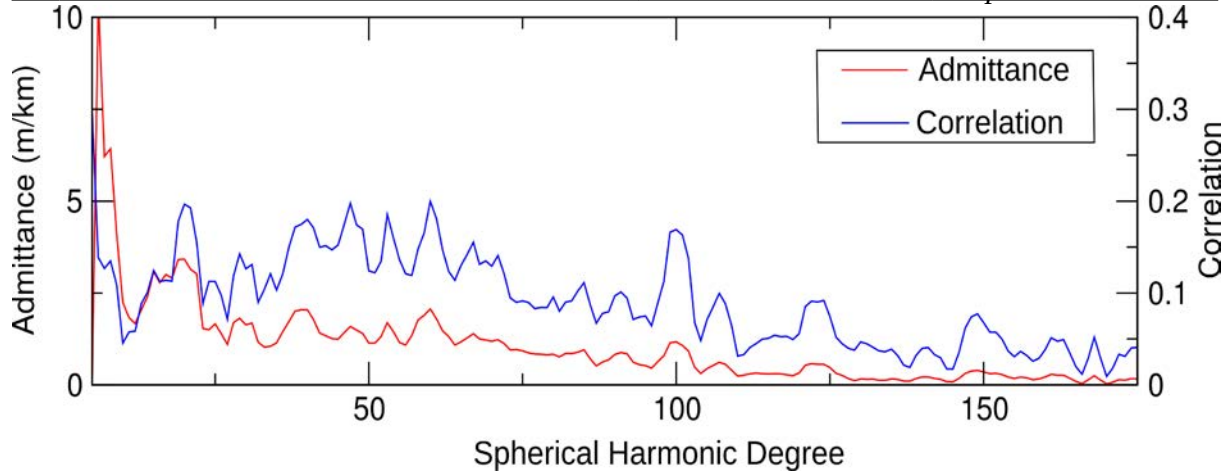


Figure 8.1. The observed geoid and topography admittance at Fortuna Tessera. The low admittance and correlation at low spherical harmonic degrees imply dynamic compensation is not required within this area.

presented in Chapter 7, two plumes were chosen as possible representations for Atla and Beta Regio. The first plume had a horizontal dimension of ~ 1000 km, similar to the dimensions required (~ 1500 km) for the plume below Maat and Ozza Mons, a dynamic topography of 1.5 km, and a geoid anomaly of 110 m.

Maat and Ozza Mons have observed elevations ranging from 4–8 km, with a total observed geoid anomaly of ~ 160 m. Thermal, Airy and regional isostasy were able to account for 3.5–6.5 km of the observed elevation and 45–52 m of the observed geoid. From lithospheric modelling, dynamic compensation was proposed to account for ~ 1.5 km and 108–115 m of the remaining elevation and geoid, respectively. Both the lithospheric and numerical models suggest Atla Regio could be supported by a mantle plume ~ 1000 km wide, which contributes 1.5 km and ~ 110 m to the observed elevation and geoid, respectively.

Due to Sapas Mons sharing a similar elevation, geoid anomalies and lava flows as the other volcanoes in Atla Regio, some authors have proposed that this volcano is the site of a second mantle plume [Senske and Head, 1992]. However, lithospheric modelling results found that

this volcano requires very minor (~ 0.5 km) and localised (width = ~ 0.5 km) dynamic compensation, possibly implying additional support comes from a small diapir rather than a primary mantle plume from the deep mantle.

The dynamic topography associated with the second plume (~ 0.4 km) shown in Chapter 7 closely approximates that required from lithospheric modelling (~ 0.3 km) at Beta Regio in Chapter 5. The amplitude of the geoid anomaly (~ 115 m) associated with the modelled plume also closely approximates the total (~ 120 m) observed geoid high at Beta Regio. Additionally, this second plume (~ 1500 km) shares a similar horizontal dimension to Beta Regio (~ 2000 km).

However, a much larger dynamic component than what was found may also be appropriate for Beta Regio since this area corresponds to the largest geoid-to-topography ratio (~ 31 m km⁻¹) of all the volcanic rises on Venus [Smrekar and Phillips, 1991; Stofan *et al.*, 1995]. The amount of dynamic uplift occurring at Beta Regio may be higher than that obtained from lithospheric modelling if the contribution from isostatic compensation has been overestimated or underestimated.

8.3.2 Pressure-Release Melting and Melt Generation Rates

Venus's surface exhibits extensive lava flows, some overlying other geological features, implying recent partial melting of the upper mantle [Smrekar and Sotin, 2012]. Prerequisites for melting do not have to be high, Nimmo and McKenzie [1996] found thinning of the lithosphere by 30% and a 200°C rise in upper mantle temperature is enough to start melting and cause variations in mantle rheology.

Partial melting results found in Chapters 4 and 7 have important implications for localised rifting and volcanism within each area. Dry melting may occur at a rate of $\sim 0.5 \text{ km}^3 \text{ yr}^{-1}$ below a thin (50 km) thermal lithosphere at Ganis Chasma. This rate was heavily dependent on both the mantle (1300°C) and plume temperatures (1500°C) used, with higher estimates (1700°C and 1500°C, respectively) providing greater rates that were inconsistent with previous studies [Nimmo and McKenzie, 1998].

The partial melting associated with an upwelling mantle plume below a rift can act as a source of basalt for the crust, weakening the lithosphere and facilitating rifting [Sleep, 2000].

Spreading rates and the amount of partial melting by decompression was correlated by Sleep [2000] for Earth, where slow spreading rifts result in smaller amounts of partial melting. The extension and thermal thinning along Ganis Chasma, the presence of volcanoes and coronae along this rift, may imply partial melting occurs within this area [Magee and Head, 1995]. All of the melt generated ($0.5 \text{ km}^3 \text{ yr}^{-1}$) from an upwelling mantle plume below Atla Regio was also found to have been efficiently extracted to form the new crust at a rate of $0.78 \text{ km}^3 \text{ yr}^{-1}$ at Ganis Chasma. However, not all of the melt associated with an upwelling mantle plume is able to form the crust within this area. This extra crust is unlikely to have been produced from cooling associated with the last global overturn event because this older crust should reside within the surrounding plains if Ganis Chasma is currently rifting. Instead, this crust may be formed from rift-related volcanism, where the extension along Ganis Chasma acts to reduce the pressure, resulting in decompression melting and extraction.

In an absence of rifting and for a 100 km thick thermal lithosphere, no partial melt is generated above an upwelling mantle plume at Ozza and Maat Mons (Chapter 4). However, melt may occur at depths $> 200 \text{ km}$ if a wet peridotite solidus is assumed, as shown in Chapter 7. Using a wet peridotite solidus from Gerya *et al.* [2006] and a temperature profile taken at

the center of a modelled mantle plume, up to 21 % of partial melt can be produced at depths greater than 200 km. This depth (200 km) is thicker than that obtained from lithospheric modelling (100 km) below the volcanoes at Atla Regio and is a result of the assumed stagnant-lid convective regime. This regime is characterised by a thick, cold, conductive lid that does not participate in localised surface motion. If rifting was simulated and occurs above an upwelling mantle plume, the associated thinning of the lithosphere and steeper "geotherm" could result in shallower wet melting and potentially, dry melting.

Therefore, localised volcanism and rifting may occur at Atla Regio, but is absent at Beta Regio, consistent with the minor dynamic compensation found from lithospheric modelling and thick crust below the central rift trough of Devana Chasma.

8.4 Implications of Lithospheric and Dynamic Modelling

The localised rifting and volcanism inferred from the lithospheric or mantle convection models have significant implications for Venus, especially since it is often considered to be within a stagnant-lid convective regime [*Kaula and Phillips, 1981; Solomon et al., 1992*]. Even though other studies suggest ultra-slow rifting would be applicable to Venus [*Jurdy and Stoddard, 2012*], they do not identify whether rifting is occurring nor do they calculate the rate of rifting.

The localised rifting and rift-related volcanism occurring at Ganis Chasma could have important implications for Venus's mantle convective regime. The high internal heating required by the best-fit numerical model may imply the interior is warming as suggested to occur before a global overturn [*Turcotte, 1993*]. The next overturn event may be initiated at Atla Regio since the significant (by ~200-250 km) thermal thinning, the mantle upwelling and

rifting all contribute to weakening of the lithosphere. Even though the episodic convective model of *Moresi and Solomatov* [1998] and *Turcotte* [1993] favours more catastrophic failure, initiation of an overturn may occur within a localised area before being transmitted globally [*Armann and Tackley*, 2012].

The localised rifting and associated volcanism presented in this study, in conjunction with previous evidence of possible volcanism at volcano and coronae dominated rises [*Smrekar et al.*, 2010], demonstrates how rifting and tectonic deformation may occur on a planet without plate tectonics, with implications for exoplanet studies, and also perhaps the evolution of the early Earth [*O'Neill*, 2012; *O'Neill et al.*, 2014].

9. Conclusions

9.1 Introduction

A planet's geological landforms can be supported by a number of short and long wavelength mechanisms including Airy isostasy, thermal isostasy, regional isostasy (flexure), and dynamic uplift. Airy isostasy from crustal thickness variations and regional isostasy from flexure of the elastic lithosphere contribute to short-wavelength support, while thermal isostasy from thinning of the thermal lithosphere and dynamic uplift associated with convective stresses in the mantle compensate long-wavelength topography. On Venus, the contribution of each of these mechanisms in supporting the observed topography is highly ambiguous since these processes are usually considered singularly rather than completely. This ambiguity is compounded further by uncertainties surrounding Venus's lithospheric structure, internal dynamics and the parameters controlling mantle convection.

However, the complexity of Venus's landforms and the overlap of short and long wavelength features, implies deformational processes operate concurrently. Furthermore, the high geoid and topography correlation within some areas suggests the surface is strongly coupled, and modified, by interior processes.

This study provides the first complete synthesis of the mechanisms supporting the two volcanic rises, Atla Regio, Beta Regio, and the crustal plateau, Fortuna Tessera. Two main aims were identified for this study:

1. To constrain the thermal structure below each area and determine the contribution of Airy, thermal and regional isostasy in shaping topography.

2. To establish a plausible model of Venus's mantle convection and identify the amount of dynamic uplift compensating each area.

9.2 Summary of Findings

9.2.1 Thermal Structure and Internal Dynamics

A reference column using a crustal and lithospheric thickness of 30 km and 300 km, respectively, provided the most plausible thermal structure below Atla and Beta Regio, their surrounding plains regions, and Fortuna Tessera (Table 9.1). Each thermal structure was constrained by simultaneously comparing the modelled results to elevation, geoid, and Bouguer gravity observables, within a 3D Cartesian geometry.

Table 9.1. Lithospheric Structure

Area	Crustal Thickness (km)	Thermal Lithosphere Thicknesses (km)
Atla Regio [†]	<1-60	50-100
Beta Regio [†]	15-75	60-100
Plains Regions [*]	20-35	250-375
Fortuna Tessera	65-80	150-340

[†] Area covered by the volcanic rise characterised by elevations between ~1-8 km

^{*} The regions surrounding the volcanic rises, Atla and Beta Regio, characterised by an elevation $\sim \leq 1$ km.

The two volcanic rises share similar thermal lithospheric thicknesses ranging from a minimum of 50-60 km below the rifts, to 100 km below the volcanoes (Table 9.1). The rifts that dissect each rise are also sites of thinner crust (< 1 km to 25 km). In comparison, a thick crust is associated primarily with the volcanoes, however, the tessera located within Beta Regio can reach crustal thicknesses of up to 75 km (Table 9.1).

A thicker thermal lithosphere occurs below the plains surrounding each volcanic rise (250-375

km) and at Fortuna Tessera (150-340 km). Crustal thicknesses within the plains range from 20-35 km and Fortuna Tessera has a crust 65-80 km thick, similar to the tessera units observed within Beta Regio (~75 km).

Global elevation and geoid observables were also used to constrain a plausible 3D spherical shell model of Venus's internal mantle convection and the associated parameters. In order to provide a realistic representation of the mantle, each simulation assumed a Venusian surface temperature, radius, gravitational acceleration, and density. Other conditions were also assumed including thermal and chemical buoyancy, temperature and pressure dependent viscosity, and phase transitions.

The mantle convection parameters that provided the best-fit model, constrained to Venus's global elevation and geoid, are shown in Table 9.2. An effective Rayleigh number of 2.5×10^7 , internal heating of 40, activation energy of 10, and a lower mantle that was 3 times more viscous than the upper mantle, resulted in ~60 localised upwellings and an average lithospheric thickness of 223 km. Most of these upwellings have elevations of ~1.5 km, corresponding to geoid anomalies of ~120 m, with some plumes having a minimum dynamic topography of ~0.5 km and a maximum of ~2.1 km.

9.2.2 Compensation Mechanisms

This study has found multiple processes operate concurrently to support the observed topography at Atla Regio, Beta Regio, and Fortuna Tessera (Figure 9.3). Both volcanic rises share similar swell elevations of ~2-4 km, however elevations reach up to 7.7 km at Maat Mons in Atla Regio (Table 9.3). Fortuna Tessera also has elevations ranging from 1-2 km, but can reach up to 4.7 km near Maxwell Montes. Most of the observed swell topography

Table 9.2. Model Parameters and Results

Parameter	Value
Rayleigh Number ^{†*}	2×10^8
Effective Rayleigh Number ^{†*}	2.5×10^7
Internal Heating [†]	40
Pre-exponential Factor ^{††}	3
Activation Energy [†]	10
Lithospheric Thickness (km)	223
Number of Plumes	60
Dynamic Topography (km)	-1.9 to 2.1
Geoid (m)	-256 to 261

[†] Rayleigh number, effective Rayleigh number, internal heating, pre-exponential factor, and activation energy are non-dimensional.

* The Rayleigh number, Ra and the effective Rayleigh number, $Ra_{effective}$ were scaled with respect to Venus's radius and mantle thickness, respectively.

^{††}For the lower mantle.

Table 9.3. Contributions to Topography

	Atla Regio	Beta Regio	Fortuna Tessera
Observed Elevation (km)	-2.0 to 7.7	-2.0 to 4.4	-1.6 to 4.7
Airy & Thermal Isostasy (km)	-1.7 to 5.5	-1.8 to 4.5	-1.7 to 5.2
Regional Isostasy (km)	0.3 to 1.5	-1.2 to 2.1	0.5 to 0.7
Estimated Dynamic Topography (km)*	0.5 to 1.5	0 to 0.3	-
Modelled Dynamic Topography (km) [†]	1.5	0.5	-

* From lithospheric modelling. Dynamic topography was estimated from the residual topography, after isostatic effects were considered.

[†] Found from the best-fit numerical model.

at each volcanic rise is supported by a combination of both Airy and thermal isostasy with minor compensation from regional isostasy and dynamic uplift.

Considering an elastic lithospheric thickness of 50 km, flexure can contribute to the swell topography at each rise (Table 9.3). The modelled, estimated, and observed geoid and topography admittance and correlation profiles for each rise also imply dynamic uplift contributes to long-wavelength compensation at degrees $\sim < 35$ -40. The dynamic topography

obtained from numerical modelling has a similar magnitude to that required from lithospheric modelling (Table 9.3). Therefore, dynamic uplift most likely contributes up to 1.5 km of the topography at Maat Mons in Atla Regio, but compensates less (< 0.5 km) at Ozza and Sapas Mons in Atla Regio, and in Beta Regio.

Admittance and correlation calculations and lithospheric modelling results imply Fortuna Tessera is primarily supported by Airy and thermal isostasy. Crustal thickness variations support most of the tessera terrain in the eastern portion of this area, with thermal thinning only occurring in the west, near Maxwell Montes. Minor, localised regional isostasy is also required along the narrow chasmata associated with the Chevron Tessera.

9.3 Implications

Whether rifting and volcanism is currently operating at these areas depends on their thermal structure and mantle dynamics. One area that may be currently rifting is Ganis Chasma in Atla Regio, as evidenced by its thin crust ($< \sim 1$ km), thin thermal lithosphere (50 km) and previous observations of outwardly dipping craters [Basilevsky, 1993; Basilevsky and Head, 2002; Jurdy and Stoddard, 2007; Matias and Jurdy, 2005; Matias *et al.*, 2004]. The thinning of the thermal lithosphere by a mantle plume in Atla Regio has weakened the lithosphere facilitating rifting at Ganis Chasma at a rate of 5-12 mm yr⁻¹.

In contrast, Devana Chasma, which is located in Beta Regio, is probably absent of current rifting due to the associated thick modelled crust (15-20 km) below the central rift trough, slightly thicker modelled thermal lithosphere (60 km) and randomly dipping craters [Basilevsky and Head, 2002; Matias and Jurdy, 2005]. The minor localised dynamic compensation (up to ~ 0.3 km) found for this area implies thermal thinning in conjunction with

the thick crust associated with the tessera terrain near Rhea Mons are most likely responsible for Beta Regio having the highest ($\sim 31 \text{ m km}^{-1}$) geoid to topography ratio of all the Venusian rises.

Previous studies have implied volcanism may be active at some of Venus's rises facilitated by partial melting above upwelling plumes [Smrekar and Sotin, 2012]. A mantle plume below Atla Regio was found to generate partial melting below the thin (50 km) lithosphere at Ganis Chasma at a rate of $0.5 \text{ km}^3 \text{ yr}^{-1}$, with all of this melt being extracted to contribute to crustal formation. Rift-related volcanism associated with localised rifting and decompression melting also assists crustal formation, since the crustal production rate ($0.78 \text{ km}^3 \text{ yr}^{-1}$) is higher than the melt generation rate from an upwelling mantle plume.

However, no partial melting from an upwelling mantle plume occurs below Ozza, Maat and Sapas Mons when a dry peridotite solidus and a thick modelled thermal lithosphere (100 km) are used. However, if the mantle is hydrated, melting below this area is possible. The best-fit numerical model produced a modelled plume that shared a similar dynamic topography and geoid height as Atla Regio. Using this corresponding temperature profile up to 21% of partial melt was generated at a depth $> 200 \text{ km}$.

9.4 Limitations

The results obtained from both the lithospheric and convection models are strongly influenced by the parameters used. However, steps were taken to constrain these parameters through the use of multiple numerical and lithospheric models and through comparison of the calculated responses to the geophysical observables. Numerical models used observed elevation and geoid anomalies to constrain Rayleigh number, internal heating, activation energy and the pre-

exponential factor, whereas each lithospheric model also used Bouguer gravity to constrain plausible lithospheric structures.

Lithospheric modelling at Atla Regio also used three different reference crustal and thermal lithospheric thicknesses to indirectly constrain the most plausible reference column at the North Polar Plains. Melt generation rates calculated for an upwelling mantle plume directly constrain the chosen lithospheric structure below Ganis Chasma and indirectly, the reference lithospheric column at the North Polar Plains.

9.5 Future Work

This thesis has constrained the thermal structure and compensation mechanisms operating at selected regions on Venus, as well as obtaining a plausible model of Venus's internal dynamics. The tectonic and volcanic implications of these results provide opportunities for future work. These include:

1. Modelling rifting within a 3D spherical shell.

By modifying the yield stress for a conductive lid, the lithosphere can experience varying degrees of mobilisation, depending on the magnitude of the parameters chosen [Moresi and Solomatov, 1998]. Under Venusian conditions, this will most likely produce episodic, rather than stagnant-lid, convection [Moresi and Solomatov, 1998]. Although a stagnant-lid regime approximates Venus's current convective style, an episodic regime is more appropriate when considering the evolution of Venus's lithosphere [Turcotte, 1993]. In an episodic regime, quiescent periods associated with thick, rigid and cold lithosphere are interspersed with overturn events characterised by resurfacing and a thin thermal lithosphere. Compared to a

stagnant-lid regime, an episodic regime is able to explain the geologically young surface ages implied from crater statistics and the complex tectonic and volcanic features observed [Turcotte, 1993]. Future models could vary the yield stress to simulate this regime and basal heating could be used to determine the time steps when convection is within a quiescent period. The velocity output obtained for these time steps can then be used to calculate rates of spreading at representative areas that experience localised rifting.

2. Modelling partial melting within a 3D spherical shell.

Tracer particles can be used in numerical modelling to calculate changes in the chemical state of the interior over time. Combining these variations with local conditions of melting and phase transformations, the volume of magma can be calculated [Dupeyrat and Sotin, 1995]. By combining these estimates with the rifting rates found in (1) the volume of melt and rate of melting can be calculate for a suitable convective model of Venus's interior.

3. Lithospheric modelling at possible subduction zones and wrinkle ridges.

In order to maintain Venus's total surface area, the new crust produced along Ganis Chasma must be either destroyed by subduction or accommodated by compression. The very slow rates of spreading at Ganis Chasma might suggest that the surrounding plains, especially the wrinkle ridges, accommodate this crust by compression [Bilotti and Suppe, 1999; Sandwell et al., 1997]. Furthermore, plains regions surrounding a volcanic rise may also be sites of subduction [Schubert and Sandwell, 1995] . Constraining the lithospheric structure within the distal plains regions could determine if they are areas of compression or subduction and possibly constrain the amount of crust that is accommodated or destroyed.

10. References

- Achauer, U., P. K. H. Maguire, J. Mechie, W. V. Green, and KRISP working group (1992), Some remarks on the structure and geodynamics of the Kenya Rift, *Tectonophysics*, 213, 257–268, doi:10.1016/0040-1951(92)90262-5.
- Afonso, J. C., G. Ranalli, and M. Fernández (2005), Thermal expansivity and elastic properties of the lithospheric mantle: results from mineral physics of composites, *Physics of the Earth and Planetary Interiors*, 149, 279–306, doi:10.1016/j.pepi.2004.10.003.
- Aitta, A. (2012), Venus’ internal structure, temperature and core composition, *Icarus*, 218(2), 967–974, doi:10.1016/j.icarus.2012.01.007.
- Anderson, F. S., and S. E. Smrekar (2006), Global mapping of crustal and lithospheric thickness on Venus, *Journal of Geophysical Research*, 111, 20 pp., doi:200610.1029/2004JE002395.
- Arkani-Hamed, J. (1993), On the tectonics of Venus, *Physics of the Earth and Planetary Interiors*, 75–96, doi:10.1016/0031-9201(93)90056-F.
- Arkani-Hamed, J., G. G. Schaber, and R. G. Strom (1993), Constraints on the thermal evolution of Venus inferred from Magellan data, *Journal of Geophysical Research: Planets*, 98(E3), 5309–5315, doi:10.1029/93JE00052.
- Arkani-Hamed, J., and M. N. Teksöz (1984), Thermal evolution of Venus, *Physics of the Earth and Planetary Interiors*, 34(4), 232–250, doi:10.1016/0031-9201(84)90065-7.
- Armann, M., and P. J. Tackley (2012), Simulating the thermochemical magmatic and tectonic

- evolution of Venus's mantle and lithosphere: Two-dimensional models, *Journal of Geophysical Research: Planets*, 117, E12003, doi:10.1029/2012JE004231.
- Arnold, G., R. Haus, D. Kappel, P. Drossart, and G. Piccioni (2008), Venus surface data extraction from VIRTIS/Venus Express measurements: Estimation of a quantitative approach, *Journal of Geophysical Research: Planets*, 113, E00B10, doi:10.1029/2008JE003087.
- Artemieva, I. M. (2006), Global $1^\circ \times 1^\circ$ thermal model TC1 for the continental lithosphere: Implications for lithosphere secular evolution, *Tectonophysics*, 416(1–4), 245–277, doi:10.1016/j.tecto.2005.11.022.
- Aubaud, C., E. H. Hauri, and M. M. Hirschmann (2004), Hydrogen partition coefficients between nominally anhydrous minerals and basaltic melts, *Geophysical Research Letters*, 31, L20611, doi:10.1029/2004GL021341.
- Banerdt, W. B., and M. P. Golombek (1988), Deformational Models of Rifting and Folding on Venus, *Journal of Geophysical Research*, 93(B5), 4759–4772, doi:10.1029/JB093iB05p04759.
- Barnett, D. N., F. Nimmo, and D. McKenzie (2000), Elastic Thickness Estimates for Venus Using Line of Sight Accelerations from Magellan Cycle 5, *Icarus*, 146(2), 404–419, doi:10.1006/icar.2000.6352.
- Barnett, D. N., F. Nimmo, and D. McKenzie (2002), Flexure of Venusian lithosphere measured from residual topography and gravity, *Journal of Geophysical Research*, 107, 21 pp., doi:10.1029/2000JE001398.
- Basaltic Volcanism Study Project (1981) *Basaltic Volcanism on the Terrestrial Planets*, Pergamon Press, Oxford.

- Basilevsky, A. T. (1986), Structure of central and eastern areas of Ishtar Terra and some problems of Venusian tectonics, *Geotectonics*, 20, 282-288.
- Basilevsky, A. T. (1993), Age of Rifting and Associated Volcanism in Atla Regio Venus, *Geophysical Research Letters*, 20(10), 883–886.
- Basilevsky, A. T. and J. W. Head (2000), Geologic units on Venus: evidence for their global correlation, *Planetary and Space Science*, 48, 75-111, doi:10.1016/S0032-0633(99)00083-5.
- Basilevsky, A. T., and J. W. Head (2002), Venus: Analysis of the degree of impact crater deposit degradation and assessment of its use for dating geological units and features, *Journal of Geophysical Research*, 107, 38 pp., doi:200210.1029/2001JE001584.
- Basilevsky, A. T., and J. W. Head (2002), Venus: Timing and rates of geologic activity, *Geology*, 30(11), 1015 -1018, doi:10.1130/0091-7613(2002)030<1015:VTAROG>2.0.CO;2.
- Basilevsky, A. T., and J. W. Head (2007), Beta Regio, Venus: Evidence for uplift, rifting, and volcanism due to a mantle plume, *Icarus*, 192(1), 167–186, doi:10.1016/j.icarus.2007.07.007.
- Basilevsky, A. T. and G. E. McGill (2007), Surface evolution of Venus, in *Exploring Venus as a Terrestrial Planet*, 23-45, American Geophysical Union, Washington.
- Basilevsky, A. T., O. V. Nikolaeva, and C. M. Weitz (1992), Geology of the Venera 8 landing site region from Magellan data: Morphological and geochemical considerations, *Journal of Geophysical Research: Planets*, 97(E10), 16315–16335, doi:10.1029/92JE01557.
- Benešová, N., and H. Čížková (2012), Geoid and topography of Venus in various thermal

- convection models, *Studia Geophysica et Geodaetica*, 56(2), 621–639, doi:10.1007/s11200-011-0251-7.
- van den Berg, A. P., P. E. van Keken, and D. A. Yuen (1993), The effects of a composite non-Newtonian and Newtonian rheology on mantle convection, *Geophysical Journal International*, 115(1), 62–78, doi:10.1111/j.1365-246X.1993.tb05588.x.
- Bevington, P. R., and D. K. Robinson (1992), *Data reduction and error analysis for the physical sciences*, McGraw-Hill Inc, New York.
- Bilotti, F., and J. Suppe (1999), The Global Distribution of Wrinkle Ridges on Venus, *Icarus*, 139(1), 137–157, doi:10.1006/icar.1999.6092.
- Bindschadler, D. L. and J. W. Head (1991), Tessera terrain, Venus: characterization and models for origin and evolution, *Journal of Geophysical Research*, 96(B4), 5889–5907, doi:10.1029/90JB02742.
- Bindschadler, D. L., and E. M. Parmentier (1990), Mantle flow tectonics: The influence of a ductile lower crust and implications for the formation of topographic uplands on Venus, *Journal of Geophysical Research: Solid Earth*, 95(B13), 21329–21344, doi:10.1029/JB095iB13p21329.
- Bindschadler, D. L., G. Schubert, and W. M. Kaula (1990), Mantle flow tectonics and the origin of Ishtar Terra, Venus, *Geophysical Research Letters*, 17(9), 1345–1348, doi:10.1029/GL017i009p01345.
- Bindschadler, D. L., G. Schubert, and W. M. Kaula (1992), Coldspots and hotspots: Global tectonics and mantle dynamics of Venus, *Journal of Geophysical Research: Planets*, 97(E8), 13495–13532, doi:10.1029/92JE01165.
- Bondarenko, N. V., J. W. Head, and M. A. Ivanov (2010), Present-Day Volcanism on Venus:

- Evidence from Microwave Radiometry, *Geophysical Research Letters*, 37(23), L23202, doi:10.1029/2010GL045233.
- Bonin, B. (2012), Extra-terrestrial igneous granites and related rocks: A review of their occurrence and petrogenesis, *Lithos*, 153, 3–24, doi:10.1016/j.lithos.2012.04.007.
- Bown, J. W., and R. S. White (1994), Variation with spreading rate of oceanic crustal thickness and geochemistry, *Earth and Planetary Science Letters*, 121(3–4), 435–449, doi:10.1016/0012-821X(94)90082-5.
- Bossman, A.B., and P.E. Keken (2013), Dynamics of plumes in a compressible mantle with phase changes: implications for phase boundary topography, *Physics of the Earth and Planetary Interiors*, 224, p 21-31.
- Brian, A. W., E. R. Stofan, J. E. Guest, and S. E. Smrekar (2004), Laufey Regio: A newly discovered topographic rise on Venus, *Journal of Geophysical Research: Planets*, 109(E7), doi:10.1029/2002JE002010.
- Brown, C. D., and R. E. Grimm (1996a), Lithospheric rheology and flexure at Artemis Chasma, Venus, *Journal of Geophysical Research*, 101, 12,697 – 12,708, doi:10.1029/96JE00834.
- Brown, C. D., and R. E. Grimm (1996b), Floor subsidence and rebound of large Venus craters, *Journal of Geophysical Research*, 101, 26,057 – 26,067, doi:10.1029/96JE02706.
- Brown, C. D., and R. E. Grimm (1999), Recent Tectonic and Lithospheric Thermal Evolution of Venus, *Icarus*, 139(1), 40–48, doi:10.1006/icar.1999.6083.
- Buck, W. R. (1992), Global decoupling of crust and mantle: Implications for topography, geoid and mantle viscosity on Venus, *Geophysical Research Letters*, 19(21), 2111–

2114, doi:199210.1029/92GL02462.

Burov, E., and A. B. Watts (2006), The long-term strength of continental lithosphere; “jelly sandwich” or “creme brulee”?, *GSA Today*, 16(1), doi:10.1130/1052-173(2006)016<4:TLTSOC>2.0.CO;2.

Cattermole, P. (1994), *Venus: the geological story*, University Collage London Press, London.

Chassefière, E., R. Wieler, B. Marty, and F. Leblanc (2012), The evolution of Venus: Present state of knowledge and future exploration, *Planetary and Space Science*, 63–64, 15–23, doi:10.1016/j.pss.2011.04.007.

Chorowicz, J. (2005), The East African rift system, *Journal of African Earth Sciences*, 43(1–3), 379–410, doi:10.1016/j.jafrearsci.2005.07.019.

Christensen, U. (1984), Convection with pressure-dependent and temperature-dependent non-Newtonian rheology, *Geophysical Journal of the Royal Astronomical Society*, 77, 343–384.

Coakley, B. J., and J. R. Cochran (1998), Gravity Evidence of Very Thin Crust at the Gakkel Ridge (Arctic Ocean), *Earth and Planetary Science Letters*, 162(1–4), 81–95, doi:10.1016/S0012-821X(98)00158-7.

Davies, G.F. (2000), *Dynamic Earth: Plates, Plumes and Mantle Convection*, Cambridge University Press, Cambridge.

Dupeyrat, L., and C. Sotin (1995), The effect of the transformation of basalt to eclogite on the internal dynamics of Venus, *Planetary and Space Science*, 43(7), 909–921, doi:10.1016/0032-0633(94)00227-I.

Elkins-Tanton, L. T., S. E. Smrekar, P. C. Hess, and E. M. Parmentier (2007), Volcanism and

- volatile recycling on a one-plate planet: Applications to Venus, *Journal of Geophysical Research: Planets*, 112, E04S06, doi:10.1029/2006JE002793.
- Ernst, R. E., K. L. Buchan, and D. W. Desnoyers (2007), Plumes and Plume Clusters on Earth and Venus: Evidence from Large Igneous Provinces (LIPs), *Superplumes: Beyond Plate Tectonics*, edited by D. A. Yuen, S. Maruyama, S.-I. Karato, and B. F. Windley, 537–562, Springer Netherlands.
- Ernst, R., and D. Desnoyers (2004), Lessons from Venus for understanding mantle plumes on Earth, *Physics of the Earth and Planetary Interiors*, 146(1–2), 195–229, doi:10.1016/j.pepi.2003.10.012.
- Ernst, R., D. Desnoyers, J. Head, and E. Grosfils (2003), Graben–fissure systems in Guinevere Planitia and Beta Regio (264°–312°E, 24°–60°N), Venus, and implications for regional stratigraphy and mantle plumes, *Icarus*, 164(2), 282–316, doi:10.1016/S0019-1035(03)00126-X.
- Filiberto, J. (2014), Magmatic diversity on Venus: Constraints from terrestrial analog crystallization experiments, *Icarus*, 231, 131–136, doi:10.1016/j.icarus.2013.12.003.
- Ford, P. (1986), Pioneer Venus hypsometry, 12 pp., Center for space research, Institute of Technology, Cambridge.
- Ford, P. G., and G. H. Pettengill (1992), Venus Topography and Kilometer-Scale Slopes, *Journal of Geophysical Research*, 97(E8), 13,103–13,114, doi:10.1029/92JE01085.
- Foster, A., and F. Nimmo (1996), Comparisons between the rift systems of East Africa, Earth and Beta Regio, Venus, *Earth and Planetary Science Letters*, 143(1–4), 183–195, doi:10.1016/0012-821X(96)00146-X.

- Fowler, C. M. R. (2004), *The Solid Earth: An Introduction to Global Geophysics*, 2nd ed., Cambridge University Press, United Kingdom.
- Fowler, A. C., and S. B. G. O'Brien (1996), A mechanism for episodic subduction on Venus, *Journal of Geophysical Research: Planets*, 101(E2), 4755–4763, doi:10.1029/95JE03261.
- Fullea, J. (2007), *Development of numerical methods to determine the lithospheric structure combining geopotential, lithostatic and heat transport equations. Application to the Gibraltar Arc system*. Unpublished doctoral dissertation, University of Barcelona, Spain.
- Fullea, J., J. C. Afonso, J. A. D. Connolly, M. Fernàndez, D. García-Castellanos, and H. Zeyen (2009), LitMod3D: An Interactive 3-D Software to Model the Thermal, Compositional, Density, Seismological, and Rheological Structure of the Lithosphere and Sublithospheric Upper Mantle, *Geochemistry Geophysics Geosystems*, 10, Q08019, 21 pp., doi:2009 10.1029/2009GC002391.
- Fullea, J., M. Fernàndez, J. C. Afonso, J. Vergés, and H. Zeyen (2010), The structure and evolution of the lithosphere-asthenosphere boundary beneath the Atlantic-Mediterranean Transition Region, *Lithos*, 120, 74-95. doi: 10.1016/j.lithos.2010.03.003.
- Fullea, J., M. Fernàndez, H. Zeyen, and J. Vergés (2007), A rapid method to map the crustal and lithospheric thickness using elevation, geoid anomaly and thermal analysis. Application to the Gibraltar Arc System, Atlas Mountains and adjacent zones, *Tectonophysics*, 430(1-4), 97–117, doi:10.1016/j.tecto.2006.11.003.
- Galgana, G. A., P. J. McGovern, and E. B. Grosfils (2011), Evolution of large Venusian volcanoes: Insights from coupled models of lithospheric flexure and magma reservoir

- pressurization, *Journal of Geophysical Research*, 116,
doi:201110.1029/2010JE003654.
- Gallardo Delgado, L. A., M. A. Pérez Flores, and E. Gómez Treviño (2003), A versatile algorithm for joint 3D inversion of gravity and magnetic data, *Geophysics*, 68(3), 949–959, doi:10.1190/1.1581067.
- Garcia-Castellanos, D. (2002), Interplay between lithospheric flexure and river transport in foreland basins, *Basin Research*, 14(2), 89–104, doi:10.1046/j.1365-2117.2002.00174.x.
- Garvin, J. B., J. W. Head, G. H. Pettengill, and S. H. Zisk (1985), Venus Global Radar Reflectivity and Correlations With Elevation, *Journal of Geophysical Research*, 90(B8), 6859–6871, doi:198510.1029/JB090iB08p06859.
- Gerya, T. V. (2014), Plume-induced crustal convection: 3D thermomechanical model and implications for the origin of novae and coronae on Venus, *Earth and Planetary Science Letters*, 391, 183–192, doi:10.1016/j.epsl.2014.02.005.
- Gerya, T. V., J. A. D. Connolly, D. A. Yuen, W. Gorczyk, and A. M. Capel (2006), Seismic implications of mantle wedge plumes, *Physics of the Earth and Planetary Interiors*, 156(1–2), 59–74, doi:10.1016/j.pepi.2006.02.005.
- Ghent, R. R., and I. M. Tibuleac (2002), Ribbon spacing in Venusian tessera: Implications for layer thickness and thermal state, *Geophysical Research Letters*, 29,
doi:200210.1029/2002GL015994.
- Gilmore, M. S., M. A. Ivanov, J. W. Head, and A. T. Basilevsky (1997), Duration of tessera deformation on Venus, *Journal of Geophysical Research: Planets*, 102(E6), 13357–13368, doi:10.1029/97JE00965.

- Glaze, L. S. (1999), Transport of SO₂ by explosive volcanism on Venus, *Journal of Geophysical Research: Planets*, 104(E8), 18899–18906, doi:10.1029/1998JE000619.
- Glaze, L. S., S. M. Baloga, and J. Wimert (2011), Explosive volcanic eruptions from linear vents on Earth, Venus, and Mars: Comparisons with circular vent eruptions, *Journal of Geophysical Research: Planets*, 116(E01011), doi:10.1029/2010JE003577.
- Griffiths, R. W. (1986), The differing effects of compositional and thermal buoyancies on the evolution of mantle diapirs, *Physics of the Earth and Planetary Interiors*, 43(4), 261–273, doi:10.1016/0031-9201(86)90016-6.
- Grimm, R. E. (1994), Recent deformation rates on Venus, *Journal of Geophysical Research: Planets*, 99(E11), 23163–23171, doi:10.1029/94JE02196.
- Grimm, R.E. (1994), The Deep Structure of Venusian Plateau Highlands, *Icarus*, 112(1), 89–103, doi:10.1006/icar.1994.1171.
- Grimm, R. E., and P. C. Hess (1997), The crust of Venus, in *Venus II: Geology, Geophysics, Atmosphere and Solar Wind Environment*, 1205–1244, The University of Arizona Press, Arizona.
- Grimm, R. E., and R. J. Phillips (1990), Tectonics of Lakshmi Planum, Venus: Tests for Magellan, *Geophysical Research Letters*, 17(9), 1349–1352, doi:10.1029/GL017i009p01349.
- Grimm, R. E., and R. J. Phillips (1991), Gravity anomalies, compensation mechanisms, and the geodynamics of Western Ishtar Terra, Venus, *Journal of Geophysical Research: Solid Earth*, 96(B5), 8305–8324, doi:10.1029/91JB00055.
- Grimm, R. E., and S. C. Solomon (1988), Viscous Relaxation of Impact Crater Relief on Venus: Constraints on Crustal Thickness and Thermal Gradient, *Journal of*

- Geophysical Research*, 93(B10), 11911–11929, doi:10.1029/JB093iB10p11911.
- Grinspoon, D. H. (1993), Implications of the high D/H ratio for the sources of water in Venus' atmosphere, *Nature*, 363(6428), 428–431, doi:10.1038/363428a0.
- Hamilton, V. E., and E. R. Stofan (1996), The Geomorphology and Evolution of Hecate Chasma, Venus, *Icarus*, 121(1), 171–194, doi:10.1006/icar.1996.0077.
- Hansen, V. L. (2013), Venus crustal plateaus and an analog for Archean cratons and SCLM, *Mineralogical Magazine*, 77(5), 1255.
- Hansen, V. L. (2007), LIPs on Venus, *Chemical Geology*, 241(3–4), 354–374, doi:10.1016/j.chemgeo.2007.01.020.
- Hansen, V. L., B. K. Banks, and R. R. Ghent (1999), Tessera terrain and crustal plateaus, Venus, *Geology*, 27(12), 1071–1074, doi:10.1130/0091-7613(1999)027<1071:TTACPV>2.3.CO;2.
- Hansen, V. L., R. R. Ghent, and B. K. Banks (1998), Ribbon terrain: fingerprint of ancient mantle upwellings and crustal plateaus, Venus, *29th Annual Lunar and Planetary Science Conference*.
- Hansen, V. L., and A. Olive (2010), Artemis, Venus: The largest tectonomagmatic feature in the solar system?, *Geology*, 38(5), 467–470, doi:10.1130/G30643.1.
- Hansen, V. L., and R. J. Phillips (1995), Formation of Ishtar Terra, Venus: Surface and gravity constraints, *Geology*, 23(4), 292–296, doi:10.1130/0091-7613(1995)023<0292:FOITVS>2.3.CO;2.
- Hansen, V. L., and J. J. Willis (1998), Ribbon Terrain Formation, Southwestern Fortuna Tessera, Venus: Implications for Lithosphere Evolution, *Icarus*, 132(2), 321–343,

doi:10.1006/icar.1998.5897.

Head, J. W., L. S. Crumpler, J. C. Aubele, J. E. Guest, and R. S. Saunders (1992), Venus volcanism: classification of volcanic features and structures, associations, and global distribution from Magellan data, *Journal of Geophysical Research*, 97(E8), 13,153-13,197, doi:10.1029/92JE01273.

Head, J. W. and L. Wilson (1992), Magma reservoirs and neutral buoyancy zones on Venus: implications for the formation and evolution of volcanic landforms, *Journal of Geophysical Research*, 97(E3), 3877-3903, doi:10.1029/92JE00053.

Herrick, R. R., J. Dufek, and P. J. McGovern (2005), Evolution of large shield volcanoes on Venus, *Journal of Geophysical Research*, 110, E01002, doi:10.1029/2004JE002283.

Herrick, D. L., and E. M. Parmentier (1994), Episodic large-scale overturn of two-layer mantles in terrestrial planets, *Journal of Geophysical Research: Planets*, 99(E1), 2053–2062, doi:10.1029/93JE03080.

Herrick, R. R., and R. J. Phillips (1992), Geological correlations with the interior density structure of Venus, *Journal of Geophysical Research: Planets*, 97(E10), 16017–16034, doi:10.1029/92JE01498. Herrick, R. P., V. L. Sharpton, M. C. Malin, S. N. Lyons, and K. Feely (1997). Morphology and morphometry of impact craters, in *Venus II Geology, Geophysics, Atmosphere and Solar Wind Environment*, 1015-1046, The University of Arizona Press, Arizona.

Herzberg, C., P. Raterron, and J. Zhang (2000), New experimental observations on the anhydrous solidus for peridotite KLB-1, *Geochemistry, Geophysics, Geosystems*, 1(11), 1051, doi:10.1029/2000GC000089.

Hirschmann, M. M. (2000), Mantle solidus: Experimental constraints and the effects of

- peridotite composition, *Geochemistry, Geophysics, Geosystems*, 1(10), 2000GC000089, doi:10.1029/2000GC000070.
- Höink, T., A. Lenardic, and M. Richards (2012), Depth-dependent viscosity and mantle stress amplification: implications for the role of the asthenosphere in maintaining plate tectonics, *Geophysical Journal International*, 191(1), 30–41, doi:10.1111/j.1365-246X.2012.05621.x.
- Huang, J., A. Yang, and S. Zhong (2013), Constraints of the topography, gravity and volcanism on Venusian mantle dynamics and generation of plate tectonics, *Earth and Planetary Science Letters*, 362, 207–214, doi:10.1016/j.epsl.2012.11.051.
- van Hunen, J., S. Zhong, N. M. Shapiro, and M. H. Ritzwoller (2005), New evidence for dislocation creep from 3-D geodynamic modeling of the Pacific upper mantle structure, *Earth and Planetary Science Letters*, 238(1–2), 146–155, doi:10.1016/j.epsl.2005.07.006.
- Inoue, T. (1994), Effect of water on melting phase relations and melt composition in the system $\text{Mg}_2\text{SiO}_4\text{-MgSiO}_3\text{-H}_2\text{O}$ up to 15 GPa, *Physics of the Earth and Planetary Interiors*, 85(3–4), 237–263, doi:10.1016/0031-9201(94)90116-3.
- Ivanov, M. A. (1988), The results of morphometric study of the tessera terrain of Venus from Venera 15/16 data, *Abstracts of the Lunar and Planetary Science Conference*, 19, 537–538.
- Ivanov, M. A., and J. W. Head (2009), Geological mapping of the Fortuna Tessera quadrangle (V-2), Venus: Preliminary results, *40th Lunar and Planetary Science Conference*.
- Ivanov, M. A., and J. W. Head (2010), The Lada Terra rise and Quetzalpetlatl Corona: A region of long-lived mantle upwelling and recent volcanic activity on Venus,

- Planetary and Space Science*, 58(14-15), 1880–1894, doi:10.1016/j.pss.2010.08.018.
- Ivanov, M. A., and J. W. Head (2011), Global geological map of Venus, *Planetary and Space Science*, 59(13), 1559–1600, doi:10.1016/j.pss.2011.07.008.
- Ivanov, M. A., and J. W. Head (2013), The history of volcanism on Venus, *Planetary and Space Science*, 84, 66–92, doi:10.1016/j.pss.2013.04.018.
- James, P. B., M. T. Zuber, and R. J. Phillips (2013), Crustal thickness and support of topography on Venus, *Journal of Geophysical Research Planets*, 17, doi:10.1029/2012JE004237.
- Jaupart, C., and J. C. Mareschal (2007), Heat flow and thermal structure of the lithosphere, *Treatise on Geophysics*, 6, 217–251.
- Jiménez-Munt, I., M. Fernández, J. Vergés, J. C. Afonso, D. Garcia-Castellanos, and J. Fulla (2010), Lithospheric structure of the Gorrige Bank: Insights into its origin and tectonic evolution, *Tectonics*, 29, 16 pp., doi:10.1029/2009TC002458.
- Johnson, C. L., and D. T. Sandwell (1994), Lithospheric flexure on Venus, *Geophysical Journal International*, 119(2), 627–647, doi:10.1111/j.1365-246X.1994.tb00146.x.
- Jull, M. G., and J. Arkani-Hamed (1995), The implications of basalt in the formation and evolution of mountains on Venus, *Physics of the Earth and Planetary Interiors*, 89(3–4), 163–175, doi:10.1016/0031-9201(95)03015-O.
- Jurdy, D. M., and P. R. Stoddard (2007), The coronae of Venus: Impact, plume, or other origin?, *Geological Society of America Special Papers*, 430, 859–878, doi:10.1130/2007.2430(40).
- Kargel, J. S., G. Komatsu, V. R. Baker, and R. G. Strom (1993), The Volcanology of Venera

- and VEGA Landing Sites and the Geochemistry of Venus, *Icarus*, 103(2), 253–275, doi:10.1006/icar.1993.1069.
- Kaula, W. M. (1990), Venus: A Contrast in Evolution to Earth, *Science*, 247(4947), 1191–1196, doi:10.1126/science.247.4947.1191.
- Kaula, W. M. (1995), Venus reconsidered, *Science*, 270(5241), 1460–1464.
- Kaula, W.M., Lenardic, A., Bindshadler, D.L., and J. Arkani-Hamed (1997), Ishtar Terra, in *Venus II: Geology, Geophysics, Atmosphere and Solar Wind Environment*, 879–900, The University of Arizona Press, Arizona.
- Kaula, W. M., T. Owen, S. K. Runcorn, and D. C. Tozer (1994), The Tectonics of Venus [and Discussion], *Philosophical Transactions of the Royal Society of London*, 349(1690), 345–355, doi:10.1098/rsta.1994.0137.
- Kaula, W. M., and R. J. Phillips (1981), Quantitative tests for plate tectonics on Venus, *Geophysical Research Letters*, 8, 1187–1190.
- Keep, M. and V. L. Hansen (1994), Structural history of Maxwell Montes, Venus: implications for Venusian Mountain Belt formation, *Journal of Geophysical Research*, 99(E12), 26,015–26,028, doi:10.1029/94JE02636.
- Kiefer, W. S., and B. H. Hager (1991), A Mantle Plume Model for the Equatorial Highlands of Venus, *Journal of Geophysical Research*, 96(E4), 20947–20966, doi:10.1029/91JE02221.
- Kiefer, W. S., and B. H. Hager (1991), Mantle Downwelling and Crustal Convergence: A Model for Ishtar Terra, Venus, *Journal of Geophysical Research*, 96(E4), 20,967–20,980, doi:10.1029/91JE02219.

- Kiefer, W. S., and E. K. Potter (2000) Gravity anomalies at Venus shield volcanoes: Implications for lithospheric thickness, *Lunar and Planetary Science, XXXI*, abstract 1924.
- Kiefer, W. S., and L. C. Swafford (2006), Topographic analysis of Devana Chasma, Venus: implications for rift system segmentation and propagation, *Journal of Structural Geology*, 28(12), 2144–2155, doi:10.1016/j.jsg.2005.12.002.
- Koga, K., E. Hauri, M. Hirschmann, and D. Bell (2003), Hydrogen concentration analyses using SIMS and FTIR: Comparison and calibration for nominally anhydrous minerals, *Geochemistry, Geophysics, Geosystems*, 4(2), n/a–n/a, doi:10.1029/2002GC000378.
- Konopliv, A. S., W. B. Banerdt, and W. L. Sjogren (1999), Venus Gravity: 180th Degree and Order Model, *Icarus*, 139(1), 3–18, doi:10.1006/icar.1999.6086.
- Konopliv, A., and W. L. Sjogren (1994), Venus Spherical Harmonic Gravity Model to Degree and Order 60, *Icarus*, 112(1), 42–54, doi:10.1006/icar.1994.1169.
- Konopliv, A. S., and C. F. Yoder (1996), Venusian k2 tidal Love number from Magellan and PVO tracking data, *Geophysical Research Letters*, 23(14), 1857–1860, doi:10.1029/96GL01589.
- Krassilnikov, A. S. and J. W. Head (2002), Geology, classification and evolution of Novae on Venus, *Lunar and Planetary Science, XXXIII*, abstract 1463.
- Krassilnikov, A. S., V.-P. Kostama, M. Aittola, E. N. Guseva, and O. S. Cherkashina (2012), Relationship of coronae, regional plains and rift zones on Venus, *Planetary and Space Science*, 68(1), 56–75, doi:10.1016/j.pss.2011.11.017.
- Kryuchkov, V. P. (1990), Ridge Belts: are they compressional or extensional structures?, *Earth, Moon and Planets*, 50-51, 471-491, doi:10.1007/BF00142403.

- Kucinskas, A. B., and D. L. Turcotte (1994), Isostatic Compensation of Equatorial Highlands on Venus, *Icarus*, 112(1), 104–116, doi:10.1006/icar.1994.1172.
- Kucinskas, A. B., D. L. Turcotte, and J. Arkani-Hamed (1996), Isostatic compensation of Ishtar Terra, Venus, *Journal of Geophysical Research*, 101(E2), 4725–4736, doi:10.1029/95JE02979.
- Kulikov, Y. N., H. Lammer, H.I.M. Lichtenegger, N. Terada, I. Ribas, C. Kolb, R. Lundin, E.F. Guinan, S. Barabash, H.K. Biernat (2006), Atmospheric and water loss from early Venus, *Planetary and Space Science*, 54(13–14), 1425–1444, doi:10.1016/j.pss.2006.04.021.
- Kumar, P., X. Yuan, R. Kind, and J. Mechie (2012), The Lithosphere-Asthenosphere Boundary Observed with USArray Receiver Functions, *Solid Earth*, 3(1), 149–159, doi:10.5194/se-3-149-2012.
- Lacis, A. A., G. A. Schmidt, D. Rind, and R. A. Ruedy (2010), Atmospheric CO₂: Principal Control Knob Governing Earth's Temperature, *Science*, 330(6002), 356–359, doi:10.1126/science.1190653.
- Lachenbruch, A. H., and P. Morgan (1990), Continental extension, magmatism and elevation; formal relations and rules of thumb, *Tectonophysics*, 174, 39–62.
- Leftwich, T. E., R. R. B. von Frese, H. R. Kim, H. C. Noltimier, L. V. Potts, D. R. Roman, and L. Tan (1999), Crustal analysis of Venus from Magellan satellite observations at Atalanta Planitia, Beta Regio, and Thetis Regio, *Journal of Geophysical Research*, 104(E4), 8441–8462.
- Lenardic, A., W. M. Kaula, and D. L. Bindschadler (1991), The tectonic evolution of Western Ishtar Terra, Venus, *Geophysical Research Letters*, 18(12), 2209–2212,

doi:10.1029/91GL02734.

Lopes, R.M.C., K.L. Mitchell, D. Williams, and G. Mitri (2010) Beyond Earth: how extra-terrestrial volcanism has changed our definition of a volcano, *The Geological Society of America Special Paper*, 470, 11-30.

Mackwell, S. J., M. E. Zimmerman, and D. L. Kohlstedt (1998), High-temperature deformation of dry diabase with application to tectonics on Venus, *Journal of Geophysical Research: Solid Earth*, 103(B1), 975–984, doi:10.1029/97JB02671.

Magee, K. P., and J. W. Head (1995), The role of rifting in the generation of melt: Implications for the origin and evolution of the Lada Terra-Lavinia Planitia region of Venus, *Journal of Geophysical Research: Planets*, 100(E1), 1527–1552, doi:10.1029/94JE02334.

Matias, A., and D. M. Jurdy (2005), Impact craters as Indicators of Tectonic and Volcanic Activity in the Beta-Atla-Themis Region, Venus, *Geological Society of America Special Papers*, 388, 825–839, doi:10.1130/0-8137-2388-4.825.

Matias, A., Jurdy, D.M, and P.R. Stoddard (2004), Stereo Imaging of Impact Craters in the Beta-Atla-Themis (BAT) Region, Venus., *Abstracts of the 35th Lunar and Planetary Science Conference*, 1383-1384.

McFadden, L.-A., P. Weissman, and T. Johnson (2006), *Encyclopedia of the Solar System*, 992 pp., Academic Press, San Diego.

McGill, G. E. (1993), Wrinkle ridges, stress domains, and kinematics of Venusian plains, *Geophysical Research Letters*, 20(21), 2407–2410, doi:10.1029/93GL02635.

McGovern, P., Simons, M., and S. Solomon (1995), Estimates of elastic lithosphere thickness and heat flux beneath large volcanoes on Venus, *Abstracts of the 26th Lunar and*

Planetary Science Conference, 941–942.

McGovern, P. J., and S. C. Solomon (1998), Growth of large volcanoes on Venus: Mechanical models and implications for structural evolution, *Journal of Geophysical Research*, 103, 11,071 – 11,101, doi: 10.1029/98JE01046.

McKenzie, D. (1994), The Relationship between Topography and Gravity on Earth and Venus, *Icarus*, 112(1), 55-88, doi:10.1006/icar.1994.1170.

McKenzie, D., and M. J. Bickle (1988), The Volume and Composition of Melt Generated by Extension of the Lithosphere, *Journal of Petrology*, 29(3), 625–679.

McKenzie, D., P. G. Ford, C. Johnson, B. Parsons, D. Sandwell, S. Saunders, and S. C. Solomon (1992), Features on Venus generated by plate boundary processes, *Journal of Geophysical Research: Planets*, 97(E8), 13533–13544, doi:10.1029/92JE01350.

McKenzie, D., and F. Nimmo (1997), Elastic Thickness Estimates for Venus from Line of Sight Accelerations, *Icarus*, 130(1), 198–216, doi:10.1006/icar.1997.5770.

McKinnon, W. ., K. . Zahnle, B. A. Ivanov, and H. J. Melosh (1997), Cratering on Venus: Models and observations, in *Venus II: Geology, Geophysics, Atmosphere and Solar Wind Environment*, 969–1014, The University of Arizona Press, Arizona.

Melosh, H. J. (2011), *Planetary surface processes*, Cambridge University Press, New York.

Michaels, G. A., R. S. Saunders, and E. R. Stofan (1992), Morphology of Regional Fracture Systems on Venus, *Abstracts of the Lunar and Planetary Science Conference*, 23, 903–904.

Miler, M. S., and Levander (2010), Lithospheric Structure Beneath the Western US using USArray Data, *IRIS Core Proposal*, 3, II–148.

- Moore, P. (2002), Venus, Cassell Illustrated, Great Britain.
- Moore, W. B., and G. Schubert (1995), Lithospheric thickness and mantle/lithosphere density contrast beneath Beta Regio, Venus, *Geophysical Research Letters*, 22(4), 429–432, doi:199510.1029/94GL02055.
- Moore, W. B., and G. Schubert (1997), Venusian Crustal and Lithospheric Properties from Nonlinear Regressions of Highland Geoid and Topography, *Icarus*, 128(2), 415–428, doi:10.1006/icar.1997.5750.
- Moresi, L., and B. Parsons (1995), Interpreting gravity, geoid, and topography for convection with temperature dependent viscosity: Application to surface features on Venus, *Journal of Geophysical Research*, 100(E10), 21,155–21,171, doi:199510.1029/95JE01622.
- Moresi, L., and V. Solomatov (1998), Mantle convection with a brittle lithosphere: thoughts on the global tectonic styles of the Earth and Venus, *Geophysical Journal International*, 133(3), 669–682, doi:10.1046/j.1365-246X.1998.00521.x.
- Morgan, J. P., W. J. Morgan, and E. Price (1995), Hotspot melting generates both hotspot volcanism and a hotspot swell?, *Journal of Geophysical Research*, 100(B5), 8045–8062, doi:199510.1029/94JB02889.
- Morgan, P., and R. J. Phillips (1983), Hot spot heat transfer: Its application to Venus and implications to Venus and Earth, *Journal of Geophysical Research: Solid Earth*, 88(B10), 8305–8317, doi:10.1029/JB088iB10p08305.
- Morley, C. K. (1989), Extension, detachments, and sedimentation in continental rifts (with particular reference to East Africa), *Tectonics*, 8(6), 1175–1192, doi:10.1029/TC008i006p01175.

- Mueller, N., J. Helbert, G. L. Hashimoto, C. C. C. Tsang, S. Erard, G. Piccioni, and P. Drossart (2008), Venus surface thermal emission at 1 μm in VIRTIS imaging observations: Evidence for variation of crust and mantle differentiation conditions, *Journal of Geophysical Research: Planets*, 113, E00B17, doi:10.1029/2008JE003118.
- Musser, G. S., and S. W. Squyres (1997), A coupled thermal-mechanical model for corona formation on Venus, *Journal of Geophysical Research: Planets*, 102(E3), 6581–6595, doi:10.1029/96JE03044.
- Namiki, N., and S. C. Solomon (1994), Impact crater densities on volcanoes and coronae on Venus: implications for volcanic resurfacing, *Science*, 265(5174), 929–933, doi:10.1126/science.265.5174.929.
- Namiki, N., and S. C. Solomon (1998), Volcanic degassing of argon and helium and the history of crustal production on Venus, *Journal of Geophysical Research: Planets*, 103(E2), 3655–3677, doi:10.1029/97JE03032.
- Nikolaeva, O. V., and A. A. Ariskin (1999), Geochemical constraints on petrogenic processes on Venus, *J. Geophys. Res.*, 104(E8), 18889–18897, doi:10.1029/1996JE000337.
- Nimmo, F. (2002), Why does Venus lack a magnetic field?, *Geology*, 30(11), 987–990, doi:10.1130/0091-7613(2002)030<0987:WDVLAM>2.0.CO;2.
- Nimmo, F., and D. McKenzie (1996), Modelling plume-related uplift, gravity and melting on Venus, *Earth and Planetary Science Letters*, 145(1-4), 109–123, doi:10.1016/S0012-821X(96)00200-2.
- Nimmo, F., and D. McKenzie (1998), Volcanism and Tectonics on Venus, *Annual Review of Earth and Planetary Sciences*, 26(1), 23–51, doi:10.1146/annurev.earth.26.1.23.
- Noack, L., D. Breuer, and T. Spohn (2012), Coupling the atmosphere with interior dynamics:

- Implications for the resurfacing of Venus, *Icarus*, 217(2), 484–498,
doi:10.1016/j.icarus.2011.08.026.
- Ogawa, M. (2000), Numerical models of magmatism in convecting mantle with temperature-dependent viscosity and their implications for Venus and Earth, *Journal of Geophysical Research: Planets*, 105(E3), 6997–7012, doi:10.1029/1999JE001162.
- Olson, P., G. Schubert, and C. Anderson (1993), Structure of Axisymmetric Mantle Plumes, *Journal of Geophysical Research: Solid Earth*, 98(B4), 6829–6844,
doi:10.1029/92JB01013.
- O'Neill, C. J. (2012), Tectonothermal evolution of solid bodies: terrestrial planets, exoplanets and moons, *Australian Journal of Earth Sciences*, 59(2), 189–198,
doi:10.1080/08120099.2012.644403.
- O'Neill, C., Lenardic, A., Coltice, N., L. Moresi (2014), Mantle convection and outgassing on terrestrial planets, *Comparative Climatology of Terrestrial Planets*, University of Arizona Press Space Science Series volume, Arizona.
- O'Neill, C., L. Moresi, D. Müller, R. Albert, and F. Dufour (2006), Ellipsis 3D: A Particle-In-Cell Finite-Element Hybrid Code for Modelling Mantle Convection and Lithospheric Deformation, *Computers and Geosciences*, 32(10), 1769–1779,
doi:10.1016/j.cageo.2006.04.006.
- Orth, C. P., and V. S. Solomatov (2011), The Isostatic Stagnant Lid Approximation and Global Variations in the Venusian Lithospheric Thickness, *Geochemistry Geophysics Geosystems*, 12(7), 1525–2027.
- Papale, P. (1997), Modeling of the solubility of a one-component H₂O or CO₂ fluid in silicate liquids, *Contributions to Mineralogy and Petrology*, 126(3), 237–251,

doi:10.1007/s004100050247.

Papuc, A. M., and G. F. Davies (2012), Transient mantle layering and the episodic behaviour of Venus due to the “basalt barrier” mechanism, *Icarus*, 217(2), 499–509, doi:10.1016/j.icarus.2011.09.024.

Parmentier, E. M., and P. C. Hess (1992), Chemical differentiation of a convecting planetary interior: Consequences for a one plate planet such as Venus, *Geophysical Research Letters*, 19(20), 2015–2018, doi:10.1029/92GL01862.

Pasyanos, M. E. (2010), Lithospheric thickness modeled from long-period surface wave dispersion, *Tectonophysics*, 481(1–4), 38–50, doi:10.1016/j.tecto.2009.02.023.

Petford, N. (2000), Dyke widths and ascent rates of silicic magmas on Venus, *Geological Society of America Special Papers*, 350, 87–95, doi:10.1130/0-8137-2350-7.87.

Pauer, M., K. Fleming, and O. Čadež (2006), Modeling the dynamic component of the geoid and topography of Venus, *Journal of Geophysical Research*, 111(E11), doi:10.1029/2005JE002511.

Pettengill, G. H., E. Eliason, P. G. Ford, G. B. Lorient, H. Masursky, and G. E. McGill (1980), Pioneer Venus Radar results altimetry and surface properties, *Journal of Geophysical Research: Space Physics*, 85(A13), 8261–8270, doi:10.1029/JA085iA13p08261.

Pettengill, G. H., P. G. Ford, W. T. K. Johnson, R. K. Raney, and L. A. Soderblom (1991), Magellan: Radar Performance and Data Products, *Science*, 252(5003), 260–265, doi:10.1126/science.252.5003.260.

Pham, L. B. S., Ö. Karatekin, and V. Dehant (2011), Effects of impacts on the atmospheric evolution: Comparison between Mars, Earth, and Venus, *Planetary and Space Science*, 59(10), 1087–1092, doi:10.1016/j.pss.2010.11.010.

- Phillips, R. J. (1990), Convection-driven tectonics on Venus, *Journal of Geophysical Research: Solid Earth*, 95(B2), 1301–1316, doi:10.1029/JB095iB02p01301.
- Phillips, R. J. (1994), Estimating Lithospheric Properties at Atla Regio, Venus, *Icarus*, 112(1), 147–170, doi:10.1006/icar.1994.1175.
- Phillips, R. J. H. (1998), Geological evolution of Venus: Rises, plains, plumes, and plateaus, *Science*, 279(5356), 1492.
- Phillips, R. J., R. E. Grimm, and M. C. Malin (1991), Hot-Spot Evolution and the Global Tectonics of Venus, *Science*, 252(5006), 651 –658, doi:10.1126/science.252.5006.651.
- Phillips, R. J. and V. L. Hansen (1994), Tectonic and magmatic evolution of Venus, *Annual Review of Earth and Planetary Sciences*, 22, 597-656, doi:10.1146/annurev.ea.22.050194.003121.
- Phillips, R. J., C. L. Johnson, S. L. Mackwell, P. Morgan, D. T. Sandwell, and M. T. Zuber (1997), Lithospheric Mechanics and Dynamics of Venus, in *Venus II: Geology, Geophysics, Atmosphere and Solar Wind Environment*, 1163–1205, The University of Arizona Press, Arizona.
- Pieters, C.M., J. W. Head, W. Patterson, S. Pratt, J. Garvin, V. L. Barsukov, A. T. Basilevsky, I. L. Khodakovsky, A. S. Selivanov, A. S. Panfilov, Yu. M. Gektin, Y. M. Narayeva (1986), The Color of the Surface of Venus, *Science*, 234(4782), 1379–1383, doi:10.1126/science.234.4782.1379.
- Pritchard, M. E., V. L. Hansen, and J. J. Willis (1997), Structural evolution of western Fortuna Tessera, Venus, *Geophysical Research Letters*, 24(18), 2339–2342.
- Pronin, A.A. (1986) The structure of Lakshmi Plateau, an indication of asthenosphere horizontal flows on Venus, *Geotectonika*, 20, 271-280.

- Ranalli, G. (1995) *Rheology of the Earth*, Chapman and Hall, London.
- Rappaport, N. J., A. S. Konopliv, A. B. Kucinskas, and P. G. Ford (1999), An Improved 360 Degree and Order Model of Venus Topography, *Icarus*, 139(1), 19–31, doi:10.1006/icar.1999.6081.
- Rappaport, N., and J. J. Plaut (1994), A 360-Degree and -Order Model of Venus Topography, *Icarus*, 112(1), 27–33, doi:10.1006/icar.1994.1167.
- Rasool, S. I., and C. De Bergh (1970), The Runaway Greenhouse and the Accumulation of CO₂ in the Venus Atmosphere, *Nature*, 226(5250), 1037–1039, doi:10.1038/2261037a0.
- Ratcliff, J. T., P. J. Tackley, G. Schubert, and A. Zebib (1997), Transitions in thermal convection with strongly variable viscosity, *Physics of the Earth and Planetary Interiors*, 102(3–4), 201–212, doi:10.1016/S0031-9201(97)00013-7.
- Rathbun, J. A., D. M. Janes, and S. W. Squyres (1999), Formation of Beta Regio, Venus: Results from measuring strain, *Journal of Geophysical Research*, 104(E1), 1917–1927, doi:10.1029/1998JE900026.
- Reese, C. C., V. S. Solomatov, and L.-N. Moresi (1998), Heat transport efficiency for stagnant lid convection with dislocation viscosity: Application to Mars and Venus, *Journal of Geophysical Research: Planets*, 103(E6), 13643–13657, doi:10.1029/98JE01047.
- Reese, C. C., V. S. Solomatov, and L.-N. Moresi (1999), Non-Newtonian Stagnant Lid Convection and Magmatic Resurfacing on Venus, *Icarus*, 139(1), 67–80, doi:10.1006/icar.1999.6088.
- Reynolds, J. M. (1997), *An introduction to applied and environmental geophysics*, John Wiley and Sons, West Sussex, England.

- Richards, M. A., W.-S. Yang, J. R. Baumgardner, and H.-P. Bunge (2001), Role of a low-viscosity zone in stabilizing plate tectonics: Implications for comparative terrestrial planetology, *Geochemistry, Geophysics, Geosystems*, 2(8), 1026, doi:10.1029/2000GC000115.
- Riley, K. M., R. C. Anderson, and B. J. Peer (1995), Lineament analysis of Fortuna Tesera, Venus: Results from an ongoing study, *Abstracts of the Lunar and Planetary Science Conference*, 26.
- Roberts, K. M., and J. W. Head (1990), Western Ishtar Terra and Lakshmi Planum, Venus: Models of formation and evolution, *Geophysical Research Letters*, 17(9), 1341–1344, doi:10.1029/GL017i009p01341.
- Robinson, E. M., B. Parsons, and S. F. Daly (1987), The effect of a shallow low viscosity zone on the apparent compensation of mid-plate swells, *Earth and Planetary Science Letters*, 82(3–4), 335–348, doi:10.1016/0012-821X(87)90207-X.
- Robinson, C. A., G. D. Thornhill, and E. A. Parfitt (1995), Large-scale volcanic activity at Maat Mons: Can this explain fluctuations in atmospheric chemistry observed by Pioneer Venus?, *Journal of Geophysical Research: Planets*, 100(E6), 11755–11763, doi:10.1029/95JE00147.
- Rogers, N. (2008), *An introduction to our dynamic planet*, Cambridge University Press, United Kingdom.
- Rogers, P. G., and M. T. Zuber (1998), Tectonic evolution of Bell Regio, Venus: Regional stress, lithospheric flexure and edifice stresses, *Journal of Geophysical Research*, 103, 16,841–16,853, doi:10.1029/98JE00585.
- Romeo, I., and D. L. Turcotte (2008), Pulsating continents on Venus: An explanation for

- crustal plateaus and tessera terrains, *Earth and Planetary Science Letters*, 276(1–2), 85–97, doi:10.1016/j.epsl.2008.09.009.
- Ryan, M.P. (1994), *Magmatic Systems; Neutral-Buoyancy controlled magma transport and storage in mid-ocean ridge magma reservoirs and their sheeted-dike complex: a summary of basic relationships*, 97-135. Academic Press: California.
- Sandwell, D. T., C. L. Johnson, F. Bilotti, and J. Suppe (1997), Driving Forces for Limited Tectonics on Venus, *Icarus*, 129(1), 232–244, doi:10.1006/icar.1997.5721.
- Sandwell, D. T., and M. L. Renkin (1988), Compensation of swells and plateaus in the north Pacific: No direct evidence for mantle convection, *Journal of Geophysical Research: Solid Earth*, 93(B4), 2775–2783, doi:10.1029/JB093iB04p02775.
- Sandwell, D. T., and G. Schubert (1992), Flexural ridges, trenches and outer rises around coronae on Venus, *Journal of Geophysical Research*, 97, 16069–83, doi:10.1029/92JE01274.
- Schaber, G. G., R. G. Strom, H. J. Moore, L. A. Soderblom, R. L. Kirk, D. J. Chadwick, D. D. Dawson, L. R. Gaddis, J. M. Boyce, and J. Russell (1992), Geology and distribution of impact craters on Venus: What are they telling us?, *Journal of Geophysical Research: Planets*, 97(E8), 13257–13301, doi:10.1029/92JE01246.
- Shellnutt, J. G. (2013), Petrological modeling of basaltic rocks from Venus: A case for the presence of silicic rocks, *Journal of Geophysical Research: Planets*, doi:10.1002/jgre.20094.
- Schubert, G., D. Bercovici, and G. A. Glatzmaier (1990), Mantle Dynamics in Mars and Venus: Influence of an Immobile Lithosphere on Three-Dimensional Mantle Convection, *Journal of Geophysical Research*, 95(B9), 14,105–14,129, doi:10.1029/JB095iB09p14105.

- Schubert, G., and C.A.P. Goldman (2012), Mantle plume interaction with an endothermic phase change, *Journal of Geophysical Research*, 100, B5, 8245-8256.
- Schubert, G., W. B. Moore, and D. T. Sandwell (1994), Gravity over Coronae and Chasmata on Venus, *Icarus*, 112(1), 130–146, doi:10.1006/icar.1994.1174.
- Schubert, G., and D. T. Sandwell (1995), A Global Survey of Possible Subduction Sites on Venus, *Icarus*, 117(1), 173–196, doi:10.1006/icar.1995.1150.
- Schubert, G., V. S. Solomatov, P. J. Tackley, and D. L. Turcotte (1997), *Mantle convection and the thermal evolution of Venus*, 1245-1288, The University of Arizona Press, Arizona.
- Schubert, G., D. L. Turcotte, and P. Olson (2001), *Mantle convection in the earth and planets*, Cambridge University Press, New York.
- Seeds, M. A. (2005). *Foundations of astronomy*, Thomson Brooks/Cole, Australia.
- Senske, D. A. (1993), Rifting at Devana Chasma, Venus: Structure and estimation of the effective thickness of the elastic lithosphere, *Abstracts of the 24th Lunar and Planetary Science Conference*, 1277–1278.
- Senske, D. A., and J. W. Head (1992), Atla Regio, Venus: Geology and Origin of a Major Equatorial Volcanic Rise, *Papers presented to the International Colloquium Venus*, 107–109.
- Senske, D. A., J. W. Head, E. R. Stofan, and D. B. Campbell (1991), Geology and structure of Beta Regio, Venus: Results from Arecibo Radar Imaging, *Geophysical Research Letters*, 18(6), 1159–1162.
- Senske, D. A., G. G. Schaber, and E. R. Stofan (1992), Regional Topographic Rises on Venus: Geology of Western Eistla Regio and Comparison to Beta Regio and Atla Regio, *Journal of Geophysical Research*, 97(E8), 13395-13420.

- Self, S. (2006), The effects and consequences of very large explosive volcanic eruptions, *Philosophical Transactions of the Royal Society*, 364(1845), 2073–2097, doi:10.1098/rsta.2006.1814.
- Simons, M., S. C. Solomon, and B. H. Hager (1997), Localization of gravity and topography: constraints on the tectonics and mantle dynamics of Venus, *Geophysical Journal International*, 131(1), 24–44, doi:10.1111/j.1365-246X.1997.tb00593.x.
- Sjogren, W. L., W. B. Banerdt, P. W. Chodas, A. S. Konopliv, G. Balmino, J. P. Barriot, J. Arkani-Hamed, T. R. Colvin, and M. E. Davies (1997), The Venus gravity field and other geodetic parameters, in *Venus II: Geology, Geophysics, Atmosphere and Solar Wind Environment*, 1125–1161, The University of Arizona Press, Arizona.
- Simons, M., B. H. Hager, and S. C. Solomon (1994), Global Variations in the Geoid/Topography Admittance of Venus, *Science*, 264(5160), 798–803, doi:10.1126/science.264.5160.798.
- Simons, M., S. C. Solomon, and B. H. Hager (1997), Localization of gravity and topography: constraints on the tectonics and mantle dynamics of Venus, *Geophysical Journal International*, 131(1), 24–44, doi:10.1111/j.1365-246X.1997.tb00593.x.
- Sleep, N. H. (2000), Evolution of the mode of convection within terrestrial planets, *Journal of Geophysical Research: Planets*, 105(E7), 17563–17578, doi:10.1029/2000JE001240.
- Smrekar, S. E. (1994), Evidence for Active Hotspots on Venus from Analysis of Magellan Gravity Data, *Icarus*, 112(1), 2–26, doi:10.1006/icar.1994.1166.
- Smrekar, S. E., L. Elkins-Tanton, J. J. Leitner, A. Lenardic, S. Mackwell, L. Moresi, C. Sotin, and E. R. Stofan (2007), Tectonic and thermal evolution of Venus and the role of volatiles: implications for understanding the terrestrial planets, in *Exploring Venus as*

a terrestrial planet, 45–71, American Geophysical Union, Washington.

Smrekar, S. E., W. S. Kiefer, and E. R. Stofan (1997), Large Volcanic Rises on Venus, in *Venus II: Geology, Geophysics, Atmosphere and Solar Wind Environment*, 845–878, The University of Arizona Press, Arizona.

Smrekar, S. E., and E. M. Parmentier (1996), The Interaction of Mantle Plumes with Surface Thermal and Chemical Boundary Layers: Applications to Hotspots on Venus, *Journal of Geophysical Research*, 101(B3), 5397–5410, doi:10.1029/95JB02877.

Smrekar, S. E., and R. J. Phillips (1991), Venusian Highlands: Geoid to Topography Ratios and their Implications, *Earth and Planetary Science Letters*, 107(3-4), 582–597, doi:10.1016/0012-821X(91)90103-O.

Smrekar, S. E., and C. Sotin (2012), Constraints on mantle plumes on Venus: Implications for volatile history, *Icarus*, 217(2), 510–523, doi:10.1016/j.icarus.2011.09.011.

Smrekar, S. E., E. R. Stofan, N. Mueller, A. Treiman, L. Elkins-Tanton, J. Helbert, G. Piccioni, and P. Drossart (2010), Recent Hotspot Volcanism on Venus from VIRTIS Emissivity Data, *Science*, 328(5978), 605–608, doi:10.1126/science.1186785.

Solomatov, V. S. (1995), Scaling of temperature and stress dependent viscosity convection, *Physics of Fluids*, 7(2), 266, doi:10.1063/1.868624.

Solomatov, V. S., and L.-N. Moresi (1996), Stagnant Lid Convection on Venus, *Journal of Geophysical Research*, 101(E2), 4737–4753, doi:10.1029/95JE03361.

Solomatov, V. S. and V. N. Zharkov (1990), The thermal regime of Venus, *Icarus*, 84, 280–295, doi:10.1016/0019-1035(90)90038-B.

Solomon, S. C., and J. W. Head (1982), Mechanisms for lithospheric heat transport on Venus:

- Implications for tectonic style and volcanism, *Journal of Geophysical Research: Solid Earth*, 87(B11), 9236–9246, doi:10.1029/JB087iB11p09236.
- Solomon, S. C., and J. W. Head (1984), Venus banded terrain: tectonic models for band formation and their relationship to lithospheric structure, *Journal of Geophysical Research*, 89, 6885–6897.
- Solomon, S. C., and J. W. Head (1990), Lithospheric Flexure Beneath the Freyja Montes Foredeep, Venus: Constraints on Lithospheric Thermal Gradient and Heat Flow, *Geophysical Research Letters*, 17(9), 1393–1396, doi:10.1029/GL017i009p01393.
- Solomon, S. C., and J. W. Head (1991), Fundamental issues in the geology and geophysics of venus, *Science*, 252(5003), 252–260, doi:10.1126/science.252.5003.252.
- Solomon, S. C., S. E. Smrekar, D. L. Bindschadler, R. E. Grimm, W. M. Kaula, G. E. McGill, R. J. Phillips, R. S. Saunders, G. Schubert, S. W. Squyres, and E. R. Stofan (1992), Venus tectonics: an overview of Magellan observations, *Journal of Geophysical Research*, 97(E8), 13,199–13,255, doi:10.1029/92JE01418
- Spohn, T., and G. Schubert (1983), Convective thinning of the lithosphere: A mechanism for rifting and mid-plate volcanism on Earth, Venus, and Mars, *Tectonophysics*, 94(1–4), 67–90, doi:10.1016/0040-1951(83)90010-0.
- Squyres, S. W., D. M. Janes, G. Baer, D. L. Bindschadler, G. Schubert, V. L. Sharpton, E. R. Stofan (1992), The morphology and evolution of coronae on Venus, *Journal of Geophysical Research*, 97(E8), 13,611–13,634, doi:10.1029/92JE01213.
- Squyres, S. W., D. M. Janes, G. Schubert, D. L. Bindschadler, J. E. Moersch, D. L. Turcotte, and E. R. Stofan (1993), The spatial distribution of coronae and related features on

- Venus, *Geophysical Research Letters*, 20(24), 2965–2968, doi:10.1029/93GL00866.
- Stein, C., A. Fahl, and U. Hansen (2010), Resurfacing events on Venus: Implications on plume dynamics and surface topography, *Geophysical Research Letters*, 37(1), L01201, doi:10.1029/2009GL041073.
- Steinberger, B., S. C. Werner, and T. H. Torsvik (2010), Deep versus shallow origin of gravity anomalies, topography and volcanism on Earth, Venus and Mars, *Icarus*, 207(2), 564–577, doi:10.1016/j.icarus.2009.12.025.
- Steinbach, V., and D. A. Yuen (1992), The effects of multiple phase transitions on Venusian mantle convection, *Geophysical Research Letters*, 19(22), 2243–2246, doi:10.1029/92GL02319.
- Stevenson, D. L., T. Spohn, and G. Schubert (1983), Magnetism and thermal evolution of terrestrial planets, *Icarus*, 54, 466–489.
- Stoddard, P. R., and D. M. Jurdy (2011), Topographic comparisons of uplift features on Venus and Earth: implications for Venus tectonics, *Icarus*, 524–533, doi:10.1016/j.icarus.2011.09.003.
- Stofan, E. R., V. E. Hamilton, D. M. Janes, and S. E. Smrekar (1997), Coronae on Venus: morphology and origin, in *Venus II: Geology, Geophysics, Atmosphere and Solar Wind Environment*, 931–965, The University of Arizona Press, Arizona.
- Stofan, E. R., J. W. Head, D. B. Campbell, S. H. Zisk, A. F. Bogomolov, O. N. Rzhiga, A. T. Basilevsky, and N. Armand (1989), Geology of a rift zone on Venus: Beta Regio and Devana Chasma, *Geological Society of America Bulletin*, 101(1), 143–156, doi:10.1130/0016-7606(1989)101<0143:GOARZO>2.3.CO;2.
- Stofan, E. R., and S. E. Smrekar (2005), Large topographic rises, coronae, large flow fields,

- and large volcanoes on Venus: Evidence for mantle plumes?, *Geological Society of America Special Papers*, 388, 841–861, doi:10.1130/0-8137-2388-4.841.
- Stofan, E. R., S. E. Smrekar, D. L. Bindshadler, and D. A. Senske (1995), Large Topographic Rises on Venus: Implications for Mantle Upwelling, *Journal of Geophysical Research*, 100(E11), 23317–23327, doi:10.1029/95JE01834.
- Stofan, E. R., S. E. Smrekar, S. W. Tapper, J. E. Guest, and P. M. Grindrod (2001), Preliminary analysis of an expanded corona database for Venus, *Geophysical Research Letters*, 28(22), 4267–4270, doi:10.1029/2001GL013307.
- Sukhanov, A. L. (1986), Parquet: Regions of areal plastic dislocations, *Geotectonics*, 20, 294–305.
- Tackley, P. J. (2000), Self-consistent generation of tectonic plates in time-dependent, three-dimensional mantle convection simulations, *Geochemistry, Geophysics, Geosystems*, 1(8), doi:10.1029/2000GC000036.
- Tan, E., E. Choi, P. Thoutireddy, M. Gurnis, and M. Aivazis (2006), GeoFramework: Coupling multiple models of mantle convection within a computational framework, *Geochemistry, Geophysics, Geosystems*, 7, Q06001, doi:10.1029/2005GC001155.
- Tan, E., M. Gurnis, L. Armendariz, L. Strand, and S. Kientz (2012), *CitcomS User Manual Version 3.2.0*, Computational Infrastructure for Geodynamics (CIG).
- Taylor, J. R. (1982), *An introduction to error analysis*, 327 pp., University Science Books, Mill Valley, California.
- Titov, D. V., H. Svedhem, D. Koschny, R. Hoofs, S. Barabash, J.L. Bertaux, P. Drossart, V. Formisano, B. Hausler, O. Korablev, W. J. Markiewicz, D. Nevejans, M. Patzold, G. Piccioni, T. L. Zhang, D. Merritt, O. Witasse, J. Zender, A. Accomazzo, M. Sweeney,

- D. Trillard, M. Janvier, and A. Clochet (2006), Venus Express science planning, *Planetary and Space Science*, 54(13–14), 1279–1297, doi:10.1016/j.pss.2006.04.017.
- Turcotte, D. L. (1993), An Episodic Hypothesis for Venusian Tectonics, *Journal of Geophysical Research*, 98(E9), 17,061–17,068, doi:199310.1029/93JE01775.
- Turcotte, D. L. (1995), How does Venus lose heat?, *Journal of Geophysical Research: Planets*, 100(E8), 16931–16940, doi:10.1029/95JE01621.
- Turcotte, D. L., and Schubert (2001), *Geodynamics*, 2nd ed., Cambridge University Press, New York.
- Vezolainen, A. V., V. S. Solomatov, A. T. Basilevsky, and J. W. Head (2004), Uplift of Beta Regio: Three-dimensional models, *Journal of Geophysical Research*, 109, E08007, doi:200410.1029/2004JE002259.
- Vorder Bruegge, R. W. V., and J. W. Head (1989), Fortuna Tessera, Venus: Evidence of horizontal convergence and crustal thickening, *Geophysical Research Letters*, 16(7), 699–702, doi:198910.1029/GL016i007p00699.
- Vorder Bruegge, R. W. V., and J. W. Head (1990), Tectonic Evolution of Eastern Ishtar Terra, Venus, *Earth Moon Planets*, 50-51(1), 251–304, doi:10.1007/BF00142396.
- Watson, S., and D. a. N. McKenzie (1991), Melt Generation by Plumes: A Study of Hawaiian Volcanism, *Journal of Petrology*, 32(3), 501–537, doi:10.1093/petrology/32.3.501.
- Weertman, J. (1970), The creep strength of the Earth's mantle, *Reviews of Geophysics*, 8(1), 145–168, doi:10.1029/RG008i001p00145.
- Weinstein, S. A. (1995), The effects of a deep mantle endothermic phase change on the structure of thermal convection in silicate planets, *Journal of Geophysical Research:*

- Planets*, 100(E6), 11719–11728, doi:10.1029/95JE00710.
- Weinstein, S. A. (1996), The potential role of non-Newtonian rheology in the resurfacing of Venus, *Geophysical Research Letters*, 23(5), 511–514, doi:10.1029/96GL00387.
- Wessel, P., and W. H. F. Smith (1991), *Free Software Helps Map and Display Data*, EOS Transactions, American Geophysical Union, Washington.
- Wessel, P., and W. H. F. Smith (1998), *New, improved version of Generic Mapping Tools released*, EOS Transactions, American Geophysical Union, 79(49), 579.
- White, R. S. (1993), Melt Production Rates in Mantle Plumes, *Philosophical Transactions of the Royal Society of London. Series A: Physical and Engineering Sciences*, 342(1663), 137–153, doi:10.1098/rsta.1993.0010.
- Wieczorek, M. A. (2007), Gravity and Topography of the Terrestrial Planets, *Treatise on Geophysics*, 165–206.
- Wieczorek, M. A., and F. J. Simons (2005), Localized spectral analysis on the sphere, *Geophysical Journal International*, 162, 655–675.
- Wieczorek, M. A., and F. J. Simons (2007), Minimum-Variance Multitaper Spectral Estimation on the Sphere, *Journal of Fourier Analysis and Applications*, 13(6), 665–692, doi:10.1007/s00041-006-6904-1.
- Wolfe, C. J., M. K. McNutt, and R. S. Detrick (1994), The Marquesas archipelagic apron: Seismic stratigraphy and implications for volcano growth, mass wasting, and crustal underplating, *Journal of Geophysical Research*, 99(B7), 13,591–13,608, doi:10.1029/94JB00686.
- Wood, J. A., W. R. Buck, E. Anders, J. W. Morgan, E. Stolper, D. L. Anderson, W. M. Kaula,

- G. J. Consolmagno, A. E. Ringwood, and H. Wänke (1981), Geophysical and cosmochemical constraints on properties of mantles of the terrestrial planets, in *Basaltic volcanism on the terrestrial planets*, Pergamon Press, New York.
- Young, H. D. (1962), *Statistical treatment of data*, McGraw-Hill Inc, New York.
- Zhong, S., A. McNamara, E. Tan, L. Moresi, and M. Gurnis (2008), A benchmark study on mantle convection in a 3-D spherical shell using CitcomS, *Geochemistry, Geophysics, Geosystems*, 9(10), doi:10.1029/2008GC002048.
- Zhong, S., M. T. Zuber, L. Moresi, and M. Gurnis (2000), Role of temperature-dependent viscosity and surface plates in spherical shell models of mantle convection, *Journal of Geophysical Research: Solid Earth*, 105(B5), 11063–11082, doi:10.1029/2000JB900003.
- Zienkiewicz, O. C., R. L. Taylor, and J. Z. Zhu (2005), *The finite element method: its basis and fundamentals*, Elsevier Butterworth-Heinemann, Amsterdam.
- Zuber, M. T. (1987), Constraints on the lithospheric structure of Venus from mechanical models and tectonic surface features, *Journal of Geophysical Research: Solid Earth*, 92(B4), E541–E551, doi:10.1029/JB092iB04p0E541.
- Zuber, M. T., and E. M. Parmentier (1989), Lithospheric necking: a dynamic model for rift morphology, *Earth and Planetary Science Letters*, 373–383, doi:10.1016/0012-821X(86)90147-0.
- Zuber, M. T., and E. M. Parmentier (1990), On the relationship between isostatic elevation and the wavelengths of tectonic surface features on Venus, *Icarus*, 85(2), 290–308, doi:10.1016/0019-1035(90)90118-S.

A1. CitcomS Input File

```
# specify output files
datadir="global_14"
datafile="globe"
output_format=ascii
output_optional=geoid,stress,horiz_avg,surf,botm
output_ll_max=80

write_q_files=500

file_vbcs=0
vel_bound_file="velbc/velbc_full"

coor=0
coor_file="coor32.dat"

mat_control=0
mat_file=""

lith_age=0
lith_age_file=""

tracer=0
tracer_file=""

# processors, mesh grid information
nproc_surf=12
nprocx=2
nprocy=2
nprocz=2
nodex=65
nodey=65
nodez=65
mgunitx=4
mgunity=4
mgunitz=4
levels=4

# the calculation region definition
radius_inner=0.55
radius_outer=1.0

theta_min=1.0708
theta_max=2.0708

fi_min=1.0708
fi_max=2.0708

# restart info
```

```
tic_method=-1
#tic_method=0
#restart=on
restart=off
post_p=0
datadir_old="global_13"
#datadir_old="global_20"
datafile_old="globe"
solution_cycles_init=42000
zero_elapsed_time=off

# timestepping information
minstep=1
maxstep=30000
#maxstep=80000
#maxtotstep=80000
maxtotstep=30000
storage_spacing=500
cpu_limits_in_seconds=1000000000

# Initial conditions
num_perturbations=1
perturbmag=0.1
perturbl=3
perturbm=2
perturblayer=5

# Boundary Conditions
topvbc=0
    topvbxval=0.0
    topvbyval=0.0
botvbc=0
    botvbxval=0.0
    botvbyval=0.0

toptbc=1
    toptbcval=0.0
bottbc=1
    bottbcval=1.0

lith_age_time=0
lith_age_depth=0.031400
mantle_temp=0.800000
temperature_bound_adj=0
depth_bound_adj=0.157000
width_bound_adj=0.087270
half_space_age=100.0

# miscellaneous information
```

```
stokes_flow_only=0
inputdiffusivity=1.0
inputdiffusivity=1.0
rayleigh=2e8 # equiv 1.87e07
Q0=40

# required information
Problem=convection
Geometry=sphere
Spacing=regular
Solver=multigrid
node_assemble=1

# Depth Information
z_lith=0.0066116
z_410=0.0811 #also depth of 410-phase change
z_lmantle=0.114 #also depth of 670-phase change
z_cmb=0.49 # depth of another phase change

# Viscosity Information
Viscosity=system
rheol=7
visc_smooth_method=3

VISC_UPDATE=on
num_mat=4

TDEPV=on
viscE=10,10,10,10
viscT=0.292,0.292,0.292,0.292
visc0=1,1,3,1
viscZ=1.88e-6,1.88e-6,1.88e-6,1.88e-6

visc_layer_control=off
visc_layer_file="viscosity-file-FBRun5lA30D015-96.dat"

SDEPV=off
sdepv_expt=1,1,1,1
sdepv_misfit=0.020

PDEPV=off
pdepv_a=1.36e4,1.36e4,1.36e4,1.36e4
pdepv_b=0,0,0,0
pdepv_y=1.36e4,1.36e4,1.36e4,1.36e4
pdepv_eff=on
pdepv_offset=0

low_visc_channel=off
low_visc_wedge=off
lv_min_radius=0.9764
```

lv_max_radius=0.9921
lv_channel_thickness=0.0047
lv_reduction=0.5

VMIN=on
visc_min=1.0e-2
VMAX=on
visc_max=2.0e4

Tracer information
tracer=off

tracer_ic_method=0
tracers_per_element=10
tracer_file="tracer.dat"

tracer_flavors=0
ic_method_for_flavors=0
z_interface=0.700000

regular_grid_deltheta=1.0
regular_grid_delphi=1.0

chemical_buoyancy=on
buoy_type=1
buoyancy_ratio=1.0
reset_initial_composition=off

Phase Change Information
Ra_410=0.0
clapeyron=0.0494
transT410=0.78
width410=0.017

Ra_670=0.0
clapeyron=-0.0494
transT670=0.875
width670=0.017

Ra_cmb=0.0
clapeyroncmb=-0.0235
transTcmb=0.875
widthcmb=0.0058

Dimensional Information
radius=6050e3
density=3300
thermdiff=8.1e-7
gravacc=8.87
thermexp=2.0e-5
refvisc=2e21
cp=1200

```
density_above=60.0  
density_below=6600.0
```

```
# Data input and program debugging  
DESCRIBE=off  
BEGINNER=off  
VERBOSE=off
```

```
verbose=off  
see_convergence=1
```

```
# Solver Related Matters  
mg_cycle=1  
down_heavy=3  
up_heavy=3  
vlowstep=20  
vhighstep=5
```

```
piterations=375  
accuracy=1.0e-3
```

```
ADV=on  
fixed_timestep=0.0  
finetunedt=0.7  
adv_sub_iterations=2  
adv_gamma=0.5
```

```
precond=on  
aug_lagr=on  
aug_number=2.0e3
```

```
remove_rigid_rotation=on
```

```
# Age information  
start_age=4.0  
reset_startage=0
```


A2. Processes Forming Volcanic Topography at Atla Regio, Venus

Elyse Schinella¹, Craig O'Neill¹, Juan Carlos Afonso¹

Department of Earth & Planetary Science, GEMOC ARC National Key Centre, Macquarie University, Sydney, NSW, 2109

Summary: Venus and Earth share a similar size, mass and density, however Venus's high surface temperatures, pressures, dehydrated crust and absence of subduction zones, makes the surface unique. One area which shares similar volcanic landforms to Earth's is the equatorial highland Atla Regio, which extends from 170°E-220°E 30°N-10°S. The similarity of these volcanic features to Earth based examples and an understanding of the processes which produced them, can help to constrain the deformational mechanisms that may have operated at Atla Regio. This study will aim to compare volcanic topography at Atla Regio to topography observed within the Hawaiian and Cape Verde Archipelagos, Earth to determine if similar deformational processes occurred within Atla Regio. On Earth, three main processes act to produce volcanic topography and include: 1) uplift associated with a mantle plume impinging on the underside of the lithosphere; 2) rifting and volcanism associated with the mantle plume and; 3) volcanic loading, where the extra volcanic mass is compensated by flexure of the lithosphere. An understanding of the processes that gave rise to topography at Atla Regio is fundamental to determine a suitable rheological profile within this area.

Keywords: Atla Regio, Venus, Hawaii, Cape Verde, mantle plume, volcanism, lithospheric flexure

1. Introduction

Venus consists of three main types of geological landforms, including highland areas, lowland volcanic plains and lowland plains regions, which encompass 8%, 27% and 65% of Venus's surface, respectively [1]. One highland located along the equator is Atla Regio, which is marked by three large volcanoes, Ozza Mons in the south-east, Maat Mons in the south-west and Sapas Mons in the north-west, as well as three rifts, Ganis Chasma, Dali Chasma and Parga Chasma that form a triple junction at Ozza Mons (Figure 1) [2]. Due to the presence of these rifts and volcanoes, in conjunction with this region's broad domal morphology, gravity high, extensive lava flows, high elevation (~3 km) and absence of compressional features, Atla Regio is considered to be a volcanic rise [2]. Atla Regio shares similar characteristics to Earth's hot-spots, where volcanism is associated with mantle plumes [1, 2]. On the basis of the localised topography and gravity observed at Ozza Mons and Sapas Mons, each of these areas may be sites of mantle upwellings, implying Atla Regio may have two mantle plumes acting to produce the topography and gravity anomalies within this area [2].

Volcanic topography on Earth can result when an upwelling mantle plume impinges onto the base of the lithosphere causing volcanism and uplifted topography forming a volcanic rise [3] (Figure 2). Generally these areas also have large dimensions > 1000 km, suggesting that the topography is not solely supported by lithospheric strength, but by a deeper source such as a mantle plume [4]. Two currently active, Earth hot-spots are Hawaii, situated along the Hawaiian-Emperor Seamount chain and Cape Verde, located west of Senegal, Africa [5, 6].

Currently Hawaii and the Cape Verde Islands are located above mantle plumes, which cause uplifted topography and a volcanic rise [5, 6, 7, 8]. Aside from uplift and volcanism, the presence of a mantle plume can be further constrained by an excess temperature, since mantle

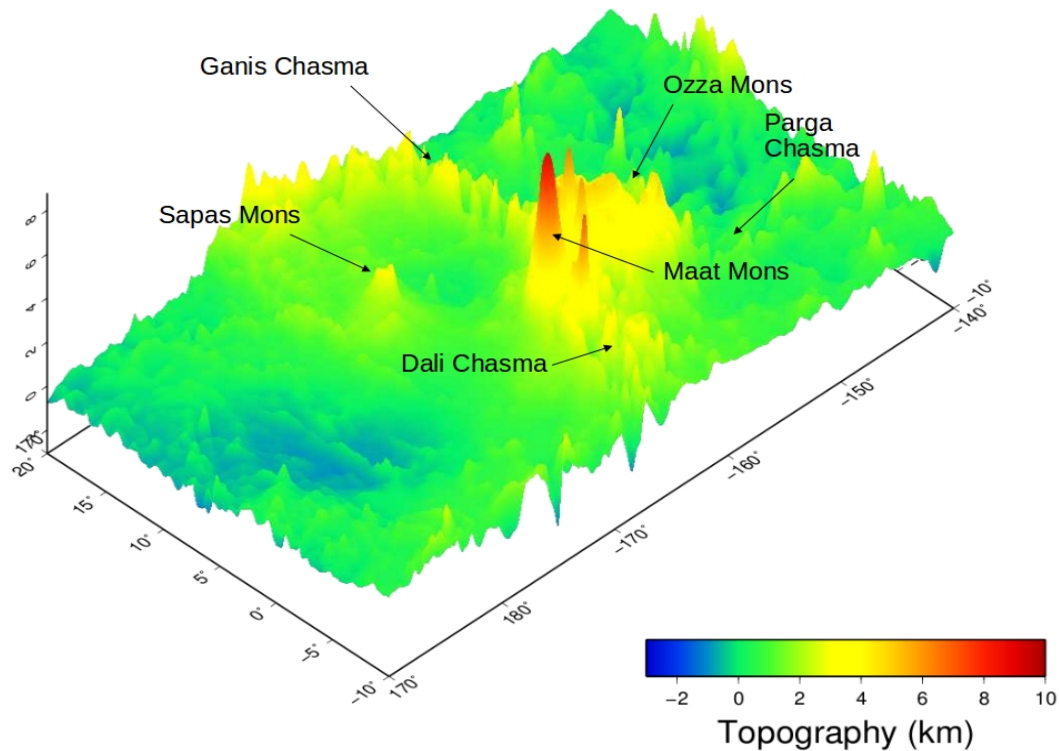


Figure 1. A 3D map showing the topography at Atla Regio. This area is dominated by three large volcanoes; Ozza and Maat Mons to the south and Sapas Mons to the north. A triple junction rift, comprising Ganis, Parga and Dalia Chasma meet at Ozza Mons.

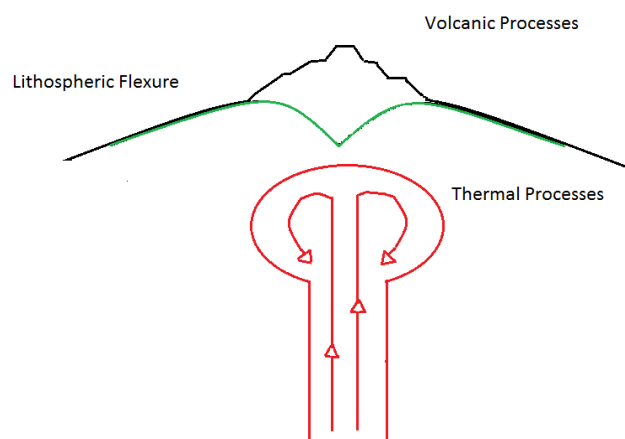


Figure 2. Schematic showing the three processes that can give rise to volcanic topography. Red line is an upwelling mantle plume, which can produce uplift, volcanism and the production of volcanic topography. The volcanoes produced can act as loads and cause the lithosphere to bend (green line).

plumes may represent extra heat, which is superimposed on the background temperature associated with mantle convection [8, 9]. These temperatures rely on a stagnation distance (r_s), which is the distance that separates the upwelling plume material from the normal asthenosphere and a plume channel thickness (A), which is the diameter of the asthenospheric conduit that connects the plume from the core-mantle boundary to the base of the lithosphere [8, 9]. Sleep [8] calculated an average excess temperature of 230-300 °C for stagnation distances of 350-450 km and a plume channel thickness of 100 km for the Hawaiian swell.

The origin and structure of mantle plumes on Venus is highly unconstrained with some authors proposing that plume channels may not extend throughout the entire depth of the mantle [10]. However, if a plume channel exists below Atla Regio it should be thicker ($\sim 200 \pm 100$ km), than those estimated for Hawaii ($\sim 100 \text{ km} \pm 16 \text{ km}$), due to Venus's hotter mantle [8, 11, 12]. Also coronae are possible surface expressions of mantle plumes, therefore their range of diameters 200-600 km could represent a range of possible stagnation distances [13].

The presence of a mantle plume can also be associated with a buoyancy flux, where a thermal mass is upwelling to the lithosphere per second, by a plume [8, 9, 12]. Since plume buoyancy is proportional to heat flow, the excess heat flow associated with this plume can also be calculated [8, 9, 12].

For Earth, the calculation of buoyancy flux relies on the knowledge of the absolute velocity of a hot-spot, which is defined as the motion of the hot-spot relative to the plate it resides on [8, 9]. Therefore, lower heat fluxes associated with the mantle plume component of heat flow are on the order of 10-20 mW m⁻² at slower-moving hot-spots, such as Cape Verde and Bermuda, compared to the higher mantle plume heat flux obtained at faster-moving hot-spots, such

Hawaii [8, 9, 14].

Turcotte & Schubert [12] used a plate velocity of 90 mm yr^{-1} for the Hawaiian hot-spot with a cross-sectional area of 1.13 km^2 , to calculate a buoyancy flux of 7.4 Mg s^{-1} , which represents a mantle plume heat flux of $3 \times 10^{11} \text{ W}$ or less than 1% of total global heat flow of Earth at this location. Venus, however, has a stationary lithosphere and the closest Earth analog for these features may be for a slow-moving plate, since these areas may be closer to thermal equilibrium [14, 15]. Cape Verde is one example of a hot-spot located on a slow-moving plate [8, 14, 15]. The buoyancy flux, and in turn, the heat flow due to a mantle plume within this area is 1.6 Mg s^{-1} and 20 mW m^{-2} [8, 14]. Models by Smrekar & Parmentier [16] suggest that buoyancy fluxes, and in turn the extra heat fluxes from a mantle plume, which are most representative of Venus hot-spots, may not be large [14, 15].

Volcanoes associated with the impingement of a mantle plume can also initiate rifting and volcanism, contributing to the topography observed [17]. Hawaii is dominated by shield volcanoes, which are characterised by their broad shapes, low elevations and undulating slopes [17]. This morphology is also consistent with Venusian volcanoes, however, these volcanoes generally have larger basal diameters and flatter profiles in comparison to those found at Hawaii [18]. The larger basal diameters of Venusian volcanoes could be caused from an absence of plate motion, since a mantle plume would produce volcanism for longer time frames on a stationary lithosphere [1]. The lower elevations and shallower slopes of Venusian volcanoes could result from: 1) high temperatures within the crust and at the surface that may have acted to slow cooling of rising magma; 2) low lava viscosities; 3) highly effusive, large volumes of magma; 4) extensive lava flow formation from lava tubes; 5) slow cooling of lava flows due to high atmospheric temperatures [18, 19, 20].

Modelling of gravity anomalies over Alta Regio can be useful to determine a suitable density distribution and therefore, geological structure below the highland [13]. The highland topography associated with volcanism at Atla Regio should correspond to a high free-air gravity anomaly, high geoid anomaly and a low bouguer anomaly [2]. Free-air gravity anomalies at short-wavelengths correspond well to local topography [12]. Bouguer anomalies, however, tend to exhibit structure associated with long-wavelength, isostatically compensated topography [12]. At sites of large-scale topography a negative bouguer anomaly is usually observed since the excess mass of the highland is isostatically compensated by a low-density crustal “root” or a low-density partial melt and magma chamber associated with volcanism [12]. The geoid anomaly, defined as the elevation difference between a reference equipotential surface (geoid) and the measured geoid, also reflects deeper density anomalies [12, 21, 22].

The presence of these volcanoes on the surface can act as loads which force the lithosphere downwards at the center of the load, whilst the surrounding area bulges upwards (Figure 3) [12]. By modelling this flexural response the elastic lithosphere thickness, which is the portion of the lithosphere that is rigid enough to sustain elastic stresses for long periods, can be determined [12]. This elastic lithosphere thickness can be used to determine a suitable temperature at the base of this layer, and in turn a thermal gradient and heat flux through an area [23].

Previous authors have determined a range of elastic lithosphere thicknesses for Atla Regio to reside between 20-52 km [14, 15, 24]. Even though these authors used spectral analysis of gravity and topography to determine elastic lithosphere thickness, their estimates are valuable for comparison purposes [14, 15, 24]. Phillips [15] used spectral analysis and Monte Carlo modelling to suggest a range of elastic lithosphere thicknesses between 40-50 km and a mean elastic lithosphere thickness of 45 km. Using this elastic lithosphere thickness as a guide, a

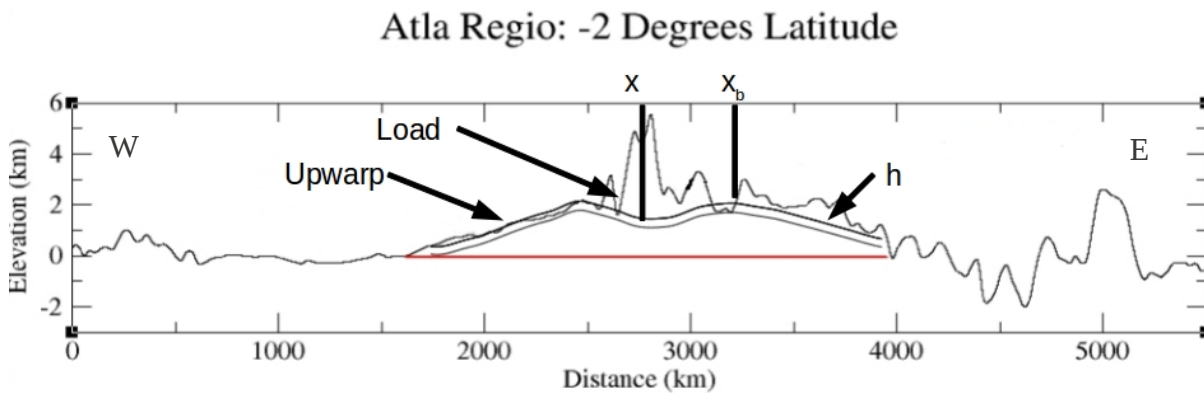


Figure 3. An east-west profile showing the upwarping of the lithosphere associated with a volcanic load at Atla Regio. The distance between the center of the load (x) and the maximum amplitude of the forebulge (x_b) can be used to determine elastic lithosphere thickness (h). The red line is the inferred line of constant depth.

thermal gradient of $7\text{--}10\text{ K km}^{-1}$ was found from moment-curvature relationships [15]. The elastic thickness estimate for Atla Regio was consistent with those obtained over the uplifted portion of the slow-moving, East African hot-spots (43–49 km), which experience a total heat flow (from mantle convection and a possible mantle plume) of $20\text{--}50\text{ mW m}^{-2}$ and a temperature gradient of $5\text{--}12.5\text{ K km}^{-1}$ [15, 25].

Phillips [15] inferred Atla Regio to share a similar thermal environment as the East African hot-spots and used an Earth-scaled heat flux of 74 mW m^{-2} as a guide to determine total heat flow within this area. Assuming a lower bound total heat flow of 80 mW m^{-2} for Atla Regio and a temperature gradient of 20 K km^{-1} , an elastic lithosphere thickness of 20 km was found [15]. However, this elastic lithosphere thickness is significantly lower than spectral analysis suggested, which led Phillips [15] to propose that Atla Regio should have a lower total heat flow (i.e. $< 80\text{ mW m}^{-2}$) than what is ascertained from Earth scaling alone.

Phillips [15] also used the mean elastic lithosphere thickness and thermal gradient within Atla Regio to propose a 100 km thick thermal lithosphere, which comprises the crust and top-most portion of the upper-mantle, to occur below this area. A thin thermal lithosphere below Atla Regio, compared to the plains regions (~350 km) could suggest that the area experiences possible heating from the tail of a mantle plume [15].

Turcotte & Schubert [12] estimated the elastic lithosphere thickness below the Hawaiian Archipelago, by taking the distance from the center of the Island of Oahu to the surrounding arch. Using this distance (250 km), a flexural parameter and rigidity of 80 km and 2.4×10^{23} N m, respectively, an elastic lithosphere thickness of 34 km was found for this area [12]. The total heat flux at the Hawaiian swell was found from measurements to be $\sim 52.9 \pm 2.3$ mW m⁻² by Von Herzen *et al.* [26].

Spectral admittance studies suggest that the thickness of the elastic lithosphere may vary between 20-29 km below the Cape Verde Islands [6]. Best fit surface/subsurface loading models, however, suggest an elastic lithosphere thickness closer to 29 km [6]. Heat flow measurements taken across the Cape Verde Rise were found to increase over the middle of the swell up to 16 ± 4 mW m⁻² above the 45.5 ± 3.4 mW m⁻² heat flow of normal 125 Myr old crust [27].

2. Methodology

Parameters used to calculate the excess temperature associated with a mantle plume at Atla Regio, Oahu and Cape Verde are listed in Table 1.

Table 1. Parameters used to calculate excess temperature, buoyancy flux and heat flow.

	Parameter	Atla Regio (Venus)	Oahu (Earth)	Cape Verde (Earth)
Cross-sectional area (km ²)	W	3056*	1188*	1097*
Mantle density (kg m ⁻³)	ρ_m	3330**	3330 [†]	3330 [†]
Surface density (kg m ⁻³)	ρ_s	67 [‡]	1030 [†]	1030 [†]
Stagnation distance (km)	r_s	200-600*	350 – 450 [†]	390 [†]
Plume channel thickness (km)	A	200	100 [†]	100 [†]
Thermal expansion coefficient (x10 ⁻⁵ K ⁻¹)	α	3.10 [#]	3.00 [†]	3.00 [†]
Specific Heat (x10 ³ J kg ⁻¹ K ⁻¹) [‡]	c_p	1.25	1.25	1.25

* Values measured from topographic profiles.

** Value from [28].

‡ Values from [7].

[‡] Density of Venus's atmosphere at the surface. Value from [29].

[†] Density of water. Value from [7].

*Values from [13].

Value from [30].

These parameters and Equation [1] can be used to estimate the excess temperature (T) due to a mantle plume:

$$T = (W(\rho_m - \rho_s)) / (\pi r_s A \rho_m \alpha) \quad [1]$$

where W is the cross-sectional area, ρ_m is mantle density, ρ_s is surface density, which is considered to be atmosphere for Venus (67 kg m⁻³) and water for Earth (1030 kg m⁻³) and α is the coefficient of thermal expansion [8, 9].

The excess mass produced due to the presence of the plume can be represented by the buoyancy flux (B) delivered to the rise by the plume:

$$B = [(\rho_m - \rho_s) W u] \quad [2]$$

where W is the cross-sectional area and u is the velocity of the hot-spot relative to the lithosphere. This equation follows from Sleep [9] and the terminology in this equation is not standardised. Venus has a stationary lithosphere, therefore the closest Earth-based hot-spot analogue would be for a slow-moving plate [14]. The v values used for Venus are the lower limit plate velocity values of the slow-moving Cape Verde hot-spot (12 mm yr⁻¹) [27]. Hot-spot velocities relative to the lithosphere for the Hawaiian swell range from ~83 mm yr⁻¹ to 96 mm yr⁻¹ [4, 9, 31, 32]. A value of 90 mm yr⁻¹ was used, similar to Turcotte & Schubert [12], since this value is closer to the average plate velocity for the values from [4, 9, 31, 32].

The heat flux (Q_H) of the mantle plume could then be found using:

$$Q_H = (c_p B) / \alpha \quad [3]$$

The properties of volcanoes, which were calculated from topographic profiles over Atla Regio and the Hawaiian and Cape Verde swells, included basal diameter, height, average slope, root mean square (RMS) slope and volume. Topographic profiles across the edifice of the volcano were observed and the basal extents defined where the edifice joined the surrounding volcanic flanks. The heights, volumes, average slope and RMS slope of the volcano were then measured above the edifice base.

Modelling of the lithospheric structure below Atla Regio was completed using the finite-difference code GEO3Dmod [21]. GEO3Dmod is an interactive 3D forward modelling software, which calculates the thermal, pressure and density structure for a given model, as well as elevation, free-air gravity, bouguer gravity, geoid and heat flow [21]. By fitting these

calculated values to observables, the models are more tightly constrained than by singularly fitting each observable [21, 22, 33]. GEO3Dmod assumes a conductive thermal lithosphere, comprising the crust and the conductive portion of the upper mantle [21, 22, 33]. See [21, 22, 33] for more details.

Lithospheric flexure calculations were also used to determine the thermal gradient and in turn heat flow through an area. The half-width of the depression (x) was located beneath the load and the distance (d) to the forebulge (x_b) calculated (Figure 3).

This distance (d) was then used to determine the flexural parameter (F) using:

$$F = d / \pi \quad [4]$$

Using the flexural parameter (F), the flexural rigidity (D) of the plate was found:

$$D = F^4 (\rho_m - \rho_s) g \quad [5]$$

where g is the acceleration due to gravity (9.81 m s^{-2} for Earth and 8.87 m s^{-2} for Venus).

The flexural rigidity was then used to estimate the elastic lithospheric thickness (T_e) from:

$$T_e = [D \times 12 (1 - \nu^2) / E]^{1/3} \quad [6]$$

where ν is Poisson's ratio (0.25) and E is Young's modulus (70 GPa), similar to the values used by [12].

By using a reference lithosphere and moment-curvature relationships, Phillips *et al.* [14]

determined a suitable equation to determine a linear thermal gradient (dT/dZ) for elastic lithosphere thicknesses below certain Venusian features:

$$dT/dZ = 9.54 (T_e / 30)^{-0.817} \quad [7]$$

Using this temperature gradient (dT/dZ) and the thermal conductivity (k) at the base of the lithosphere, the total heat flux (q) of the area was determined by using the equation:

$$q = k \cdot dT/dZ \quad [8]$$

Estimates of the thermal conductivities at the base of the lithosphere were $\sim 3.3 \text{ W m}^{-1} \text{ K}^{-1}$ [30] for Venus and $2.55 \text{ W m}^{-1} \text{ K}^{-1}$ for Hawaii [34, 35]. It should also be noted that the total heat flux calculated by Equation [8] includes both a heat flux from a possible upwelling mantle plume and the background heat flux associated with mantle convection [14].

3. Results

From Equation [1] the excess temperature associated with a mantle plume below Atla Regio was found to range from 85-769°C for stagnation distances between 200-600 km. Venus has been proposed to have a stationary lithosphere (plate velocity = 0 mm yr⁻¹). However, due to the dependency of buoyancy flux and heat flow equations on a plate velocity, a hot-spot located on a slow-moving plate was considered to be the closest Earth-based analogue [9, 14].

By using a lower-limit velocity (12 mm yr⁻¹) of the Cape Verde hot-spot, relative to the lithosphere [31], and Equation [2-3], a buoyancy flux of 3.79 Mg s⁻¹ and a mantle plume heat flux of $1.53 \times 10^{11} \text{ W}$ at Atla Regio was obtained. Therefore, the the range of excess heat associated with a mantle plume on Venus would be less than $1.53 \times 10^{11} \text{ W}$.

The excess temperature associated with Oahu, a fast-moving hot-spot, was found to range from 193-249°C for stagnation distances between 350-450 km. Based on a plate velocity of 90 mm yr⁻¹ [11], a buoyancy flux of 7.79 Mg s⁻¹ and a mantle plume heat flow of 3.25x10¹¹ W was found for Oahu. The excess temperature of Cape Verde, a slow-moving hot-spot, was found to be 206 K for a stagnation distance of 390 km. Using a plate velocity of 12 mm yr⁻¹, a buoyancy flux of 0.96 Mg s⁻¹ and a heat flow of 4.0x10¹⁰ W was found.

Results for calculating the basal diameter, height, average slope and RMS slope for the three volcanoes within Atla Regio and comparing these to Hawaii and Pico de Fogo (within the Cape Verde Archipelago), can be observed in Table 2. The volcanoes located at Atla Regio have larger basal diameters (405-630 km), and except for Sapas Mons, larger volumes (30.5-42.3x10⁴ km³), than the Island of Hawaii and Pico de Fogo, which have basal diameters of 200 km and 63 km and volumes of 12.5x10⁴ km³ and 1.46x10⁴ km³, respectively.

All the volcanoes located within Atla Regio also have smaller heights (2.34, 3.85 km, 6.8km for Sapas, Ozza and Maat Mons, respectively) when compared to Hawaii (8.48 km). However, only Ozza Mons and Sapas Mons have smaller heights when comparing to Pico de Fogo (6.28 km). The RMS slope of each volcano was also calculated, however, since long slope-frequency distributions will bias the RMS slope to greater values, an average of the slopes measured for each volcanic edifice were also calculated [36, 37]. Shallower RMS slopes and average slopes were obtained for the volcanoes within Atla Regio (0.646°-2.19° and 0.537°-1.66°), compared to Hawaii (5.60° and 5.01°), and Pico de Fogo (13.55° and 12.06°). Since Pico de Fogo is a stratovolcano it has steeper slopes compared to the volcanoes within Hawaii and Atla Regio, which are shield volcanoes [17, 18, 38].

Table 2. Volcano characteristics

Volcano	Basal Diameter (km)	Height (km)	RMS Slope (degrees)	Average Slope (degrees)	Volume ($\times 10^4 \text{ km}^3$)
Sapas Mons	630	2.34	0.646	0.537	10.9
Maat Mons	405	6.8	2.19	1.66	30.5
Ozza Mons	495	3.85	0.719	0.764	42.3
Hawaii	200	8.48	5.60	5.01	12.5
Pico de Fogo	63	6.28	13.55	12.06	1.46

A possible lithospheric model below Sapas Mons is shown in Figure 4. The topographically high Sapas Mons volcano between 1000-2300 km, corresponds to a Bouguer low, reflecting the depression of the crust-mantle boundary by lithospheric flexure or a possible lower-density partial melting/magma chamber. This compares to the topographically low plains region surrounding Sapas Mons (0-1000 km) which has a thinner crust (~ 20 km). A thinner (~ 70 km) thermal lithosphere (the crust and upper mantle layers) and higher surface heat flow ($\sim 38 \text{ mW m}^{-2}$), occurs below Sapas Mons and Atla Regio, which could be associated with the presence of a mantle plume.

Flexural modelling at Atla Regio and Oahu can be observed in Figures 3 & 5. The distance between the half-width of the depression (x) and the maximum amplitude of the forebulge (x_b) were found to be 324 km, 310 km and 212 km for Atla Regio, Oahu and Cape Verde, respectively.

Using Equations [4] and [5] a flexural parameter of 103 km, 98.7 km and 67.5 km and a flexural rigidity of $8.19 \times 10^{23} \text{ N m}$, $5.34 \times 10^{23} \text{ N m}$ and $1.17 \times 10^{23} \text{ N m}$ were found for Atla Regio, Oahu, and Cape Verde, respectively. Substituting these flexural rigidity estimates into Equation [6], an elastic lithosphere thickness of 50.9 km, 44.1 km and 26.6 km were found for Atla Regio, Oahu and Cape Verde, respectively. The thermal gradient for Atla Regio was

calculated from Equation [7] and found to be 6.19 K km^{-1} . Using this thermal gradient with Equation [8] a total heat flux of 20.4 mW m^{-2} for basal lithospheric thermal conductivities of $3.3 \text{ W m}^{-1} \text{ K}^{-1}$ was found.

Since Equation [7] is specific of Venus, the thermal gradient at Oahu was found from a simple oceanic geotherm [12] and yielded a geothermal gradient of 23 K km^{-1} and 20 K km^{-1} for Oahu and Cape Verde, respectively. This gradient and a thermal conductivity of $2.55 \text{ W m}^{-1} \text{ K}^{-1}$ was used to determine a total heat flux of 59 mW m^{-2} and 51 mW m^{-2} for Oahu and Cape Verde, respectively.

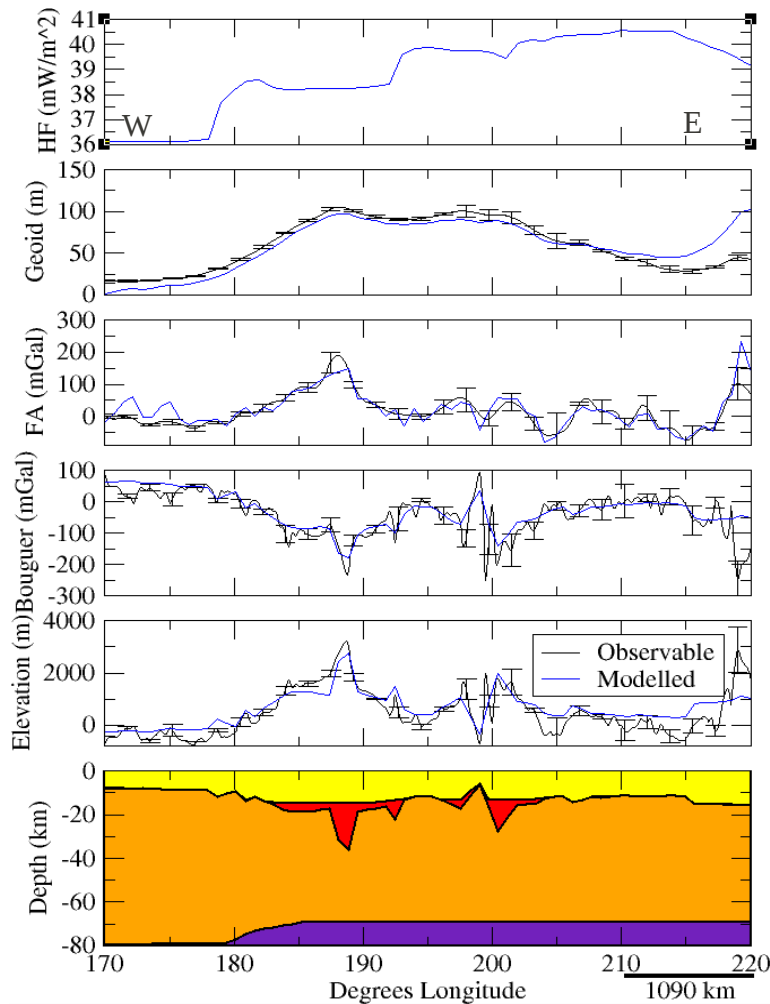


Figure 4. Profile across Sapas Mons at 8° latitude, showing the crust (yellow and red) and conductive upper mantle (orange) that comprise the thermal lithosphere. The adiabatic sub-lithosphere is shown in purple. Note: The plot of heat flow has no observable. Scale bar: 10° Longitude = 1090km.

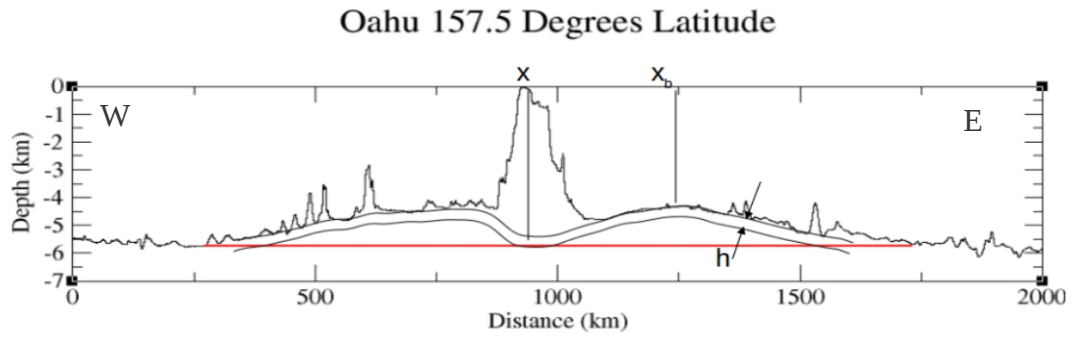


Figure 5. North-South topographic profile across Oahu, Hawaii. The red line is the constant-depth line, facing arrows infer an elastic lithosphere of thickness (h).

4. Discussion/Conclusion

The excess temperature due to a mantle plume on Venus was found to range from 85-769°C for unconstrained stagnation distances between 200-600 km, compared to the excess temperature of 193°-249°C and 206 K for more constrained stagnation distances of 350-450 km and 390 km for the Hawaiian and Cape Verde swells, respectively. One reason for a large range of excess temperatures at Atla Regio compared to Oahu and Cape Verde is that this area has a larger cross-sectional area $\sim 3056 \text{ km}^2$ compared to Oahu (1188 km^2) and Cape Verde (1097 km^2).

Due to Venus's lack of water, a higher density contrast between mantle and air also produced higher excess temperatures compared to the smaller density contrast arising from mantle and water on Earth. The equation for excess temperature also relies on a stagnation distance, which is calculated from the radial velocity of the plume, the average unperturbed asthenospheric velocity and the half plate velocity at the hot-spot (Equation 8 in [9]). The stagnation distances for the Hawaiian and Cape Verde swells are also better constrained, than those for Atla Regio, since Venus has a stationary lithosphere, with zero plate velocities. The

closest approximation of stagnation distances on Venus may be the diameter of coronae, due to their possible mantle plume origin (200-600 km) [13]. The existence of an asthenospheric channel that extends throughout the entire mantle is questionable on Venus [10], however our calculations of excess temperature assumed an asthenospheric channel thickness. This thickness was more tightly constrained for Hawaii ($\sim 100 \pm 16$ km), compared to Atla Regio ($\sim 200 \pm 100$ km) [8, 12].

The buoyancy flux and heat flow values obtained also rely on the velocity of the hot-spot relative to the lithosphere [8, 9]. For Oahu the hot-spot velocity ranged from 83 mm yr⁻¹ to 96 mm yr⁻¹ [4, 9, 31, 32], with ~ 90 mm yr⁻¹ being chosen in this study, similar to the value used by [12]. This yielded a mantle plume heat flux of 3.25×10^{11} W at Oahu, slightly higher than the mantle plume heat flux of 3×10^{11} W obtained by [12] at a similar location.

Buoyancy flux and heat flow estimates for a mantle plume at Atla Regio, however, have a greater uncertainty than values obtained for Hawaii, since Venus has a stationary lithosphere [1]. The closest Earth-based hot-spot analogue to Venus are those located on slow-moving plates [14]. By taking the lowest estimate of the plate velocity of the Cape Verde hot-spot (12 mm yr⁻¹ [27]), and taking the heat flux obtained as an upper bound, heat flux from a mantle plume through Atla Regio should range from 0 W to 1.53×10^{11} W. This compares to the heat flux of 4.0×10^{10} W found for Cape Verde. Even though the same plate velocities were used for Atla Regio and Cape Verde, the differences in cross-sectional area and surface density contrasts caused the variation in heat flow estimates for each of these areas. Despite the high uncertainties and large range of estimated values for excess temperature, buoyancy flux and heat flow, this study has showed that dynamic support from a mantle plume may be contributing to the topography at Atla Regio.

The volcanoes at Atla Regio have larger basal diameters and volumes (except Sapas Mons), but lower elevations (except Maat Mons) than Hawaii and Pico de Fogo. This is consistent with the general trend that volcanoes on Venus have larger basal diameters and volumes than shield volcanoes on Earth [1, 18]. This difference can be attributed to Venus's lack of plates and the associated velocities over hot-spots [1]. On Venus, volcanoes would remain over the hot-spot for longer time intervals compared to Earth's volcanoes, where a plate would move away from the hot-spot over time [1]. Volcanoes within Atla Regio also tend to have shallower slopes than Hawaii and Pico de Fogo, which could be due to: 1) higher temperatures within the crust and surface; 2) lower-viscosity lavas; 3) larger volumes of magma erupted at higher effusion rates; 4) propagation of lavas by lava tubes and; 5) higher surface pressures [18, 19, 20].

The thin thermal lithosphere, high heat flow and presence of a low-density root below Sapas Mons could reflect current volcanism associated with an upwelling mantle plume. The excess heat associated with a mantle plume would act to thin the thermal lithosphere, producing a geoid high, and causing partial melting below this area. The associated bouguer low could represent either this partial melt or a possible low-density magma chamber.

The elastic lithosphere thickness of 50.9 km, obtained at Atla Regio from flexural modelling, is close to the upper limit of the range (40-50 km) of elastic lithosphere thicknesses from Phillips [15], who used spectral analysis and Monte Carlo inversions. The elastic lithosphere thickness obtained at Oahu (44.1 km) is higher than that obtained by Turcotte & Schubert [12] over the Hawaiian Archipelago (34 km). The elastic lithosphere thickness at the Cape Verde Archipelago was found to be 26.6 km, within the range found by [6] from spectral admittance studies, but lower than the 29 km found from best-fit surface/subsurface loading models. These differences in estimates of elastic lithosphere thicknesses may be caused from the

difficulties associated with determining the maximum amplitude of the forebulge due to interference from the surrounding topography that acts to obscure the flexural upwarp, similar to what is observed on the left-side of the profile in Figure 4.

The thermal gradient of 6.19 K km^{-1} for Atla Regio, obtained indirectly from flexural modelling, was also within the range of thermal gradients [$7\text{-}10 \text{ K km}^{-1}$] outlined by Phillips [15]. Phillips [15] suggested Atla Regio should have a total heat flux less than what is obtained from Earth-scaling ($\sim 80 \text{ mW m}^{-2}$). From flexural modelling a total heat flux of $18.6\text{-}24.8 \text{ mW m}^{-2}$ was found for Atla Regio, which is significantly lower than that obtained by Earth scaling. The total heat flux value obtained from flexural modelling at Oahu is slightly higher (58.7 mW m^{-2}) than those obtained from total heat flux measurements taken at Hawaii ($52.9 \pm 2.5 \text{ mW m}^{-2}$ [26]), whilst the obtained heat flux value for Cape Verde is slightly less (51 mW m^{-2}) than measured values ($61 \pm 7.4 \text{ mW m}^{-2}$ [27]). Differences in the heat flow estimates obtained from flexural modelling to measured values are most likely caused from comparing these areas to a globally averaged oceanic geotherm.

The results of this study suggests that volcanic topography at Atla Regio could be produced by three processes, thermal, volcanic and flexural. The impingement of a mantle plume on the lithosphere could have initiated rifting and volcanism, resulting in volcanic loading and flexure of the lithosphere. These processes act in a similar way to those observed on Earth, but yield different results due to Venus's unique surface conditions. Future work aims to constrain the stagnation distances through finite-element modelling and to produce a plausible rheological structure below Atla Regio, which will be used to constrain these processes further.

5. Acknowledgments

The authors would like to thank the Space Policy Unit, Engineers Australia, and ASRI for providing sponsorship to attend the 10th Australian Space Science Conference in Brisbane. The authors would like to thank Dr Marc Norman and Dr Jon Clarke for their time and suggestions for improvements to this paper. Software used in this study is available at the following sites , SHTOOLS: <http://www.ipgp.fr/~wieczor/SHTOOLS/SHTOOLS.html> , GMT: <http://gmt.soest.hawaii.edu/>, Grace: <http://plasma-gate.weizmann.ac.il/Grace/>, LitMod3D: <http://www.es.mq.edu.au/staff/Software1.htm>). This is contribution 694 from the Australian Research Council National Key Centre for the Geochemical Evolution and Metallogeny of Continents (<http://www.gemoc.mq.edu.au>).

6. References

1. Moore, P. “Venus”. Cassel Illustrated, Great Britain, 2002, pp. 191.
2. Senske, D.A. & Head, J.W. “Atla Regio Venus: Geology and origin of a major equatorial volcanic rise. *Proceedings of Lunar and Planetary Science*, No. 789, 1992, pp.107-109.
3. Phillips, R.J., Grimm, R.E., & Malin, M.C. “Hot-spot evolution and the global tectonics of Venus”. *Science*, Vol. 252, No. 5006, 1991, pp. 551-658.
4. Davies, G.F. “Ocean bathymetry and mantle convection: 1. Large-scale flow and hotspots”. *Journal of Geophysical Research*, Vol. 93, No. B9, 1988, pp. 10467-10480.
5. Wilson, J.T. “A possible origin of the Hawaiian Islands”. *Canadian Journal of Physics*. Vol. 41, 1963, pp. 863-870.
6. Ali, M.Y., Watts, A.B., & Hill, I. “A seismic reflection profile study of lithospheric flexure in the vicinity of the Cape Verde Islands”. *Journal of Geophysical Research*, Vol. 108, No. B5, 2003, pp. 24.
7. Morgan, W.J. “Convection plumes in the lower mantle”. *Nature*, Vol. 230, No. 42,

- 1971, pp. 42-43.
8. Sleep, N.H. "Hotspots and mantle plumes: some phenomenology". *Journal of Geophysical Research*, Vol. 95, No. B5, 1990, pp. 6715-6736.
 9. Sleep, N.H. "Hotspot volcanism and mantle plumes". *Annual Review of Earth and Planetary Sciences*, Vol. 20, 1992, pp. 19-43.
 10. Jellinek, M.A., Lenardic, A. and Manga, M. "The influence of interior mantle temperature on the structure of plumes: Heads for Venus, Tails for Earth". *Geophysical Research Letters*, Vol. 29, 2002, pp. 4.
 11. Schubert, B., Bercovici, D, Glatzmaier, G.A. "Mantle dynamics in Mars and Venus: Influence in an immobile lithosphere on three-dimensional mantle convection". *Journal of Geophysical Research*, Vol. 95, No. B9, 1990, pp. 14105-14129.
 12. Turcotte, D.L. & Schubert, G. "*Geodynamics*" 2nd Ed, Cambridge University Press, 2002, pp. 458.
 13. Head, J.W., Crumpler, L.S., Aubele, J.C., Guest, J.E., Saunders, R.S. "Venus volcanism: Classification of volcanic features and structures, associations and global distribution from Magellan data". *Journal of Geophysical Research*, Vol. 97, No. E8, 1992, pp. 13153-13197.
 14. Phillips, R.J., Johnson, C.L., Mackwell, S.J., Morgan, P., Sandwell, D.T., & Zuber, M.T. "Lithospheric mechanics and dynamics of Venus". In *Venus II: Geology, Geophysics, Atmosphere and solar wind environment*, Bougher, S.W., Hunten, D.M. & Phillips, R.J. (eds.), 1997, The University of Arizona Press, pp. 1362.
 15. Phillips, R.J. "Estimating lithospheric properties at Atla Regio, Venus". *Icarus*, Vol. 112, 1994, pp. 147-170.
 16. Smrekar, S., & Parmentier, E.M. "The interaction of mantle plumes with surface thermal and chemical boundary layers: applications to hotspots on Venus". *Journal of Geophysical Research*, Vol. 101, 1996, pp. 5397-5410.

17. Skinner, B., Porter, S.C. & Park, J. “*Dynamic Earth: An introduction to physical geology*” 5th Ed, Wiley, 2004, United States of America.
18. Schaber, G.G. “Volcanism on Venus as inferred from the morphometry of large shields”. *Proceedings of Lunar and Planetary Science*, Vol. 21, 1991, pp. 3-11.
19. Head, J.W. & Wilson, L. “Volcanic processes and landforms on Venus: Theory, prediction and observations”. *Journal of Geophysical Research*, Vol. 91, 1986, pp. 9407-9446.
20. Wood, C.A. “Venusian volcanism: Environmental effects on style and landforms”. In *Reports of the Planetary Geology and Geophysics Programs-1979*, 1979, pp. 244-246.
21. Fullea, J., Afonso, J.C., Connolly, J.A.D., Fernandez, M., Garcia-Castellanos, D., & Zeyen, H. “LitMod3D: An interactive 3D software to model the thermal, compositional, density, seismological, and rheological structure of the lithosphere and sublithospheric upper mantle”. *Geochemistry, Geophysics, Geosystems*, Vol. 10, No. 8, 2009, pp. 1-21.
22. Afonso, J.C., Fernandez, M., Ranalli, G., Griffin, W.L., & Connolly, J.A.D. “Integrated geophysical-petrological modeling of the lithosphere and sublithospheric upper mantle: Methodology and applications”. *Geochemistry, Geophysics, Geosystems*, Vol. 9, No. 5, 2008, pp. 1-36.
23. Barnett, D.N., Nimmo, F., & McKenzie, D. “Flexure of Venusian lithosphere measured from residual topography and gravity”. *Journal of Geophysical Research*, Vol. 107, 2002, pp. 1-21.
24. Smrekar, S.E. “Evidence for active hotspots on Venus from analysis of Magellan gravity data”. *Icarus*, Vol. 112, 1994, pp. 2-26.
25. Ebinger, C.J., Bechtel, T.D., Forsyth, D.W., and Bowin, C.O. “Effective elastic plate thickness beneath the East African and Afar Plateaus and dynamic compensation of the

- uplifts". *Journal of Geophysical Research*, Vol. 94, 1989, pp. 2883-2901.
26. Von Herzen, R.P., Detrick, R.S., Crough, S.T., Epp, D. & Fehn, U. "Thermal origin of the Hawaiian Swell: Heat flow evidence and thermal models". *Journal of Geophysical Research*, Vol. 87, 1982, pp. 6711-6723.
27. Courtney, R.C. & White, R.S. "Anomalous heat flow and geoid across the Cape Verde Rise: Evidence for dynamic support from a thermal plume in the mantle". *Geophysical Journal Royal Astronomical Society*, Vol. 87, 1986, pp. 815-868.
28. Head, J.W. & Wilson, L. "Magma reservoirs and neutral buoyancy zones on Venus: Implications for the formation and evolution of volcanic landforms". *Journal of Geophysical Research*, Vol. 97, 1992, pp. 3877-3903.
29. Seiff, A. "Thermal structure of the atmosphere of Venus". In *Venus*, Hunten, D.M., Colin, L., Donahue, T.M., & Moroz, V.I. (eds.), 1983, The University of Arizona Press, pp. 215-279.
30. Johnson, C. & Sandwell, D.T. "Lithospheric flexure on Venus". *Geophysical Journal International*, Vol. 119, 1994, pp. 627-647.
31. Gordon, R.G. & Jurdy, D.M. "Cenozoic global plate motions". *Journal of Geophysical Research*, Vol. 91, 1986, pp. 12389-12406.
32. Duncan, R.A. & Clague, D.A. "Pacific plate motion recorded by linear volcanic chains". In *The ocean and basins and margins. Vol. 7A. The Pacific Ocean* (Naim, A.E.M., Stehi, F.G., Uyeda, S. eds.) 1985, New York, pp. 89-121.
33. Fulla, J., "Development of numerical methods to determine the lithospheric structure combining geopotential, lithostatic, and heat transport equations. Applications to the Gibraltar Arc System". PhD thesis, University of Barcelona, Spain, 2008, pp. 240.
34. Horai, K. "Thermal conductivity of Hawaiian basalt: A new interpretation of Robertson and Peck's data". *Journal of Geophysical Research*, Vol. 96, No. B3, 1991, pp. 4125-4132.

35. Robertson, E.C. & Peck, D.L. "Thermal conductivities of vesicular basalt from Hawaii". *Journal of Geophysical Research*, Vol. 79, No. 32, pp. 4875-4888.
36. Shepard, M.K., Campbell, B.A., Bulmer, M.H., Farr, T.G., Gaddis, L.R., & Plaut, J.J. "The roughness of natural terrain: A planetary and remote sensing perspective". *Journal of Geophysical Research*. Vol. 106, No. E12, 2001, pp. 32777-32795.
37. Kreslavsky, M.A. & Head III, J.W. "Kilometer-scale slopes on Mars and their correlation with geologic units: Initial results from Mars Orbiter Laser Altimeter (MOLA) data". *Journal of Geophysical Research*, Vol. 104, 1999, pp. 21911-21924.
38. Day, S.J., Heleno, de Silva, S.I.N., Fonseca, J.F.B.D. "A past giant lateral collapse and present-day flank instability of Fogo, Cape Verde Islands". *Journal of Volcanology and Geothermal Research*, Vol. 94, 1999, pp. 191-218.

A3. Constraining Weathering Processes on Venus from Particle Size Distributions and Magellan Synthetic Aperture Radar (SAR)

Elyse Schinella¹ and Craig O'Neill¹

Department of Earth and Planetary Science, Australian Research Council Centre of Excellence for Core to Crust Fluid Systems/GEMOC, Macquarie University, Sydney, NSW, 2109

Summary: Due to Venus's unique surface conditions the processes controlling the distribution of impact crater ejecta and sediment transport occurring on this planet are different to those on Earth. Venus's dense atmosphere acts to remove or reduce small meteors during atmospheric entry, resulting in a lack of small impact craters on the surface. Ejecta dispersal from large impacts, where the meteor was able to survive the transit through the dense atmosphere of Venus, are unconstrained. Sediment transport and the influence of the dense and sluggish atmosphere on the surface are also poorly known. Our study aims to investigate the processes responsible for the distribution and deposition of ejecta at large parabolic impact craters on Venus. From this we aim to constrain the near surface-atmospheric processes responsible for sediment transport on Venus. Large parabolic impact craters were chosen since their westward orientated ejecta blankets could suggest deposition by Venus's east-west orientated zonal winds, allowing us to investigate the atmospheric effects on crater ejecta dispersal. We used Synthetic Aperture Radar (SAR), obtained from the Magellan mission to Venus, to study the Fresnel reflectivity, emissivity, and Root-Mean Square (RMS) slope of ejecta blankets at selected sites on Venus. The particle size distribution associated with the ejecta of parabolic impact craters were dependent on the particle size interpolated to the rim of the crater, crater

radius, distance from the center of the crater, and an empirical power law coefficient. By combining RMS slope with particle size distributions we can constrain the surface-atmosphere processes acting to produce small-scale roughness and topography variations, and weathering processes on Venus.

Keywords: meteor, parabolic impact craters, Venusian atmospheric circulation, sediment transport.

1. Introduction

Venus's dense atmosphere of up to 90 bars acts to destroy or reduce small meteors less than 100 m in diameter [1]. Those meteors that are able to survive atmospheric entry can create one of the many different types of impact craters observed on the surface, including parabolic impact craters [Figure 1] [2]. Parabolic impact craters usually have their apex in the east with westward opening arms [2]. The associated crater is usually located slightly to the west of the parabolas' apex [2]. Approximately 66 of the craters on Venus exhibit some or all of these characteristic features [2]. More parabolic craters may have existed at older impact sites, however, the resulting parabolic deposits may have been redistributed by aeolian processes, which is reinforced by the presence of wind streaks at some of these deposits [2].

Campbell *et al.* [2] outlined one possible model for the formation of these features. In this model these craters were formed when an impactor was large enough to strike the surface and cause the resulting fine grained ejecta plume to have enough velocity to rise into Venus's upper atmosphere (~50-70 km altitude). Once in the upper atmosphere these particles were influenced by Venus's east-west zonal winds [2-5]. The large and dense particles, which travelled at low velocities, would not have reached the upper atmosphere, instead falling close

to the rim of the crater [2, 4]. However, the fine and light grained ejecta, which travelled at a higher velocity, would have been entrained within the ascending and expanding ejecta plume. Once in Venus's upper atmosphere the zonal winds then dispersed the falling ejecta particles into a parabolic shape over hundreds of kilometers [2, 4]. These particles then rained out of the ejecta plume and caused a parabolic ejecta blanket to be deposited on the surface [2]. However, Schultz [6] suggested that the parabolic ejecta blankets and small impact craters were most likely caused from the impactor angle and direction [2].

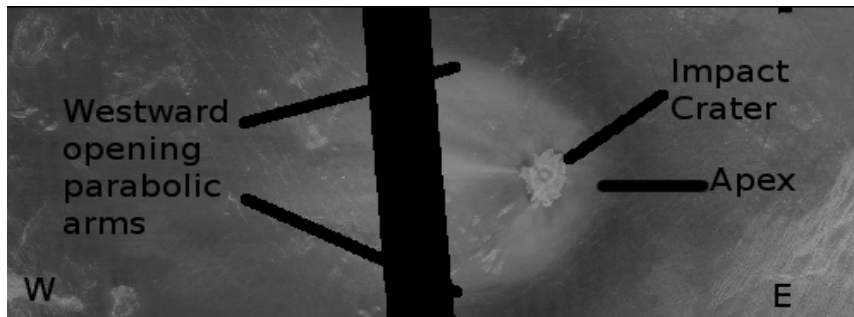


Figure 1 (Modified from [7]) Adivar, a parabolic impact crater centered at 8.92°N 76.19°E [Table 1]. The apex of the parabola is in the east with the associated impact crater slightly to the west. The arms of the parabola open towards the west.

Vervack and Melosh [4] determined a model of particle size distributions on Venus. They used an empirical power law and a reference size relationship, calculated from comparisons of predicted model parabolas and parabolas observed on the surface of Venus. Using these parameters they were able to determine the particle size distribution that was directly related to the radius of the parent crater and the distance from the crater centre [1, 5, 8]. Vervack and Melosh [4] also used the crater radius and distance from the crater in a relationship first proposed by McGetchin *et al.* [9], to determine the thickness of the ejecta blanket surrounding a crater. Applying this formula and a Gaussian distribution to the parabolic Carson crater [Table 1], the thickness of the ejecta blanket was estimated to be 0.1 m, 400 km away from the crater centre. Closer to the crater, the ejecta thickness increased to 0.3 m at 200 km and 0.5 m

at 150 km, respectively [4].

Most parent impact craters of the parabolic ejecta appear bright in Magellan Synthetic Aperture Radar. Most of these features do not appear to be cross-cut by any geological landforms, suggesting they are among the youngest features on the Venusian surface [2]. The parabolic features surrounding the parent impact crater mostly appear radar-dark, with only one crater, Cohn [Table 1], having these features appear radar-bright. Some craters can also have a combination of radar-bright and radar-dark features [2].

Table 1. Crater Parameters

Crater Name	Longitude °E ^a	Latitude °N ^a	Crater radius ^b (km)	dc (m) ^c	Parabola Type ^a	Parabola Length ^a (km)	Parabola Width ^a (km)
Adivar	76.19	8.92	15	21.95	adivar ^d	1020	860
Carson	-15.88	-24.17	19.5	14.56	dark	980	950
Cohn	-151.89	-33.24	11.5	33.22	bright	770	830
Adiah	-106.69	-47.26	8.75	50.88	inner bright, outer dark	830	822
Aurelia	-28.2	20.3	15.5	20.85	dark	640	750
Greenaway	145.12	22.92	46.15	3.8	dark	1750	1990
Montessori	-80.08	59.43	21.45	12.56	dark	1150	1300
Stuart	20.23	-30.77	33.3	6.33	dark	1220	1660
Von Schoorman	-169.99	-5.03	14.45	23.26	inner bright, outer dark	720	710

^a Values from Campbell *et al.* [2].

^b Values from Herrick *et al.* [10].

^c Calculated from Eq. [1].

^d Radar bright deposit surrounded by a radar dark deposit.

This could suggest that larger particle sizes occur close to the crater compared to the smaller particles within the parabolic deposits [2]. Based on this, RMS slope, a measure of roughness, should be greater at the impact crater due to the presence of larger particles. This compares to lower RMS slopes and smaller particles within the ejecta blanket. It could also suggest that

different erosional processes have occurred at the crater compared to the parabolic ejecta [2].

In addition to RMS slope, reflectivity and emissivity, which have non-dimensional (n.d) units, can also be useful in ejecta studies. Campbell *et al.* [2] noticed that for most areas, emissivity decreased from 0.85 to 0.80 n.d, whilst reflectivity increased from 0.10 to 0.15 n.d. RMS slope also appeared lower within the parabolic impact crater compared to the adjacent plains. Vervack and Melosh [4] suggested that the background surface roughness of the parabolic ejecta was obscured by matter that acted to decrease the radar and emissivity of these features. Campbell *et al.* [2] used surface roughness at radar dark parabolic deposits to infer an upper limit of 1 - 2 cm on particle size and ejecta depths of 7 cm – 2 m. These authors [2] also suggested that the volume and ejection height governed the dispersal of the large and coarse particles at the apex of the parabola and not Venus's zonal winds [2].

Moving outwards from a crater centre to the surrounding ejecta, RMS slope tended to decrease since larger particles occurred at the rim and smaller particles occurred in the ejecta [2]. Emissivity also decreased since the radar-bright crater rims had high emissivities compared to the dull surrounding ejecta [2]. Reflectivity, however, increased from a roughness perspective as the rough crater rims had a lower albedo compared to the smooth ejecta areas [2].

Our study aimed to develop and test an equation, which could relate RMS slope to particle size at selected large parabolic impact craters on Venus. This equation could be useful to constrain surface-atmospheric processes and their contribution to the production of small-scale roughness and topography variations, at selected sites on Venus.

2. Methodology

Left-look and full resolution images from Magellan's 12.6 cm wavelength SAR for each selected crater were downloaded and processed from the Map-A-Planet website [7]. Fresnel reflectivity, RMS slope, and emissivity were downloaded as Environmental Systems Research Institute (ESRI) grids [11]. This data was then processed using Generic Mapping Tools (GMT) [12] to obtain maps of RMS slope, which is a measure of surface roughness [13]. Large RMS slopes suggest rough and hummocky surfaces, composed of large particles, compared to low RMS slopes that suggest smooth surfaces, composed of small particles [13]. Reflectivity, or the albedo of the surface, is weakly reliant on particle size, but is strongly influenced by the type of dielectric permittivity and physical-electrical properties of the surface material, as well as the incidence angle [13]. This is also true for emissivity, which is the inverse of reflectivity [13].

Some misrepresentation occurs between the true position and the observed position within the SAR data set. This arises from errors generated when converting the time between echoes to surface distance and is common at high-relief, but small scale structures [13]. These errors are not quantified, but have been observed to influence images through distortion and layover [13]. A proportion of the reflectivity data also contains errors, the cause of which remain unidentified [13].

In order to determine the particle size distribution at the selected craters on Venus [Figure 2] we had to firstly find the reference size relationship, d_c , of each of the craters using Equation [1] from [1] and Table 1:

$$d_c \text{ (m}^{-1}\text{)} = 1500 R_c \text{ (km}^{-1}\text{)}^{-1.56} \quad [1]$$

where R_c was the radius of the crater. Schaller and Melosh [8] found that the scaling coefficient could range from 690-3330 and the power from -1.30 and -1.82.

Using this reference size relationship the particle size distributions for each crater were then found from Equation [2]:

$$d = d_c (R_c / R)^\alpha \quad [2]$$

where R_c was the crater radius, R was the distance from the crater, and α was the power law, assumed to be 2.65 +/- 0.03 from Schaller and Melosh [8].

In order to determine a relationship between particle size and RMS slope we first had to relate RMS slope, $RMSS$, to R , distance from the crater centre, through Eq. [3]:

$$\log (RMSS) = a - m \log (R) \quad [3]$$

where m was the gradient of the line of regression and a was found from Eq. [4]:

$$a = c / m \quad [4]$$

where c was the intercept value of the regression line.

The parameters c and m were found graphically from the regression line taken from graphs of $\log (R)$ vs $\log (RMSS)$ for each crater. One example of this is shown in Figure 3. The values of c and m for each crater are listed in Table 2.

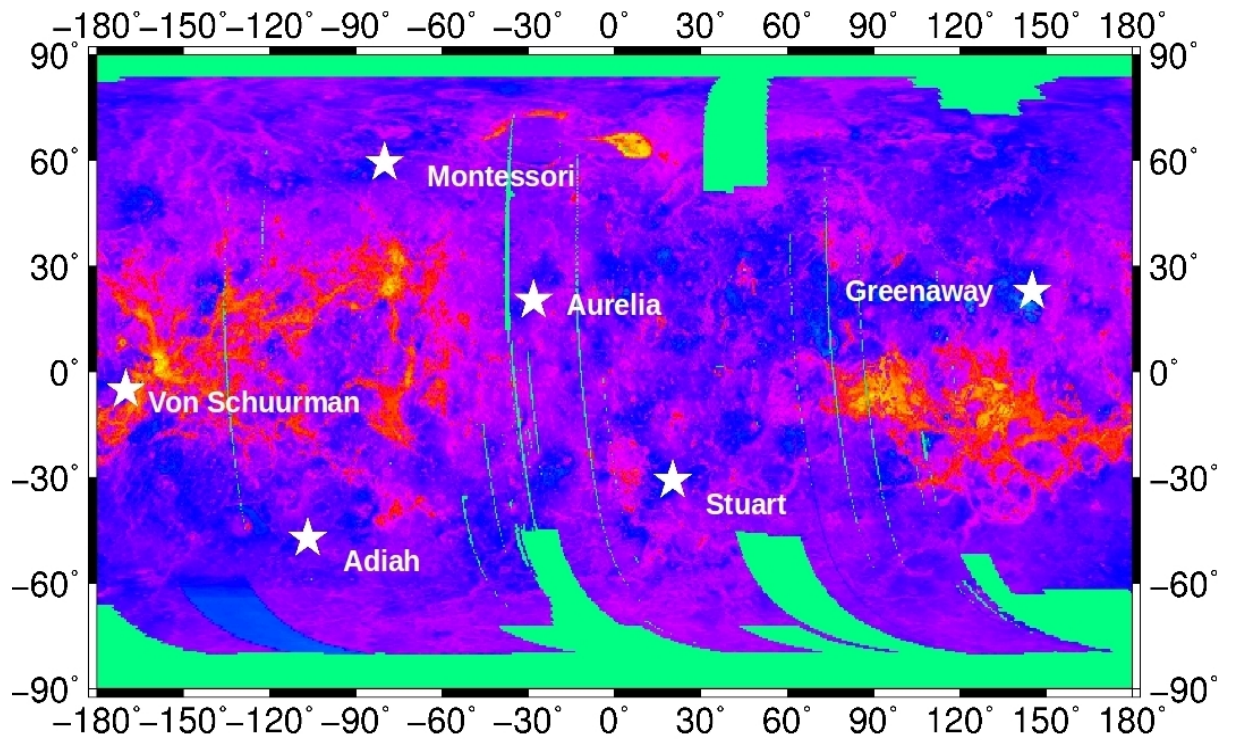


Figure 2. A pixel-registered and non-dimensional Magellan SAR map showing the location of each of the craters addressed in this study. The bright red-yellow areas represent highland regions compared to the blue areas that represent smooth plains regions.

Table 2. Regression intercept and gradient for each crater

Crater Name	c	m	a
Adiah	0.962	0.138	6.930
Aurelia	4.231	0.912	4.636
Greenaway	8.747	1.709	5.117
Montessori	-0.024	0.008	-3.122
Stuart	4.205	0.570	2.398
Von Schuurman	0.346	0.238	1.454

Adiah Log (R) vs Log (RMSS)

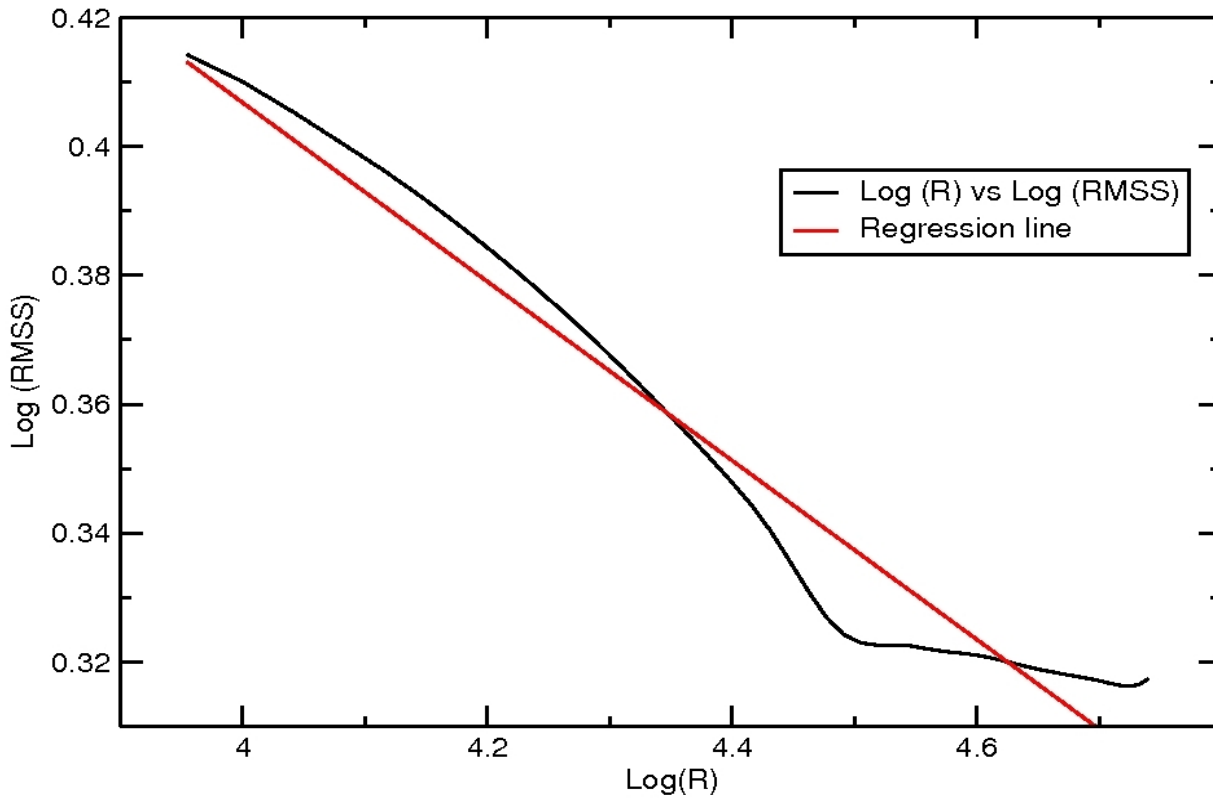


Figure 3. Graph of Log (R) vs Log (RMSS). The red line is the regression line. The gradient, m , was calculated from the regression line and the intercept, c , was calculated from the X-intercept of the regression line.

3. Results

Re-arranging Eq. [3] with respect to R and solving simultaneously with Eq. [2], an equation relating RMS slope to particle size was determined:

$$d = d_c R_c^{\alpha} \text{RMSS}^{\alpha/m} / 10^{\alpha m} \quad [5]$$

The RMS slope, compared to particle sizes from Eq. [2] and Eq. [5], for the Adiah, Aurelia, Greenaway, and Stuart craters, are shown in Figures 4 and 5. On Figures 4 and 5, our particle

sizes from Eq. [5] are shown with error bars that represent the relative error between our calculated particle sizes and those from Eq. 2. These error bars are useful in determining the suitability of our Eq. [5] compared to Eq. [2].

Moving outwards from the crater rim to a point within the ejecta blanket, RMS slope tended to decrease. Where RMS slope followed a smooth exponential decay, our particle sizes tended to correlate to those found from Eq. [2], as seen between 10 - 22 km in Figure 4A. However, if large RMS slope variations occurred over short distances, our estimated particle sizes correlated less to those found from Eq. [2]. For example, the 0.75° decrease in observed RMS slope, between 30 - 44 km, within Figure 4B, reduced our particle size estimates by 3.3 m over the same distance [Table 3]. However, particle sizes from Eq. [2] experienced less of a change between 30 - 44 km, decreasing by 1.7 m in Figure 4B. This was also observed in Figure 5A [Table 3]. Between 84 – 128 km, the RMS slope decreased by 1.9° . This RMS slope decline corresponded to a decrease in our estimated particle sizes by 0.9 m, whilst particle sizes calculated from Eq. [2] decreased by 0.35 m.

When small RMS slope variations occurred over large distances, our estimated particle sizes showed a closer correlation to those found from Eq. [2]. For example, in Figure 4C, between 64 - 94 km, a decrease in RMS slope of 2.22° occurred [Table 3]. This gentle decrease reduced our estimated particle sizes by 1.7 m compared to 0.9 m from Eq. [2]. This also occurred along the profile in Figure 4B, between 55 - 68 km, where RMS slope gently decreased by 0.07° [Table 3]. Our particle sizes followed a similar distribution with a 0.08 m decrease. This compares to particle sizes calculated from Eq. [2], which decreased by 0.13.

Similar to Figure 4B-4C, the profile within Figure 5A also showed a similar response [Table 3]. Between 165 - 195 km, the RMS slope decreased gently by 0.11° . This variation was

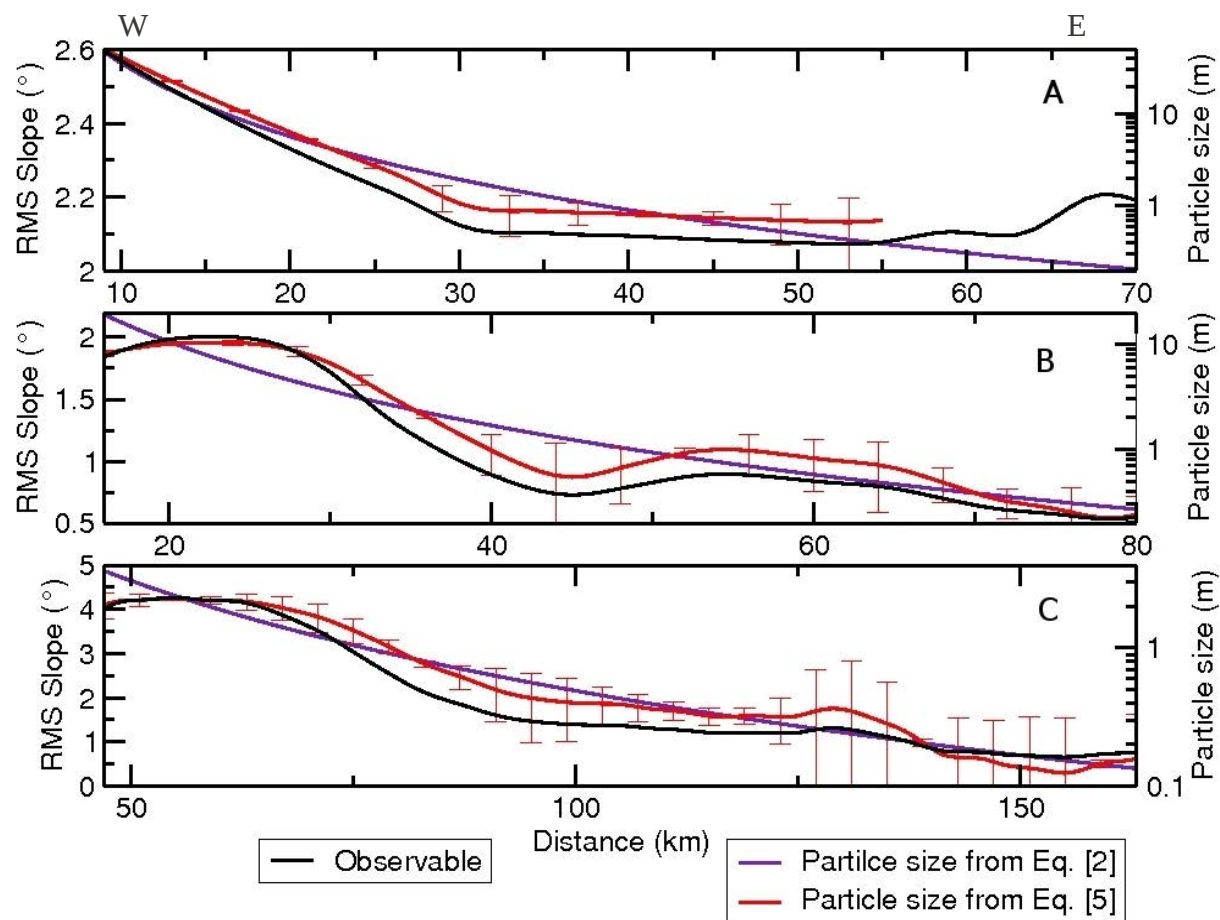


Figure 4. Graphs showing a comparison between the RMS slope (black line), the particle sizes from Equation [2] (purple line), and our particle sizes from Equation [5] (red line) for the Adiah (A), Aurelia (B), and Greenaway (C) craters. Error bars represent the relative error.

Table 3. RMS slope and particle sizes

Figure No.	Location (km)	RMS slope (°)	Particle size from Eq. [5] (m)	Particle size from Eq. [2] (m)
4B	30 - 44	-0.75	-3.3	-1.7
5A	84 - 128	-1.9	-0.9	-0.35
4C	64 - 94	-2.2	-1.7	-0.9
4B	55 - 68	-0.07	-0.08	-0.13
5A	165 - 195	-0.11	-0.03	-0.02

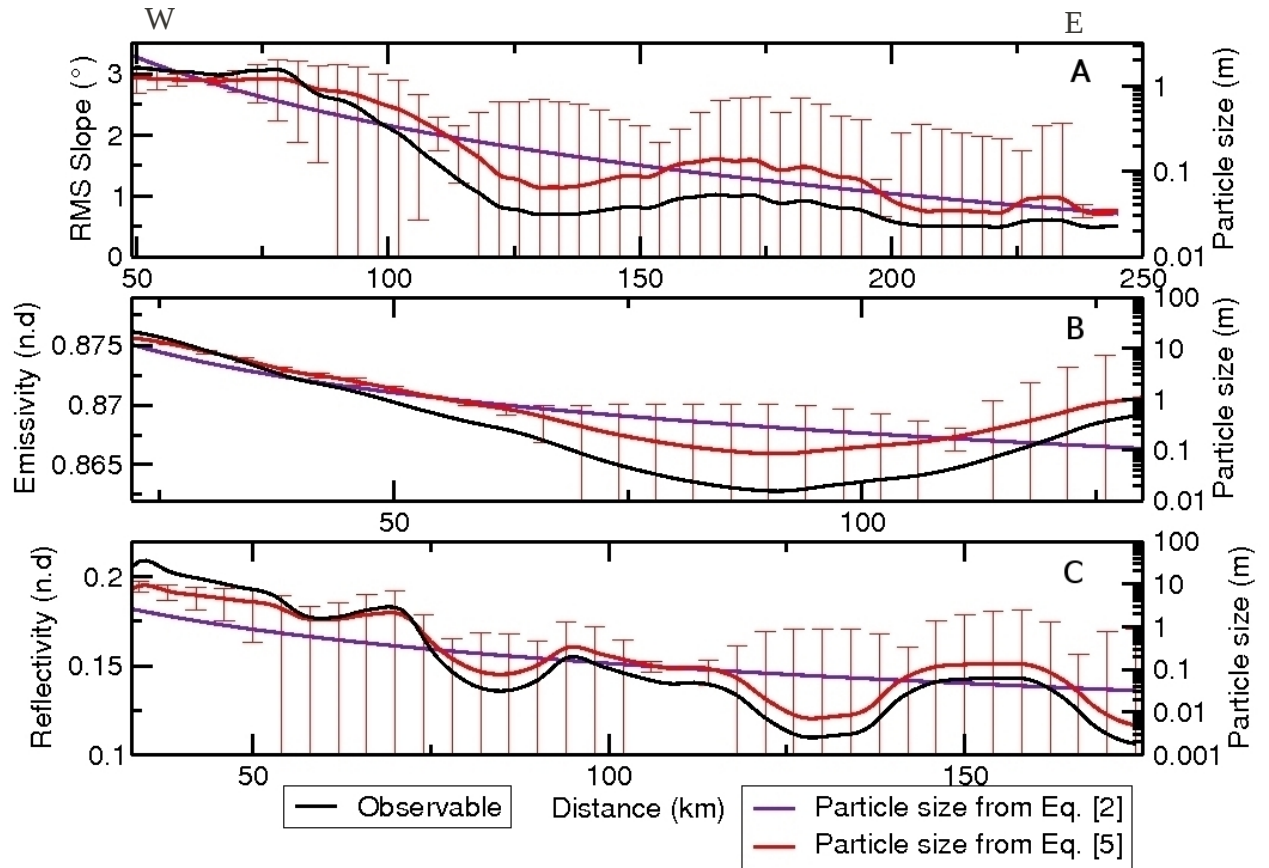


Figure 5. Profiles of the RMS slope, emissivity, reflectivity from the Stuart (A), Montessori (B), and Von Schuurman (C) craters respectively. Key is similar to Figure 4.

carried through to our particle size estimate, which had a 0.03 m decrease. This compares to the 0.02 m decrease in particle size estimate from Eq. [2].

Reflectivity and emissivity are also weakly related to the roughness of the surface and in turn, particle size. Therefore, we should be able to estimate particle size when we substitute reflectivity and emissivity values, instead of RMS slope, within Eq. [5]. This has been done for profiles from the Montessori and Von Schuurman craters and the results were plotted in Figures 5B-5C. Similar to the graphs of RMS slope, when emissivity followed a smooth exponential decay, our particle size estimates from Eq. [5] correlated well with those from Eq. [2]. For example, Figure 5B shows an emissivity profile from the Montessori crater. Between 22 - 61 km, the emissivity gradually decreased causing estimated particle sizes to follow a

similar trend decreasing by 13.4 m, compared to the 9.3 m decrease in particle size, calculated from Eq. [2] [Table 4]. However, when variations occurred within emissivity our particle size estimates also varied. Between 66 - 90 km, a decrease in emissivity of 0.005 occurred and corresponded to a decrease of 0.33 m in our particle size estimates, compared to 0.36 from Eq. [2] [Table 4].

Table 4. Emissivity and particle sizes

Figure No.	Location (km)	Emissivity	Particle size from Eq. [5] (m)	Particle size from Eq. [2] (m)
5B	22 - 61	-0.003	-13.4	-9.3
5B	66 - 90	-0.005	-0.33	0.36

A similar relation can also be observed in the reflectivity profile from the Von Schuurman crater (Figure 5C). Between 92 - 118 km and 140 - 165 km, our particle size estimates showed a greater correlation to those from Eq. [2]. For example, at 140 km the reflectivity was 0.13, and corresponded to a particle size estimate of 0.04 from Eq. [5], compared to 0.06 Eq. [2] [Table 5].

Table 5. Reflectivity and particle sizes

Figure No.	Location (km)	Reflectivity	Particle size from Eq. [5] (m)	Particle size from Eq. [2] (m)
5C	140	0.13	0.04	0.06
5C	129	0.11	0.01	0.07

Large reflectivity variations occurred over short distances between 79 - 86 km and 120 - 140 km in Figure 5C, resulting in our particle sizes exhibiting less correlation to those from Eq. [2]. At 129 km, the reflectivity was 0.11 and corresponded to an estimated particle size of 0.01 m from Eq. [5].

Figure 6 shows a simple plot of particle sizes for a range of crater radii. The RMS slope was allowed to vary for each crater radius, but the values for a and m remained the same. When substituted into Eq. [5] craters with a larger radius resulted in larger particle sizes, whilst craters with a smaller radius resulted in smaller particle sizes [Figure 6].

From Figure 7, small changes in the value of a and m caused large variations (orders of magnitude) of our calculated particle sizes. Larger values of a produced smaller particle sizes compared to lower values of a , which produced larger particle sizes. Similarly, low values of the gradient of the line of regression, m , resulted in larger particle sizes compared to high values that corresponded to smaller particle sizes [Figure 8].

4. Discussion

Our particle size estimates from Eq. [5] were more closely correlated to those determined from Eq. [2] from Vervack & Melosh [4] when we related RMS slope to particle size, instead of to emissivity and reflectivity. This was most likely due to RMS slope being a measure of surface roughness, and in turn, particle size. Emissivity and reflectivity were weakly related to surface roughness and particle size, which resulted in less correlation between our estimates from Eq. [5] and those from Eq. [2].

Due to the reliance of our equation on the values of RMS slope, our particle size estimates were strongly influenced by roughness variations. When RMS slope exhibited a smooth exponential decay, our particle size estimates showed a satisfactory correlation to those of Vervack & Melosh [4]. However, as soon as variations occurred within RMS slope, our particle size estimates became unreliable. It also appears that our estimates were strongly influenced by large RMS slope variations, over short distances, compared to small RMS slope

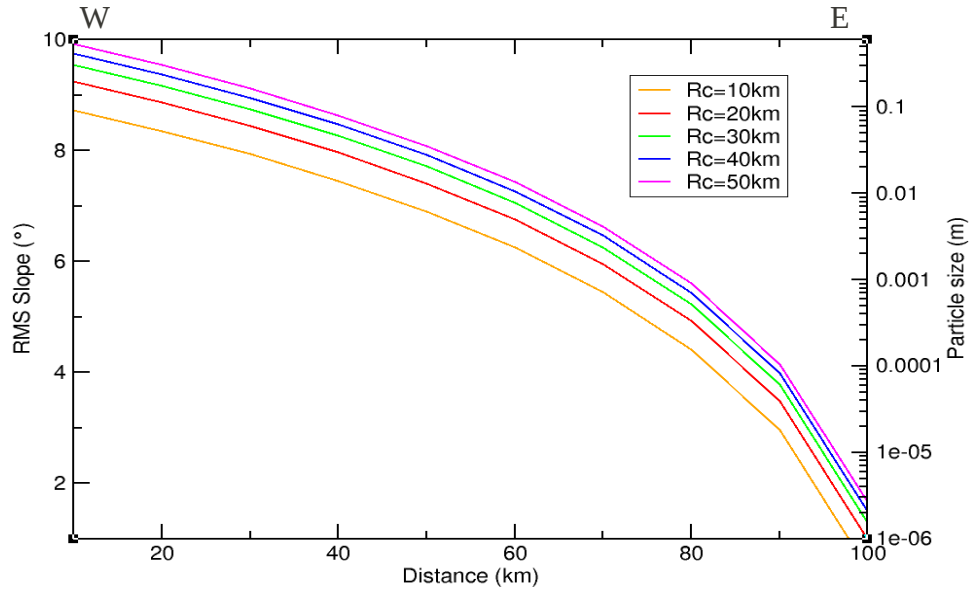


Figure 6. Plot of particle sizes for different crater radii. Craters with a smaller radius produced smaller particle sizes compared to those from larger radius craters. RMS slope was allowed to vary, however the a and m values within Eq. [5] remained constant.

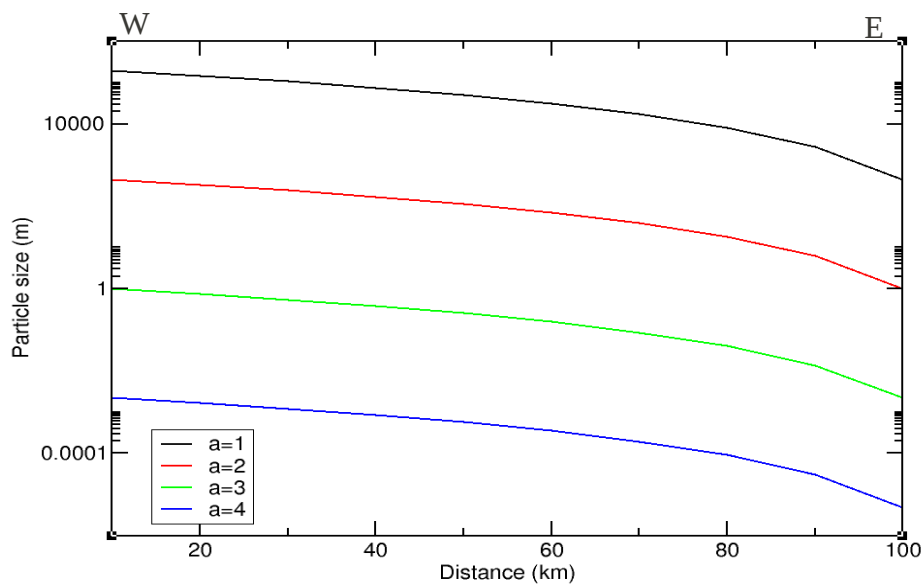


Figure 7. Graph showing the influence of varying the parameter, a , in Eq. [5], whilst R_c , d_c and m remained constant. Higher values caused smaller particle sizes compared to low values that produced larger particle sizes.

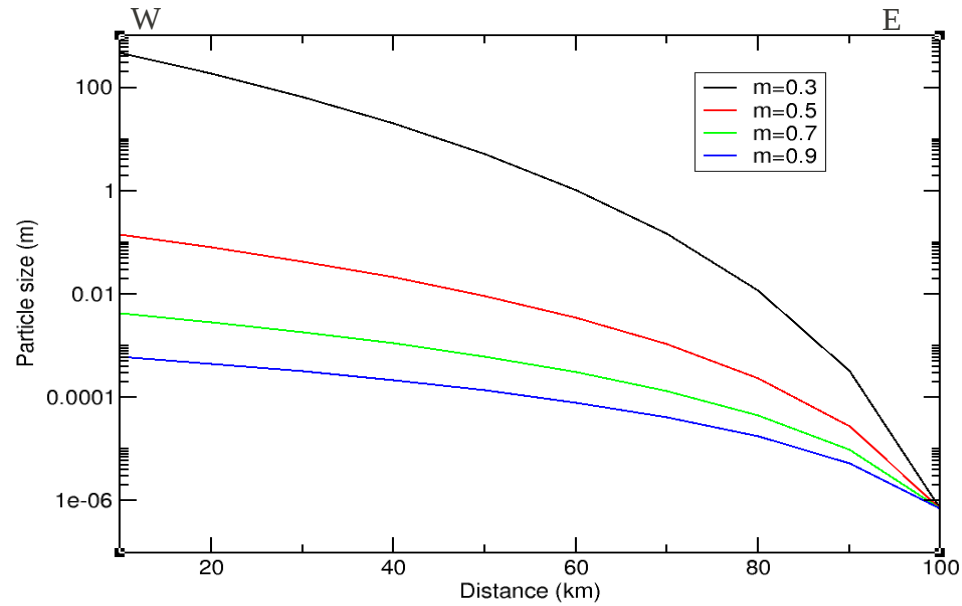


Figure 8. Graph showing the influence of varying the gradient of the line of regression, m , in Eq. [5], whilst R_c , d_c and a remained constant. Similar to Figure 7, lower values produced larger particle sizes compared to higher values that produced smaller particle sizes.

variations, over large distances.

Since the crater radius (R_c), y intercept (a), and the gradient of the line of regression (m) were included in our equation, these parameters could have influenced our calculated particle sizes. Changes to the crater radius resulted in smaller changes to our estimated particle sizes. However, changes to the values of the y-intercept and the gradient of the regression line were greater since these last two parameters were powers within our equation. The gradient and y intercept of the line of regression were based on plots of $\text{Log}(R)$ and $\text{Log}(\text{RMSS})$ for each crater profile. Thus, variations within the RMS slope could have transferred to our $\text{Log}(\text{RMSS})$ values and in turn, influenced our values for the y intercept and gradient of the regression line. These variations were most likely the cause of our unsatisfactory correlations between our particle sizes from Eq. [5] and those from Eq. [2] by Vervack & Melosh [4].

5. Conclusions

We have developed a new method of relating RMS slope or surface roughness to particle size at selected parabolic craters on Venus. Due to the reliance of our proposed equation to RMS slope, large variations within this parameter also produced large variations in our estimated particle sizes. However, if one wishes to use RMS slope to calculate particle sizes, variations will always occur within these values, due to the large roughness variations between a crater rim and ejecta blanket. Our equation could be used in future studies to estimate ejecta blanket particle sizes in order to constrain the sediment transport mechanisms acting at these craters. Understanding the surface-atmosphere interactions at these craters could, in turn, constrain the weathering process on Venus.

6. Acknowledgments

The first author would like to thank the Space Policy Unit, Engineers Australia, and the Australian Space Research Institute for sponsorship to attend the 11th Australian Space Science Conference in Canberra. Craig O'Neill acknowledges Australian Research Council support. Graphs were created using Grace: <http://plasma-gate.weizmann.ac.il/Grace/>. This is contribution 46 from the ARC Centre of Excellence for Core to Crust Fluid Systems (<http://www.ccfs.mq.edu.au>) and 811 in the GEMOC Key Centre (<http://www.gemoc.mq.edu.au>).

7. References

- [1] W. B. McKinnon, K. J. Zahnle, B. A. Ivanov, and H. J. Melosh, "Cratering on Venus: Models and observations," in *Venus II: Geology, Geophysics, Atmosphere and Solar*

- Wind Environment*, Tucson: The University of Arizona Press, 1997, p. 969-1014.
- [2] D. B. Campbell et al., "Magellan Observations of Extended Impact Crater Related Features on the Surface of Venus," *Journal of Geophysical Research*, vol. 97, no. 10, 1992, p. 277.
- [3] R. E. Avridson, V. R. Baker, C. Elachi, R. S. Saunders, and J. A. Wood, "Magellan: Overview of Venus surface modification," *Abstracts of the Lunar and Planetary Science Conference*, vol. 22, 1991, p. 33.
- [4] R. J. Vervack Jr and H. J. Melosh, "Wind interaction with falling ejecta: Origin of the parabolic features on Venus," *Geophysical Research Letters*, vol. 19, no. 6, 1992, p. 525–528.
- [5] R. J. Phillips et al., "Impact craters on Venus: initial analysis from Magellan," *Science*, vol. 252, no. 5003, 1991, p. 288-297.
- [6] P. H. Schultz, "Atmospheric Effects on Ejecta Emplacement and Crater Formation on Venus From Magellan," *Journal of Geophysical Research*, vol. 97, no. 10, 1992, p. 248.
- [7] Map-A-Planet. USGS Astrogeology Science Center, <http://astrogeology.usgs.gov>, 2011.
- [8] C. J. Schaller and J. Melosh, "Venusian parabolic halos: numerical model results," *Abstracts of the 25th Lunar and Planetary Science Conference*, 1994, p. 1201-1202.
- [9] T. R. McGetchin, M. Settle, and J. W. Head, "Radial thickness variation in impact crater ejecta: implications for lunar basin deposits," *Earth and Planetary Science Letters*, vol. 20, no. 2, 1973, p. 226-236.
- [10] R. R. Herrick, V. L. Sharpton, M. C. Malin, S. N. Lyons, and K. Feely, "Morphology and morphometry of impact craters," in *Venus II: Geology, Geophysics, Atmosphere and Solar Wind Environment*, Tucson: The University of Arizona Press, 1997, p. 1015-1046.
- [11] T. Hare, "Radar Properties", USGS Astrogeology, 2004, Available from: ftp://pdsimage2.wr.usgs.gov/pub/pigpen/venus/Radar_properties/.
- [12] P. Wessel and W. H. F. Smith, "Free software helps map and display data", *EOS Trans.*

AGU, vol. 72, no. 441, 1991.

[13] K. L. Tanaka et al., *The Venus Geological Mappers' Handbook*, 2nd ed. U.S.

Department of the Interior, U.S. Geological Survey, 2003, p. 68.